RPSEA

Final Report

09122-04.FINAL

Marcellus Shale Gas Project
09122-04

May 10, 2013

Jordan Ciezobka
Senior Engineer, Shale Gas Research

Gas Technology Institute
1700 South Mount Prospect Road
Des Plaines IL, 60018

LEGAL NOTICE

This report was prepared by Gas Technology Institute as an account of work sponsored by the Research Partnership to Secure Energy for America, RPSEA. Neither RPSEA members of RPSEA, the National Energy Technology Laboratory, the U.S. Department of Energy, nor any person acting on behalf of any of the entities:

a. MAKES ANY WARRANTY OR REPRESENTATION, EXPRESS OR IMPLIED WITH RESPECT TO ACCURACY, COMPLETENESS, OR USEFULNESS OF THE INFORMATION CONTAINED IN THIS DOCUMENT, OR THAT THE USE OF ANY INFORMATION, APPARATUS, METHOD, OR PROCESS DISCLOSED IN THIS DOCUMENT MAY NOT INFRINGE PRIVATELY OWNED RIGHTS, OR

b. ASSUMES ANY LIABILITY WITH RESPECT TO THE USE OF, OR FOR ANY AND ALL DAMAGES RESULTING FROM THE USE OF, ANY INFORMATION, APPARATUS, METHOD, OR PROCESS DISCLOSED IN THIS DOCUMENT.

THIS IS A FINAL REPORT. THE DATA, CALCULATIONS, INFORMATION, CONCLUSIONS, AND/OR RECOMMENDATIONS REPORTED HEREIN ARE THE PROPERTY OF THE U.S. DEPARTMENT OF ENERGY.

REFERENCE TO TRADE NAMES OR SPECIFIC COMMERCIAL PRODUCTS, COMMODITIES, OR SERVICES IN THIS REPORT DOES NOT REPRESENT OR CONSTIITUTE AND ENDORSEMENT, RECOMMENDATION, OR FAVORING BY RPSEA OR ITS CONTRACTORS OF THE SPECIFIC COMMERCIAL PRODUCT, COMMODITY, OR SERVICE.

Abstract

Extending throughout much of the Appalachian Basin, the Marcellus shale is stratigraphically the lowest member of the Devonian age Hamilton Group, and is divided into several sub-units. The formation is mainly composed of black shale and contains lighter shales and interbedded limestone layers as a result of sea level variations during its deposition almost 400 million years ago. It is overlain by the Mahantango shales and Tully limestone and underlain by the Onondaga limestone, Huntersville chert, and Oriskany sandstone. Having a potentially prospective area of over 44,000 square miles, the Marcellus shale is one of the largest shale plays in North America and covers portions of New York, northern and western Pennsylvania, eastern Ohio, western Maryland, and most of West Virginia. In its 2011 Annual Energy Outlook report, the EIA reported technically recoverable reserves of approximately 400 TCF of natural gas in the Marcellus shale. Recovering 400 TCF of natural gas from a shale resource requires tremendous amounts of water that is used primarily for hydraulic fracturing. Care must be taken to ensure minimal environmental impact; e.g., use of fresh water, when developing this resource while continually increasing operational efficiency.

Gas Technology Institute (GTI), with funding from the Research Partnership to Secure Energy for America (RPSEA), initiated an industry cooperative research project, that, aside from other tasks, aims to examine the contribution of gas production from natural fractures in addition to predicting the spatial distribution and population characteristics of these natural fracture systems. These natural fracture systems in conjunction with hydraulic fracturing are the key drivers for gas production. Hence, in addition to understating the natural fracture attributes, it is necessary to optimize hydraulic fracturing treatments so that a synergistic effect is achieved whereby the natural fractures are exploited for enhanced gas production. As such, much of the research was focused on hydraulic fracture design and optimization with supporting field data acquisition.

A team of experts including five universities, one national laboratory, and one industry consortium, worked together with service companies and a major producer in the heart of the Marcellus Shale. The goal was to evaluate reservoir characteristics and determine optimal completion and stimulation techniques and develop technologies that increased gas production while minimizing environmental impact. Dedicated research was focused in the areas of: geology, reservoir engineering, high-resolution rock imaging, dynamic flow behavior of shale gas, hydraulic fracture modeling and diagnostics, and microseismic imaging. The cooperative efforts resulted in better understanding of the Marcellus Shale reservoir and enhanced understanding of fracturing dynamics thus leading to more efficient fracturing techniques that reduce environmental impact while producing more gas.

Key results from these studies were:

- Combined analysis of hydraulic fracturing and microseismic parameters with production logging proved that such analyses can lead to identification of naturally fractured zones during hydraulic fracturing,

- Hydraulic fracturing operations can be altered to result in higher fracturing efficiency; i.e., minimized use of fracturing fluid for production of unit volume of produced gas,
- Spatial distribution of natural fractures can be projected through geomechanical modeling,
- Advanced reservoir simulation using artificial intelligence techniques can identify the most influential parameters in completion practices and point to most promising locations for infill drilling,
- A relatively simple bimodal production decline analysis method developed in this project can provide a valuable tool for single well production analyses
- Natural gas liquids could impede production and reduce the relative permeability to gas given the right drawdown conditions,
- It is quite clear from the microseismic event location asymmetry that S/N has a major impact on the inferred fracture geometry and it is unlikely that the fractures are as asymmetric as depicted in the microseismic survey,
- Optimal microseismic array design for accurate interpretation of focal mechanisms should consist of surface and borehole geophones

Disclaimer

This report was prepared as an account of work sponsored by **Research Partnership to Secure Energy for America (RPSEA)**. Neither RPSEA, Gas Technology Institute (GTI), nor any agency thereof, nor any of their employees, makes any warranty, express or implied, or assumes any legal liability or responsibility for the accuracy, completeness, or usefulness of any information, apparatus, product, or process disclosed, or represents that is use would not infringe privately owned rights. Reference herein to any specific commercial product, process, or service by trade name, trademark, manufacturer, or otherwise does not necessarily constitute or imply its endorsement, recommendation, or favoring by RPSEA, GTI, or any agency thereof. The views and opinions of authors expressed herein do not necessarily state or reflect those of RPSEA or GTI.

Acknowledgements

We acknowledge the support of RPSEA for funding the Marcellus Shale Gas project. Many thanks to Range Resources for providing wells of opportunity, data, cost sharing and technical guidance. Special thanks to Schlumberger for providing technical expertise and cost sharing.

Funding for this project was provided by RPSEA through the Ultra-Deepwater and Unconventional Natural Gas and Other Petroleum Resources Research and Development Program authorized by the Energy Policy Act (EPAct) of 2005. RPSEA is under contract with the U.S. Department of Energy's National Energy Technology Laboratory to administer three elements of the EPAct Section 999 Program: (1) Ultra-deepwater architecture and technology; (2) Unconventional natural gas and other petroleum resources exploration and production; and (3) Technology challenges of small producers.

RPSEA is a non-profit corporation established to help meet the nation's growing need for hydrocarbon resources produced from reservoirs in America; formed by a consortium of premier U.S. energy research universities, industry and independent research organizations. The mission of RPSEA is to provide a stewardship role in ensuring the focused research, development and deployment of safe, environmentally sensitive technology that can effectively deliver hydrocarbons from domestic resources to the citizens of the United States. RPSEA will sharply focus its experience, expertise, and capabilities on meeting the program's objectives: to maximize the value of domestic natural gas and oil resources through new technologies to increase production, and to do so in less expensive, safer and more efficient and environmentally benign ways.

Report Structure

In the present report, we will present a brief summary of results and proceed to reporting details of work performed under each task. The report is voluminous and includes many details that all of them are not necessarily of interest to all readers. In addition, electronic handling of a document exceeding several hundred pages in length with graphs and diagrams usually causes problem and frustration. To avoid these issues, we are presenting the report in a binder containing seven separate sections each reporting on one major task. Care has been taken to prepare each section as a standalone document that can be detached, copied or downloaded independent of the rest of the report. The following structure will be followed in this report.

- Section 1 Project Summary
- Section 2 Research Site
- Section 3 Summary of Results
- Section 4 Appendix of all Individual Reports

Table of Contents **Page**

Abstract 3
Disclaimer 5
Acknowledgements 5
Report Structure 6
1. Project Summary 8
2. Research Site 11
3. Summary of Results 13
Hydraulic Fracturing 13
Pumping Diagnostics 17
Microseismic Monitoring 19
Microseismic Event Location Error Considerations 21
Dr. James Rector, Professor – University of California, Berkeley 21
Hydraulic Fracturing Optimization in the Presence of Concentrated Natural Fractures 22
Optimized passive seismic survey design with simultaneous borehole and surface measurements 23
Debotyam Maity and Dr. Fred Aminzadeh - Induced Seismicity Consortium (ISC, USC) 23
Geology 25
Dr. Julia Gale – Bureau of Economic Geology 25
Nano-meter Scale Pore Imaging 27
Dr. Dmitriy Silin and Dr. Timothy Kneafsey – Lawrence Berkeley National Laboratory 27
Flow Characteristics in the Presence of Gas Liquids 28
Dr. Roland Horne – Stanford University 28
Fracture Characteristics 29
Dr. Terry Engelder – Pennsylvanian State University 29
Reservoir Engineering 30
Dr. Shahab Mohaghegh – West Virginia University 30
Technology Transfer 31
4. Appendix of Individual Reports 33
Appendix A – Topical Report: Stimulation & Completion 33
Appendix B – Comparison of Surface and Borehole Microseismic 49
Appendix C - Controlled Hydraulic Fracturing of Naturally Fractured Shales (SPE-164524) 88
Appendix D - Optimized passive seismic survey design using borehole and surface measurements 109
Appendix E – Marcellus Shale Geology 133
Appendix F – Nanometer Pore Scale Imaging 182
Appendix G – Flow Characteristics in the Presence of Gas Liquids 200
Appendix H – Fracture Characterization at the Marcellus Level 226
Appendix I – Reservoir Engineering 259

Marcellus Shale Gas Project

A Joint Industry Project Sponsored by

Research Partnership to Secure Energy for America (RPSEA)

Final Report, May 10, 2013

Gas Technology Institute (GTI)

1. Project Summary

Gas Technology Institute (GTI) with funding from Research Partnership to Secure Energy for America (RPSEA), initiated an industry cooperative research and development project in the Marcellus Shale where industry experts from four universities and one national laboratory collaborated on solving environmental and economic challenges related to development and gas production from the Marcellus Shale. The project combines the application of advanced exploration and development technologies with real-world data from elaborate field data acquisition and experiments. Marcellus Shale formation occurs mainly in New York, Pennsylvania, West Virginia, Virginia, Maryland, and Ohio, but to date gas production has been predominantly from Pennsylvania, West Virginia, and Ohio. According to a 2011 EIA report, this play is considered to be an up-and-coming natural gas resource that can provide over 6 years of natural gas to the current US gas supply. As such, development of this resource is crucial to contributing in sustaining natural gas domestic independence. However, depressed gas prices demand more now than ever that wells are developed in ways that are environmentally safe and economically viable for production from shale resources to reach its full capacity.

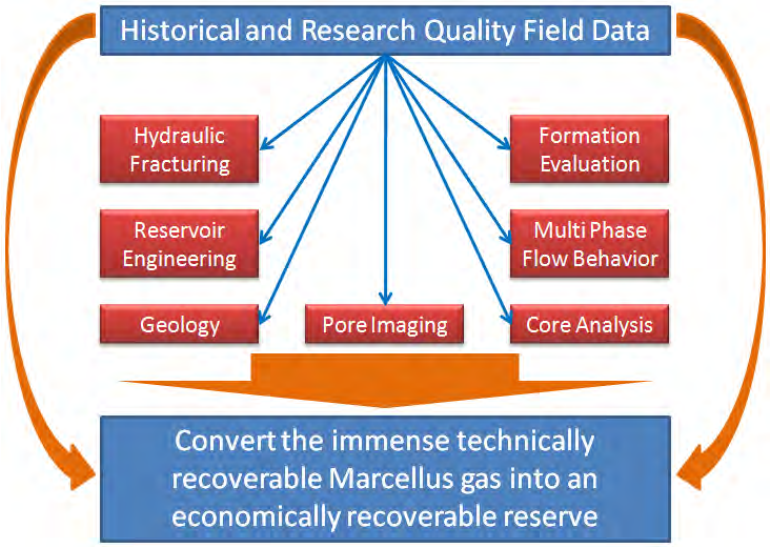

Figure 1: Elements of the Marcellus Project.

Industry participation included donated background data and provision of wells of opportunity for acquisition of research quality data. Additionally, generous cost sharing by Range Resources and Schlumberger enabled the execution of a multi well borehole microseismic survey that included monitoring of 62 hydraulic fracturing stages and 93 fracture stages with surface microseismic. Culmination of data acquisition was core evaluation, logging, and microseismic fracture diagnostic surveys on wells drilled by Range Resources. Logging efforts entailed a vertical seismic profile, advanced cement bond integrity evaluation, and production logging from individual fracture stages.

Historical and field acquired quality research data were used to perform analysis in areas of geology, formation evaluation, hydraulic fracturing, reservoir engineering, pore imaging, core analysis, and reservoir flow behavior, to enable a comprehensive understanding of parameters that influence gas production so that the immense technically recoverable Marcellus gas can be converted into economically recoverable reserves. Figure 1 shows the elements of the Marcellus research project.

Members of the project include industry partners, research team, and the principal investigator. Industry partners are comprised of Range Resources and Schlumberger. Organizations that are performing research in their respective field of expertise include GTI, West Virginia University, Bureau of Economic Geology, Stanford University, Lawrence Berkeley National Laboratory, and

Pennsylvania State University and University of California at Berkeley. Figure 2 shows the project members and their contribution to the project.

Project Manager & Principal Investigator	**Research Team** ***Research Focus***
Gas Technology Institute (GTI) *R&D, Analysis, Integration, and Coordination*	West Virginia University *Reservoir Engineering*
	Bureau of Economic Geology *Geology*
	USC-ISC *Microseismic Array Design*
Industry Partner ***Contribution***	Stanford University *Flow Property Changes Due to Condensate Dropout*
Range Resources LLC *Wells of Opportunity, Data, and Guidance*	Lawrence Berkeley National Laboratory *Nano-scale Pore Imaging*
Schlumberger *Borehole Microseismic*	Pennsylvania State University *Fracture Characterization*
	UC-Berkeley *Comparison of Surface and Borehole Microseismic Surveys*

Figure 2: Project Participants.

2. Research Site

A multiple well pad owned and operated by Range Resources Appalachia LLC located in Washington county Pennsylvania, is the site of field data acquisition (Figure 3). From the pad extend seven nearly-parallel horizontal wells traversing the Marcellus Shale. The trajectories of the well laterals are in the general northwest direction and are normal to the maximum in situ horizontal stress (σ_{Hmax}) orientation as shown in Figure 4. Spacing of the horizontal trajectories of the wellbores is approximately 500 ft with an average horizontal wellbore length of 3640 ft. The horizontal well sections are drilled in the upper section of the Marcellus shale, having a true vertical depth (TVD) of approximately 6500 ft. Considering the surface location of the wells as being centered in a rural and geographically complex setting, pad drilling was utilized at this site. Cores collected from five science wells located nearby the test site provided complete geochemical, petrological, petrophysical, and geomechanical analysis.

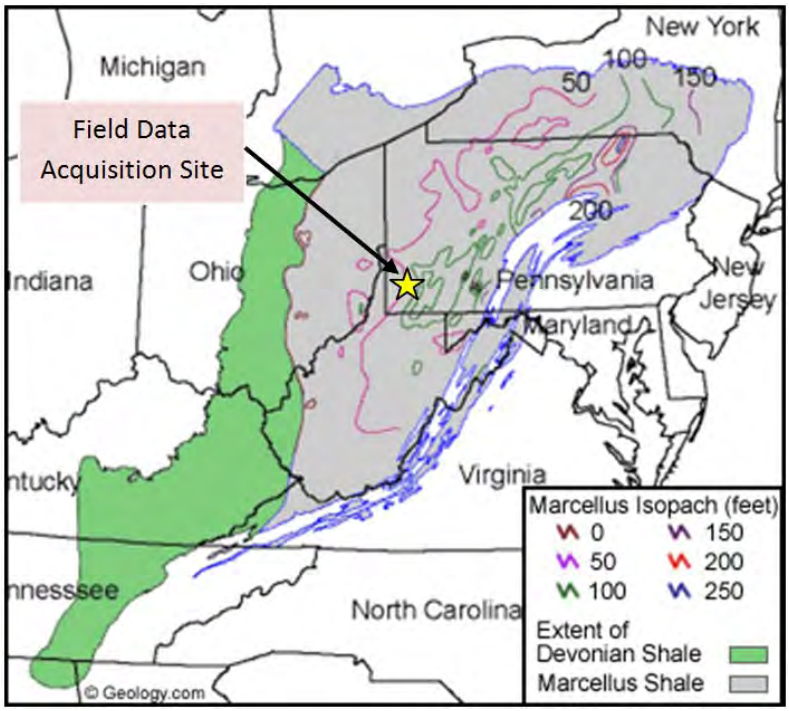

Figure 3: Location of field data acquisition site.

The gross thickness of the Marcellus shale at a nearby well located less than 3 miles from the test site is roughly 150 ft with an average porosity and permeability of 8 percent and 600 nanodarcy, respectively. Figure 5 is a shale log montage showing total gas and water saturation in the Marcellus and Marcellus-A intervals along with free and adsorbed gas content, total organic content (TOC) and the calculated permeability. Log calculated lithology, petrophysical

and geomechanical properties were correlated with core measurements. As evident from the shale log evaluation, the lower portion of the Marcellus, the Marcellus-A, is a better quality reservoir in terms of TOC, total gas saturation, porosity, permeability, and other attributes related to gas shale development. Although the lower section of the Marcellus is considered to be a better quality reservoir, the horizontal lateral is drilled in the upper section as past trails have shown that it is easier to fracture stimulate. While the well laterals are placed in the upper portion of the Marcellus, the lower portion of the Marcellus formation was also considered for production with the assumption that hydraulic fracture stimulation treatments would result in the production from the upper Marcellus. It is shown in later sections that the hydraulic fractures did in fact propagate into the lower portion of the Marcellus indicating that production from the lower zone would contribute to the total production.

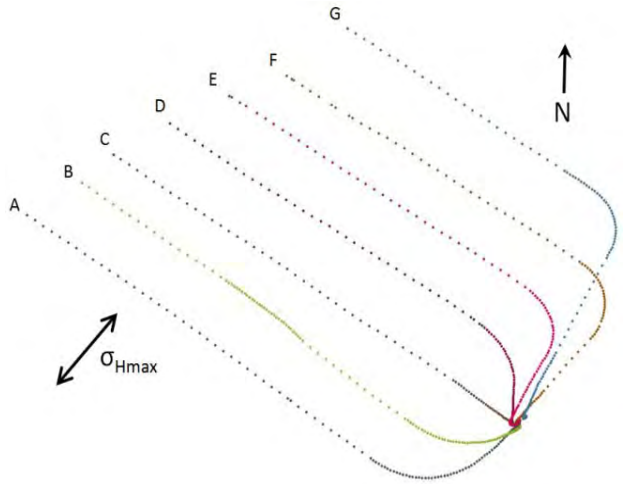

Figure 4: Experiment site well layout.

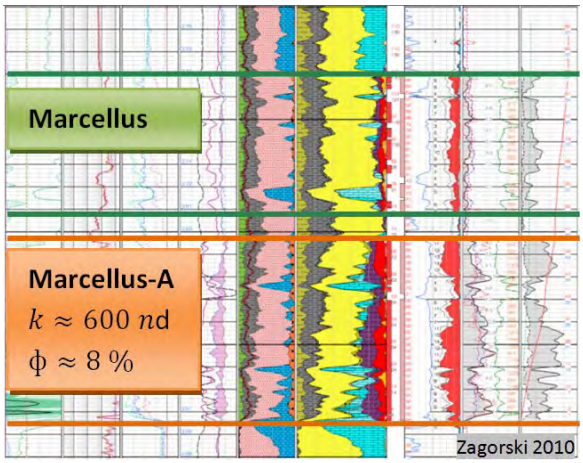

Figure 5: Shale Montage Depicting Local Marcellus Reservoir Properties (After Zagorski, 2010).

3. Summary of Results

Hydraulic Fracturing

In order to produce commercial quantities of gas from the seven wells, each well was stimulated with multiple hydraulic fracture stages. As the length of the horizontals varied from well to well so did the number of fracture stages, with one well having a minimum of 11 and another having a maximum of 17 stages. However the spacing of fracture stages and perforation clusters remained the same in each well. Hydraulic fracture treatments were comprised mainly of water, sand, and very low concentrations of fit-for-purpose additives.

The wells were completed with casing and the pump down plug-and-perf technique was utilized in between frac stages. At the end of each fracture stage, a bridge plug and a perforating gun assembly connected to wireline was pumped to the desired depth and the bridge plug was set, providing isolation for the next fracture stage from the previous one. The remaining assembly of perforating guns was pulled up the wellbore to a depth corresponding to the next fracture stage at which point the perforating guns were fired providing perforations that enabled communication between the formation and the wellbore. The wireline was then pulled out of the well and the fracture treatment started. This process was repeated until all fracture stages in each well were completed. Figure 6 shows the number of frac stages pumped in each well along with the completed lateral length and the average fluid volume pumped per frac stage. The average fluid volume pumped per stage for wells A, C, E, D, and F was about 7000 barrels

(bbl), while for well G was 8500 bbl and well B was 9900 bbl. The average lateral length for all the wells was about 3600 ft.

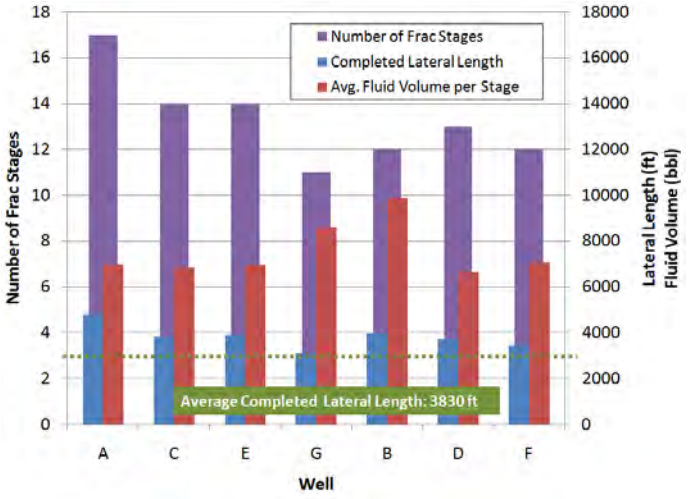

Figure 6: Comparison of Fracture Design Parameters.

It may seem as though the size of the fracture stages varies considerably from well to well. However, when fluid and proppant amounts pumped in each well are normalized on the basis of per foot of lateral, it becomes clear that five (wells A, C, E, D, and F) out of the seven wells were stimulated with the same proportions of proppant and fluid. The other two wells were stimulated with higher concentrations and amounts of proppant which also required more fluid to be pumped. Figure 7 shows the normalized fluid volume and proppant mass pumped in each well on a per-foot basis. In wells A, C, E, D, and F, an estimated 1000 lbs of proppant was pumped per each ft of completed lateral requiring about 25 bbls of fluid volume per foot of lateral. In an ongoing attempt to determine the optimal fracture treatment design, the proppant mass pumped in well G was increased by 75% (on a per foot basis) and by 100% in well B (also on a per foot basis). Because of the higher proppant mass, the amount of fluid pumped was also higher, however not proportionally to the percentage of proppant increase.

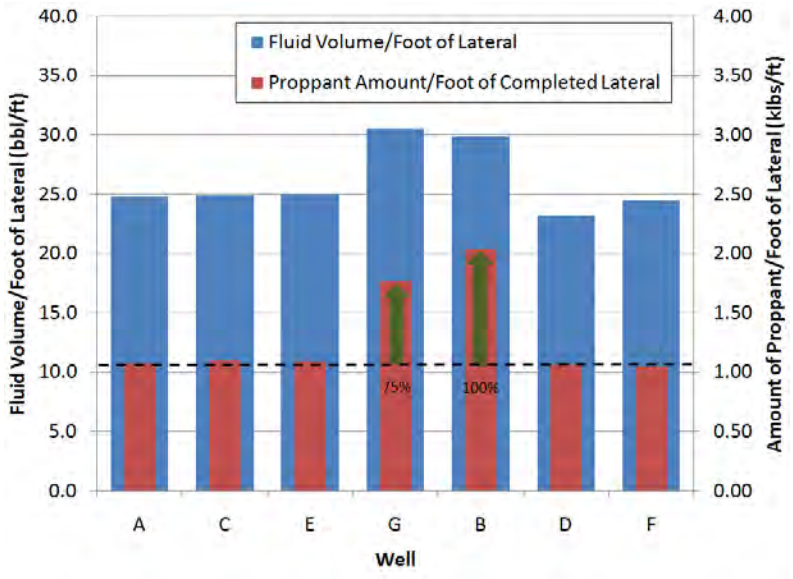

Figure 7: Fracture Design Parameters on a Per-Foot Basis.

In order to maximize hydraulic/natural fracture network complexity, the hydraulic facture stages were pumped in a modified zipper sequence. The zippering of hydraulic fractures tends to change the local stress field as a result of geomechanical and pore pressure changes induced by hydraulic fracturing. Because of the nature of the well trajectories and the number of wells, the zippering sequence was performed in five separate clusters. Each cluster was optimized for best microseismic viewing distance and fracture interference. Figure 8 shows the zipper sequence of the first cluster of frac stages that included four adjacent wells. The wells were fractured in an alternating fashion until thirteen fracture stages were executed, then the geophone position was changed to accommodate the next cluster of fracture stages.

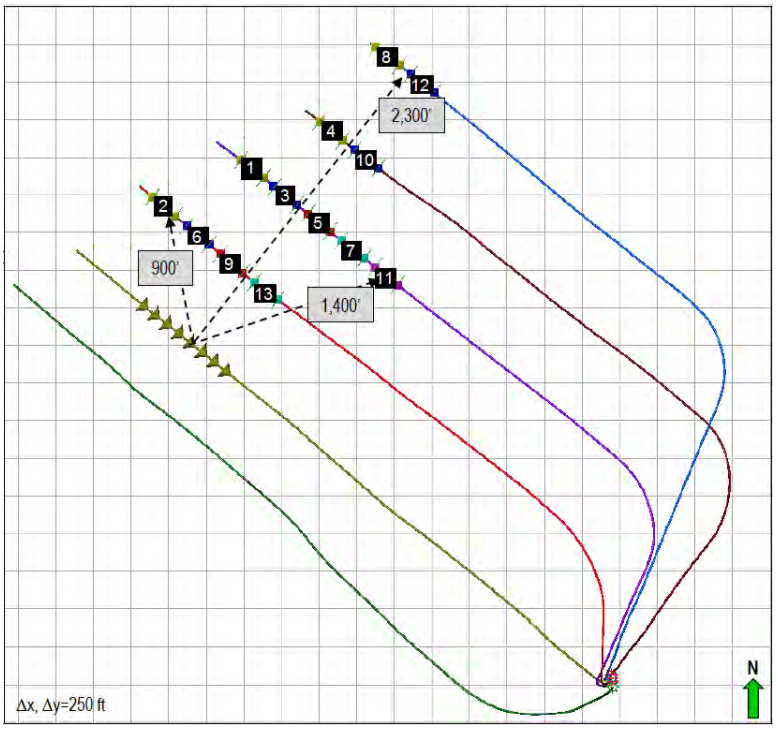

Figure 8: 1st Geophone Placement and Sequence of Frac Stages Pumped.

Figure 9 shows the position of the geophones used to monitor all the fracture stages. The first three geophone placements were used to monitor the wells located to the northeast of the observation well while the last two geophone placements were used to monitor the well located southeast of the observation well and a few remaining fracture stages on the northeast wells. After all fracture stages were pumped, coil tubing was used to drill out all the bride plugs that were used for isolation and the wells were flow tested and then put on production.

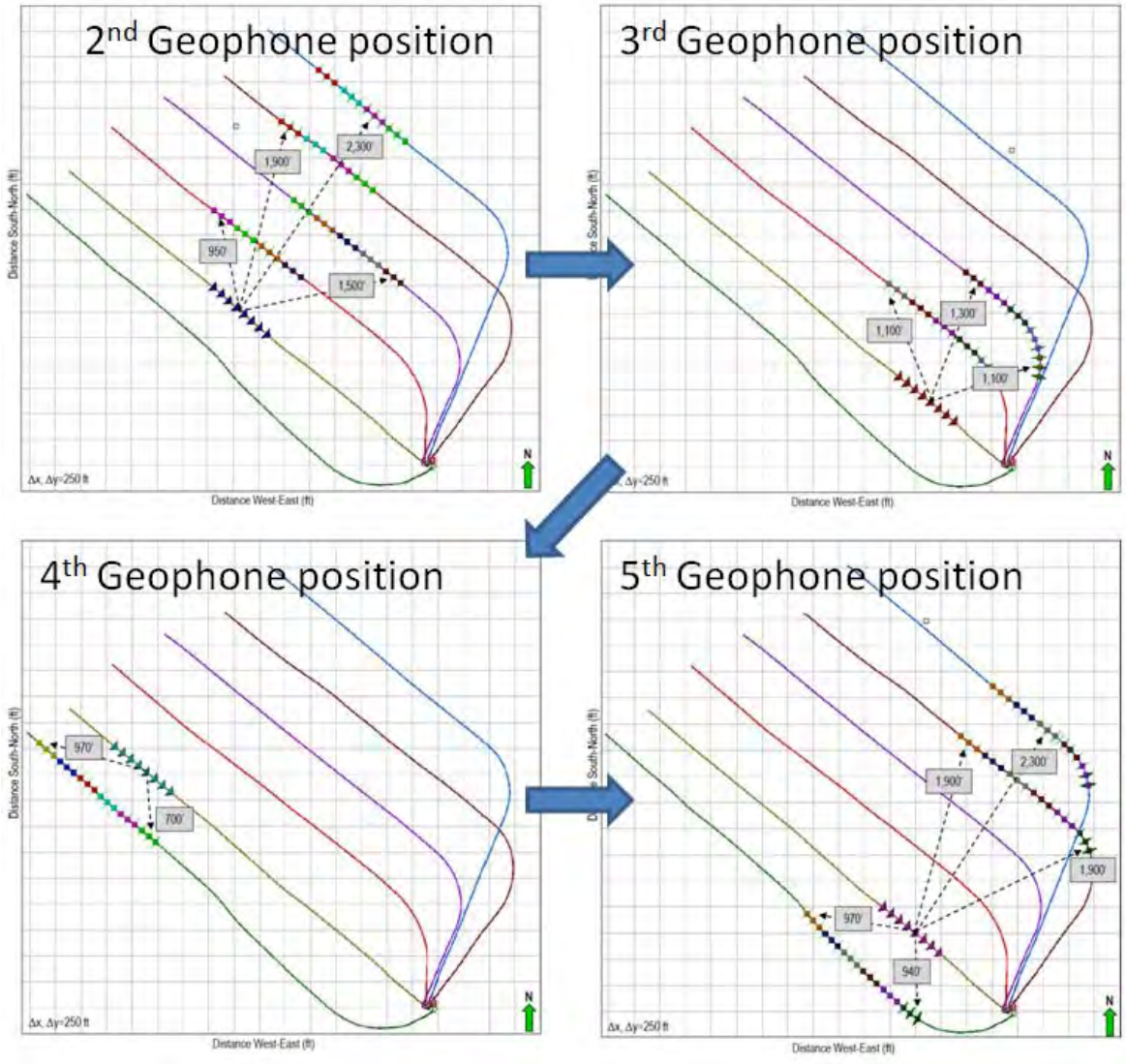

Figure 9: Remaining geophone positions used to monitor fracture stages

Pumping Diagnostics

After reviewing surface treatment data from all hydraulic fracture stages, a pressure anomaly was discovered in 3 fracture stages in adjacent wells. We believe this anomaly is related to a swarm of natural fractures that significantly contributes to production as evidenced from a production log that was ran in one of the horizontal wells. Additionally, microseismic data corresponding to the three isolated cases of anomalous pressure response reveal the estimated dimensions of the natural fracture swarm. Detailed analysis is provided in a topical report in Appendix A.

Upon further review of borehole microseismic data, a certain phenomenon related to pumping rate and microseismic event density is recurring in almost all of the fracture stages pumped. Analyses show that the majority of microseismic events are generated during the transient pumping periods. Figure 10 shows the impact of pumping rate variations on microseismic event density. The industry believes that a greater number of microseismic events contribute positively to production. Therefore, this suggests that the way in which a hydraulic treatment is executed has real implications on production. This phenomenon will be evaluated in future projects.

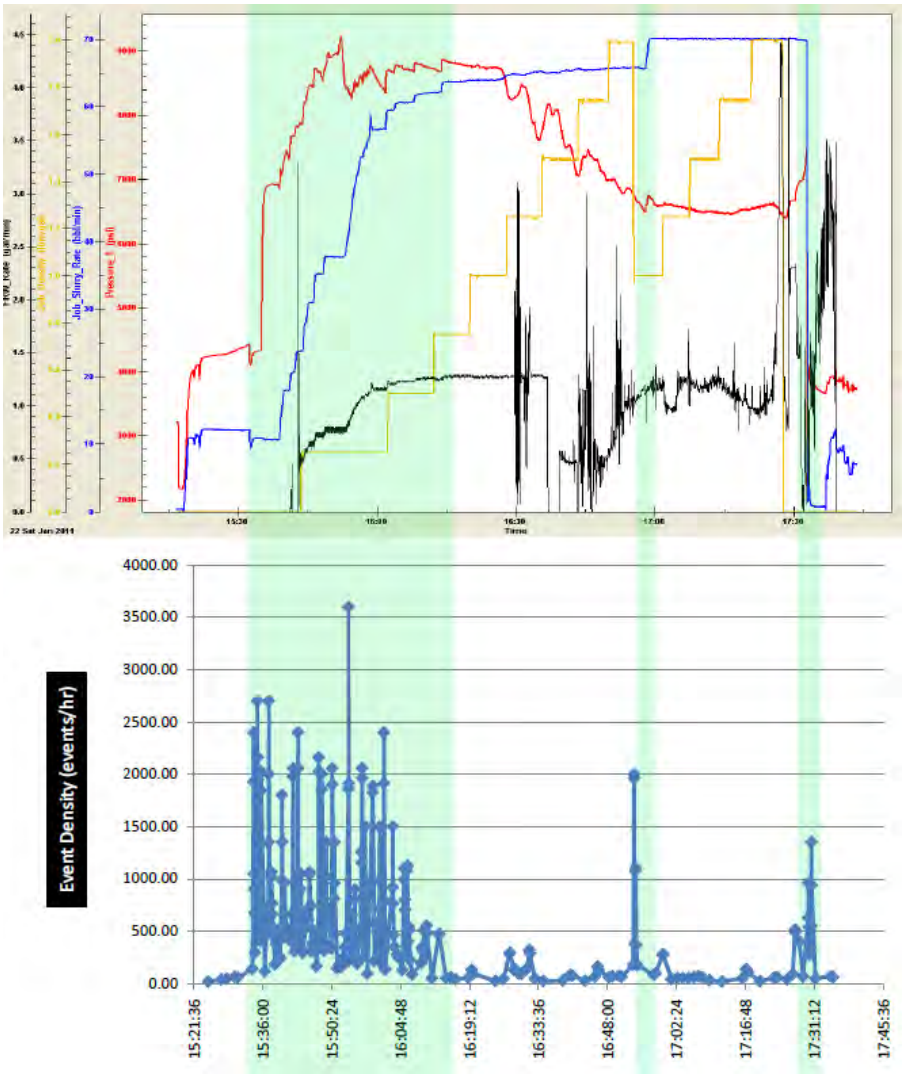

Figure 10: Surface pumping data, blue curve (top picture) synchronized with microseismic event density (bottom picture) for a single fracture stage.

Microseismic Monitoring

Microseismic surveys were utilized to determine the effectiveness of hydraulic fracture stimulation treatments and predict the created fracture geometry. A system of surface geophones in conjunction with borehole geophones was used to capture the microseismic events. In total, 93 fracture stages were recorded from seven wells with the surface system and 62 fracture stages were recorded from five wells with the borehole system. The fracturing process and the microseismic monitoring efforts took nearly a month to complete.

Downhole microseismic survey was captured with a horizontal geophone array consisting of 8 shuttles spaced 100 ft apart and placed in the horizontal section of one of the interior wells. Figure 11 shows the location of the first 3 geophone positions used in the zipper frac sequence along with the microseismic events captured. The array was moved to 5 different positions during the course of fracturing treatments in order to reduce spatial bias that would have decreased the signal to noise ratio during monitoring of 62 fracture stages. Perforation shots were used as check shots to calibrate seismic velocity in between fracture stages.

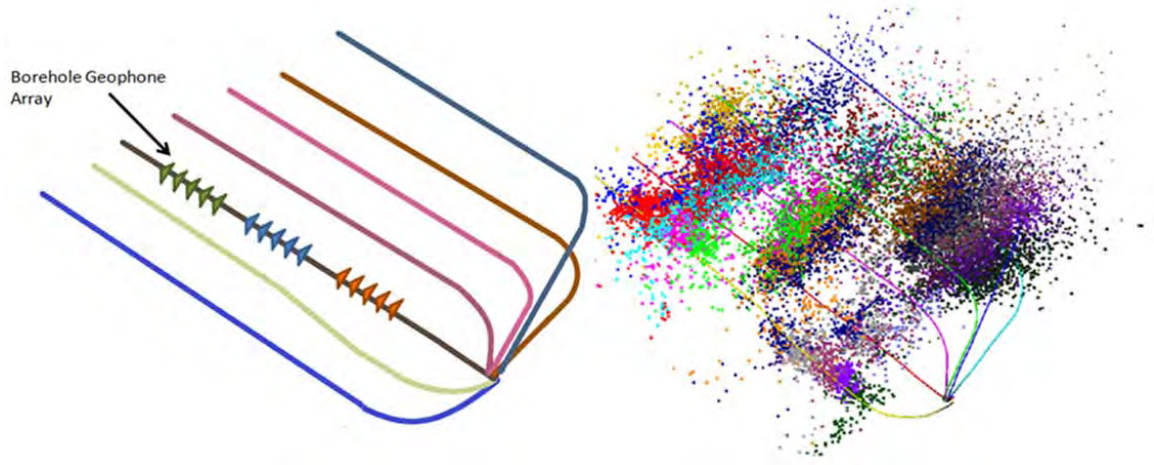

Figure 11: Left picture shows position of geophones used in downhole microseismic. Right picture shows microseismic events recorded with downhole microseismic.

The surface microseismic system was used to monitor all 93 fracture stages on all 7 wells. The surface array was comprised of geophones arranged in 10 lines radiating away from the wellbore pad. The array was constructed using 1082 geophone stations that recorded the microseismic data with a sampling rate of 2 milliseconds. Figure 12 shows the surface array that

was used to complete the microseismic survey along with the captured microseismic events. Results from the Vertical Seismic Profile (VSP) Survey were used to generate the seismic velocity model in order to determine the event locations accurately.

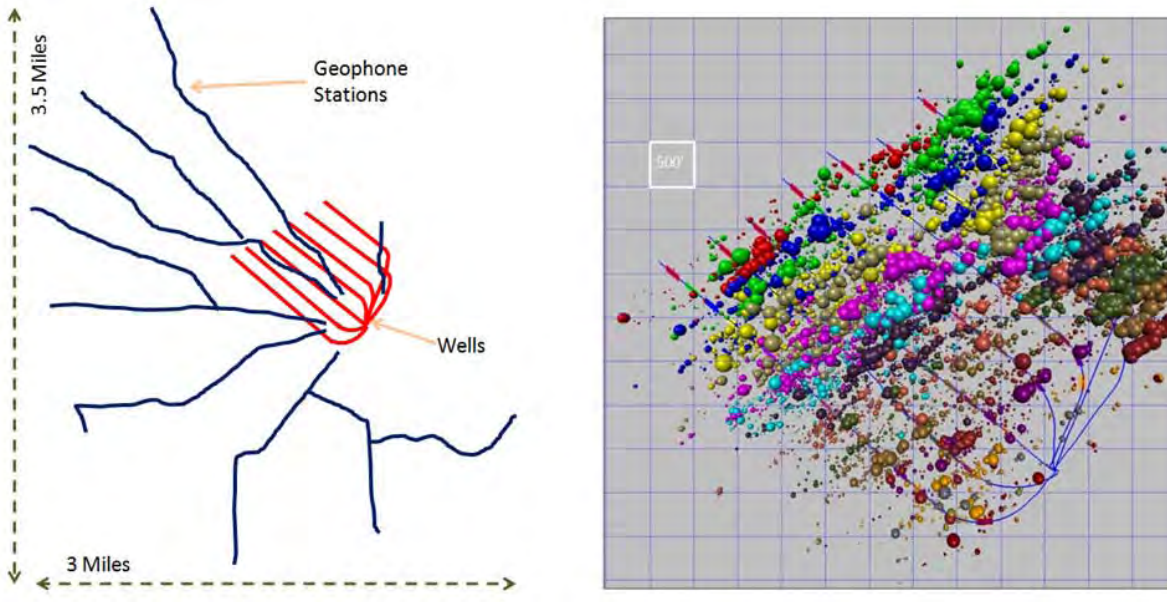

Figure 12: Left picture shows position of surface geophone array relative to well trajectories. Right picture shows microseismic events captured with surface microseismic.

Below is a summary of results and a more detailed analysis comparing the two microseismic surveys is in Appendix B:

- Microseismic data indicated that the majority of hydraulic fractures are vertically confined to the intended zone but some of them may extend a short distance into the overlying layer immediately above the lower Marcellus.
- In the majority of cases hydraulic fractures extend laterally over 500 feet and cross the neighboring horizontal wells.
- Hydraulic fracturing process is not uniform across the pad as evidenced by variations in the number of microseismic events.

- Anomalous pumping pressure variations were observed in several stages indicating the possibility of the presence of swarms of natural fractures around those stages. Production data from these zones confirms this observation

- Pressure observations during fracturing and radioactive tracer logs also indicated some communication between fractures and neighboring wells

- Calculation of stimulated reservoir volume indicated reasonable coverage but as the distinction between seismic signals from propped fractures and those from their vicinity (or the far field) is not possible, reevaluation of SRVs based on production history and reservoir simulation would clarify the ambiguities

- Results from downhole and surface microseismic imaging indicate agreement between the two surveys on fracture azimuth.

Microseismic Event Location Error Considerations

Dr. James Rector, Professor – University of California, Berkeley

Microseismic event location error plays a major role in the accuracy of assessed hydraulic fracture dimensions and SRV calculations. Dr. James Rector compared results of the two microseismic surveys by reviewing the microseismic reports from both contractors. The objectives of this analysis was to dig deeper into the contractor reports and evaluate the derived microseismic event locations in terms of the receiver geometry and the impact of these locations on inferred fracture dimensions and stimulated volumes. In addition, the review of the two reports considered the advantages and disadvantages of each system with regards to event location uncertainty and the factors that affect this uncertainty (e.g. velocity model, event type, focal mechanism, signal to noise ratio, raypath complexity/uncertainty, frequency content and receiver characteristics). For full report see Appendix B. Major conclusions are as follows.

- Given the uncertainty in fracture height, width and length, the extrapolation from event magnitude and density to SRV is very tenuous. Ignoring the uncertainty in event location and thus the fracture dimensions, the SRV values are therefore likely to be overestimated.
- The inability to deploy geophones directly above some of the stimulation wells and the bias of geophone locations toward the northwest of the stimulation wells is similar in concept to a seismic survey with irregular and biased sampling. It is well known that such survey geometries can result in migration smearing and bias of focus location. To properly characterize these effects would require forward modeling with a subset of the inferred source locations, magnitudes, frequency content and mechanism along with the surface geophone locations.
- The arrival time difference between compressional and shear (or shear converted) waves has long been used as a useful tool for event location. Given that there are

apparent long offset shear converted wave data, I am not sure why this approach is not incorporated to obtain a more accurate distance measure unless the absence of near offset shear data or uncertainties in the shear velocity profile make this approach problematic.

- In order to characterize the depth resolution of the technique (without calibration), the focusing results (Slides 5 and 6) should be presented as amplitude. Also, various criteria can be used to estimate the depth uncertainty. From the data provided it appears that a reasonable estimate for depth uncertainty for these very high S/N events is +/- 150 ft. Without calibration information, the event uncertainty may be higher for lower S/N events. If the events are located in the vicinity of large reflectors that are not incorporated into the depth migration there could also be some bias in the event location. Given the velocity model for this area, the events locations may be biased toward deeper positions.
- The types of mechanisms that would likely be recorded by vertical geophones at the surface would be vertical dip slip events. In order to obtain a good focal mechanism solution for all possible types of events, it is necessary to have a recording geometry where both P waves and S-waves are recorded across a wide range of solid angles. With only a surface array geometry or a Downhole geometry, only limited types of focal mechanisms will be discernible and therefore there may be inconsistencies between the events recorded by each.
- It is quite clear from the event location asymmetry that S/N has a major impact on the inferred fracture geometry and it is unlikely that the fractures are as asymmetric as depicted in the downhole event data.

Hydraulic Fracturing Optimization in the Presence of Concentrated Natural Fractures

Geologic studies of natural fractures in outcrops of Marcellus shale and other formations show that there are certain distances at which there is a high occurrence of natural fractures, called the characteristic spacing. High resolution imaging also shows that even though the Marcellus shale exhibits low porosity and permeability, the presence of micro-fractures enhances gas storage and potentially gas flow.

Using microseismic data, more specifically microseismic event count and the fracture length to width aspect ratio, it is possible to identify a swarm of natural fractures. Figure 13 shows a qualitative method of how to determine the extent of natural fracturing in the reservoir. On the x-axis is the microseismic event count and on the y-axis is the inverse of the length to width (L/W) aspect ratio or the width to length (W/L) aspect ratio. With increasing microseismic event count and increasing fracture W/L aspect ratio the natural fracture concentration increases. This results from fluid propagating from hydraulic fractures into natural fractures and changing direction as the hydraulic fracture intersects a natural fracture. Furthermore, increased interaction of hydraulic fractures with natural fractures causes the W/L fracture aspect ratio to increase as more fluid is pumped. The W/L aspect ratio increases as a result of frac fluid propagating through the natural fractures causing more “pops”. Having such an extensive microseismic dataset is very rare and there needs to be a way to identify the natural fracture

swarms without such a dataset. We have shown that there is very good correlation of natural fracturing with the mud log gas shows. In fact, in a very tight reservoir such as the Marcellus, the gas shows should be driven by natural fractures. Full report summarizing this study is in Appendix C.

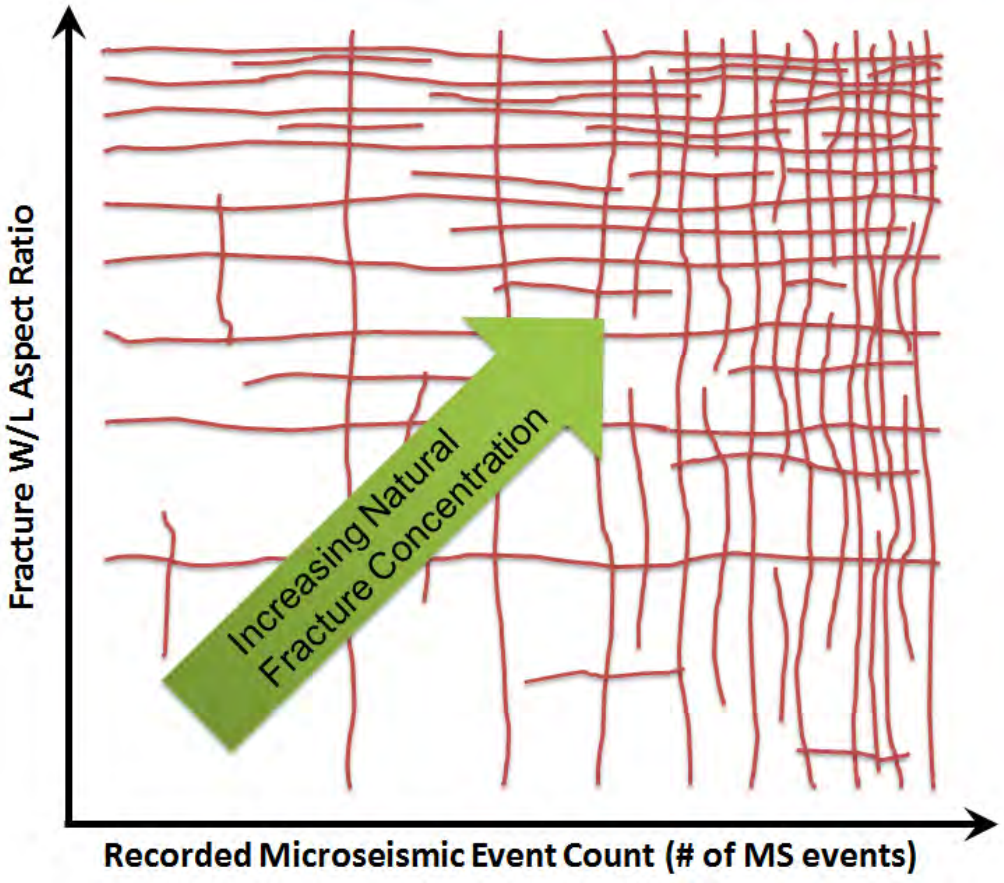

Figure 13: Indication of natural fracture concentration based in microseismic data.

Optimized passive seismic survey design with simultaneous borehole and surface measurements

Debotyam Maity and Dr. Fred Aminzadeh - Induced Seismicity Consortium (ISC, USC)

Increased use of microseismic monitoring has enabled better understanding of created fracture dimensions. There are currently two main methods of acquiring a microseismic survey. One method is to place the geophones on the surface and the other is to place the geophones in a monitor wellbore. While each geophone configuration can be used to map microseismic events, they both have advantages and disadvantages depending on reservoir depth and array configuration, as well as many other factors. This project attempts to develop a new integrated framework for optimized multi array passive seismic monitoring programs based on specific

requirements set forth at the initiation of the project. A new framework has been defined based on existing microseismic array optimization workflows and deployed this framework into a working implementation within Matlab environment for potential use. While the algorithm as tested shows a lot of promise for actual deployments in the field, tests with real data can provide the necessary confidence to use it for future programs. Main goal is aimed at understanding the elements which influence the design of multi array passive seismic monitoring programs and to develop a framework for optimization of such arrays for improved hypocentral locations and source mechanisms while optimizing deployment costs. Below is a summary of results while the full report is in Appendix D.

- Surface array is highly sensitive to subtle changes in the subsurface structure of the reservoir. (Sensitivity would normally follow the sequence surface > vertical > horizontal due to large velocity variations with depth compared with lateral variations). This is further validated by the unstable design solutions observed.
- For vertical arrays, it seems to be best to have the sensors closest to the actual zone of interest (which also makes intuitive sense as this would reduce estimation uncertainties). However, if vertical/ horizontal wells are the only observation wells, it is necessary to place a few surface sensors taking solid angle criteria into account. The other way is to have multiple wellbore arrays distributed around the zone of interest.
- Moment tensor inversions for source characterization should be done with boundary elements alone (of the subtended solid angle by the arrays) during final processing/ analysis and with the minimum number of elements possible (taking noise issues into account). However, for the array design and deployment, adequate backup is desired for some degree of redundancy.
- Actual noise conditions in the field and their impact on sensors is difficult to predict but can have substantial degrading effect and impact design suitability. High noise environments should require built in redundancy in the designs. The algorithm allows us to incorporate specific noise based weighting coefficients to receiver locations before the optimization runs begin to adequately factor it in for the optimization workflow.
- As already explained, properly designed well arrays can make large surface arrays redundant. However smaller arrays are necessary in case the number of observation wells are limited.
- More complex cost functions should be tested for to check if the solutions can be improved. However, to the best of our knowledge, this is the first time that an attempt has been made to optimize an array for multiple functions in a holistic manner.
- For poorly constrained scenarios or badly conditioned solutions, physical constraints may be imposed or multiple solutions may be compared based on local optima and conclusions drawn from such comparisons. Constraints can also provide solutions which are more stable.
- With regard to horizontal arrays and using updated velocity models based on hydrofrac generated perturbations within velocity field based on stress induced changes from stage to stage, industry seems to be reluctant to focus on working with such changes at

this point as it requires very high quality data, increased man hours for processing of the data as well as some more research on newer workflows/ algorithms. However fairly complex lateral velocity models are used (based on available information) to improve results when working with horizontal arrays.

- While it would seem that the optimal vertical observation array design can remove some of the sensors in the middle section of the well (observations from optimization runs in this work), in the actual field implementations, it is not seen not practical as tools have standardized length interconnects and it makes more sense to cover the complete acquisition instead of using a complex array design.
- While only ray-trace focusing and Moment tensor inversion optimizations have been tested, other factors can also be easily added within the optimization framework. Potential candidates include arrival time differentials (based on moveout), event amplitudes, attenuation pseudo factors, polarity, etc.

Geology

Dr. Julia Gale – Bureau of Economic Geology

Operators exposed to the development of tight shale reservoirs are aware of the importance of natural fractures. The most common fractures documented in the Marcellus Shale in core and outcrops are sub vertical opening-mode fractures that are broadly strike parallel (J1) or cross-fold joints (J2). These natural fractures are important because of their interaction with hydraulic treatment fractures that are produced using hydraulic fracturing stimulation. At the scale of hydraulic fracture stimulation, natural fracture patterns and in situ stress can be highly variable, even though a broad tectonic pattern may be consistent over 100s of miles. Thus, site-specific evaluation of the natural fractures and in situ stress is necessary. Open fractures are observed in a few cases in core. Fracture-size scaling, coupled with fracture-size control over sealing cementation and a subcritical growth mechanism that favors clustering suggests that open fractures are likely to be concentrated in clusters spaced hundreds of feet apart. The goal for this project is to characterize the fractures and identify the characteristic spatial arrangement of fractures, including potential clusters of large fractures. Efforts leading to understating of the fracture characteristics included field data sampling, core sampling and analysis, and laboratory tests to determine the subcritical crack index, leading to spatial organization of natural fractures. Summary of geological studies is below and the full report is attached in Appendix E.

- In the Marcellus Shale there are two to three sets of subvertical natural fractures: in the quarry exposures near Union Springs, NY, J1 fractures trend 075°, and J2 fractures trend 335°. In the Marcellus reservoir in SW Pennsylvania in the well experiment location for

the project there are three trends: NE (which we interpret as J1), NW (which we interpret as J2) and a third set trending ENE. Fractures in outcrop are up to 40 m long and the tallest is at least 3 m high.

- Induced fractures in the reservoir trend NE-SW.
- An analysis of the spatial organization of the calcite-sealed fractures in the Union Springs quarry location we found J1 fractures have a weak preferred spacing at 0.2m, 1 m, ~7 m and 14 m. J2 fractures show preferred spacing at 2, 4 and 14 m.
- J2 fractures in the Gulla Unit #10H horizontal well image log show a preferred spacing at 12.5 m, which is comparable to the vertical distance between limestone beds observed in the nearby Paxton Isaac Unit #7 well. This may be a characteristic mechanical layer thickness, which is reflected somewhat in the fracture spacing.
- Samples from the Paxton Isaac Unit #7 well yield subcritical indices from 38 to 131, with a mean of 75, and fracture toughness, KIc, typically from 1.0 – 1.7 MPa sqrm.
- Geomechanical models using measured and selected input parameters specific to the subsurface close to the Gulla and Paxton Isaac wells yield fracture spacing patterns comparable to those measured directly proving that geomechanical modeling is a useful predictive tool.
- Horizontal fractures seen in cores were not observed in outcrop.
- The fractures in the outcrop are mostly barren, with the exception of a few examples including those at the Wolfe Quarry in Union Springs.
- Fractures in core are mostly sealed. Barren fractures do occur, but where orientation is known these are parallel to S_{Hmax} and are interpreted as drilling-induced fractures.
- Sealing cements in fractures are calcite, quartz, pyrite, barite and anhydrite. The cement crystals may be sub-euhedral, anhedral or fibrous. Cements commonly show crack-seal texture indicating multiple opening events.
- Larger fractures (> 5 mm wide) may be partly open, with euhedral cement lining open pores: examples were observed in the Onondaga Lst. in the Hardie Unit #1 core, and in the shale facies in other proprietary cores outside this study. Fractures in the shale that are narrower than this are completely sealed, but fractures as narrow as 1 mm have been observed with fracture porosity within a carbonate in the Dunn Clingermann well. There is also some fracture porosity in fractures that are contained within concretions.

- Fluid inclusions are present in some but not all of the fracture cements (hydrocarbon and aqueous). They are typically absent or are too small to observe with a petrographic microscope in the fibrous cements.
- Preliminary O18 and C13 stable isotope data in calcite cements indicates variation in composition of fluids from which cements were precipitated.

Nano-meter Scale Pore Imaging

Dr. Dmitriy Silin and Dr. Timothy Kneafsey – Lawrence Berkeley National Laboratory

The principal objective of this study is identification and analysis of specific petrophysical properties of Marcellus shale reservoir. The proposed approach relies on three dimensional pore-scale imaging of reservoir rock samples followed by analysis of pore space connectivity, pore size distribution, and evaluation of two-phase fluid flow properties of the rock. Micron-scale pores make the matrix permeability comparable to that of a concrete wall; therefore, conventional core laboratory experiments are prohibitively time-consuming. Petrophysical analysis based on 3D imaging utilizing FIB milling techniques offer an alternative approach, which can provide insights and measurements of otherwise unavailable properties of the rock. Results are based on first-of-its kind complex research where micron and nanometer-scale properties of the rock will be coupled with the field study and well data focusing on a specific gas-producing region. Full report describing the approach and analysis performed in this study is in Appendix F, and a summary of results with conclusions is given below. A number of Marcellus shale samples were available and analyzed. The samples were analyzed with different imaging techniques: 1) Low-resolution computed tomography, 2) Micro-tomography at the Advanced Light Source Facility, 3) FIB/SEM.

- Each imaging technique revealed rock properties at different scales.
- Heterogeneity is present in all scales.
- The porosity is low in all scales.
- Micro-CT data shows development of micro cracks near quartz grain and pyrite inclusions. We speculate that such micro cracks may enhance rock permeability and gas recovery.

Flow Characteristics in the Presence of Gas Liquids

Dr. Roland Horne – Stanford University

The Marcellus shale usually contains higher hydrocarbons and quite possibly behaves as a light gas-condensate reservoir. The gas usually consists of mainly methane and other light hydrocarbons but can also contain heavier components. In this case, the reservoir temperature lies between the critical temperature and the cricondentherm. Initially, the reservoir pressure is at a point that is above the dew point curve so the reservoir is in the gaseous state only. During production, the reservoir pressure declines isothermally and at the dew point, and thus liquid starts to condense and if the reservoir pressure decreases further, more liquid is condensed in the reservoir. A gas-condensate reservoir is special as when the pressure decreases, instead of having gas evolution, there is liquid condensation resulting in the reduction of permeability to gas leading to reduced gas production.

The objective of this research was to gain a better understanding of the possible condensate blocking in Marcellus shale and reduction in the relative permeability. The knowledge gained is important for optimizing the producing strategy aimed at reducing the impact of condensate banking and improving the ultimate gas recovery.

In order to achieve the research objective, the following experiments were conducted:

1. Computerized tomography (CT) scanner experiment on dry cores.
2. Permeability measurement using the pressure pulse decay apparatus.
3. Porosity measurement.
4. Gas-condensate core flooding experiment.
5. Compositional measurement using Gas Chromatography (GC).
6. Saturation measurement using the X-ray CT scanner.

The results indicate that: The coreflooding experiment of the Berea sandstone and the Marcellus shale core using the Marcellus gas-condensate gas mixture confirm the expectation based on earlier experiments (which used synthetic binary gas mixtures) that the composition of Marcellus shale gas mixture would change during production. The change in the gas composition is caused by the dropout of the heavier components into the liquid condensate phase below the dew point pressure.

A full report in Appendix G presents the recent results of the CT scanner experiment conducted on the dry cores and also highlights the results of gas-condensate core flooding experiment.

Fracture Characteristics

Dr. Terry Engelder – Pennsylvanian State University

The principal objective of this task is to understand and characterize hydraulic fracturing at the Marcellus level through detailed analysis of microseismic events during hydraulic fracturing. Microseismic events associated with stimulation of gas shales can be of two types: single couple (mode I) or double couple (mode II or III). The first type of event is much like a laboratory acoustic emission which is a single couple seismic mechanism. A single couple event is the record of the noise associated with the opening of a mode I crack. The motion of the walls of a mode I crack is normal to the plane of the crack. Seismic noise from mode I cracks tends toward the relatively low energy end of the seismic spectrum. The second type of event is typical of earthquakes where the motion of the walls of the crack is parallel to the plane of the crack. In this case, the crack acts like an earthquake fault and the seismic event is a double couple mechanism. During shear slip, typically a larger amount of seismic energy is released as compared to opening mode cracks. It is this latter seismic signal that is most easily detected by microseismic techniques associated with stimulation of gas shales. Different fracturing modes will have different permeability and hence different effects on production and will have a different response in the seismogram.

Although the stimulated volume could be estimated from the 3D plot of microseismic events, different stages might contain different fractions of each mode of fracturing. Therefore the fracturing modes bring uncertainty in the estimation of production based on the spatial distribution of microseismic events. The way to draw a distinction between the modes of fracturing is by analysis of moment tensor data of each event. Moment tensor data could be calculated from seismogram wave form plus information about the mechanical properties of rock formations the seismic wave travelled through (which is represented in a Green function). By inversion of moment tensor from full wave form (or a certain part of frequency domain of the seismogram) and Green's function, it might be possible to assess the modes of fracturing of each event. Working under this task, seismic data was interpreted to develop a complete

understanding of the nature of fractures that are contributing to the production of gas from black shales. The order of analysis follows:

- Draw a distinction between single and double couple mechanisms.
- After step #1 is completed, draw a distinction between fault mechanisms as a consequence of man-made fractures vs. the opening and propping of natural fractures.
- After step #2 is completed, draw a distinction between stimulation of local joints J_{fault} and regional sets J_1 and J_2.
- After step #3 is completed, draw a distinction between stimulation of regional sets J_1 and J_2. (These two joint sets are subnormal and may offer differing permeability levels because of their position in the earth stress field).

The full report describing fracture analysis is in Appendix H.

Reservoir Engineering

Dr. Shahab Mohaghegh – West Virginia University

Reservoir simulation is the industry standard approach to understanding reservoir behavior and predicting future performance. The intent of this study was to assess the potential of Marcellus Shale formation using a novel and integrated workflow that incorporates field production data and well logs using a series of traditional reservoir engineering analyses complemented by artificial intelligence and data mining techniques. The model developed using this technology is a full field model built on integration of static and dynamic measurements and its objective is to predict future well performance in order to recommend field development strategies, also called Top-Down Intelligent Reservoir Model.

Traditional reservoir simulation and modeling is a bottom-up approach that starts with building a geo-cellular model of the reservoir and then populating the model with the best available petrophysical and geophysical information at the time of development. Engineering fluid flow principles are then added and solved numerically in order to generate a dynamic reservoir model. Typically, the full field model is calibrated using historic pressure and production data in a process referred to as "history matching." Once the full field subsurface reservoir model has been successfully calibrated, it is used to predict future reservoir production under a series of potential scenarios, such as drilling new wells, injecting various fluids or stimulation.

Top-Down Intelligent Reservoir Modeling approaches the reservoir simulation and modeling from reverse standpoint by attempting to make an insight into reservoir by starting with actual field measurements (well production history). The production history is augmented by core, log, well test, and seismic data in order to increase the accuracy of the Top-Down modeling technique. The database of this study focuses on 136 horizontal wells of Marcellus Shale Gas Reservoir located in Washington County. Results of statistical analysis of given data, the dynamic well behavior by using the production history ,and the first results of Top-Down modeling are presented in Appendix I, while a summary of the results follows.

- Most of the wells are located in pads with more than 3 wells that are similar in tract of land, although some single wells can be seen in this area.
- Four BTU regions (varies from dry to wet) are defined for the wells that shows the amount of condensate in gas. Most of the wells are located in area 2 and 3 which condensate content changes from medium to low.
- Static properties of Upper and Lower Marcellus show that the lower part of Marcellus is much more prolific than the upper part.
- More than 70% of the given wells are completed and come to production in 2009 and 2010; therefore, the history of production is relatively short.
- Number of stages for the wells changes from 4 to 17 while more than 50% of the wells have been fractured by 8 to 10 stages.
- The amount of pumped proppant in most wells is between 4 million lb to 6 million lb. the average amount of injected proppant is 4.5 million lb per well.
- Between 100000 to 150000 barrels of fluid is being used for fracturing the wells in this area. The average volume of clean fluid is 124000 barrel for each well.
- The average injection rate and pressure is 68.5 barrel per min and 6500 Psi for each well respectively.

Technology Transfer

Our past company experience has proved technical workshops as the most efficient technology transfer vehicle along with presentations made at industry recognized events. We held several workshops during the course of this project. In these workshops, results were presented to engineers and geoscientist in interactive sessions where the participants took part in the discussions and received hands-on training on application of the methods and techniques. A

final Industry Workshop was held in Canonsburg PA, on May 7th 2013 to disseminate all the research results. Over 95 attendees were present at the workshop and all researchers from the project presented their results. Presentations were also given at conferences and industry sponsored consortiums. Table 1 shows a list of technology transfer efforts made by GTI.

Table 1: Technology transfer efforts for the Marcellus Shale Research Project.

Date	Event	City	Venue	Notes
January 26, 2011	Illinois Basin Petroleum Technology Transfer Council Workshop	Evansville, IN	The Centre	Presentation - Iraj Salehi: Results from New Albany Shale project and summary of the Marcellus Shale project Presentation - Jordan Ciezobka: Approach to Successful Stimulation Techniques in Shale and Tight Sand Plays
April 19-20, 2011	RPSEA Unconventional Gas Conference 2011	Denver, CO	Denver Marriott City Center	Presentation - Jordan Ciezobka: New Albany and Marcellus Shale Gas Projects - A review and update
June 24, 2011	45th American Rock Mechanics (ARMA) Symposium and Workshop	San Francisco, CA	The Westin San Francisco Market Street	Presentation - Jordan Ciezobka: Multiple Hydraulic Fractures and Fracture Reorientation
June 27-29, 2011	Optimizing Shale Oil & Gas Wells	Denver, CO	Renaissance Denver Hotel	Presentation - Jordan Ciezobka: Fracturing Techniques in the Marcellus. What have we learned?
September 25-28, 2011	AAPG Eastern Section Meeting and Workshop PTTC/DOE/RPSEA Gas Shales Workshop	Arlington, VA	Hyatt Regency, Crystal City	Presentation - Jordan Ciezobka: Marcellus Shale Hydraulic Fracturing
October 30 - November 2, 2011	SPE ATCE (Annual Technical Conference and Exhibition)	Denver, CO	Colorado Convention Center	Salehi & Ciezobka, Poster : Marcellus Gas Shale, A GTI-Industry-RPSEA Cooperative R&D Project Salehi & Ciezobka Poster: New Albany Shale, An Industry-RPSEA Cooperative R&D Project
November 10, 2011	American Institute of Chemical Engineers Midwest Regional Conference	Chicago, IL	University of Illinois - Chicago	Presentation - Jordan Ciezobka: Gas Shales - A Supply Game Changer, If Done Right!
November 15-17, 2011	DUG East Conference	Pittsburgh, PA	David L. Lawrence Convention Center	Salehi & Ciezobka Poster: Marcellus Gas Shale, A GTI-Industry-RPSEA Cooperative R&D Project Salehi & Ciezobka Poster: New Albany Shale, An Industry-RPSEA Cooperative R&D Project
December 12-13, 2011	OURF Symposium	Tulsa, OK	Double Tree Downtown Hotel	Presentation - Jordan Ciezobka: New Albany and Marcellus Shale Gas Research Projects, A Review and Update
January 19, 2012	Chicago Council on Science and Technology	Chicago, IL	Northwestern University	Presentation - Jordan Ciezobka: Marcellus Fracturing and Shale Gas Development
May 7, 2013	Industry Workshop	Canonsburg, PA	Hilton Garden Inn	Held an Industry Workshop disseminating all research results with all researchers

4. Appendix of Individual Reports

Appendix A – Topical Report: Stimulation & Completion

the Energy to Lead

Marcellus Gas Shale Project
RPSEA Project 9122-04

Topical Report
Stimulation and Completion

Prepared by:
Jordan Ciezobka
August 16, 2011

Gas Technology Institute
1700 S. Mount Prospect Rd.
Des Plaines, Illinois 60018

Introduction

Extending throughout much of the Appalachian Basin, the Marcellus shale is stratigraphically the lowest member of the Devonian age Hamilton Group, and is divided into several sub-units. The formation is mainly composed of black shale and contains lighter shales and interbedded limestone layers as a result of sea level variation during its deposition almost 400 million years ago (Harper et al. 2004). It is overlain by the Mahantango shales and Tully limestone and underlain by the Onondaga limestone, Huntersville chert, and Oriskany sandstone as shown in Figure 1 (Milici et al. 2006). Having a potentially prospective area of over 44,000 square miles, the Marcellus shale is one of the largest shale plays in North America as it covers portions of New York, northern and western Pennsylvania, eastern Ohio, western Maryland, and most of West Virginia.

Gas production from ultra low permeability reservoirs such as the Marcellus shale and tight sands can only be achieved commercially with appropriate completion and stimulation techniques due to their inherent reservoir properties. Because these reservoirs exhibit low porosity and ultra low permeability, large volumes of this type of reservoir have to be considered to assure commercial in-place gas quantities. In addition, flow restriction due to low permeability has to be overcome with an effective stimulation program such as hydraulic fracturing. Presence and interaction of natural fractures with created hydraulic fractures can further aid in gas production by creating a complex fracture network that drains a larger portion of the reservoir.

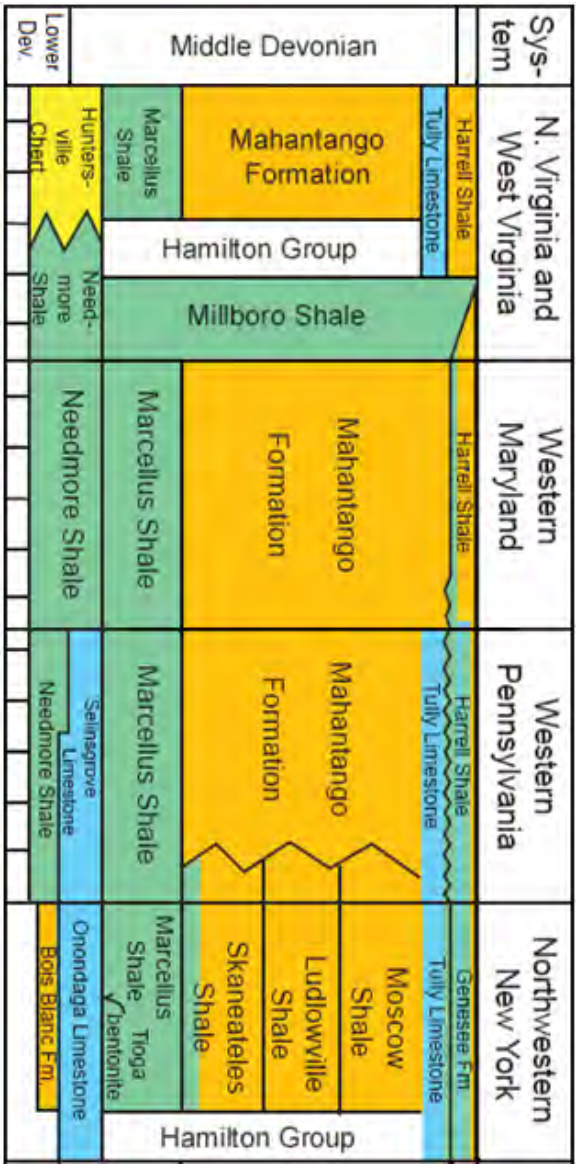

Figure 1: Stratigraphic Section Showing Marcellus Shale

Gas Technology Institute (GTI), with funding from the Research Partnership to Secure Energy for America (RPSEA), has initiated an industry cooperative research project, that, aside from other tasks, aims to examine the contribution of gas production from natural fractures in addition to predicting the spatial distribution and population characteristics of these natural fracture systems through the measurement of the subcritical crack index. The subcritical crack index, *n*, is the exponent in the power law

relationship between crack propagation velocity *V*, and mode I stress intensity, K_I, as shown in Equation 1. The subcritical crack index and the pre-exponent, A, can be measured in the laboratory.

$$V = A \cdot K_I^n$$

Equation 1

Evidence suggests that subcritical crack growth is an important parameter in natural fracture creation. By measuring this parameter locally from core samples, one can extrapolate fracture patterns to a larger scale (Holder et al. 2001). In addition, pumping diagnostics of hydraulic fracture stimulation treatments coupled with production data were used to infer local extent of natural fracturing and their interaction with the created hydraulic fractures.

After reviewing initial data in this research project, we were able to directly identify a cluster of natural fractures that intersects a number of horizontal wells at a particular portion of each well that has a significant impact on production and pumping of hydraulic fracturing treatments. We were able to verify the existence of this local cluster of natural fractures by examining pre and post completion data on multiple wells that we believe intersect this cluster. Examined data included mud logs, hydraulic fracturing diagnostics, radioactive tracer (RA) logs, surface and borehole microseismic surveys, production logs, and check shot seismic velocity profiles.

Experiment Site

A multiple well pad owned and operated by Range Resources Appalachia LLC located in Washington county Pennsylvania is the site of field data acquisition. The pad includes seven nearly-parallel horizontal wells. The trajectories of the well laterals are in the general northwest direction and are normal to the maximum in situ horizontal stress (σ_{Hmax}) orientation as shown in Figure 2. Spacing of the horizontal sections of the wellbores is approximately 500 ft with an average horizontal wellbore length of 3640 ft. The horizontal well sections lie along the lower portion of the Marcellus shale, (the Marcellus-A) having a true vertical depth (TVD) of approximately 6500 ft. Pad drilling was utilized in this case as the surface location of the wells is centered in a rural and geographically complex setting.

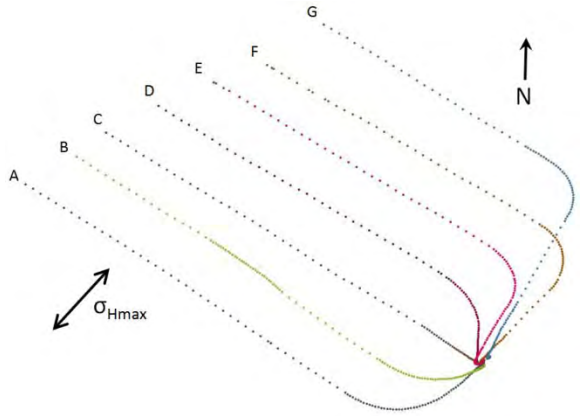

Figure 2: Experiment Site Well Trajectories

The gross thickness of the Marcellus shale at a nearby well located less than 3 miles from the test site is roughly 150 ft with an average porosity and permeability of 8 percent and 600 nanodarcy, respectively. Figure 3 is a shale log montage and shows the total gas and water saturation (third track from the right) in the Marcellus and Marcellus-A intervals along with free and adsorbed gas content (first track from right). Second track from the right shows the total organic content (TOC) along with the calculated permeability. As evident from the shale log evaluation, the lower portion of the Marcellus, the Marcellus-A, is a better reservoir in terms of TOC, total gas saturation, porosity

and permeability. However, the operator chose to place the horizontal sections of the wells in the upper interval. The well laterals were placed in the upper portion of the Marcellus due to previous success of fracture placement, the lower portion of the Marcellus formation was also considered for production with the assumption that hydraulic fracture stimulation treatments would result in the production from the lower Marcellus. It is shown in later sections that the hydraulic fractures did in fact propagate into the lower portion of the Marcellus indicating that production from the lower zone would contribute to the total production.

Hydraulic Fracturing

In order to produce commercial quantities of gas from the seven wells, each well was stimulated with multiple hydraulic fracture stages. As the length of the horizontals varied from well to well so did the number of fracture stages, with one well having a minimum of 11 and another having a maximum of 17 stages. However the spacing of fracture stages and perforation clusters remained the same in each well. Hydraulic fracture treatments were comprised mainly of water, sand, and very low concentrations of fit-for-purpose additives.

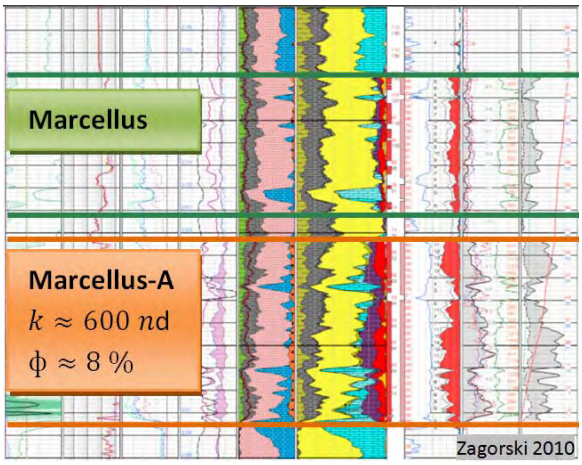

Figure 3: Shale Montage Depicting Local Marcellus Reservoir Properties (After Zagorski, 2010)

The wells were completed with casing and the pump down plug-and-perf technique was utilized in between frac stages. At the end of each fracture stage, a bridge plug and a perforating gun assembly connected to wireline was pumped to the desired depth and the bridge plug was set, providing isolation for the next fracture stage from the previous one. The remaining assembly of perforating guns was pulled up the wellbore to a depth corresponding to the next fracture stage at which point the perforating guns were fired providing perforations that enabled communication between the formation and the wellbore. The wireline was then pulled out of the well and the fracture treatment started. This process was repeated until all fracture stages in each well were completed. Figure 4 shows the number of frac stages pumped in each well along with the completed lateral length and the average fluid volume pumped per frac stage. The average fluid volume pumped per stage for wells A, C, E, D, and F was about 7000 barrels (bbl), while for well G was 8500 bbl and well B was 9900 bbl. The average lateral length for all the wells was about 3800 ft.

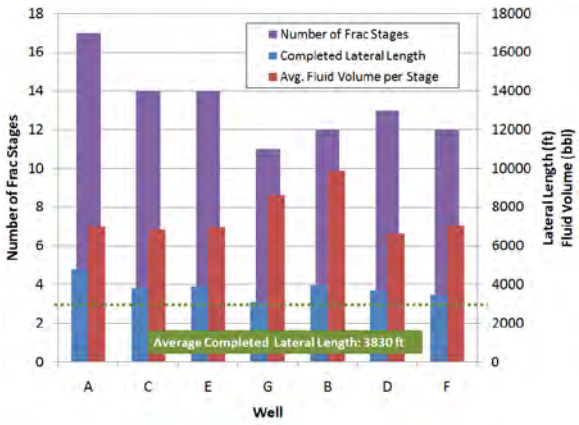

Figure 4: Comparison of Fracture Design Parameters

It may seem as though the size of the fracture stages varies considerably from well to well. However, when fluid and proppant amounts pumped in each well are normalized on the basis of per foot of lateral, it becomes clear that five (wells A, C, E, D, and F) out of the seven wells were stimulated with the same proportions of proppant and fluid. The other two wells were stimulated with higher concentrations and amounts of proppant which also required more fluid to be pumped. Figure 5 shows the normalized fluid volume and proppant mass pumped in each well on a per-foot basis. In wells A, C, E, D, and F, an estimated 1000 lbs of proppant was pumped per each ft of completed lateral requiring about 25 bbls of fluid volume per foot of lateral. In an ongoing attempt to determine the optimal fracture treatment design, the proppant mass pumped in well G was increased by 75% (on a per foot basis) and by 100% in well B (also on a per foot basis). Because of the higher proppant mass, the amount of fluid pumped was also higher, however not proportionally to the percentage of proppant increase.

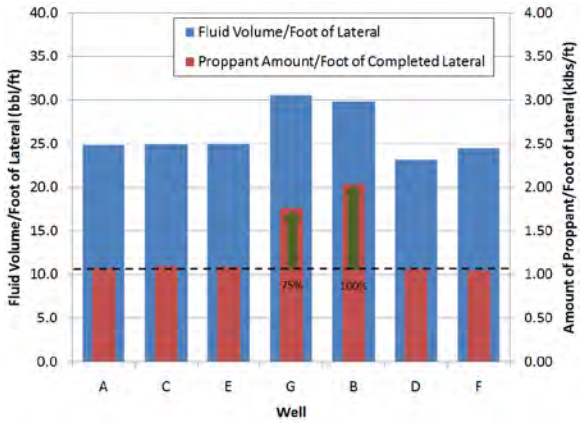

Figure 5: Fracture Design Parameters on a Per-Foot Basis

In order to maximize hydraulic/natural fracture network complexity, the hydraulic facture stages were pumped in a modified zipper sequence. The zippering of hydraulic fractures tends to change the local stress field as a result of geomechanical and pore pressure changes induced by hydraulic fracturing as shown by Singh (Singh et al. 2008) and evidenced in previous GRI experiments such as the Mounds Drill Cuttings Injection Project (Moschovidis et al. 2000). Because of the nature of the well trajectories and the number of wells, the zippering sequence was performed in five separate clusters. Each cluster was optimized for best microseismic viewing distance and fracture interference. Figure 6 shows the zipper sequence of the first cluster of frac stages that included four adjacent wells. The wells were fractured in an alternating fashion until thirteen fracture stages were executed, then the geophone position was changed to accommodate the next cluster of fracture stages.

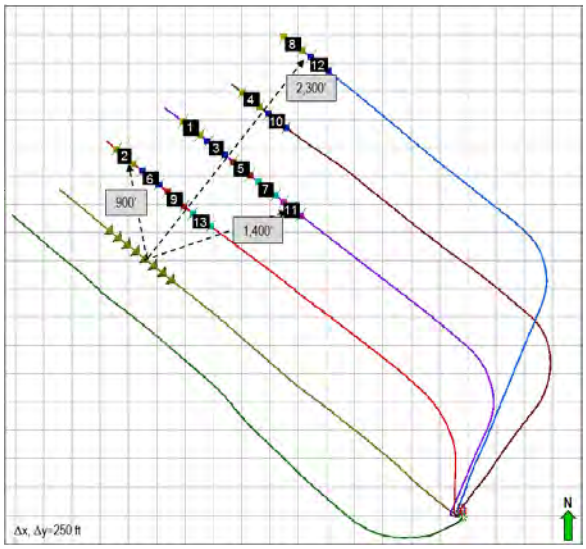

Figure 6: 1st Geophone Placement and Sequence of Frac Stages Pumped

Figures 7, 8, 9, and 10, show the four other positions of the geophones and the cluster of fracture stages that were executed and monitored. The first three geophone placements were used to monitor the wells

located to the northeast of the observation well while the last two geophone placements were used to monitor the well located southeast of the observation well and a few remaining fracture stages on the northeast wells. After all fracture stages were pumped, coil tubing was used to drill out all the bride plugs that were used for isolation and the wells were flow tested and then put on production.

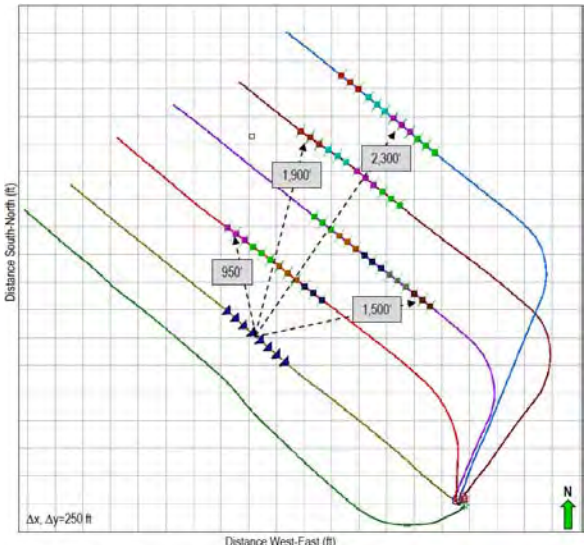

Figure 7: 2nd Geophone Placement and Frac Stages Pumped

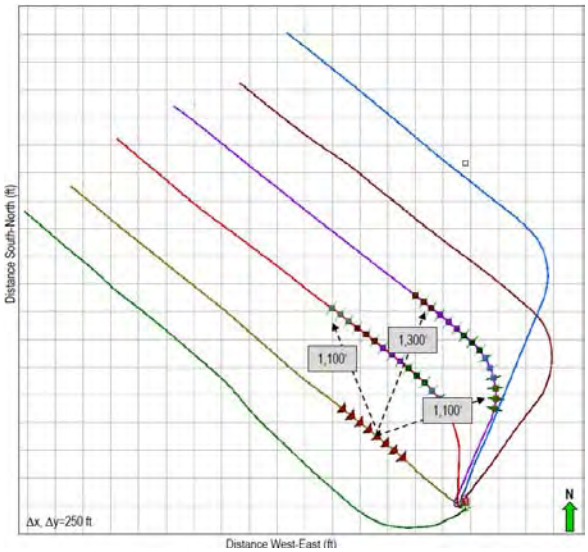

Figure 8: 3rd Geophone Placement and Frac Stages Pumped

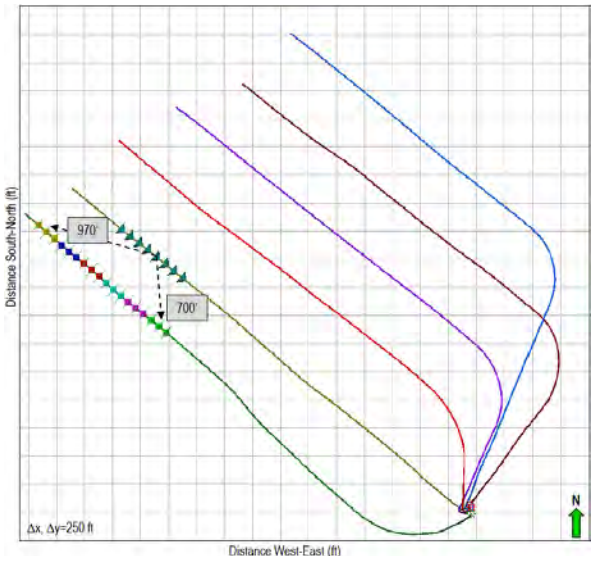

Figure 9: 4th Geophone Placement and Frac Stages Pumped

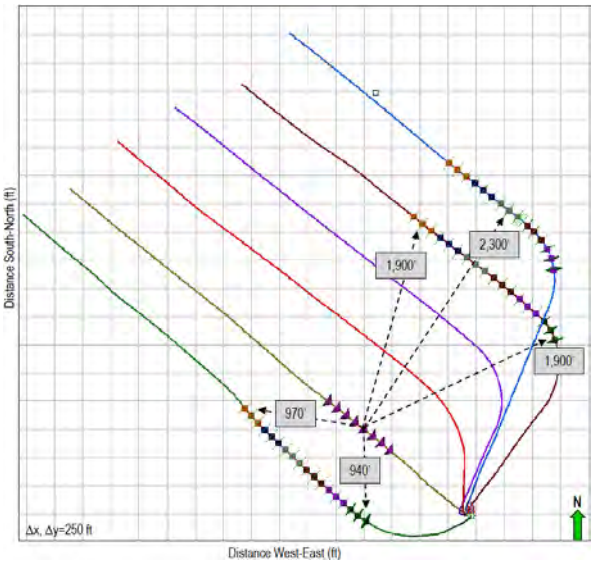

Figure 10: 5th Geophone Placement and Frac Stages Pumped

Microseismic Monitoring

Microseismic monitoring was performed in order to understand the hydraulic fracture geometry, including the extent of upwards and downwards growth, the fracture azimuth, interference of fractures as a result of the modified zipper technique, and calculation of the stimulated reservoir volume (SRV). Two distinct monitoring systems were utilized to

complete the microseismic surveys. The results from the two systems were compared for similarities and differences in terms of fracture geometry and azimuth orientation.

The first system, which was used to monitor all 93 fracture stages on all 7 wells, was a surface monitoring array comprised of geophones arranged in 10 lines radiating away from the wellbore pad. The array was constructed using 1082 geophone stations that recorded the microseismic data with a sampling rate of 2 milliseconds. Figure 11 shows the surface array that was used to complete the microseismic array. Results from the Zero Offset Vertical Seismic Profile (VSP) Survey were used to generate the seismic velocity model in order to determine the event locations accurately. The costs of surface microseismic imaging were covered by Range Resources but the results were made available to the research team.

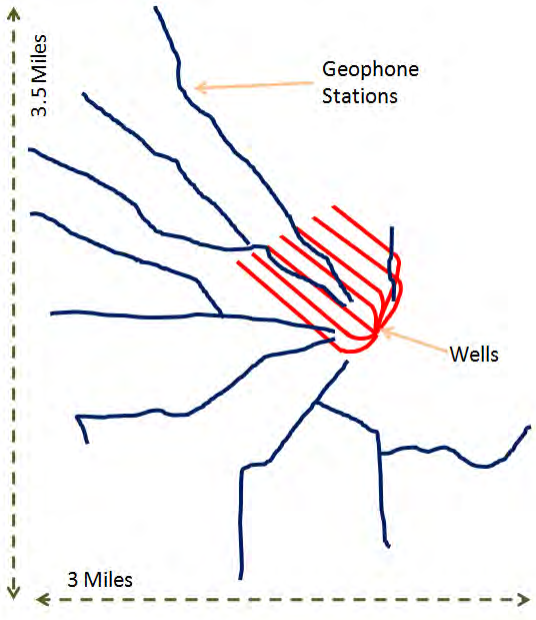

Figure 11: Lines Showing the Location of Surface Geophones Used to Complete the Surface Microseismic Survey

The second monitoring system was a borehole microseismic system positioned in one of the horizontal wells (Well C) and consisted of 8 shuttles spaced 100 ft apart. As previously mentioned, the geophone array was moved to 5 positions to best capture the microseismic events in terms of signal amplitude and quality. Results from the Zero Offset Vertical Seismic Profile Survey were used to generate the velocity model. In addition, seismic signals generated by firing perforating guns in between fracture stages were used as check shots to calibrate the horizontal velocity between the check shot position and the borehole receiver. In total, 62 fracture stages were monitored using the borehole system. Fracture stages in Well A were not monitored due to financial constraints and fracture stages in Well C were not monitored for the obvious reason of geophone utilization. The cost of the survey was shared between Range Resources and GTI, and the remainder was cost-shared by Schlumberger, the service provider completing the borehole microseismic imaging. Figure 11 shows the frac stages that were monitored with the borehole system.

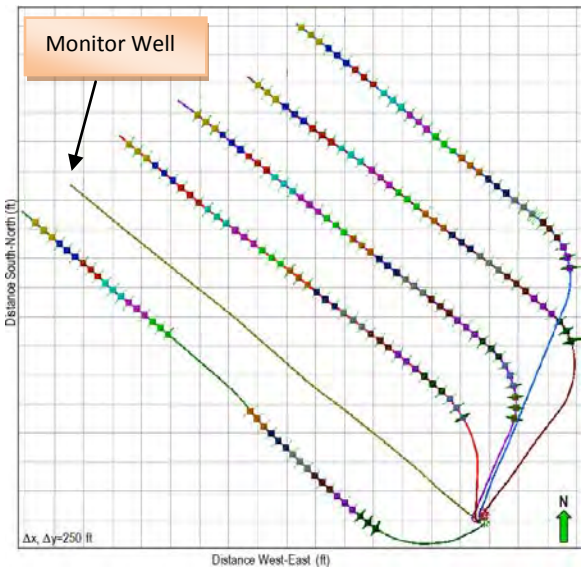

Figure 12: Wells and Frac Stages Monitored with Borehole Microseismic

The results of the two microseismic surveys, shown in figure 13 and 14, show similar results in fracture geometry, azimuth and overall event population. The azimuth of the hydraulic fractures seems to be normal to the orientation of the horizontal laterals, indicating that the wells were in fact drilled perpendicular to the plane of maximum horizontal stress (σ_{Hmax}). Although the borehole microseismic survey does not include microseismic events from wells A & C, there are clear similarities in the location of concentrated events, mainly in the toe stages of the wells and the stages close to the curves in wells E, F, and G. Another similarity in the two sets of data shows that there are much fewer recorded events in wells A, B, C, D, in the horizontal portion of the well that extends from about the middle of the horizontal to the curve. This phenomenon is more pronounced in the survey recorded with the surface microseismic system. The data acquired with the borehole system does show a decreased amount of events in the aforementioned interval, however, because wells A and C were not monitored with the borehole system, a survey including these two wells might have been considerably different. In addition to event population similarities, there is a region near the curve sections of wells F and G where the fracture azimuth seems to be slightly more oriented in the northeasterly direction. This phenomenon is not yet explained and will be looked into further; one possibility is that stress interaction from previous fracs might have changed the local azimuth.

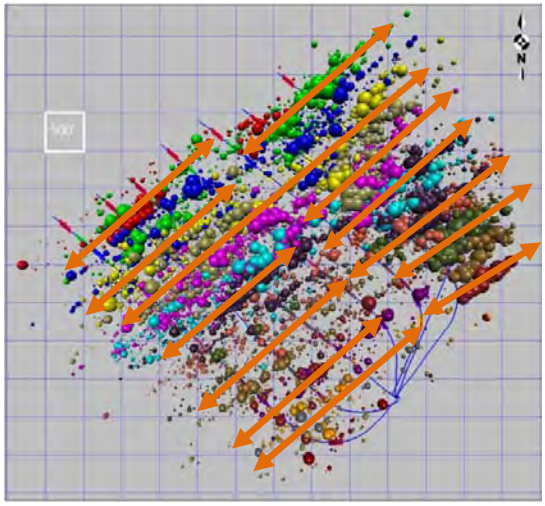

Figure 13: Map View of Microseismic Events Recorded with Surface Microseismic Imaging

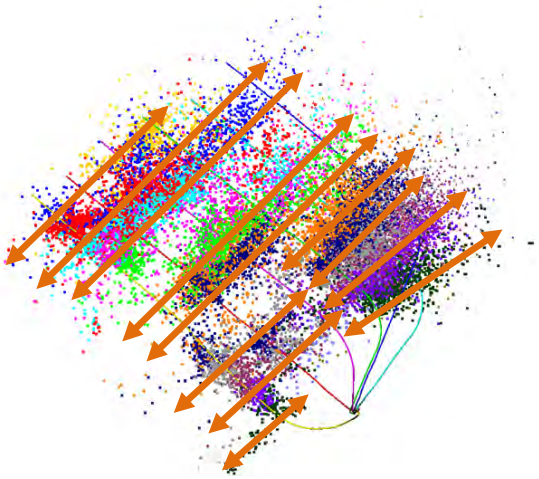

Figure 14: Map View of Microseismic Events Recorded with Borehole Microseismic Imaging

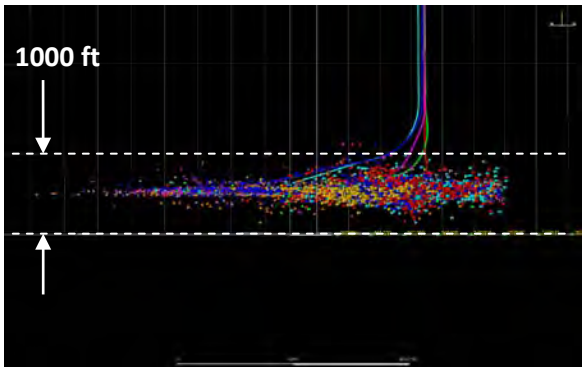

Figure 15: Front View of Microseismic Events Captured with Borehole System

The majority of the microseismic cloud is contained in a vertical window that is less than 1000 ft. Figure 15 shows the front view of the borehole microseismic survey data. Although the horizontals were drilled into the lower Marcellus as previously mentioned, the data shows a good deal of microseismic activity in the upper portion of the Marcellus, thus leading to believe that it was stimulated as well.

Production Logging

A production log utilizing a spinner flowmeter conveyed with coiled tubing was performed on well D in order to determine production contribution from individual stimulated perforation clusters. Because of a restriction in the wellbore, the tool was conveyed just past a depth corresponding to stage 4 frac perforations and the remainder of the stimulated wellbore up to the last perforation cluster was logged. The total production contribution from the first 3 frac stages, which were not logged due to restriction in the well, contributed 10% to the total production after the well was on production for about 3 months.

The next set of perforation clusters, corresponding to stage 4 frac interval, showed a contribution of 22% of total production. This was by far the highest production from any single frac stage in this well. Other notable intervals that contributed to production in double digit percentages were stage 8 and 12 perf intervals, which produced 14 and 13 percent respectively. Figure 16 shows the production contribution from individual frac stages.

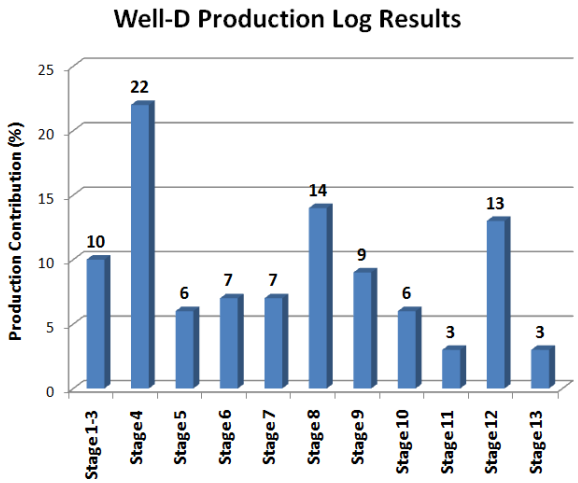

Figure 16: Production Contribution from Individual Frac Stages in Well-D

Analysis and Conclusions

After reviewing borehole microseismic data, production logging results, fracture surface treatment parameters, and RA tracer survey results, we believe that we have identified a local cluster of natural fractures that intersect a few of the project wells and is substantially different from the other natural fractures that may exist and intersect the remaining wells. This cluster of natural fractures may be contributing to higher than average production.

Production logging results from Well-D show that production from perforation clusters corresponding to Stage 4 frac account for much higher than average production (22% of the total well). In addition, surface fracturing pressure is very erratic, suggesting opening of natural fractures, plugging and then diversion.

Figure 17 is the surface treatment plot from Stage 4 frac of well D. This is the only stage in well D that exhibits this much pressure fluctuation while keeping the rate almost constant after the designed job rate is achieved.

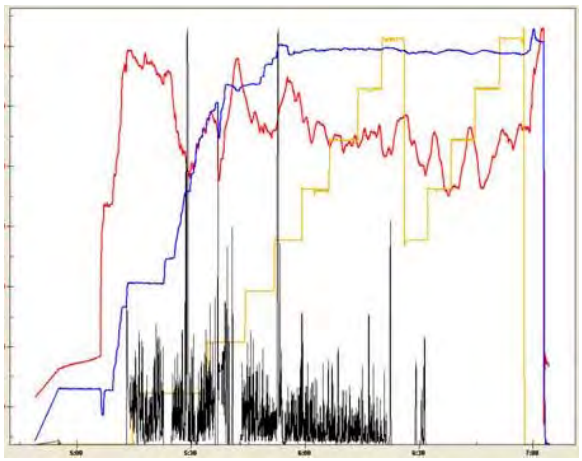

Figure 17: Treatment Data from Stage 4 Frac in Well D

In this figure, the red curve is the surface treating pressure, the blue curve is treatment rate, the yellow curve is wellhead proppant concentration, and the black curve is the friction reducer concentration.

Coincidently, Stage 5 frac in well B and Stage 5 in well E exhibit a similar erratic surface pressure response that is not seen in the remaining frac stages of the said wells. These two frac stages along with stage 4 of well D all fall mostly in line. Figure 18 shows the surface treatment data from well E stage 5. Pressure fluctuations due to rate changes are not considered to be formation related.

Figure 19 shows the surface treatment data from well B stage 5 frac. Again, if pressure changes due to rate fluctuations are not considered, there is some erratic behavior in the pressure response during the treatment that is not evidenced in other frac stages.

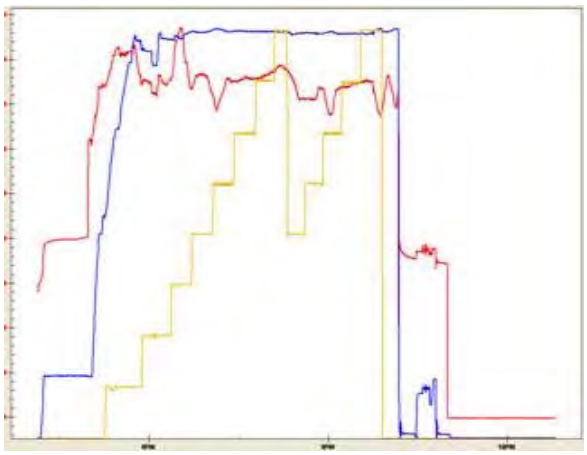

Figure 18: Treatment Data from Well E Stage 5 Frac

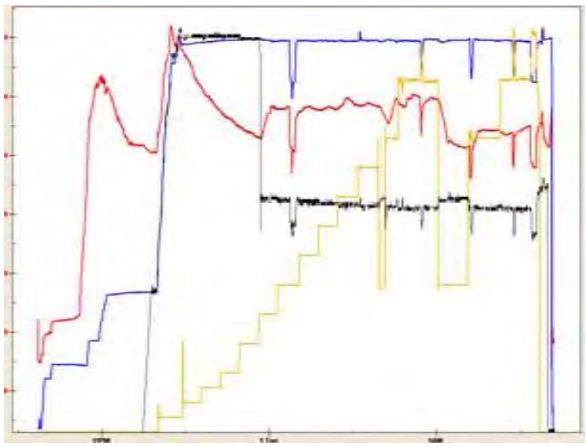

Figure 19: Treatment Data from Well B Stage 5 Frac

The radioactive tracer survey overlaid on top of the production log shows that there is some communication between this zone (stage 4 frac) and some other zone, possibly the previous frac stage (stage 3). In Figure 20, the right most track shows the radioactive isotope that was used to trace the fracturing fluid in each frac stage. Red is Iridium, blue is Antimony, and yellow is Scandium. Based on the log, Iridium, denoted by the red box in the right most track, was pumped in stage 4 and there seems to be no trace of it as the log only shows Scandium, shown by the yellow spikes in the dashed light green box in Figure 20. The interval that produced 14% of the total gas (frac stage 8) in Well-D also showed some RA isotope mixing with the adjacent frac stage (stage 9).

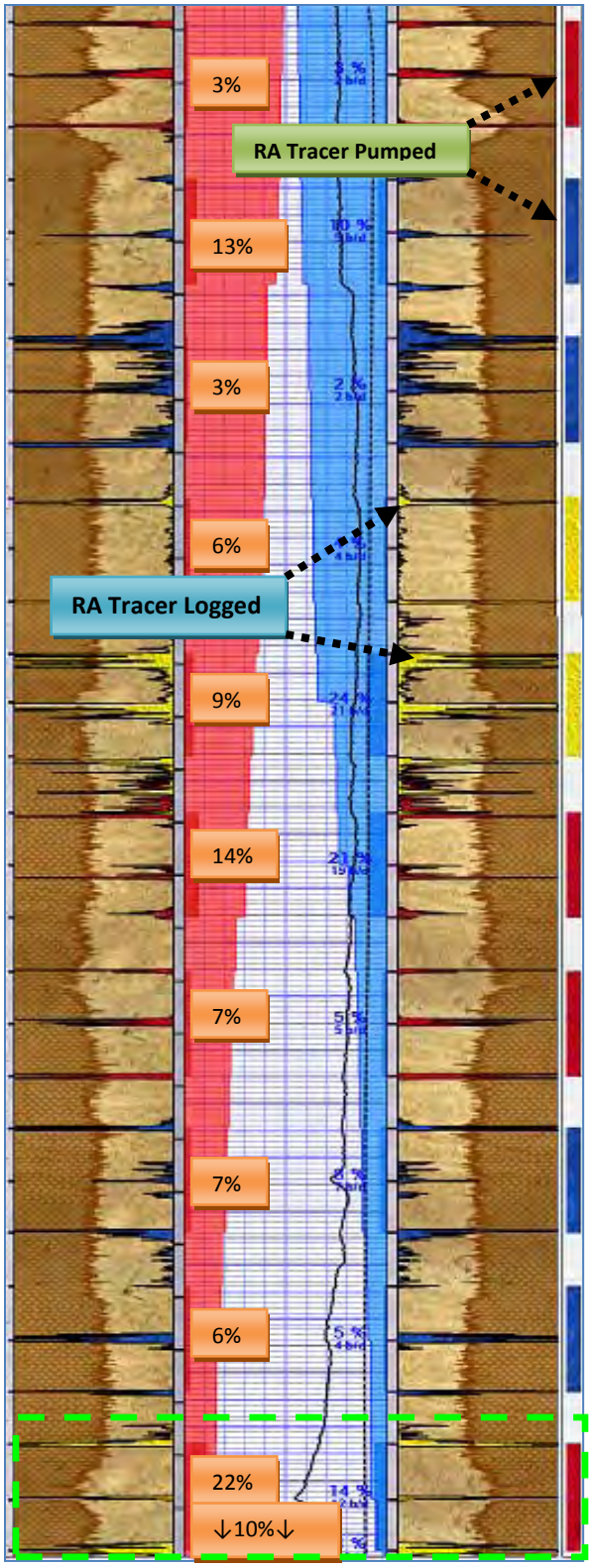

Figure 20: Well-D Production Log Results Overlaid on top of RA Tracer Log

As previously mentioned, the three fracture stages that exhibit the erratic pressure response in three separate wells all lie mostly in a line as shown in Figure 21.

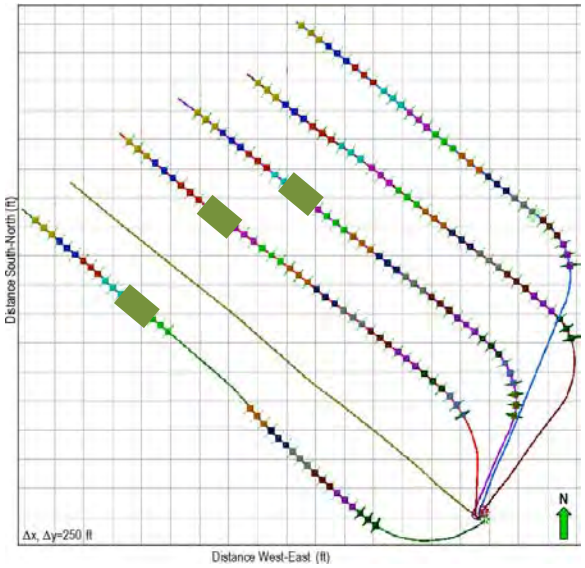

Figure 21: Fracture Stages that Exhibit an Erratic Treating Pressure Response (Green Boxes)

Microseismic events that correspond to these three particular fracture stages are clustered as shown in Figure 21, and indicate that there is in fact a local phenomenon that could point to a swarm of natural fractures that caused the erratic surface treating response and a much higher than average production rate from well D stage 4 frac. As evidenced in Figures 13 and 14, there are areas of concentrated microseismic events that could suggest other swarms of natural fractures. However the erratic treating pressure response is not clearly visible in other fracture stages besides the ones mentioned previously in this discussion. It is not clear at this point accounting for pump rate fluctuations and friction reducer concentration changes what operational parameters could be causing this difference in the pressure response.

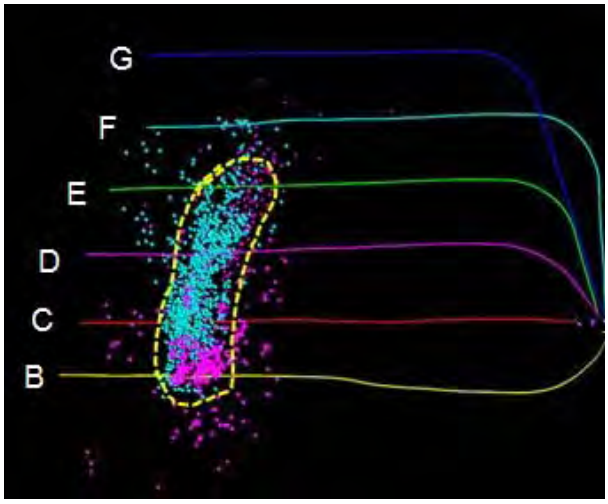

Figure 22: Microseismic Events from Well-B Stage 5 Frac, Well-D Stage 4 Frac, & Well-E Stage 5 Frac

Furthermore, microseismic events from Well D stage 4 frac (blue dots in Figure 22) traverse wells C, B and E. This could further be an indication of a group of natural fractures as the fracturing fluid was able to dilate the natural fractures and propagate farther than it would have in the absence of the inferred natural fractures.

In the next phase of this project, microseismic event source mechanism will be evaluated in order to determine if the signal was generated by shear or tensile failure, indicating whether a natural fracture was dilated or a new hydraulic fracture was created. In addition, check shot seismic velocity will be compared for adjacent frac stages to determine the extent of natural discontinuities that are present. The idea is that if there are concentrated local swarms of natural fractures, the seismic velocity should considerably slow down.

One of the project objectives was to determine the optimal fracture treatment design based on production results. Although a production log is only available from well D, total production from wells D, F, C, E and G is available. In this set of wells, three distinct frac designs were pumped as mentioned previously and shown in Figure 4. Because all of the wells had different completed lateral lengths it would be difficult to interpret which fracture treatment had the best impact on production. However, when gas production is normalized to the length of the completed lateral, a clear picture emerges.

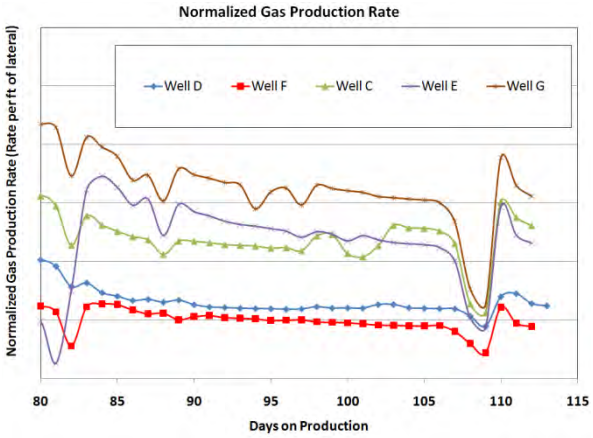

Figure 23: Normalized Gas Production Rate

Figure 23 shows the normalized gas production on a per-foot of completed lateral from 5 wells; well D, F, C, E, and G. Production from the other two wells, well A and B, was not available. The fracture treatment that was pumped in well G had 75% more proppant per foot than wells D, F, C, and E. Perhaps that's why it has the highest production rate on a per-foot-basis of completed lateral. It is not clear if well's G higher production rate is solely a result of higher proppant concentration since there is no well that offsets it immediately to the East. Thus, the only other well that is competing for gas reserves will well G is well F. In the case of the middle wells, wells B, C, D, E, and F, each well has an offset well both to the East and West. However, based on previous experiments performed by Range Resources (Curry et al. 2010), higher proppant amounts and concentrations lead to improved production rates and higher ultimate recoveries (EUR).

Because this is early production data, only after about 115 days on production, inference of long term production and ultimate recovery cannot be accurately assumed. Additional analysis of production will be made as more production data becomes available and a second production log is completed in well D within the next six months.

Stimulated Reservoir Volume (SRV) is another important parameter to consider when evaluating stimulation effectiveness relative to production rates. The drawback of making conclusion from SRV is that it is a calculated value based on microseismic event occurrence and distribution. Moreover, it is difficult to predict which microseismic events correspond to a producing portion of the reservoir, since some events are generated in reservoir locations that will never be connected to the wellbore due closure of un-propped fractures or insufficient fracture conductivity. Other factors that can affect SRV are low microseismic event count resulting from background noise and event magnitude being below the detection threshold.

Nonetheless, we were able to determine the SRV for each of the stimulated wells that were monitored with the borehole microseismic system. Figure 24 shows the estimated SRV cloud for well D. Based on the location and extent of the SRV cloud it would be logical to conclude that different portions of the well would produce at different rates and in fact that is true. Utilizing the production log results from well D, it is possible to overlay the gas production contribution from selected well depths on top of the SRV cloud, as shown in Figure 23. Well locations corresponding to 22% and 14% of total production have a well developed SRV cloud, while locations with a production contribution of 6% and 3% have a very small SRV cloud. The location of the well that shows a 13% production contribution does not have a well developed SRV cloud, yet production from this zone is the third highest in the well. Frac stages 1 through 3 together contribute 10% to the total production of well D even as the SRV cloud toward the toe of the well is well developed.

We are beginning to see more anomalies related to the estimated SRV volume and production rates, like the one just discussed, but on a larger scale. Figure 25 shows the total calculated SRV for each well that was monitored utilizing borehole microseismic along with the normalized gas production rates (which is a data subset of Figure 23) after the wells have been 100 days on production. Left vertical axis corresponds to the calculated SRV while the right vertical axis shows the normalized gas production rate.

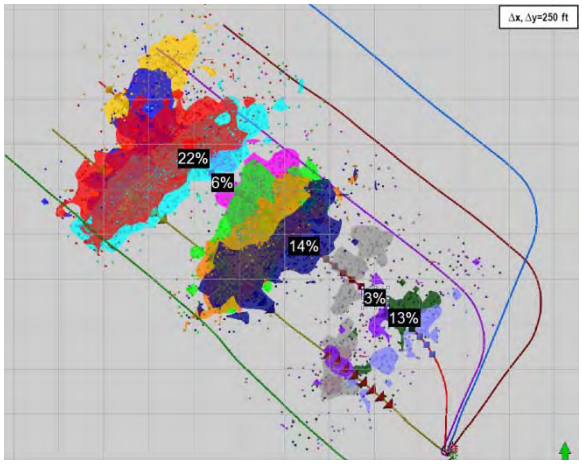

Figure 24: Estimated SRV Cloud from Well-D and Associated Gas Production Contribution

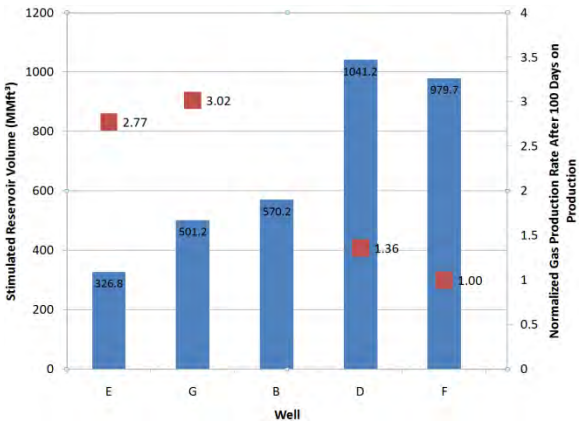

Figure 25: Stimulated Reservoir Volume Calculated from Borehole Microseismic Survey

What is very interesting is that the production rates in wells E and G are almost triple the production rates in wells D and F although the calculated SRV in wells D and F is much higher than in wells E and G, almost double in magnitude. Production data for well B was unavailable. These types of anomalies demonstrate that the calculated SRV by itself is not always reliable and other factors need to be considered in order to predict production.

In multi well scenarios such as this one, the SRV cloud crosses multiple wells and it is difficult to predict how much of one well's SRV cloud contributes to another well's production. A true measure of SRV's impact on production can only be calculated for a single well if production and SRV clouds from nearby wells do not merge.

Summary of Ongoing & Future Work

Data analysis is ongoing and as more data becomes available it will be compared and evaluated in order to make meaningful correlations that can predict the influence of various parameters on production. There is strong evidence that natural fractures at this experiment site manifest themselves in concentrated swarms and have a profound impact on gas production. In support of this discovery, future work will aim to determine the source mechanism of the microseismic events in order to find out if the signals are generated by breaking new rock or dilating natural fractures, or both. Subcritical Crack Index testing may also confirm the spatial characteristics of the natural fractures, the testing will commence as soon as cores from the test site are available. In addition, it may be possible to compare perforation check shot velocity variations in order to determine areas of decreased velocity that might result from concentrated natural discontinuities such as clusters of natural fractures.

Acknowledgement

*We would like to thank **RPSEA** for providing funding for this much needed research project.*

*In addition, we also express our thanks to **Range Resources** for providing substantial cost sharing, data, and wells of opportunity and **Schlumberger** for their generous cost-sharing.*

References

1. **Harper, J., Laughrey, C., Kostelnik, J., Gold, D., Doden, A.** *Trenton and Black River Carbonates in the Union Furnace Area of Blair and Huntingdon Counties, Pennsylvania : Introduction.* s.l. : Pennsylvania Geological Survey, 2004.

2. **Milici, R., Swezey, C.**, *Assessment of Appalachian Basin Oil and Gas Resources: Devonian Shale–Middle and Upper Paleozoic Total Petroleum System. Open-File Report Series 2006-1237.* United States Geological Survey, 2006.

3. **Holder, J., Olson, J., Philip, Z.,** *Experimental determination of subcritical rack growth parameters in sedimentary rock,* Geophysical Research Letters, Vol. 28, No. 4, pages 599-602, University of Texas at Austin, February 15, 2001

4. **Singh, V., Roussel, N., Sharma, M.,** *Stress Reorientation Around Horizontal Wells*, SPE-116092. s.l. : Society of Petroluem Engineers, 2008.

5. **Moschovidis, Z., Steiger, R., Peterson, R., Warpinski, N., Wright, C., Chesney, E., Hagan, J., Abou-Sayed, A., Keck, R., Frankl, M., Fleming, C., Wolhart, S., McDaniel, B., Sinor, A., Ottesen, S., Miller, L., Beecher, R., Dudley, J., Zinno, D., Akhmedov, O.,** *The Mounds Drill-Cuttings Injection Field Experiment: Final Results and Conclusions*, SPE-59115. s.l. : Society of Petroluem Engineers, 2000.

6. **Curry, M., Maloney, T., Woodroof, R., Leonard, R.** *Less Sand May Not Be Enough SPE-131783.* s.l. : Society of Petroluem Engineers, 2010.

Appendix B – Comparison of Surface and Borehole Microseismic

Evaluation of Surface and Downhole Microseismic Event Analysis Consulting Report Compiled by Dr. James Rector

Overview

In January and February of 2011 Range Resources conducted a microseismic monitoring experiment on a series of horizontal wells that were drilled and stimulated in the Marcellus Shale. Seismic sensors were placed in a dense surface array that was stationary for all stimulated wells. In addition, seismic sensors were placed in one of the horizontal wells and the sensors were moved during different stages of the stimulation so that the stimulated zone in each well was roughly at the same horizontal position along the borehole as the sensors. Reports were generated for each stimulated well for both the surface array (Microseismic Inc), and the downhole array (Schlumberger). These reports summarize estimated characteristics of the microseisms such as event location and event time relative to treatment history. Each report also estimated a stimulated volume of rock. In addition to these common characteristics, the data from the surface array were used to estimate event focal mechanism and event magnitude.

The objectives of this report are to dig deeper into the contractor reports and evaluate the derived microseismic event locations in terms of the receiver geometry and the impact of these locations on inferred fracture dimensions and stimulated volumes. In addition the report will evaluate the advantages and disadvantages of each system with regards to event location uncertainty and the factors that affect this uncertainty (e.g. velocity model, event type, focal mechanism, signal to noise ratio, raypath complexity/uncertainty, frequency content and receiver characteristics). Finally, recommendations will be made for improved hydrofracture microseism characterization.

Surface Acquisition and Event Location Analysis

Slide 1 shows the well geometry and surface array configuration for the surface acquisition of microseisms. Overall, 435 total hours were recorded. Ninety-three fracture treatments comprising 254 hours (approximately 2.5 hours per stage) were recorded by the surface array In addition, 93 Perf/Plug Stages and 264 perforation shots were recorded. The horizontal wells were located at approximately 6,850 ft TVD from KB and all depths were measured relative to KB. The inability to deploy geophones directly above some of the stimulation wells and the bias of geophone locations toward the northwest of the stimulation wells is similar to a seismic survey with irregular and biased sampling. It is well known that such survey geometries can result in migration smearing and bias of focus location. To properly characterize these effects would require forward modeling with a subset of the inferred source locations, magnitudes, frequency content and mechanism along with the surface geophone locations.

A summary of surface background noise levels was provided. Background noise values were calculated by percentile of 1 second rms values over the data. Values are given by day and by stage. Average values are given at the 50^{th} percentile. The average noise level for the project was 31.5 dB by day (averaged over 24 hours). The average noise level for the project was 31.8 dB by stimulation stage (averaged over the different stimulations). There was no other discussion of this in the final report and therefore other than relative db measurements or without using Microseismic Inc's own internal noise database, it is unclear what this

measurement means. Moreover, a db measurement represents all frequencies and could be quite different if it were not filtered to the frequency range used in the microseismic analysis (10-60 Hz).

The velocity model used for event focusing and location was constructed from a VSP in a nearby vertical well without the aid of 3-D seismic. Based presumably on the perf shot data, the entire velocity model was increased 36%. This is very strange. I do not see how a velocity model 36% higher than a known 1-D velocity model near the treatment well can be viewed as valid. Assuming that the VSP velocities are correct, one must ask how and why the velocity field from the perf shot data are 36% higher than a well constrained velocity function from a VSP. However, Slides 2 and 3 show the nmo'd perf shot calibration data for two perf shot events and Slide 4 shows a stronger microseismic event after nmo correction. The adjusted velocities (36% higher than VSP derived velocities) appear to align the first-arriving events quite well, suggesting that the velocity model is largely 1-D and that the velocity adjustment is warranted. The only possible explanation that I can think of in this adjustment is that the VSP velocity versus depth function was assumed to be a subsea depth. If the depth were actually TVD the velocity would have been underestimated and the true velocity would be approximately 1/3 higher which closely resembles the 36% increase applied.

Note also in Slide 4 that there are events with negative moveout for increasing offsets. These events are most likely reflections from deeper horizons that propagate with a higher apparent velocity than the primary event. Incorporating these events into event location if 3-D seismic data were available for calibration would potentially be an extremely useful enhancement. Also note that the longer offsets appear to have strong shear (probably shear converted) events. The arrival time difference between compressional and shear (or shear converted) waves has long been used as a useful tool for event location. I am not sure why this approach is not incorporated to obtain a more accurate distance measure unless the absence of near offset shear data or uncertainties in the shear velocity profile make this approach problematic.

In Slides 5 and 6, we can see the results of applying this adjusted velocity model and focusing the energy from the events at different depths. Its important to note in these plots that the vertical scale is Energy, which is amplitude squared. In order to characterize the depth resolution of the technique (without calibration), the data should be presented as amplitude. Various criteria can be used to estimate the depth uncertainty. From the figures provided it appears that a reasonable estimate for depth uncertainty in these very high S/N events is +/- 150 ft. Without calibration information, the event uncertainty may be higher for lower S/N events. If the events are located in the vicinity of large reflectors that are not incorporated into the depth migration there could also be some bias in the event location. Given the velocity model for this area, the events locations may be biased toward deeper positions.

The report also summarizes event locations based on string shots and ball drop events. I believe this summary is misleading. While the event locations correspond remarkably well to the borehole positions I believe (though I have no confirmation), that timing information for the ball drops and the string shots was available. If there were an absolute time reference, the depth resolution would be substantially better than the focusing approach summarized in Slide 5.

Unfortunately, absolute time is not available for the microseismic events. If there were a correlation between downhole and surface microseismic events and the events were located close to the downhole sensors, the sensor timing may be useful in calibration.

Event Location

The event location summaries for each of the wells and each of the wells were reviewed. The objective of this effort was to determine if there were any apparent biases (observed in fracture asymmetry relative to the wellbore) in event location due to the recording geometry. Note that geology and/or local stresses may also account for fracture asymmetry—e.g. it may be real.

Slides 7,8,9,10 show the results for Well A, C, E and G, which were the first wellbores stimulated in sequence. Note that on Well A and C, and G that the higher magnitude events are somewhat biased to the NE of the stimulation well while for Well E the events are biased to the SW. Other than Well C the events generally lie deeper than the stimulation well.

Slides 11,12, show the event location results for Well B, D and 1A which were stimulated subsequently and represent areas where, presumably there have been fractures opened by the initial stimulations in A-G and, potentially modifications of the local in situ stresses. Well B was drilled to a different depth and has a few events that are somewhat chaotic in nature (in the conclusion slide it is noted that the fracture grew down and communicated with earlier states—this is also borne out by the Schlumberger downhole data). Well D and 1A look very similar to Well E and Well G. The event locations appear to be biased beneath the borehole.

It appears that geologic factors may account for the fracture asymmetry in Well E, G, D and 1A. Well C is unique in that it is the only well with event biases above the well. If strong reflecting horizons are present (such as the interface between the Marcellus and the Onondaga), the event times would be biased toward later times and deeper locations would be estimated.

Event Focal Mechanism

Slide 14 is a summary of the focal mechanisms derived from the microseismic data. All focal mechanisms derived were vertical dip slip. This is not surprising given the nature of the recording geometry. The longest source/receiver offsets are approximately twice the depth of the events with most of the receivers confined to less than the event depth. Consequently, most of the radiated P-wave energy from the event would need to have a takeoff angle of less than 60 degrees from the vertical in order to be observed at the surface. There have been a number of recently published studies about the focal mechanisms created by microseisms and the influence of receiver-array geometry and signal-to noise ratios on the types of focal mechanisms that can be resolved (see, e.g. Eaton, et al, 2011, and Du, et al, 2011).Slide 15 and 16 are summaries of the radiation patterns from different types of source mechanisms and a Source/Type diagram. The only types of mechanisms that would likely be recorded by vertical geophones at the surface would be vertical dip slip events. Horizontal strike slip events and tensile fractures would be virtually impossible to observe at the surface (Slide 17). Moreover, CLVD events (combination of double couple source and volumetric change would only be

observed if the surface array were oriented perfectly. Unless a very dense 3-D array were deployed this mechanism would not be observed at the surface.

In most studies it is emphasized that in order to obtain a good focal mechanism solution for all possible types of events, it is necessary to have a recording geometry where both P waves and S-waves are recorded across a wide range of solid angles. With only a surface array geometry or a downhole geometry, only limited types of focal mechanisms will be discernable and therefore there may be inconsistencies between the events recorded by each.

Conclusions

Microseismic Inc. concluded that there was communication between individual fracture stages in a particular well, and that some well (A C and B) exhibited communication. The average fracture height was estimated to be 380 ft and the average fracture length was estimated at 930 feet with a SRV value of about 225,000 acre feet. None of these inferences take into account event location uncertainty.

Given that the event depth uncertainty is about 150 ft I would have preferred the conclusions to show a mean height and a variance (e.g. 380 ft +-150 feet). Similarly, it would have been useful to show a horizontal position uncertainty. Without seeing the focusing results it is difficult to evaluate the validity of the estimated length. One measure of horizontal resolution is a ½ Fresnel Zone, another is a 1/4 wavelength (Rayleigh's resolution criteria). A common measure that I think is useful is something in between. . For this data, an approximate ½ Fresnel zone is 800 ft and an approximate 1/4 wavelength is 100 ft. Taking the mean of these two numbers would yield a horizontal resolution of about 450 ft. Thus the fracture half length would be estimated at 930 ft +-450 ft. This estimate would be appropriate without calibration data. Given that there are perf shot events, the half length uncertainty may be an upper bound.

In addition to the uncertainty in fracture height, width and length, the extrapolation from event magnitude and density to SRV is very tenuous. It requires the assumption that a microseismic event in a particular cell is directly related to potential flow. It is well known in the literature that many rock fracture mechanisms, particularly focal mechanisms that do not have a volumetric component may not result in potential flow. Ignoring the uncertainty in fracture dimensions the SRV values are thus likely to be overestimated. These conclusions are summarized in Slide 17.

The report itself lacks many details such as velocity model compensation reasons, raypath summaries, example data demonstrating focal mechanisms, raw data examples, spectra, and event uncertainty/bias ellipsoids. These data would be quite useful to a geophysicist attempting to evaluate the validity of the findings and the results.

There are a number of particular observations, that if addressed, that would better help characterize events:

- The inability to deploy geophones directly above some of the stimulation wells and the bias of geophone locations toward the northwest of the stimulation wells is similar in concept to a seismic survey with irregular and biased sampling. It is well known that such survey geometries can result in migration smearing and bias of focus location. To properly characterize these effects would require forward modeling with a subset of the inferred source locations, magnitudes, frequency content and mechanism along with the surface geophone locations.

- The arrival time difference between compressional and shear (or shear converted) waves has long been used as a useful tool for event location. Given that there are apparent long offset shear converted wave data, I am not sure why this approach is not incorporated to obtain a more accurate distance measure unless the absence of near offset shear data or uncertainties in the shear velocity profile make this approach problematic.

- In order to characterize the depth resolution of the technique (without calibration), the focusing results (Slides 5 and 6) should be presented as amplitude. Also, various criteria can be used to estimate the depth uncertainty. From the data provided it appears that a reasonable estimate for depth uncertainty for these very high S/N events is +/- 150 ft. Without calibration information, the event uncertainty may be higher for lower S/N events. If the events are located in the vicinity of large reflectors that are not incorporated into the depth migration there could also be some bias in the event location. Given the velocity model for this area, the events locations may be biased toward deeper positions.

- The types of mechanisms that would likely be recorded by vertical geophones at the surface would be vertical dip slip events. In order to obtain a good focal mechanism solution for all possible types of events, it is necessary to have a recording geometry where both P waves and S-waves are recorded across a wide range of solid angles. With only a surface array geometry or a downhole geometry, only limited types of focal mechanisms will be discernible and therefore there may be inconsistencies between the events recorded by each.

Downhole Acquisition and Event Location Analysis

I received summary reports for downhole data recorded by Schlumberger from stimulations performed in the E, G, D and 1A wells. In addition I received a summary file that documented the number of events, the interpreted fracture top and bottom, the interpreted stimulated length, the interpreted stimulated azimuth and the interpreted stimulated volume for each of the stages in these wells along with each stage in the B well. The only information about the data acquisition that I was given is shown in Slide 18. The C well was used as the monitor well and an 8 element (100 ft between elements) geophone array was used to collect the data. The array was moved 5 times during the acquisition to positions roughly perpendicular to the stage being stimulated. There was no information in the reports on the exact location of the arrays. I was

informed that both P and S waves (polarizations unknown) were to find event azimuth relative to each receiver. Using the anisotropic velocity model (Slide 19), the differential traveltimes between the P and S waves were used to backproject along the measured orientation and the direct raypath assumed by the velocity model. Only the direct arrival was used. No attempt was made to incorporate head waves or other events. Given the low velocities in the shale, it is possible that head waves and reflection arrivals may affect the measured direct arrival times and, potentially the measured polarization although without the actual data this hypothesis cannot be confirmed or denied. In a recent study by Zimmer (2011), the effects of location uncertainty using just first arrivals as opposed to using direct arrivals. Shear waves were not incorporated into this analysis. For longer distances using direct arrivals only, event location uncertainties increase.

The only information on event magnitude was a summary QC plot for each of the stimulated wells monitored Slides 20-23, which showed a range of event magnitudes for each estimated distance from the geophone array along with a S/N threshold for each stimulated well. Note that the S/N and the event magnitude threshold was held constant except for the most distant well (G) where the event magnitude was allowed to be slightly lower and the S/N was larger. In these figures we see a S/N histogram that depicts event count versus some unknown attribute (presumably S/N). Presumably the events are fractally distributed in event magnitude and the lower S/N events are more numerous than the higher S/N events. There is no information in the report depicting event magnitude as a function of location.

Slides 24-27 show side and map views of the event locations for each of the stimulated wells, color coded by event stage. From the cross-sectional views it is apparent that the events are centered around the stimulation depth, with a slight tendency for the events to extend further downward than upward. The wells closer to the receiver well (D and E) have substantially more variation in the vertical positioning of events than do the wells more distant from the receiver well, which are tightly grouped around the stimulation depth. One question that obviously arises is whether these differences are due to real fracture differences or whether they are due to some other factor. A recent RPSEA Topical Report (Ciezobka, August 16, 2011) concluded that there may be a natural fracture swarm in the vicinity of wells D and E. This natural fracture swarm could explain the larger distribution of event locations as fluids move away from a primary fracture zone.

Alternatively, there may be other factors at play. From the Zimmer study cited above the event locations should exhibit more uncertainty with increasing distance. Therefore, I believe the increased event scatter for nearby stimulation wells may due to interference effects. In the data example cited by Zimmer (2011), it is easy to distinguish the head wave and the direct arrival based on arrival time. As the path length shortens, the differential arrival times shorten and there may be substantial interference effects between the direct and the head wave arrivals. This is particularly true because the low velocity interval is relatively thin and the velocity contrasts are large. Without the benefit of examining the real data, these interference effects could be a contributing factor to the large scatter observed on D and E stimulations. This could also affect inferred direction.

Slides 28-31 show map views of the event locations. It does appear that the event clouds are asymmetric about the treatment well. This is more apparent when examining the map views of the stimulated volumes where all the fractures appear heavily one sided. While this may be a real effect, it is more likely that the more distant microseisms that define the NE wing of the fracture are below the S/N threshold. Thus the apparent fracture asymmetry is most likely due to event S/N and not geology.

Focal Mechanisms

Without any real data it is difficult to determine what the fracture focal mechanism is. Schlumberger made no attempt in its report to address this issue. As a generalization on the types of events we might expect to observe on the different geophone components, we can refer to Slide 15. It would appear that with the downhole recording geometry employed, that strike slip focal mechanisms oriented perpendicular to the treatment wells would result in P-waves recorded on the oriented horizontal component with little shear wave energy (either SV or SH). Dip slip events oriented perpendicular to the treatment wells would result in SV waves observed on the vertical component and minimal P-wave and SH energy. Given that it was reported that both P and SV waves were used in the event locations, it is possible that the focal mechanisms were a combination of dip and strike slip event. It could also be possible that the strike slip event had some component of fracture opening or closing. Tensile events oriented perpendicular to the treatment wells would result in SH waves on the horizontal component oriented along the receiver wellbore with little P-wave or SV wave energy.

Conclusions

Without real data examples it is difficult to evaluate the reliability of event locations or their uncertainty and it is impossible to evaluate potential focal mechanisms. This is particularly true if there are substantial interference arrivals. Ignoring these potential interference effects and assuming a reliable velocity model the downhole-derived event locations should have substantially less uncertainty than the surface-derived locations. Assuming a center frequency of 100Hz and path lengths ranging from 0 to 1000 ft, we would expect that the Fresnel zones would range from 0 to 100 ft. Event location uncertainty would be expected to be a fraction of that should therefore be a fraction of that assuming no interference effects. It is quite clear from the event location asymmetry that S/N has a major impact on the inferred fracture geometry and it is unlikely that the fractures are as asymmetric as depicted in the downhole event data.

Reconciliation of Surface Microseismic and Downhole Microseismic

A recent study by Eisner, et al (2010) compared event locations derived from surface and downhole microseismic data. Unlike the current study, the downhole recordings were made in a vertical well.

A small subset of high-S/N events with similar origin times were identified and were determined to be almost certainly associated with the same microseism recorded on both the surface array and the downhole array. One of the most interesting findings of the study was that the location uncertainty was comparable between the two receiver geometries. In fact, the downhole

locations had more vertical scatter than the surface locations. As in the current study, I believe that this effect may be due to arrival interference although without any real data it is impossible to confirm this hypothesis.

In theory downhole event location should have much less uncertainty than surface event location. However, theory assumes minimal interference and high-S/N. It is well known in crosswell surveys that the direct arrival is often impossible to identify when the receiver is located at a similar depth to the crosswell source. This is particularly true when both source and receiver are located in low velocity rocks. Likewise, if the microseismic source were located in low velocity rocks, there may be a problem with identifying the direct arrival event in the geometry used in the Well Study.

Recommendations

It is quite clear from the studies that an effort to reinterpret the downhole and surface data and integrate into a composite study would be beneficial. In particular the following general investigations are suggested:

- Analysis of downhole microseismic events and integration with finite difference forward modeling through a realistic velocity model and with realistic focal mechanisms to better define downhole event location uncertainty and focal mechanism sensitivity
- Integration of non direct arrivals such as shear arrivals and P reflections from surface microseismic events to better define event location and focal mechanisms along with characterization of acquisition geometry on event location uncertainty and bias
- Identification of coseismic events and reconciliation of same to better compare surface and microseismic event locations.

References

Eaton, et al, 2011, Solid angles and the impact of receiver-array geometry on microseismic moment-tensor inversion, Geophysics, 76, 6, WC77-WC85.

Eisner, et al, 2010, Comparison of surface and borehole locations of induced seismicity, Geophysical Prospecting, 58, 809-820.

Zimmer, 2011, Microseismic design studies, Geophysics, 76, 6, WC17-WC25.

Surface MS Geophone Lines

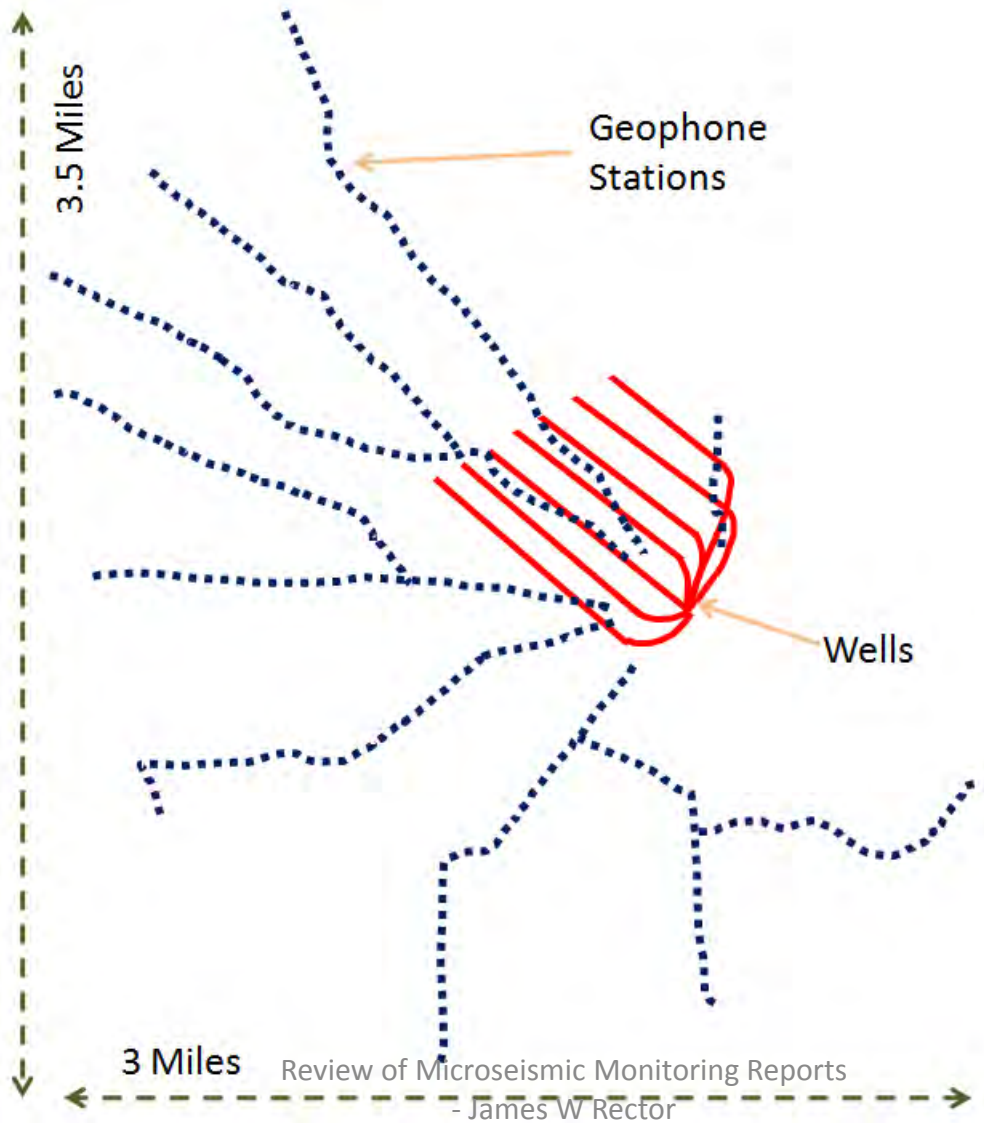

Review of Microseismic Monitoring Reports
- James W Rector

Perf Shot After NMO

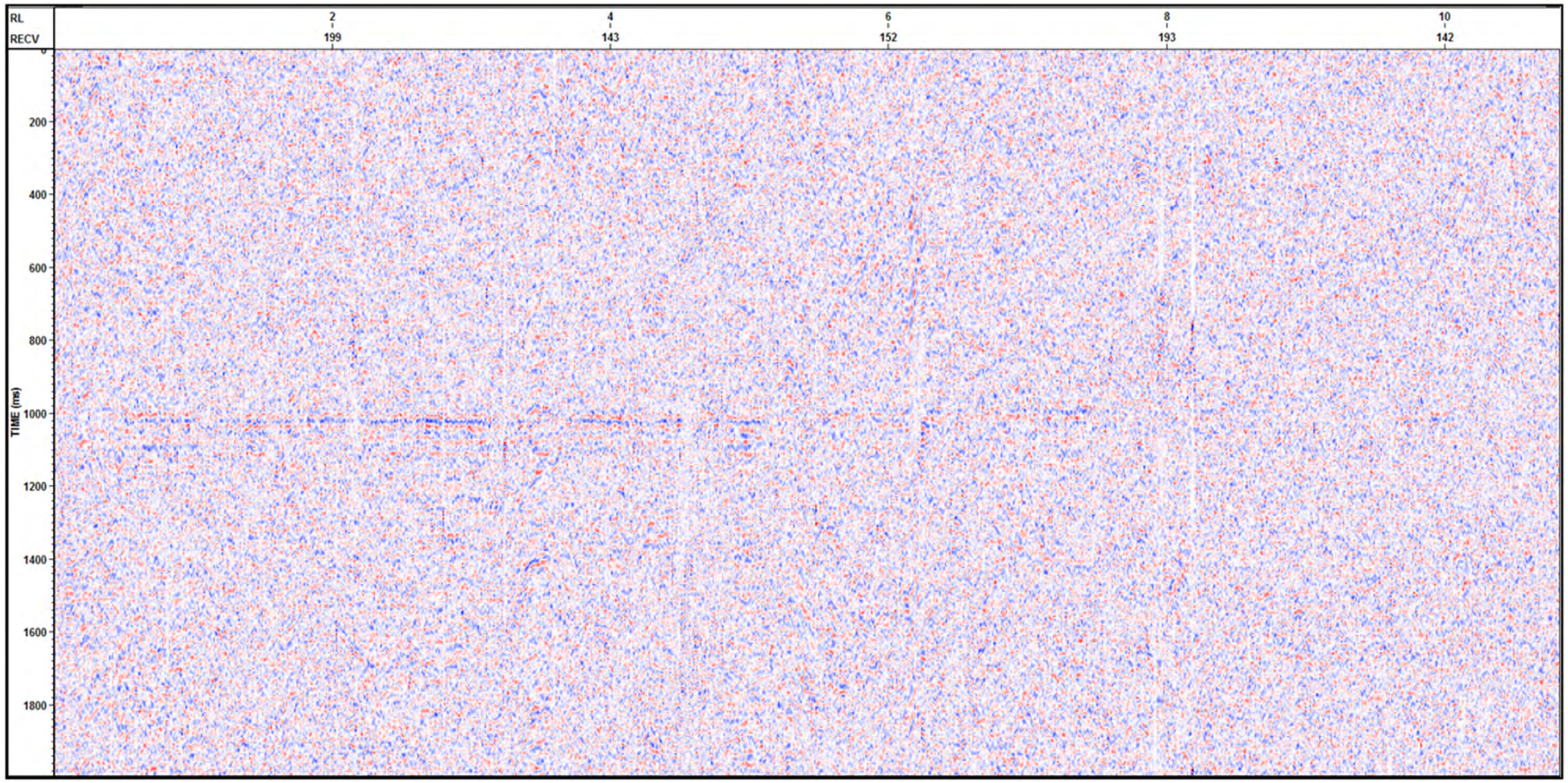

Perf 2

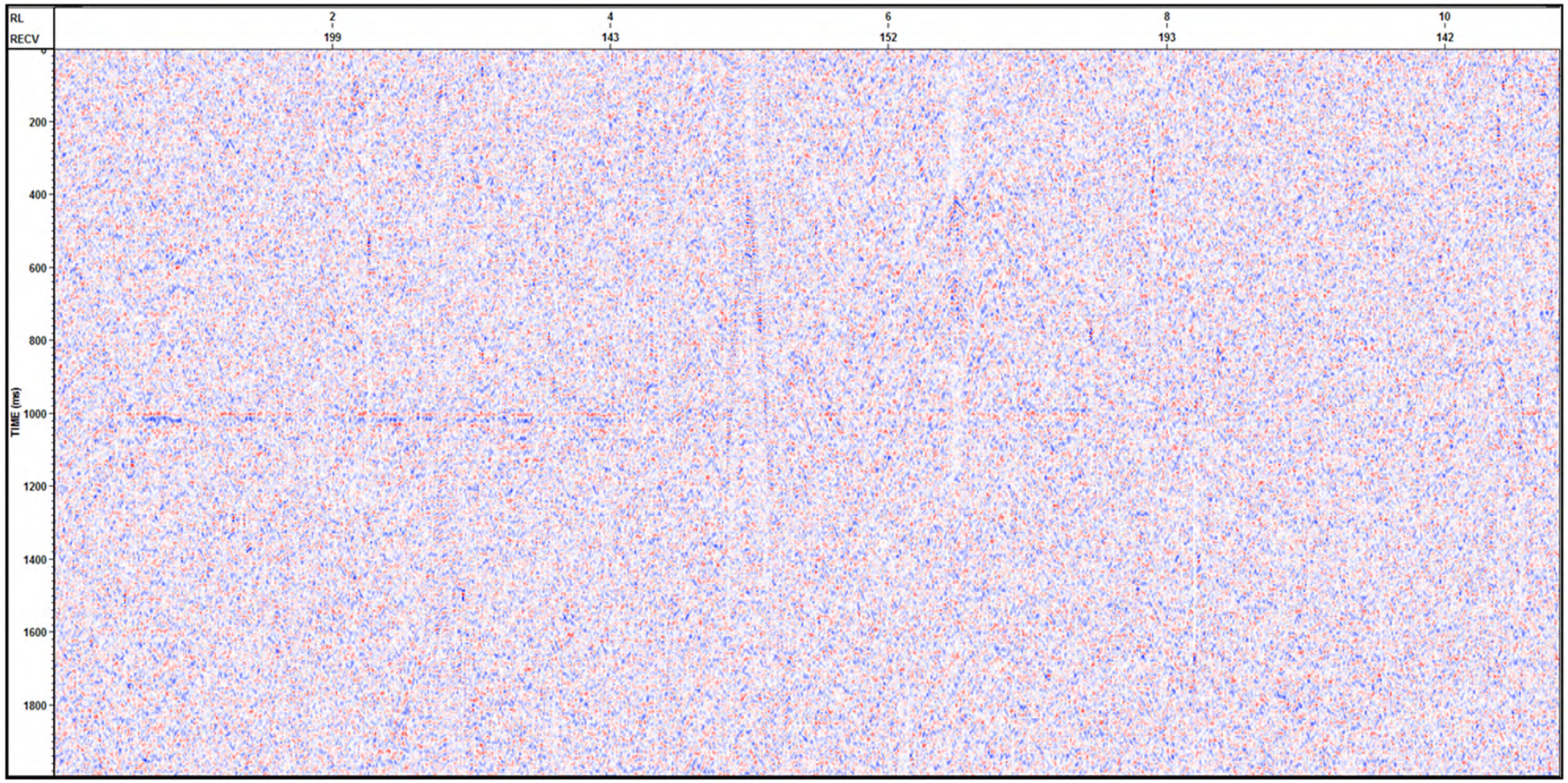
RL
RECV
2
199
4
143
6
152
8
193
10
142
TIME (ms)
200
400
600
800
1000
1200
1400
1600
1800

Large MS event

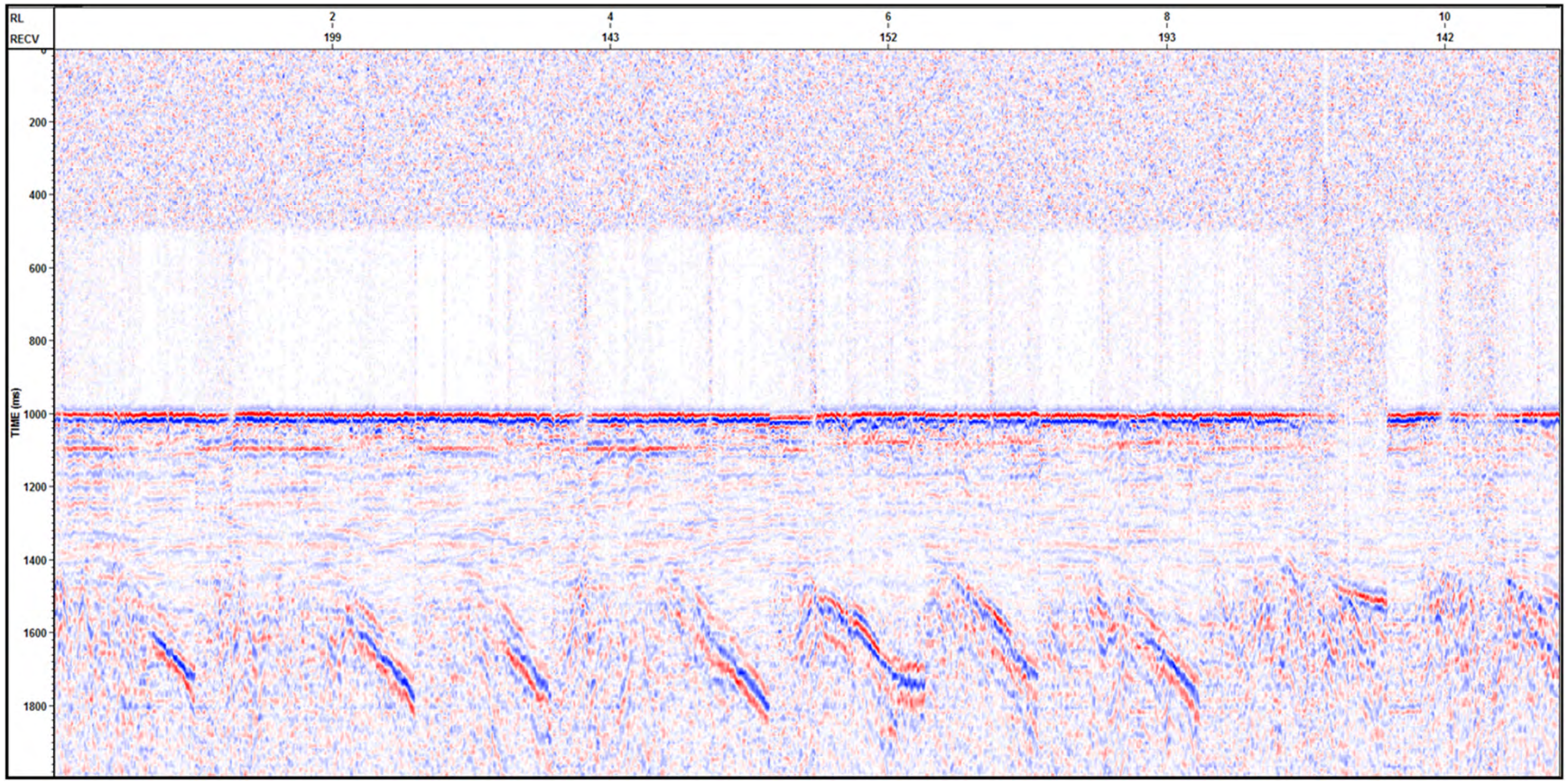

Focused Event Energy Versus Depth

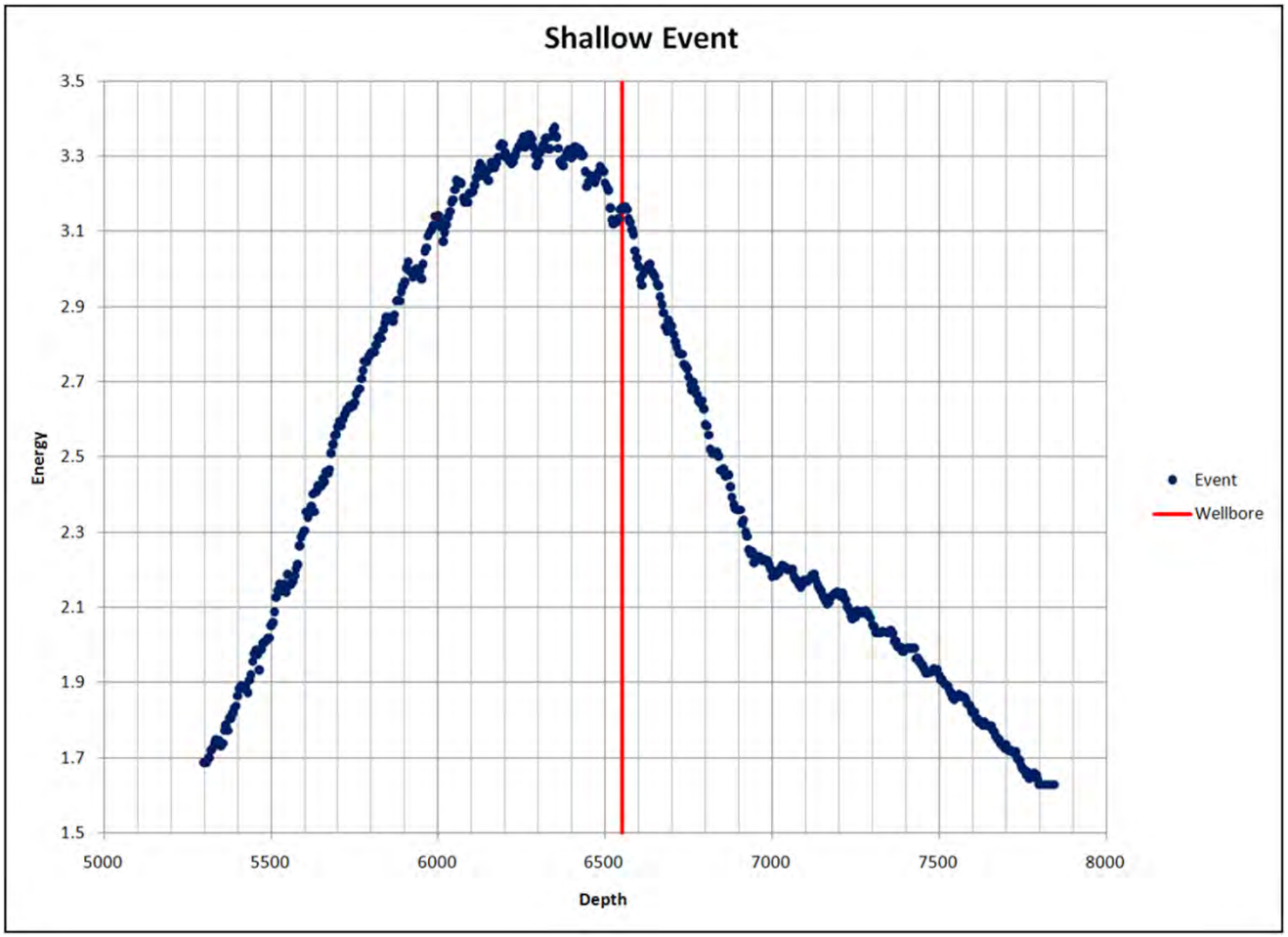

Focused event energy versus depth

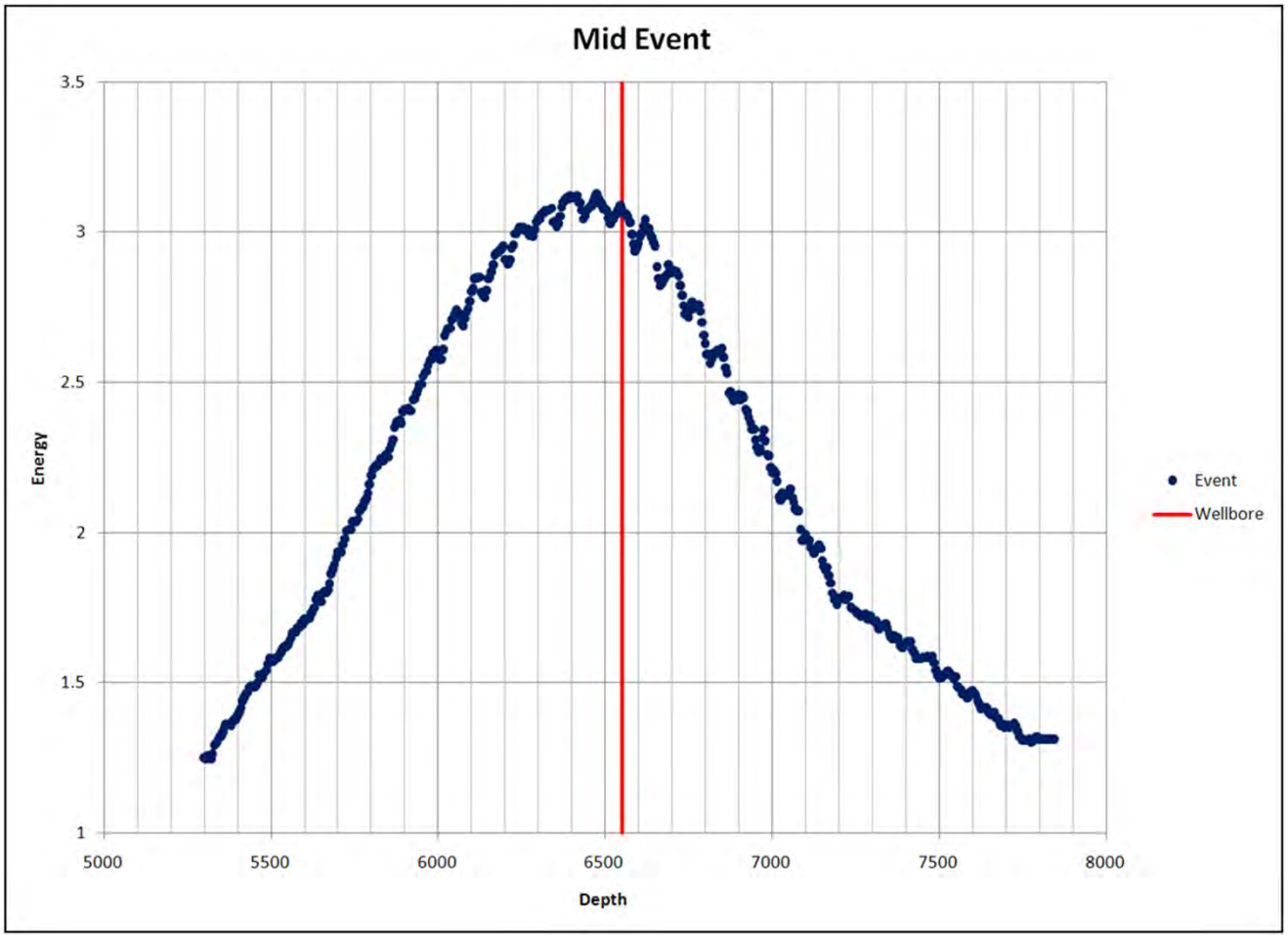

Event Locations Well A

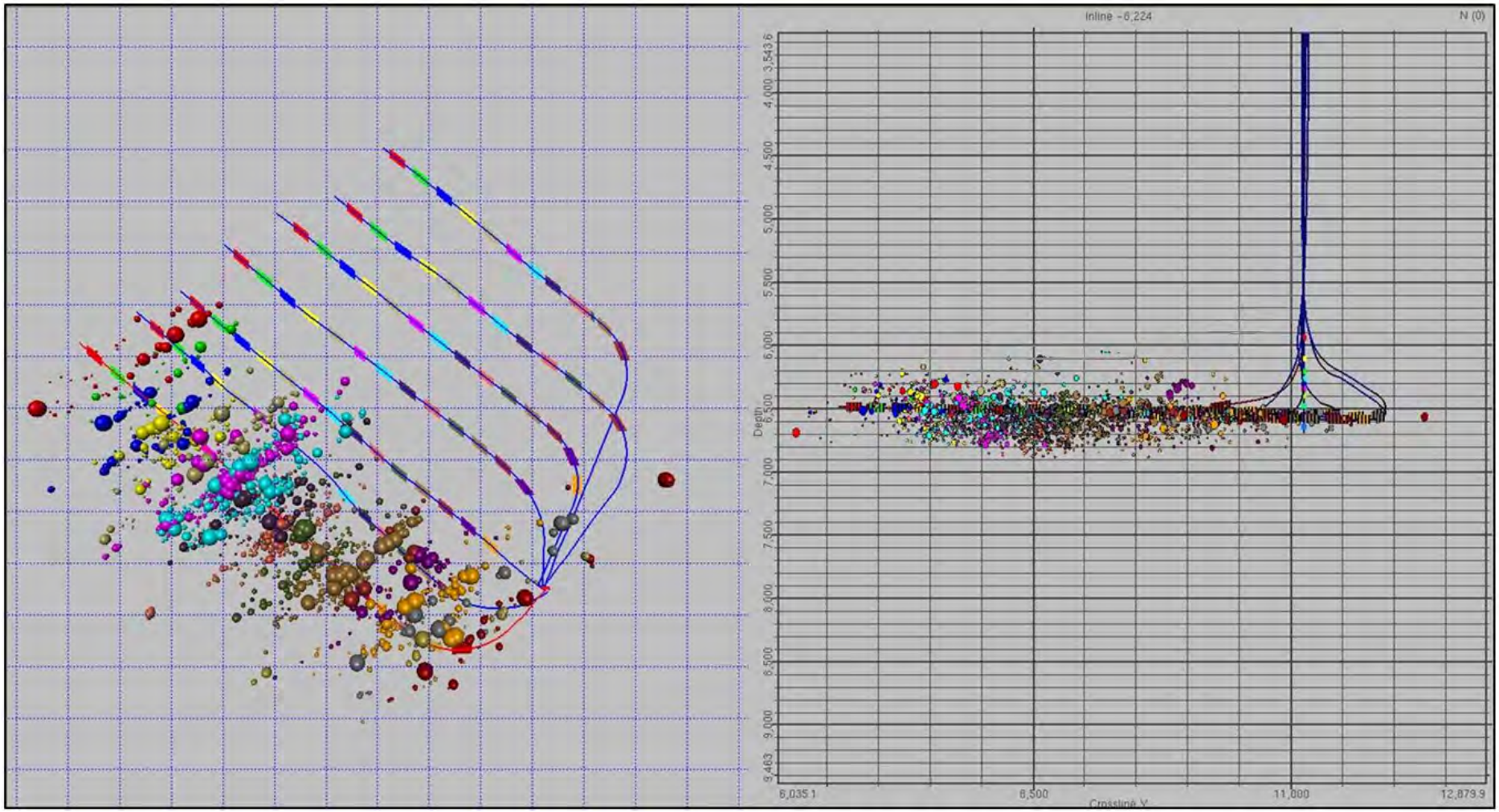

Event Locations Well C

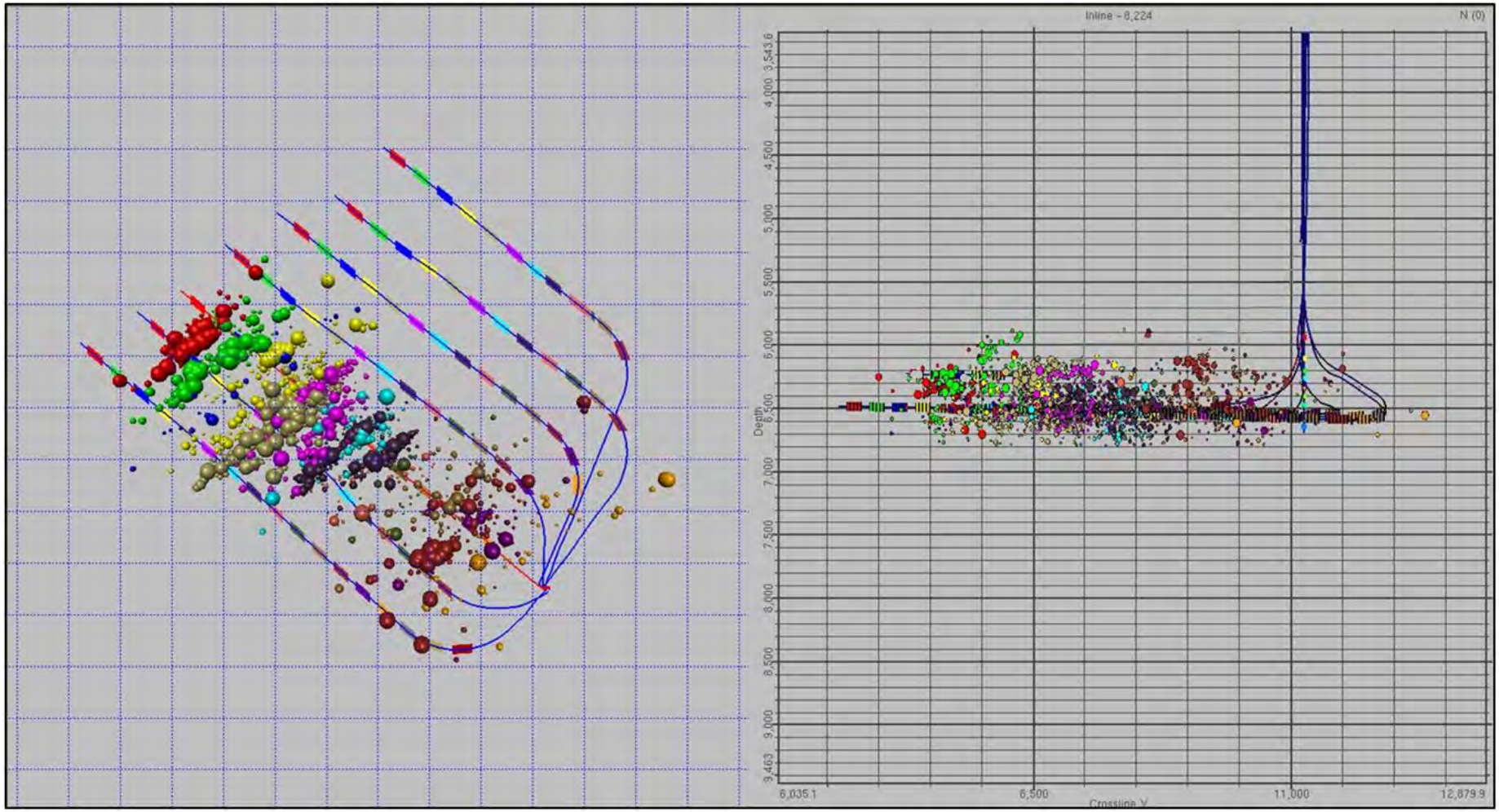

Event Locations Well E

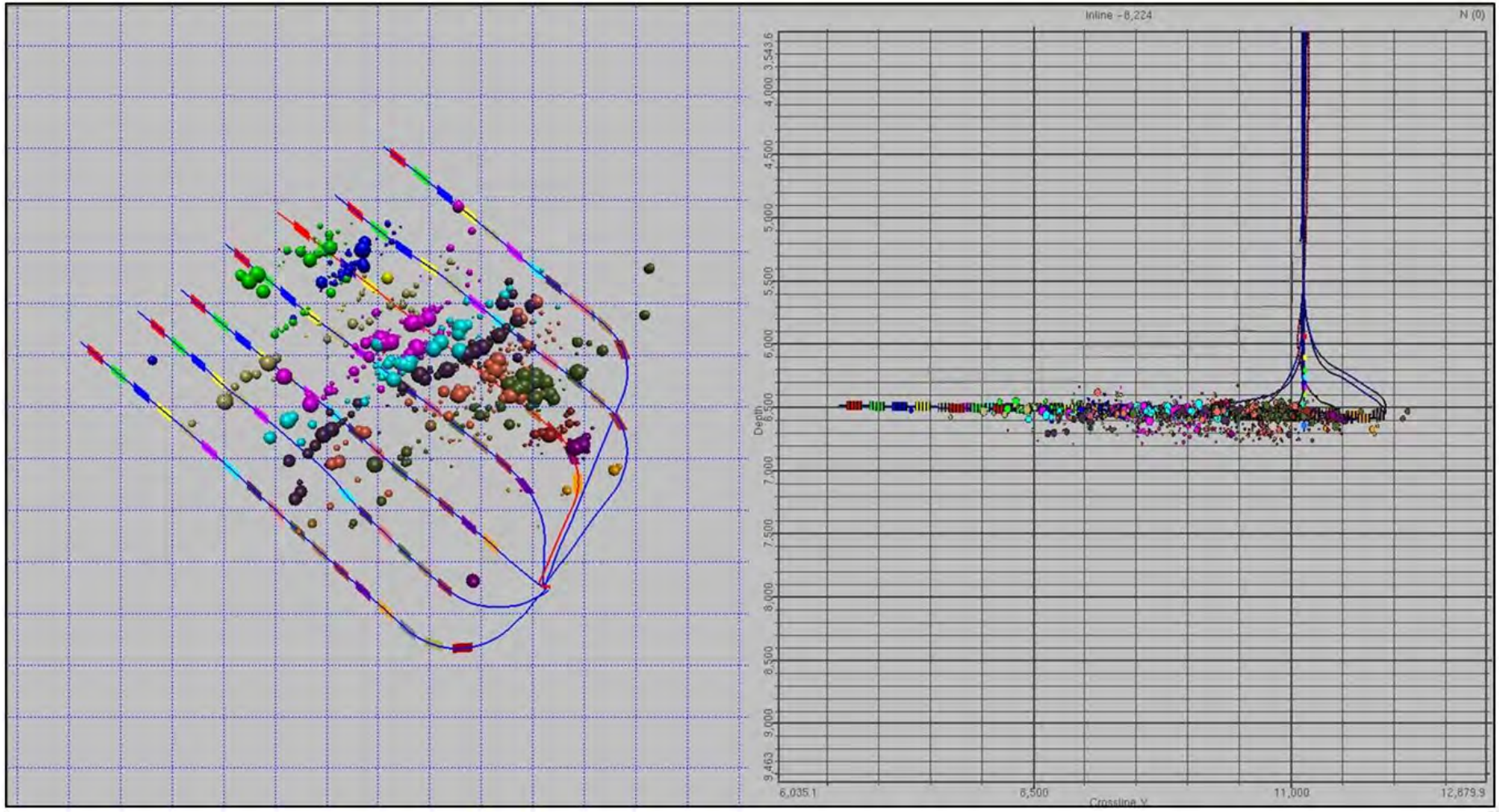

Event Location Well G

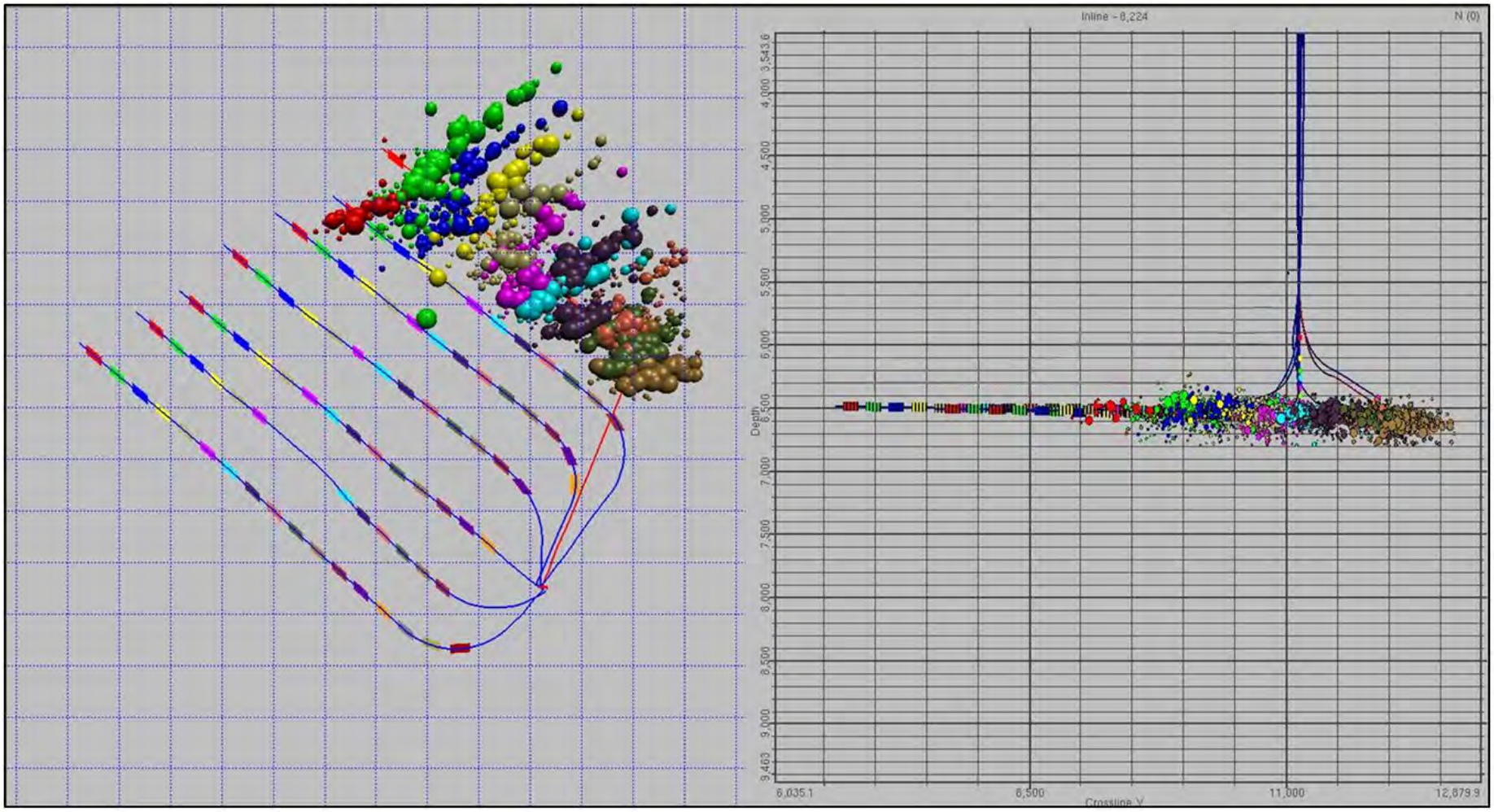

Event Locations Well D

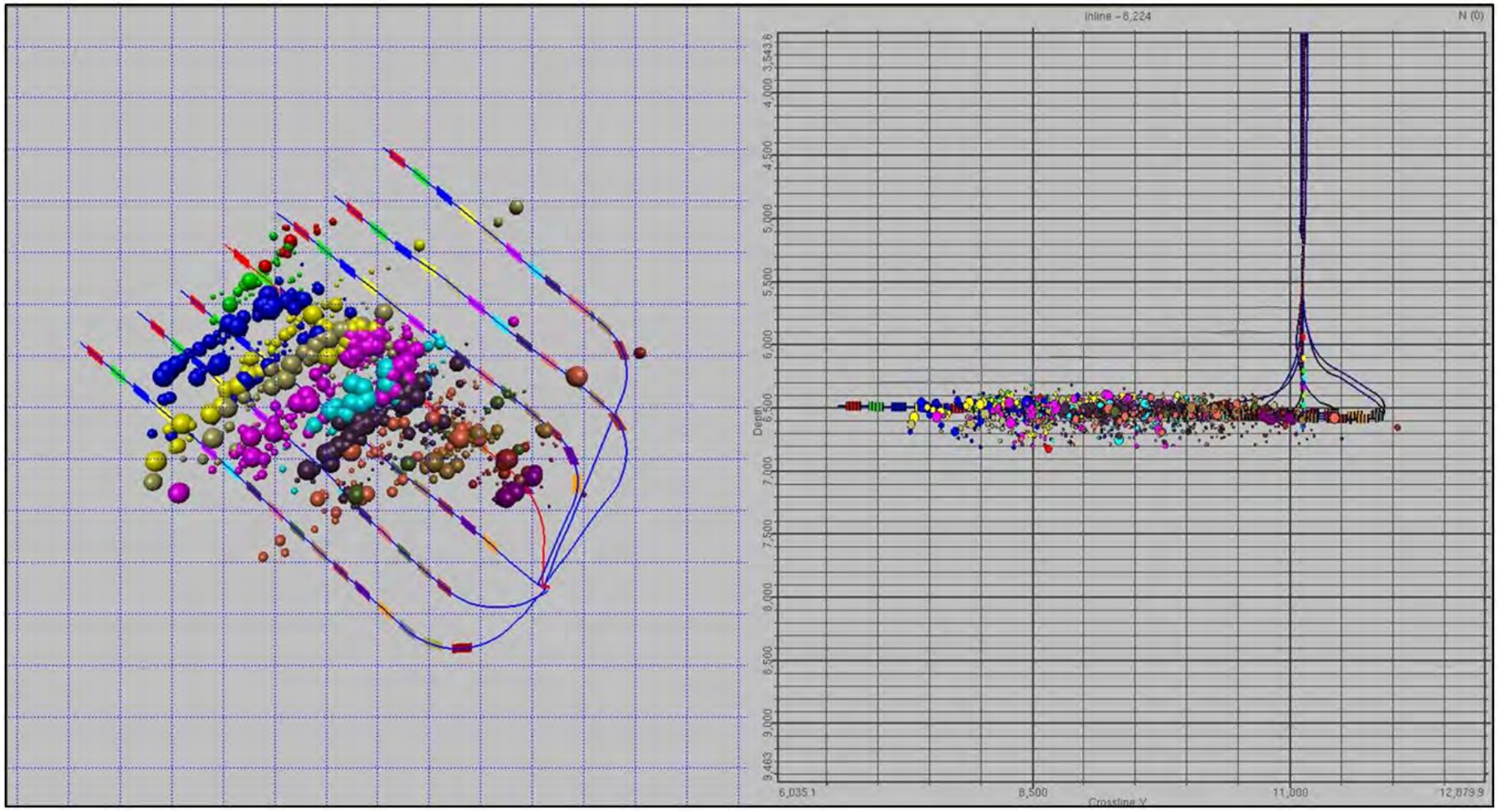

Event Locations Well F

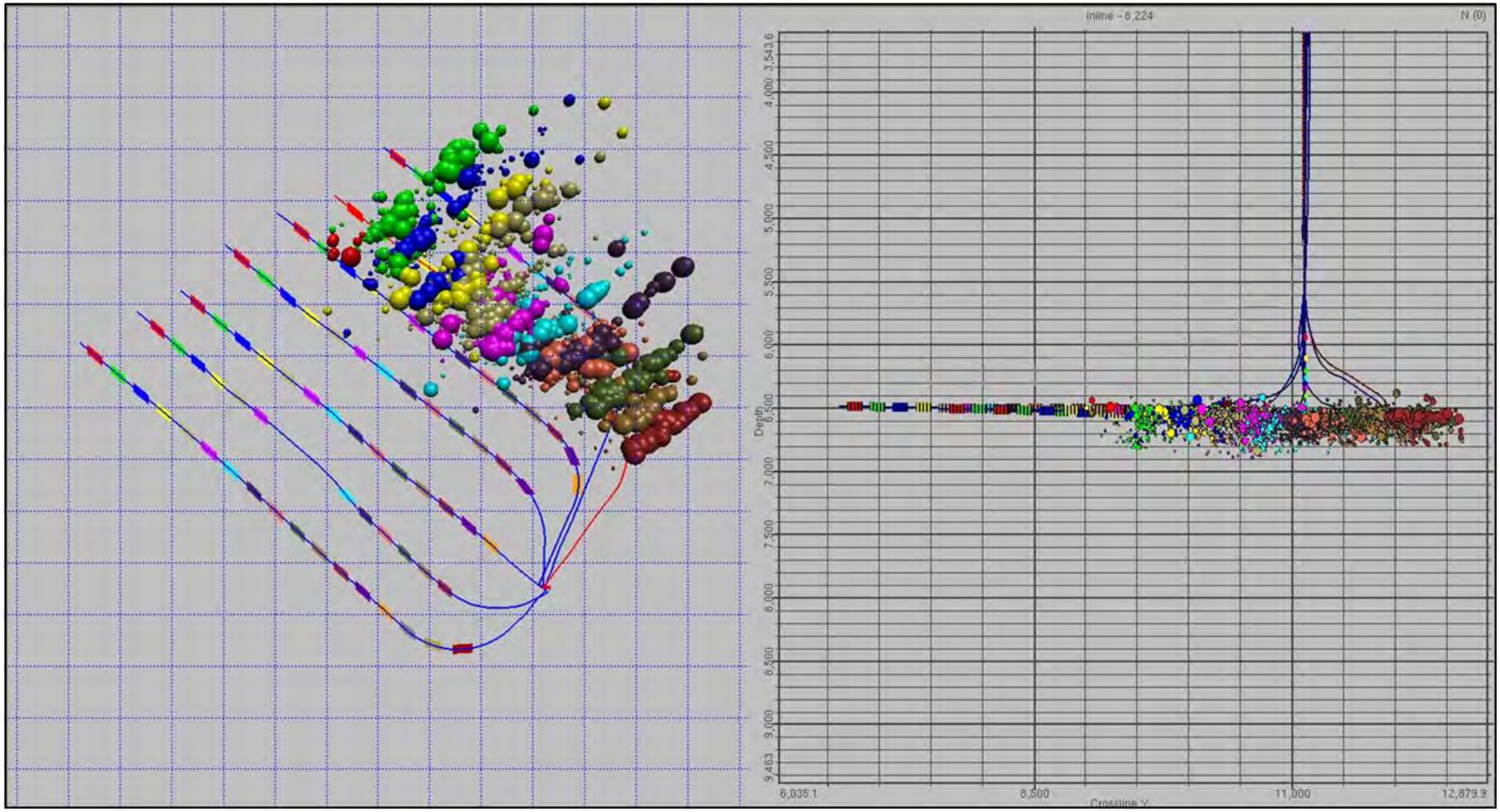

Wellbore Layout

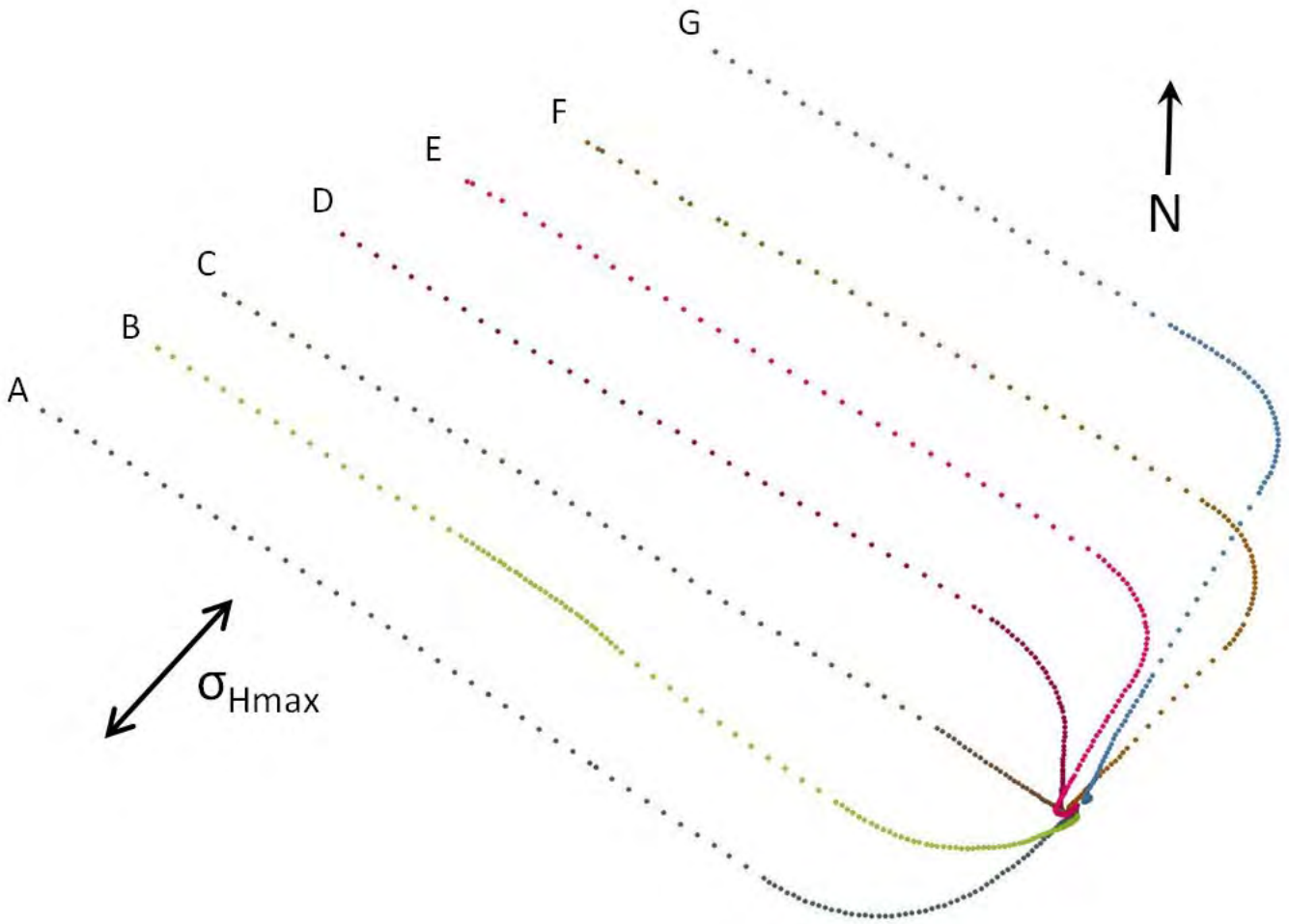

Focal Mechanisms Derived from Surface MS Data

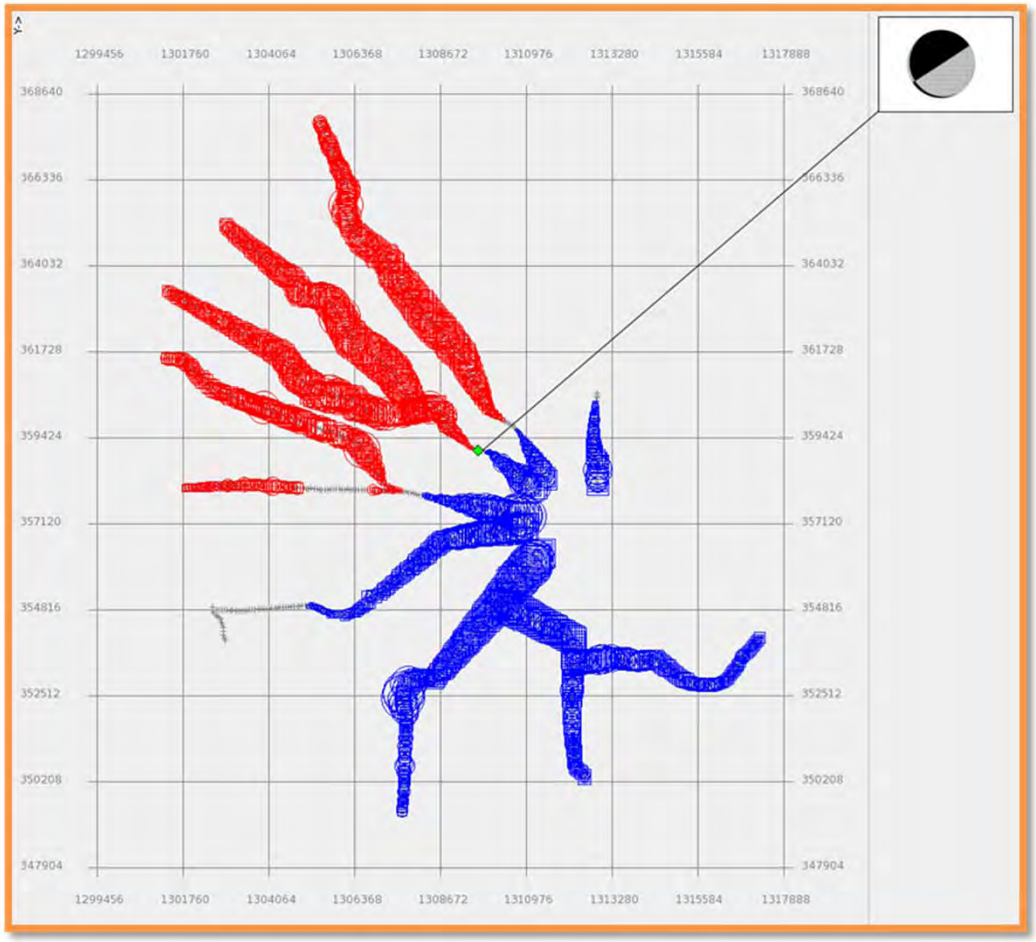

Radiation patterns of different ms source mechanisms

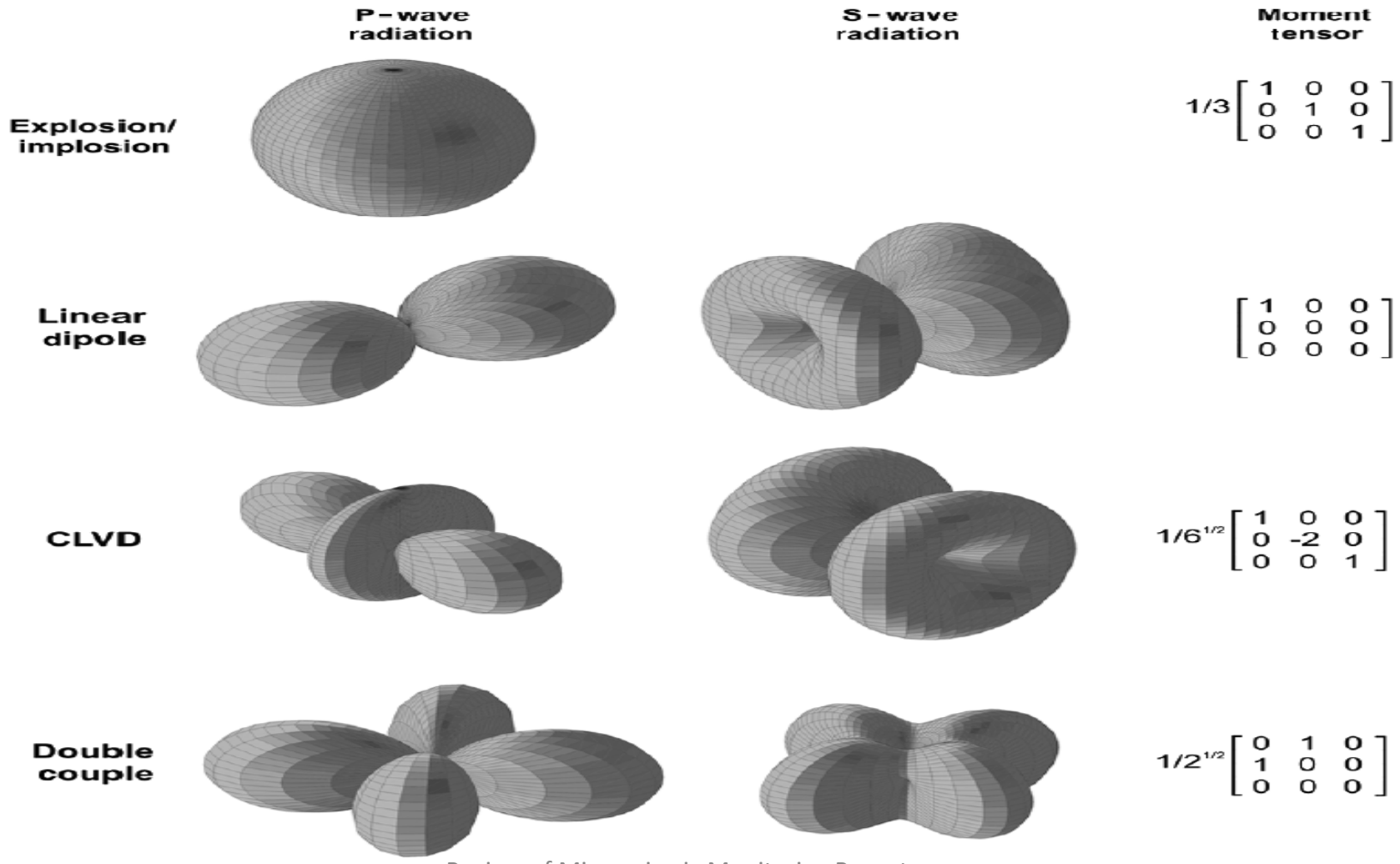

Conclusions: Surface MS

- Event Locations
  - Vertical Extent: 380 ft +/- 150 ft
  - Horizontal Extent: 930 +/- 450 ft
- Focal Mechanism
  - Vertical Dip Slip
  - Only Mechanism Easily Detectable
- Recommendations
  - Incorporation of S-wave and other scattered arrivals for better event location and potentially other focal mechanism solutions

Downhole Recording Geometry

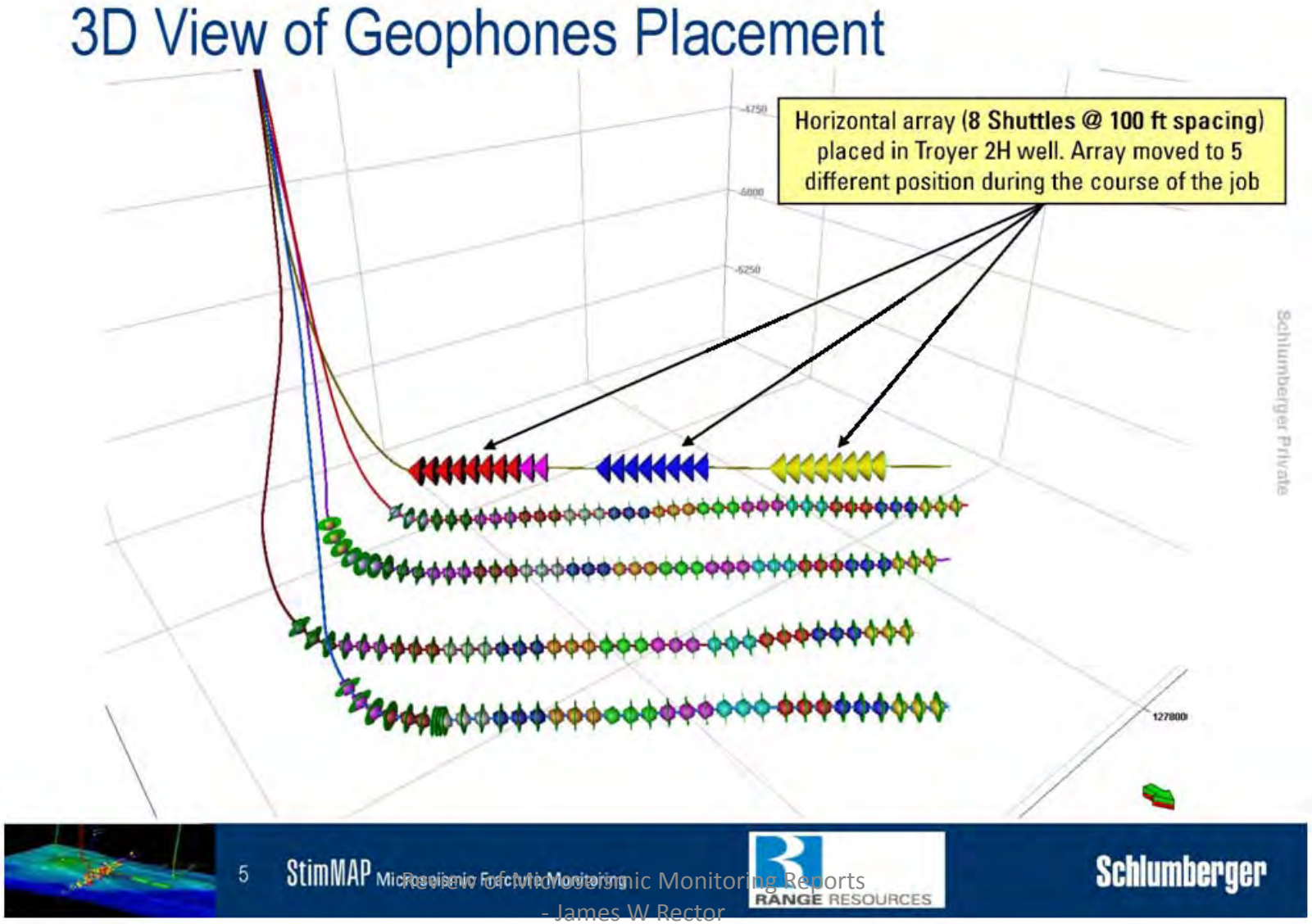

Review of Microseismic Monitoring Reports
- James W Rector

Anisotropic Velocity Model

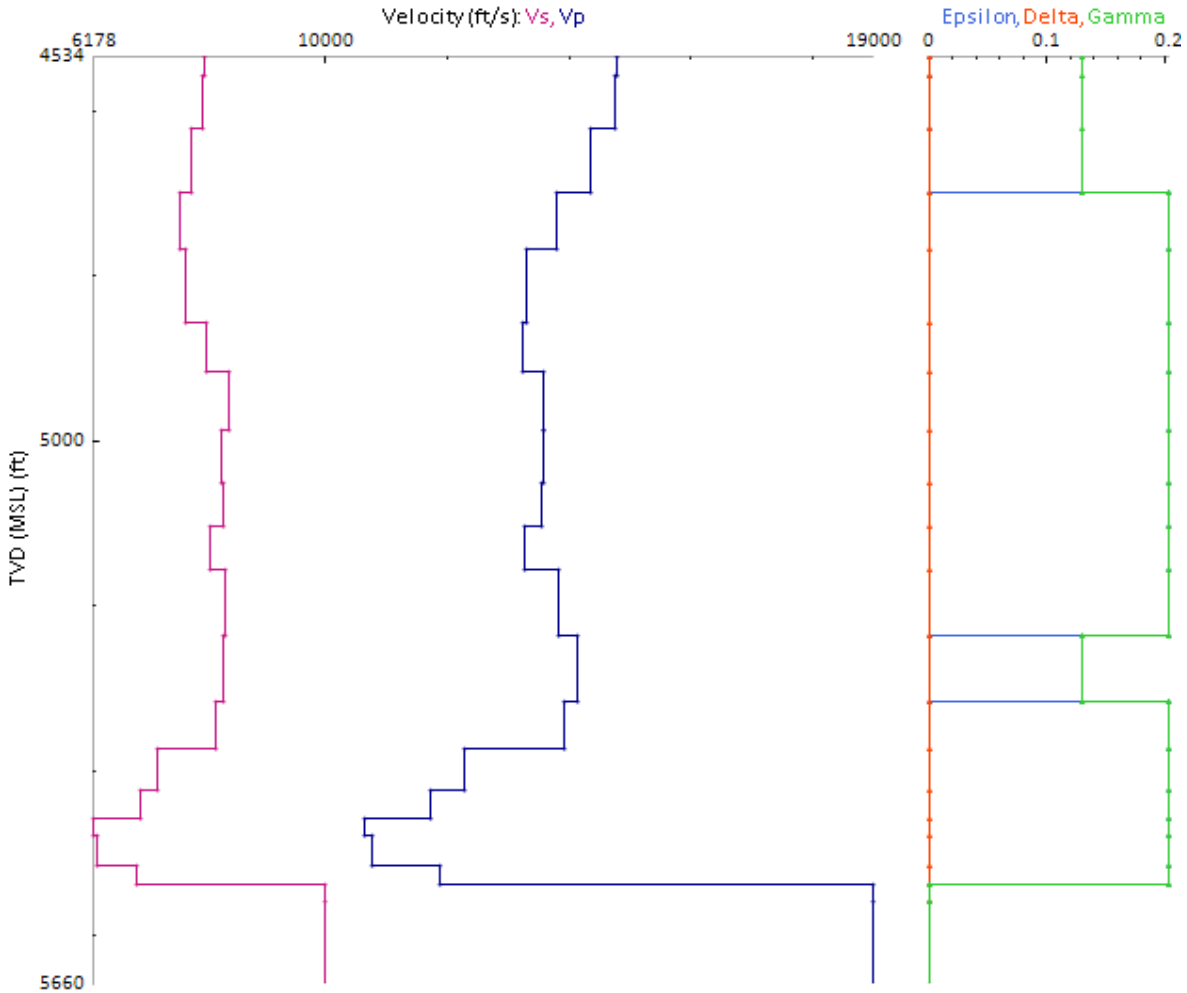

Review of Microseismic Monitoring Reports
- James W Rector

QA

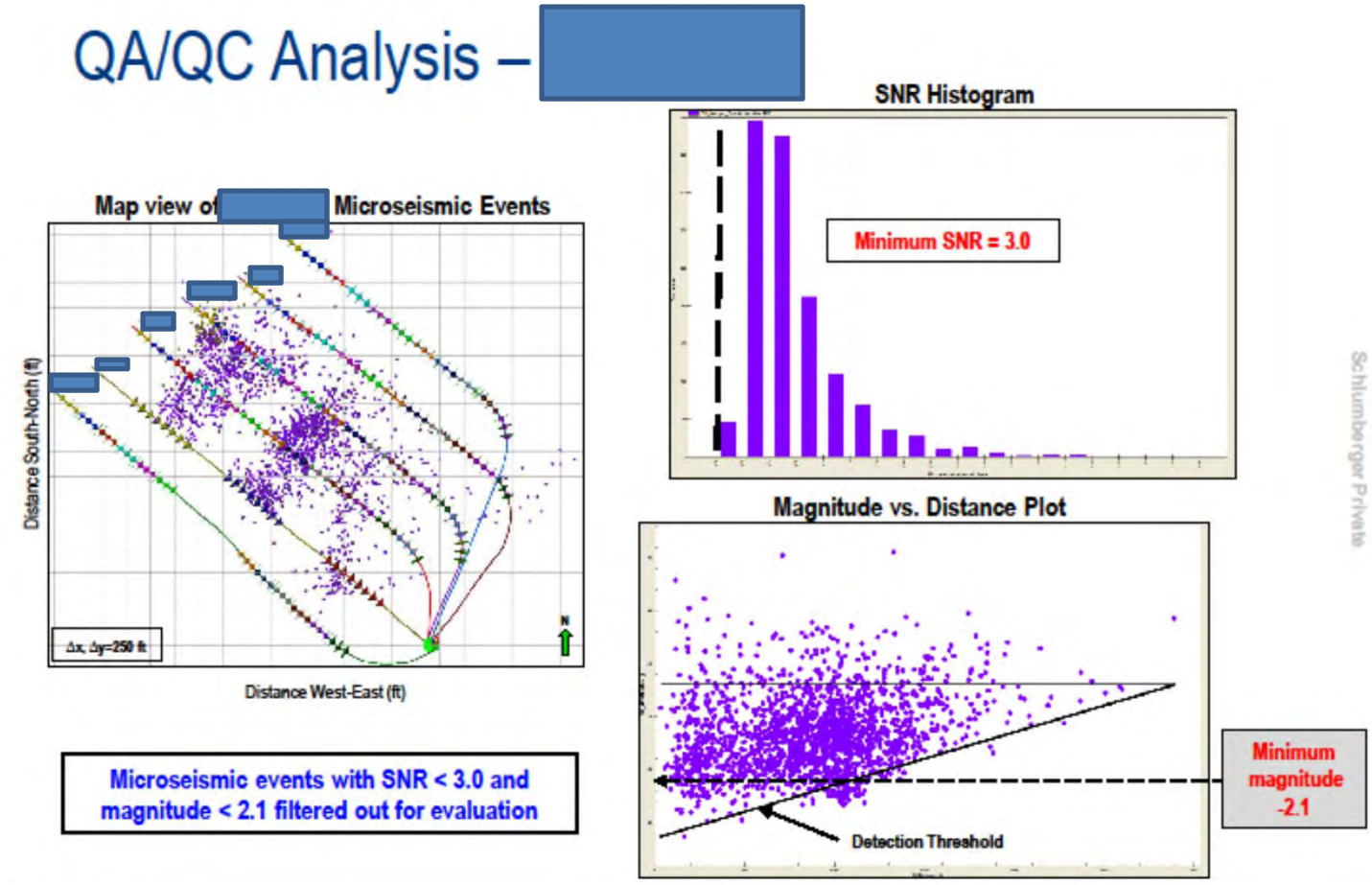

QA

QA/QC Analysis – [redacted]

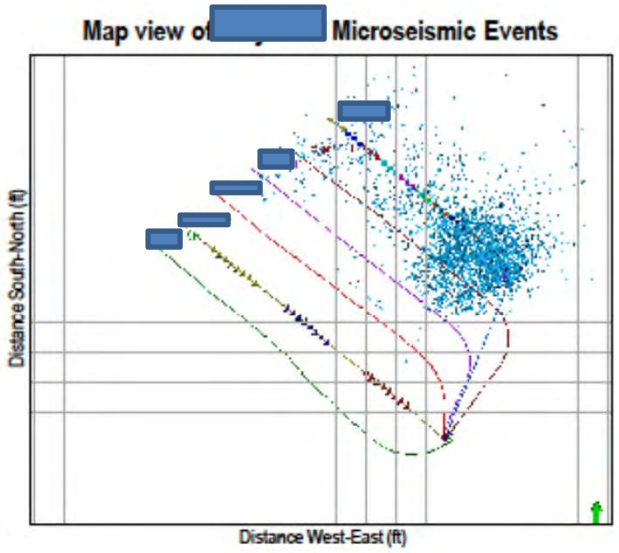

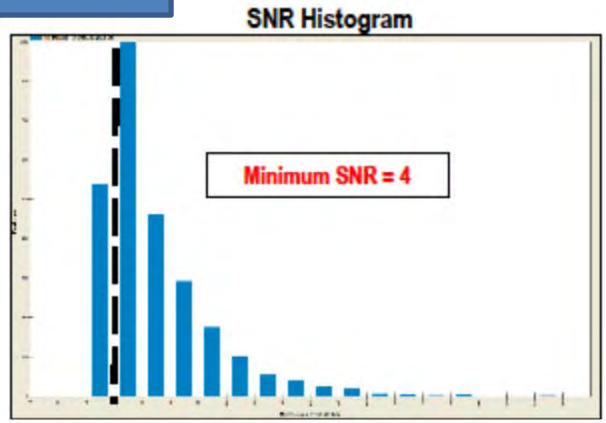

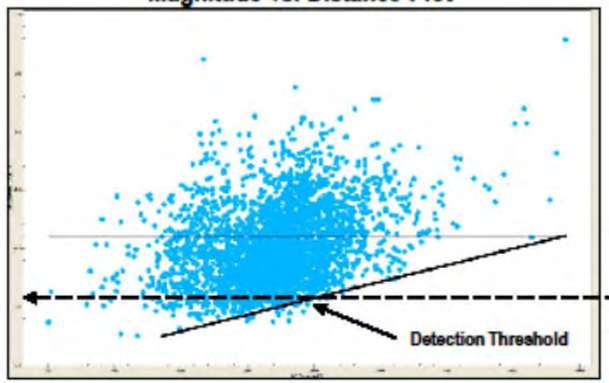

Microseismic events with SNR < 4.0 and magnitude < 1.9 filtered out for evaluation

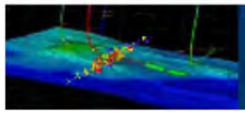

Review of Microseismic Monitoring Reports
- James W Rector

QA

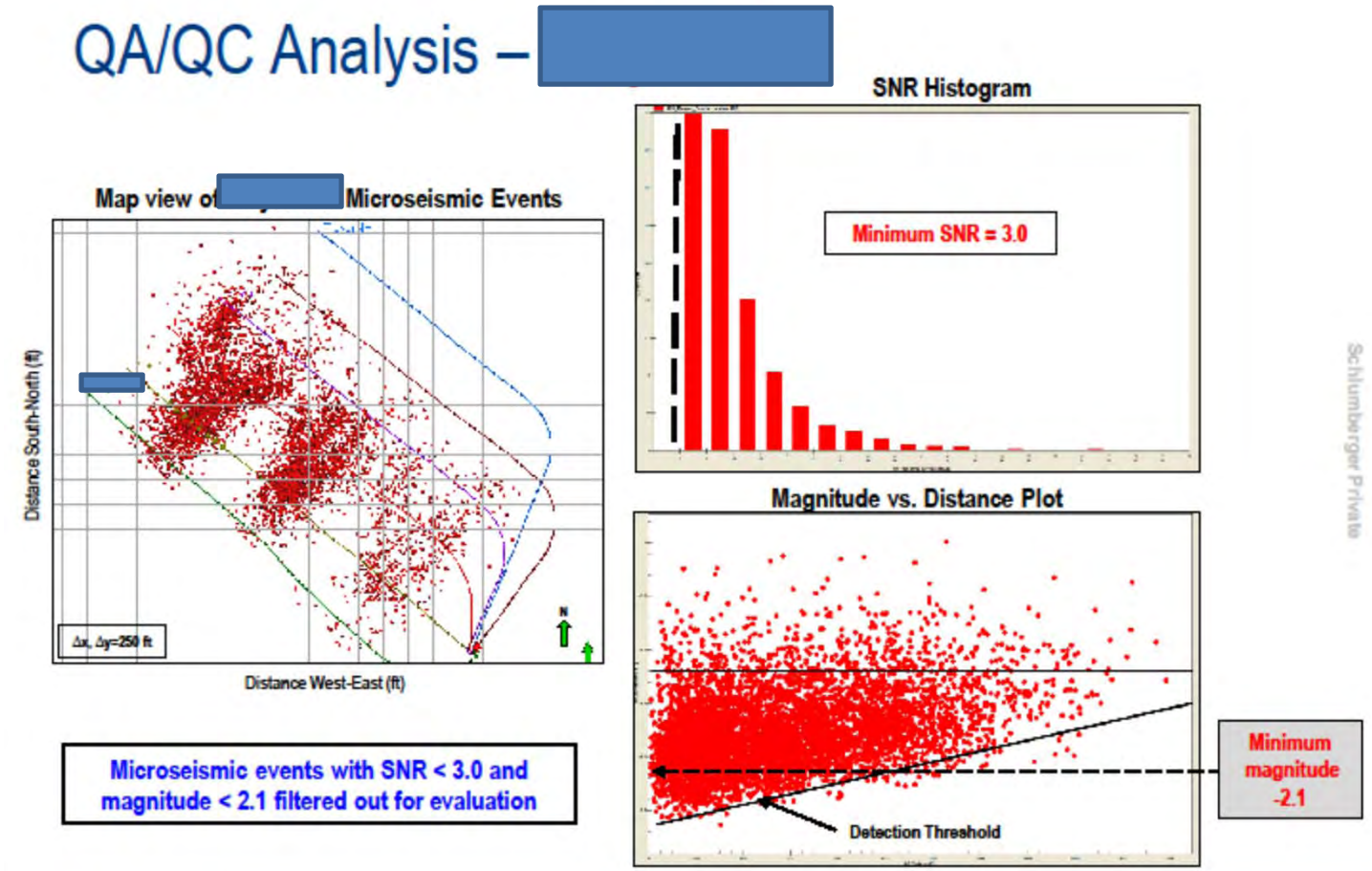
QA/QC Analysis –
SNR Histogram
Minimum SNR = 3.0
Map view of Microseismic Events
Distance South-North (ft)
Distance West-East (ft)
Δx, Δy=250 ft
N
Magnitude vs. Distance Plot
Minimum magnitude -2.1
Detection Threshold
Microseismic events with SNR < 3.0 and magnitude < 2.1 filtered out for evaluation
Schlumberger Private

QA

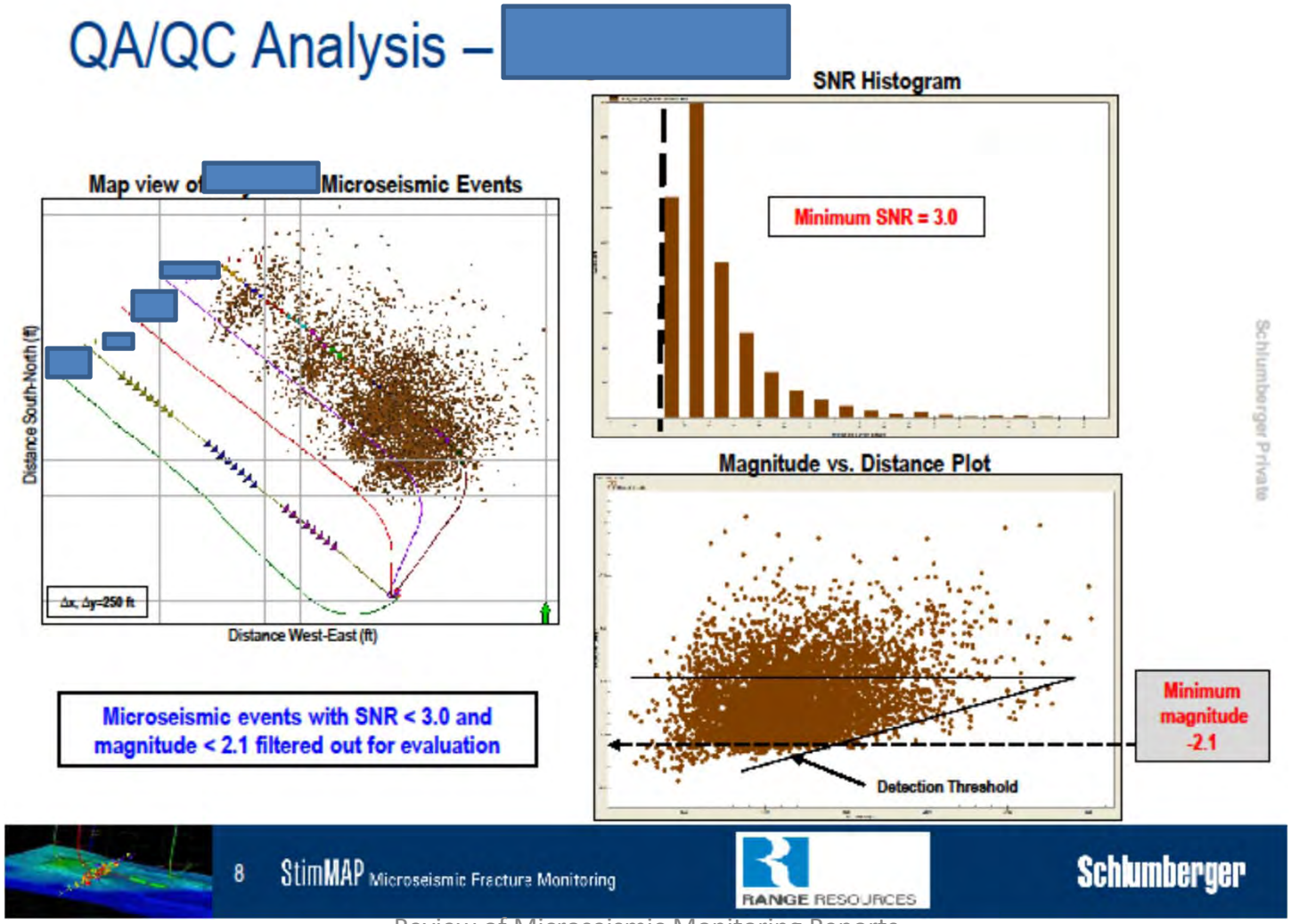

Side view

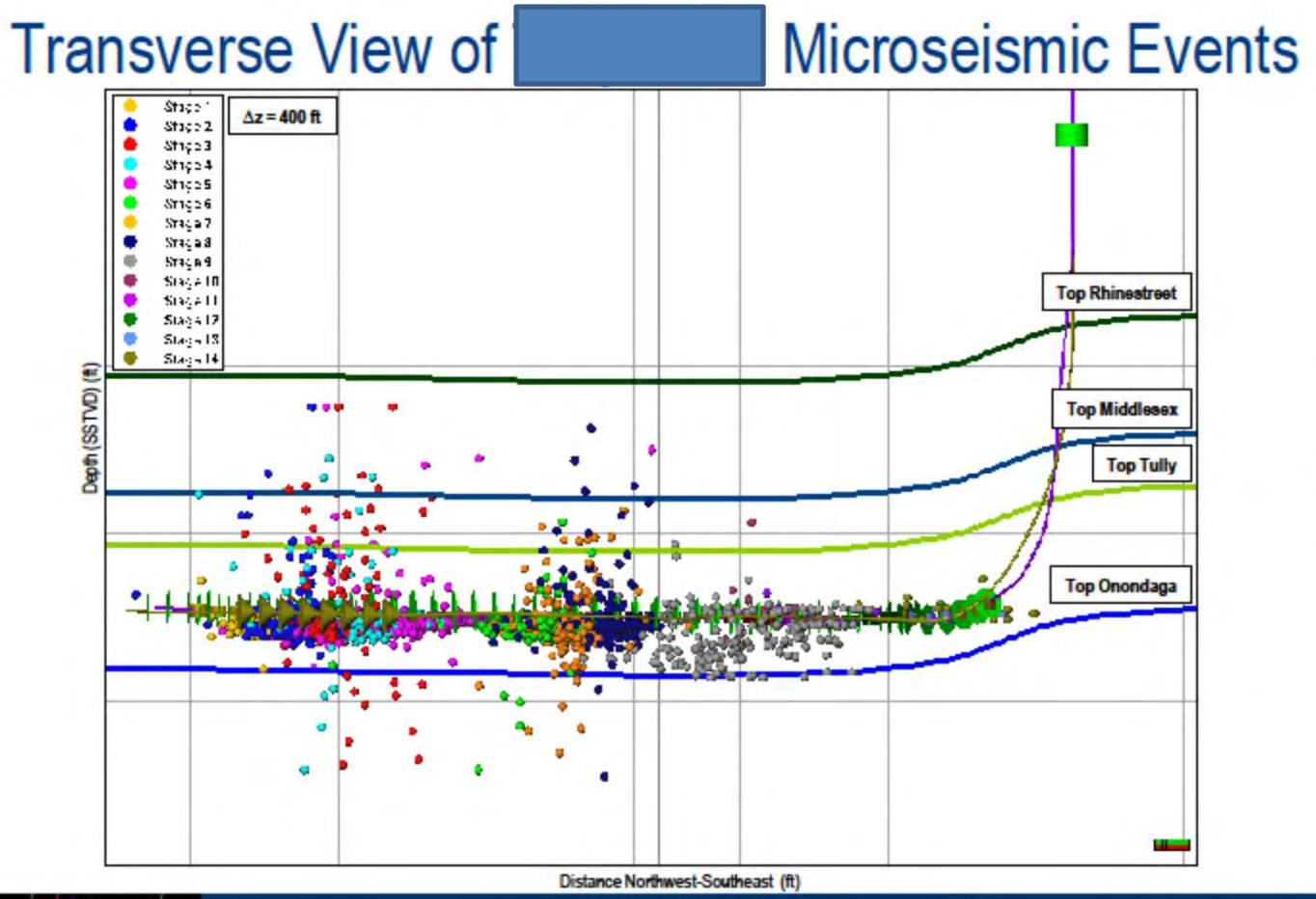
Transverse View of [redacted] Microseismic Events
Δz = 400 ft
Top Rhinestreet
Top Middlesex
Top Tully
Top Onondaga
Depth (SSTVD) (ft)
Distance Northwest-Southeast (ft)
Schlumberger Private

Side View

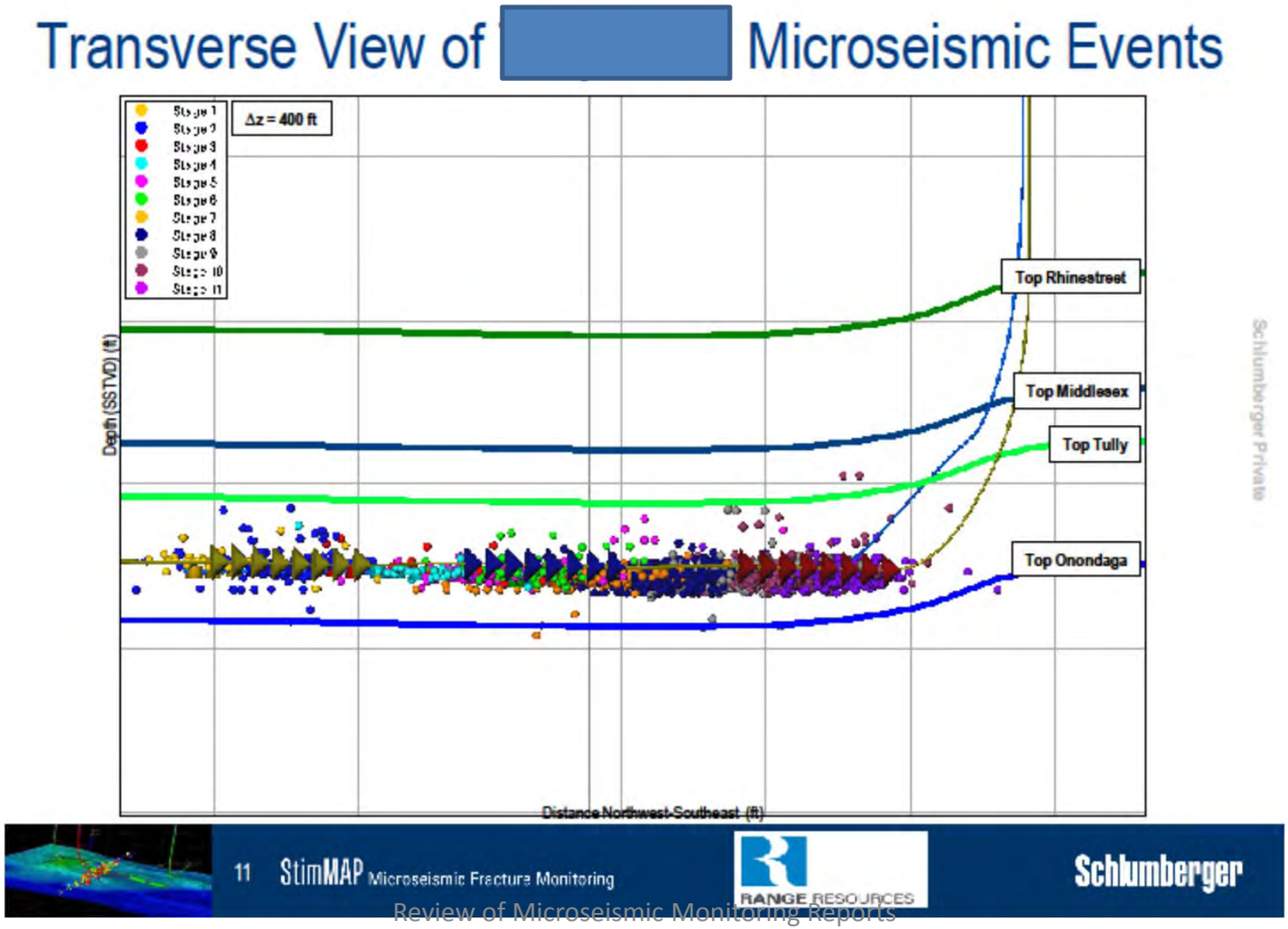
Transverse View of
Microseismic Events
Δz = 400 ft
Top Rhinestreet
Top Middlesex
Top Tully
Top Onondaga
Depth (SSTVD) (ft)
Distance Northwest-Southeast (ft)
Schlumberger Private
11
StimMAP Microseismic Fracture Monitoring
RANGE RESOURCES
Schlumberger

Side View

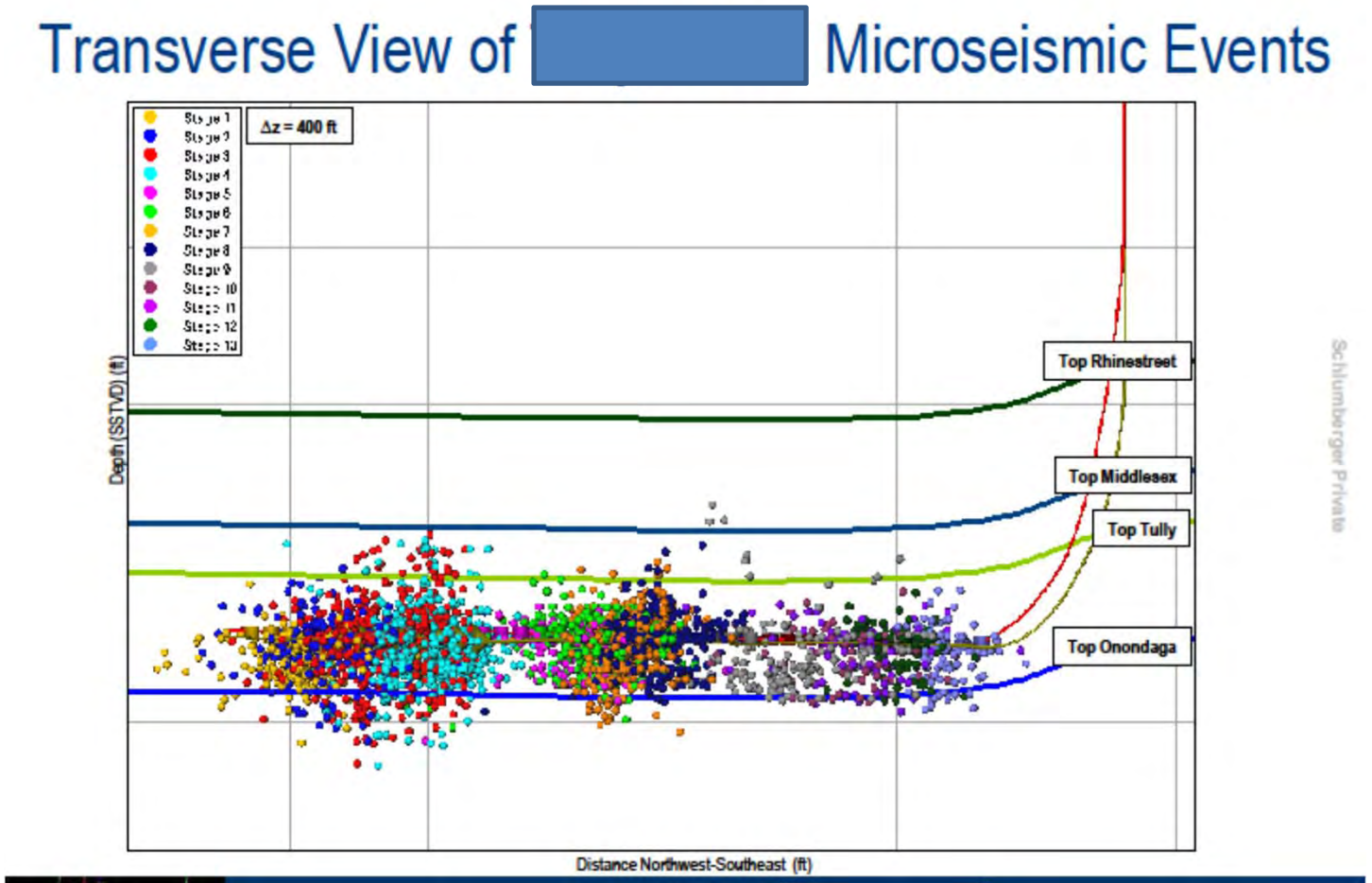
Transverse View of [redacted] Microseismic Events
Δz = 400 ft
Top Rhinestreet
Top Middlesex
Top Tully
Top Onondaga
Depth (SSTVD) (ft)
Distance Northwest-Southeast (ft)
Schlumberger Private
11
StimMAP Microseismic Fracture Monitoring
RANGE RESOURCES
Schlumberger

Side View

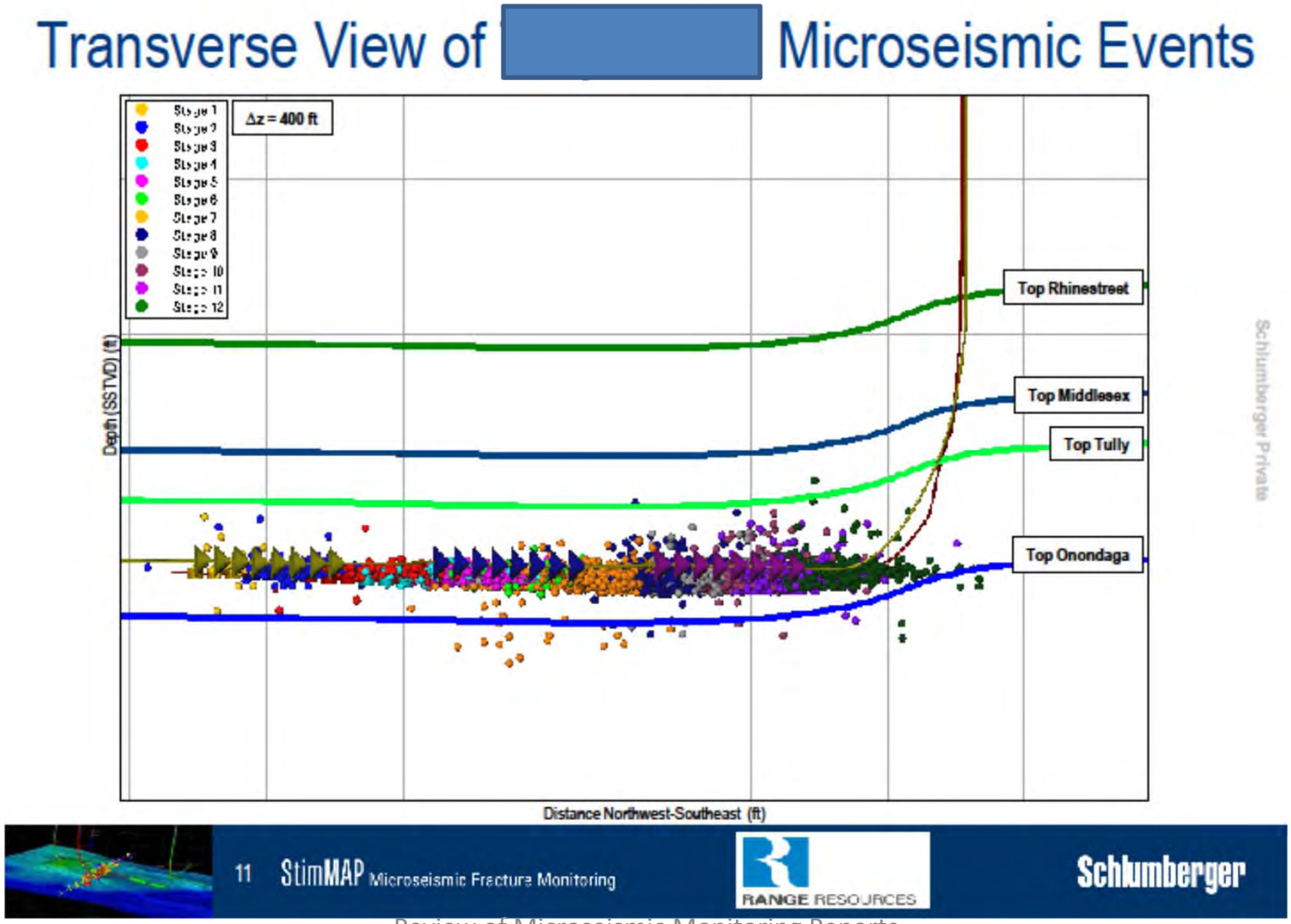
Transverse View of [redacted] Microseismic Events
Δz = 400 ft
Top Rhinestreet
Top Middlesex
Top Tully
Top Onondaga
Depth (SSTVD) (ft)
Distance Northwest-Southeast (ft)
Schlumberger Private
11
StimMAP Microseismic Fracture Monitoring
RANGE RESOURCES
Schlumberger

Map View

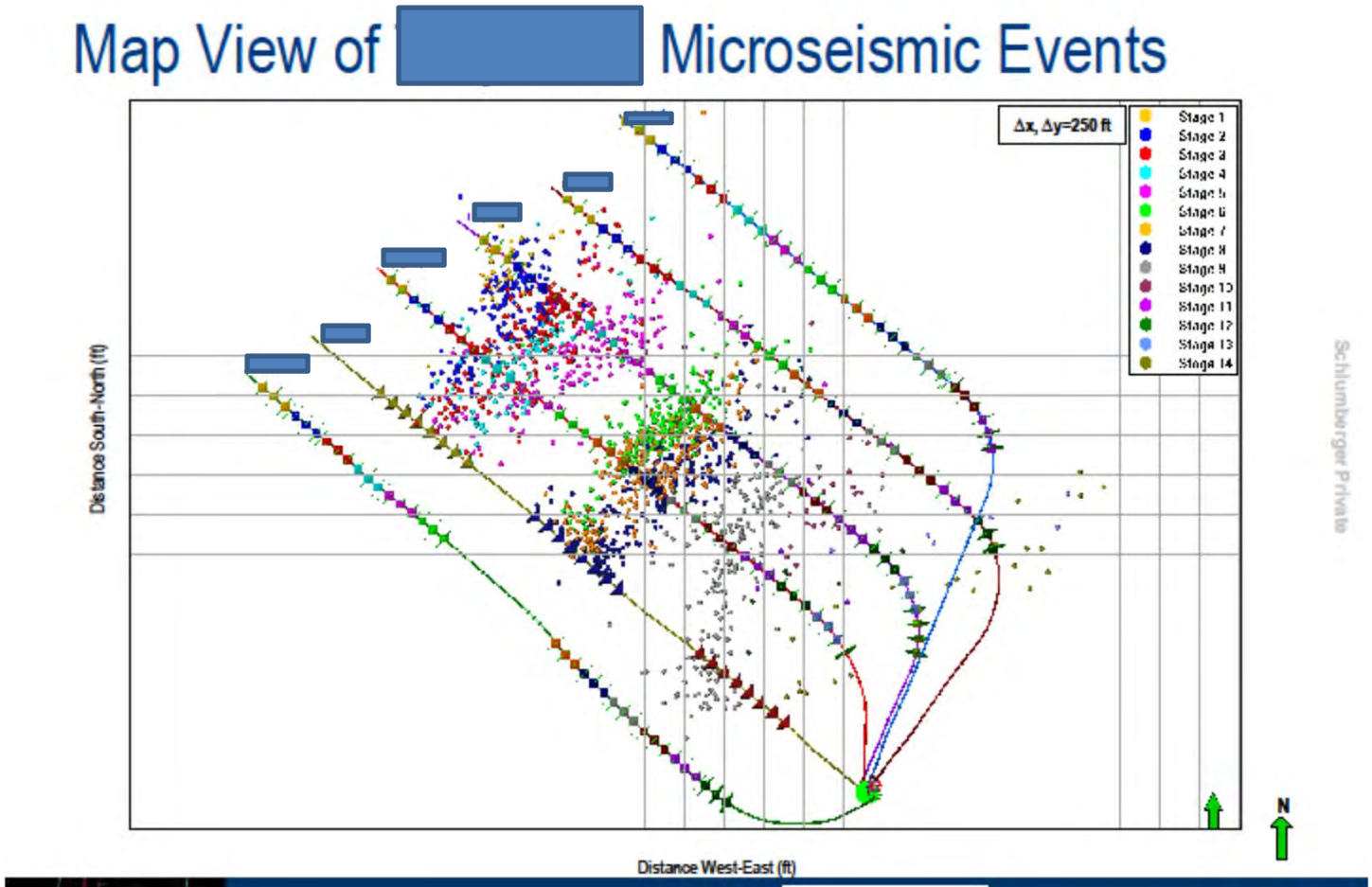
Map View of [redacted] Microseismic Events
Δx, Δy=250 ft
Stage 1
Stage 2
Stage 3
Stage 4
Stage 5
Stage 6
Stage 7
Stage 8
Stage 9
Stage 10
Stage 11
Stage 12
Stage 13
Stage 14
Distance South-North (ft)
Distance West-East (ft)
N
10
StimMAP Microseismic Fracture Monitoring
RANGE RESOURCES
Schlumberger
Schlumberger Private

Map View

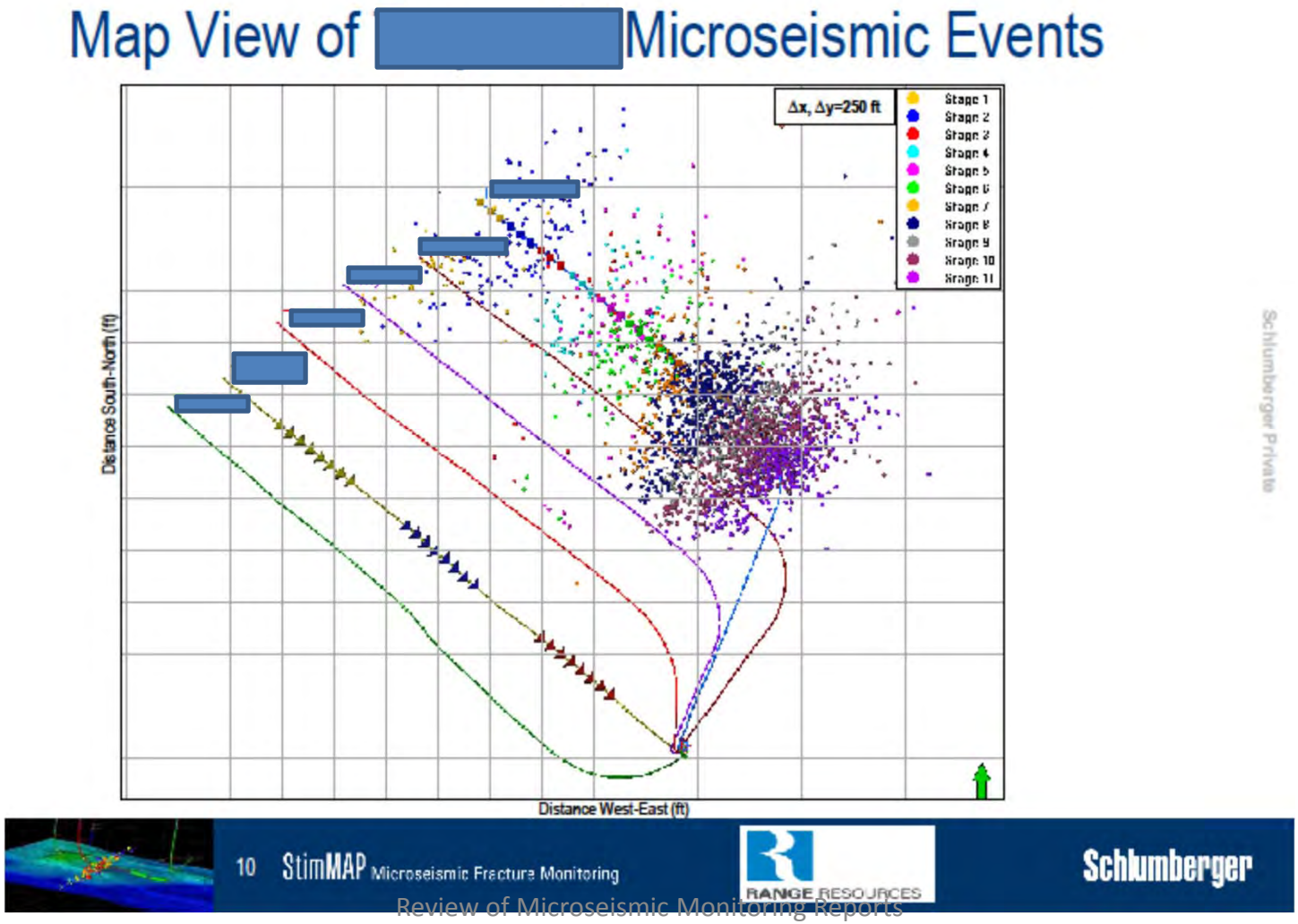
Map View of [redacted] Microseismic Events
Δx, Δy=250 ft
Stage 1
Stage 2
Stage 3
Stage 4
Stage 5
Stage 6
Stage 7
Stage 8
Stage 9
Stage 10
Stage 11
Distance South-North (ft)
Distance West-East (ft)
10
StimMAP Microseismic Fracture Monitoring
RANGE RESOURCES
Schlumberger
Schlumberger Private

Map View

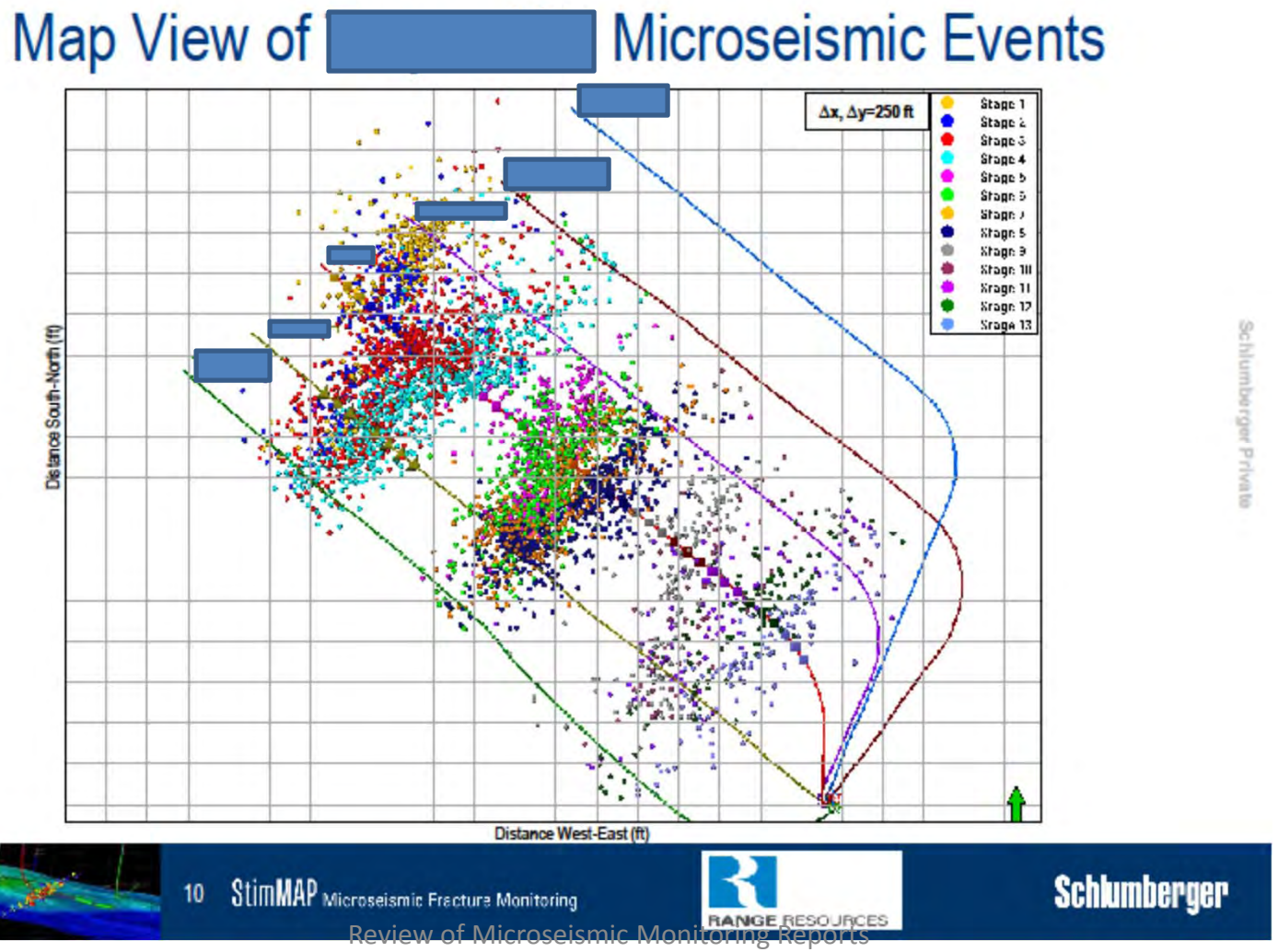

Map View

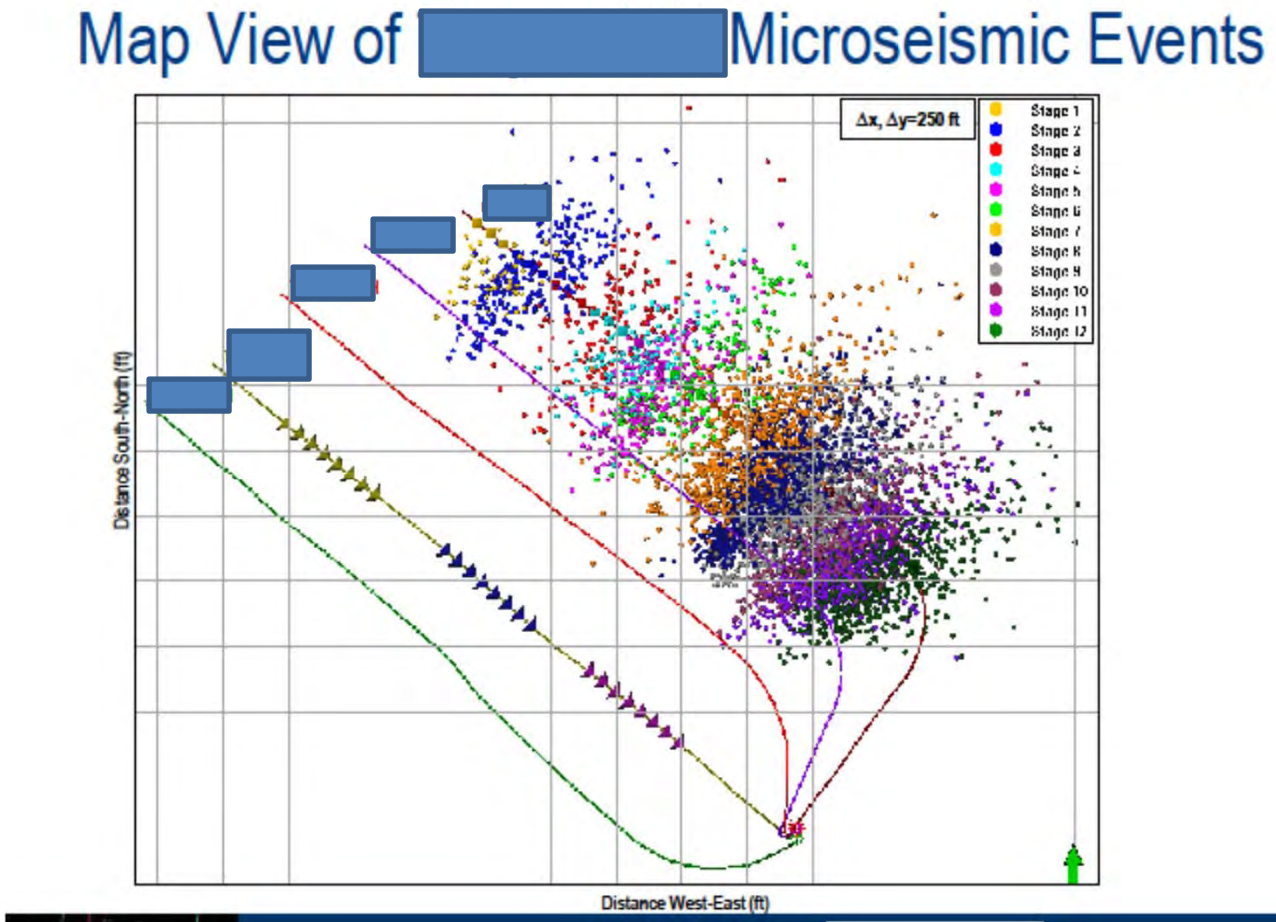

Appendix C - Controlled Hydraulic Fracturing of Naturally Fractured Shales (SPE-164524)

SPE-164524-MS

Controlled Hydraulic Fracturing of Naturally Fractured Shales - A case study in the Marcellus Shale examining how to identify and exploit natural fractures.

Jordan Ciezobka and Iraj Salehi, Gas Technology Institute

This paper was prepared for presentation at the Unconventional Resources Conference-USA held in The Woodlands, Texas, USA, 10–12 April 2013.

Abstract

This case study will illustrate how natural fractures were identified in real time through analysis of surface pumping parameters and confirmed with microseismic data and multiple production logs. Furthermore, subsurface natural fracture distribution will be examined in an approximately 1 square mile area using microseismic and production data. Additionally, gas shows from mud logs will be examined and correlated to production. Finally, methods for real-time fracture optimization will be explored based on natural fracture identification through analysis of fracturing parameters along the horizontal wellbore.

It is well known in the oil and gas industry that natural fractures, either open or prone to opening during hydraulic fracturing, greatly improve hydrocarbon production in tight sand and shale reservoirs. There are many techniques available to identify natural fractures; including image logs, mud logs, G-function analysis leading to pressure dependent leakoff (PDL), core analysis, and many more. However, these techniques have many limitations when used for optimizing the interaction of hydraulic fractures with natural fractures to create a complex fracture network. The limitations result from small sample size when using core analysis, inaccurate or unpredictable measurements from mud logs; or in the case of horizontal image logs, they are extremely costly and uneconomical to run regularly. Recent research related to subcritical index testing has shown that subterranean natural fractures manifest themselves in clusters that are not uniformly distributed along a horizontal wellbore. Therefore, it would be advantageous to gain insight into natural fracture occurrence and distribution before designing the fracturing program and then positively identify natural fracture clusters along the horizontal wellbore in real time and optimize hydraulic fracturing parameters on-the-fly.

Background

Gas Technology Institute (GTI) is currently engaged in a research and development project focused on the development of techniques and methods for delineation of the stimulated reservoir volume and characterization of operational parameters influencing growth and attributes of hydraulic fractures. The project has been funded by Research Partnership to Secure Energy for America (RPSEA). Range Resources Appalachia LLC partnered in the project by provision of cash cost sharing, background data, technical support, and access to several wells in the Marcellus play in southwest Pennsylvania (Figure 1) for field data acquisition. Technical support and significant cost sharing was also provided by Schlumberger.

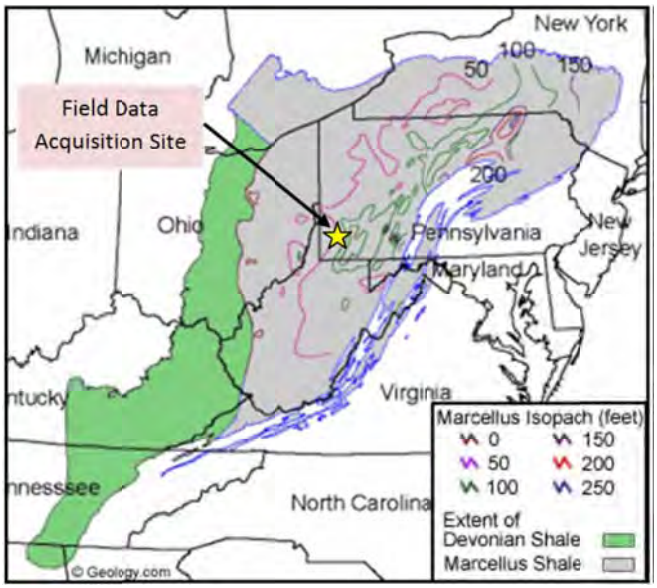

Figure 1: Field data acquisition site.

A team of experts from GTI, Bureau of Economic Geology (BEG) at the University of Texas – Austin, Lawrence Berkeley National Laboratory (LBL) and; Stanford, West Virginia University (WVU), and Pennsylvania State University (PSU) began research on this multidisciplinary project in early 2011. The project is nearing completion in March 2013.

Great emphasis was placed on comprehensive fracture diagnostics, coupled with analysis of microsesimci data, fracture geometry, and production data as means for determining fracturing efficiency (Ciezobka 2011). In the meantime, realizing that the state and spatial distribution of natural fractures are significant parameters influencing growth and volumetric extent of fracture networks, extensive efforts were also placed on characterization of natural fractures as the prerequisite for thorough analysis of hydraulic fracturing data, determination of the stimulated reservoir volume and ultimately; development of optimized completion strategy for Marcellus and other fractured shale formations. This paper is focused on identifying natural fractures before designing the stimulation program combined with real-time redesign of hydraulic fracturing parameters as a practical means for optimization of fracture stimulation procedures. The overall project structure and flow of information and results are shown on Figure 2. Detailed description of observations and proposed methodologies will follow a brief summary of results from geological studies and micron level imaging that fed into fracture analysis.

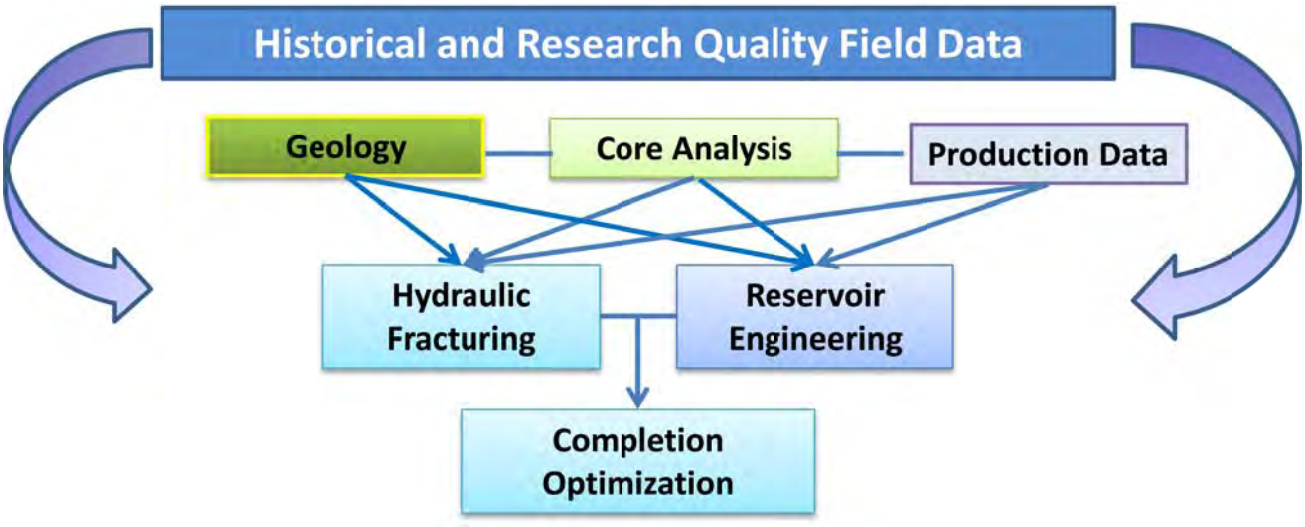

Figure 2: Project structure

Experiment Site

A multiple well pad owned and operated by Range Resources Appalachia LLC located in Washington county Pennsylvania is the site of field data acquisition. The pad includes seven nearly-parallel horizontal wells. The trajectories of the well laterals are in the general northwest direction and are normal to the maximum in situ horizontal stress (σ_{Hmax}) orientation as shown in Figure 3. Spacing of the horizontal sections of the wellbores is approximately 500 ft with an average horizontal wellbore length of 3640 ft. The horizontal well sections lie along the lower portion of the Marcellus shale, (the Marcellus-A) having a true vertical depth (TVD) of approximately 6500 ft. Pad drilling was utilized in order to minimize land use and the surface location of the wells is centered in a rural and geographically complex setting. The gross thickness of the Marcellus shale at a nearby well located less than 3 miles from the test site is roughly 150 ft with an average porosity and permeability of 8 percent and 600 nanodarcy, respectively. Data from five nearby science wells was used to characterize the Marcellus reservoir. Whole cores and a suite of advanced electric logs were used to determine petrophysical, mechanical and other rock properties. The cores were also used to calibrate the electric logs. Surface microseismic tools were installed in a roughly 3 square mile area and 93 fracture stages were monitored. Borehole microseismic tools were placed in one of the horizontal wells and 62 fracture stages were monitored.

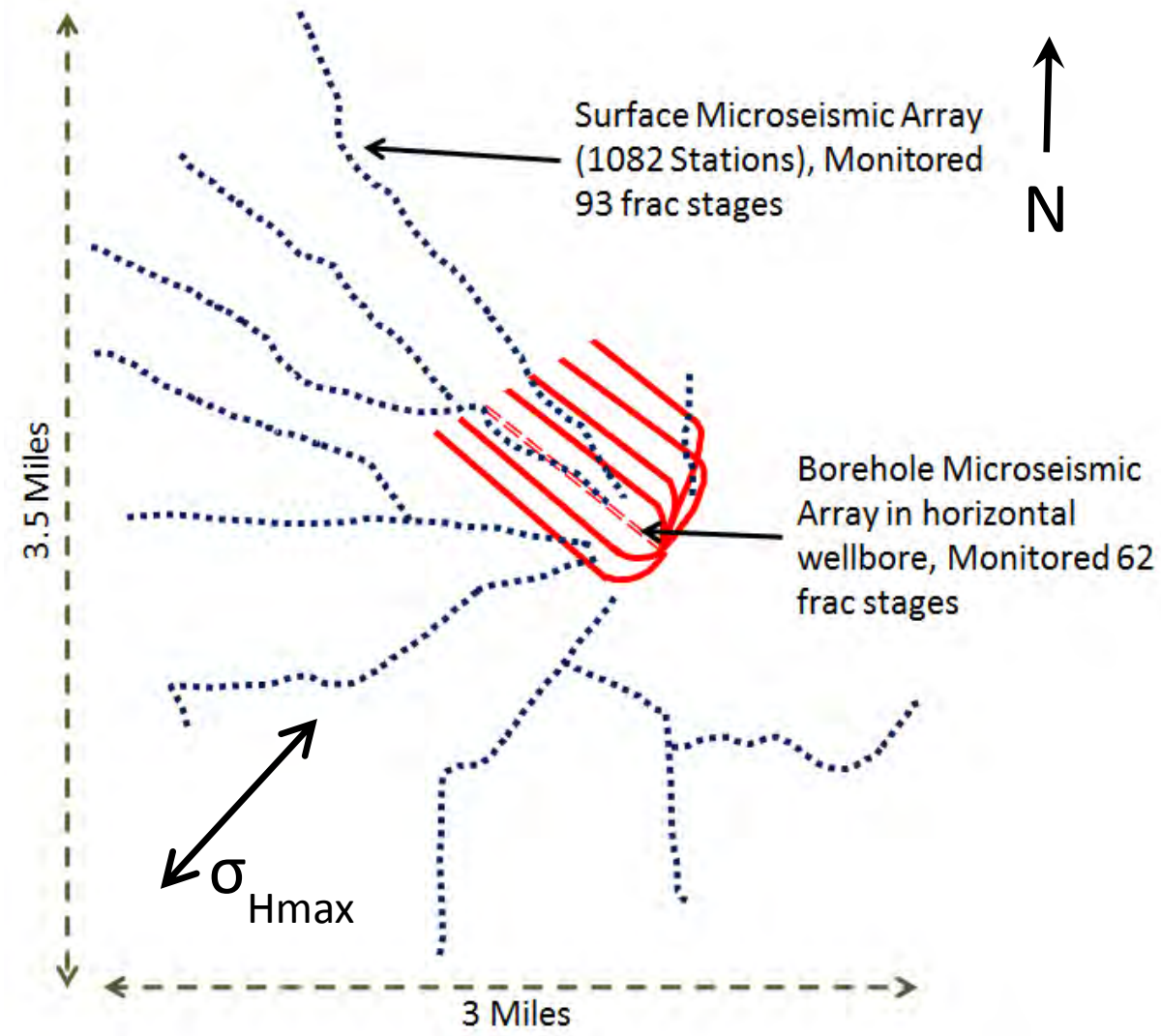

Figure 3: Layout of surface and borehole microseismic arrays and horizontal well trajectories.

Geologic Studies

Emphasis of geological studies were on characterizing, quantifying, and modeling of natural fractures through a combination of

observations at a range of scales, detailed petrographic and microstructural observation of cement fills, and geomechanical modeling. Geomechanical modeling included measurement of subcritical indices, which is an important parameter when considering natural fracture clustering, (Holder et al. 2001) of samples from cores and outcrops and statistical modeling of spatial distribution of natural fracture based on data from outcrops and borehole images. Note that large natural fractures; open or sealed, are typically sparsely sampled in cores and image logs. Yet these are the fractures that would have the most effect in augmenting gas flow or influencing the growth of hydraulic fractures. In the face of this difficulty, geomechanical modeling approach overcomes the sampling problem by use of fracture size and spatial scaling analysis leading to predictions of fracture attributes in the absence of extensive sampling.

Fracture morphology, orientation, spatial organization and cementation were analyzed using datasets from the project wells in SW Pennsylvania. A dataset from a geological field trip was also included to evaluate the use of outcrop fracture data in reservoir characterization and providing a means for expanding the relevance of the study beyond the specific area in SW Pennsylvania. Some key results from geological studies are summarized below:

- In general, there are two and sometimes three sets of subvertical natural fractures in the Marcellus Shale. There are three fracture trends in the project area in southwest Pennsylvania. These are the NE trending strike pall (J1), NW cross-fold (J2) and a third set trending ENE. Fractures in outcrop are up to 40 m long and the tallest is at least 3 m high.
- Induced fractures in the reservoir trend NE-SW.
- J2 fractures in a horizontal well image log in the study area showed a preferred spacing at 12.5 m, which is comparable to the vertical distance between limestone beds observed in a nearby well. This may be a characteristic mechanical layer thickness, which is somewhat reflected in the fracture spacing. Samples from a vertical well yield subcritical indices from 38 to 131, with a mean of 75 indicating moderate clustering propensity. Fracture toughness typically ranges from 1.0 to 1.7 MPa sqrm.
- Analysis of spatial organization of fractures in the Union Springs quarry location showed clustering propensity of fractures in the Marcellus shale. Note that J1 fractures have a weak preferred spacing at 0.2m, 1 m, 7 m and 14 m. while J2 fractures show preferred spacing at 2, 4 and 14 m as shown in Figure 4a and 4b.

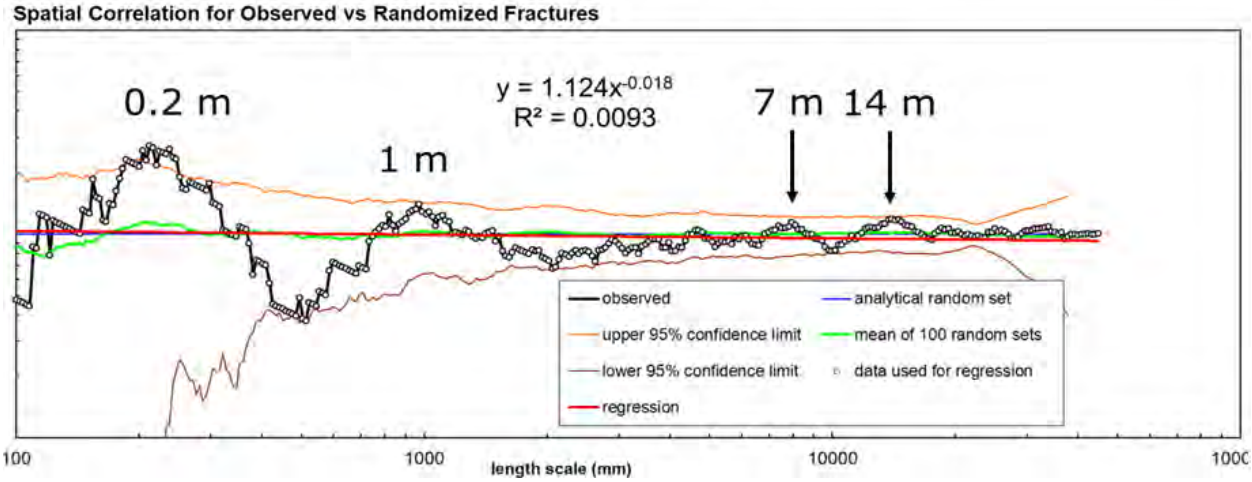

Figure 4a: Spatial correlation plots for J1 fractures in the Union Springs Member of the Marcellus Shale in the Wolfe Quarry at Union Springs, NY

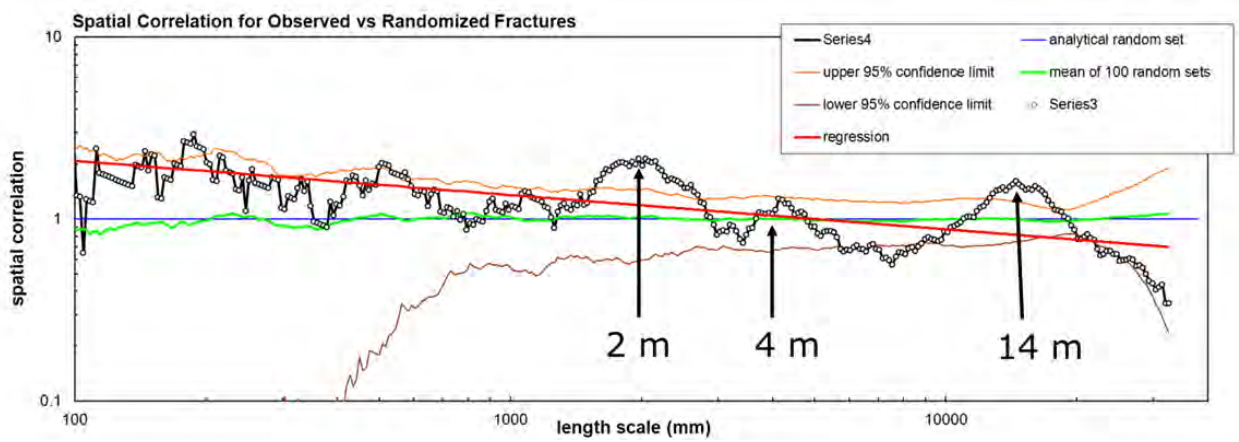

Figure 4b: Spatial correlation plots for J2 fractures in the Union Springs Member of the Marcellus Shale in the Wolfe Quarry at Union Springs, NY

As will be seen in the proceeding sections, clustering of natural fractures in the study area was well substantiated through microseismic imaging and pumping diagnostics.

Core Analysis

Range Resources drilled and cored multiple vertical research wells in the vicinity of the project site. Well logs and results of core analysis were made available to the research team and have been incorporated in all analyses. In addition, samples from these cores were provided for measurement of subcritical indexes by BEG. Lawrence Berkeley National Laboratory (LBL) performed nanometer-scale imaging of core samples, and Stanford University performed flow tests through cores to determine production conditions resulting in condensate drop-out in the reservoir, thus reducing effective permeability.

Work by LBL included

1. Low-resolution computed tomography
2. Micro-tomography at the Advanced Light Source Facility
3. FIB/SEM and diamond knife/SEM

In summary, it was reported that each imaging technique reveals rock properties at different scales; heterogeneity is present and porosity is low in all scales. Micro-CT data shows development of microcracks near quartz grain and pyrite inclusions. Pores were reported to be present at a variety of spatial scales and those observed in material surrounding framboidal pyrite grains were on the order of tens to hundreds of nanometers in diameter. Microfractures at grain boundaries were also observed although they may not be well connected. It was also concluded that permeability in the Marcellus shale may be dominated by the overall layered structure of the rock as seen in the low-resolution scans. Figure 5 shows some results of the nanometer-scale imaging.

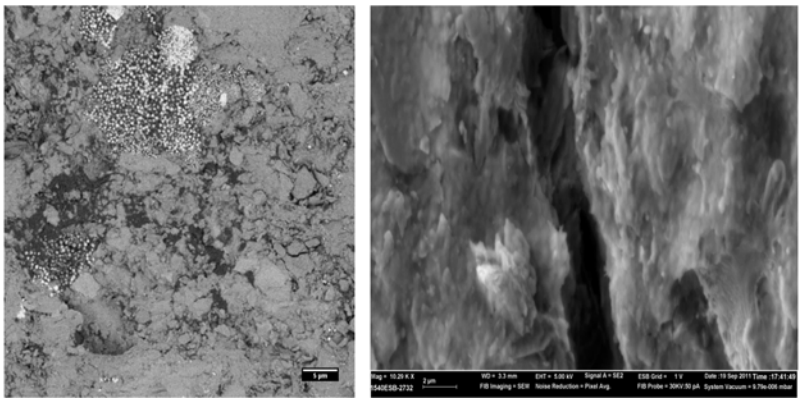

Figure 5: Left – SEM image of diamond-knife cut Marcellus shale sample. Right – SEM image of Marcellus shale sample showing the structure of a microcrack.

Hydraulic Fracturing

The seven research wells were stimulated using multi-stage hydraulic fracturing with slick water and sand at a designed rate of 70 bpm. Acid was used ahead of each fracture stage to reduce entry friction. Five wells (wells A,C,E,D,F) out of the seven wells were stimulated with the same proportions of proppant and fluid. The other two wells were stimulated with higher concentrations and amounts of proppant which also required more fluid to be pumped. Figure 6 shows the normalized fluid volume and proppant mass pumped in each well on a per-foot basis. In wells A, C, E, D, and F an estimated 1000 lbs of proppant was pumped per each foot of completed lateral requiring about 25 barrels of fluid volume per foot of lateral. The proppant mass pumped in well G was increased by 75% (on a per foot basis) and by 100% in well B (also on a per foot basis). Based on previous experiments performed by Range Resources (Curry et al. 2010), higher proppant amounts and concentrations lead to improved production rates and higher ultimate recoveries. As such, the various fracture designs were pumped to determine the optimal proppant concentration, mass, and fluid volume.

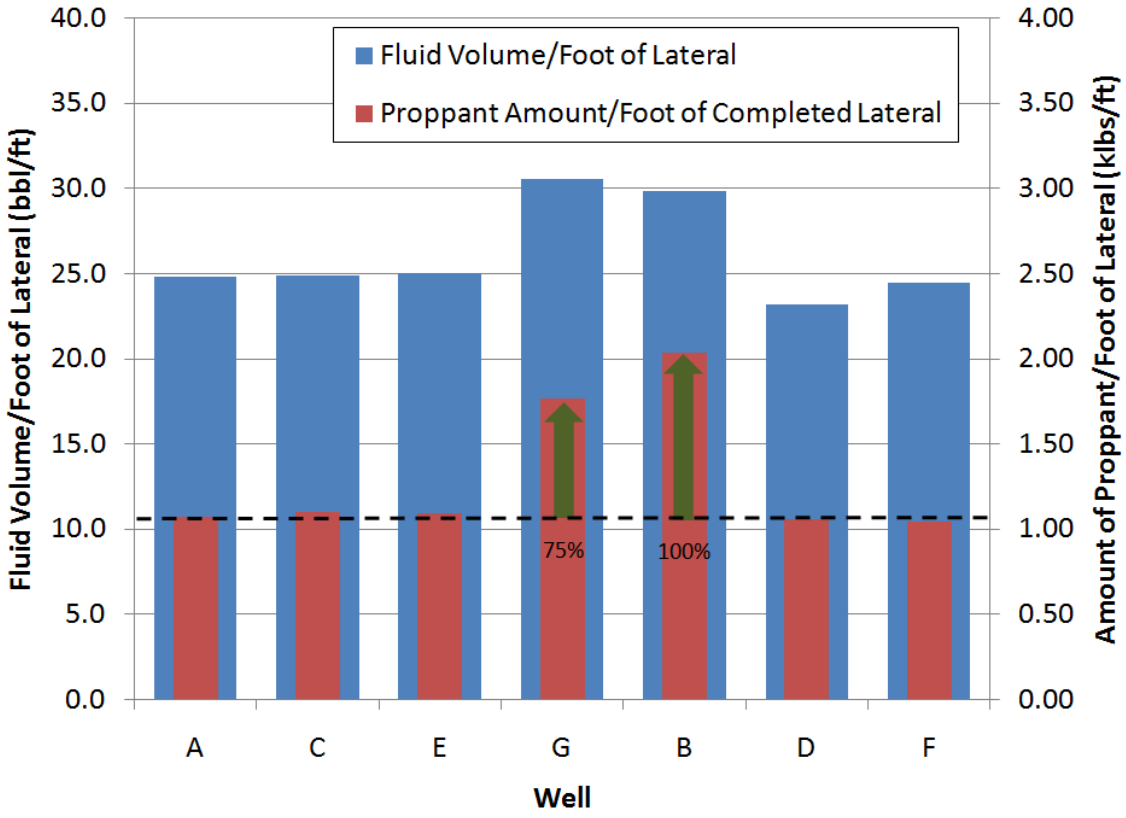

Figure 6: Normalized fluid and proppant volume for each well.

During stimulation, a total of 93 hydraulic fracture stages were pumped in seven horizontal wells. Of these 93 fracture stages all were monitored with a surface microseismic array as shown in Figure 3, and 62 of the 93 fracture stages were monitored with borehole array placed in well C as shown in Figure 7. Due to variations in array geometries and major difference in the distance between the microseismic signal source and the surface and borehole arrays, there were significantly fewer events recorded with the surface microseismic array for each fracture stage. However there were many areas in the reservoir that showed very similar patterns in microseismic event concentration and fracture geometries when comparing the two different microseismic surveys. This is evident in the composite plots showing the microseismic event distribution for the entire pad as shown in Figure 8. There are areas with concentrated microseismic events from not just one fracture stage, but from multiple fracture stages. Coincidently, there are areas where there is very little microseismic activity, even if multiple fracture stages should have intersected. Both surveys show very similar results on a large scale and hence increase the validity of each other.

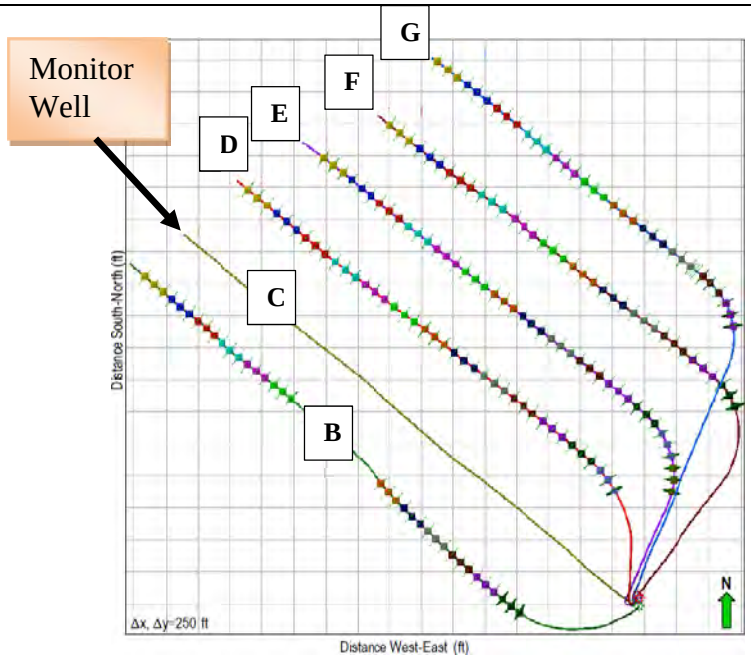

Figure 7: Fracture stages monitored with borehole microseismic.

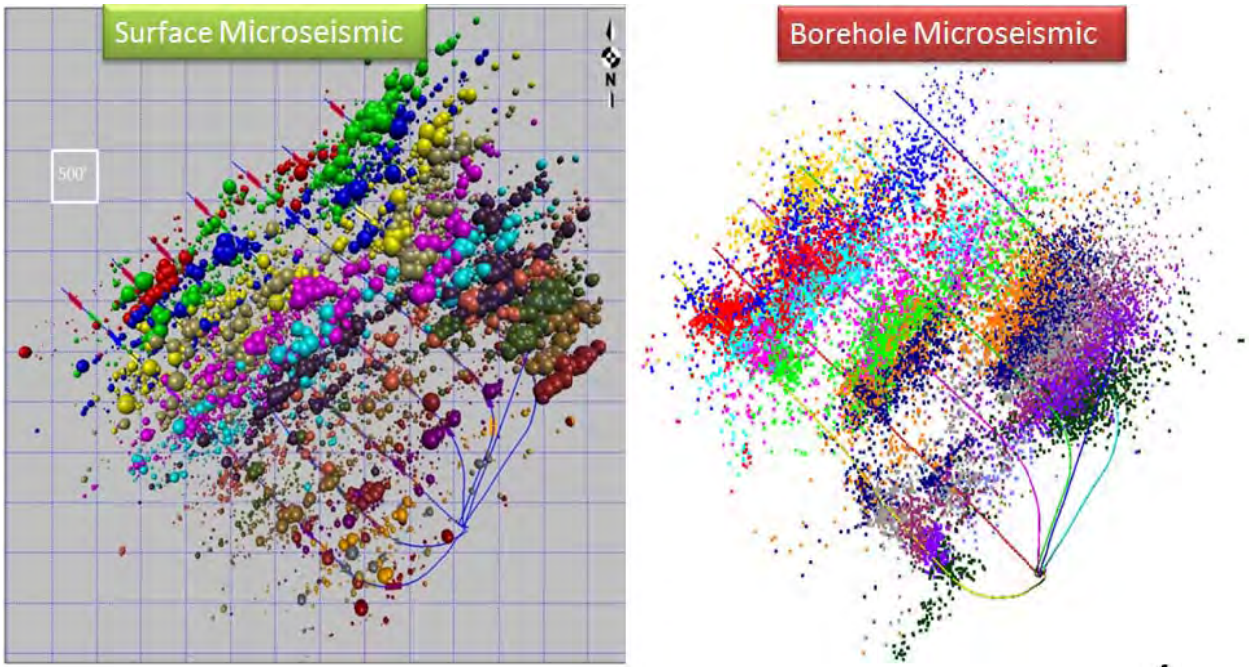

Figure 8: Microseismic event distribution from a surface survey (left) and borehole survey (right).

Natural Fracture Identification from Stimulation

After initial review of borehole microseismic data, production logging results, fracture surface treatment parameters, and RA tracer survey results, a local cluster of natural fractures was identified that intersects a few of the wells and is substantially different from the other natural fractures that may exist and intersect the remaining wells. This cluster of natural fractures may be contributing to higher than average production. Production logging results from Well-D show that production from perforation clusters corresponding to Stage 4 frac account for much higher than average production (22% of the total well). In addition, surface

treating pressure is very erratic, suggesting opening of natural fractures, plugging and then diversion. Figure 9 is the surface treatment plot from Stage 4 frac of well D. This is the only stage in well D that exhibits this much pressure fluctuation while keeping the rate almost constant after the designed job rate is achieved.

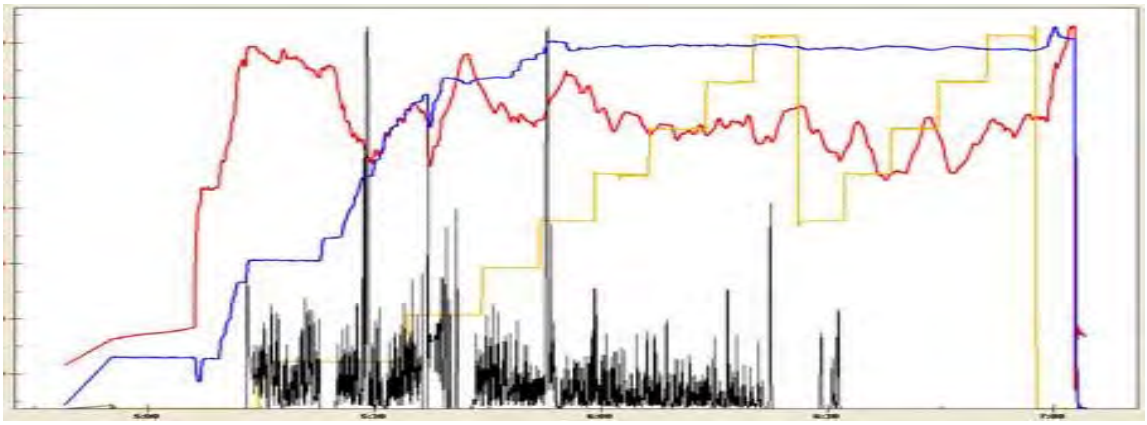

Figure 9: Treatment Data from Stage 4 Frac in Well D

In Figure 9, the red curve is the surface treating pressure, the blue curve is treatment rate, the yellow curve is wellhead proppant concentration, and the black curve is the friction reducer concentration. Coincidently, Stage 5 frac in well B and Stage 5 frac in well E exhibit a similar erratic surface pressure response that is not seen in the remaining frac stages of the said wells. These two frac stages along with stage 4 of well D all fall mostly in line. Figure 11 shows the surface treatment data from well E stage 5. Pressure fluctuations due to rate changes are not considered to be formation related. Figure 10 shows the surface treatment data from well B stage 5 frac. Again, if pressure changes due to rate fluctuations are not considered, there is some erratic behavior in the pressure response during the treatment that is not evidenced in other frac stages.

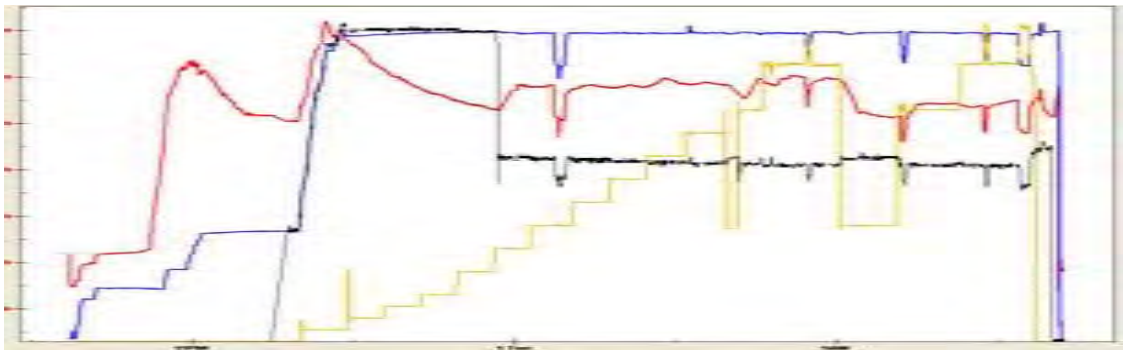

Figure 10: Surface Treatment Data from Well B Stage 5 Frac.

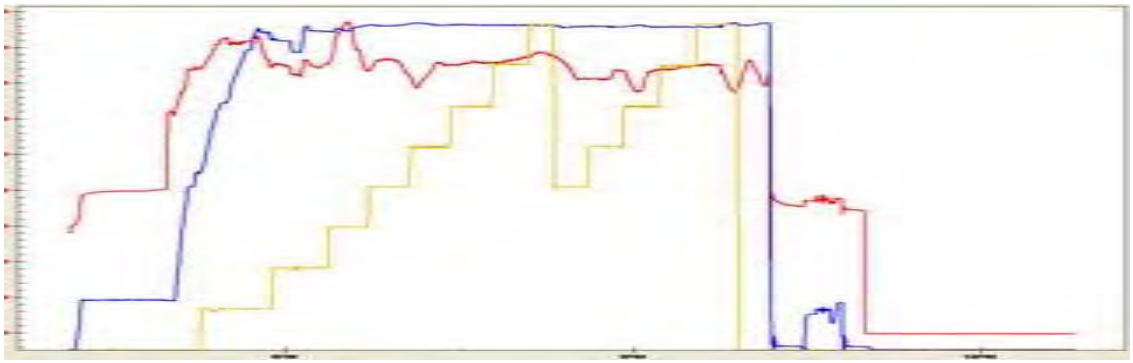

Figure 11: Treatment Data from Well E Stage 5 Frac.

The results of the radioactive tracer survey indicated that there was communication between this zone (stage 4 frac) and some

other zone, possibly the previous frac stage (stage 3). As previously mentioned, the three fracture stages that exhibit the erratic pressure response in three separate wells all lie mostly in line as shown in Figure 12.

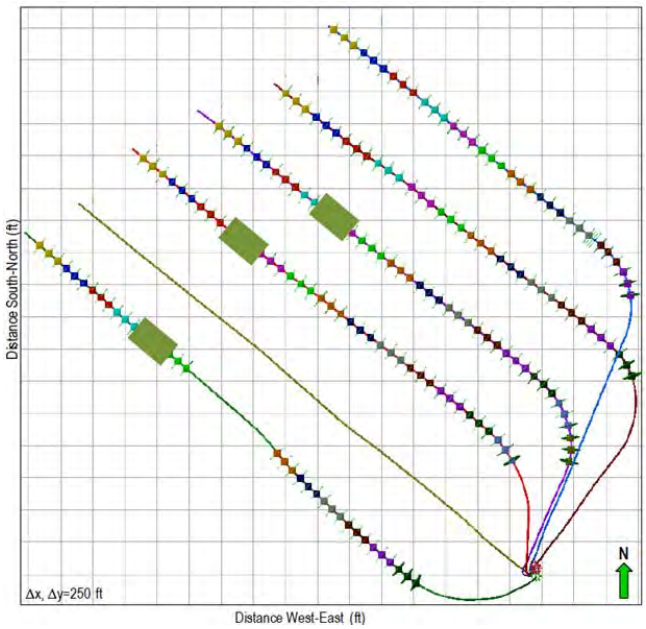

Figure 12: Fracture Stages that Exhibit an Erratic Treating Pressure Response (Green Boxes).

Microseismic events that correspond to these three particular fracture stages are clustered as shown in Figure 13, and indicate that there is in fact a local phenomenon that could point to a swarm of natural fractures causing the erratic surface treating response and a much higher than average production rate from well D stage 4 frac. As evidenced in Figure 8, there are areas of concentrated microseismic events that could suggest other swarms of natural fractures. However the erratic treating pressure response is not clearly visible in other fracture stages besides the ones mentioned previously in this discussion. It is not clear at this point why the pressure fluctuation was so pronounced in these three fracture stages. Other fracture stages exhibited some pressure variation, however friction reducer concentration changes and pump rate changes could not be ruled out as the cause. Furthermore, microseismic events from Well D stage 4 frac (light blue dots in Figure 13) traverse wells C, B and E. This could further be an indication of a swarm of natural fractures since the fracture network is wide and penetrated multiple wells during pumping.

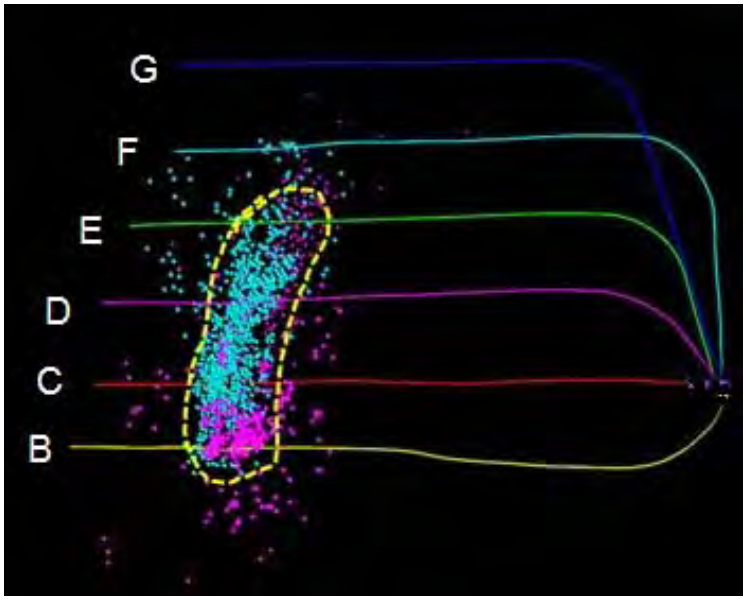

Figure 13: Microseismic Events from Well-B Stage 5 Frac, Well-D Stage 4 Frac, & Well-E Stage 5 Frac.

Natural Fracture Identification from Microseismic and Mud Log Data

Using gas shows data from mud logs, fracture Length to Width aspect ratio (microseismic cloud length divided by width as shown in Figure 14), microseismic event count for each fracture stage, and the results from the post frac production log, we can compare how hydraulic fracture dimensions affect production and relate the gas production to the initial gas that was encountered during drilling from the mud logs. In areas along the horizontal lateral where the wellbore intersects a concentrated swarm of natural fractures, it is expected that gas encountered during drilling to be in high amounts as the natural fractures provide a conduit to gas flow. High gas shows in ultra-low permeability reservoirs can be attributed to natural fractures, since the gas shows are primarily a result of gas being discharged from the natural fractures as well as gas flow from the shale matrix into the natural fractures and into the wellbore, especially during underbalanced drilling. On the other hand, in the areas along the wellbore where there are no natural fractures or the natural fracture concentration is low, the gas present in the drilling mud should be low.

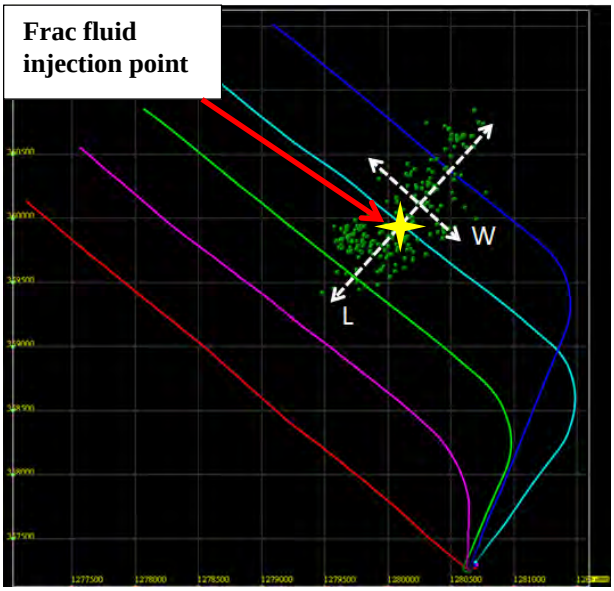

Figure 14: Plan view of horizontal wells witch microseismic data for a single frac stage showing the fracture geometry in terms of fracture width and length. The fracture width here is the width of the fracture network and not the fracture aperture.

When considering the fracture dimensions of each individual fracture stage along a horizontal wellbore, we can quantify the fracture geometry in terms of the fracture Length and Width. The fracture length is the extent of the microseismic events at a distance normal to the wellbore and the fracture width is the extent of the microseismic cloud along the wellbore. Thus the fracture width presented here is the fracture network width and not individual fracture aperture, as shown in Figure 14. In the areas where there are little or no natural fractures present, we can expect to see a simple hydraulic fracture or fractures that are long and closely spaced. Conversely, in areas along the wellbore that exhibit a high degree of natural fracturing we would expect to see many hydraulic fractures spaced far apart and intersect with natural fractures, thus forming a complex and wide fracture network. However, this complex fracture network should be shorter than an individual hydraulic fracture since much of the fracturing fluid is used to expand the fracture network along the wellbore and connect the natural fractures as opposed to creating a single long hydraulic fracture. In the case where there is a moderate degree of natural fracturing along the horizontal wellbore, the created hydraulic fractures should exhibit some complexity due to the interaction with natural fractures and should be longer than a complex fracture network that is created in the presence of high natural fracturing. But this moderately complex fracture network should be shorter than a simple hydraulic fracture that is created in the absence of natural fractures as shown in Figure 15.

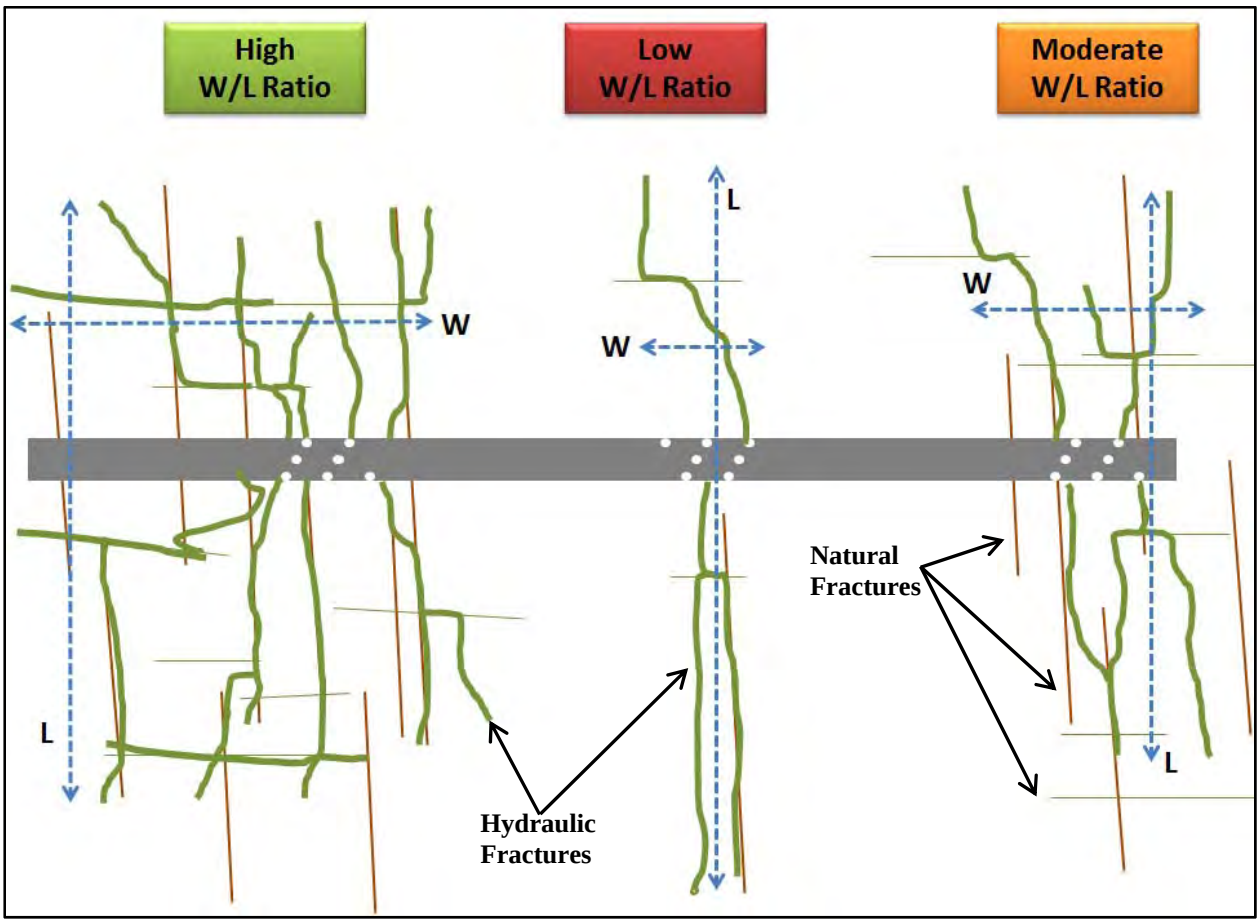

Figure 15: Fracture network creation in the presence of natural fractures.

Another important parameter to consider when evaluating stimulation efficiency is the number of microseismic events captured during a hydraulic stimulation treatment. This parameter heavily depends on proximity of geophones to the signal source and when in close proximity, the geophones should record a large number of microseismic events. As the events occur farther and farther from the geophones, they should still be recorded, although with lesser location accuracy.

If we consider the three cases shown in figure 15; where the wellbore intersects a concentrated swarm of natural fractures, few natural fractures, and almost no natural fractures, we can qualitatively predict the number of microseismic events that would be recorded in each case. In the case of a hydraulic fracture or fractures intersecting a concentrated swarm of natural fractures, we can expect a large number of recorded microseismic events. This is due to the fracturing fluid changing direction many times and breaking up new rock while intersecting natural fractures and creating a complex fracture network. In cases where there are few natural fractures that intersect and are near the wellbore, there should be fewer recorded events relative to the previous case. This is a result of fewer hydraulic fractures intersection with natural fractures and changing direction. In the third case, where there are few or no natural fractures at all, we expect to record a low number of microseismic events. This happens because the hydraulic fracture is simple as it does not have a chance to intersect with natural fractures and change direction while creating signal events. Furthermore, under this condition, the hydraulic fracture quickly propagates away from the wellbore and many of the microseismic signals are too far from the geophones to be recorded and located accurately. Figure 16 shows the results of the borehole microseismic survey from the test site mentioned earlier. There are areas that exhibit a high concentration of microseismic events, moderate concentration of microseismic events, and areas of few or no microseismic events. These results are quite surprising given that the fracture spacing in all wells was almost identical and large fluid and proppant volume pumped. Additionally, the geophones in the horizontal monitoring well were moved 5 times along the wellbore to reduce the listening distance, or spatial bias, as the fracturing treatments were executed in a zipper sequence. This evidence, along with mentioned geologic studies and fracture diagnostics related to pressure variations during pumping clearly substantiate the notion that natural fractures in the Marcellus manifest themselves in swarms or clusters. This evidence is further supported by results from a production log. Even

though all perforation clusters contribute to production, the areas where there is evidence if swarms of natural fractures the productivity is much higher as discussed in later sections.

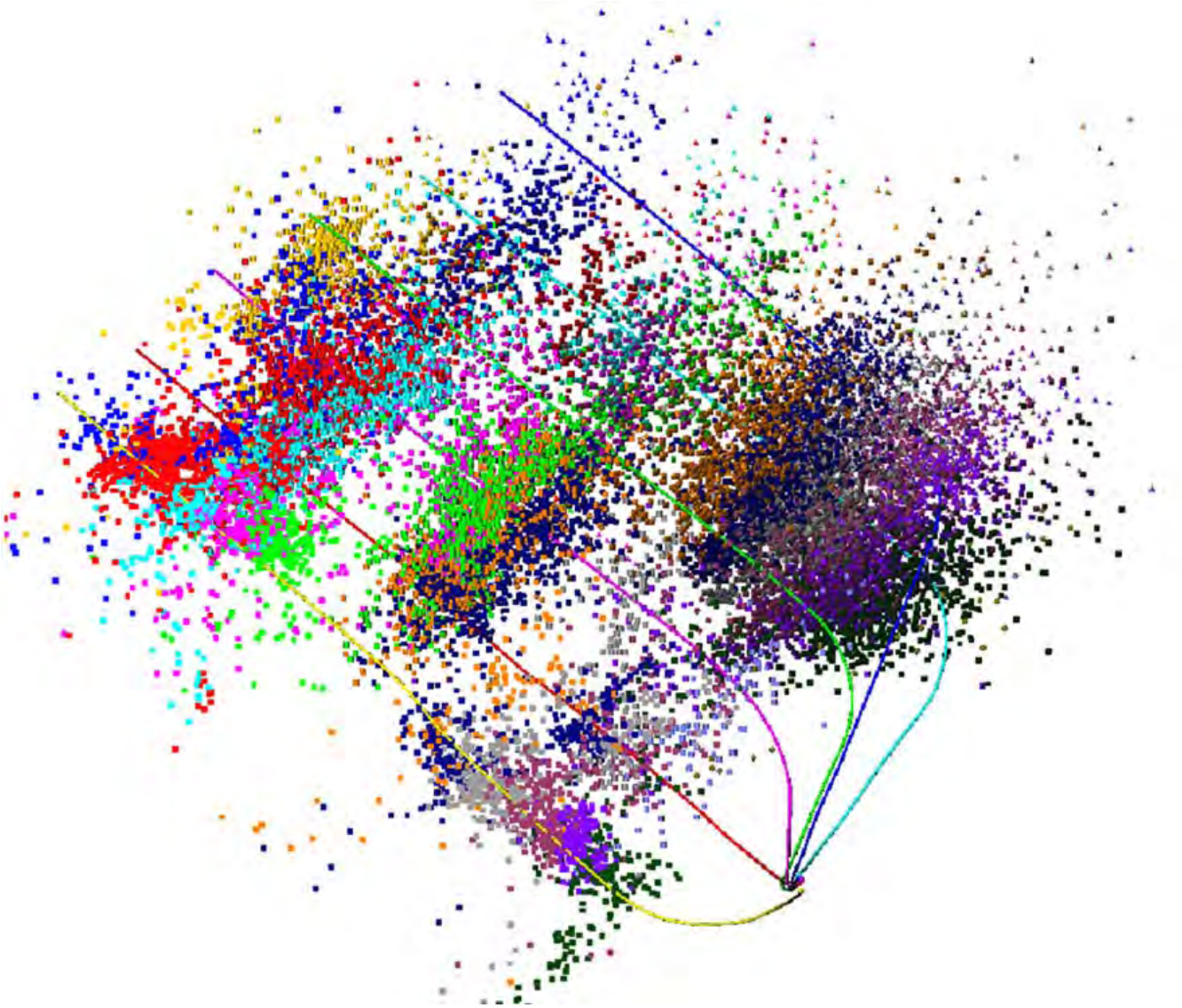

Figure 16: Results of the microseismic survey showing the recorded events for each frac stage.

Reservoir Quality

When looking at the production log and trying to determine the factors that might have contributed positively to the production at each perforated interval, it is essential to consider and understand the reservoir quality along the horizontal lateral. Aside from reservoir quality, there are many factors that influence production from each fracture stage. Critical factors related to stimulation include: fracture and perforation cluster spacing, fluid and proppant volumes pumped, fracturing treatment pump rate, proppant concentration and mesh size, etc. One way to determine the reservoir quality and check for uniformity is to look at the gamma ray acquired during drilling of the horizontal section. Figure 17 shows the gamma ray for 2 wells adjacent to the microseismic monitoring well. These two wells (Well D and E) were chosen because the gamma ray data was available for only these two wells. The gamma ray is fairly uniform throughout the lateral section of the two wellbores. This is indicative of the horizontal lateral staying in the pay zone as the reservoir quality is uniform throughout. If the horizontal section of wellbore diverged from the pay zone, the gamma ray would quickly indicate this as can be seen in the curve section on both wells and in the toe section of well D.

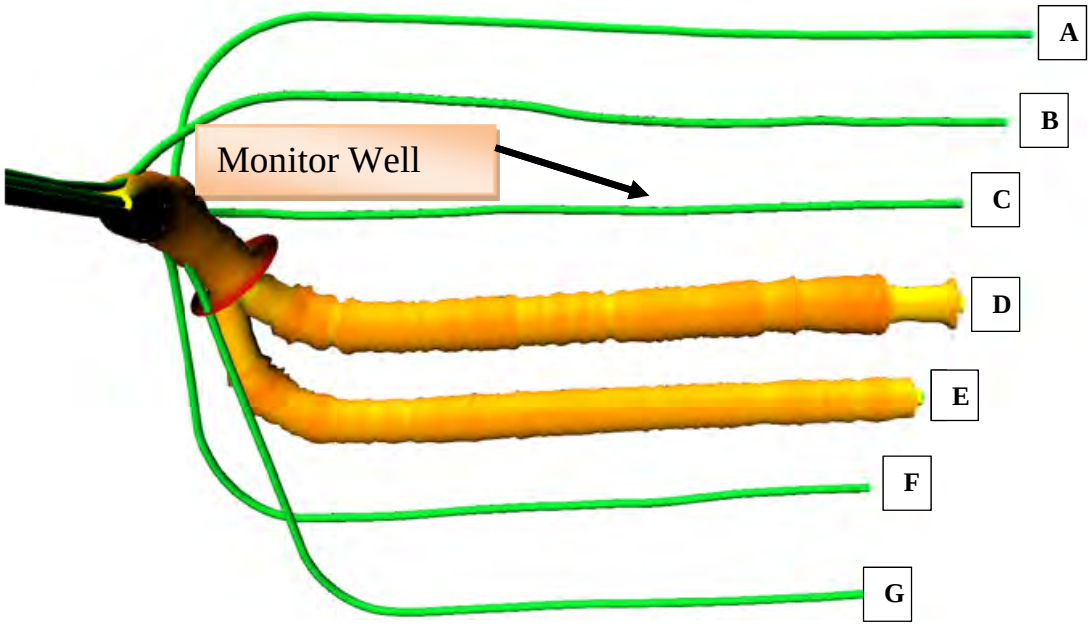

Figure 17: Plan view of horizontal wells with gamma ray logs in two selected wells closest to the microseismic monitoring well.

With the gamma ray being uniform throughout the wellbore, we can cautiously assume that the rock is fairly homogenous, however when looking at the gas shows there are significant variations in the gas distribution from the heel of the well to the toe. In all cases, there were significant gas shows recorded throughout the horizontal lateral with some areas being much more active than others. For example, well D has very few gas shows near the heel and the gas shows increase towards the middle of the horizontal. Then towards the toe of the well, there are fewer and fewer gas shows with significant voids. This could be an indication that either the reservoir quality may have changed or the toe section of this well may have come out of the pay zone judging by the major decrease in the gamma ray. In either case, the lack of gas shows in this section of the wellbore could be explained by poor reservoir quality. In another example, well E, there are again numerous gas shows throughout the lateral; however again, there is high variability in the distribution of the recorded gas shows. Well E has reasonably good shows towards the heel of the well and the gas shows fade towards the middle of the well. Then, starting at the middle there are again significant shows; however the gas shows decrease towards the toe of the well as shown in Figure 18. With the gamma ray being uniform, there have to be other drivers for the gas shows to vary this much, and hence there is a good chance that natural fractures are present in clusters along the horizontal lateral.

Comparing the gamma ray data from the heel section and toe section of well D, it is evident that the gamma ray is similar. Given that these wells were drilled toe-up to aid in liquid drainage, there is a chance that the toe of the lateral may be at the boundary of the Marcellus and the overlying formation. Natural fracture clusters are not confined just to the Marcellus, they extend through multiple formations as seen in cores and geologic studies. Therefore, if a swarm of natural fractures intersects the toe section of well D, production from this section should not be impacted even if this section was outside of the Marcellus. This is because the created fracture network resulting from stimulation and composed of hydraulic and natural fractures will connect the wellbore to the Marcellus. The significant spike in the gas show at the very end of well D in figure 18 indicates that there might be some natural fractures present.

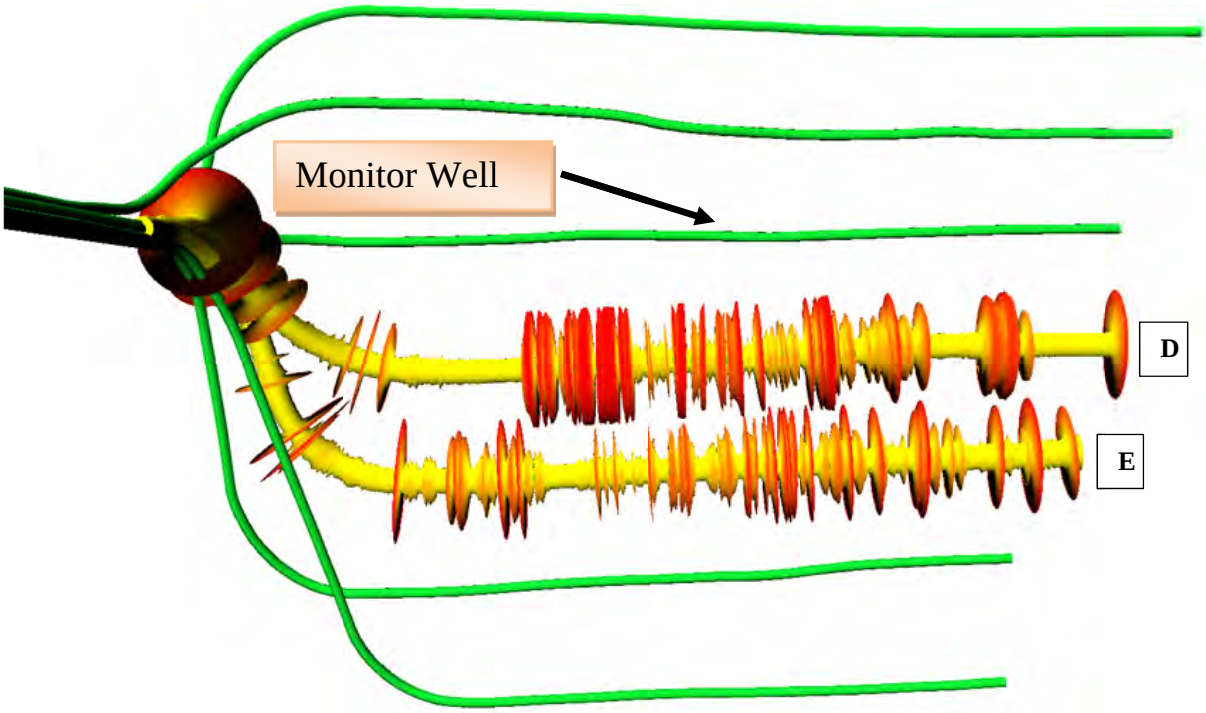

Figure 18: Plan view of horizontal wells with mud log gas shows in two selected wells closest to the microseismic monitoring well.

Combining the gas show data, along with fracture Length to Width aspect ratio, microseismic event count and also the early production log, many clear trends can be observed. Beginning at the heel section of the well D (1st shaded area), mud log data shows very little gas (1 in figure 19), the created fractures in this area are long and the fracture network is narrow as indicated by the high Length to Width aspect ratio (2 in Figure 19). The microseismic event count is low (3 in figure 19) and gas production is high from one of the perforation clusters (4 in Figure 19). By looking at the gas shows we can conclude that not many natural fractures were present. This is supported by the narrow fracture geometry that is long and has a low event count. The high production from just one perforation cluster suggests that the long narrow fracture geometry connected to a natural fracture network somewhere nearby this increasing production in one perforation cluster.

The second position along the wellbore that has high production is in the middle. Here there were significant gas shows, the created fracture network is wide as indicated by the low length to width aspect ratio, and the microseismic event count is high. All of the data suggests that in this area there is a minor natural fracture cluster. The reason why it is minor is because the high production is limited to 1 perforation cluster. However the microseismic event count is high and the L/W aspect ratio is low in the neighboring fracture stages.

Looking at the last 2/3 of the wellbore towards the toe, we see many perforation clusters with high gas contribution. The last production logging data point in Figure 19, which is closest to the toe of the well, is the total production from fracture stages 1 through 3, as the production logging tools were not able to be conveyed all the way to the toe. There are significant gas shows in the mud log, the length to width aspect ratio is consistently low and the microseismic event count is extremely high in almost all the frac stages in this area. All the data suggest that there is a large concentrated natural fracture swarm in this area that is driving the high production. Finally, the very end of the wellbore, the toe section that had the first two fracture stages shows very few gas shows, the length to width aspect ratio is increasing and the event count is decreasing. There is no production log data for this section as the tools were unable to be conveyed all the way to the toe. However, considering that the gamma ray here is low and very different from the rest of the wellbore, it is assumed that the wellbore is out of the pay zone. This is confirmed by the lack of gas shows. Even though there were no gas shows, the microseismic data indicates that the natural fractures are present and are not just confined to the Marcellus. This can be seen from a relatively high microseismic event count for each fracture stage and by the low length to width aspect ratio.

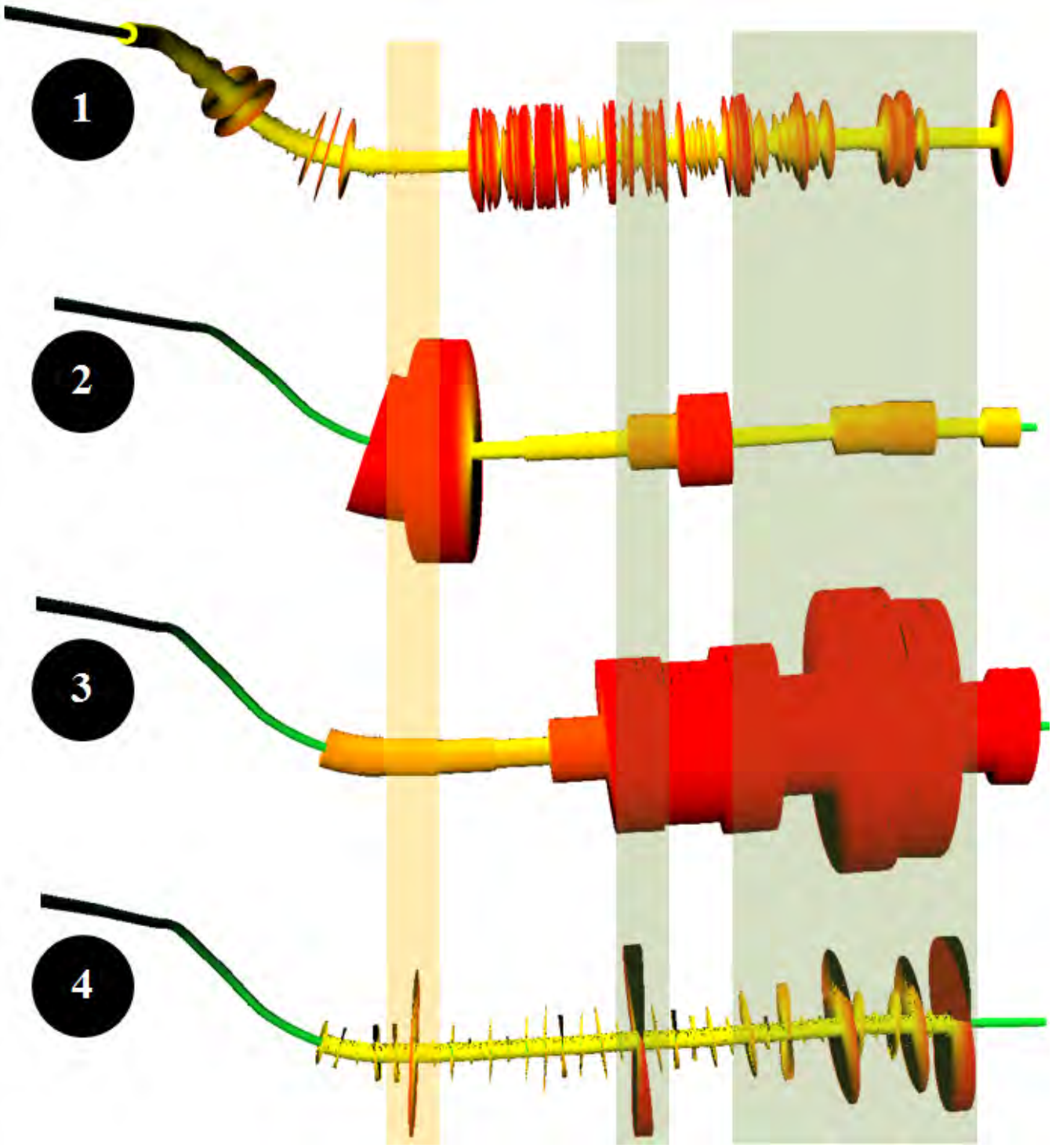

Figure 19: Plan view of horizontal well D. 1: Mud log gas shows. 2: Fracture Length/Width aspect ratio from microseismic data for each frac stage. 3: Microseismic event count for each fracture stage. 4: Gas production from each perforation cluster based on production log ran after 4 months on production.

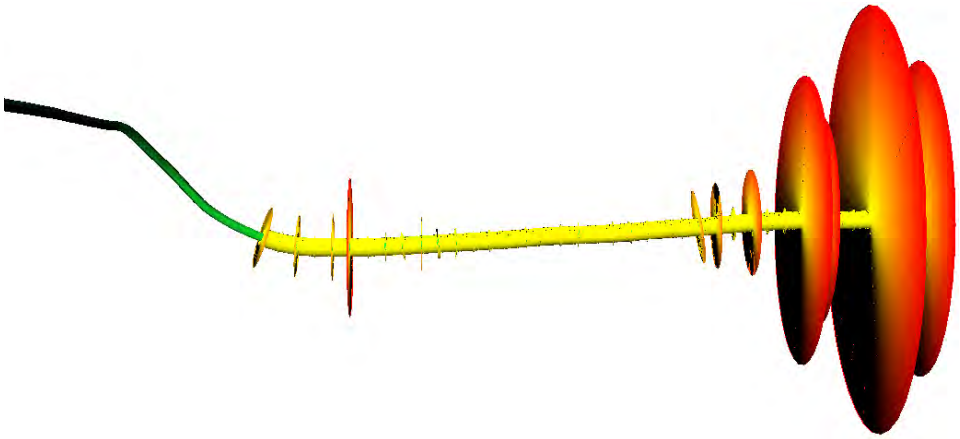

Figure 20: Plan view of well D showing gas production from each perforation cluster based on production log ran after 13 months on production.

A second production log was run in well D to determine production contribution from each perforation cluster and how it changes over time. During the second production log, tools were able to reach and log the perforated lateral from the toe to the heel with the exception of the first two perforation clusters in the first fracture stage. The well was chocked back slightly to accumulate fluid in the lateral to cut the friction forces since the tools in the first production log were not able to reach the toe of the wellbore. As a consequence, the production contribution from individual perforation clusters in the first 3 fracture stages was not determined in the first production log. Instead, the production from the first 3 fracture stages was recorded as aggregate. By holding some back pressure during the second production logging run it restricted flow from a portion or all of the stages. There is a chance that liquid could stack up in the horizontal section toward the heel of this toe-up well due to choking back the flow at the surface. However, this effect might be limited since the production log shows higher production in the heel section of the wellbore than in the middle section of the wellbore.

Based on the results, the majority of gas production comes from the toe section of the wellbore with some significant production coming in at the heel section as shown in Figure 20 (The scale in this figure is increased to show detail. The total production recorded in the second production log, as expected, is significantly lower due to depletion, than total production recorded in the first production log. The two production logs were run 9 months apart.) The relatively high production contribution in the toe section compared with the rest of the wellbore can be attributed to two factors. First, there exists a natural fracture swarm near the toe section of this particular wellbore that has been identified through various analyses as shown before. Second, higher production contribution can be expected in the toe and heel sections of the wellbore after the well has been on production for some time because a reservoir that is penetrated with multiple horizontal wells will be depleted first in the area that contains the horizontal wells and then the highest production should be at the toe and heel as shown in Figure 21. The heel and toe sections of all the wells will be recharged with gas from the reservoir that is not penetrated by any wellbores thus having a higher long term production contribution.

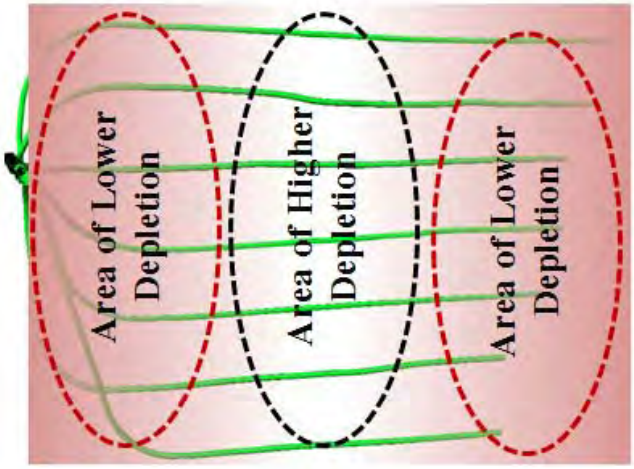

Figure 21: Plan view showing depletion areas of a penetrated reservoir with multiple horizontal wells.

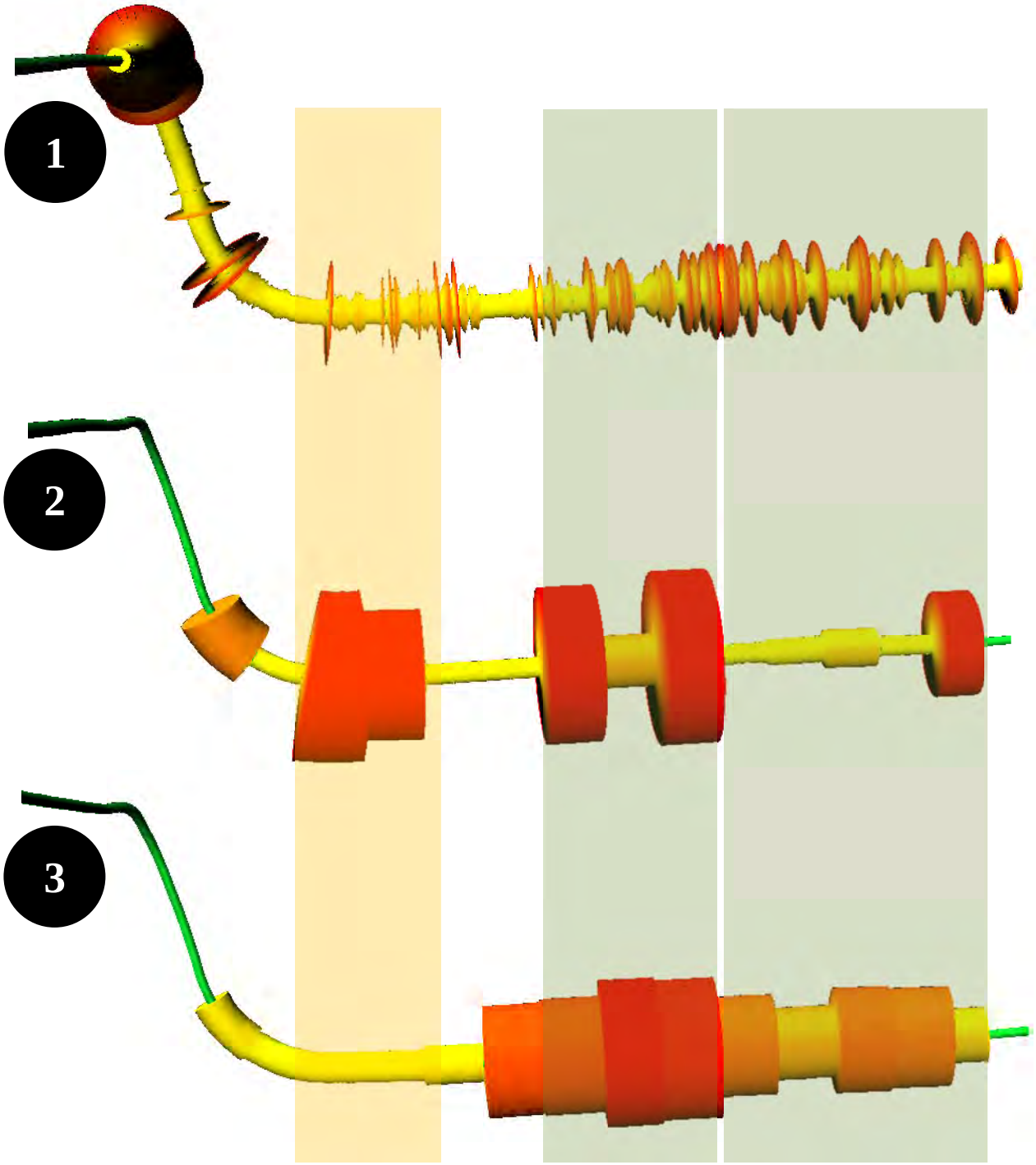

Figure 22: Plan view of horizontal well E. 1: Mud log gas shows. 2: Fracture Length/Width aspect ratio from microseismic data for each frac stage. 3: Microseismic event count for each fracture stage.

A similar analysis to determine natural fracture occurrence and concentration can be performed on another well with available mud log data. Well E, which is adjacent to well D, does not have a production log, however microseismic data is available for all the fracture stages performed in this well. Therefore, the fracture geometry data including microseismic event count and Length to Width aspect ratio can be compared.

Beginning at the heel of well E, the mud log shows few small gas shows that are spaced far apart (1 in Figure 22). The hydraulic fractures in this area are long and the fracture length to width aspect ratio is high (2 in Figure 22), indicating little hydraulic

fracture interaction with natural fractures. The microseismic event count is low (3 in figure 22), thus again indicating a lack of natural fractures that would interact with hydraulic fractures and create a complex fracture network. With the microseismic event count low, the Length to Width aspect ratio high and relatively low gas shows, there is good indication that there are few or no natural fractures present in this area of the wellbore. This agrees with analysis performed at the heel section of the adjacent well, Well D.

The area in the middle of the wellbore indicates some gas shows that are spaced far apart and are moderately high. The microseismic event count is significant and there is an alternating high-low-high fracture Length to Width aspect ratio. There is clear indication that there are some natural fractures present in this area by the significant microseismic event count and by the alternating length to width aspect ratio. The mud log data confirms this as the gas shows fade in and out. This is again in agreement with the adjacent well, Well D, and implies that the minor natural fracturing extends across these two wells.

Looking at the last 2/3 of the wellbore towards the toe, there are significant gas shows in the mud log, the length to width aspect ratio is consistently low and the microseismic event count is consistently high in almost all the frac stages in this area. All the data suggest that there is a large concentrated natural fracture swarm in this area that is driving the high gas shows in the mud log. The gamma ray at the toe section in this well is consistent with the rest of the wellbore, suggesting that the entire wellbore is in the pay zone. The mud log data confirms this by showing good gas shows. However the natural fracture swarm may be fading out towards the very end of the wellbore. The microseismic count is beginning to decrease and the length to width aspect ratio is begging to increase. This implies that the fracture complexity is decreasing. Again, this is confirmed by the gas shows being less and less frequent.

Big Picture

Results from the previous analysis provide a very strong case that suggests natural fractures in the Marcellus manifest themselves in concentrated swarms. We have shown that the Length to Width aspect ratio along with microseismic event count is a good indicator of the presence and concentration of natural fractures. Furthermore, this is supported by the mud log gas shows. Using the entire microseismic data set we can plot the Length to Width aspect ratio for every fracture treatment on this pad to examine how the natural fractures are spread out. Figure 23 is a surface plot that shows the Length to Width aspect ratio for all 93 hydraulic fracturing treatments. The warm colors indicate long, narrow hydraulic fractures, while the cool colors indicate shorter but wider hydraulic fracture networks tied together with natural fractures. The wellbore orientation relative to the surface plot is shown below the surface plot.

There are areas in the plot that indicate that the natural fracture swarms extend across multiple wells then fade out and eventually start again. Area 1 in Figure 23 shows a valley that extends across multiple wells indicating a significant natural fracture swarm that was confirmed in the previous analysis of well D and E. The lowest part of Area 2 in Figure 23 in the plot coincides with the middle if the wellbores D and E. Previous analysis suggests that there could be a small natural fracture swarm present in this area, and based on the surface plot the natural fracture swarm is fading out and eventually disappears in the middle and top of area 2. Area 3 in Figure 23 shows a very deep valley, indicating another natural fracture swarm. This seems to be just the beginning of the swarm as it begins to widen towards the top as the data ends. Area 4 in figure 23 indicates a lack of natural fractures due to the high length to width aspect ratio. In this area the fractures are long and fairly simple due to lack of hydraulic fracture-natural fracture interaction. Area 4 coincides with the previous analysis of the heel sections of the two wellbores where there were very few gas shows and the fractures were long and simple. The heel of well D is right below area 4. This is where the production log showed one perforation cluster with significant production. Although the hydraulic fractures in the area showed to be long and simple, there is a good chance that they eventually connect to a natural fracture network that can be seen to be starting below section 4, indicated by the cool colors, or the valley.

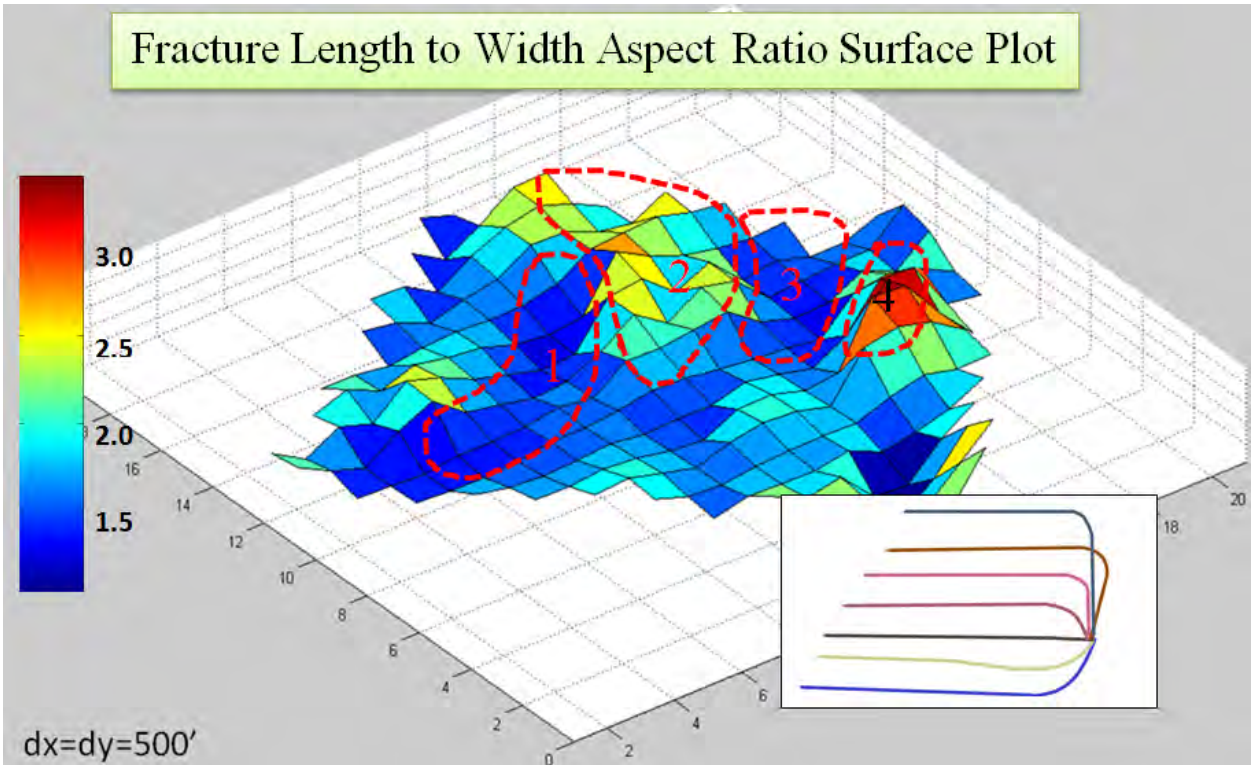

Figure 23: Surface plot of the Length to Width aspect ratio for the entire pad.

Conclusions

Geologic studies of natural fractures in outcrops of Marcellus shale and other formations show that there are certain distances at which there is a high occurrence of natural fractures, called the characteristic spacing. High resolution imaging also shows that even though the Marcellus shale exhibits low porosity and permeability, the presence of micro-fractures enhances gas storage and potentially gas flow. Together with the analysis described in the above sections, it is possible to determine where the natural fracture swarms are located and the extent of the fracture concentration.

Using microseismic data, more specifically microseismic event count and the fracture length to width aspect ratio, it is possible to identify a swarm of natural fractures. Figure 24 shows a qualitative method of how to determine the extent of natural fracturing in the reservoir. On the x-axis is the microseismic event count and on the y-axis is the inverse of the length to witdh (L/W) aspect ratio or the width to length (W/L) aspect ratio. With increasing microseismic event count and increasing fracture W/L aspect ratio the natural fracture concentration increases. This results from fluid propagating from hydraulic fractures into natural fractures and changing direction as the hydraulic fracture intersects a natural fracture. Furthermore, increased interaction of hydraulic fractures with natural fractures causes the W/L fracture aspect ratio to increase as more fluid is pumped. The W/L aspect ratio increases as a result of frac fluid propagating through the natural fractures causing more "pops". Having such an extensive microseismic dataset is very rare and there needs to be a way to identify the natural fracture swarms without such a dataset. We have shown that there is very good correlation of natural fracturing with the mud log gas shows. In fact, in a very tight reservoir such as the Marcellus, the gas shows should be a driven by natural fractures.

Microseismic data shows that in the areas with swarms of natural fractures, stimulation is very efficient. This can be seen by the very high microseismic event count, low L/W aspect ratio, and high production contribution from perforation clusters in this area. However, in the areas that do not contain many natural fractures, stimulation efficiency is greatly reduced. This is the area that requires more thorough stimulation. Given that the natural fractures manifest themselves in swarms in the Marcellus shale, there is a good chance that pumping more fracture stages in areas that have little or no gas shows, will lead to better stimulation by inducing more hydraulic fractures, and increasing the chances to connect with nearby natural fracture swarm. It is possible that hydraulic fracture spacing in areas with high gas shows can be reduced without decreasing production significantly as these areas will produce effectively because of the natural fractures. The data and the results of the analysis presented here suggest that more focus should be placed on stimulating areas that do not have good gas shows but where the gamma indicates the wellbore is still in the pay zone. When designing the stimulation program, hydraulic fracture spacing could be determined by the gas shows and

more fracs pumped in areas of no gas shows instead of equally spacing the hydraulic fracture stages.
Furthermore, surface pressure variations during pumping of a hydraulic fracture stage have shown to be a reliable indicator of the presence of natural fractures and can be used to confirm and compare against the mud log gas shows. It is therefore possible to optimize the fracture spacing in real time if such pressure variations are observed.

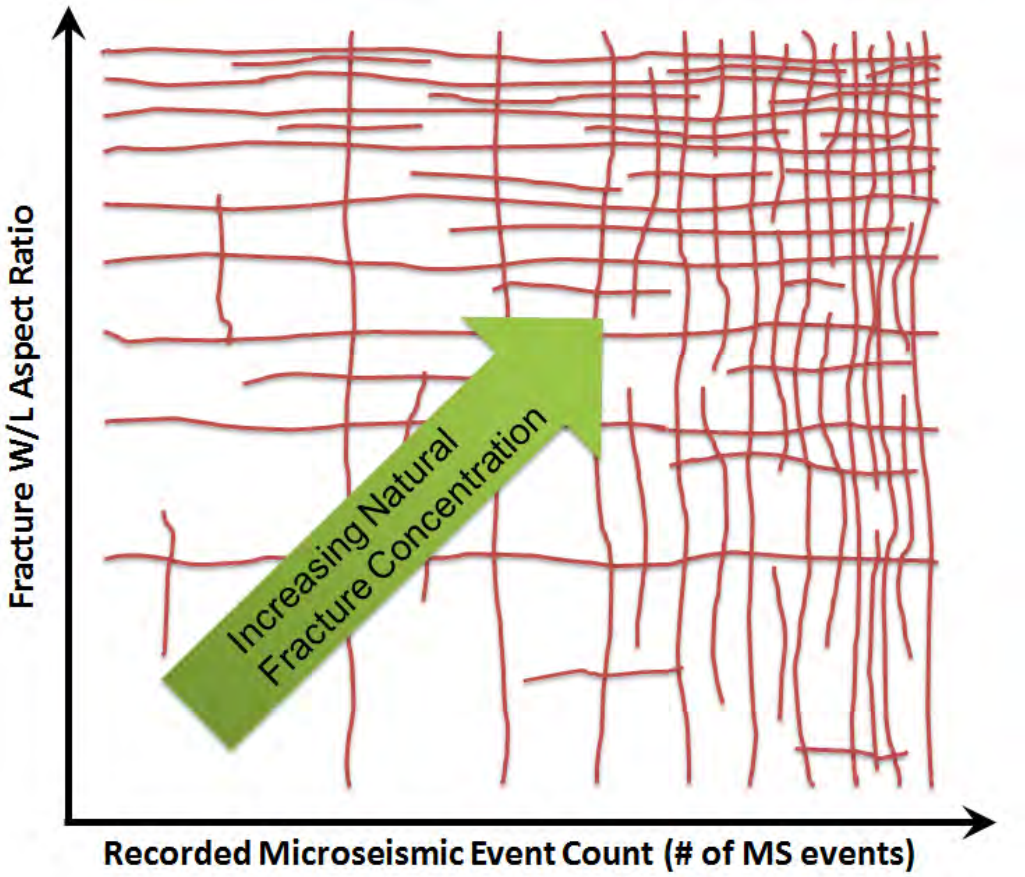

Figure 24: Indication of natural fracture concentration based in microseismic data.

Acknowledgement
We would like to thank RPSEA for providing funding for this research project. In addition, we also express our thanks to Range Resources for providing substantial cost sharing, data, and wells of opportunity and Schlumberger for their generous cost-sharing.

References

Ciezobka, J., *Topical Report on Stimulation and Completion, Marcellus Gas Shale Reseach Project*, August 25, 2011, www.rpsea.org

Holder, J., Olson, J., Philip, Z., *Experimental determination of subcritical rack growth parameters in sedimentary rock,* Geophysical Research Letters, Vol. 28, No. 4, pages 599-602, University of Texas at Austin, February 15, 2001

Curry, M., Maloney, T., Woodroof, R., Leonard, R. *Less Sand May Not Be Enough SPE-131783.* s.l. : Society of Petroluem Engineers, 2010.

Appendix D - Optimized passive seismic survey design with simultaneous borehole and surface measurements

Optimized passive seismic survey design with simultaneous borehole and surface measurements

Debotyam Maity, Fred Aminzadeh

Induced Seismicity Consortium (ISC, USC)

Date: January 18th, 2013

Report ISC-2013-1

USC Viterbi
School of Engineering

Table of Content

TABLE OF CONTENT 2
SUMMARY: 3
INTRODUCTION: 3
THEORETICAL ASPECTS: 3
SELECTED OPTIMIZATION FRAMEWORK ELEMENTS: 5
EXPERIMENTAL SETUP: 8
RESULTS: 9
OBSERVATIONS & RECOMMENDATIONS: 17
FUTURE WORK: 19
ALGORITHM: 19
ACKNOWLEDGEMENT: 20
REFERENCES: 20
APPENDIX A: 20

Summary:

This project attempts to develop a new integrated framework for optimized multi array passive seismic monitoring programs based on specific requirements set forth at the initiation of the project. We have defined a new framework based on existing microseismic array optimization workflows and deployed this framework into a working implementation within Matlab environment for potential use. While the algorithm as tested shows a lot of promise for actual deployments in the field, tests with real data can provide the necessary confidence to use it for future programs. This project has been funded by a GTI grant and is aimed at understanding the elements which influence the design of multi array passive seismic monitoring programs and to develop a framework for optimization of such arrays for improved Hypocentral locations and source mechanisms while optimizing deployment costs. This report provides an extensive background on the optimization framework used in tour work as well as results with necessary observations and recommendations for future multi array receiver deployments. (Refer Appendix A for the original proposal and work plan).

Introduction:

With the increasing potential for use of multiple microseismic arrays in hydraulic fracturing and waste water injection programs, there is a need to look into a standardized scheme for optimizing the design and layout of the different arrays so as to improve upon the observations, processing and interpretations which can be made through each of the individual or the combined arrays. The aim is to maximize the information that can be gleaned from the data collected through these arrays in order to obtain the best possible results during the actual stimulation through improved (high resolution) event mapping, source mechanisms, velocity, stress, other property estimates, etc. This is essential as each monitoring program will have its own unique dynamics which need to be taken into account while designing the arrays. We propose to look at this problem at multiple levels to identify and develop elements of the workflow to design an optimized multi-array survey which works to improve the applicability of the sensor arrays themselves as well as reduce the final deployment costs by taking into account the relevant limits to be placed on the design including for redundancy if the cost benefit analysis requires us to do so. Such a workflow will provide relevant deployment schemes for any future multi-array monitoring programs and provide us with a valuable tool to get the best value for money.

Theoretical Aspects:

Most hydraulic-fracturing experiments can benefit tremendously with properly designed micro-seismic arrays and their optimum deployment in ways which cover all potential waveform propagation pathways in the subsurface. Moreover, the limitations and advantages associated with different deployment schemes (such as high noise artifacts and deployment costs for surface data, etc) are now well documented. This places a very high premium on the final deployment costs if we were to design arrays which are exhaustive and designed to cover for all possibilities without checking for possible redundancy. Moreover, in order to save costs, most situations demand the placement of arrays in existing wells and surface locations which are more conducive from an “operational” point of view. While there are existing procedures to optimize micro-seismic array design for either surface phones or

borehole measurements, simultaneous optimization for both measurements continues to be underexplored. The challenge becomes even more daunting if additional design constraints (such as tooling design, legal restrictions, etc) come into the picture. Figure 1 shows a generalized listing of some of the design elements which place constraints on any microseismic survey. Which elements within this matrix gets higher importance often depends on the location and the operator and the service provider has to come up with an optimal solution within these restrictions. Figure 2 shows typical deployment possibilities with different seismic & microseismic monitoring programs implemented in the field and indicates the potential complexities which such deployments may face when we try to optimize them.

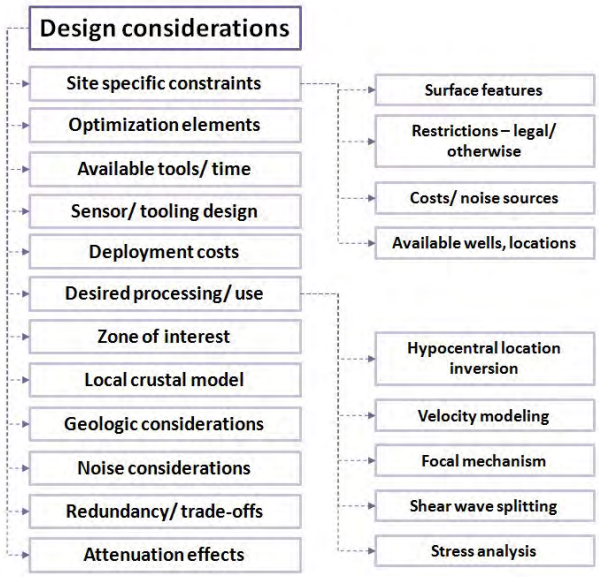

Figure 1: Global design framework

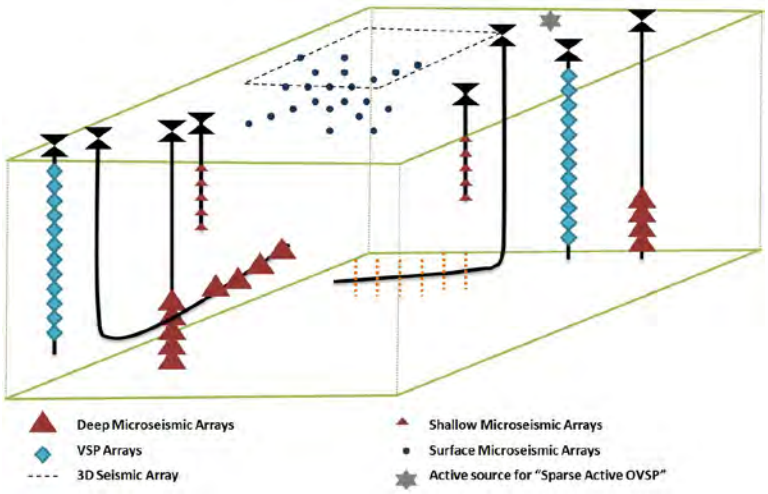

Figure 2: Schematic view of complex survey designs with deep, shallow and surface arrays for passive seismic as well as active arrays for improved reservoir characterization.

The aim therefore is to design and implement a monitoring program which makes the best possible use of the available assets (such as available wells, etc) and to design the program in such a way so as to

optimize the design parameters for all of the planned arrays to get the best possible results from the data during processing (for locations, focal mechanisms, etc). This can be achieved through modeling of the arrays and potential ray paths and identifying the specific inversion schemes to used during processing and can be very exhaustive depending on the level of complexity involved. A large number of variables generally define these design parameters. These include the crustal or the local velocity structure, major faults and discontinuities, operational factors (such as operational drilling programs, pumping schemes, etc and their proximity), cost/ time/ resource limitations and finally the "desired degree of precision" in the final results. There are many potential monitoring arrays and their combinations which can be examined. Under this project, we have developed algorithms which provide the ability to add complex array designs in 3D and optimize over the entire search volume. Down-hole (both vertical and horizontal), shallow verticals, surface, etc can all be combined based on existing conditions but the method does require some prior knowledge on the actual zone of interest.

Selected Optimization framework elements:

Based on the requirements identified by GTI and our own analysis at ISC, specific elements from within the design framework (figure 1) were selected for implementation within the optimization algorithm. Elements of the defined work plan (Appendix A) were incorporated and followed as necessary. Based on the potential location of the monitoring arrays and receiver patch design, the receiver locations were modeled in 3D. Similarly, based on the identified zones of interest, artificial sources were placed at depth of interest to mimic actual events that may occur during the monitoring phase of the project. The first component for optimization was the actual ray traces based on all source receiver pairs. The separation of the ray traces and the actual ray lengths have a direct bearing on the final results obtained during inversion runs. The second component that was looked into was the actual moment tensor inversion algorithm (least square inversion for focal mechanism) to be used. Here the stability of the inversion matrix (in the presence of noise and attenuation effects) plays the most important role as far as design considerations go. Figure 3 shows a schematic view of both these elements and how their optimization relates to their evaluation methodology.

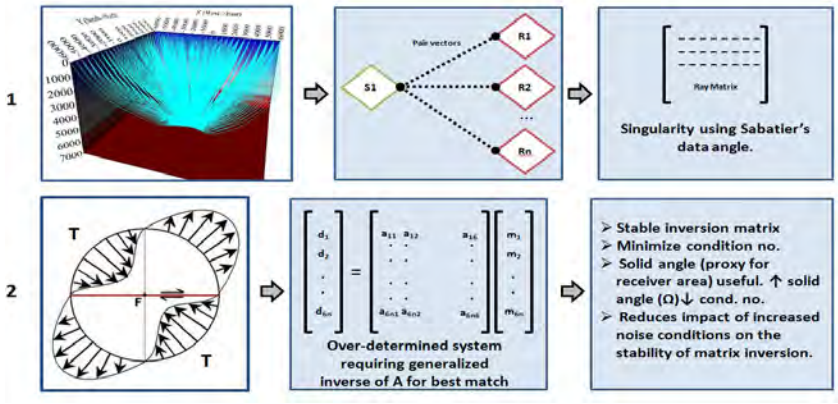

Figure 3: Background on selected design elements.

It is important to note that there are many other design criteria which may be implemented and the method proposed here is just one among the many techniques available in theory. There is considerable body of literature available which can be referenced in order to look at some of these methods. To cite a few examples, Genetic Algorithms (GA) based optimization techniques have been used in the past and can be looked into for improved results (Raymer et al., 2004). We did run implementations of GA based optimization but switched to the more exhaustive search method as we also had moment tensor inversion optimization criteria which led to certain implementation issues. Another technique involves the analysis or error ellipsoids observed during hypocentral location inversions. This involves generating synthetic data (based on array design) and running location algorithms with good error quantification and optimizing the array by removing elements showing highest errors (Chen, 2006). Figure 4 shows some examples of such error evaluations for different depths from cited work.

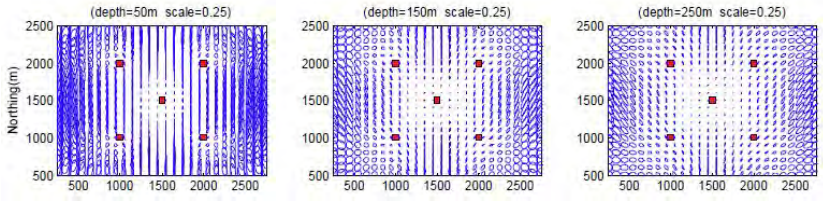

Figure 4: Error ellipses at different depths for 5 receivers (Chen, 2006).

Methods based on analysis of noise levels for different configurations also provide interesting guidelines on array design (Eisner et al., 2010). Other techniques from electrical engineering (which make use of signal processing concepts) are also available and provide unique insights for some diverse perspective. However, we will look at the specific elements within the framework that were utilized in this study.

In case of ray trace focusing, the starting point is to understand any standard inversion method which may be used in hypocentral location algorithms. A generalized solution for arrival time based on model slowness can be represented as $d = A_s M$. Here the ij^{th} element of the A_s matrix denotes the ray-length within the corresponding element. Based on the inverse solution obtainable, the $A_s^T A_s$ matrix can be decomposed numerically and the Eigen values provide an indication of how relevant the information is that can be obtained for the corresponding source-receiver pair (ray trace). While the eigenvalues based quality measure and optimization is a possible pathway to follow (Linear statistical experimental designs by Curtis, 2004), another alternative technique is to use the concept of singularity where zero or near zero eigenvalues for the identified matrix occur if rows in A_s are a linear combination of other rows which in turn indicates redundancy in the data. This approach has been used (Curtis et al., 2004) to design passive surveys in the past and modified implementations are available for use in the open source (experimental design applet for a seismic network: http://alomax.free.fr/projects/expdesign/). The generalized equation for quality measure used is as follows:

$$Quality_{target\ \ Rec.} = \sum_{other\ Rec.} \{ \sum_{sources} [(1 - \frac{\left| a_{target\ \ Rec.} \cdot a_{other\ Rec.} \right|}{\left\| a_{target\ \ Rec.} \right\| \left\| a_{other\ Rec.} \right\|}) \frac{w_{target\ \ Rec.} w_{other\ Rec.}}{w_{max}^2}] \}$$

Where a gives the partial derivative of the source/ receiver pair and w gives the relative weights assigned to each datum based on ray-length function used as proxy for attenuation. Since each row of A_s

corresponds to a single datum, hence singularity of A_s would indicate that there must be redundancy in the dataset (as per discussion on "data angle" by Sabatier, 1977). The method involves starting with a design which involves all the potential source/ receiver pairs. The dot product of each row with every other row is summed and the same is done for each receiver in turn (they may be weighted by expected data uncertainties, i.e., noise and attenuation affects as well as weights to focus on model subspace). The resulting measure shows the weighted angle between each row and the space spanned by all other rows in the matrix. For a row with angle close to zero, it would indicate that row lies completely within the space associated with all other rows in question indicating data redundancy. On the other hand, if data is adding new information, the angle should be non zero and hence the magnitude of Sabatier's angle measure can be used as a proxy quality measure for receivers. At the end of each iteration, receivers whose pairs show the smallest measure are pruned and the process in continued with the shortened array till adequate number of receivers have been removed. The final quality measure for the component associated with the iteration is calculated as follows:

$$QF_1 = W_1 \times Quality_{target\ \ Rec.}$$

The second component looked into in this work is the moment tensor inversion component. Generalized lease square inversion of 3C amplitudes of P and S wave direct arrivals can be used to retrieve the moment tensor for any event. The relation between observed first arrival data and moment tensor elements can be written in matrix form as:

$$d = Am + noise$$

$$d = \left(a_1^P, a_2^P, a_3^P, a_1^S, a_2^S, a_3^S\right)^T \ which\ give\ the\ observed\ amplitudes\ of\ the\ direct\ arrivals$$

$$m = (M_{11}, M_{22}, M_{33}, M_{12}, M_{13}, M_{23})^T \ defines\ the\ components\ of\ moment\ tensor$$

A matrix can be evaluated using P and S wave particle motion equations which makes use of direction cosines(γ), travel times(τ), density(ρ), phase velocities(α & β) and displacement - time function at the source (w) to solve for moment tensor (Aki et al., 2002):

$$u_i^P(x,t) = (4\pi r\rho\alpha^3)^{-1}\{\gamma_i\gamma_j\gamma_k M_{jk}\}w(t - \tau_P)$$

$$u_i^S(x,t) = (4\pi r\rho\beta^3)^{-1}\{(\delta_{ij} - \gamma_i\gamma_j)\gamma_k M_{jk}\}w(t - \tau_s)$$

Due to large number of source - receiver pairs, a least square solution has to be obtained for the resulting over determined system.

$$m = (A^T A)^{-1} A^T d$$

The influence of array design on the computation of generalized inverse has been extensively studied by Eaton (2011) where the stability of the inversion for matrix $B = A^TA$ (condition number of B) is tested. The condition number indicates the stability of the matrix and can be obtained from the eigenvalues as per the following relation:

$$k(B) = \frac{|\lambda_{max}|}{|\lambda_{min}|}$$

We use 'k' as a proxy for the degree of instability of the generalized inverse. Eaton has shown that for the purpose of stable inversion for seismic moment tensors, receivers located at the perimeter of the array are the most important. Since numerical tests indicate that the area of receiver patch may in itself not be a sufficient indicator (it will also depend on the distance of the patch from the source), solid angle is used as a good proxy for parameterization of the optimization problem. Both the observations (high solid angle and peripheral sensors) are based on numerical tests and summarized for a sample case in Figure 5. The final quality measure for the moment tensor inversion component is given by:

$$QF_2 = W_2 \times k(B)$$

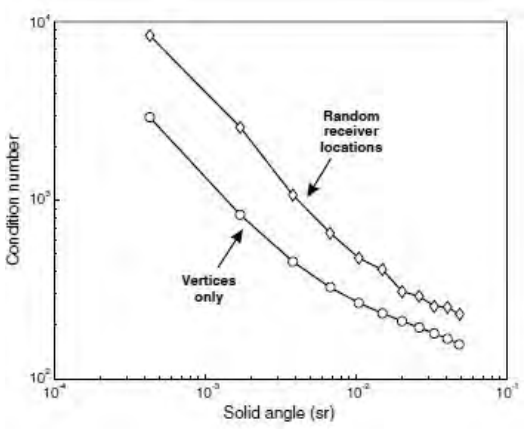

Figure 5: Condition no. vs. solid angle subtended by receiver array validating the major contribution of sensors at the vertices on stability of the inversion (Eaton, 2011).

Experimental setup:

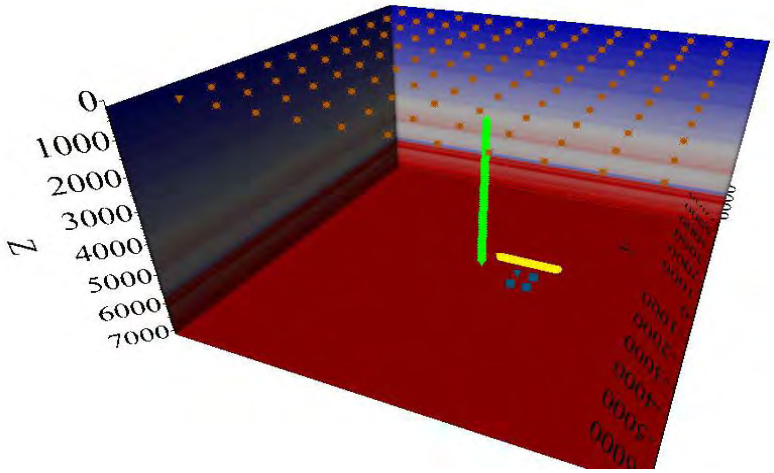

Figure 6: Setup with surface, subsurface vertical & horizontal arrays with pseudo sources.

In order to understand the effect of different arrays on the two selected design criteria, the first step was to create an experimental setup including the necessary observation wells, production well, potential source locations, receiver spread and adequately representative velocity models. Based on regional velocity models available in open source and 1D model provided by GTI, a 3D velocity model was generated with adequate "perturbations" through the introduction of multiple dipping layers. However, since exact data on the specifics of the setup were not available, a more generalized setup with rectangular surface array and down-hole vertical/ horizontal arrays was created and tested for optimization possibilities. Figure 6 shows the 3D model slice as well as the surface/ subsurface well setup and some pseudo sources as per the actual deployment in the field. Once the setup was finalized, based on the velocity model, an adequately effective ray-tracing algorithm was used to generate ray-paths for source - receiver pairs as per the setup. Figure 7 shows sample ray-traces for a single source and surface receivers for reference.

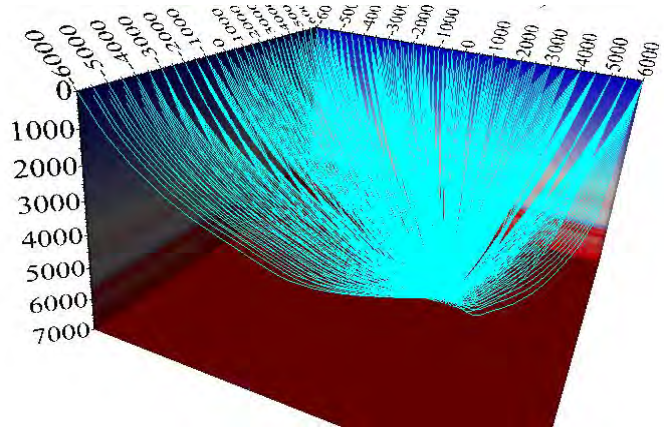

Figure 7: Results from a typical ray-tracing algorithm for partial setup of source - receiver pairs.

Results:

Initial tests were run with a constant velocity model and a single source located on the central vertical axis. This was done in order to validate the final algorithm implementation and to make generalized observations on the behavior of the optimization workflow for the two separate optimization criteria described in the earlier sections. Figure 8 (a, b & c) shows three examples of sample runs with different weights assigned to the two different quality measures as obtained from the two separate optimization elements (ray-trace focusing & Moment tensor inversion). The quality measures are referred to as QF_1 & QF_2 which are used to generate the optimization parameter ($w_1QF_1 + w_2QF_2$). We observe that optimization with a higher stress on ray focusing tends to prune receivers from the periphery before moving towards the central section of the receiver patch. On the other hand, for moment tensor inversion optimization, the receivers at the periphery hold more importance and the receivers closer to the subsurface source tend to get pruned first. Solid angle based analysis shared in subsequent discussions does tend to reinforce this observation. We observe that with equal weight given to both quality measures, the selected sensors seem to be closer to the actual source and the sensors from the periphery get pruned. However, sensors at the corner zones (showing highest possible solid angle)

remain important. Moreover, the radial pattern (as is seen being deployed by many service companies) also tends to indicate that it is an optimal design under given conditions.

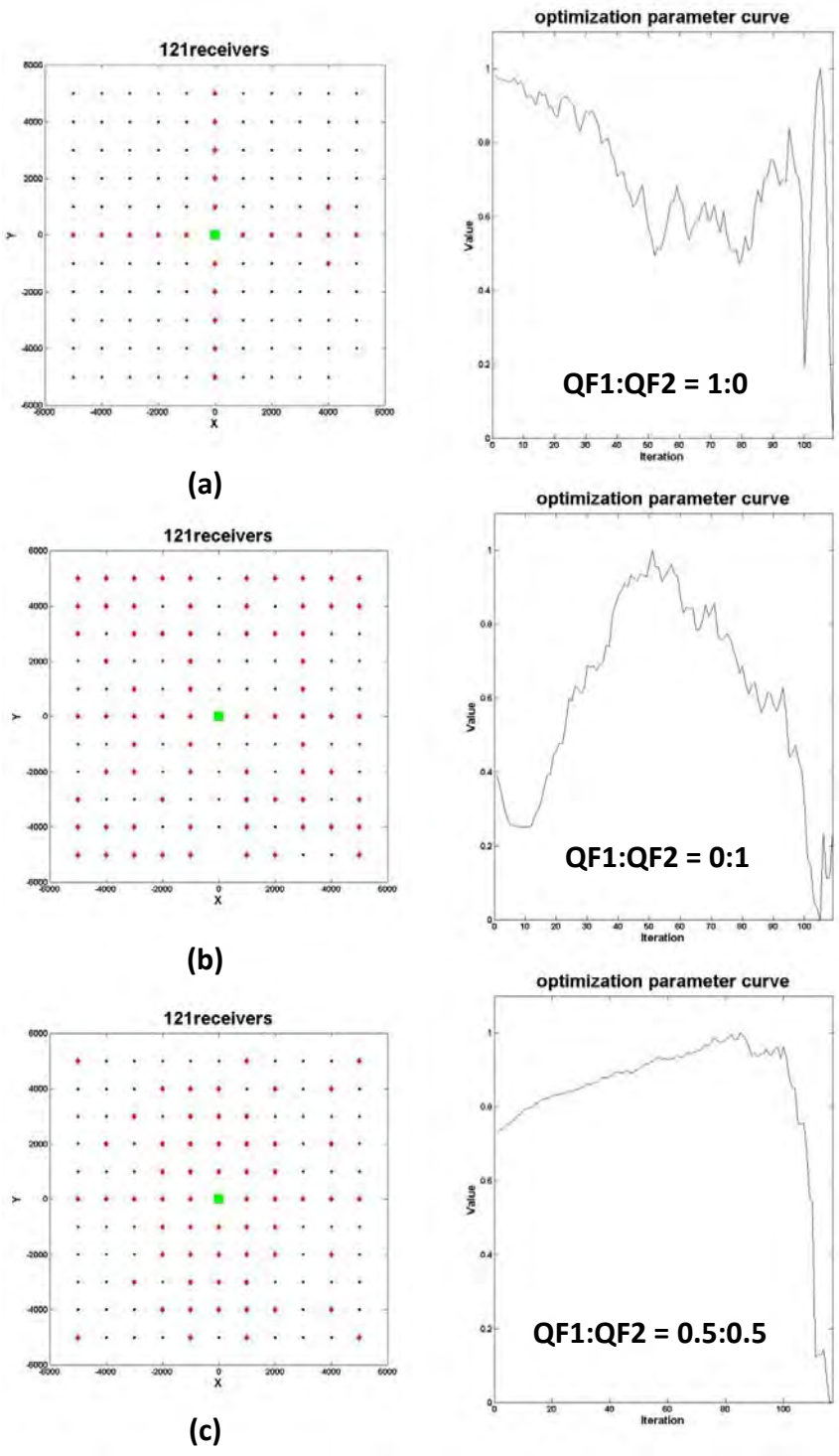

Figure 8: Sample runs with non-variant velocity model, surface receiver array and source at central vertical. (a) shows results with full weight for ray-trace focusing, (b) shows results for full weight on moment tensor inversion and (c) shows results with equal weight assigned to the two components. Red dotted locations are those finally selected based on parameter.

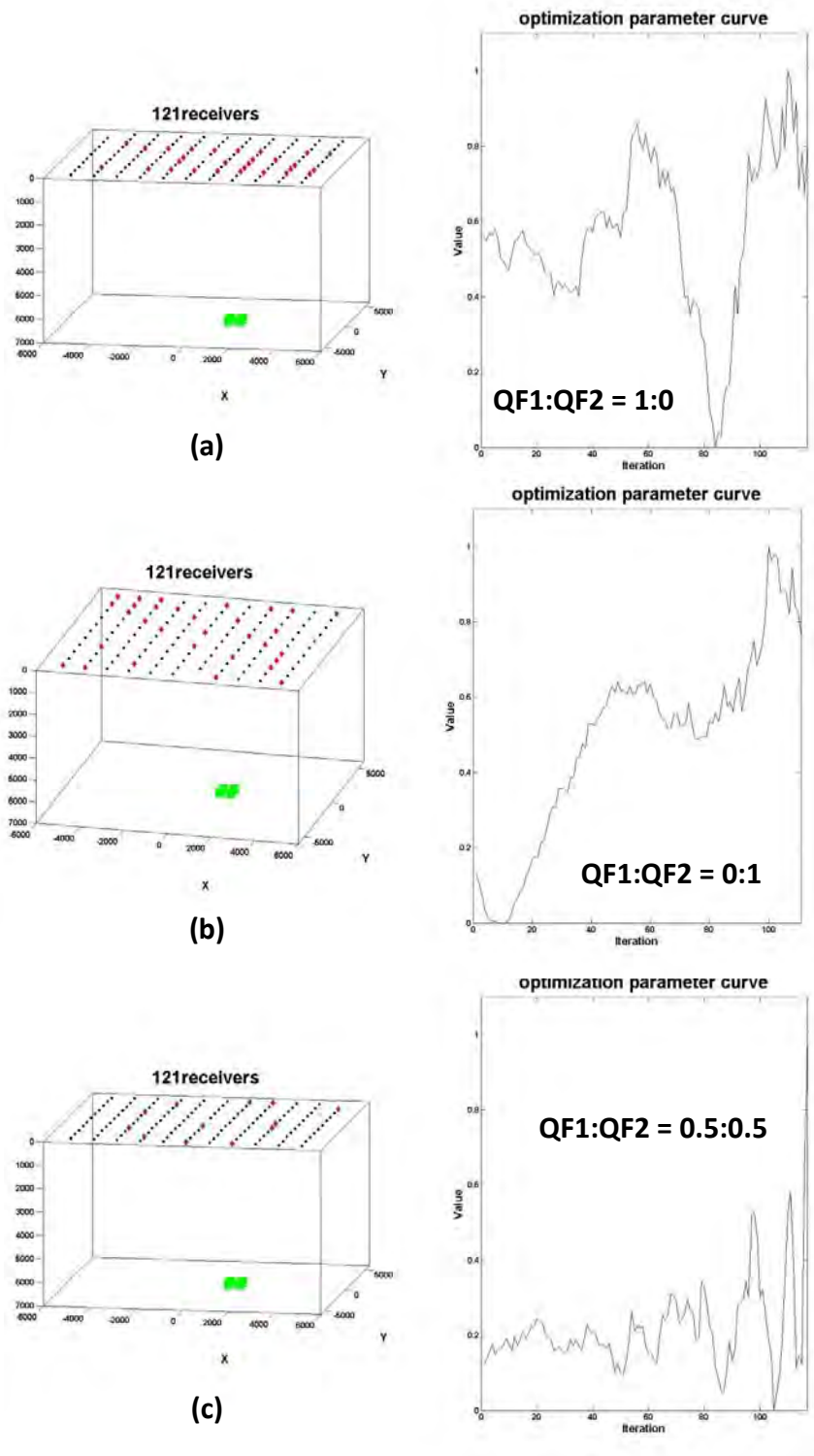

Figure 9: Sample runs with complex velocity model, surface receiver array and source at lateral offset. (a) shows results with full weight for ray-trace focusing, (b) shows results for full weight on moment tensor inversion and (c) shows results with equal weight assigned to the two components. Red dotted locations are those finally selected based on parameter.

Once the algorithm was validated, tests were conducted with sources located at lateral offsets (from origin) and various receiver configurations as per the baseline configurations introduced in the earlier section. For a simple equally spaced rectangular array (Figure 9), again the ray trace focusing based optimization leads to denser receiver spread close to the actual event cloud and the pruning moves from outer periphery towards the zone of interest. For moment tensor inversion optimization, receivers at the corners and the periphery seem to hold importance. The optimization curves also show that the results are relatively poorly conditioned for all the test cases which seem to be a problem with most surface deployments. We hypothesize this as an artifact of source - receiver separation which is the highest for the surface array. Moreover slight variations in velocity profiles (dipping layers incorporated in our tests) lead to substantial perturbations in the ray trace matrix (compared with scenario with no velocity variations). It is important to remember that through solid angles can be used as a good proxy for identifying the best receivers from among all receivers within the patch; receivers beyond critical separation must be pruned as attenuation effects can lead to significant degradation in SNR.

The next case (Figure 10) involved a single vertical array at a lateral offset from the source locations (zone of interest). We again observe that in case of ray trace focusing based optimization, the sensors closest to the zone of interest remain important. In case of moment tensor inversion optimization, the final array tends to be segmented with maximum possible separation angle between the two arrays. However, in this particular case, the shape of optimization parameter curve indicates the failure of the moment tensor based inversion scheme to work for a vertical array (figure 10b). This could be due to the inherent limitations of a vertical array to provide good moment tensor inversion results. Such arrays also show zero solid angle further validating the observation. However, a segmented array seems to provide the most optimum solution in case only a single vertical array is deployed. However, an improved solution could be the presence of a few receivers at the surface and the main vertical array within the wellbore close to the zone of interest. This becomes necessary considering cost/ design issues associated with geophones for wellbore deployments.

Figure 11 shows sample runs with both the surface and the vertical array deployed at one go. This allowed analysis of the impact of first array on selection of receiver locations on the second array and vice versa. Again maximum weight on ray trace focusing based optimization leads to selection of receivers closets to the zone of interest. For optimized moment tensor inversion problem, the surface array provides the best solution (and the vertical array seems redundant). However, solid angle analysis may provide different results as selecting some receivers of the wellbore array may provide good solid angle projections when considered in conjunction with surface receiver locations (though such deployments cannot provide backup receivers due to design). Such analysis has not been conducted for this study. Again the parameter solutions for the three test cases show highly unconditioned results (considered to be carried over effect of surface arrays). We consider optimization based on selections made from among locally optimal solutions in subsequent discussion. Another important scheme not tested for is the presence of multiple vertical arrays which can provide adequate sensor count for good moment tensor inversion results thereby making surface arrays redundant (specifically within wellbores around the zone of interest).

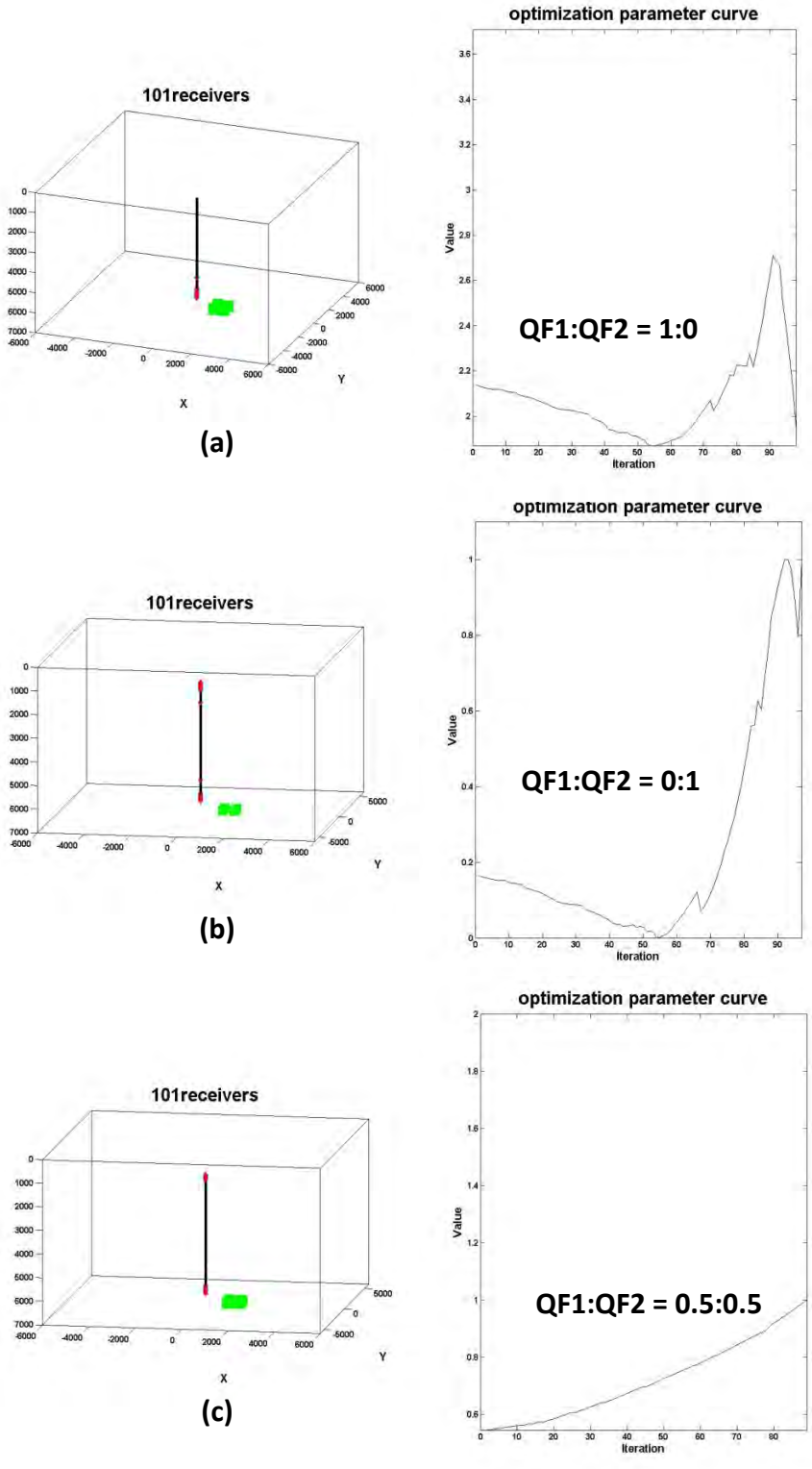

Figure 10: Sample runs with complex velocity model, vertical receiver array and source at lateral offset. (a) shows results with full weight for ray-trace focusing, (b) shows results for full weight on moment tensor inversion and (c) shows results with equal weight assigned to the two components. Red dotted locations are those finally selected based on parameter.

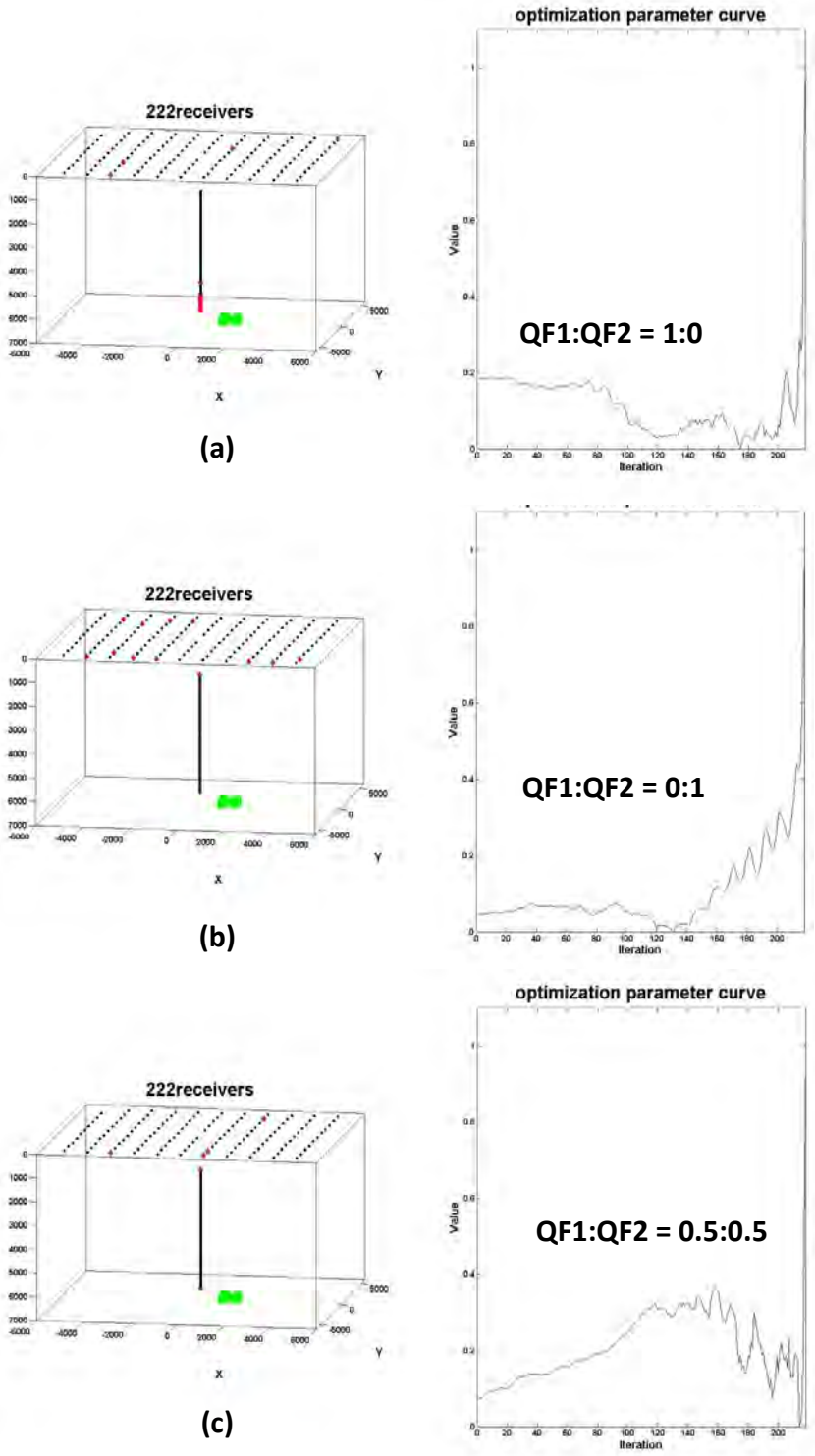

Figure 11: Sample runs with complex velocity model, surface + vertical receiver array and source at lateral offset. (a) shows results with full weight for ray-trace focusing, (b) shows results for full weight on moment tensor inversion and (c) shows results with equal weight assigned to the two components. Red dotted locations are those finally selected based on parameter.

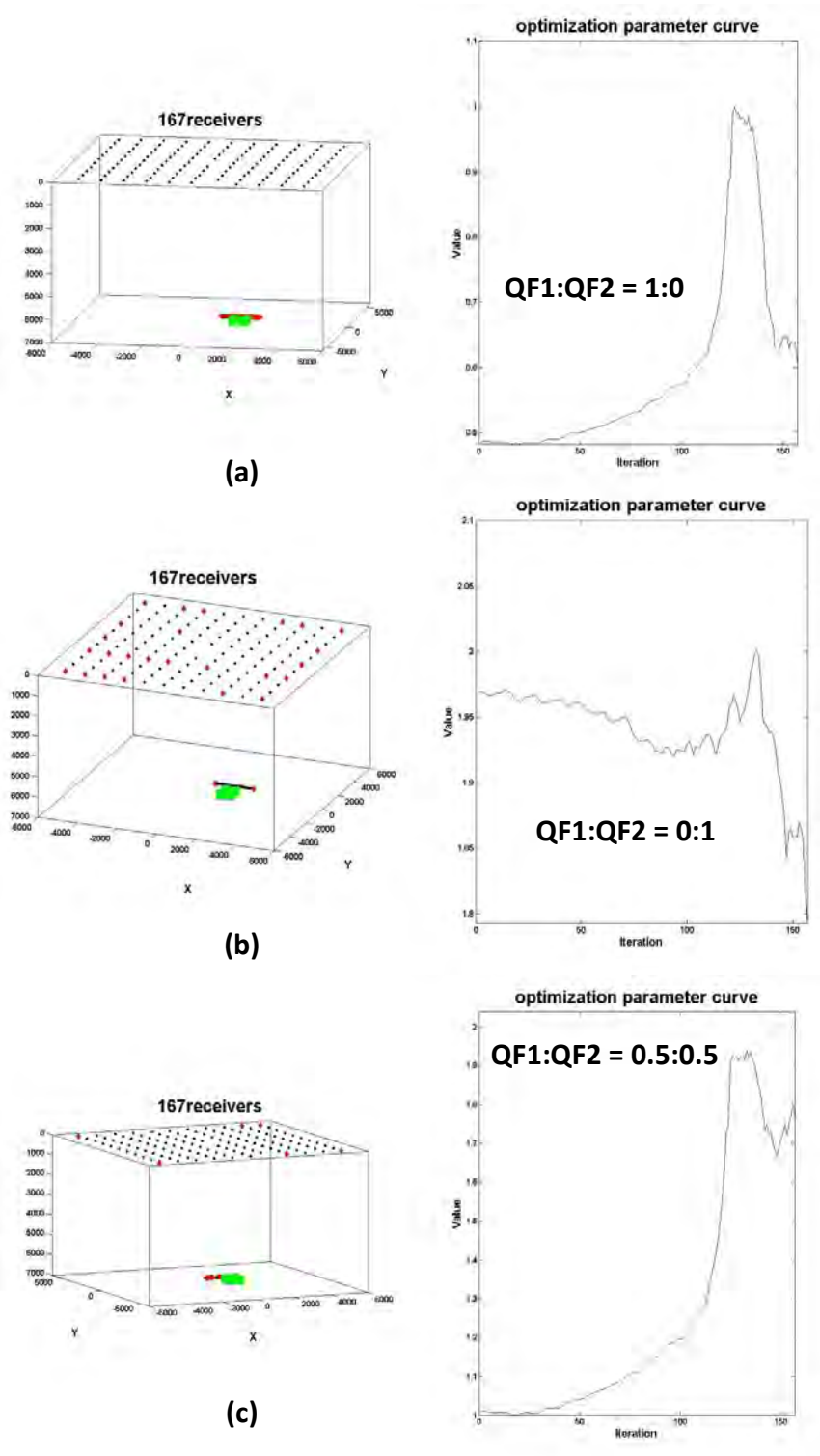

Figure 12: Sample runs with complex velocity model, surface + horizontal receiver array and source at lateral offset. (a) shows results with full weight for ray-trace focusing, (b) shows results for full weight on moment tensor inversion and (c) shows results with equal weight assigned to the two components. Red dotted locations are those finally selected based on parameter.

Final configuration tested for involves both horizontal as well as surface arrays (Figure 12). The horizontal array was configured as parallel (laterally offset but at same depth from reference sources). Again the receivers in the wellbore got preference when ray focusing based optimization had the highest weighted impact on design. Within wellbore, those receivers closest to the zone get pruned first and the process seems to spread away from the center (zone) towards the periphery of the receiver array. Optimized runs tended to select some sources at the surface as well (as moment tensor inversion based optimization requires laterally separated receivers creating relatively large solid angle which is not possible with a single horizontal wellbore array. Thus the presence of wellbore array again indicates that a relatively small surface array may suffice (few well positioned receivers based on design considerations).

Based on the results obtained for various configurations, we also extracted receiver locations for local optimum for few test cases in order to verify their possible use as candidate receiver configurations. This exercise is recommended and is particularly useful in case we have highly irregular and unconditioned outputs in order to make an optimal choice. Figure 13 shows examples of such locally optimal solutions for two sample runs.

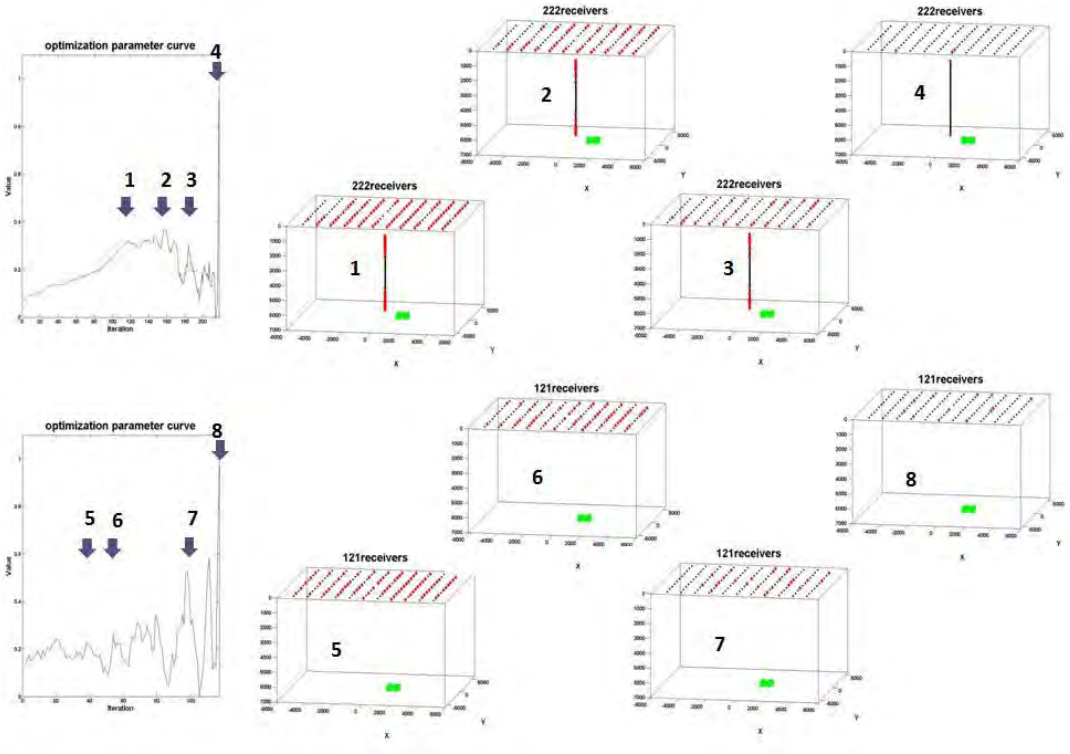

Figure 13: Local maximums from optimized parameter curve as potential design solutions.

Solid angle analysis can also be carried out to validate observations made from optimized array designs or as one of the selection criteria for optimal design from multiple potential candidate designs. The best method is to encode maximum solid angle calculation for designs within the optimization algorithm and use it as an additional element of selection. While this has not been implemented within the optimization algorithm at this point, some initial solid angle analysis has been carried out for typical

receiver configurations (based on selected end points within receiver patch). Figure 14 shows two such configurations and Table 1 shows the results for test cases. The solid angle is computed as per the following equation which should work for n dimensional patch at the surface:

$$\tan\left(\frac{\Omega}{n}\right) = \sqrt{\tan\left(\frac{\theta_s}{2}\right)\prod_{i=1}^{n}\tan\left(\frac{\theta_s - \theta_i}{2}\right)} \qquad \text{where } \theta_s = \frac{1}{2}\times\sum_{j=1}^{n}\theta_i \qquad \text{and } \theta_i \text{ are the vertex angles}$$

A thorough investigation should involve solid angle analysis for all possible receiver combinations (for a receiver patch on a pseudo surface).

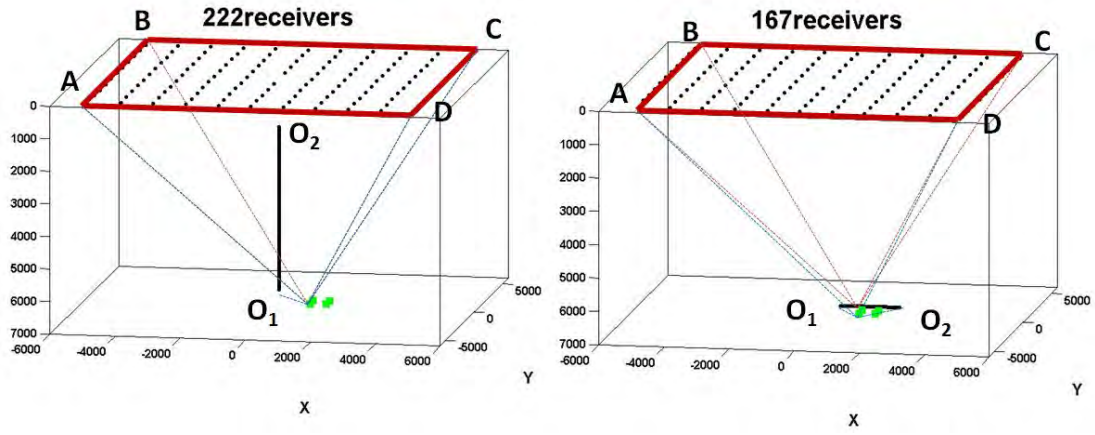

Figure 14: Sample solid angle calculations for reference.

Receiver array design	Vertex angles	Solid angle (Ω)
Surface	57°, 62°, 64°, 59°	~ 179
Vertical	61°, 97°	0
Horizontal	58°, 66°	0
Surface + Vertical (A,D,C,O_1)	39°, 27°, 61°	~53
Surface + Vertical (A,D,C,O_2)	59°, 27°, 84°	~ 274
Surface + Horizontal (A,D,C,O_1)	58°, 41°, 74°	~ 24
Surface + Horizontal (A,D,C,O_2)	91°, 41°, 129°	~ 23

Table 1: Sample solid angle results for selected receivers from designs for reference.

Observations & Recommendations:

1. Surface array is highly sensitive to subtle changes in the subsurface structure of the reservoir. (Sensitivity would normally follow the sequence surface > vertical > horizontal due to large velocity variations with depth compared with lateral variations). This is further validated by the unstable design solutions observed.

2. For vertical arrays, it seems to be best to have the sensors closest to the actual zone of interest (which also makes intuitive sense as this would reduce estimation uncertainties). However, if vertical/ horizontal wells are the only observation wells, it is necessary to place a few surface sensors taking solid angle criteria into account. The other way is to have multiple wellbore arrays distributed around the zone of interest.

3. Moment tensor inversions for source characterization should be done with boundary elements alone (of the subtended solid angle by the arrays) during final processing/ analysis and with the minimum number of elements possible (taking noise issues into account). However, for the array design and deployment, adequate backup is desired for some degree of redundancy.

4. Actual noise conditions in the field and their impact on sensors is difficult to predict but can have substantial degrading effect and impact design suitability. High noise environments should require built in redundancy in the designs. The algorithm allows us to incorporate specific noise based weighting coefficients to receiver locations before the optimization runs begin to adequately factor it in for the optimization workflow.

5. As already explained, properly designed well arrays can make large surface arrays redundant. However smaller arrays are necessary in case the number of observation wells are limited.

6. More complex cost functions should be tested for to check if the solutions can be improved. However, to the best of our knowledge, this is the first time that an attempt has been made to optimize an array for multiple functions in a holistic manner.

7. For poorly constrained scenarios or badly conditioned solutions, physical constraints may be imposed or multiple solutions may be compared based on local optima and conclusions drawn from such comparisons. Constraints can also provide solutions which are more stable.

8. With regard to horizontal arrays and using updated velocity models based on hydrofrac generated perturbations within velocity field based on stress induced changes from stage to stage, industry seems to be reluctant to focus on working with such changes at this point as it requires very high quality data, increased man hours for processing of the data as well as some more research on newer workflows/ algorithms. However fairly complex lateral velocity models are used (based on available information) to improve results when working with horizontal arrays.

9. While it would seem that the optimal vertical observation array design can remove some of the sensors in the middle section of the well (observations from optimization runs in this work), in the actual field implementations, it is not seen that often as tools have standardized length interconnects and it makes more sense to cover the complete acquisition instead of using a complex array design.

10. While only ray-trace focusing and Moment tensor inversion optimizations have been tested, other factors can also be easily added within the optimization framework. Potential candidates include arrival time differentials (based on moveout), event amplitudes, attenuation pseudo factors,

polarity, etc (Figure 15). Moreover, based on known limitations on the availability of wells, surface conditions, etc, preset arrays can be designed for and included and only those arrays can be set for optimization which provide such flexibility (hasn't been tested).

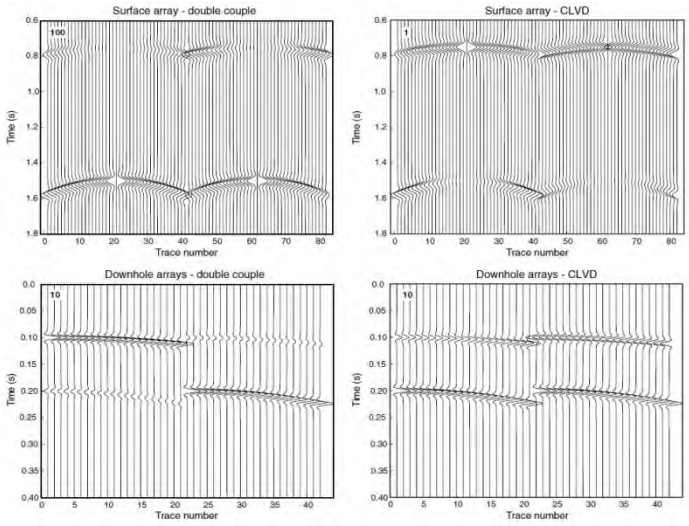

Figure 15: Examples of synthetic seismograms obtained for two different source mechanisms (double couple & compensated linear vector dipole) for surface and wellbore vertical arrays (Eaton et al., 2011).

Future work:

Based on the analysis carried out for the test cases, we have adequate confidence on the designed framework and propose testing of the framework for more complex array deployment schemes including multiple down-hole arrays. Moreover, additional inputs within the optimization framework can be looked into to improve the versatility of the designed arrays. Also, tests with real deployments can be conducted with validation based on synthetically generated seismograms for pruned arrays or comparison of actual passive seismic data from deployed arrays (with final selections based on test results). Improved models for inversion algorithms can also allow optimizations based on inversion schemes (with minimization of associated errors). Moreover, increased receiver density can provide better indication of ideal deployment "zones" of interest for receivers.

Algorithm:

A. Read velocity model.
B. Read Source/ Receiver locations and generate ray traces based on velocity model (ray-tracing algorithm).
C. Generate ray-length matrix based on defined 3D gridding.
D. Generate moment tensor inversion matrix based on ray traces and ray lengths.
E. Compute quality factors as defined in previous sections for both elements and normalize the measures before final quality measure for iteration is defined.

F. Remove receiver location with lowest quality measure (as per definition).
G. Store cumulative measure at said iteration as quality parameter.
H. Iterate steps E through G till the number of receivers is down to very low number (user selected minimum).
I. Select array (receiver locations) corresponding to highest measure over all stored iterations as the final selected design.

Note: The effect of pruned locations on subsequent iterations is unknown and therefore this process is not exhaustive. However, at least for the ray trace focusing section of the algorithm, the results are similar to results obtained through either mote exhaustive or more "smart" techniques (Genetic Algorithms).

Acknowledgement:

We would like to acknowledge Dr. Iraj Salehi from GTI for his valuable support and suggestions throughout the project. We would also like to acknowledge Dr. Martin Karrenbach from SR2020 for his helpful insights into actual array design and deployment issues in the field as well as access to their proprietary software for generating necessary models and use of appropriate ray tracing algorithms for actual tests. We would also like to thank our sponsors at ISC for their continued support.

References:

1. Aki, K., & P. G. Richards, (2002), 'Quantitative Seismology: University Science Books'.
2. Chen, Z., (2006), 'Guidelines for the geometry design or local microseismic arrays', CREWES Research Report - vol. 18.
3. Curtis, A., A. Michelini , D. Leslie & A. Lomax, (2004), 'A deterministic algorithm for experimental design applied to tomographic and microseismic monitoring surveys', Geophys. J. Int., 157.
4. Eaton, D. W., (2011), 'Solid angles and the impact of receiver-array geometry on microseismic moment-tensor inversion', Geophys. J. Int., 76.
5. Eisner, L., B. J. Hulsey, P. Duncan, D. Jurick, H. Werner, & W. Keller, (2010), 'Comparison of surface and borehole locations of induced seismicity. Geophysical Prospecting, doi: 10.1111/j.1365-2487.2010.00867.x.
6. Raymer, D., & Y. Ji, (2004), 'Genetic algorithm design of microseismic injection monitoring networks in the Tengiz field', SEG Annual Meeting, Denver, CO.
7. Sabatier, P. C., (1977), 'On geophysical inverse problems and constraints', Geophys. J. Int., 43.

Appendix A:

GTI Proposal for reference:

Introduction

With the increasing use of multiple microseismic arrays in hydraulic fracturing and waste water injection programs, there is a need to look into a standardized scheme of optimizing the design and layout of the different arrays so as to optimize the observations and interpretations which can be made through each of the individual arrays. The aim is to maximize the information that can be collected through these arrays in order to obtain the best possible results during the actual stimulation through improved (high resolution) event mapping, source mechanisms, velocity and other property estimates, etc. This is essential as each monitoring program will have its own unique dynamics which need to be taken into account while designing the arrays. We propose to look at this problem at multiple levels to develop a workflow to design an optimized multi-array survey which works to improve the applicability of the sensor arrays themselves as well as reduce the final deployment costs by taking into account the relevant limits to be placed on the design if the cost benefit analysis requires so. Such a workflow will provide relevant deployment schemes for any future multi-array monitoring experiments and provide the users with a valuable tool to get the best value for money.

Scope of Work

Most hydraulic-fracturing experiments can benefit tremendously with properly designed micro-seismic arrays and their optimum deployment in ways which cover all potential waveform propagation pathways in the subsurface. Moreover, the limitations and advantages associated with different deployment schemes (such as high noise artifacts from surface data, higher deployment costs for relatively deep horizontal arrays, etc) are now well documented. This places a very high premium on the final deployment costs if we were to design arrays which cover all possibilities. Moreover, in order to save costs, most situations demand the placement of arrays in existing wells and surface locations which are more conducive from an "operational" point of view. While there are existing procedures to optimize micro-seismic array design for either surface phones or borehole measurements, simultaneous optimization for both measurements continues to be a challenge.

The aim therefore is to design and implement a monitoring program which makes the best possible use of the available assets (such as wells, etc) and to design the program in such a way so as to optimize the design parameters for both of the planned arrays to get the best possible results. This can be achieved through modeling of the arrays and potential ray-paths using waveform inversion schemes and can be very exhaustive depending on the level of complexity involved. A large number of variables will define these design parameters. These include the crustal or the local velocity structure, major faults and discontinuities, operational factors (such as operational drilling programs, pumping schemes, etc and their proximity), cost/ time/ resource limitations and finally the "desired degree of precision" in the final results.

There are many potential monitoring arrays and their combinations which can be examined. Down-hole (both vertical and horizontal), shallow verticals, surface, etc can all be potentially combined. ISC aims to use linear statistical experiment design techniques to optimize on the relevant parameters associated with the geophysical experiments at hand. Soft computing tools such as genetic algorithms can be used to optimize on specific parameters as desired. Potential data redundancies can be removed depending on the optimized cross-well and surface tomographic designs. It is also important to note that ray-path

coverage alone is poor criterion for designing model parameterizations and therefore holistic model based optimization schemes are necessary if we want to optimize on the basic array designs. In case of highly non linear mapping between the collected and extracted data and the model parameters (which is possible under certain situations requiring optimization), techniques such as "entropy criteria evaluation", Bayesian design, etc can be used.

The work-plan for the project is defined as follows:

1. *Pre-project study phase: This will include collection of critical information on the field in question including publicly available local velocity fields, exact shales (within Mahantango or other formations) being targeted, typical pumping volumes, etc.*
2. *The next step will be to model for sample stages based on a broad understanding of the stages developed during the provided monitoring experiment. With information on locations of arrays for each cluster of hydrofrac stages, we will generate synthetic datasets to understand the viability of the results as observed through our modeling work by making use of any available information on MEQ orientations, densities, etc. This will include the surface placement as well as the 5 "zippering" geophone placements as was conducted during the provided monitoring experiment.*
3. *Once the models have been validated, the next step would be to modify the arrays (both surface and down-hole) based on identified operational limits to simulate results as obtained from different array configurations. These will include modifying the number and placement of sensors, offsets, etc.*
4. *Optimization will be carried out (for both linear and non-linear mappings) based on preselected criteria. A more detailed description of techniques applicable for specific arrays can be developed and provided as required. Final decision on optimization workflow to be used will depend on the results obtained during the modeling phase.*
5. *Given the fact that simultaneous optimization of borehole and surface measurements will require proper weighting of the each objective, we will run tests and make recommendations on the choice of those weight factors based on different operational considerations.*
6. *Finally, ISC will provide an optimized multi-array design technique based on the observations as discussed above. The complexity of the methods to be used (such as potential full waveform inversion, etc) will be contingent upon mutually agreeable requirements as identified for this project.*

Deliverables

The project deliverables include the following:

1. *Optimized array design procedure for the current industry cooperative research project in Marcellus with a focus on quantifying the potential improvements as obtained through our modeling studies. While the parameters will be optimized for a typical velocity model in the Marcellus shale area, the attempt will be made to easily generalize the results elsewhere.*

2. *Develop a broad workflow for any future array design program including cost effective techniques to optimize multi-array designs and techniques to compare and contrast different array configurations in both qualitative and quantitative manner.*
3. *Project report and multi-array design workflow.*

Duration

The project is envisaged to be spread over a period of 3 months with the deliverables spread over the same duration. The actual model parameter optimizations and optimized array designs will be provided by the beginning of 1Q, 2013.

Cost

The cost to carry out this project is estimated at $75K. The contribution from RPSEA/GTI towards the project cost will be $50K. The remainder ($25K) will be cost share from USC.

Appendix E – Marcellus Shale Geology

Marcellus Shale BEG Natural Fracture Project
Final Report

Julia F.W. Gale, Stephen E. Laubach, Laura Pommer
Bureau of Economic Geology,
Jon E. Olson, Jon Holder, Kashif Naseem
Department of Petroleum and Geosystems Engineering
The University of Texas at Austin

Objectives

Background

Operators in the Marcellus Shale gas play are aware of the importance of natural fractures and there has been substantial work on the fracture systems in core and outcrop in the large region covered by this play (Eastern Shale Gas Project reports; Evans, 1980, 1994, 1995; Engelder et al. 2009 and references therein; Lash and Engelder, 2005, 2007, 2009). The most common fractures documented by these authors in core and outcrop are subvertical opening-mode fractures that are broadly strike parallel (J1) or cross-fold joints (J2). Evans (1995) also found strike-parallel veins that post-date the J2 set and Lash and Engelder (2005) describe bitumen-filled microcracks developed during catagenesis. Gale and Holder (2010) found in a study of several gas-shales that narrow, sealed, subvertical fractures are typically present in most shale cores. In shale-gas plays that are produced using hydraulic fracturing stimulation these fractures are nevertheless important because of their interaction with hydraulic treatment fractures (Gale et al., 2007). At the scale of hydraulic fracture stimulation, natural fracture patterns and in situ stress can be highly variable, even though a broad tectonic pattern may be consistent over 100s of miles. Thus, site-specific evaluation of the natural fractures and in situ stress is necessary. Open fractures are observed in a few cases in core. Fracture-size scaling, coupled with a fracture-size control over sealing cementation and a subcritical growth mechanism that favors clustering suggests that open fractures are likely to be concentrated in clusters spaced hundreds of feet apart (Gale, 2002; Gale et al., 2007). Our goal for this project is to characterize the fractures and identify the characteristic spatial arrangement of fractures, including potential clusters of large fractures.

Our emphasis is on characterizing, quantifying and modeling fractures that have grown in the subsurface in a chemically reactive environment through a combination of observation at a range of scales, detailed petrographic and microstructural observation of cement fills, and geomechanical modeling (cf Marrett et al., 1999; Gale, 2002; Laubach 1997, 2003; Olson, 2004). Large natural fractures, open or sealed, are typically sparsely sampled in core or image logs. Yet these are the fractures that would have the most effect in augmenting gas flow or influencing the growth of hydraulic fractures. Our approach overcomes the sampling problem by use of fracture size and spatial scaling analysis coupled with geomechanical modeling. That is, we may make predictions about their attributes without sampling them.

Fracture morphology, orientation, spatial organization and cementation were analyzed using datasets from the project well-experiment area in SW Pennsylvania. We added a dataset from a field area to evaluate the use of outcrop fracture data in reservoir

characterization in the Marcellus, thus expanding the relevance of the study beyond the well-experiment area in SW Pennsylvania.

Summary of Results

- In the Marcellus Shale there are two to three sets of subvertical natural fractures: in the quarry exposures near Union Springs, NY, J1 fractures trend 075°, and J2 fractures trend 335°. In the Marcellus reservoir in SW Pennsylvania in the well experiment location for the project there are three trends: NE (which we interpret as J1), NW (which we interpret as J2) and a third set trending ENE. Fractures in outcrop are up to 40 m long and the tallest is at least 3 m high.
- Induced fractures in the reservoir trend NE-SW.
- An analysis of the spatial organization of the calcite-sealed fractures in the Union Springs quarry location we found J1 fractures have a weak preferred spacing at 0.2m, 1 m, ~7 m and 14 m. J2 fractures show preferred spacing at 2, 4 and 14 m.
- J2 fractures in the Gulla Unit #10H horizontal well image log show a preferred spacing at 12.5 m, which is comparable to the vertical distance between limestone beds observed in the nearby Paxton Isaac Unit #7 well. This may be a characteristic mechanical layer thickness, which is reflected somewhat in the fracture spacing.
- Samples from the Paxton Isaac Unit #7 well yield subcritical indices from 38 to 131, with a mean of 75, and fracture toughness, KIc, typically from 1.0 – 1.7 MPa sqrm.
- Geomechanical models using measured and selected input parameters specific to the subsurface close to the Gulla and Paxton Isaac wells yield fracture spacing patterns comparable to those measured directly: geomechanical modeling is a useful predictive tool.
- Horizontal fractures seen in cores were not observed in outcrop.
- The fractures in the outcrop are mostly barren, with the exception of a few examples including those at the Wolfe Quarry in Union Springs.
- Fractures in core are mostly sealed. Barren fractures do occur, but where orientation is known these are parallel to S_{Hmax} and are interpreted as drilling-induced fractures.
- Sealing cements in fractures are calcite, quartz, pyrite, barite and anhydrite. The cement crystals may be sub-euhedral, anhedral or fibrous. Cements commonly show crack-seal texture indicating multiple opening events.
- Larger fractures (> 5 mm wide) may be partly open, with euhedral cement lining open pores: examples were observed in the Onondaga Lst. in the Hardie Unit #1 core, and in the shale facies in other proprietary cores outside this study. Fractures in the shale that are narrower than this are completely sealed, but fractures as narrow as 1 mm have been observed with fracture porosity within a carbonate in the Dunn Clingermann well. There is also some fracture porosity in fractures that are contained within concretions.

- Fluid inclusions are present in some but not all of the fracture cements (hydrocarbon and aqueous). They are typically absent or are too small to observe with a petrographic microscope in the fibrous cements.
- Preliminary O18 and C13 stable isotope data in calcite cements indicates variation in composition of fluids from which cements were precipitated.

Fracture Characterization from Well Data

Project planning
Project strategy and planning for data acquisition were discussed at a meeting at Range Resources, Carbondale, PA on 12/14/2010. The experimental well for the project was confirmed as the Troyer Space Management Unit #10 in Washington County, PA, and preparations were made for data on five nearby wells to be made available.

Slabbed sections of four Range Resources cores housed at TerraTek in Salt Lake City were examined and photographed on 3-4 March 2011. Sampling took place on November 15-16 after further work on the cores by a third party had been completed. The cores are:

Range Resources Paxton Isaac Unit #7	(Washington Co.)
Range Resources Hardie Unit #1	(Greene Co.)
Great Lakes Energy Dunn Clingerman Unit #4	(Washington Co.)
Great Lakes Energy Stewart Nancy Unit #4	(Washington Co.)

The cores are in Washington and Greene Counties in SW Pennsylvania (Fig. 1). They are taken through the target interval for the Troyer well, which had already undergone hydraulic fracturing with microseismic monitoring at the time of core examination. The aim of the core examination is to characterize the natural fracture system in the vicinity of the Troyer well in order to better understand the behavior of hydraulic fracture treatments, and the permeability system of the Marcellus Shale. A horizontal image log from a fifth well, the Gulla Unit # 10H, in Washington County was provided for fracture orientation and spatial organization analysis.

Sampling of Cores
In November 2011 the cores were sampled for fracture cements, non-cemented fracture surfaces and for subcritical index and tensile strength of fracture planes testing. We used the observations of the archived half of the core, as described above and in the Terratek reports, to select depths from the sampling halves. The sampling inventory is provided in Appendix B.

Additional cores samples were obtained by Edgar Pinzon (GTI) from the Eastern Shale Gas Project #5 (Connie Sokovitz #1) well in Lawrence Co., PA (received at the Bureau facility on June 15th). These samples were collected for subcritical crack index work. The well is located more than 60 miles north of the focus area for the project so the results cannot be used for modeling of the fracture system in the vicinity of the well experiment. Test results would, however, be used to constrain the variability of subcritical index in the Marcellus. Pinzon (pers. comm.) did not observe natural fractures in the cores from

which the samples came. The cores were full diameter, however, and the outer surfaces were rough, which may have obscured any hairline fractures present.

Figure 1. Google Earth base map of New York and Pennsylvania showing field area and well experiment location. Green boxes are enlargements of the well experiment location.

Fracture Characterization and Fracture Cement Petrography

Fracture characterization had already been completed by TerraTek for the two cores that were oriented using scribing techniques: the Paxton Isaac Unit #7 and Hardie Unit #1 cores. The fracture orientations obtained from the core had been calibrated with image logs. Our aim was to augment, not repeat, this work. We used the existing fracture reports to establish that most of the fractures in the whole core are represented in the slabbed viewing half. During the March 2011 visit we photographed the fractures in the slabbed viewing half of these cores and examined the TerraTek fracture description reports provided by Range. We concur with the overall findings of these reports in terms of fracture types. There are some differences in our interpretation of features on a fracture-by-fracture basis and these discrepancies are discussed below.

Fracture descriptions were made of the two unoriented cores (Dunn Clingerman Unit #4; Stewart Nancy Unit #4) as this had not previously been done. These data are included in Appendix A.

The main fracture types described from the cores were sampled and fracture cements observed in thin section using conventional petrography and cold-cathode CL. Calcite is the dominant fracture cement, with quartz, pyrite, barite and anhydrite also present in some fractures. Cements may be fibrous or anhedral-blocky. Characteristic cement types and morphologies are summarized in the photo-panels and captions that follow each fracture core description section.

Range Resources Paxton Isaac Unit #7

This core extends through the entire interval of interest from 5,849 ft in the Rhinestreet Fm. to 6,533 ft in the Onondaga Lst. Fracture types include (1) networks in carbonate concretions, (2) tall, narrow, steeply-dipping, sealed fractures, (3) bedding –parallel sealed fractures (4) shallow-angle faults and (5) drilling-induced fractures. These are described below. The orientations of natural and induced fractures presented in the TerraTek reports are interpreted in relation to the J1/J2 terminology established for the Appalachian basin shales by Engelder and other workers (see Engelder et al., 2009 and references therein) (Fig. 2).

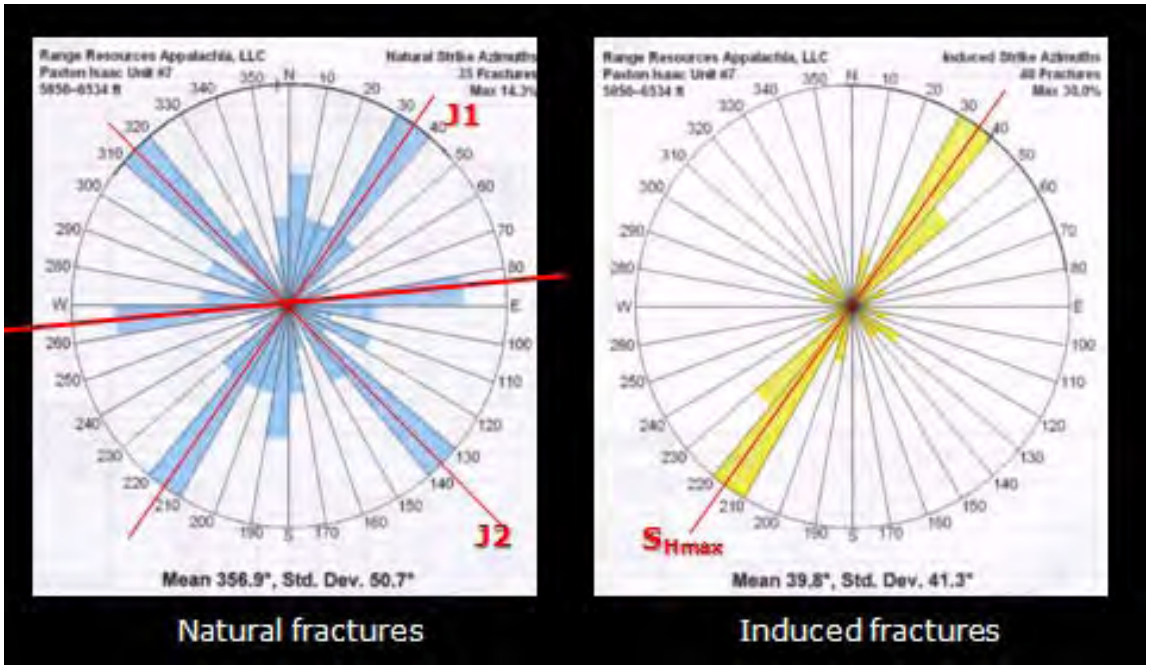

Figure 2. Orientation of natural and induced fractures in the Paxton Isaac Unit #7 core, calibrated by image log. Data collected by TerraTek, red interpretation lines by Gale, this study.

Complex networks that are contained within carbonate concretions (Fig. 3a). While these fractures are unlikely to contribute significantly to reservoir permeability, the cements in the fractures may offer insights into fluid processes operating some time after concretions were established. The concretions themselves might affect propagation of hydraulic fractures.

(a) (b)

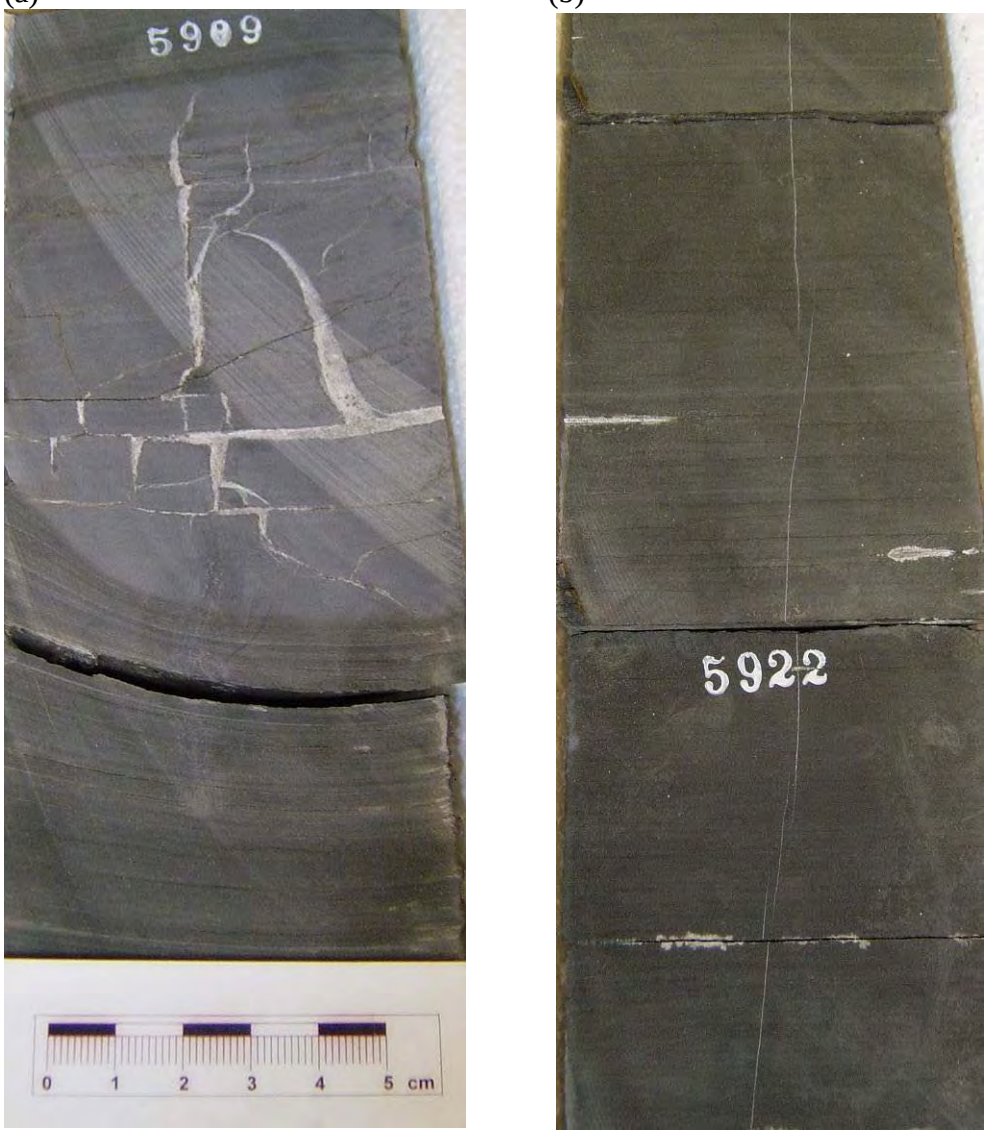

Figure 3. Sealed natural fractures in the Paxton Isaac Unit #7 core, (a) fracture network contained within carbonate concretion (b) tall, segmented steep fractures. Sealing cement is calcite.

Tall (up to 4 ft), steep (dip > 70°), sealed fractures are common in this and the other cores examined (Fig. 3b). These are similar to the fractures described by Gale *et al*., (2007) in the Barnett Shale, and are interpreted to be part of a fracture population that has a power –law or exponential size distribution. The fractures observed here likely represent the smaller size fraction of the wider population. In some parts of the core (e.g. 6,916 ft) fractures of this type are parallel to the slabbed face and are easily missed.

(a) (b)

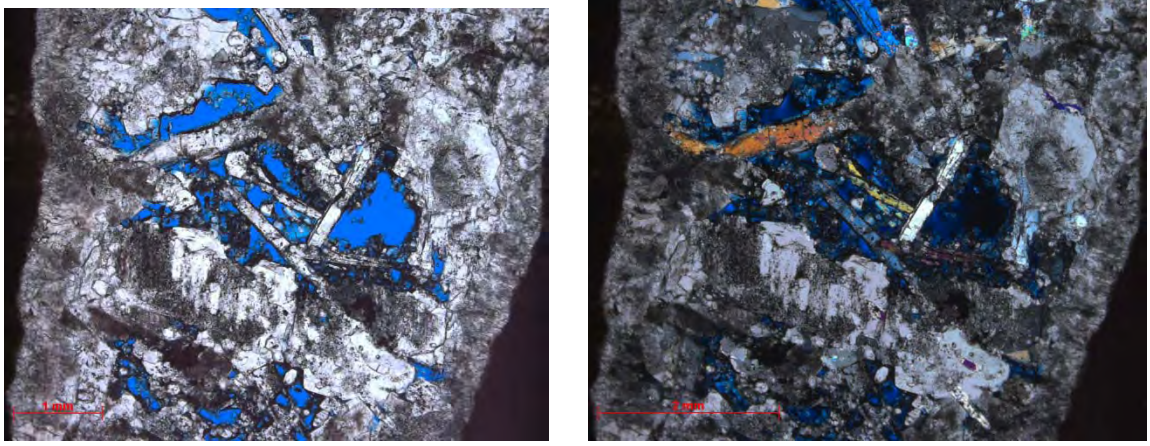

Figure 4. (a) plane light, (b) crossed polars photomicrographs of anhydrite laths growing in fracture pore space. The fracture walls are calcite. This fracture is contained inside a carbonate concretion (Fig. 3a); fracture inside concretions commonly show a different cement pattern and morphology from the fractures cutting the shale. Sample from 5909 ft.

(a) (b)

Figure 5. (a) Plane light and (b) crossed polars photomicrographs of fracture cement in a subvertical fracture similar to the example in Fig. 3b. The cement is fibrous calcite with a median line. Adjacent fibers have a common crystallographic orientation so that blocks of fibers move into extinction together (b). Fibres are normal to fracture walls in this case indicating no shear component to the opening. Sample depth 6,231.5 ft.

Bedding-parallel fractures constitute a third fracture type. They are commonly sealed with fibrous calcite (Fig. 6a, b) but others contain blocky calcite cement. These fractures are not common in the core but several are observed together between 6,483 and 6,485 ft in the organic-rich part of the Marcellus Fm. (Fig. 7a). We speculate that these fractures may be associated with fluid overpressure during catagenesis (c.f. Lash and Engelder, 2005) although we did not observe hydrocarbon fluid inclusions in the fibrous cements in this well. Single phase oil inclusions were noted in a horizontal fracture in the Dunn Clingermann well (see section on this well below). In addition to the planar bedding-parallel fractures there are networks of shallow angle, non-planar fractures that may have slickensides along the surfaces and where the host rock is brecciated (Fig. 7b). These are interpreted as zones of shear. In an example at 6,488.2 ft a pyrite-rich layer has been displaced by approximately 2 mm of reverse shear along a shallow-angle fault (Fig. 7c).

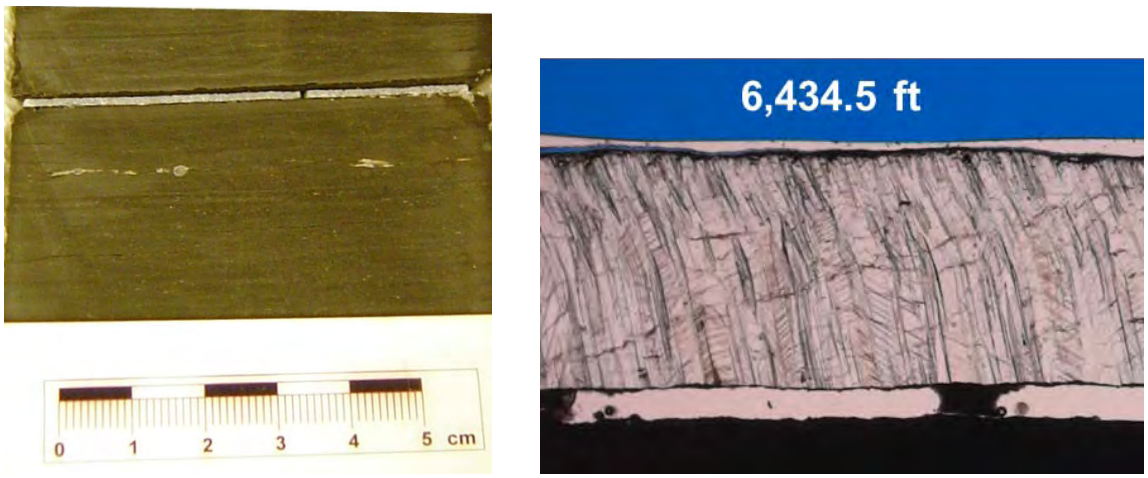

Figure 6. (a) Bedding-parallel fracture at 6,434.5 ft, with fibrous calcite cement. (b) thin section of fracture in (a). Curved fibers indicate a minor horizontal shear component in addition to opening normal to the fracture wall. Oxygen and carbon stable isotopes were analyzed for this sample.

(a) (b)

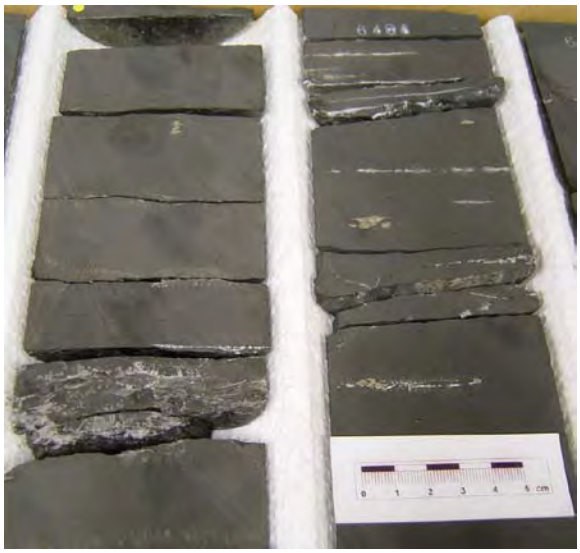

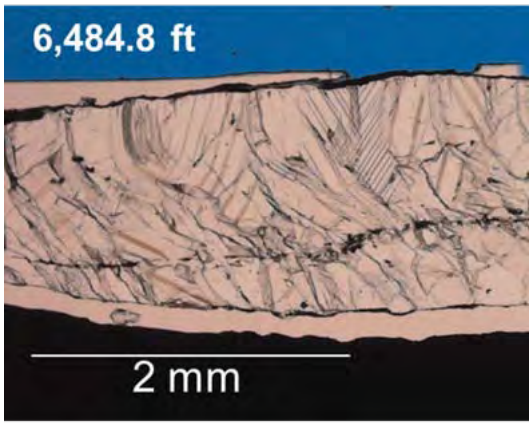

(c) (d)

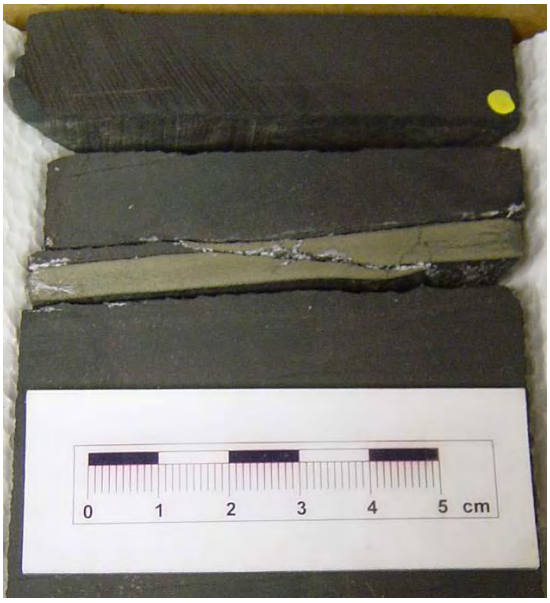

Figure 7. (a) Bedding parallel opening-mode fractures, (b) Plane light photomicrograph of fracture cement in a fracture from bedding parallel fracture in the (Fig. 7a). Curved fibers indicate a minor horizontal shear component in addition to opening normal to the fracture wall. Oxygen and carbon stable isotopes were analyzed for this samples, (c) low angle shears in the Paxton Isaac well, (d) low angle shear cutting a pyrite layer at 6,488.2 ft.

Range Resources Hardie Unit #1

Fracture types present in the Paxton Issac Unit #7 were also observed in the Hardie Unit #1. In addition, there are examples of long fractures originally interpreted as induced, petal centerline fractures (Fig. 8a, b). We reinterpret these fractures as being reactivated natural fractures on the basis of two factors: 1) the dips of the fractures are not subvertical but approximately 70°; they are not truly ‘centerline’, although the fractures do curve at the upper terminus and have a ‘petal’ geometry. 2) There are hairline sealed natural

fractures in apparently the same orientation in adjacent parts of the core (Fig. 8c, d). In any case it is likely that the strike of these fractures is close to both the paleo- and present day S_{Hmax}.

There are several examples of fractures within carbonate or pyrite concretions that contain a several phases of cement (Fig. 9). We will sample these. While these fractures may not provide conduits for hydrocarbons the cements may reveal information about the fluids and temperature conditions in the basin. The concretions can preserve the pre-compaction state of the shale (Fig. 10).

(a) (b) (c) (d)

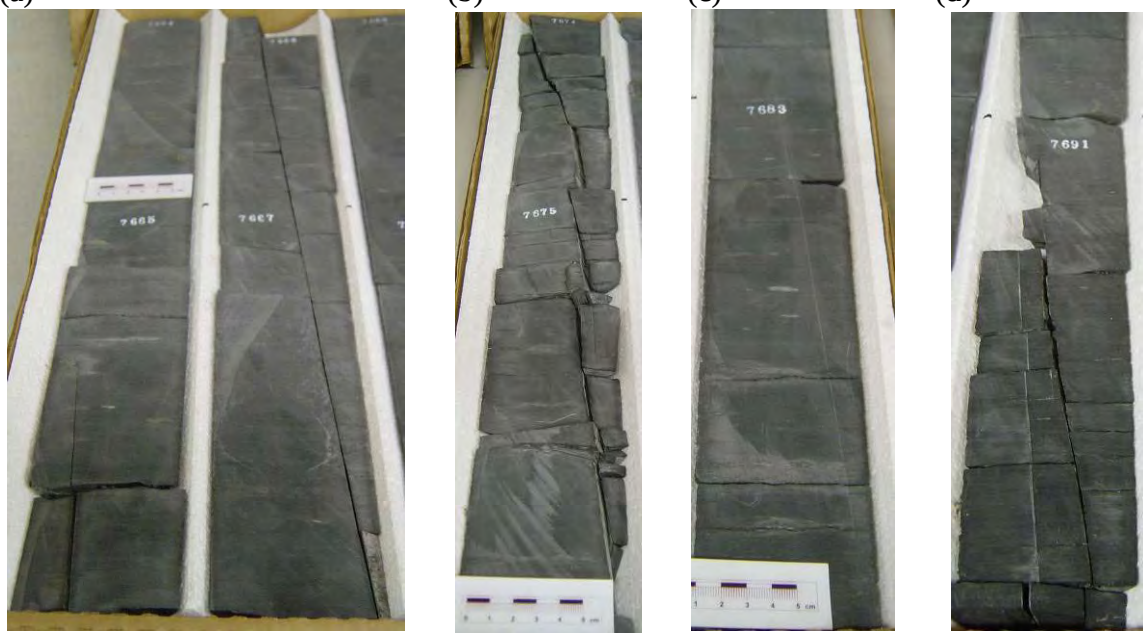

Figure 8. (a, b) Apparently barren, planar fractures dip at 70° and curve at the upper terminus with a 'petal' geometry. These had been interpreted as induced petal centerline fractures. Depths 7,664-7,668 ft and 7,674 ft (c, d) Natural fractures sealed with calcite with similar orientation in adjacent sections of core. Depths 7,683 and 7,691 ft. Hardie Unit #1 core.

(a) (b)

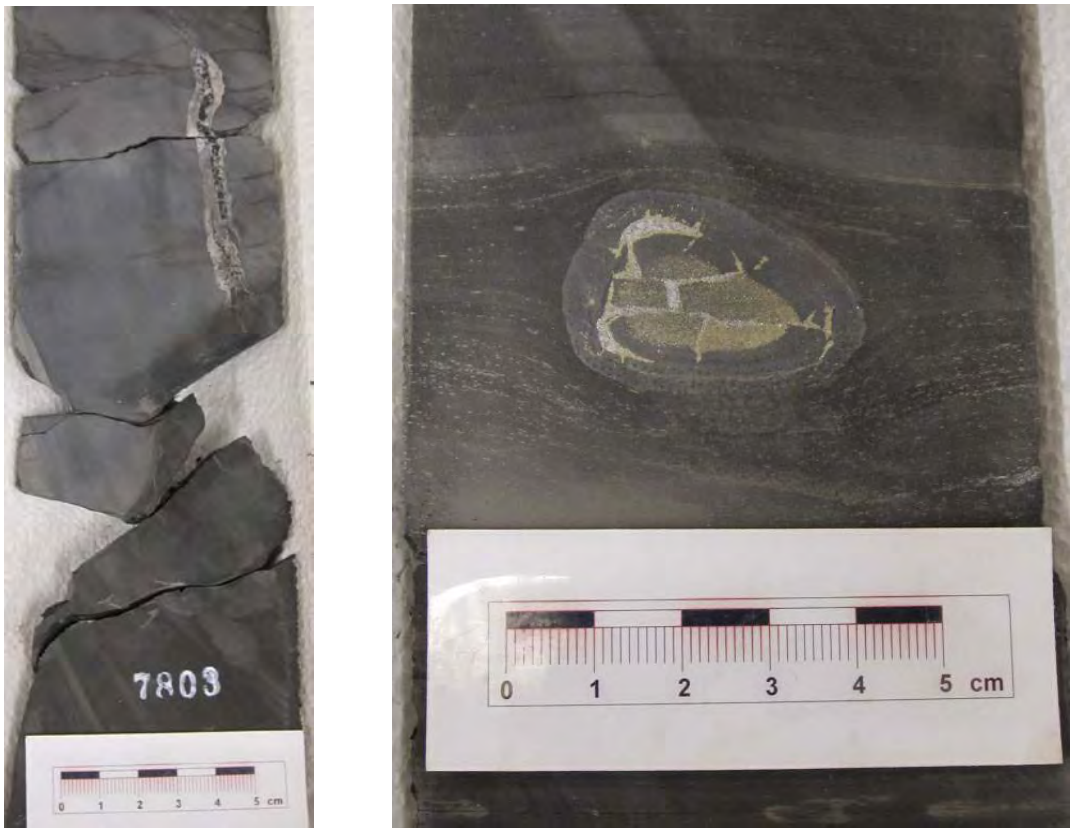

(c)

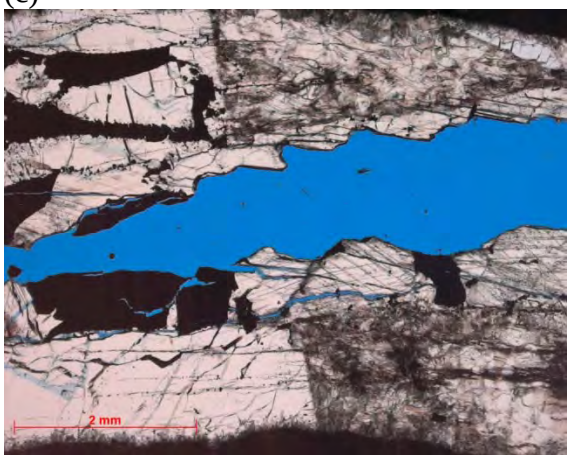

Figure 9. Fractured carbonate/pyrite concretions with multiple phases of fracture sealing cement, Hardie Unit #1 core. Samples from (a) 7,803 ft and (b) 7,817.5 ft. (c) Plane light photomicrograph of anhydrite, calcite and pyrite cements in the fracture in (a). These are similar to the fractures in the Paxton Isaac well concretions.

Figure 10. Fossils are preserved with their original geometry within a carbonate concretion, but are compacted in the surrounding layers. This is evidence that the concretions grew before compaction of the sediment was complete. Hardie Unit #1 core, 7,847 ft.

In addition to the steep planar fractures with large height to width aspect ratios (Fig. 3b, 8) there are fractures with much lower aspect ratios that occur in en echelon arrays at 7,881 to 7,883 ft (Fig. 11). These are sealed with fibrous carbonate cement. The relationship between these two groups is not known.

(a) (b)

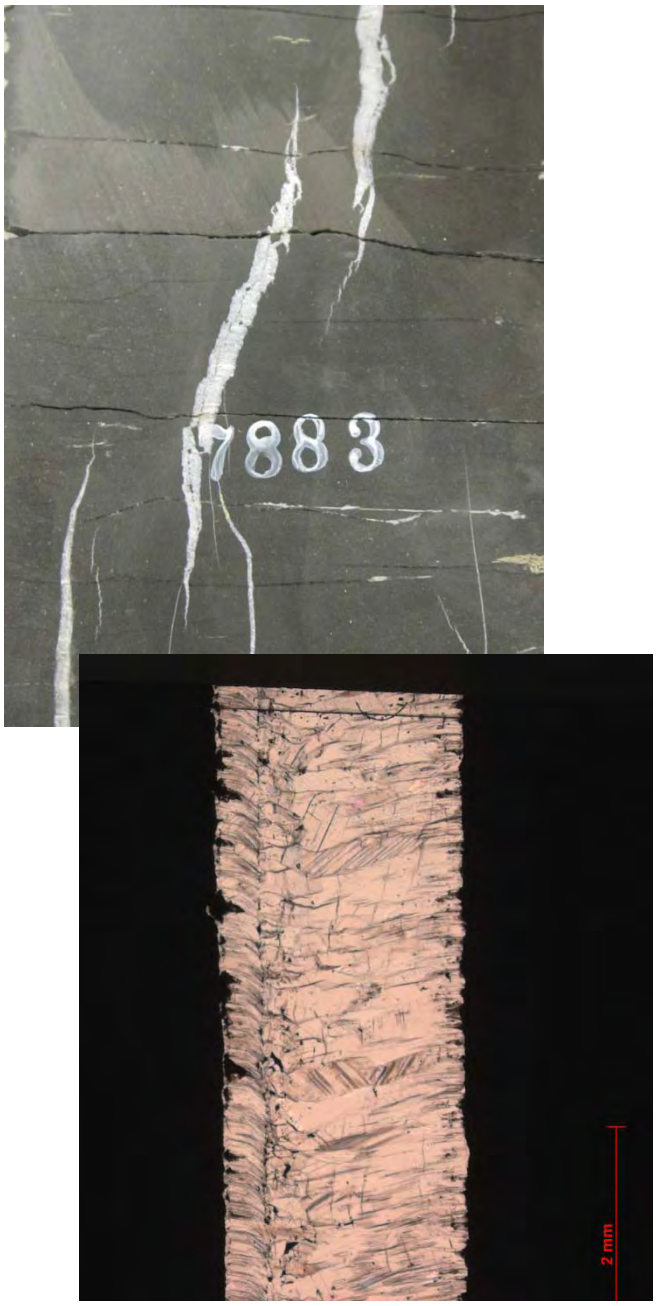

Figure 11. (a) En echelon arrays of low height to width aspect ratios. (b) Thin section photomicrograph showing fibrous calcite fracture fill with variable fiber width and orientation.

The en echelon arrays may also contain complex branching structures near the tips of each segment (Fig. 11a). In other cases fractures may be dominantly vertical but have horizontal (bedding parallel) offshoots (Fig. 12).

Complex branching low angle fractures are also present (Fig. 13; c.f. Fig. 7). Some are bedding-parallel, opening-mode fractures with either blocky or fibrous fill (top of figure). Others have shear offsets and slickensides along them (center of figure).

The unit below the Marcellus, the Onondaga Limestone contains en echelon fractures with vuggy openings in calcite cement (Fig. 14).

(a)

Figure 12 (a) Vertical fracture with fibrous calcite fill and horizontal component at the top break. (b) Both fractures have detached from the fracture walls, and possibly from each other in thin section. Both show curved fibers, which are consistent with contemporaneous opening. The vertical fracture has a median line consistent with growth from the center outwards (antitaxial) whereas the horizontal fracture does not, and has the widest crystals in the center, which is consistent with syntaxial growth from the walls inwards. Sample depth 7897.5 ft.

(b)

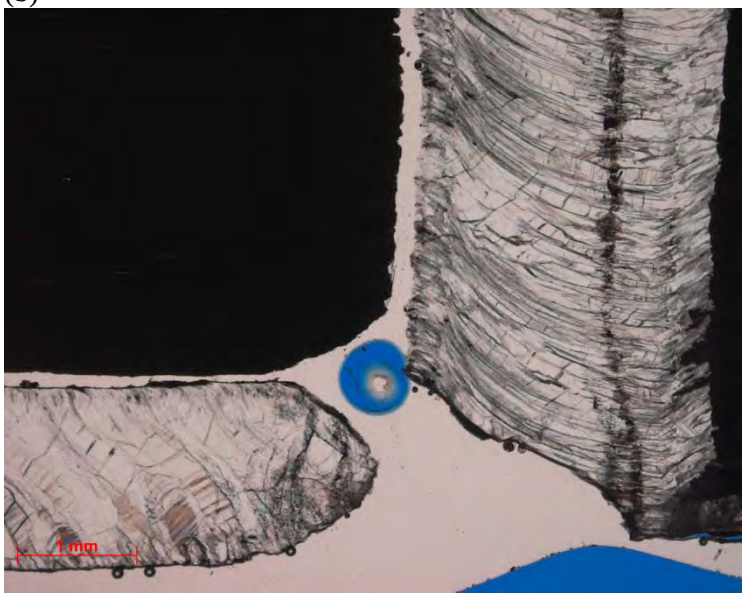

(a) (b)

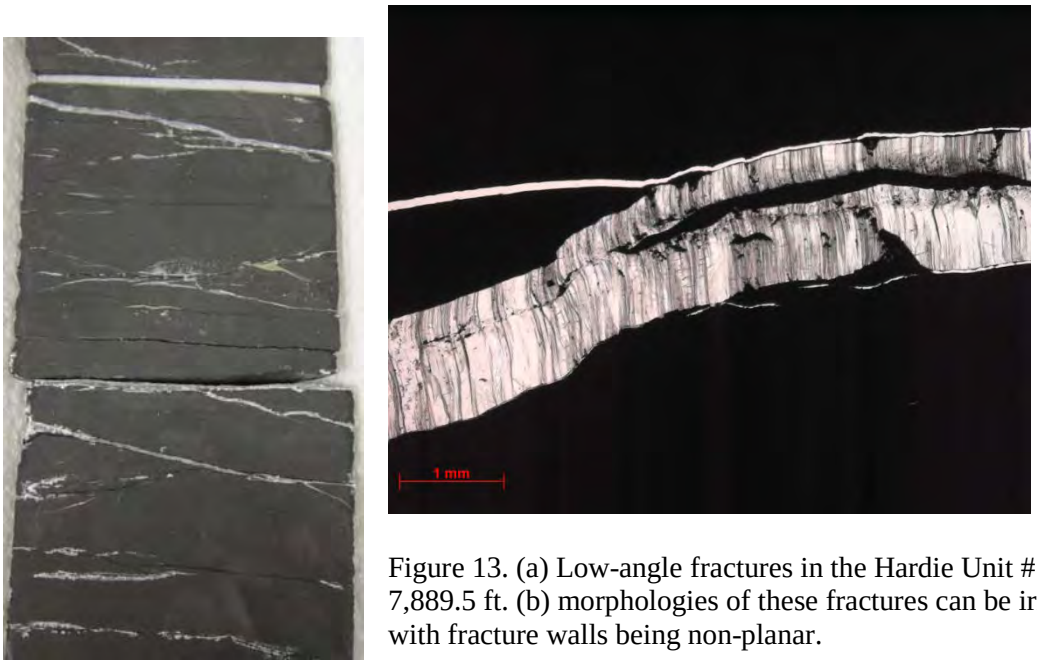

Figure 13. (a) Low-angle fractures in the Hardie Unit #1 core, 7,889.5 ft. (b) morphologies of these fractures can be irregular, with fracture walls being non-planar.

(a) (b)

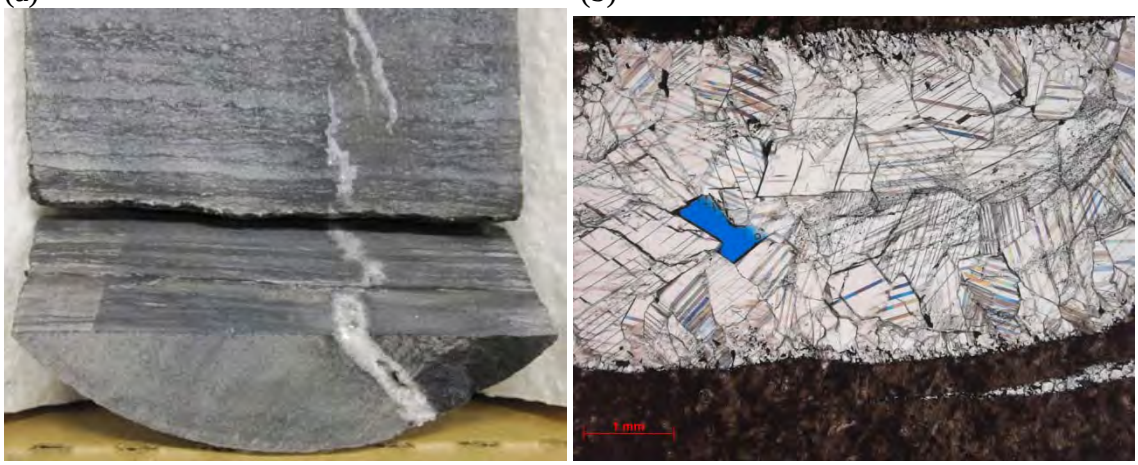

Figure 14. (a) Partly open fractures in the Onondaga Lst. at 7935.8 ft (b) plane light photomicrograph of fracture porosity (blue epoxy) in calcite cement in the sample in (a).

Great Lakes Energy Dunn Clingerman Unit #4

This core is unoriented and a systematic fracture description had not been done previously. We present a spreadsheet showing some of the measurable parameters and descriptive characterization (Appendix A). Here, we present a summary of the findings. As for the other cores described in this report, there are both drilling induced and natural fractures present. We first give examples of fractures similar to those found in the two oriented cores.

Steeply dipping fractures sealed with calcite in the shale section (Fig. 15a), but partly open in the underlying limestone section (Fig. 15b), sealed horizontal fractures,

sometimes associated with pyrite (Fig. 16) and low angle fractures (Fig. 17) are present at several locations in this core.

Also present are steep barren fractures (e.g. 6,515.5 to 6,521 ft) that we interpret as drilling induced fractures.

Figure 15. (a) Vertical calcite-sealed fractures at 6,579 to 6,583ft in mudrock, and partly open at 6,620 ft in limestone. We do not know if the fracture sets are the same.

(a)

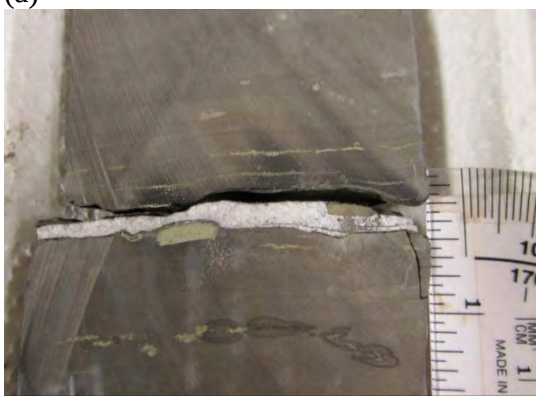

(b)

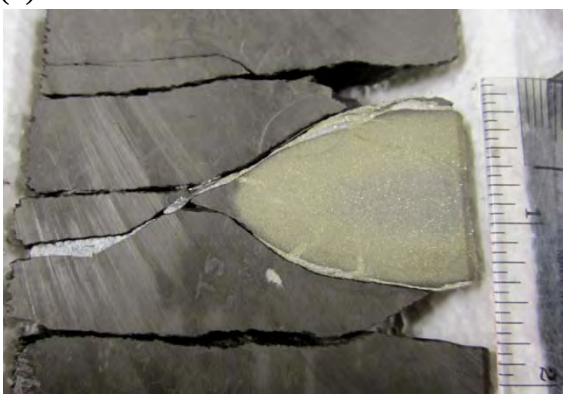

(c)

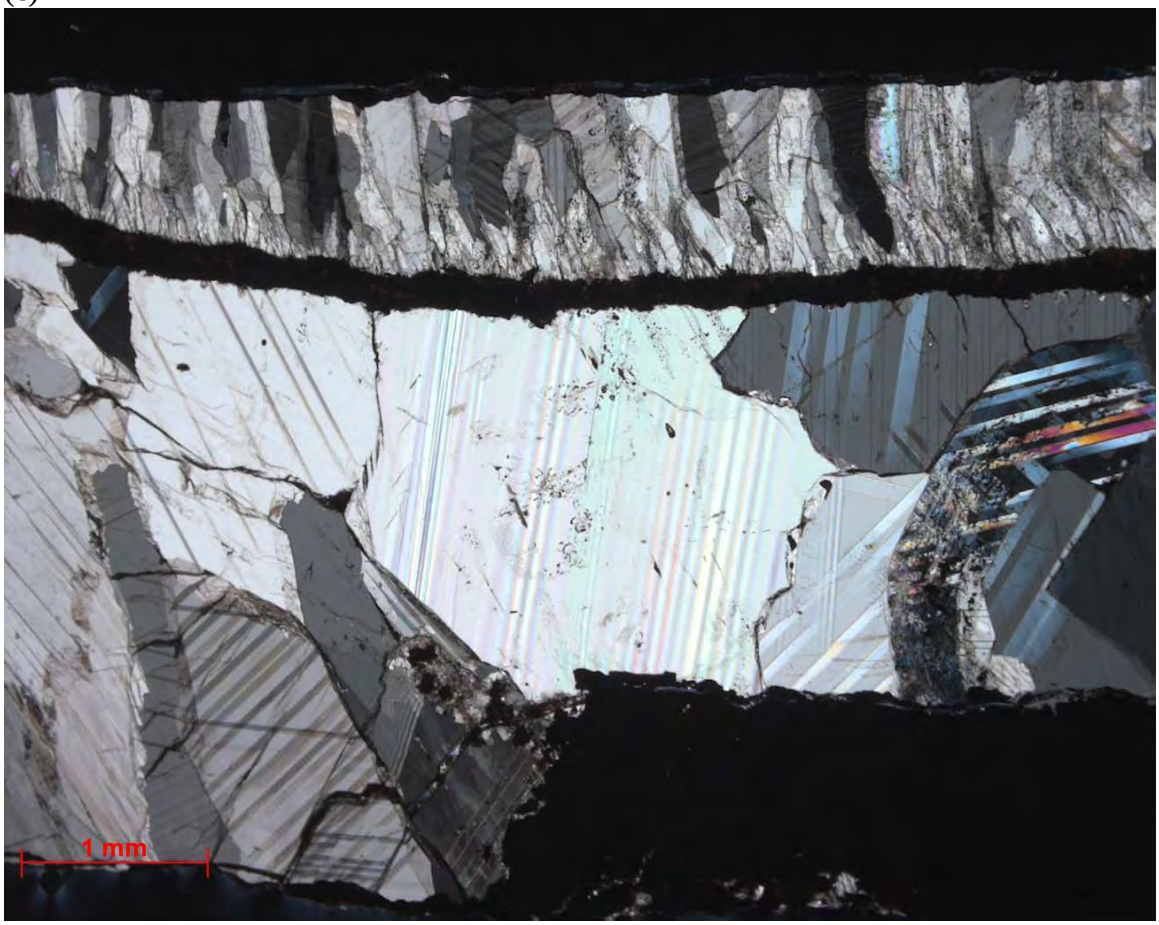

Figure 16. Horizontal fractures sealed with calcite and associated with pyrite layers or nodules at (a) 6,507.6 ft and (b) 6,570.4 ft (c) crossed polars photomicrograph of calcite cement in the

fracture in (a). Two different calcite morphologies are present; a coarse blocky cement at the base and a fibrous layer at the top.

Figure 17. Low angle fracture at 6,567.6 ft.

There are many locations in all wells where there are horizontal accumulations of pyrite. In the Paxton Isaac Unit #7 well there are several of these near the top of the cored interval. Terratek had interpreted these as fractures (Fig. 18a) and many of them are notably crenulate.

(a) (b)

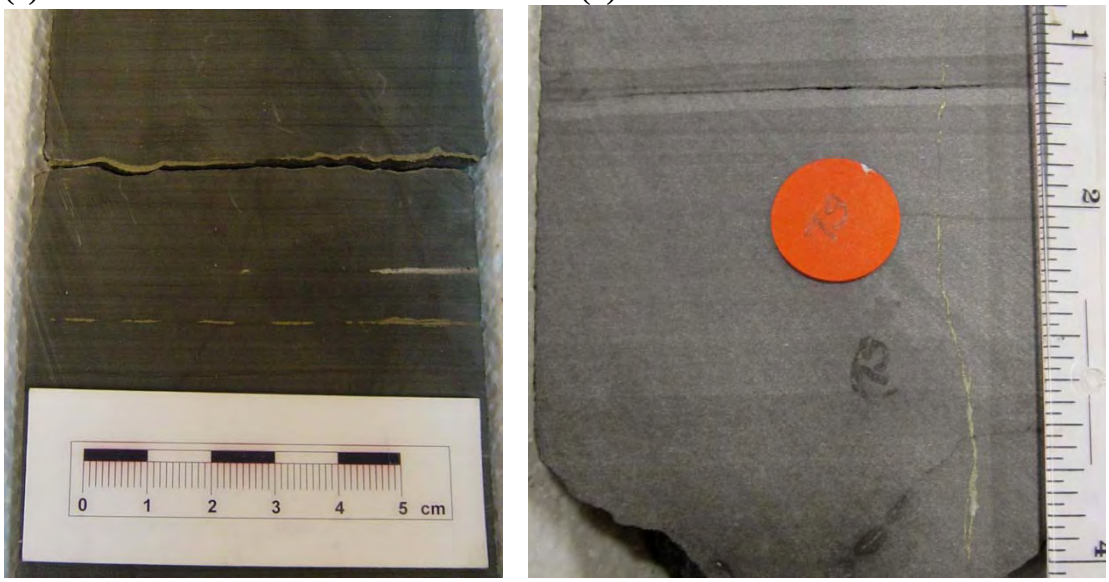

Figure 18. (a) Horizontal accumulations of pyrite of uncertain origin in the Paxton Isaac Unit #7 core at 5,882 ft. (b) Vertical, pyrite-filled fracture in the Dunn Clingerman Unit #4 core at 6,600.5 ft.

We consider that they are not fractures but are likely sedimentary or diagenetic in origin, with the crenulate forms possibly being pyrite replacement of fossils. However, in the

Dunn Clingerman well there are vertical, pyrite–filled fractures (Fig. 18b). The origin of the pyrite accumulations is therefore unresolved, but we suspect there is more than one mechanism.

In the crinoidal limestone at the base of the core there are subvertical stylolites, which must be tectonic in origin. We have not established the relationship between the stylolites and the fractures in the limestone. Tectonic stylolites at a high angle to J2 fractures are observed in outcrop in the Tully Limestone in the river section below Taughannock Falls, NY. Engelder and Engelder (1977) described the strain recorded in fossils, including crinoids, and due to solution cleavage in the Appalachian Plateau, concluding that horizontal shortening was of the order of 10%.

Great Lakes Energy Stewart Nancy Unit #4

This core is unoriented and a systematic fracture description had not been done previously. We present a spreadsheet showing some of the measurable parameters and descriptive characterization (Appendix B). This core is notably more disked (many horizontal breaks) than the other cores, which may reflect its composition. There are several accumulations of silt and pyrite that can superficially resemble horizontal fractures (Fig.19). There are very few natural fractures in the core, however, most being concentrated in the lowest 4 ft, where there are sealed fractures associated with concretions and a few calcite-sealed subvertical fractures (Fig. 20).

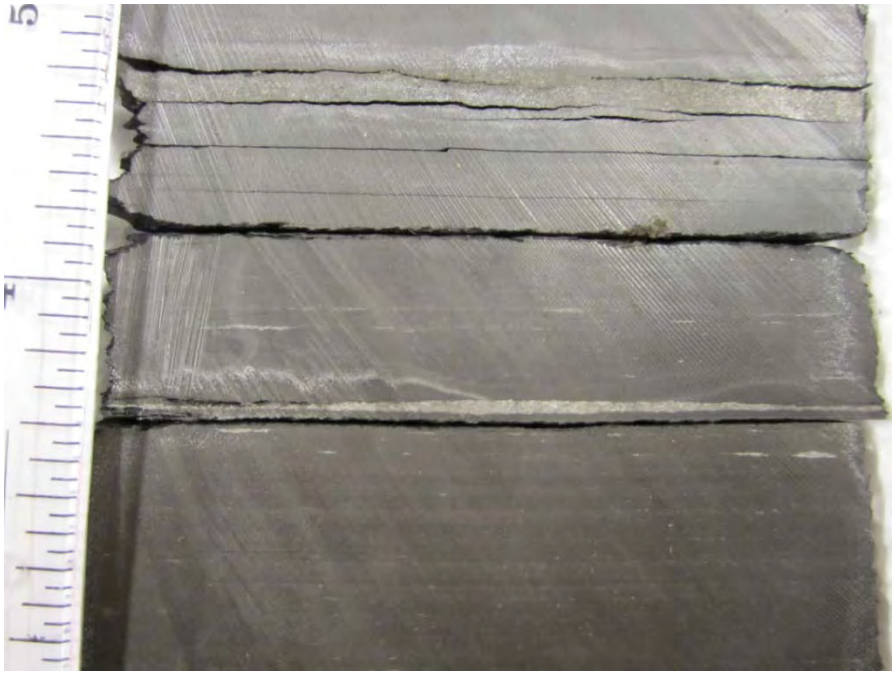

Figure 19. Silt (center) and pyrite (top) accumulations at 6,279.2 ft.

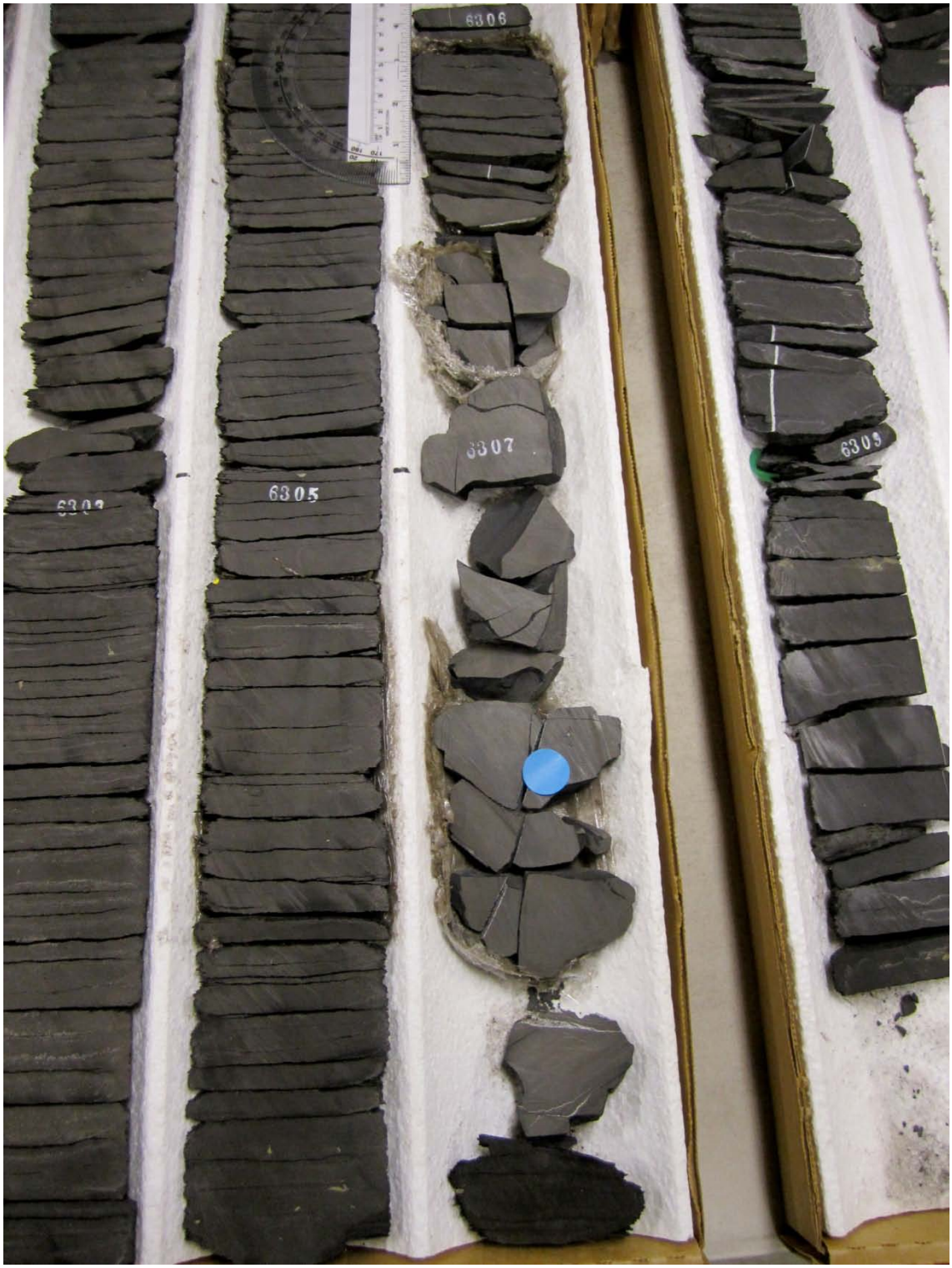

Figure 20. Bottom box of Stewart Nancy unit #4 core showing ‘poker chip’ breaks in the mudrock interval. A fracture network sealed with calcite and pyrite occurs in the paler grey carbonate concretion and vertical, calcite-sealed fractures are present at the base (6,302 to 6,310 ft).

Additional work

A Petra project was constructed by Laura Pommer (Graduate Research Student, BEG) and Edgar Pinzon (GTI) so that intervals of interest relative to the Troyer Space Management Unit #10 could be identified (Fig. 22). Tops identified on the cores and well log analysis were used to construct tops on the different members in the section and correlate from well to well. The Hardie well depths are greater than those in Washington County. In addition to the target zone for the well itself, units above and below are of interest as they are likely to be reached by the hydraulic fracture treatment.

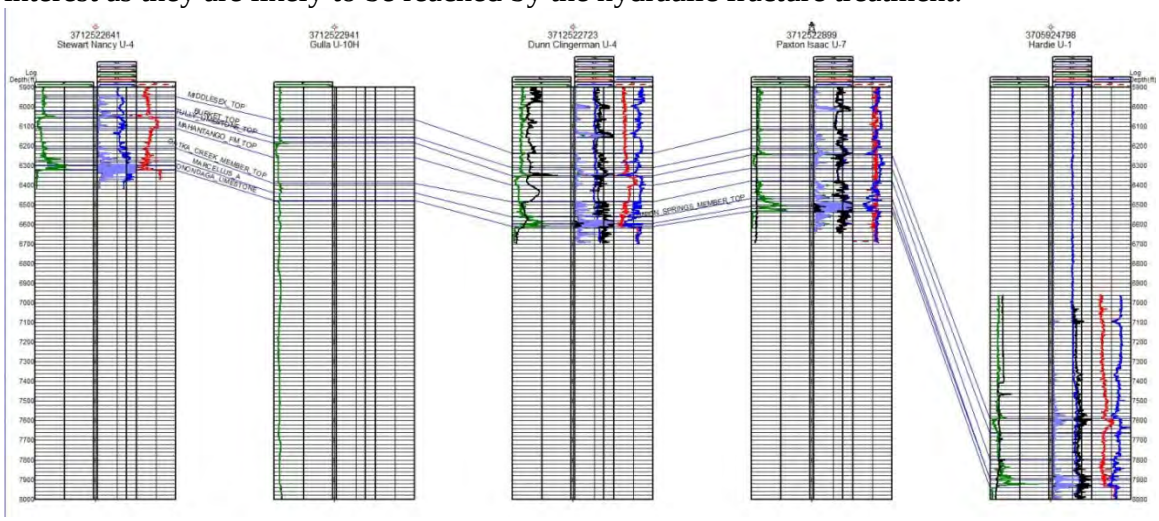

Figure 22. Cross-section constructed using the well logs from the project area. Construction done using Petra.

Field Work

Two field trips occurred during the first year of the project. Dr. Terry Engelder (Pennsylvania State University) led a field trip to several outcrop locations in central Pennsylvania and the Finger Lakes district of New York State on June 2-3, 2011 (Fig. 23). The purpose of the trip was to examine the fracture expression in outcrop in the Marcellus and overlying shale-bearing sequences in the region, and to discuss the overall gas-plume model for natural hydraulic fracturing that Engelder has developed. For this project there were two additional objectives:

1) To compare findings in outcrop with the fracture characterization previously reported for cores from Washington and Greene Counties, SW Pennsylvania in the project focus area. We also viewed two cores at the Penn. State Geology Department core laboratory for comparison.

2) To assess whether additional fieldwork would be beneficial for the project.

As a result of the first trip a data-acquisition trip took place during September 29-31, 2011. The outcrop fracture patterns in the Marcellus Shale have been the subject of many studies over several decades. This second trip was aimed at addressing questions that have not previously been answered. Namely, the apparent anomaly in the number of fractures observed with cement in the subsurface in cores (many) vs. the number of fractures observed with cement in outcrop (few). A further anomaly is that many fractures in core dip at around 70-75°, whereas the joints in outcrop are mostly subvertical (where bedding is horizontal). The only exception observed is one cluster of steeply dipping (~ 70°) J2 fractures adjacent to subvertical ones in Fillmore Glen State Park.

Work by Engelder (2009) suggests that joint sets visible in outcrop represent those in the subsurface as seen in core and borehole image logs. The joints, in both outcrop and subsurface, are observed to be in two main orientations and are hypothesized to have formed "close to peak burial depth as natural hydraulic fractures induced by abnormal fluid pressures generated during thermal maturation of organic matter" (Engelder et al., 2009). If this is correct then outcrop and quarry observations in the Marcellus Shale can thus be used as a proxy for subsurface joint orientation and fracture modeling, as the fractures are essentially "fossil reservoir fractures" (Fidler Thesis, 2011). We collected samples of cement from both fracture sets with the aim of determining whether the cements indeed indicate fracturing occurred at depths (temperatures and pressures) equivalent to the present day Marcellus reservoir. Analysis of these samples is ongoing as part of Pommer's thesis, results of which will be available upon completion. We will compare results with Evans (1995) who found progressively mature hydrocarbon fluid inclusions in fracture cements from fractures of decreasing age in Devonian shales from the Appalachian Basin, relative timing having been established through cross-cutting and abutting relationship. Evans (1995) related these findings using a burial history curve such that the latest fractures developed at peak burial for the Devonian shales.

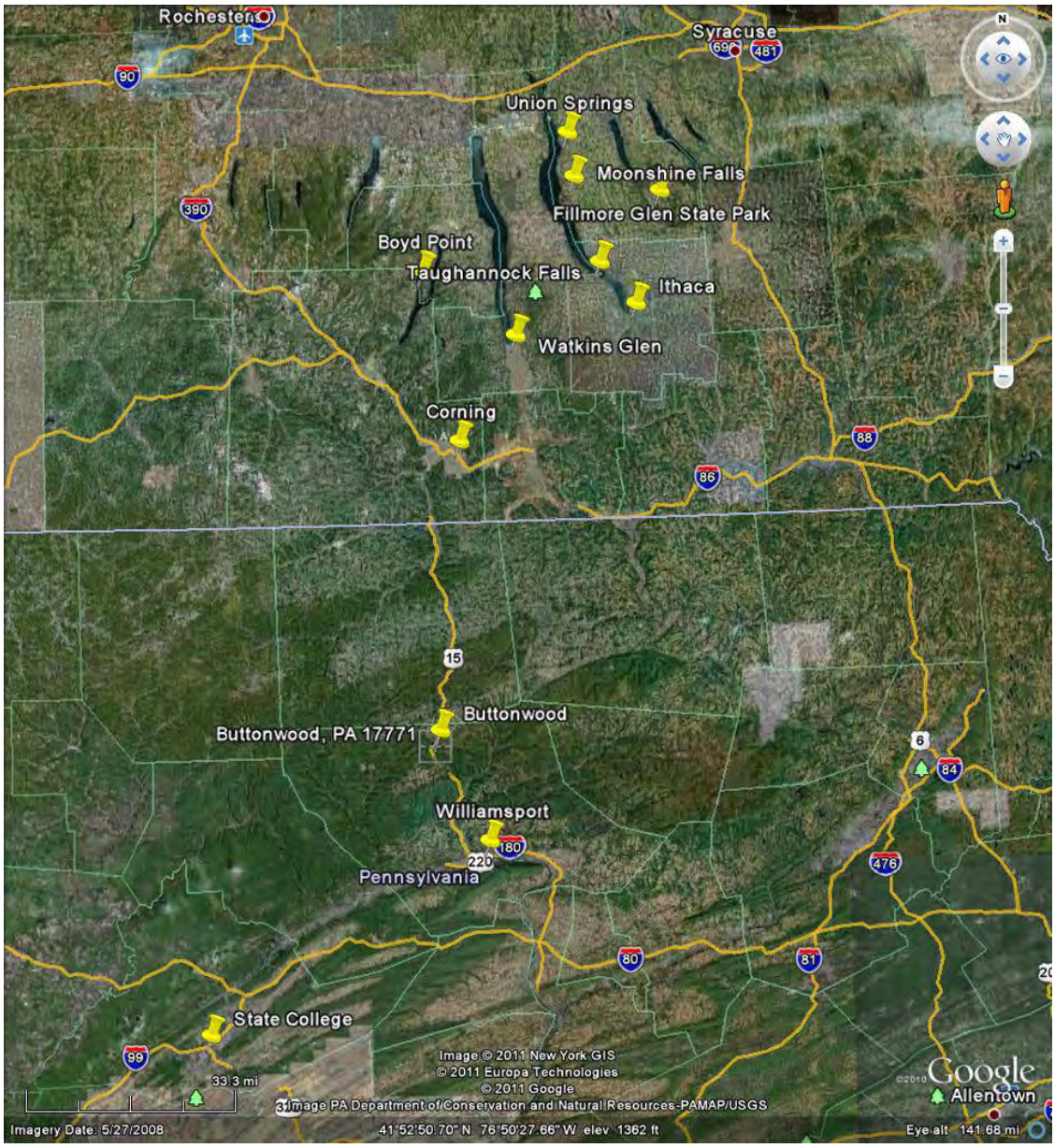

Figure 23. Map of outcrop locations examined during the June 2-3 field trip. Mapped with GoogleEarth.

Summary of findings

Key observations in outcrop are that there is a consistent fracture organization in terms of orientation and relative timing. Consistencies are seen across the outcrop belt and vertically through the section, with repeated patterns of fracture intensity in black and grey shales. These are summarized by Engelder and Gold (2008) field guide, in which some “conundrums” concerning our understanding of these fracture systems are discussed, and by Engelder et al. (2009). There are three main fracture sets: J1 joints,

trending ENE-WSW and best developed in the black shales such as the Marcellus, Geneseo and Middlesex Formations; J2 joints, trending approximately NNW-SSE, normal to fold axes and best developed in the grey shales; J3 which are sub-parallel to J1 but which tend to be curviplanar and are interpreted to have developed during uplift in the modern day stress field.

Fractures in outcrop mostly manifest themselves as barren joints with clear surface-propagation features such as plumose structure and arrest marks. Lacazette and Engelder (1992) documented an example in the Ithaca Sandstone and there are many other examples throughout the section (e.g. Fig. 24).

Figure 24. J2 joint with plumose structure showing several different horizons where fracture growth initiated. Catskill Delta Sherman Creek Formation sandstone south of Buttonwood on west side of I99.

J1 fractures are best developed in the black shale, and J2 are dominant in the grey shales. Both J1 and J2 occur in the grey shales directly overlying black shales (Fig. 25). There are in fact two sets of J2 joints, with the later set striking a little clockwise from the earlier set. At the Boyd Point stream outcrop the later J2 set are oriented 008/78 E (Fig. 26) and both J2 sets are also present at Taughannock Falls State Park, NY. (Fig. 27).

Figure 25. Both joint sets are present in Middlesex Shale in the streambed at Boyd Point, Keuka Lake, NY. A J2 joint is parallel to the scale (oriented (343/89NE here) and is at a high angle to J1 joints (oriented 077/90), which are offset along J2 joints in some places.

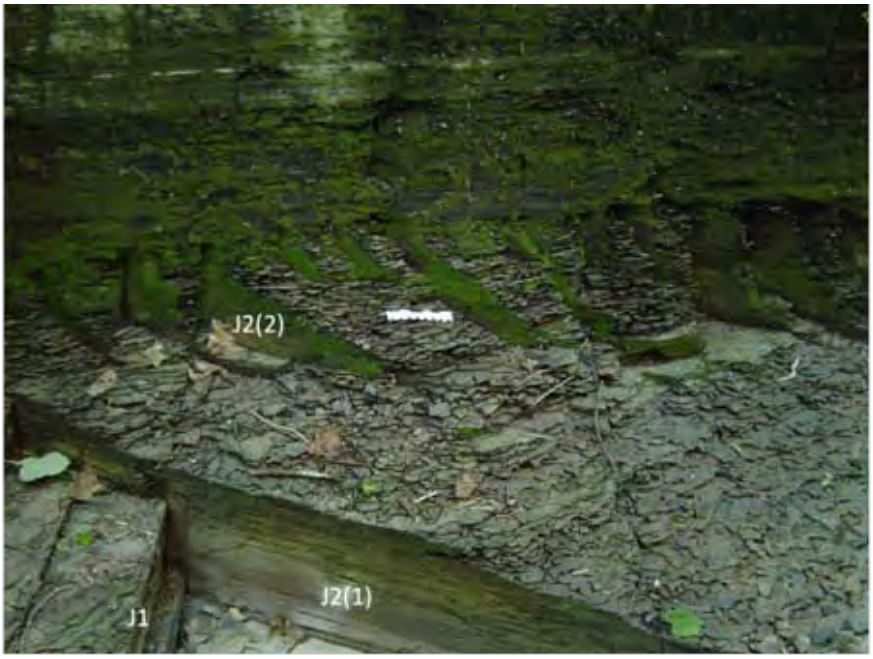

Figure 26. J1 and both J2 joint sets are present in the streambed at Boyd Point, Keuka Lake, NY.

Figure 27. J2 joint sets, J2(1) and J2(2), are present in the Ithaca Formation at Taughannock Falls State Park, NY. Multiple J2(2) joints propagate down from the siltstone shale interface (Engelder and Gold, 2008).

Very few fractures have cement in them although there are exceptions (Fig. 28). A quarry near Union Springs, NY contains several well-exposed J1 joint surfaces with calcite and pyrite cement in the Union Springs Member of the Marcellus (J2 fractures also have cement). Further examples of cemented J2 joints are documented by Engelder and Gold (2008) in the Union Springs Member of the Marcellus along the Conrail railroad cut at Newton-Hamilton, PA. Partly open J2 fractures also occur in the Onondaga Limestone at the same location.

There are two sets with abutting and offset relations indicating an older J1 set that trends ENE-WSW and a younger J2 set trending NNW-SSE. Both are steeply dipping and sealed with calcite and pyrite. Kinematic apertures of these fractures are up to 1 mm and the cement-wall rock bond is weak.

Figure 28. J1 fracture with calcite and pyrite cements on the surface. Plumose structure can be seen in the cement at right. Location: Wolfe Quarry, The Village at Union Springs, NY.

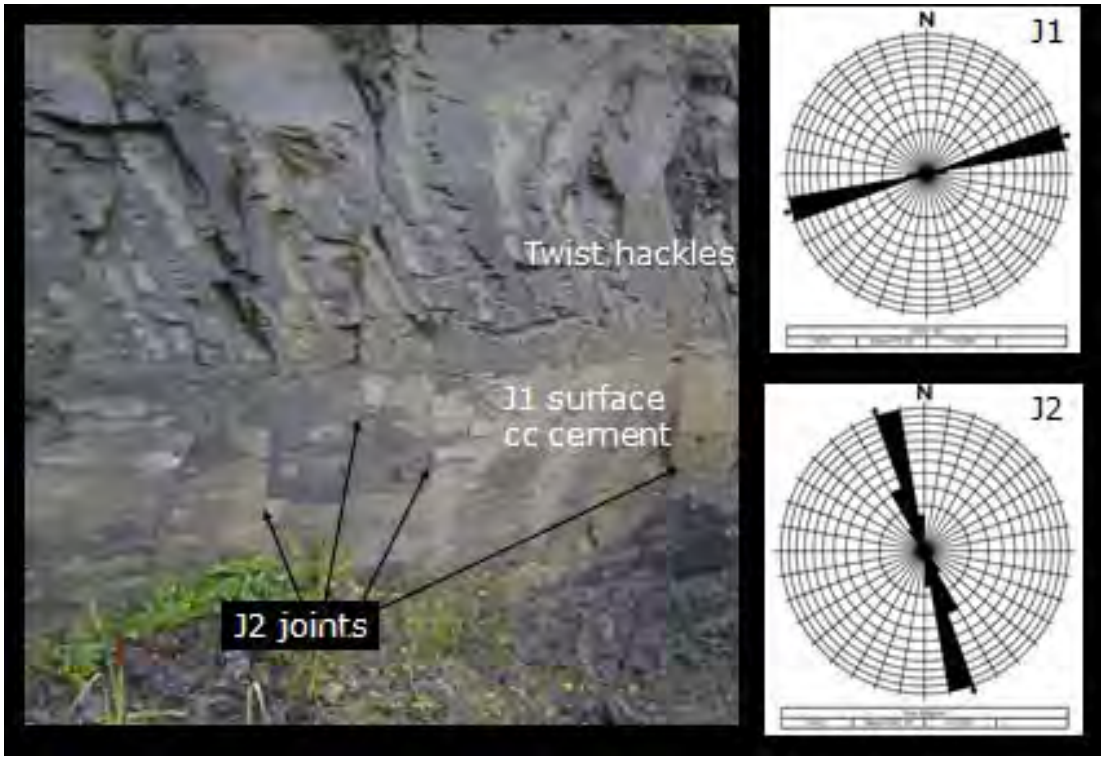

Figure 29. J1 fracture face with patchy calcite cement on the surface. Twist hackles have developed in the upper part of the fracture. Several J2 fractures cut the J1 fracture plane; J2 spacings, widths and other attributes were collected here using a scanline constructed along the J1 surface at approximately 1 m above the quarry floor. Inset rose diagrams; trends of J1 (n = 52) and J2 fractures (n = 42) measured at this location. Location: Wolfe Quarry, The Village at Union Springs, NY.

Natural fracture spatial organization.

Fracture spacing data were collected for both fracture sets. J1 spacing data were collected along a scanline normal to J2 fractures in the quarry floor. J2 data were collected along a scanline on a J1 joint surface that forms the back wall of the quarry (Fig. 29). Plots of fracture aperture versus position along scanline give a sense of the degree to which fractures are clustered. The J1 fractures are somewhat clustered (Fig. 30a), while the J2 fractures appear to be more strongly clustered (Fig. 30b). No mineral cement was seen in the J2 fractures in the scanline along the J1 that forms the back wall of the quarry although elsewhere in the quarry J2 fractures contain cement fill.

(a)

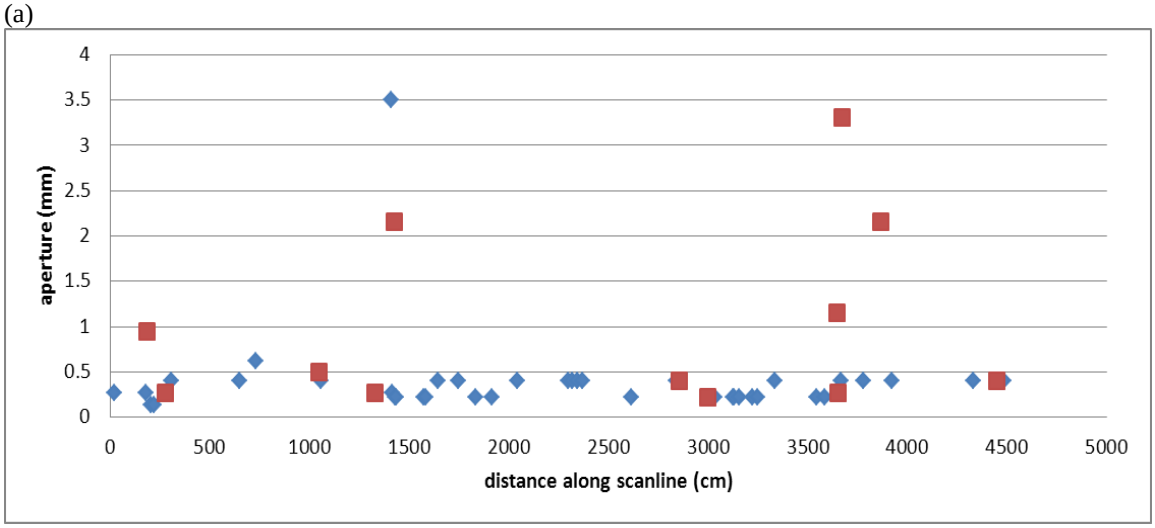

(b)

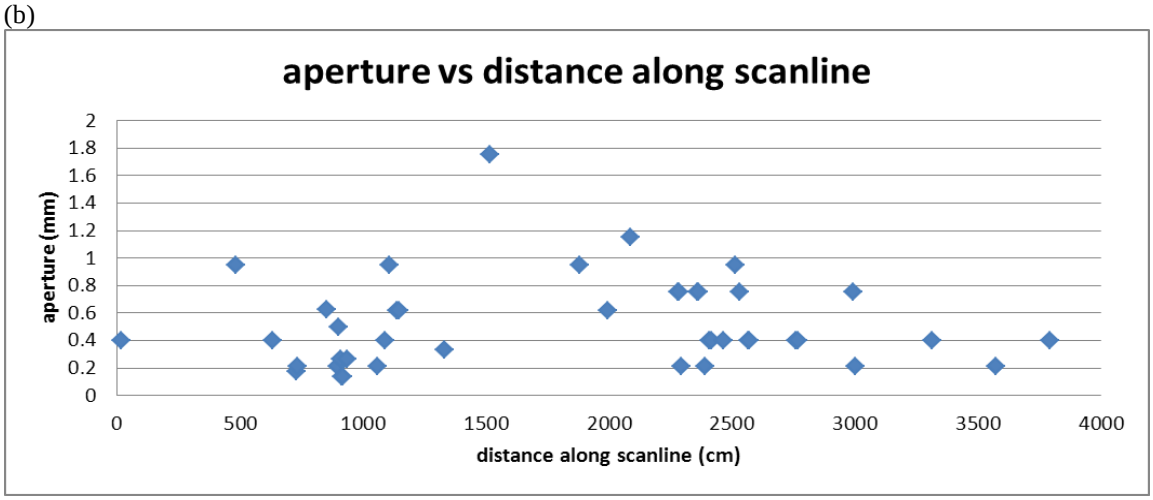

Figure 30. Plots of fracture aperture versus distance along scanline for (a) J1 joints, where orange = sealed fractures, blue = apparently barren fractures, and (b) J2 joints. Data were collected from scanlines normal to each joint set.

Plots of spacings, as shown in Figure 30, give a sense of clustering but do not allow quantification of clustering. To do this we analyzed the spacing data using a geostatistical method based on a two point correlation integral – the normalized correlation count (Fig.

31). This method, developed by Marrett et al. (2005) and Gomez (2007), allows quantification of the degree to which fractures are clustered relative to the clustering expected in a random distribution. The difference between the correlation count for a random set (normalized to 1) and the observed correlation count is termed the spatial correlation. Peaks in the observed data represent length scales at which spatial correlation is greater than random (Fig. 31). The J1 fractures have a weak preferred spacing at 0.2m, 1 m, ~7 m and 14 m (Fig. 31a). The J2 fractures show preferred spacing at 2, 4 and 14 m (Fig. 31b). The common correlation for both sets at 14 m is noteworthy and we speculate this may reflect an intrinsic mechanical layer thickness for the Union Springs at this location that persisted during burial and governed fracture spacing for two fracture sets that developed at two different times.

(a)

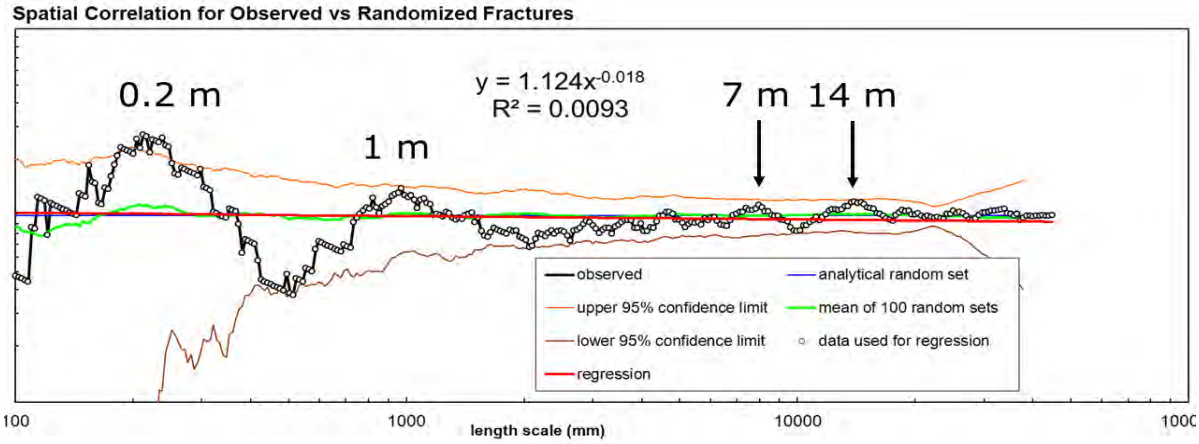

(b)

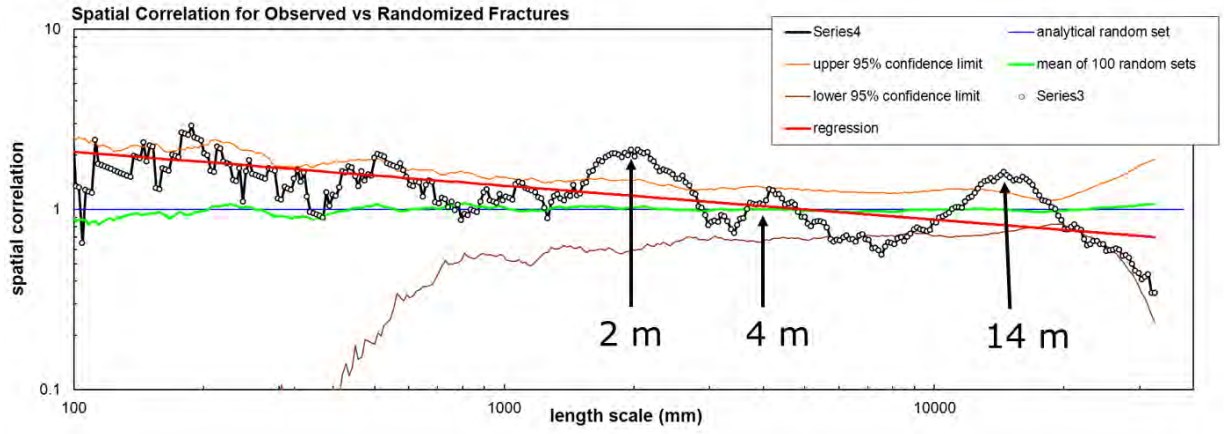

Figure 31. Spatial correlation plots for (a) J1 fractures and (b) J2 fractures in the Union Springs Member of the Marcellus Shale in the Wolfe Quarry at Union Springs, NY. Spacing data were collected along scanlines normal to each fracture set. The plots show the deviation of the observed data (open circles and black line) from analytical random spatial correlation (blue line) and 100 randomized arrangements of the data (green line) together with the 95% confidence limits of the randomized data. Peaks indicate greater spatial correlation at that length scale, troughs indicate lower correlation.

Natural fracture spatial organization: analysis of resistivity image log (GVR tool), Gulla Unit #10H Horizontal well, Washington Co., PA

The Gulla Unit #10H well in Washington Co. SW Pennsylvania is part of the group of five wells used in this project to characterize the natural fracture pattern in the Marcellus Shale. Of the five wells it is the only horizontal well. Fractures along the length of the wellbore, both natural and induced, were imaged with a Schlumberger GVR log, and bedding and fractures were interpreted and depths and orientations were plotted (picked) by Schlumberger. We extracted the fracture orientation data from an Excel spreadsheet of the fracture picks and plotted them as lower hemisphere stereographic projections (Fig. 32).

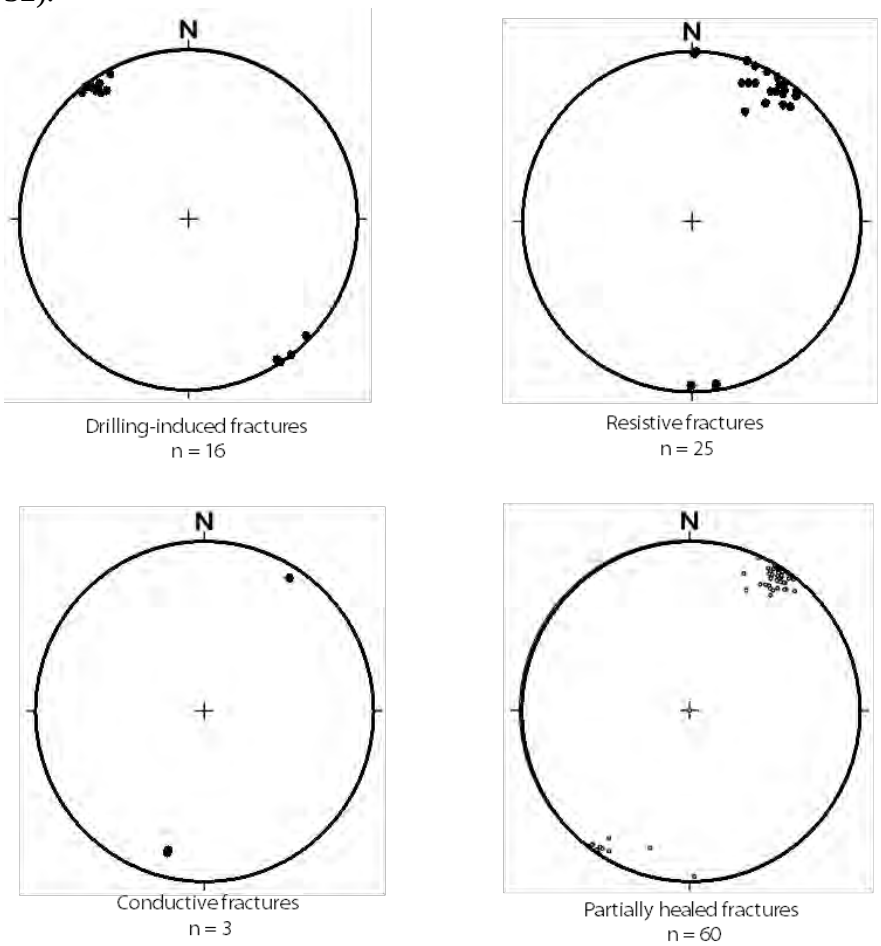

Figure 32. Compilation of lower hemisphere stereographic projections of poles to fractures for different fracture types identified in the Gulla Unit #10H image log. The drilling azimuth is 329°, which is normal to the drilling-induced fractures.

We also examined the fracture picks using the WellEye viewing tool and compared them with the fracture data obtained from core and image logs in the other wells in Washington Co. The orientations of different fracture types obtained from the image log in the Gulla Unit #10H well are similar to fracture orientations in the other wells at comparable depths. According to the directional survey the well becomes horizontal at about 6,366 ft (TVD) which corresponds to a MVD of 6,620 ft allowing for the curve around the heel of the well. This is close to the top of the Marcellus A.

Natural fractures with various degrees of resistivity trend WNW-ESE (these are interpreted as being part of the regional J2 set). Resistivity is an indicator of whether the fracture is open to conductive fluid. Conductive fractures are commonly interpreted as being open. Fractures with openings may have linings of cement on walls or may have been reactivated and opened during drilling. Partly open fractures may have discontinuous cement fill. Resistive fractures are likely to be filled with cement. The presence of all three degrees of mineral fill in a single set is consistent with models of cementation that show a size-dependence of fracture fill for synkinematic cement, or heterogeneity of fracture fill for postkinematic cements (Laubach 2003).

The orientation of fractures in this well and their measured depths along the length of the well allow us to examine the fracture spatial organization of the different fracture types. Examination of fracture occurrence along the length of the wellbore gives a qualitative sense of clustering (Fig. 33). Plots of fracture location along the borehole, from 6,660 to 7,208 ft (Fig. 33a) and from 7000 to 8364 ft (Fig. 33b) reveal the different fracture types are not evenly distributed. There are gaps in natural fracture occurrence between 6,800 and 7,000 ft and between 8,000 and 8,200 ft.

Drilling induced fractures trend NE-SW. It is possible some or all of the fractures interpreted as drilling induced are in fact natural J1 fractures. Otherwise, there are 88 J2 fractures, zero J1 fractures and 16 drilling-induced fractures in 1350 ft of lateral. Induced fractures (yellow in Fig. 33) are concentrated midway along the imaged borehole with a few at each end. The significance of this clustering of induced fractures (or J1) is not known at this point in the study. We will attempt to investigate further whether these fractures are natural or induced.

The deviation survey for the well indicates a drilling azimuth of 329°, which is normal to the induced fractures. An orientation sampling bias would lead to undersampling of WNW-ESE fractures more so than those trending at a high angle to the wellbore. We conclude that even if all the “induced fractures” are in fact J1 natural fractures, the J2 set is more intense than the J1 set at this locality.

(a)

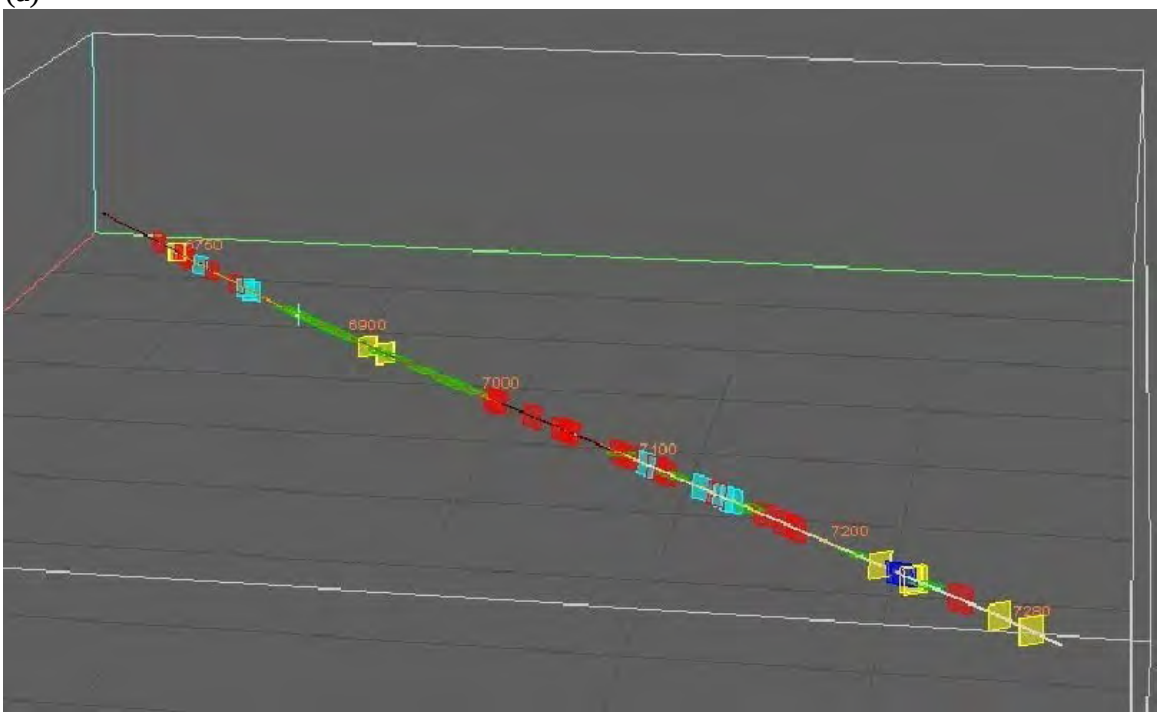

(b)

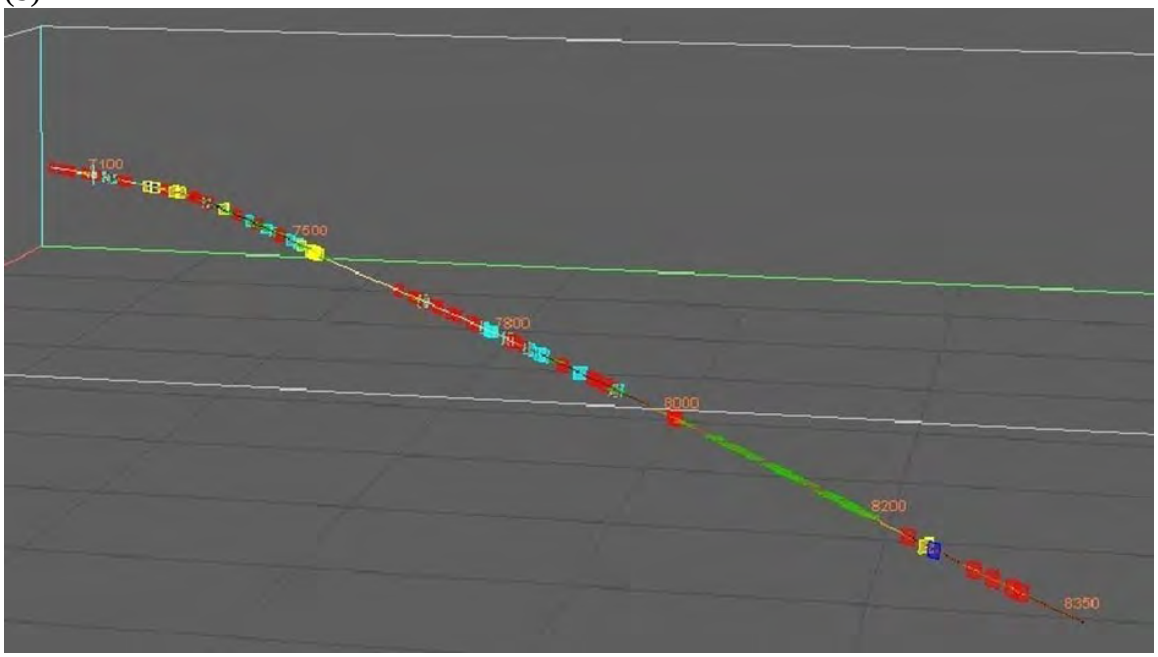

Figure 33. Fracture locations along the length of the Gulla Unit 10H horizontal well (picks by Schlumberger) (a)from 6,660 to 7,208 ft and (b) from 7000 to 8364 ft. Note overlap in the plots. Different fracture types are color coded: Red = partially healed fracture; Light blue = resistive fracture; Blue = conductive fracture; Yellow = drilling-induced fracture; Green = bed boundary.

The first step in our quantitative spatial analysis is to take the measured vertical depths along the wellbore and compute the spacings between all the fractures in the set. Corrections for non-oblique fractures can be made at this stage or after the correlation count analysis. The technique requires that the width (kinematic aperture, that is the wall to wall dimension of the fracture including porosity and cement) of the fractures be included so that mid-point positions for each fracture can be established. In the case of data collected in outcrop or horizontal core these would be directly measured, but because it is not possible to measure the widths of the fractures in the GVR log we assign arbitrary widths to the fractures. The widths are typical of those seen in core and range from 0.05 to 1 mm. A plot is made of the position of the fracture along the length of the wellbore, together with the assigned aperture size for each (Fig. 34). Comparison of the plot with the visualization of the wellbore for the drilling induced fracture shows how the plot captures the concentration of the fractures in the midsection of the well.

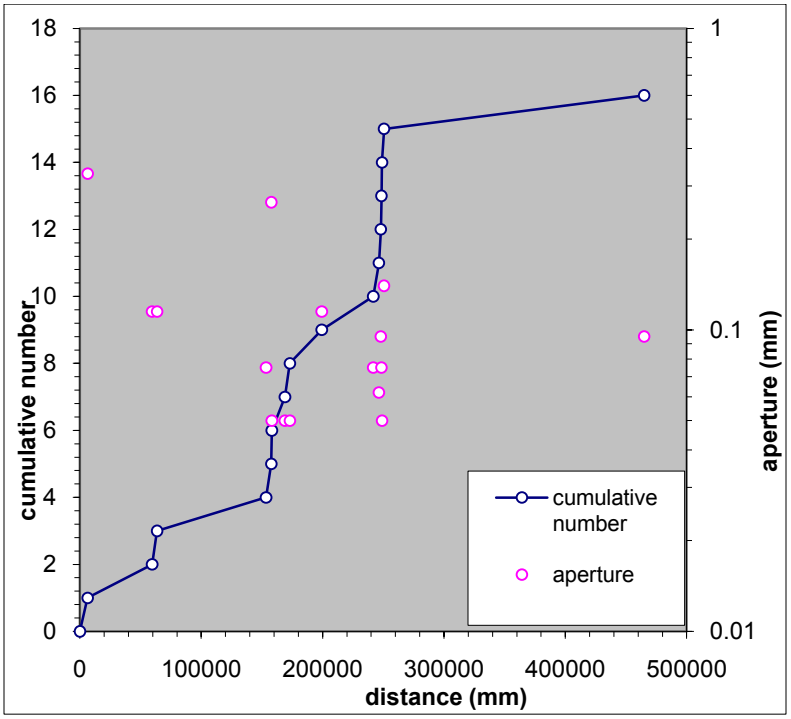

Figure 34. Plot of fracture location along the well bore (distance), shown as a cumulative fracture count (cumulative number). Widths (apertures) of each fracture are also shown. Drilling induced fractures.

We then use a modified correlation count technique, which is a geostatistical method based on a two point correlation integral. This method, developed by Marrett et al. (2005) and Gomez (2007), allows quantification of the degree to which fractures are clustered relative to the clustering expected in a random distribution. The difference between the correlation count for a random set (normalized to 1) and the observed correlation count is termed the spatial correlation (Fig. 35). Peaks in the observed data represent length scales at which spatial correlation is greater than random. In general, the larger the data set available the more representative it will be.

The plot for the drilling induced fractures shows a statistically significant peak around 80,000 mm (262 ft) (Fig. 35). This reflects the spacing of clusters of fractures seen around 170,000 and 250,000 mm in the plot of distance along borehole vs. cumulative number (Fig. 34) and in the yellow fractures in the borehole visualization close to marked depths of 7,280 and 7,500 ft (Fig. 33). Thus despite there being only 16 drilling induced fractures the correlation signal is high, indicating a strong spatial organization. The section of the plot from 1000 to 30,000 mm shows a spatial correlation progressively decreasing with increasing length scale. This is a mix of signal and artifact. The stepwise decrease with incremental decrease in length scale is due to the signal being obtained over progressively shorter distance as the length scale increases. However, the overall downward trend likely indicates a fractal spacing distribution within the clusters. Cluster width is approximately at the crossover on the x-axis at 16, 613 mm (55 ft)

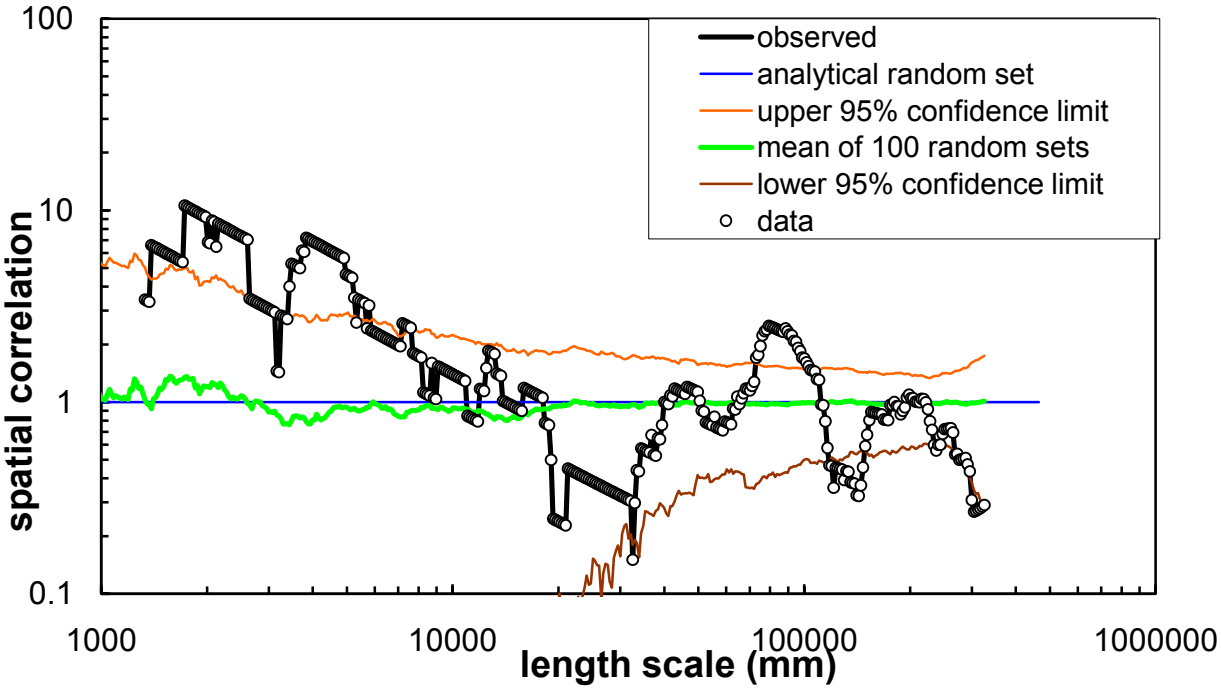

Figure 35. Spatial correlation plot for drilling induced fractures in the Gulla 10H well image log. The points up to 30,000 mm (~100 ft) indicate a fractal spacing distribution within clusters, while the peak at ~80,000 mm is an indication of a characteristic spacing, and it is statistically significant as it rises above the 95% confidence limit.

Although the natural fractures in the GVR log were split into three different groups on the basis of degree of mineral fill we argue above that these can be treated as a single set (J2). The combined data are plotted (Fig. 36) and analyzed (Fig. 37). In this case, in the absence of measured apertures, the apertures were assigned using a data set from an outcrop of Austin Chalk, where the largest fracture is 100 mm wide. These values are used to assign the midpoint of the fracture and have no further utility in this study. The cumulative number plot (Fig. 36) indicates the segments of the well bore along which there are many fractures (blue curve is steep) and those segments where there are no fractures (blue curve is flat).

The spatial correlation analysis (Fig. 37) shows a significant peak at 7,000, (23 ft) and weaker ones at 13,300 (44 ft) and 24,670 (81 ft). These all need to be corrected as the borehole is at a low angle to the fractures. If we take the mean trend of the fractures as 300° and the borehole direction as 329° then the correction to be applied is:
True spacing = apparent spacing (sin 29°)
Or, True spacing ≈ half apparent spacing
Thus the preferred spacings for J2 fractures are approximately at 3.5 m (11.5 ft), 6.75 m (22 ft) and 12.34 m (40 ft). The latter two are likely harmonics of the first. Unlike the plot for the induced fractures the natural fractures do not show a strong correlation at small length scales, progressively decreasing to zero or negative correlation. Rather, there is a single peak at 1500 -1700 mm (5 ft).

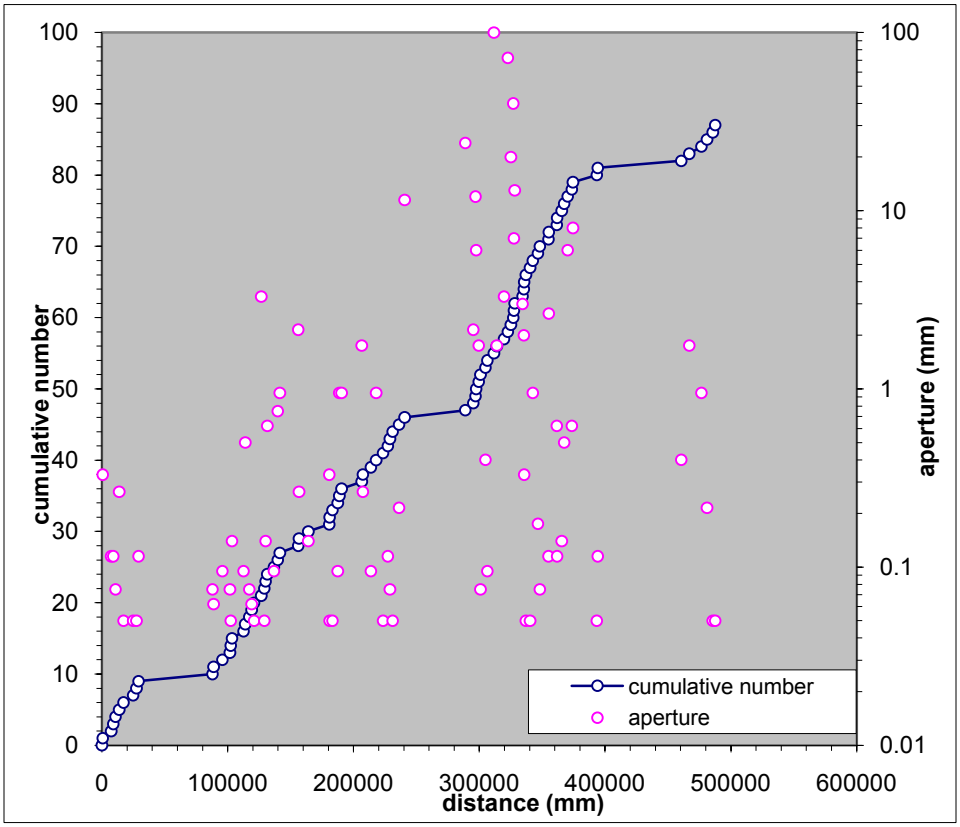

Figure 36. Plot of fracture location along the well bore (distance), shown as a cumulative fracture count (cumulative number) and fracture width (aperture) for natural fractures in the J2 set.

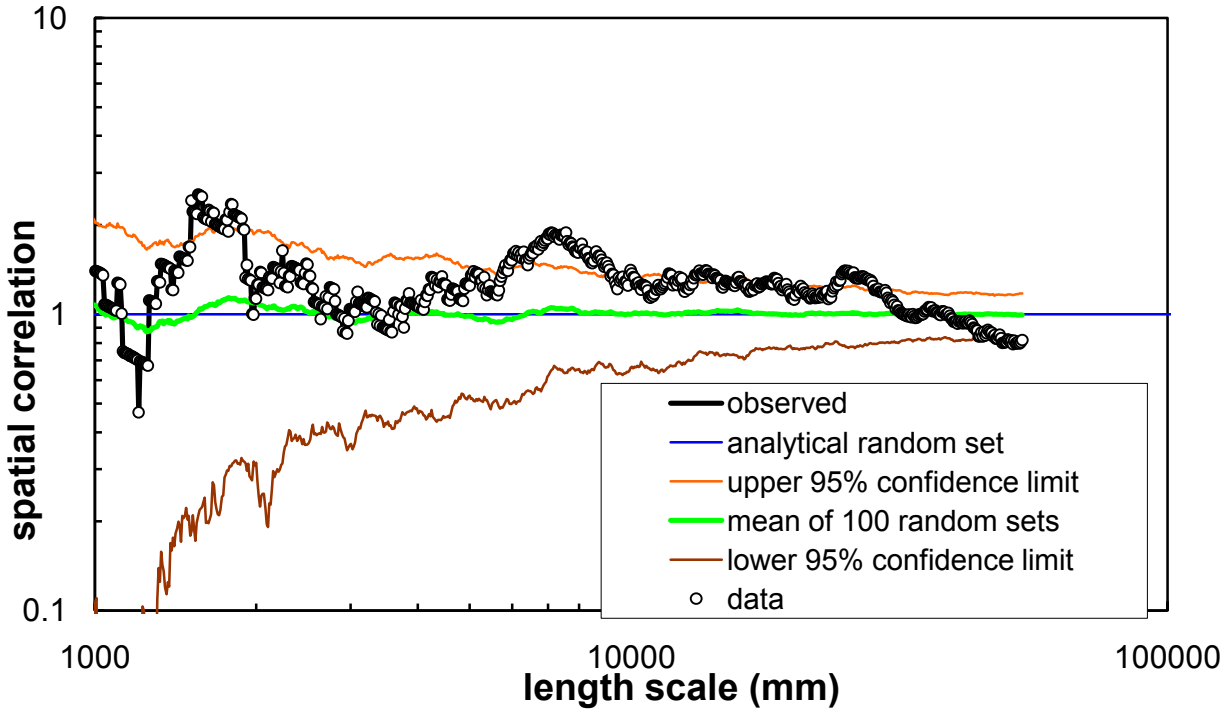

Figure 37. Spatial correlation plot for natural fractures in the Gulla 10H well image log. Significant spatial correlation is seen at approximately 1.5, 3.5, 6.8 and 12.3 m.

We now compare these results with fracture spacing data obtained from Marcellus Shale in a quarry at Union Springs, NY. In outcrop the J1 fractures have a weak preferred spacing at 0.2m, 1 m, ~7 m and 14 m. (These latter three spacings are not quite at the 95% confidence limit). The J2 fractures show preferred spacing at 2, 4 and 14 m. We highlighted the common correlation for both sets at 14 m in the field section of this report and speculated this may reflect an intrinsic mechanical layer thickness for the Union Springs at this location that persisted during burial and governed fracture spacing for two fracture sets that developed at two different times. The spacings for J2 obtained here are comparable to the spacings in outcrop. One would not expect a direct one to one correlation as the outcrop and reservoir are almost 300 miles apart and the actual spacings are sensitive to mechanical layer thickness. But the tendency to develop clusters and for these to be spaced perhaps 12-14 meters apart with some smaller scale clustering is common to both data sets. Inspection of the vertical pilot well logs for the Paxton Isaac well revealed thin limestone units at this 12.5 m spacing, and indeed we interpret the preferred spacing of fractures to reflect this mechanical layer thickness (Fig. 38). Spacings will modified by subcritical index also.

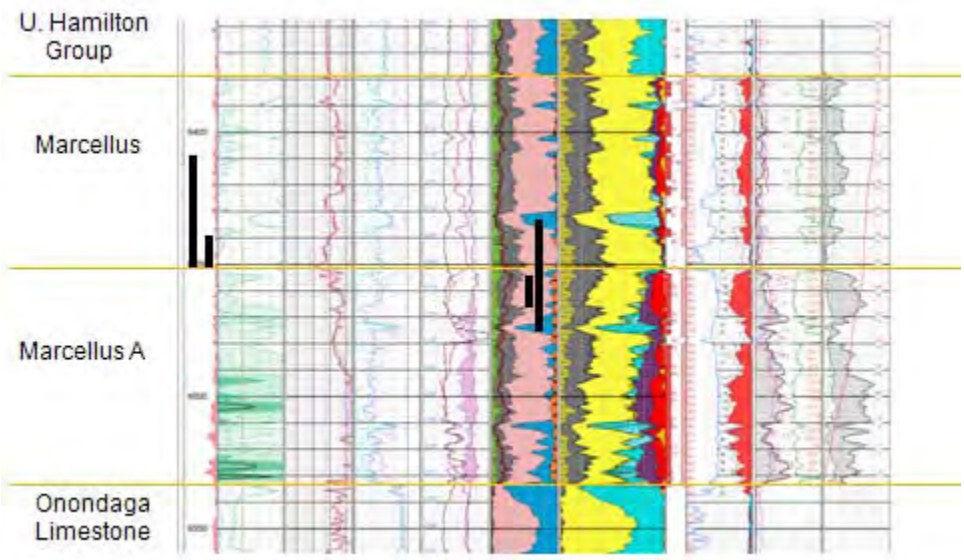

Figure 38. Paxton Isaac well log suite. The ECS shows limestone layers spaced at 12.5 m and 3 m. These may form boundaries to mechanical layers, which in turn control fracture height and thereby spacing.

The comparison with J1 is more problematic. If we assume all the "Induced fractures" are in fact J1 fractures that were reactivated during drilling there is still no similarity. In outcrop the J1 set were also clustered with clusters spaced weakly at around 14 m (with smaller spaced clusters within), but in the Gulla well these are spaced at 80 m. The difference could be due to the fact that the Gulla well samples a much longer distance normal to fracture strike than the outcrop. It is possible that our outcrop study contained just one large cluster of J1 as it was only about 45 m long.

Comparing empirically-derived spatial organization data with geomechanical modeling of fracture growth

The next phase of the spatial organization study was to compare the results from the outcrop and image log study with spatial analysis of fractures generated through geomechanical modeling of fracture growth. The modeling was done using JOINTS software, previously developed by Dr. Olson at The University of Texas at Austin. Modeling requires measurement of a mechanical rock property, the subcritical crack index (Holder et al., 2001). Measurements of subcritical crack index, fracture toughness and mechanical layer thickness from the Paxton Isaac well logs and samples were used as model input.

Geomechanical Testing

Core segments from the Paxton Isaac Unit #7 from Washington Co. (PI) and EGS#5 well (EG) from Lawrence County, were sampled for measurements of subcritical crack index (SCI) and Mode I fracture toughness (KIc, MPa-sqrt(m)). The reported Marcellus interval

in the EGS#5 well is 4010 to 4132 ft. The sample from 4082.2 ft yielded four test specimens, but the other samples (from 4099.4, 4106.7, 4119.2 and 4122 ft) could not be prepared because there was too little material for testing. SCI and K1c were determined from dual torsion measurements. The thicknesses of the test specimens are included in the tabulation. SCI was determined for 3 load decay measurements, followed by loading to failure (for K1c). Results are summarized in Tables 1 and 2.

Mean SCIs are 75, and 31, for the PI and EGS material. KIc values are generally 1 - 2 MPa-sqrt(m) for the Paxton Isaac samples and 0.7 MPa-sqrt (m) for the EGS#5.

Sample	Thickness	subcritical index					KIC
	(in)	1	2	3	4	5	Mpa-sqrt(m)
PI29S-4	0.084	78	95	92			0.36
PI29S-8	0.071	45	75	79			1.4
PI29S-9	0.075	65	80	88			1.4
PI85S-4	0.094	38	70	43			1.0
PI85S-6	0.082	67	73	57			1.2
PI85S-7	0.079	50	78	99			1.4
PI85S-8	0.075	81	123	131			2.2
PI85S-9	0.078	58	79	87			1.4
PI84S_A	0.080	76					1.3
PI84S_C	0.088			86			1.2
PI84S_D	0.085	60					1.7
PI84S_E	0.089	49					

Table 1. Subcritical crack index and fracture toughness results from tests on samples from the Paxton Isaac #7 well.

Sample	Thickness	subcritical index					KIC
	(in)	1	2	3	4	5	Mpa-sqrt(m)
EGSP4_1	0.075	27					
EGSP4_2	0.075	35					0.72
EGSP4_3	0.068	33	30				0.71

Table 2. Subcritical crack index and fracture toughness results from tests on samples from the EGS#5 well.

Geomechanical Modeling

In order to generate sufficient numbers of fractures to compare with outcrop and well datasets the output from the *JOINTS* geomechanical model was modified. The length of the model normal to fracture strike was extended while keeping the length parallel to fracture strike at least 5 times the layer thickness. We experimented with three different mechanical layer thicknesses: 1, 5 and 10 m. With this approach we were able to generate a model 200 m long so that a scanline constructed normal to the fractures intersected 39 fractures. This is comparable to the number of fractures observed in the field in 40 m scanlines and in the Gulla Unit #10H well. Spatial organization analyses of these different data sets are then compared.

We show a model using these input parameters and using a mechanical layer thickness of 10 m (Fig. 39). Although the fracture intensities are different and the number of fractures is low there are just sufficient (39) to give a signal in the spatial correlation plot (Fig. 40) so that spatial organization of these different data sets could be compared.

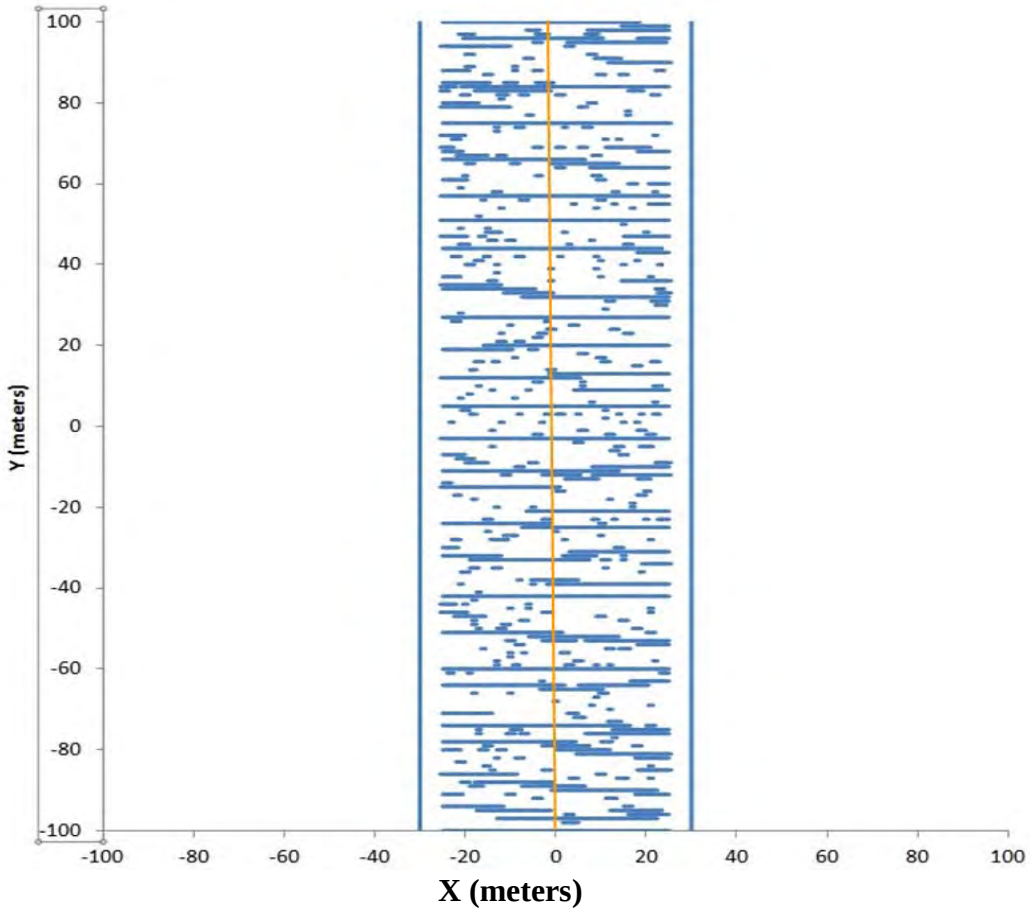

Figure 39. Map view of *JOINTS* geomechanical model of one set of natural fractures in Marcellus Shale using measured subcritical index (n= 80) and fracture toughness KIc = 1.3 MPa sqrm. Mechanical layer thickness is 10 m. Young's modulus and Poisson's ratio are chosen at 20 GPa and 0.2 respectively. Spacings and apertures were measured in the model along the orange line constructed normal to fractures at x = 0.

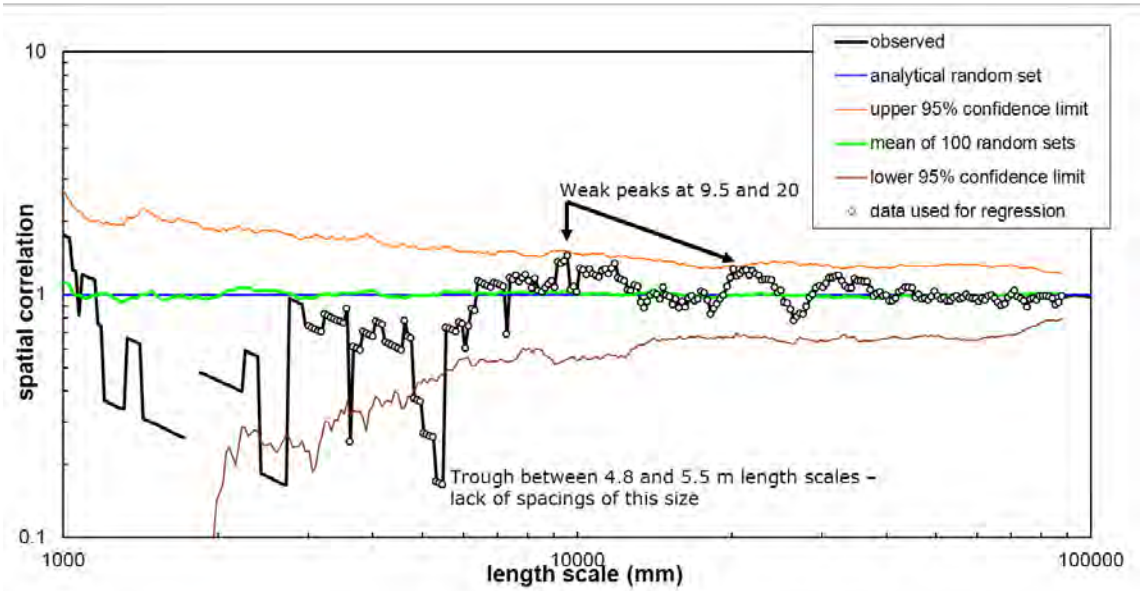

Figure 40. Spatial correlation plot for modeled fractures shown in Fig. 39.

Weak spatial correlation is seen at approximately 9.5 and 20 m. These correlation reflect the effect of mechanical layer thickness on fracture spacing. The subcritical index for this modeled example is 80, which is moderate to high and close to the mean for the sampels measured. Subcritical indices higher than this value would lead to more clustering of fractures, whereas indeices lower than 80 would lead to less clustering, but the mechanical layer thickness would still exert a strong control. The large trough between the 4.8 and 5.5 m length scale indicates lack of fracture spacings at this size.

Fracture Cement Studies: stable isotope work

Stable isotope work on some of the fracture cement samples expanded the original RPSEA project scope of work. Four samples of fracture calcite cement (2 outcrop from a quarry near Union Springs in that member, and 2 core samples from the Paxton Isaac well) were micro-drilled for analysis in a pilot study of $\delta^{13}C$ and $\delta^{18}O$ values. The samples from the outcrop J1 fractures show several narrow layers of calcite cement and a blocky cement section (Fig. 41). We interpret the layers as crack-seal texture, that is, repeated breaking and sealing of the fracture. The blocky cement is most commonly found in the fracture center but in some cases it is at the margin, which we interpret in terms of variation in the location of breaking from fracture to fracture. The J2 fracture we sampled has only blocky cement.

The fractures in the Paxton Isaac well sampled for the pilot study are both low angle, containing fibrous calcite cement fill (Fig. 42). We selected these as the most likely candidates to give a contrast in isotopic composition to the vertical sealed fractures from

the outcrop.

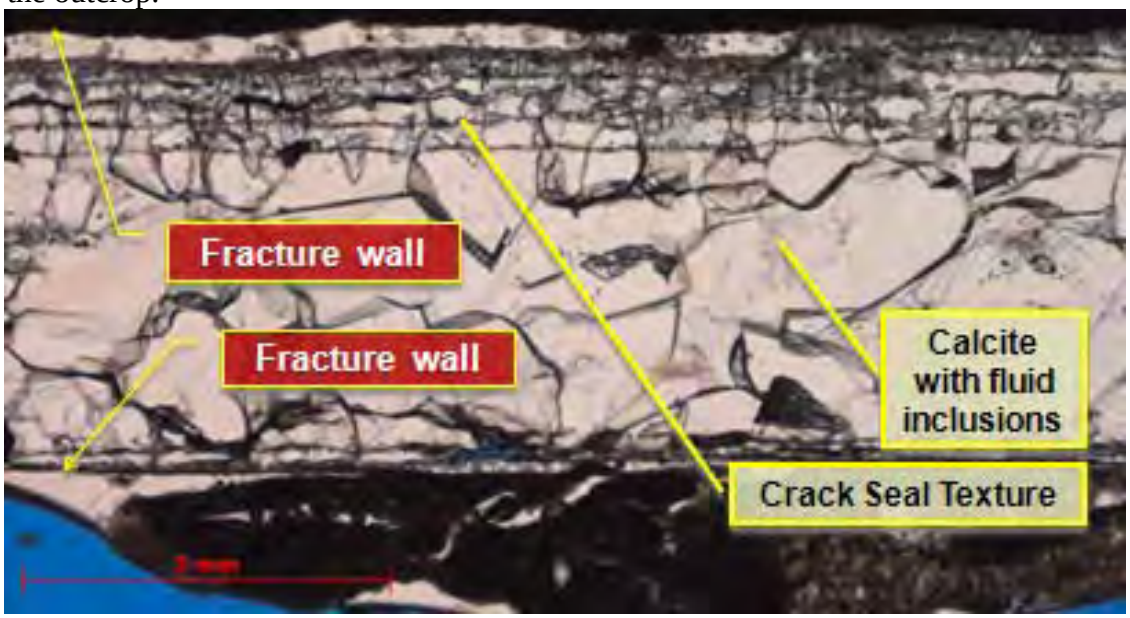

Figure 41. Photomicrograph of cement textures in a J1 fracture Marcellus fracture. Note the crack seal texture, delineated by of the presence of small, host rock inclusions parallel to fracture orientation. Blocky cement in the fracture center contains abundant fluid inclusions.

(a) **(b)**

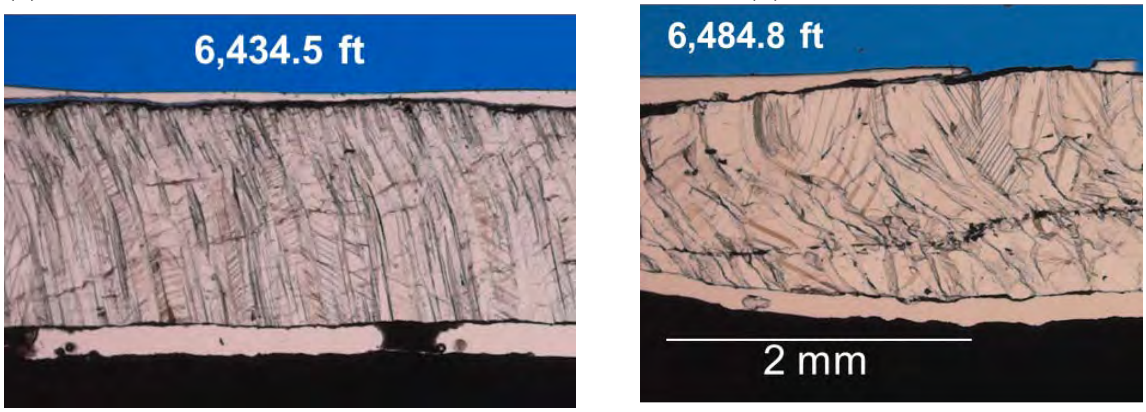

Figure 42. Fibrous calcite from horizontal and low angle fractures in the Paxton Isaac well. These samples were analyzed for $\delta^{13}C$ and $\delta^{18}O$.

The results of the stable isotope study are shown in Fig. 43. The samples from outcrop J1 and J2 have higher $\delta^{13}C$ and less negative $\delta^{18}O$ than those from the Paxton Isaac core (red circles). The interpretation of stable isotope data requires that temperature and growth rate effects be taken into account before concluding that source fluids are different. This study is outside the scope of the RPSEA project, but will be a major part of MS student Laura Pommer's thesis work. Pommer's thesis will be publicly available through the University of Texas at Austin library, and RPSEA funding will be acknowledged and the relation to the wider, GTI-led, Marcellus project will be made clear.

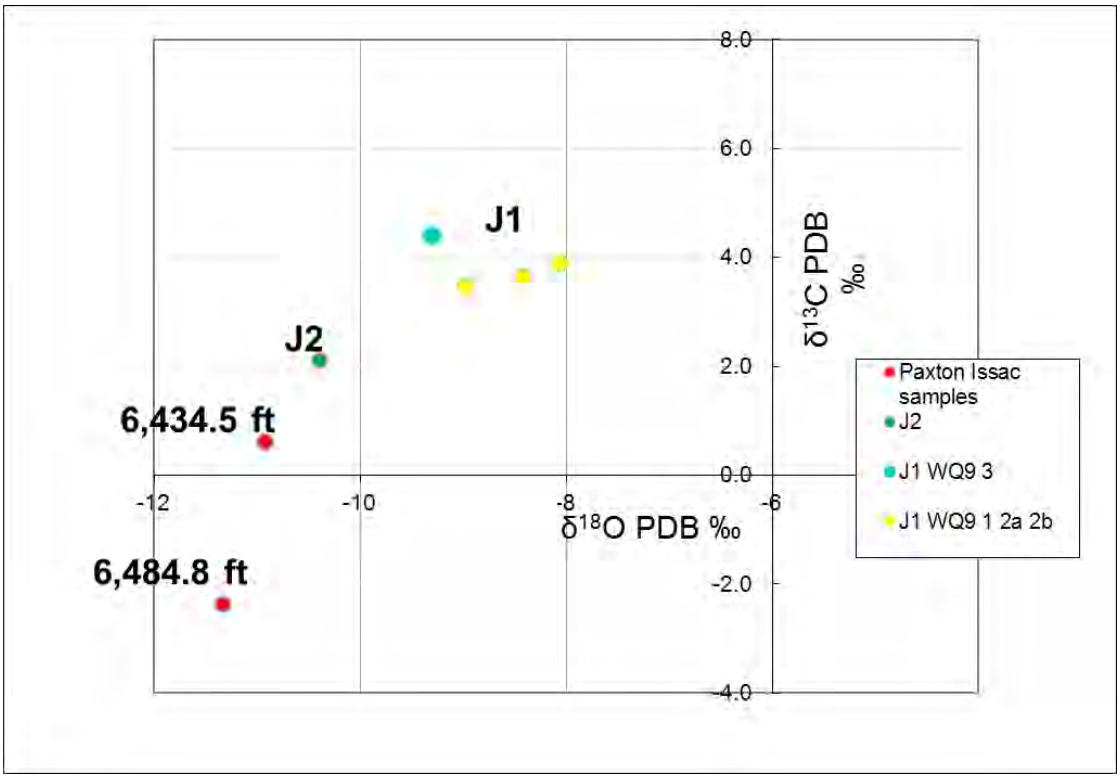

Figure 43. Isotopic composition of calcite cements from outcrop samples from J1 and J2 fractures in the quarry at Union Springs and core samples from the Paxton Isaac well.

Preliminary results.

For the purposes of this project the preliminary stable isotope results can be taken to indicate that there is potential in using stable isotope signatures of fracture cements to help distinguish fracture sets and sealing events in the Marcellus Shale. Fracture porosity and the strength of fracture planes are both dependent on the degree to which fractures are sealed so that knowledge of the sealing events is desirable.

Comparison of Fractures in Outcrop and Core

The striking difference between the outcrops and core is the degree of mineral fill observed. In core there are many filled fractures, whereas in outcrop most of the joint surfaces do not appear to have cement on them. There are exceptions, as noted above. An additional difference is that in core there are many examples of low-angle or horizontal filled fractures, but none were observed in the outcrops.

Technology Transfer

April 19-20th, 2011: Oral presentation (J.F.W. Gale) “Comparisons of natural fractures in the Marcellus Shale with fractures in other shale-gas plays. RPSEA Unconventional Gas Conference, Denver, Colorado.

September 25-27th 2011: Poster entitled “Natural Fracture Characterization in Shale-Gas Reservoirs: Spatial Organization and Fracture Sealing” presented at AAPG Eastern Section meeting, Arlington (Gale, Pommer and Ouyang).

September 28th 2011: Oral presentation (J.F.W. Gale) RPSEA Marcellus Workshop, Arlington.

October 31st, 2011: Guest lecture (J.F.W. Gale) on “Marcellus Shale Geology - Natural Fracture systems”, Graduate Level Class "Advances in Unconventional Shale Gas Resources", University of Texas at Austin.

November 8th, 2011: Oral presentation (J.F.W. Gale) on “Marcellus Shale Geology - Natural Fracture systems” given to the Fracture Research and Application Consortium (FRAC) 2011 Sponsors’ group meeting in Santa Barbara, CA. FRAC is an Industrial Associates program at The University of Texas at Austin.

February 20th-21st, 2012: J.F.W. Gale presented a poster at the Houston Geological Society Applied Geoscience Mudrocks Conference on “Natural Fracture Characterization in Shale-Gas Reservoirs: Spatial Organization and Fracture Sealing”, where Marcellus examples from this project were included. The conference was attended by close to 400 people.

March 6th, 2012: J.F.W. Gale gave a talk on “Marcellus Shale Geology - Natural Fracture systems” at the Bureau of Economic Geology Mudrocks Industrial Associates sponsors’ group meeting. The consortium has over 20 companies involved in North American and global mudrocks exploration and development.

March 31st, 2012: Laura Pommer presented her MS thesis work on “Fracture cementation in the Marcellus Shale” at The Jackson School of Geosciences Masters Saturday event, which was attended by students, faculty, industry sponsors and members of the public., Jackson School of Geosciences, The University of Texas at Austin.

April 17th, 2012: J.F.W. Gale oral presentation “Natural Fracture Attributes: Spatial Organization, Marcellus Gas Shale Project 09122-04” at the RPSEA Unconventional Gas Conference, Canonsburg, PA, 17-18th April, 2012.
April 24th, 2012: J.F.W. Gale and L. Pommer presented a poster on “Natural Fracture Characterization in Shale-Gas Reservoirs: Spatial Organization and Fracture Sealing” at the AAPG Annual Meeting in Long Beach, CA.

References

DOE Eastern Shale Gas Project reports (NETL website)

Engelder, T. and Engelder, R., 1977, Fossil distortion and décollement tectonics of the Appalachian Plateau, Geology, 5, 457-460.

Engelder, T. and Gold, D.P., 2008, Structural geology of the Marcellus and other Devonian gas shales: Geological conundrums involving joints, layer-parallel shortening strain, and the

contemporary tectonic stress field. Pittsburgh Association of Petroleum Geologists Field Trip (Sept. 12-13, 2008) AAPG-SEG Eastern Section Meeting Field Trip (Oct. 11-12, 2008).

Engelder , T., Lash, G.G. and Uzcategui, R.S., 2009, Joint sets that enhance production from Middle and Upper Devonian gas shales of the Appalachian Basin. AAPG Bulletin, v.93, p. 857-889.

Evans, M.A., 1980, Fractures in oriented Devonian shale cores from the Appalachian Basin: unpublished M.S. Thesis, Morgantown, West Virginia University, p. 278.

Evans, M.A., 1994, Joints and décollement zones in the Middle Devonian shales: Evidence for multiple deformation events in the central Appalachian Plateau: Geological Society of America Bulletin, v. 106, p. 447–460.

Evans, M. A., 1995, Fluid inclusion microthermometry: multiple vein sets from Middle Devonian shales GSA Bulletin, v. 107, p. 327–339.

Gale, J. F.W., 2002, Specifying lengths of horizontal wells in fractured reservoirs: Society of Petroleum Engineers Reservoir Evaluation and Engineering, Paper No. SPE 78600, p. 266–272.

Gale, J. F. W., and Holder, J., 2008, Natural fractures in the Barnett Shale: constraints on spatial organization and tensile strength with implications for hydraulic fracture treatment in shale-gas reservoirs, *In* 42nd U.S. Rock Mechanics Symposium and U.S.-Canada Rock Mechanics Symposium, San Francisco, June 29–July 2: ARMA, American Rock Mechanics Association, paper ARMA 08-96, 9 p.

Gale, J. F. W., and Holder, J., 2010, Natural fractures in some U.S. shales and their importance for gas production: The Geological Society, London, Petroleum Geology Conference Series, v. 7, p. 1131−1140.

Gale, J. F. W., and Laubach, S. E., 2010, New Albany shale fracture characterization: The University of Texas at Austin, Bureau of Economic Geology. Final report prepared for Research Partnership to Secure Energy in America (RPSEA), under GTI Contract Project No. S-48, 26 p.

Gale, J. F. W., S. E. Laubach, R. A. Marrett, J. E. Olson, J. Holder, and R. M. Reed, 2004, Predicting and characterizing fractures in dolostone reservoirs: Using the link between diagenesis and fracturing, *In* C. J. R. Braithwaite, G. Rizzi, and G. Darke, eds., The geometry and petrogenesis of dolomite hydrocarbon reservoirs: Geological Society (London) Special Publication 235, p. 177– 192.

Gale, J. F. W., Reed, R. M. and Holder, J., 2007. Natural fractures in the Barnett Shale and their importance for hydraulic fracture treatments. American Association of Petroleum Geologists Bulletin, 91, 603–622.

Gomez, L.A., 2007, Characterization of the Spatial Arrangement of Opening-Mode Fractures. Ph.D. Dissertation, UT Austin.

Harper, J., 2008, The Marcellus Shale—An Old “New” Gas Reservoir in Pennsylvania. Pennsylvania Geology, v. 38, no.1, Pennsylvania Bureau of Topographic and Geologic Survey.

Holder, J., J. E. Olson, and Z. Philip. 2001. Experimental determination of subcritical crack growth parameters in sedimentary rock. Geophysical Research Letters 28: 599–602.

Lacazette, A., and T. Engelder, 1992, Fluid-driven cyclic propagation of a joint in the Ithaca siltstone, Appalachian Basin,New York, in B. Evans and T.-F. Wong, eds., Fault mechanics and transport properties of rocks: London, Academic Press, p. 297–324.

Lash, G. G. and Engelder, T. 2005. An analysis of horizontal microcracking during catagenesis: example from the Catskill delta complex. American Association of Petroleum Geologists Bulletin, 89, 1433–1449.

Lash, G.G., and Engelder, T., 2007, Jointing within the outer arc of a forebulge at the onset of the Alleghanian Orogeny: Journal of Structural Geology, v. 29, p. 774–786.

Lash, G., and Engelder, T. 2009, Tracking the burial and tectonic history of Devonian shale of the Appalachian Basin by analysis of joint intersection style. Geological Society of America Bulletin, v. 121 p. 265 – 277.

Laubach, S. E., 1997, A method to detect natural fracture strike in sandstones: AAPG Bulletin, v. 81, p.604– 623.

Laubach, S. E., 2003, Practical approaches to identifying sealed and open fractures: AAPG Bulletin, v. 87, no. 4, p. 561–579.

Laubach, S.E., Olson, J.E., and Gale, J.F.W., 2004, Are open fractures necessarily aligned with maximum horizontal stress? Earth & Planetary Science Letters, v. 222, no. 1, 191-195.

Marrett, R., O. Ortega, and C. Kelsey, 1999, Extent of power-law scaling for natural fractures in rock: Geology, v. 27, no. 9, p. 799– 802.

Marrett, R.A., Gale, J.F.W. and Gomez, L.A., 2005, Spatial Arrangement of Fractures III − Correlation Analyses. Unpublished report prepared for University of Texas Fracture Research and Application Consortium.

Olson, J. E., 2004, Predicting fracture swarms—The influence of subcritical crack growth and the crack-tip process zone on joint spacing in rock, in J. W. Cosgrove and T. Engelder, eds., The initiation, propagation, and arrest of joints and other fractures: Geological Society (London) Special Publication 231, p. 73–87.

Appendix A

Dunn Clingerman and Nancy Stewart core fracture descriptions

Dunn Clingerman fracture descriptions

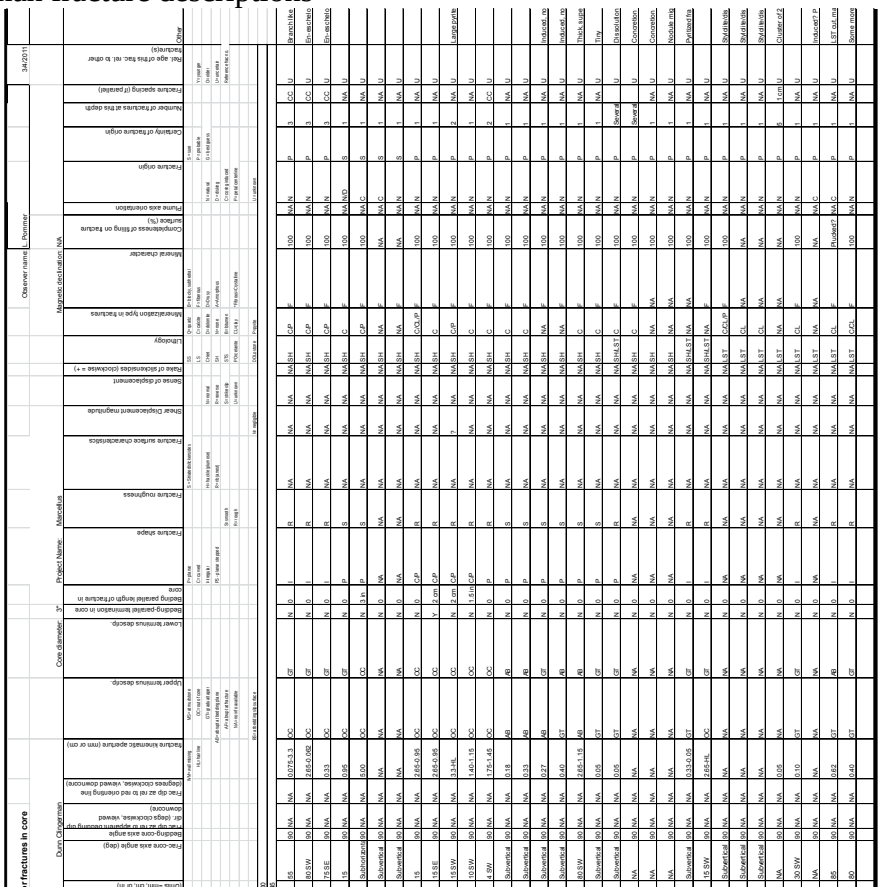

Nancy Stewart fracture descriptions

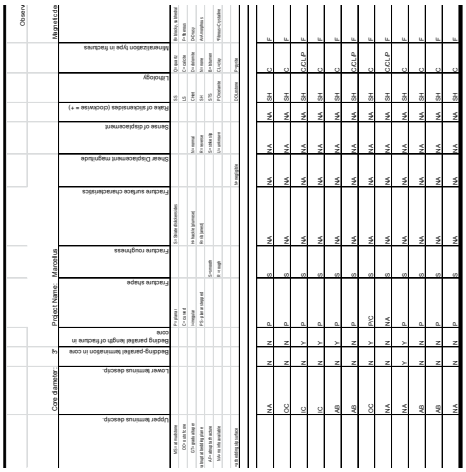

Appendix B

Sampling inventory for petrography and geomechanical tests. Samples labeled “double polished, standard thin sections with blue epoxy fill” were used for petrographic work, samples labeled “SCI” were used in geomechanical tests. Samples labled “gold coat” were to be analyzed with SEM for surface features, but this was not possible within the scope of the project.

Core samples from well experiment area

Sample	Sample type	Core Number-Terratek	Box Number-Terratek	Depth
PI 5909	2x3 Double polished, standard TS with blue epoxy fill	2	na	5909'
PI 5920.25	Bending test	2	na	5920' 2.5" -5920'7"
PI 5921.8	Double polished, standard TS with blue epoxy fill	2	na	5921' 8" - 5922'
PI 6231.5	Double polished, standard TS with blue epoxy fill	8	na	6231' 6" - 6232' 1"
PI 6382.1	Double polished, standard TS with blue epoxy fill	11	na	6382' 1" - 6382' 4"
PI 6384.8	SCI	11	na	6384' 8" - 6385'
PI 6429	SCI	12	na	6428' 10" - 6429' 3"
PI 6434.5	Double polished, standard TS with blue epoxy fill	12	na	6434' 5.5" - 6434' 11"
PI 6463	Double polished, standard TS with blue epoxy fill	12	na	6462' 7" - 6463' 3"
PI 6474	Double polished, standard TS with blue epoxy fill	12	na	6474' - 6474' 8"
PI 6484.5	Double polished, standard TS with blue epoxy fill AND GOLD COAT	13	na	6484.5' - 6484' 8"
PI 6484.8	Double polished, standard TS with blue epoxy fill	13	na	6484' 8"- 6485' 7"
H 7667.4	Gold coat	1	2	7667' 4' - 7668' 1"
H 7683	Double polished, standard TS with blue epoxy fill	1	8	7682' 11" - 7683' 3"
H 7691.4	Double polished, standard TS with blue epoxy fill	1	11	7691' 4" - 7691' 7"
H 7795.9	Double polished, standard TS with blue epoxy fill	3	5	7795' 11 " - 7796' 6"
H 7802.7	Double polished, standard TS with blue epoxy fill	3	7	7802' 7" - 7802' 11"
H 7827.2	Double polished, standard TS with blue epoxy fill	3	16	7827' 2" - 7827' 5"
H 7831.5	Gold coat	3	18	7831' 5" - 7832' 2"
H 7836.4a	Double polished, standard TS with blue epoxy fill	3	18	7836' 4" - 7838' 6"
H 7836.4b	Double polished, standard TS with blue epoxy fill	3	18	7836' 4" - 7838' 6"
H 7836.4c	Double polished, standard TS with blue epoxy fill	3	18	7836' 4" - 7838' 6"
H 7861	Double polished, standard TS with blue epoxy fill AND GOLD COAT	4	7	7861' - 7861'5"
H 7882.1	Double polished, standard TS with blue epoxy fill	5	3	7882' 1" - 7882' 11"
H 7889.25	Double polished, standard TS with blue epoxy fill	5	6	7889' 3" - 7890
H 7897.5	Double polished, standard TS with blue epoxy fill	5	8	7897' 6" - 7898' 1"
H 7899.6	Double polished, standard TS with blue epoxy fill	5	9	7899' 6" - 7900' 4.5"
H 7936	Double polished, standard TS with blue epoxy fill	6	2	7935' 11"- 7936' 1"
DC 6507.5	Double polished, standard TS with blue epoxy fill AND GOLD COAT	1	10	6507'6" - 6508'
DC 6570	Double polished, standard TS with blue epoxy fill	2	11	6570' - 6570'2"
DC 6572.2	Double polished, standard TS with blue epoxy fill	2	12	6572'3" - 6572' 6"
DC 6581.8	Double polished, standard TS with blue epoxy fill	2	15	6581'8" - 6582
DC 6592.1	Double polished, standard TS with blue epoxy fill	2	19	6592'1" - 6592'7"
DC 6593.5	Double polished, standard TS with blue epoxy fill	2	20	6593'6" - 6593'8"
DC 6600.5	Double polished, standard TS with blue epoxy fill	2	22	6600'6" - 6600' 10"
NS 6277.9	Double polished, standard TS with blue epoxy fill	3	16	6277'10" - 6278'6"
NS 6307.5	Double polished, standard TS with blue epoxy fill	4	4	6307'6" - 6308'

Field samples from quarry at Union Springs, NY

Sample	Sample type	Orientation Relative to Field Orientation	Notes
WQ1	Double polished, standard TS with blue epoxy fill	Horizontal	Horizontal relative to bedding for sampling vertical filled fracture J1
WQ2a	Double polished, standard TS with blue epoxy fill	Horizontal	Want caliche crust too if possible (on side)-Horizontal relative to bedding for sampling vertical filled fracture J1
WQ2b	Double polished, standard TS with blue epoxy fill	Horizontal	Horizontal relative to bedding for sampling vertical filled fracture J1
WQ3a	Double polished, standard TS with blue epoxy fill	Horizontal	Horizontal relative to bedding for sampling vertical filled fracture J1
WQ3b	Double polished, standard TS with blue epoxy fill	Horizontal	Horizontal relative to bedding for sampling vertical filled fracture J1
WQ4	Double polished, standard TS with blue epoxy fill	Horizontal	Horizontal relative to bedding for sampling vertical filled fracture J1
WQ5	Double polished, standard TS with blue epoxy fill	Mixed/Horizontal	Cement collection lined up parallel and cut across bottom
WQ6	Double polished, standard TS with blue epoxy fill	Horizontal	Little cement-Horizontal relative to bedding for sampling vertical filled fracture J1
WQ7	Double polished, standard TS with blue epoxy fill	Horizontal	Little cement-Horizontal relative to bedding for sampling vertical filled fracture J1
WQ8a	Double polished, standard TS with blue epoxy fill	Horizontal	Little cement-Horizontal relative to bedding for sampling vertical filled fracture J1
WQ8b	Double polished, standard TS with blue epoxy fill	Horizontal	Little cement-Horizontal relative to bedding for sampling vertical filled fracture J1
WQ9	Double polished, standard TS with blue epoxy fill	Mixed/Horizontal	Cement collection lined up parallel and cut across bottom
WQ10	Double polished, standard TS with blue epoxy fill	Mixed/Horizontal	Cement collection lined up parallel and cut across bottom
WQ11	Double polished, standard TS with blue epoxy fill	Mixed/Horizontal	Cement collection lined up parallel and cut across bottom

Appendix F – Nanometer Pore Scale Imaging

Nanometer-scale imaging and evaluation of Marcellus Shale

Project Report

Timothy Kneafsey and Dmitriy Silin*
*now at Shell

Lawrence Berkeley national Laboratory

Earth Sciences Division

1 Cyclotron Road, MS 90R1116

Berkeley, CA 94720

Berkeley, CA

October 22, 2012

Objectives

The principal objective of our effort was to perform high-resolution imaging of pores and natural fracture characterization of Marcellus Shale samples. We imaged samples of Marcellus shale samples provided to us by GTI using low-resolution x-ray CT scanning, x-ray micro tomography, and focused ion beam and diamond knife milling combined with scanning electron microscopy.

Imaging Marcellus shale samples

Imaging scales and techniques

In this work, two scales of computed tomography were used, as well as Focused Ion Beam/Scanning Electron Microscopy (FIB/SEM). To gain a general understanding of the structure of the shale, medical-scale low-resolution CT scanning of core-scale rock was performed, providing a three-dimensional density distribution at the 194 micron x 194 micron x 1000 micron scale. X-ray micro-CT was performed on millimeter-scale rock samples to provide a three-dimensional density distribution at the cubic micron scale. Focused Ion Beam/Scanning Electron Microscopy was performed to provide images of layers of the rock with a resolution of tens of nanometers (comparable voxel size 0.04 cubic microns) over a volume of thousands of cubic microns.

X-ray computed tomography (X-ray CT)

X-ray CT images the sample interior in a non-destructive manner. CT imaging is a complex procedure involving acquisition of a large number of X-ray projections followed by a computationally intensive numerical reconstruction. A stack of two-dimensional slices is constructed into a three-dimensional image. Within a slice, the data are arranged in a two-dimensional array of pixels. A pixel with the third dimension, which is the distance between two consecutive slices, is a voxel.

For a regular core, low-resolution CT data provide overview information about the heterogeneity and hidden damage in the core which helps in identifying the most suitable regions for smaller-scale imaging. If only irregular pieces are available, the micro-CT sample selection is based on visual inspection and optical micrographs. The samples were scanned using a modified Siemens Somatom HiQ medical computed tomography (CT) scanner providing 194 micron × 194 micron × 1000 micron voxels. Homogeneous samples of light element materials having known density were also scanned to provide a density calibration curve to allow estimation of densities throughout the samples.

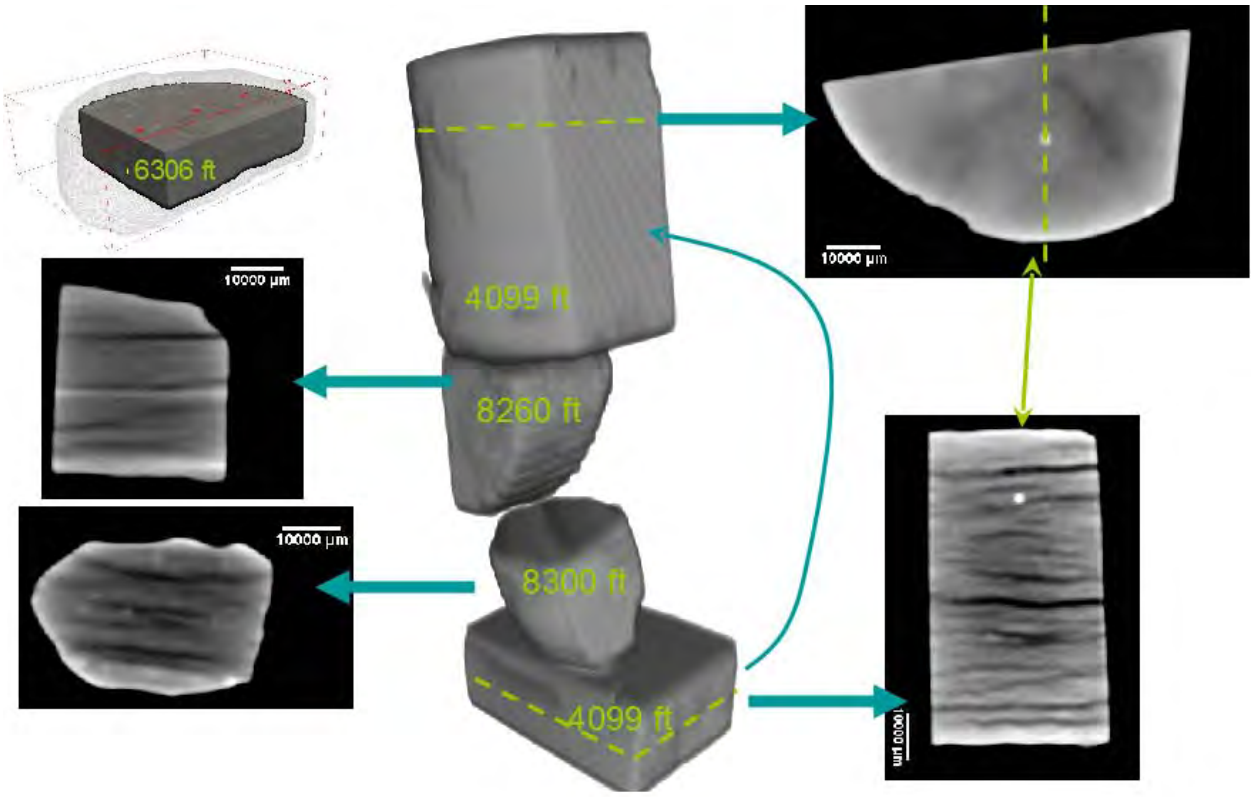

Figure 1. CT images of Marcellus shale samples with the depths indicated. Note: the 4099 ft sample was imaged twice at different orientations relative to the scanning plane (right).

Figure 1 shows low resolution CT scans of three Marcellus shale samples (the 4099 ft sample was imaged twice with different orientations to the scanning plane). The top-left image and the images in the middle are 3D reconstructions of the CT data. The cross-section views with scale bars reveal the layered structure of the rock. The layer thickness is of the order of a few millimeters, and the density variation is on the order of ~0.4 g/cm^3 from lightest to darkest shades. The lighter color indicates a denser material. The orientation of the scanned sample in the CT scanner is important because the voxels for the medical CT scanner are not isometric: the two cross-sections on the right are from the same sample at two different angles. The top right image does not show the layered structure of the sample well, even though a larger volume is scanned. The cross section indicated by the dashed line (note bright spot) is at the intersection of the planes of the right-top and right-bottom images. The bottom-left cross-section image shows a distribution of dense inclusions (brighter spots). Note that the samples from the depths of 4099 ft and 8260 ft show fewer dense inclusions than the 6306 and 8300 ft depth samples. Without information about orientation of the cored samples we assume that the layering is horizontal or close to horizontal.

Although low-resolution CT images of these samples show no hidden fractures inside the cores, the samples are not strongly consolidated and the layering is obvious. Some layers are almost separating. Cutting rock for high-resolution imaging without damaging the material turned out to be far from straightforward. This is not unusual for Marcellus shale samples. It is yet to be understood whether this

fragility of the Marcellus shale samples is a distinctive rock property or a consequence of core storage and preparation.

X-ray micro-CT at the Advanced Light Source

The LBNL x-ray micro-tomography facility is based at Beamline 8.3.2 at the Advanced Light Source (ALS) at Lawrence Berkeley National Laboratory. The x-rays are produced from a superbend magnet source and pass through a monochromator comprised of two multilayer mirrors, which can be altered in angle to select the required x-ray energy. X-ray energies from 8 KeV to 45 KeV are available. X-ray energy was adjusted to a given total attenuation of the sample of ~1500 to 2000 arbitrary absorption units. The samples were mounted on an air bearing stage that can be adjusted in three dimensions relative to the x-ray beam. The x-rays transmitted through the sample then interacted with a $CdWO_4$ single crystal scintillator that fluoresces the shadowgram x-ray image as visible light. This image was then magnified through a selection of microscope objectives and relayed onto a 4008×2672 pixel CCD camera (Cooke PCO 4000). The CCD pixel size is 9 µm. With a 10× objective, the reconstructed image pixel size is 0.9 µm. To achieve such high resolution, the sample diameter is limited to a maximum of about 3 mm. The samples were rotated in the x-ray beam from angles 0 to 180 degrees. The most common angular increment was 0.125 degrees, resulting in 1441 projections, as this was shown to be a good compromise point between the greater reconstructed image quality derived from collecting a greater number of raw images and scan time. Single image exposure times ranged from a minimum of several hundred microseconds to several seconds. Multiple images at a single angular location were averaged to avoid detector saturation during longer exposure times. The raw data were reconstructed using the commercial software package Octopus using a filtered backprojection algorithm.

Although the resolution of micro CT images may be insufficient to image the pore structure of Marcellus shale samples, they show features which cannot be detected with the other techniques. Figure 2 shows a micro CT cross section of a sample that was also imaged by Ingrain. Many items of interest are seen in this cross section, including an inclusion of grains with internal porosity (upper left), and several pyrite inclusions (light color). Although no obvious microfractures are seen, many regions of potentially connected small-scale porosity can be seen. Figure 3 shows a slice of micro CT data with pixels size of 0.9 µm. The scattered white spots are thought to be inclusions of pyrite. A number of quartz grains with sizes on the order of tens of microns are embedded in fine material (uniform medium gray objects). The pores look like small dark wormholes, with the relative volume on the order of just few percent. The zoomed area in the right-hand picture shows microcracks (dark) near quartz grains (medium gray) and pyrite (white) inclusions. Although the microfractures shown may be not have necessarily developed in-situ, they suggest a possible permeability enhancement mechanism by strain discontinuity at the interfaces between the fine-grain clay-rich material and quartz gains and pyrite inclusions. The length of some microfractures shown in Figure 4 approaches 1 mm. Image analysis does not reveal a connected network of fractures. However, fractures having apertures less than a micrometer wide cannot be seen but may provide some connectivity. The geometry and connectivity of microfractures requires additional study.

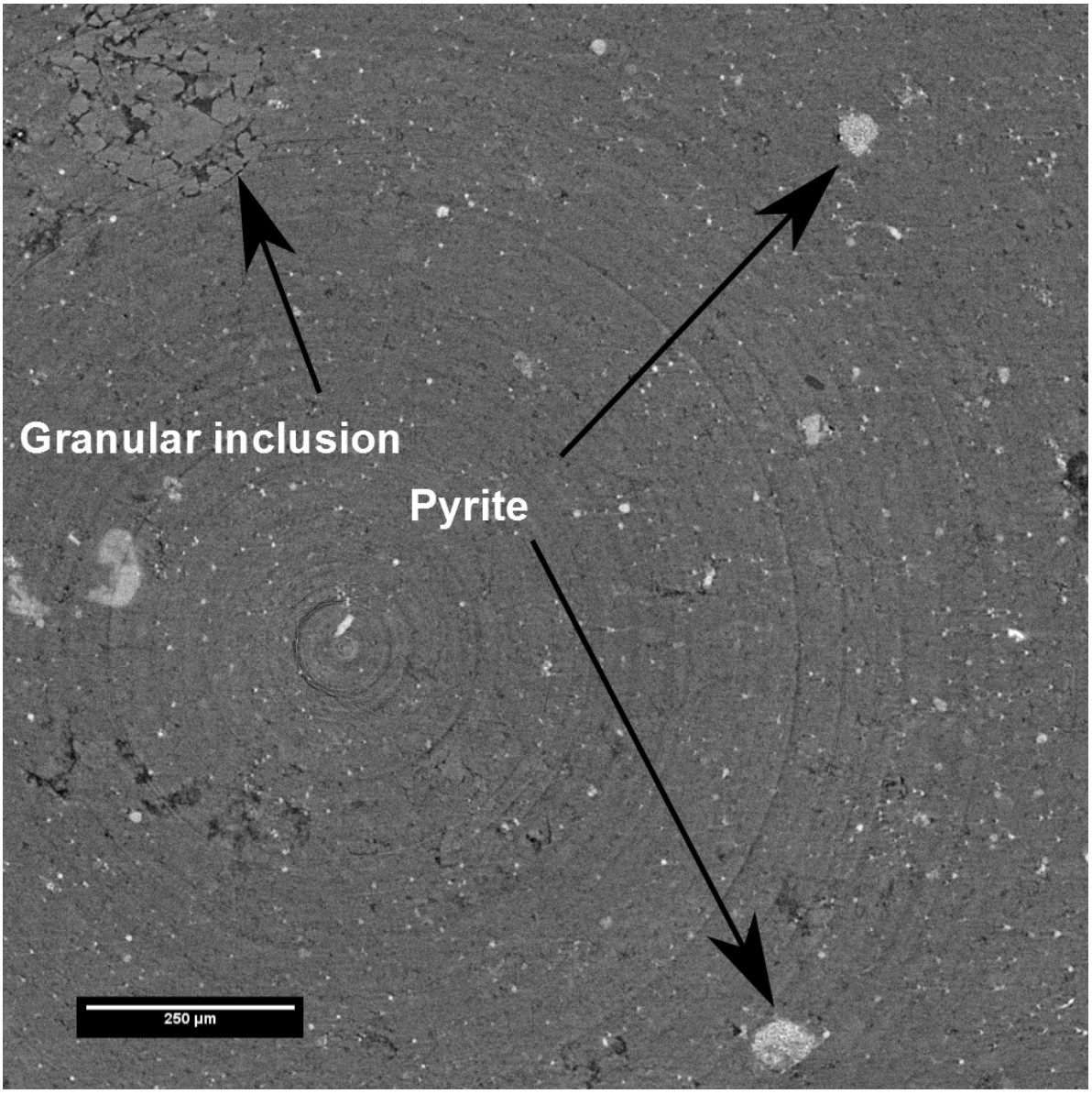

Figure 2. A granular inclusion is hundreds microns in diameter with grains of the order of 10 microns. The rings are artifacts of tomography reconstruction.

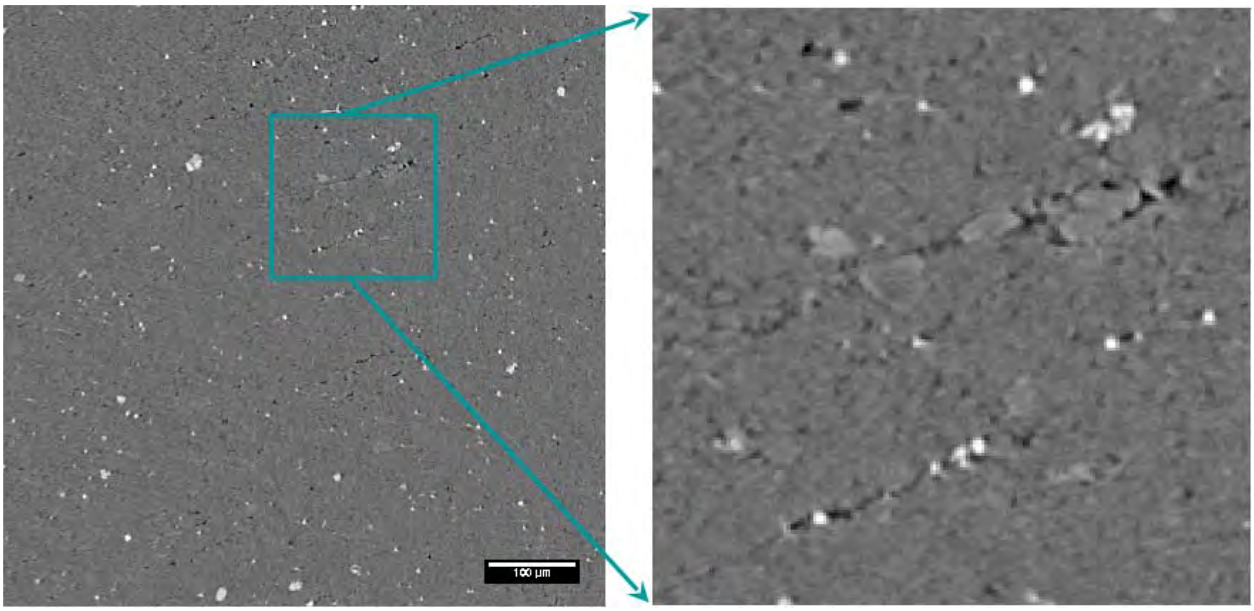

Figure 3. Micro CT images of a Marcellus shale sample with pixels size 0.9 µm. Note apparent cracks (dark) and pyrite grains (white).

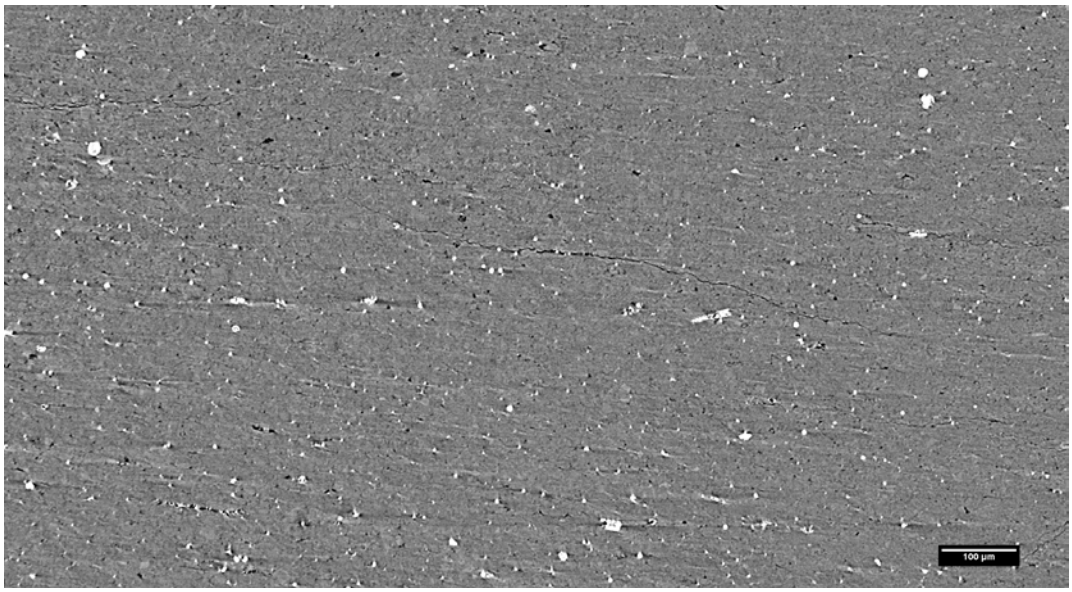

Figure 4. Micro CT images of microfractures in a Marcellus shale sample. The horizontal fracture just above the center of the image is on the order of 1 mm long.

Figure 5 shows micro CT images of four different gas-shale samples. Although extremely low porosity and permeability are common features of all samples, they also have noticeable distinctive features. The

images of New Albany and Haynesville shale show more pyrite inclusions, and the size of individual inclusions is large relative to the images of Marcellus and Barnett shales. The porosity of the Barnett shale sample is the highest among the four images. The image of Barnett shale also shows larger grains that are likely quartz and are, on average, larger and more densely distributed than in the images of other three samples.

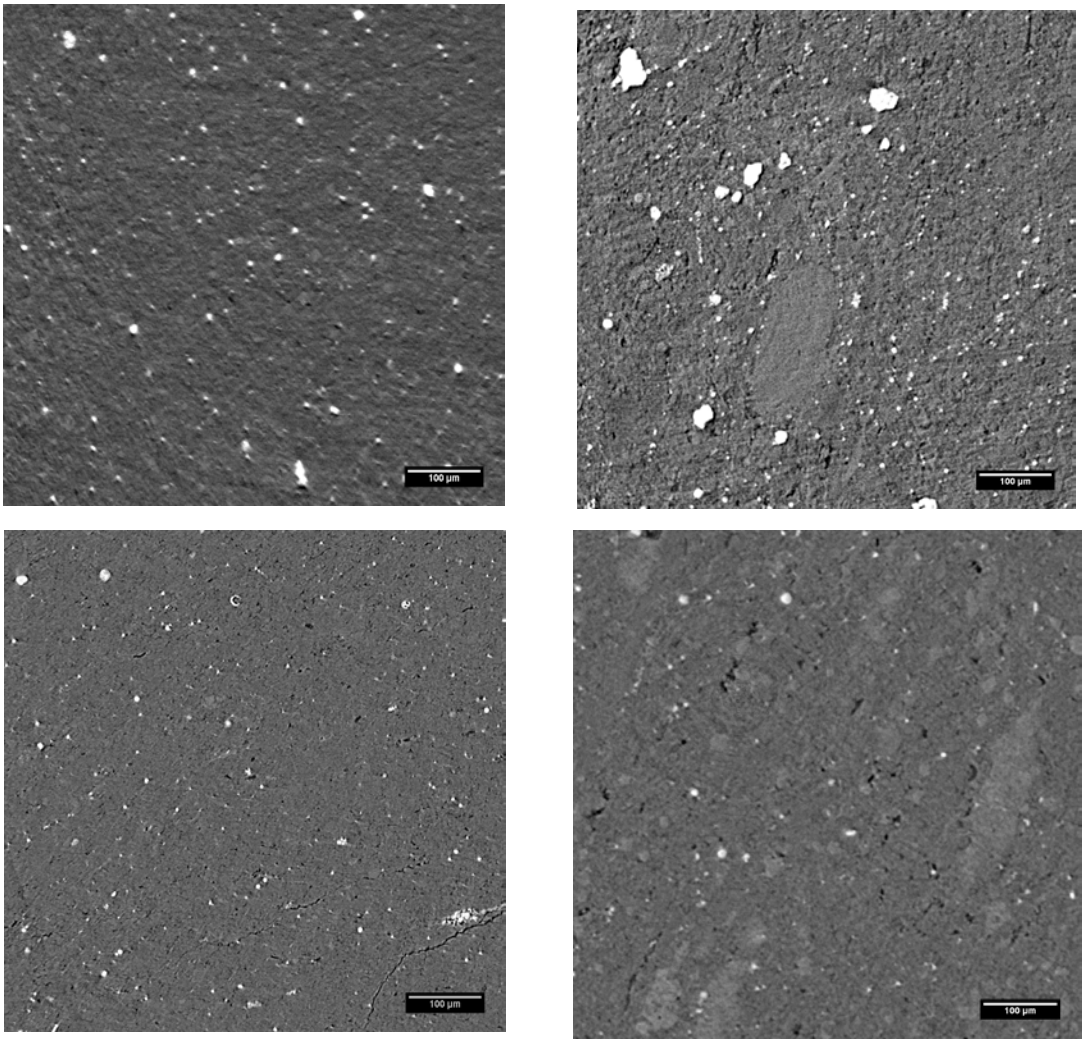

Figure 5. Micro CT images of four shale samples. Top row: New Albany shale (left) and Haynesville shale (right); bottom row: Marcellus shale (left) and Barnett shale (right).

Micro CT data of two subsamples of a Marcellus shale sample that were also imaged by Ingrain show microfractures and granular inclusions (see Figures 6 and 7). The lighter color in CT data means higher-density material. For example, the framboidal conglomerates of pyrite appear as bright spots. The grain material (not pyrite) in the inclusions does not show up as bright. Figure 7 suggests that the grains may prevent fracture closure. The Marcellus shale samples studied are fragile and friable. Sample splitting makes imaging of a fresh fracture surface or weak planes possible. Figure 8 shows an SEM image of such

a surface. Note the large (tens of microns) crystal grains. We speculate that such grains may serve as micro-proppant keeping the microfracture open. These grains are consistent with the grains filling the microfracture in Figure 6. In the data, the fractures filled with grains are penny-shaped. Such openings are usually close to microcracks like those in Figure 9. Fracture aperture in Figure 9 is about 10 microns.

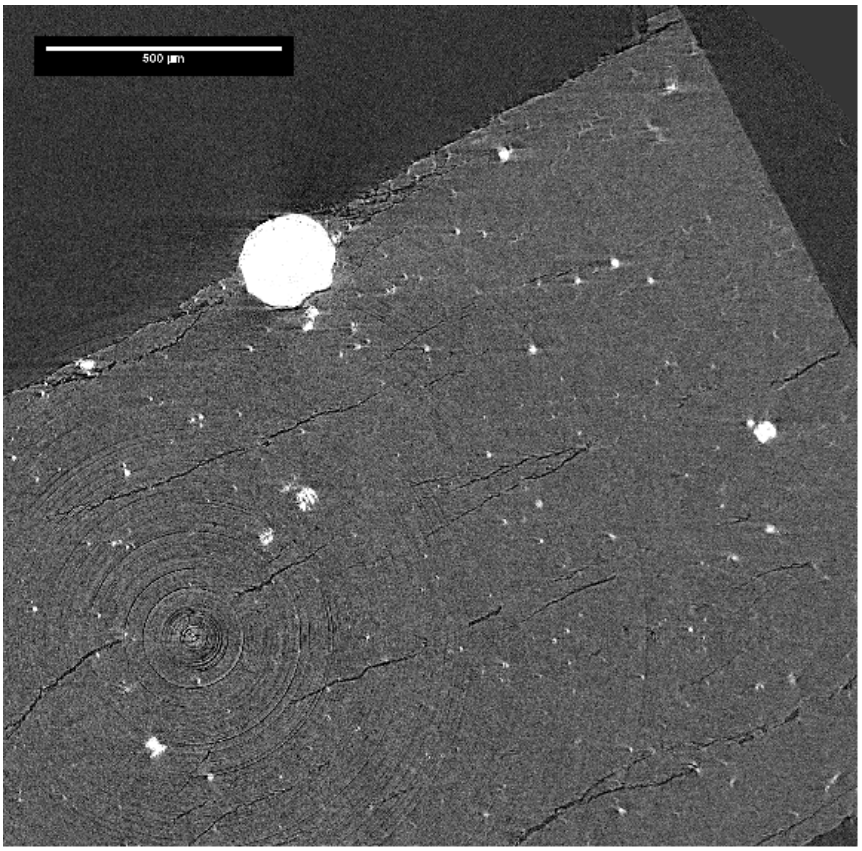

Figure 6. MicroCT image of a Marcellus shale subsample for comparison to a subsample that was also imaged by Ingrain. The concentric circles are artifacts of the image reconstruction.

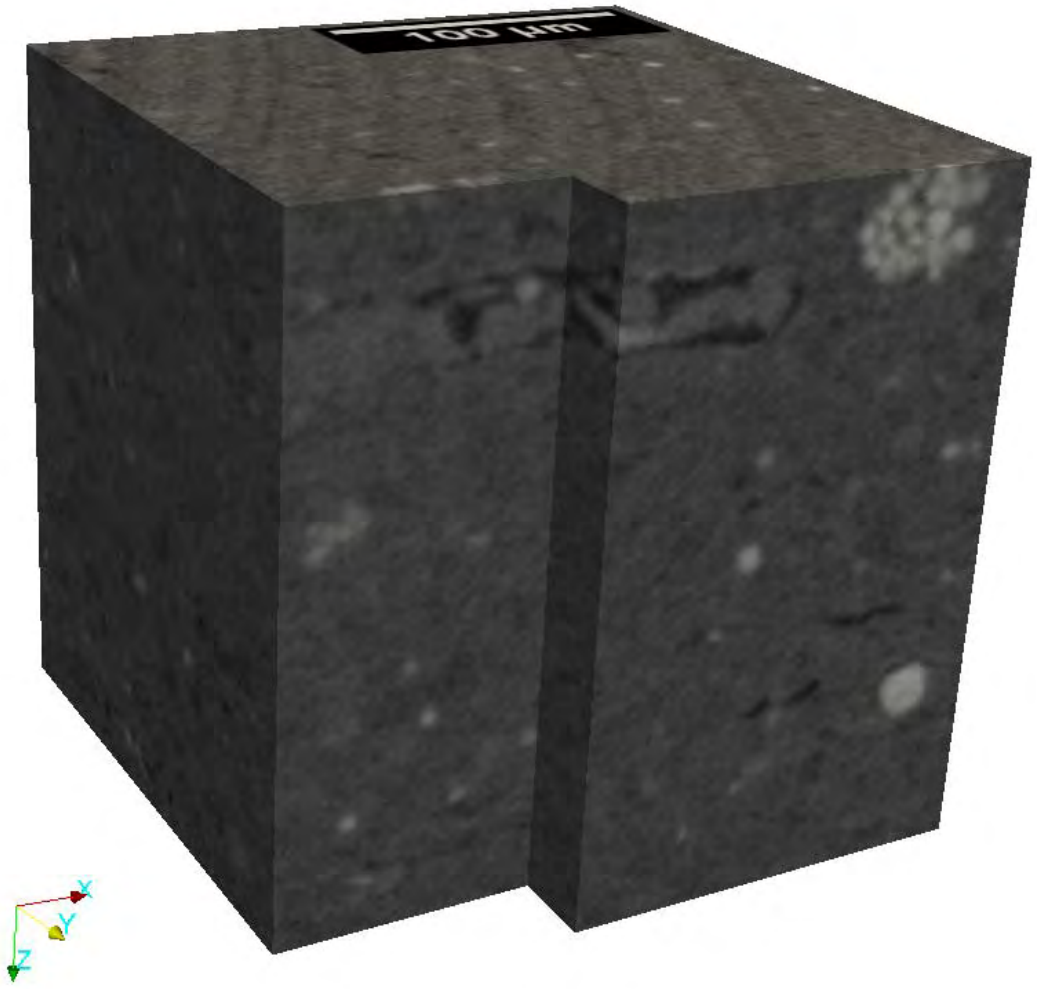

Figure 7. The granular inclusion to the left from the framboidal pyrite structure at the top right corner fills a micro-fracture.

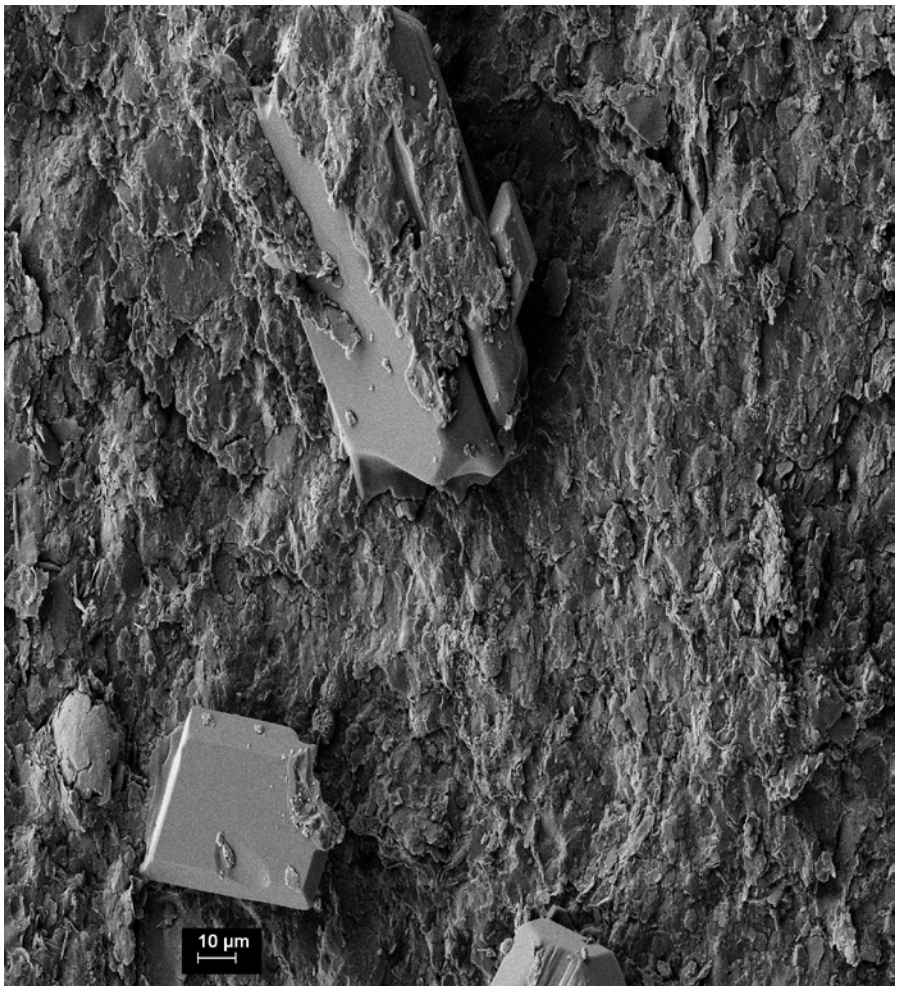

Figure 8. Crystal structures on fracture surface.

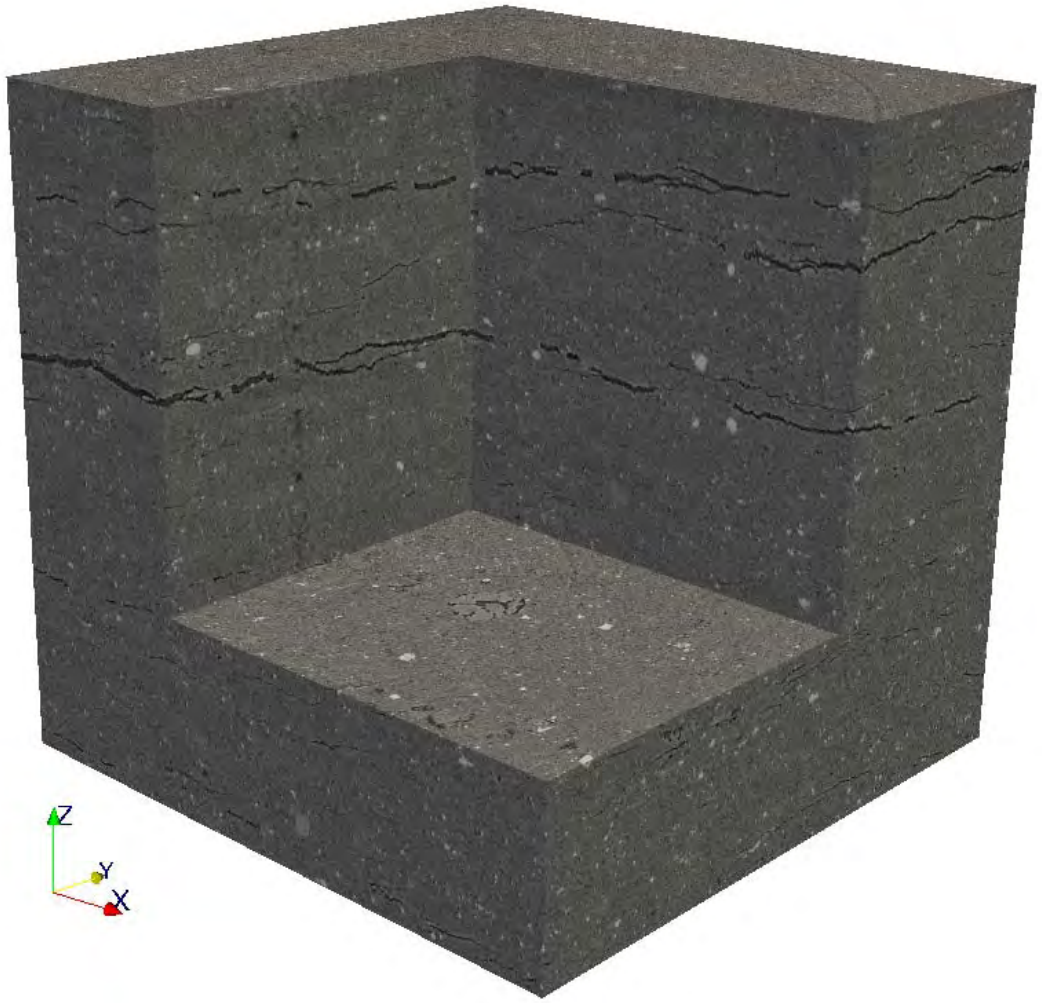

Figure 9. The image of 1.3 mm cubed volume shows micro fractures. The cracks are apparently aligned with the orientation of the layers. Note the granular inclusion visible in the horizontal (orthogonal to Z) section of the image.

Focused Ion Beam / Scanning Electron Microscopy

To obtain a fine three-dimensional structure of shale samples and their pore space, we imaged samples using a scanning electron microscope (SEM) coupled with a focused ion beam (FIB) to provide milling capability. The FIB/SEM instrument, housed at the Molecular Foundry at Lawrence Berkeley National Laboratory, is a Zeiss XB1540 EsB having a GEMINI® field emission column (FESEM) with the Orsay

Physics focused ion beam. The instrument has a maximum resolution of 1.1 nm at 20 kV and 2.5 nm at 1kV, the FIB column uses a liquid gallium source and has a resolution of 7-5 nm at 30 kV. Sample manipulation is performed on a 6-axis fully eucentric motorized stage.

To do our imaging, we use the FIB to mill a flat surface which we image using the SEM, and then repeat the process a number of times, each time milling a fixed thickness of sample. Thicknesses of the milled slices depend on the milling current, with high currents (order of nA) milling thicker and less precise slices. Slices have thicknesses ranging from 25 nm to 75 nm. Registering (aligning) and stacking the images provides a three dimensional digital reconstruction of the sample, which can then be manipulated by computer. In the SEM/FIB system, the electron beam and ion beam are positioned 54 degrees from each other. Because of this configuration, any reasonably flat location on a sample can be milled and imaged. To avoid repositioning the sample so that the surface is orthogonal to the SEM following each FIB slice, the SEM images are adjusted numerically to account for the angle.

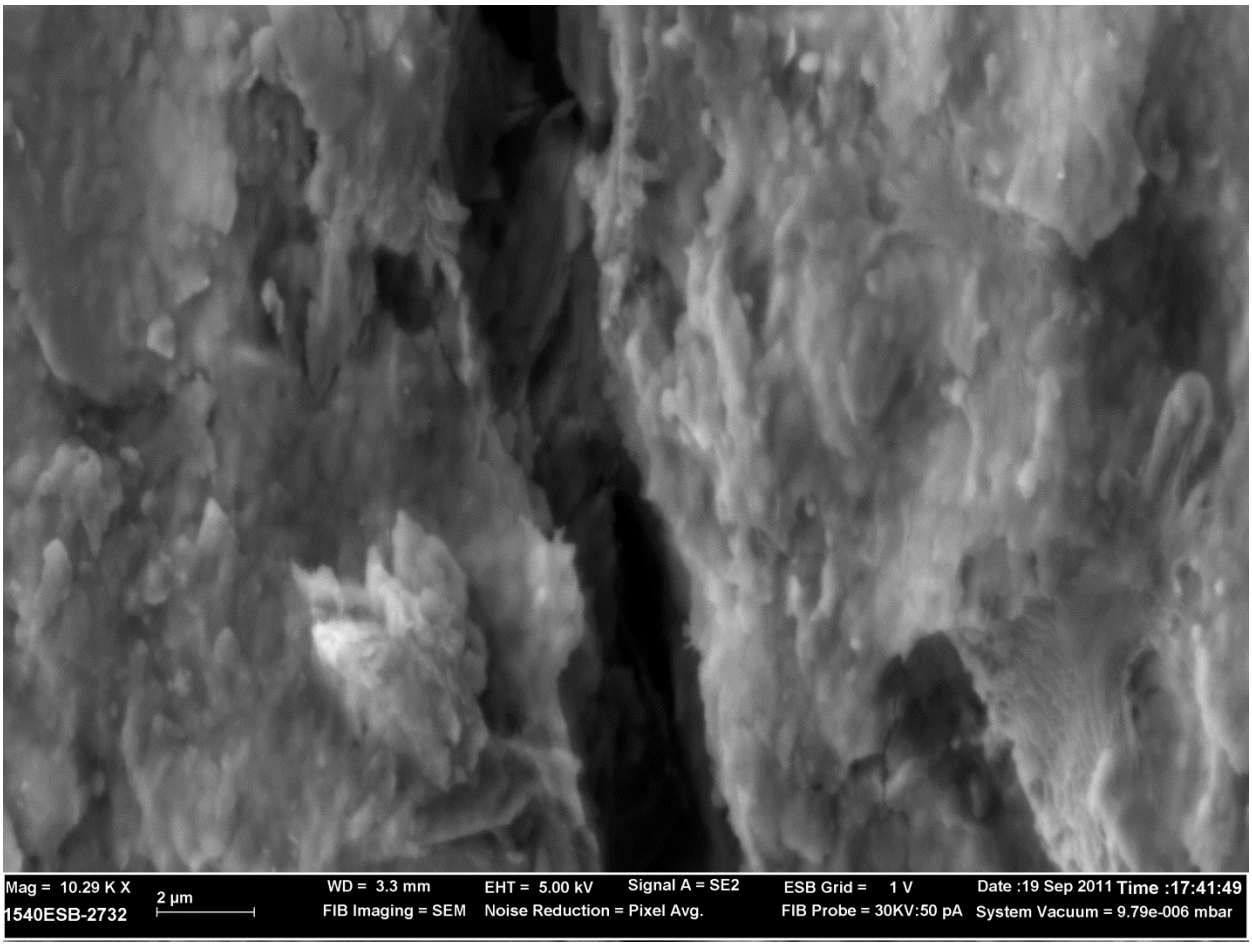

Figure 10. SEM image of Marcellus shale sample shows the structure of a microcrack.

Figure 10 shows the structure of a microfracture in a Marcellus shale sample. The fracture was probably created during sample handling; the surfaces composed of clay plates are clean of any deposited material, which means that the fracture is likely an artifact of sample preparation.

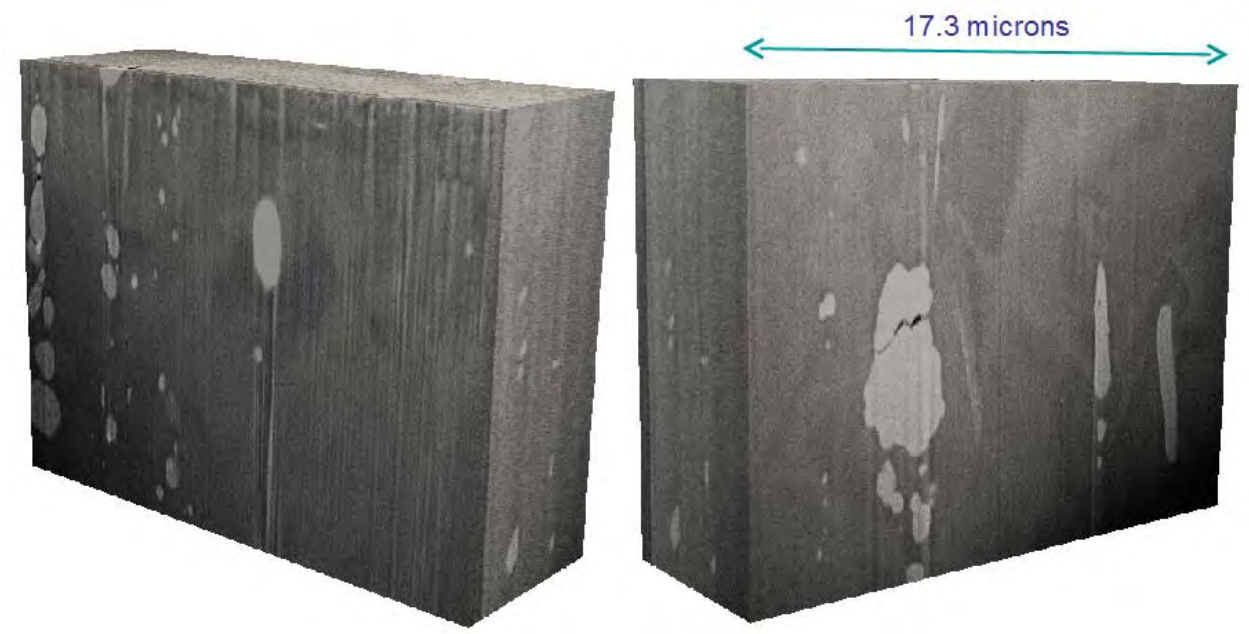

Figure 11. FIB/SEM reconstruction of Marcellus shale sample. SEM image resolution is 11.56 nm.

Figure 11 shows an example of a 3D reconstruction of a Marcellus shale sample obtained by the FIB/SEM technique. The 11.56 nanometer resolution data reveal practically zero porosity. The only visible pores are the cracks in a pyrite structure. The images demonstrate the challenges of FIB/SEM technique. The study area of 20 µm across can entirely occur in a large solid inclusion. The high contrast between material properties of different minerals in the sample complicates tuning the ion beam parameters which would mill flat surface within reasonable time and, simultaneously, preserve the nanometer-scale geometry of the pore space.

Figure 12 shows a 3D reconstruction and single slice of Marcellus shale at resolution of 50 nm. Unlike the data in Figure 10, the image surface was prepared by diamond knife cutting. Evaluation of this new technique is beyond the scope of this project. We remark, however, that the big advantage of this technique in comparison with FIB milling is the large size of the imaged area. At the same time, an ion-beam prepared surface better preserves the pore-scale structure of the rock. Imaging with diamond-knife surface preparation was performed at Gatan Inc., with the company's proprietary technology.

Figure 12 shows multiple framboidal pyrite structures. It is interesting that a more concentrated grouping of pyrite grains overlaps with a structure of larger pyrite grains. The dark color has been interpreted to indicate a relatively high presence of organic matter. Based on this interpretation, the left-hand image in Figure 12 shows organic contents close to 10%.

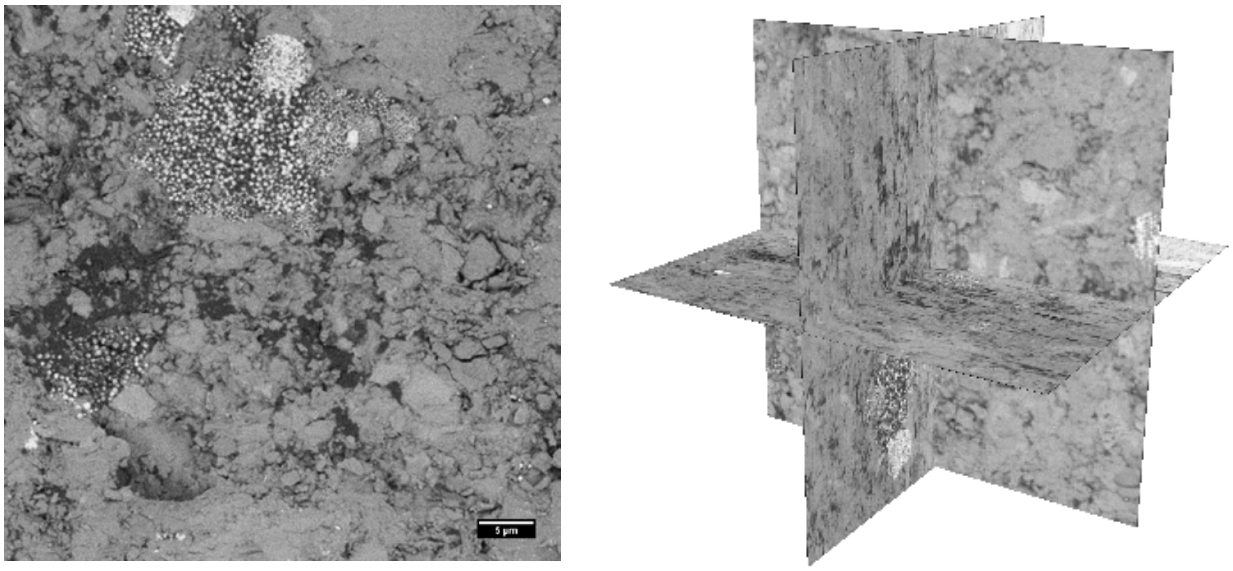

Figure 12. SEM image of diamond-knife cut Marcellus shale sample: a single slice (on the left) and orthoslices of the 3D reconstruction (on the right). Pixels size is 50 nm. Data: courtesy of Joel Mancuso, Gatan Inc.

Figure 13 shows a FIB slice of a framboidal pyrite structure. The space between the grains is filled with porous organic material. It is very interesting to note the variety of pore sizes (tens to hundreds of nanometers) within the framboidal pyrite structure. The importance of these pores to gas flow has not been established, as they typically exist within spherical inclusions in the shale and do not extend laterally into the sample.

Figure 14 identifies another type of porosity observed in the Marcellus samples. This is porosity surrounding a mineral grain. This is similar to the porosity surrounding the multigrain inclusion in Figure 2. Close examination of the fracture indicates the presence of some pore-filling minerals, indicating that this fracture was probably present in-situ. The contribution of such fractures to flow would depend on interconnectedness to other fractures.

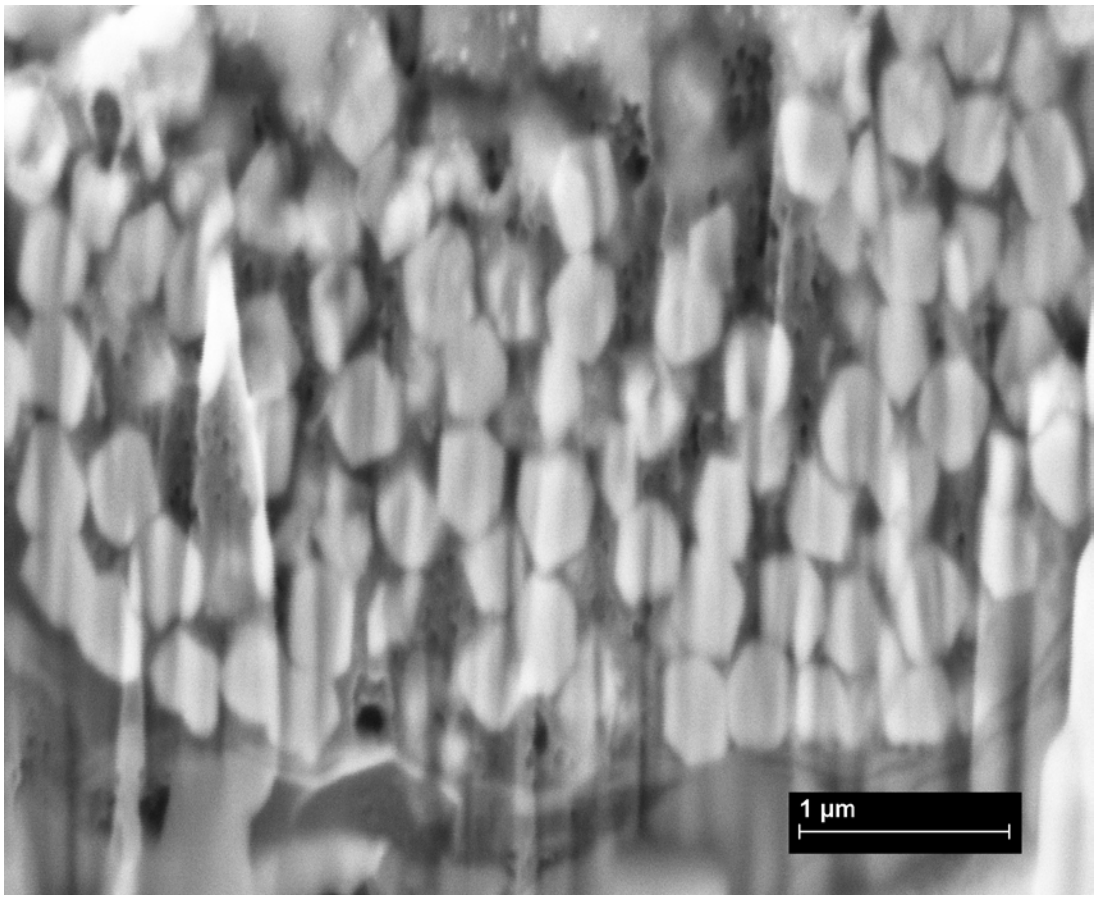

Figure 13. The space between the grains in this Pyrite framboidal inclusion is filled with porous organic material.

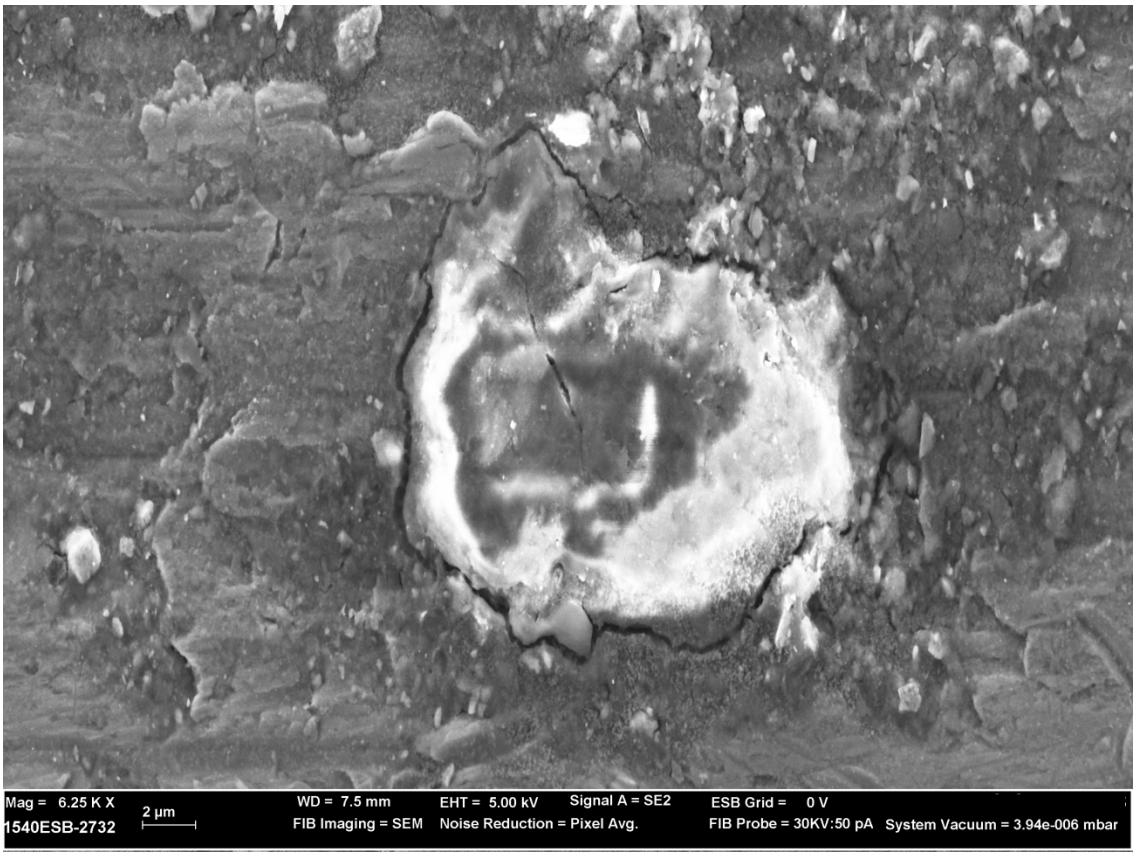

Figure 14. Fractures surrounding a granular inclusion. Some fracture-filling minerals present in the fracture indicate that the fracture was present in the sample at depth.

Conference and invited presentations

The results of this effort were included in the following conference presentations

1. Natural gas production from shales: Imaging tight media and analysis of flow. Timothy J. Kneafsey, Dmitriy Silin, and Stefano Cabrini, 2012 Molecular Foundry and National Center for Electron Microscopy. Berkeley, CA, October 4-5 2012
2. A study of shale-gas recovery mechanisms. Dmitriy Silin and Timothy Kneafsey. Gulf Publishing Shale Energy Technology Conference, Houston, TX, August 24-25 2011.
3. Tight gas: from pore-scale to well decline curve analysis. Dmitriy Silin, Timothy Kneafsey. 2011 Geologic Society of America Annual Meeting, Minneapolis, MN, October 9-12 2011
4. Imaging Gas Shales: Insights and Extension to Observed Behavior. Timothy J. Kneafsey, Dmitriy Silin, and Stefano Cabrini. 2011 Molecular Foundry and National Center for Electron Microscopy. Berkeley, CA, October 5-6 2011

5. Gas Shale: From Nanometer-Scale Observations to Well Modeling. CSUG/SPE Paper 148489. Dmitriy Silin and Timothy Kneafsey. 2011 CSUG/SPE Canadian Unconventional Resources Conference, Calgary, Canada, November 15-17 2011.
6. Shale Gas: Nanometer-Scale Observations and Well Modelling, D. Silin and T. Kneafsey, accepted, Journal of Canadian Petroleum Technology, expected publication November 2012

Invited presentation:

1. Imaging and modeling tight-gas rocks, at Ingrain, Inc., Houston, TX, August 26 2011

Conclusions

A number of Marcellus shale sample were received from GTI. The samples were analyzed with different imaging techniques:

1. Low-resolution computed tomography
2. Micro-tomography at the Advanced Light Source Facility
3. FIB/SEM and diamond knife/SEM

Each imaging technique reveals rock properties at different scales. Heterogeneity is present in all scales. The porosity is low in all scales. Micro-CT data shows development of microcracks near quartz grain and pyrite inclusions. We speculate that such microcracks may enhance rock permeability and gas recovery. Scanning electron microscopy, SEM used with focused ion beam milling and with diamond knife milling provide other insights into the porespace in Marcellus shale. Pores are present at a variety of spatial scales. Pores observed in material surrounding framboidal pyrite grains were observed to be on the order of tens to hundreds of nanometers in diameter. These pores are not likely well connected to other porosity however. Microfractures at grain boundaries have also been observed. These too may not be well connected.

Permeability in the Marcellus shale may be dominated by the overall layered structure of the rock as seen in the low-resolution scans. A comparison between the porespace in the higher density and lower density shale layers would be valuable. Because the scale of the rock laminations falls in a region where low-resolution scanning clearly identifies it but microCT does not clearly describe the porosity at the desired scale, additional efforts should be directed to comparing the connectedness of pores in these contrasting layers. We did see possible “proppant” in the low-density layer, showing a potential difference.

Appendix G – Flow Characteristics in the Presence of Gas Liquids

STANFORD UNIVERSITY
ENERGY RESOURCES ENGINEERING
SCHOOL OF EARTH SCIENCES

Marcellus Shale Gas Project

Final Report

By

Maytham Al Ismail

Roland Horne

Department of Energy Resources Engineering

May 26, 2013

Introduction

This report highlights the results of a work- conducted at SUPRI-D research group. The objective of the research work was to investigate the flow behavior of a gas-shale well through a series of laboratory core flood experiments on Marcellus shale core and gas samples. Previous work was conducted on a Berea sandstone core using a synthetic two-component gas-condensate system. However, in this work, the flow behavior of actual reservoir fluid samples through shale cores obtained from the Marcellus was studied.

The ultimate objective of the research is to gain better understanding about shale gas production behavior and how condensate dropout affects the well productivity. The research also investigated the effect of compositional variation on flow behavior.

In previous update reports, the following experiments were discussed:

1. Computerized tomography (CT) scanner experiment on dry shale cores
2. Binary (C1-nC4) gas-condensate flooding experiments on Berea sandstone core
3. Shale core preparations

In this report, the results of the following experiments will be discussed:

1. Permeability measurements using pressure pulse decay apparatus
2. Analysis of PVT experiments conducted on Marcellus gas-condensate sample
3. Gas-Chromatography (GC) calibration for natural gas analysis
4. Marcellus gas-condensate flooding experiment on Berea sandstone core
5. Numerical simulations of gas-condensate flooding experiment on Marcellus shale core
6. Marcellus gas-condensate flooding experiment on Marcellus shale core

Permeability Measurement

A. Sandstone Core

The permeability of the sandstone was measured using the Darcy flow technique. In the experiment, nitrogen gas was used. Figure 1 shows the gas permeability as a function of reciprocal mean pressure. The plot indicates that the absolute liquid permeability is 105 md for this core.

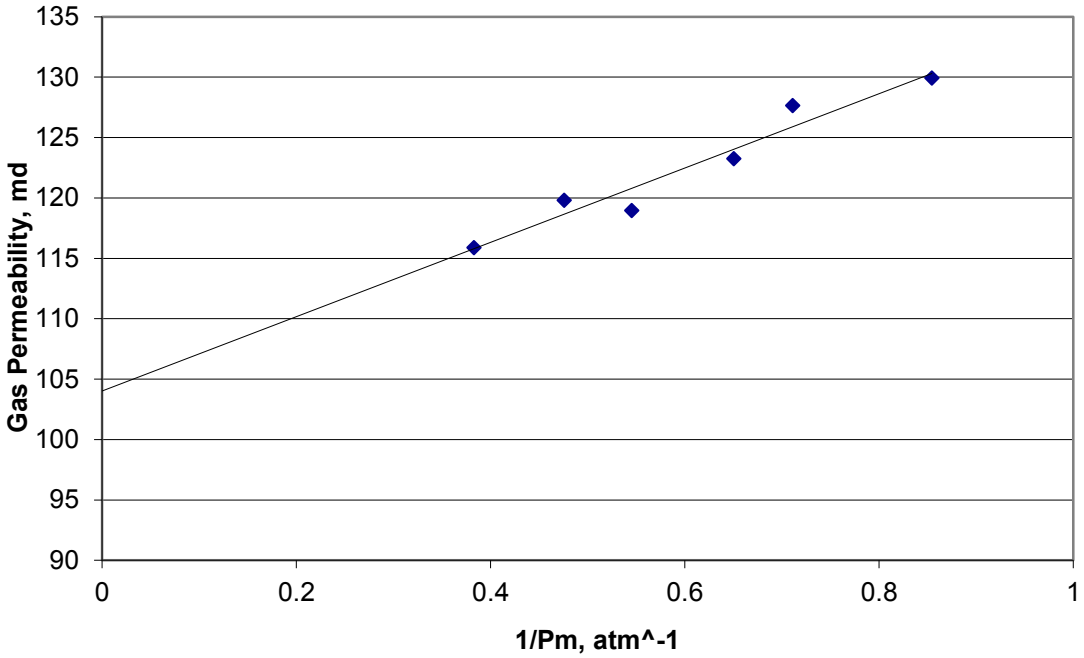

Figure 1: Absolute permeability measurement for the Berea sandstone core

B. Marcellus Shale Core

A 1-in diameter core was cut and prepared to study the permeability of the Marcellus shale at different effective pressures. The Marcellus shale core sample from which the 1-in diameter core was cut is shown in Figure 3. The permeability measurements were obtained using pressure pulse decay apparatus as shown in Figure 4.

This technique was first developed by Brace et al. (1968) to measure permeability of granites. The principle of this technique is to create a dynamically changing flow across the sample and then backing out permeability by fitting the resulting pressure curves to a flow model. In our experiment, a pressure pulse of around 50 psi was introduced at the upstream side and maintained constant, creating an effective infinite reservoir volume. Helium gas was used in the experiment to remove adsorption effects and to only test the impacts of effective stress on shale permeability.

Figure 2: Core sample dimensions

Figure 3: Marcellus shale core sample

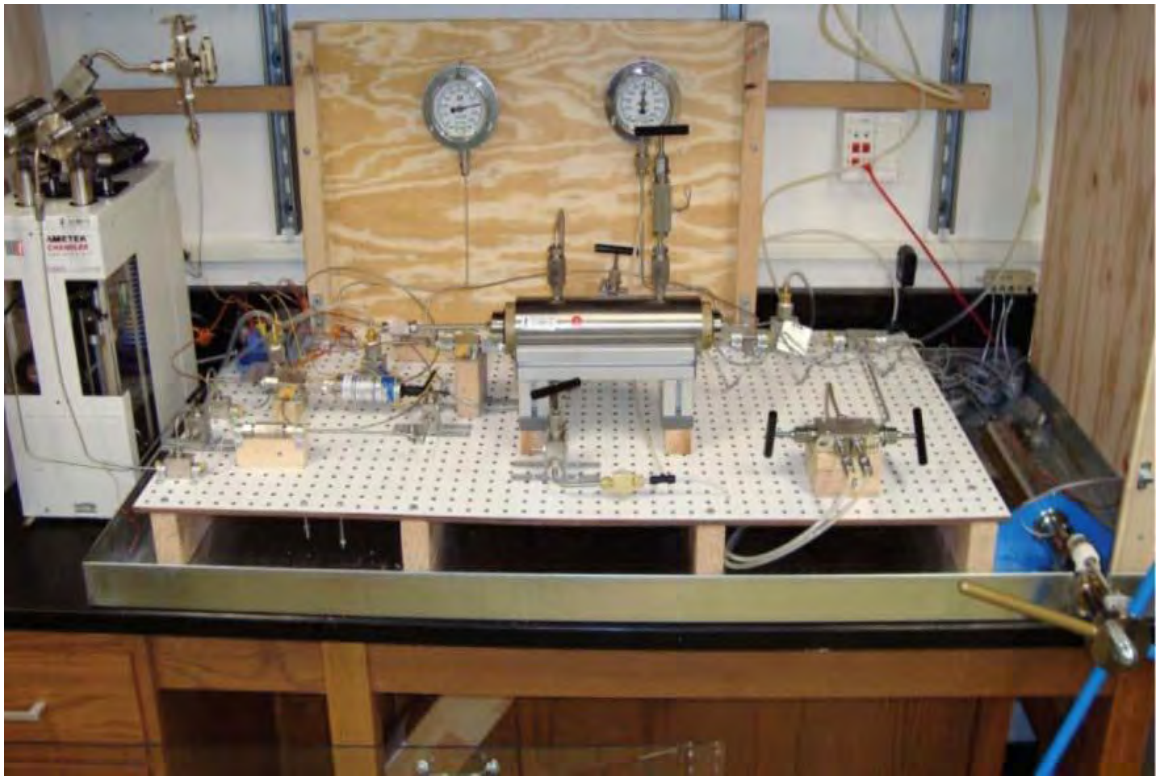

Figure 4: Pressure pulse decay apparatus for permeability measurement

Figure 5 shows a typical plot of a pressure step obtained for the Marcellus core at 320 psi pore pressure and 1,060 psi effective pressure. As shown in the figure, the upstream pressure was maintained constant and the downstream pressure was allowed to rise. To compute permeability, the following equations were used:

$$\Delta p(t) = \Delta p_o e^{-\alpha t}$$

$$\alpha = \frac{k\,A}{\beta\,V_{down}\,L\,\mu}$$

where $\Delta p(t)$ is the difference in pressure between the upstream and downstream at time t, Δp_o is the difference in pressure at time $t = 0$, k is the rock permeability, A is the core cross-sectional area, β is the gas compressibility, V_{down} is the downstream volume, L is the length of the core and μ is the gas viscosity.

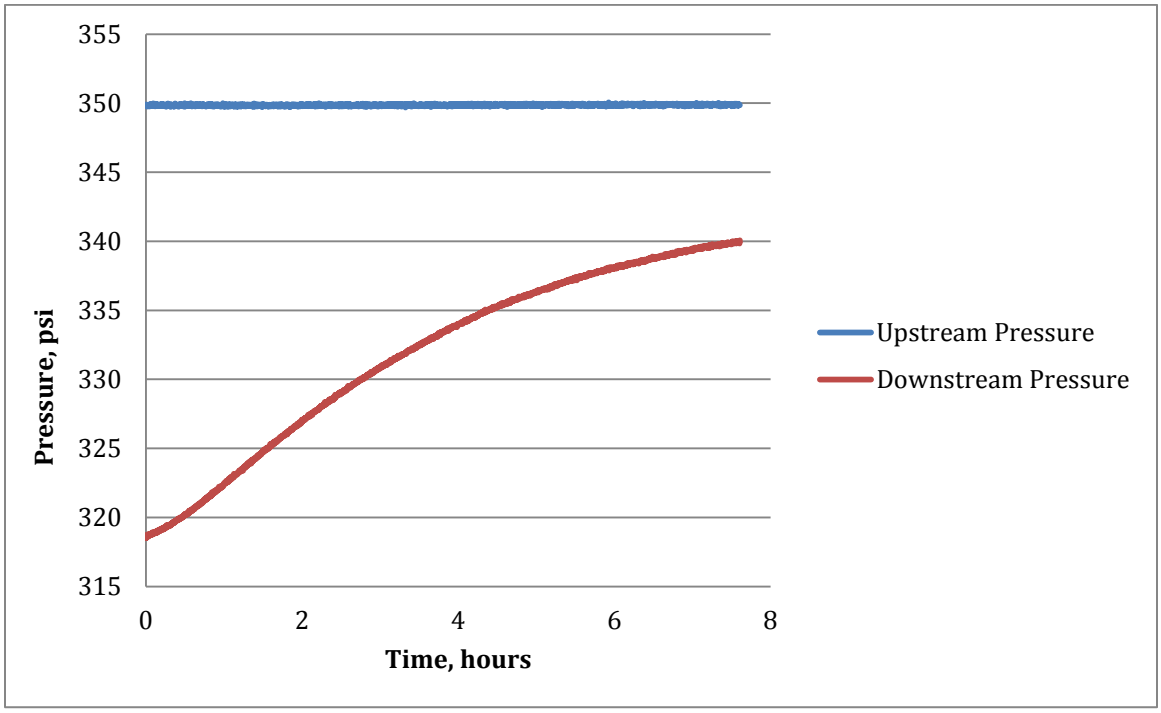

Figure 5: Example of pressure pulse decay experiment

When $\ln(\Delta p(t)/\Delta p_o)$ is plotted as a function of time, the decay shows a linear trend as shown in Figure 6. As indicated by the equations, the slope of the line is α and therefore, it is used to estimate the permeability.

Permeability estimates were obtained at different effective pressures, where $(p_{eff} = p_{confining} - p_{pore})$ and at each effective pressure, permeability estimates were obtained at different pore pressures in order to be able to calculate the effective pressure law as will be discussed later. Figure 7 shows the core permeability as a function of effective pressure. The results indicate that the permeability decreased with increasing effective pressure which is as expected. Higher effective pressures mean that core is squeezed and the grains are pushed closer to each other. Over the experimental conditions, the core permeability ranged from 25 to 65 nanodarcies.

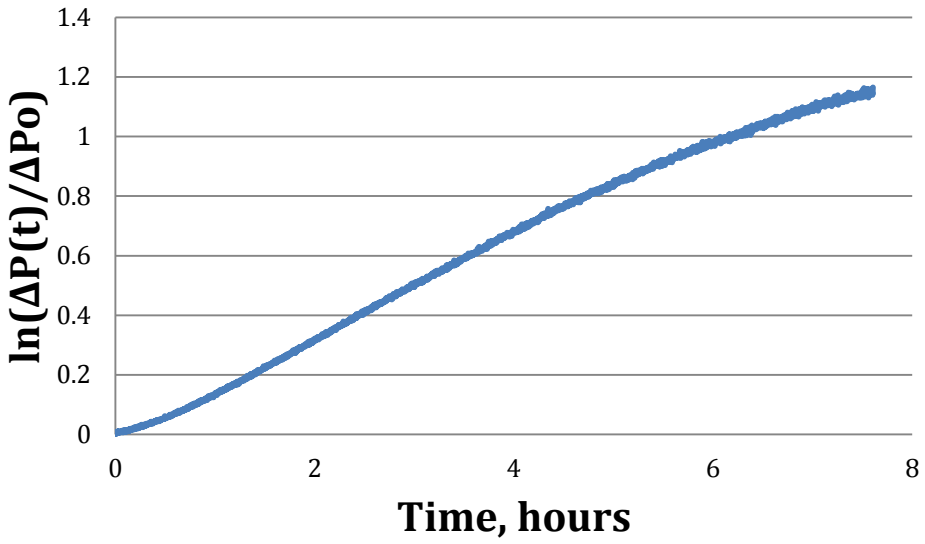

Figure 6: The decay of the pressure difference between the upstream and downstream sides

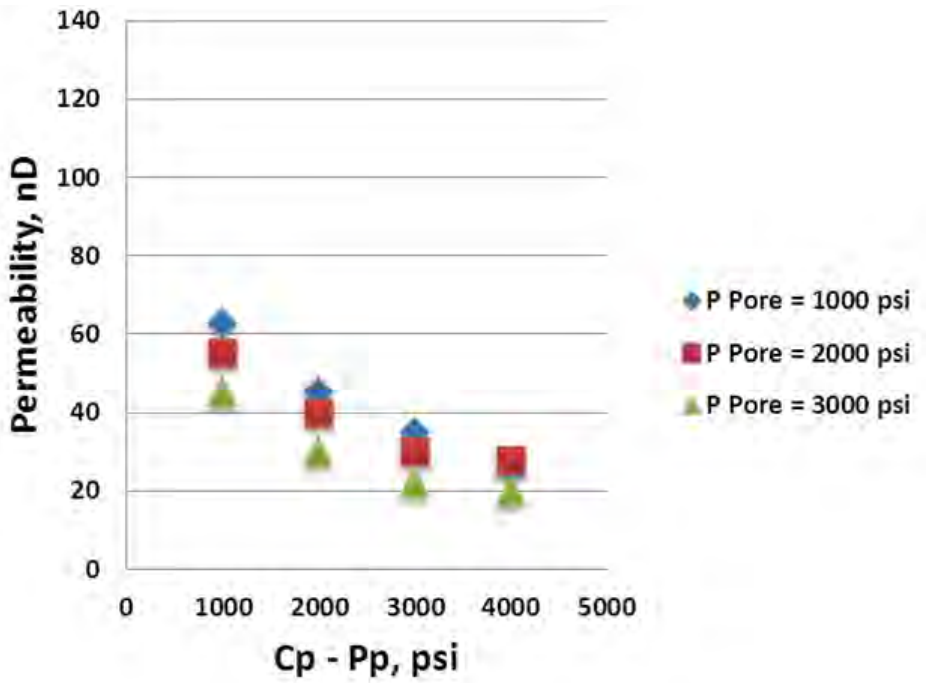

Figure 7: Marcellus shale permeability as a function of effective pressure

As mentioned earlier, one of the objectives of the pulse decay experiment is to estimate the effective pressure law, χ. The effective pressure law defines the relative sensitivity of permeability to changes in pore and confining pressures. As described by Kwon et al. (2001), it is the change in permeability with change in pore pressure at a given confining pressure divided by the change in permeability with change in confining pressure at a given pore pressure. Mathematically, the effective pressure law, χ, can be written as:

$$\chi = -\frac{\left(\frac{\partial \log k}{\partial p_p}\right)_{p_c}}{\left(\frac{\partial \log k}{\partial p_c}\right)_{p_p}}$$

In our experiment, the effective pressure law, χ, was estimated to be 0.42 ($\chi \leq 1$). Illustrations of what could the effective pressure law lead to are shown on Figure 8. The left plot is for pure quartz sandstone, the middle plot is for clay-bearing sandstones in which the clays line the pores and the right plot is for shales and mudstones with high clay contents. For the clay-bearing sandstones (middle), fluid conduit dimensions is more strongly influenced by pore pressure than confining pressure due to the high compressibility of the clay lining pores, resulting in $\chi \geq 1$. For clay-rich shales (right plot), clays form a connected matrix and the conduit dimension is more strongly affected by confining pressure than pore pressure resulting in $\chi \leq 1$. Therefore, the latter fluid flow model (clay-rich shale) is expected for this Marcellus shale core.

Compared to the clay-rich shale, the permeability of the organic-rich shale is expected to be higher. Organic-rich shale is the major productive shale in the Marcellus. Therefore, the permeability values measured for this core sample represent a low-end of the permeability range of the productive zone in the Marcellus shale.

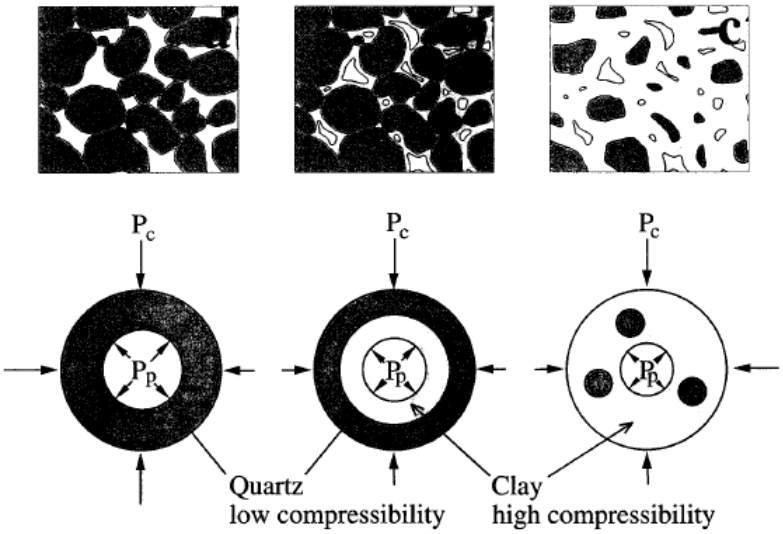

Figure 8: Effective pressure laws for porous media made up of two solids, quartz and clay minerals

PVT Analysis

An important prerequisite for using an EOS-based compositional model is achieving satisfactory agreement between equation of state (EOS) results and laboratory fluid property measurements (PVT). Hence, a commercial simulator was used to match the laboratory PVT results. The PVT study included constant volume depletion (CVD), constant composition expansion (CCE) and fluid compositional analysis at separator conditions.

The first step in the PVT simulation was to define the components that comprise the fluid system. The 11-component system contained 10 well-defined components: N2, CO2, C1, C2, C3, i-C4, n-C4, i-C5, n-C5 and C6, and one pseudocomponent (C7+) into which the heavy components were lumped. Coats and Smart (1986) argued that extensive splitting of the C7+ fraction to match laboratory data was generally unnecessary. In compositional simulation, lumping has been a common industry practice in order to significantly speed up the simulation process.

As outlined by Coats and Smart (1986), nonlinear regression was then applied on Ω_a and Ω_b of the C7+ fraction. The adjustment of Ω_a and Ω_b should be interpreted as an adjustment to the critical properties because they are related by cubic EOS parameters, a and b as shown in the following equations:

$$a = \Omega_a \frac{R^2 T_c^2}{p_c}$$

$$b = \Omega_b \frac{RT_c}{p_c}$$

Ω_a and Ω_b of C1 were also included in the nonlinear regression as recommended by Coasts and Smart (1986). Using sensitivity analysis, it was determined that the fluid model is very sensitive to the binary interaction coefficients between methane and the plus fractions. Binary interaction coefficients are introduced in order to compensate for the nonsphericity of the heavy hydrocarbons (Pederson et al., 1989). Therefore, methane-plus fraction binary interaction coefficients were included in the nonlinear regression.

Figure 9 shows the liquid saturation match for the CVD experiment and Figure 10 shows the relative volume match for the CCE experiment. The observed dew-point pressure was 3,085 psia and it was matched by the model estimates.

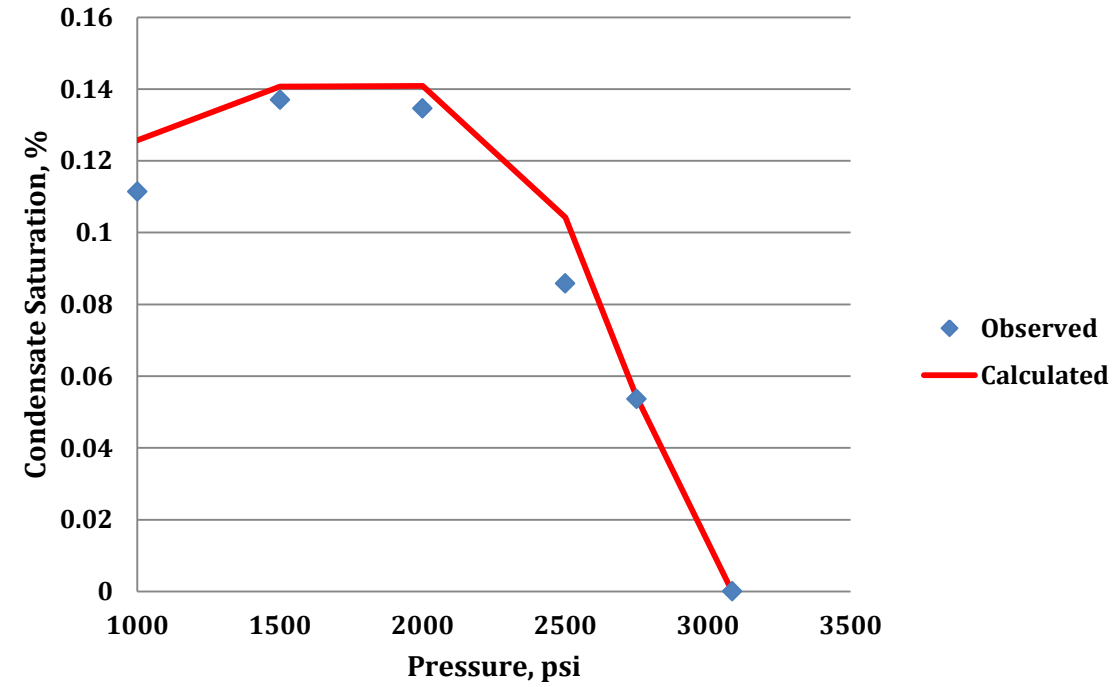

Figure 9: Condensate saturation plot during CVD experiment

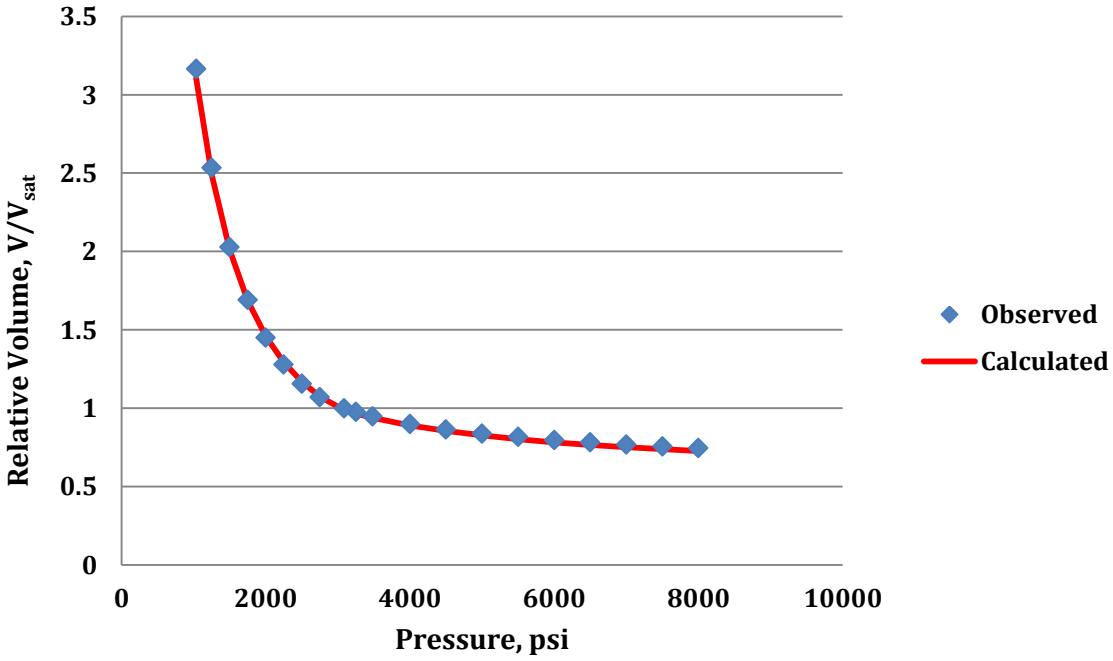

Figure 10: Pressure-volume relations of reservoir fluid during CCE experiment

Compositional data of the separator fluid samples were used to confirm the accuracy of the EOS model. When the fluid model was flashed to separator sampling conditions of 293 psia pressure and 83 ^{o}F temperature, a good agreement between the measured and calculated compositions for vapor and liquid phases was observed as illustrated on Figure 11 and Figure 12, respectively.

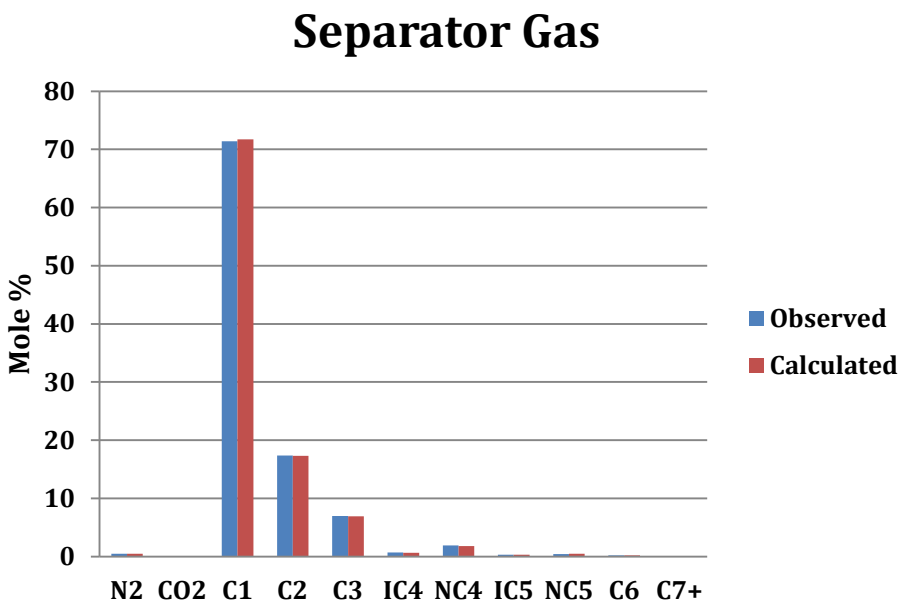

Figure 11: Measured and calculated separator gas composition

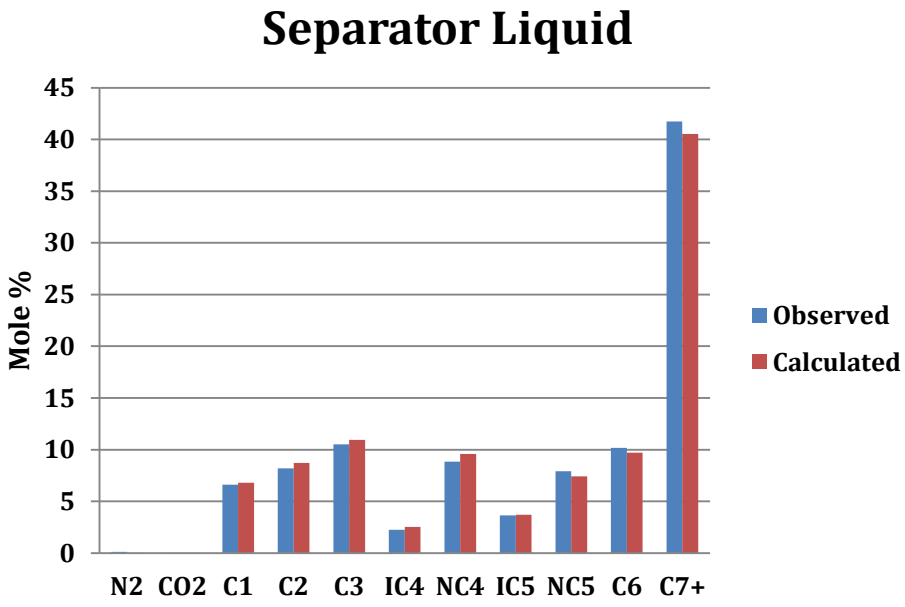

Figure 12: Measured and calculated separator liquid composition

The fluid phase envelope was generated for the gas-condensate system as shown on Figure 13. The plot indicates that for the core flooding experiment with the Marcellus natural gas-condensate system to be properly implemented, the upstream pressure should be maintained at the dew point pressure of 3,085 psi and the system temperature to be maintained at reservoir temperature of 138 ^{o}F. Therefore, a heating mechanism was introduced to the experimental apparatus as will be illustrated later.

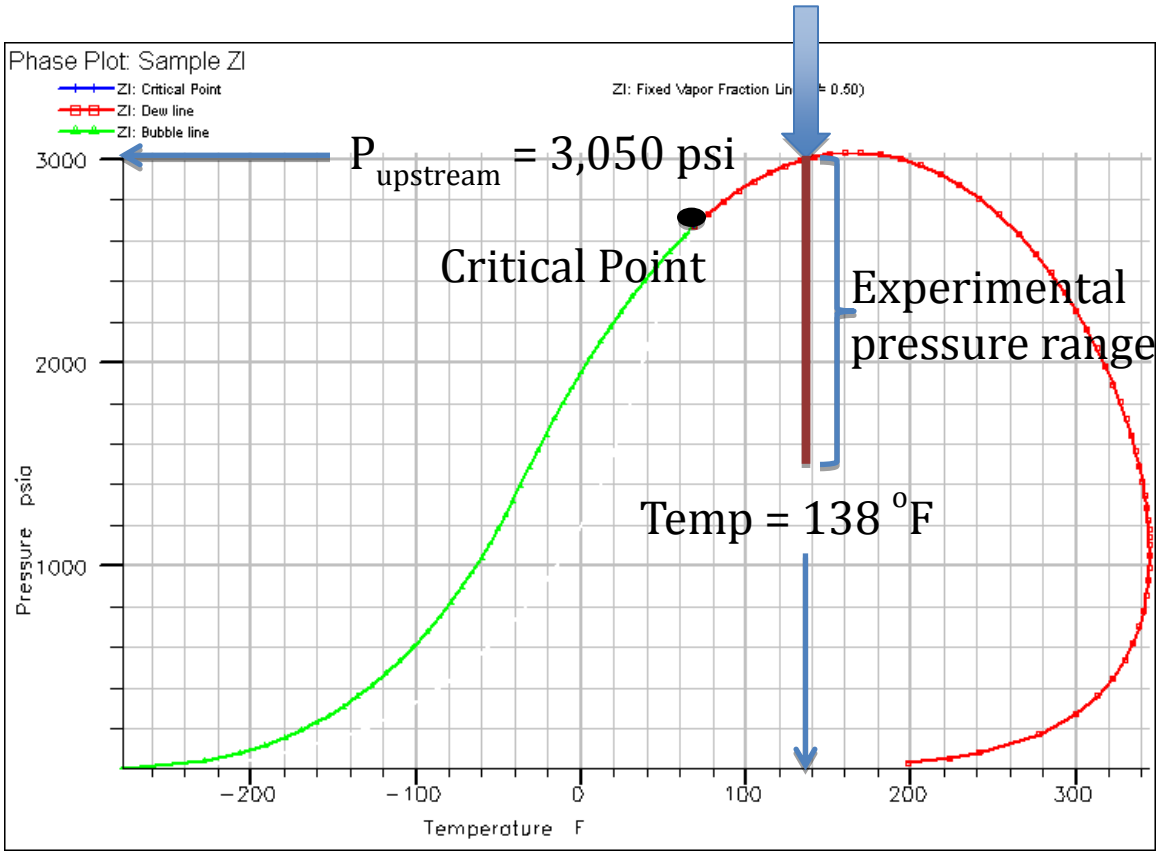

Figure 13: Phase evnvelope for the Marcellus gas sample

Gas Chromatography (GC) Calibration

The gas chromatography (GC) shown on Figure 14 is used to analysis the gas samples collected during the core flooding experiment. In order to be able to analyze the Marcellus gas samples that were injected and collected in the experiment, the GC has to be calibrated with a natural gas mix with known compositions. The calibration process involves running the sample in the GC and identifying the corresponding peak for each component as shown on Figure 15. The GC is able to identify peaks up to nC4. A good match was achieved between the GC results and the known composition of the calibration gas as shown in Figure 16.

Figure 14: Gas chromatography

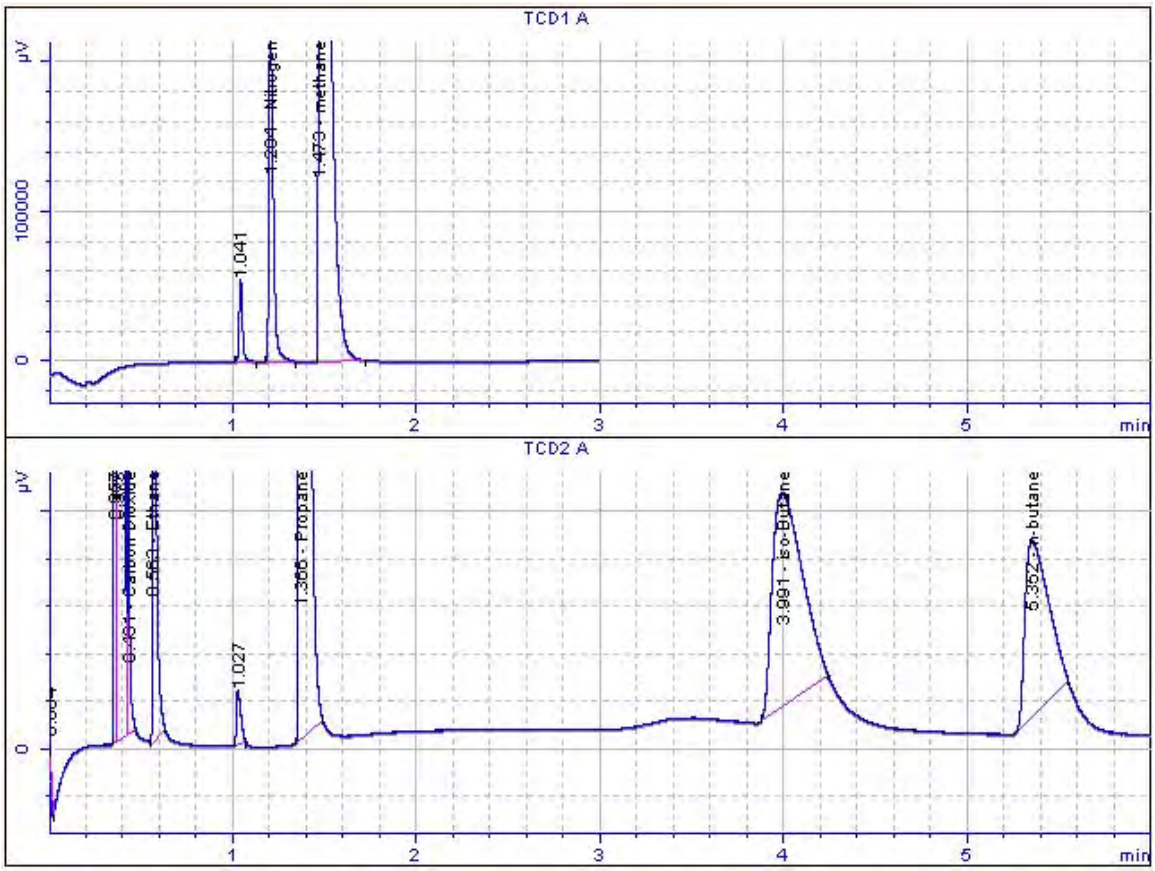

Figure 15: Peaks identified on the GC

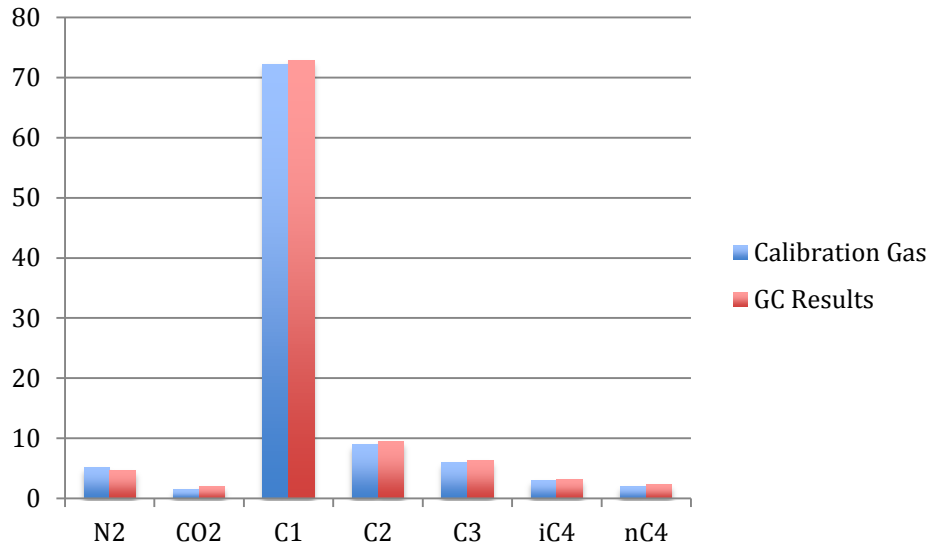

Figure 16: Calibration gas vs. GC composition results

Berea Sandstone Coreflooding Experiment Using Marcellus Gas

As mentioned earlier, in order to mimic the fluid flow in the reservoir, the experiment has to be conducted at both reservoir pressure and reservoir temperature. The reservoir pressure is controlled by allowing connecting a high pressure nitrogen cylinder to the piston gas cylinder as shown on Figure 17.

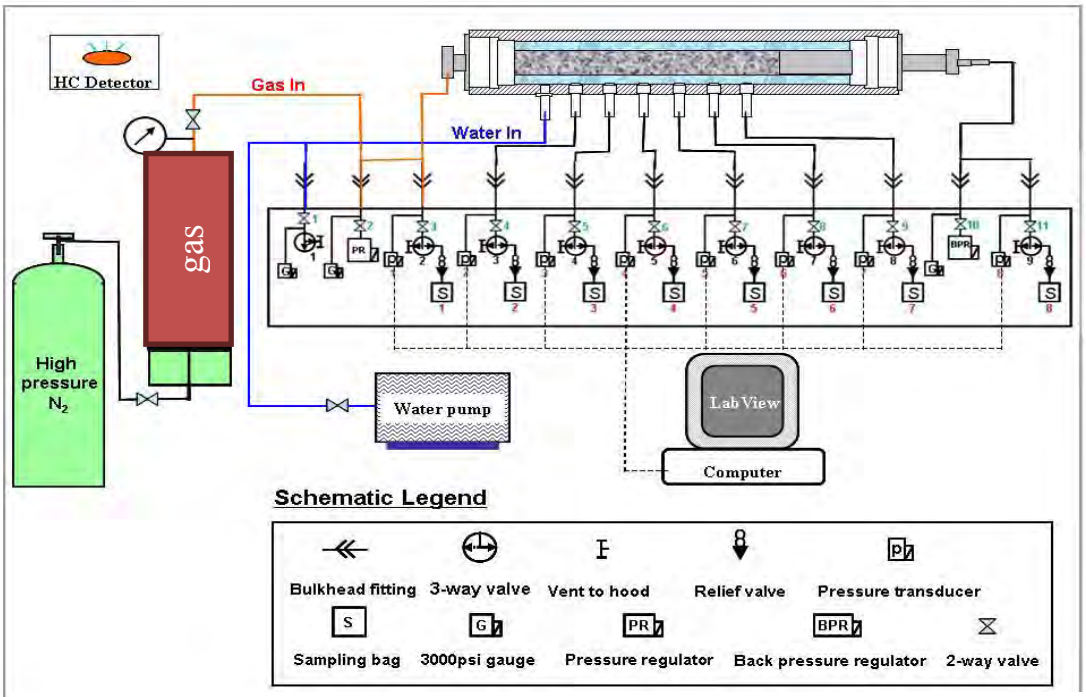

Figure 17: Core flooding experimental apparatus (from Shi 2009)

On the other hand, the temperature of the system is controlled by wrapping the whole system, including the gas cylinder, with heating tapes and insulators as shown on Figure 18. The temperature of the system is monitored by thermocouples installed at different locations throughout the experimental apparatus.

Figure 18: Photo of core flooding experimental apparatus

One experiment was conducted on the apparatus by flowing the Marcellus gas system across 11 in of Berea sandstone core in the core holder. The objective of this experiment was to test the apparatus at high temperatures and to gain a good handle on dealing with the natural gas system before loading the Marcellus shale cores.

In this experiment, the temperature experimental apparatus was first elevated to 138 ^{o}F. Then, gas was injected at an upstream pressure of 3,000 psi which is approximately the dew point pressure of the natural gas. The downhole pressure during the experiment was 2,000 psi. While the gas was flowing, five samples were collected across the core. The composition of the collected samples was later analyzed using the GC.

The composition results indicate that as the pressure drop increased from left to right across the core holder, more liquid dropped out in the core and hence, the flowing gas phase became lighter. Figure 19 plots Propane concentration in the gas phase with the gas flowing from left to right.

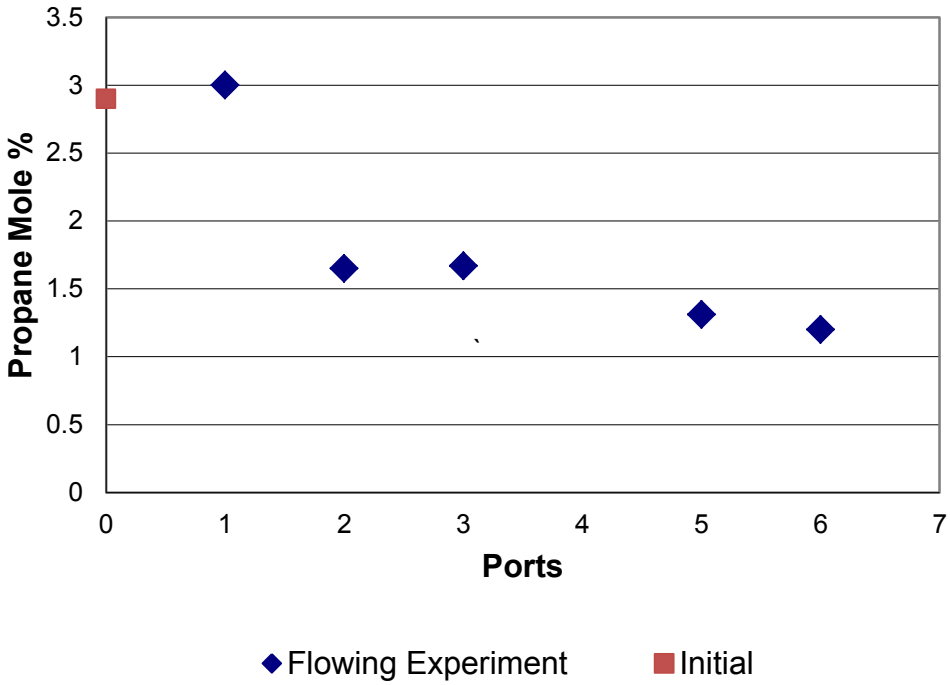

Figure 19: Propane concentration in the gas phase during the flowing experiment

Marcellus Shale Coreflooding Experiment Using Marcellus Gas

A. Numerical simulations

The fluid model presented earlier was included in a compositional simulator in order to simulate the core flooding and flowing experiment. The objective of the numerical simulation is to define the optimum experimental parameters for the "more challenging" shale core flooding experiment. The experimental parameters that need to be defined include experiment duration, upstream pressure and downstream pressure.

A one-dimensional Cartesian coordinate system was used in the simulation as shown on Figure 20. The core was constructed using a square cross section with an area equivalent to the area of the cylindrical core in order to maintain the pore volume. In the x-direction, the 6.5 in core was divided into 65 grid blocks. The injection pressure was controlled by a well assumed in the first grid block and the downstream pressure as controlled by assuming a producer in the last grid block. The temperature inside the core is assumed to be 140 ^{o}F (reservoir temperature).

Figure 20: Gridding for numerical simulation of the core (from Vo 2010)

Three experimental scenarios were simulated as follows:

I. Gas charging into the shale core
II. Gas flowing across the shale core at constant injection pressure
III. Gas flowing across the shale core with a shut-in injection well (no injector)

I. Gas charging into the shale core

Based on the PVT lab experiment, the dew point pressure of the gas is estimated by to 3,085 psi. In this simulation experiment, the core is saturated with the gas-condensate fluid until the upstream and downstream pressures reach equilibrium. The inject pressure is maintained at 3,085 psi (210 atm) and the producer is considered shut-in.

The results indicate that approximately 60-70 hours are required in order for the upstream and downstream pressures to reach equilibrium where the core is assumed to be fully saturated with the gas-condensate fluid. The pressure behavior across the core is plotted on Figure 21.

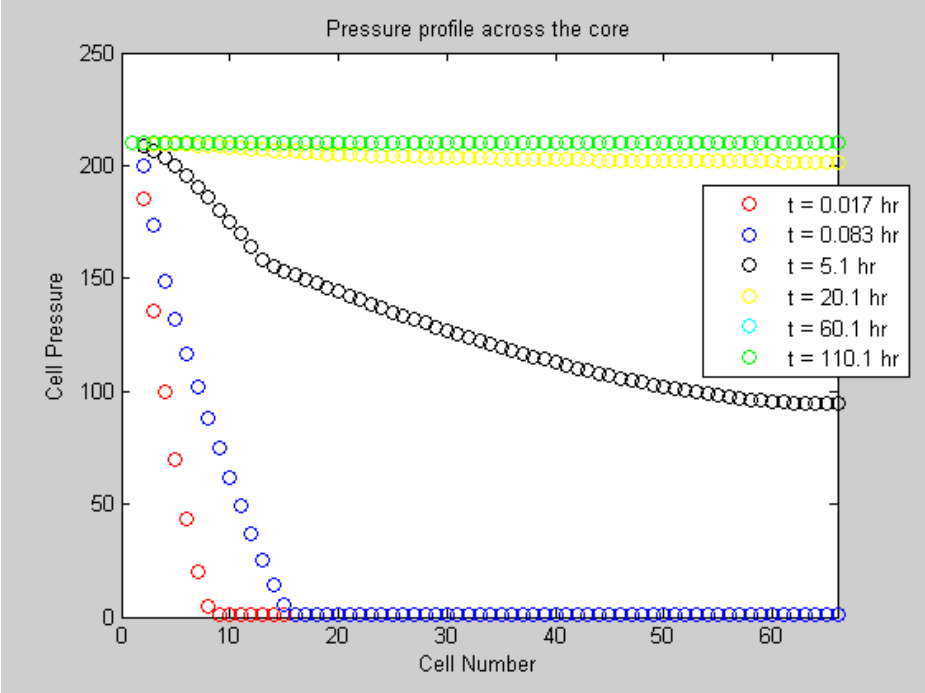

Figure 21: Pressure profile across the core during the core charging experiment

II. Gas flowing across the shale core with injection

During this simulation scenario, the saturated shale core is allowed to flow at a constant upstream pressure of 3,085 psi (210 atm) and a controlled downstream pressure of 2,000 psi (135 atm). The pressure, the condensate saturation and the composition of each component up to C7+ in the gas and liquid phase are monitored at each grid block along the core.

The results indicate that the experiment needs to be conducted for a minimum of 20 hours to allow for a substantial volume of condensate to dropout as shown on Figure 22. Hence, the composition of the gas and liquid phases is modified across the core.

Similar to the results observed on the sandstone core flooding experiment, the flowing gas phase becomes lighter from left (upstream) to right (downstream) as plotted on Figure 23 where the propane concentration is monitored across the core during the flow experiment. The plot indicates that the propane concentration in the gas phase goes down across the core. On the other hand, the propane concentration in the liquid phase increases.

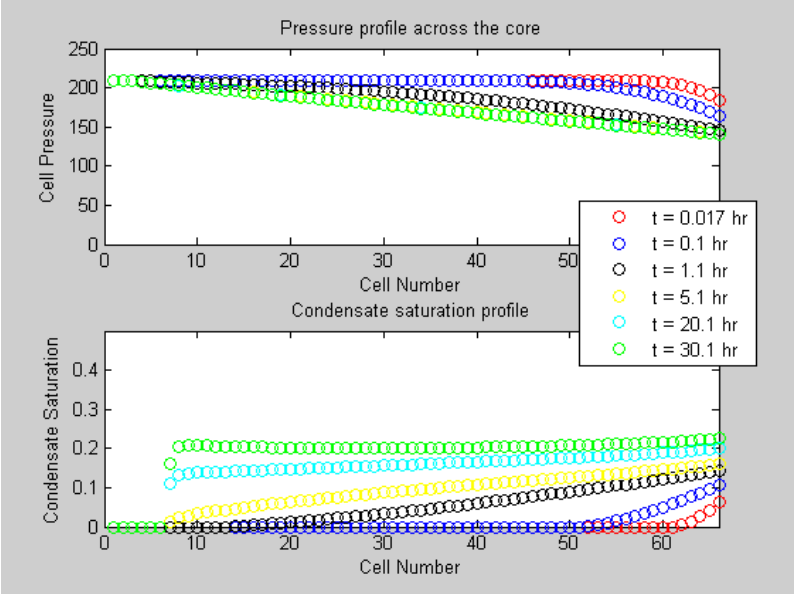

Figure 22: Pressure and condensate saturation profile during the core flowing experiment with an injector

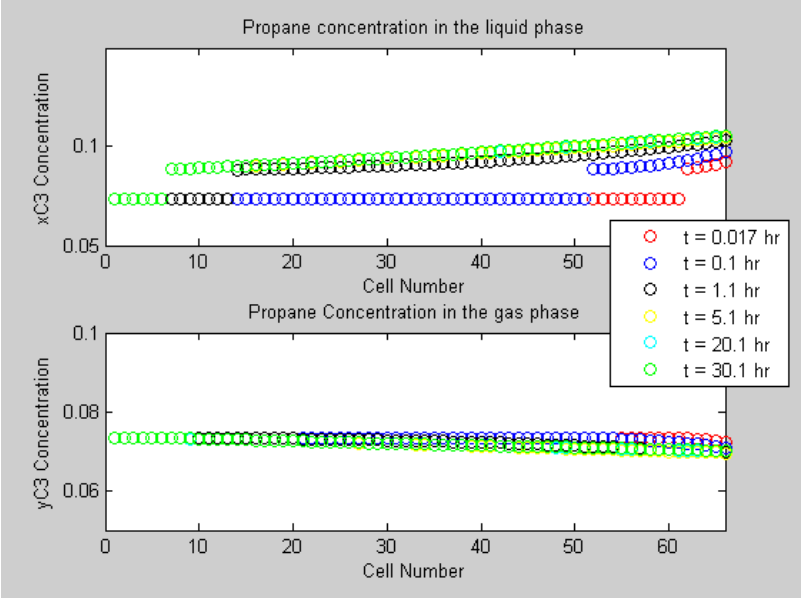

Figure 23: Propane composition in the gas and liquid phase across the core

III. Gas flowing across the shale core without injection

During this simulation scenario, the initially saturated core at 3,085 psi (210 atm) is allowed to flow at a constant downstream pressure of 2,000 psi (135 atm) while the injector well in the upstream is kept shut-in. Unlike the previous scenario, the required time for a substantial volume of condensate to dropout is only 2 hours as shown on Figure 24. Therefore, the composition of the gas and liquid phase in this experimental scenario should alter at a faster pace compared to the previous experimental scenario.

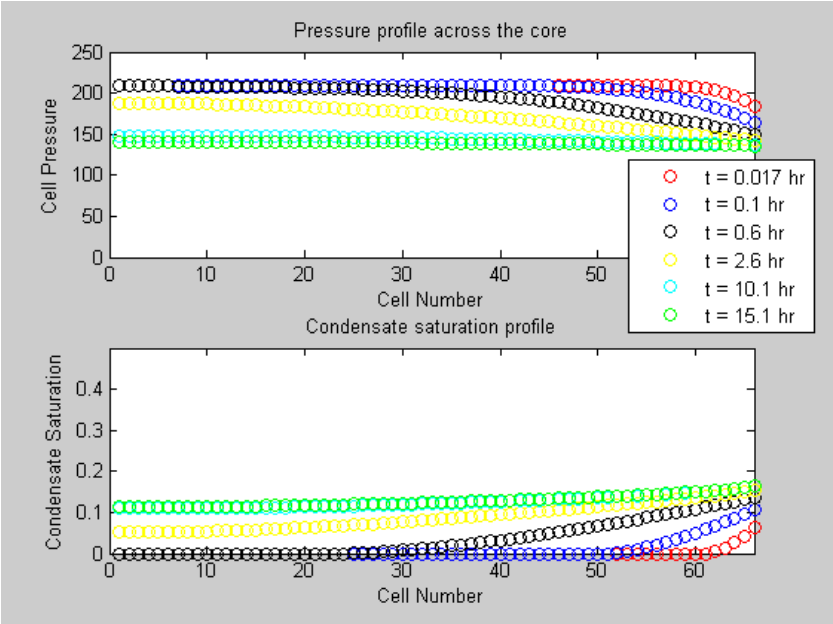

Figure 24: Pressure and condensate saturation profile during the core flowing experiment at 2,000 psi (136 atm) BHP without an injector

This scenario has also been simulated at lower BHP typical to that of the field. The investigated BHPs were 1,500 psi, 1,000 psi and 500 psi. The results for each BHP are plotted on Figure 26, Figure 26 and Figure 27. The results indicate that with additional pressure drawdown, the condensate saturation across the core starts to level off. The 500 psi BHP simulation case was repeated with a longer flowing period and the results; shown on Figure 28, indicate that the condensate saturation starts to drop slightly across the core possibly due to revaporization.

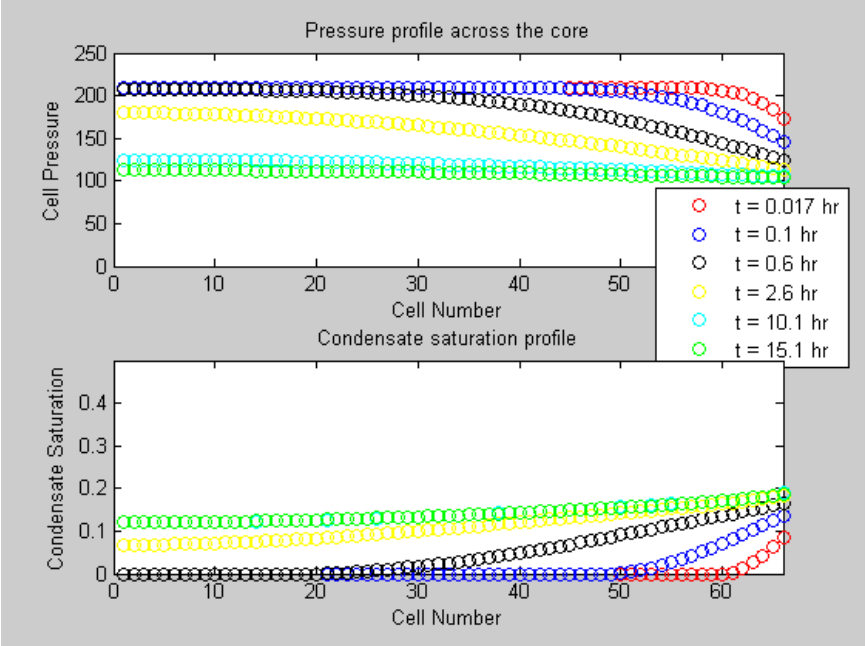

Figure 25: Pressure and condensate saturation profile during the core flowing experiment at 1,500 psi (102 atm) BHP without an injector

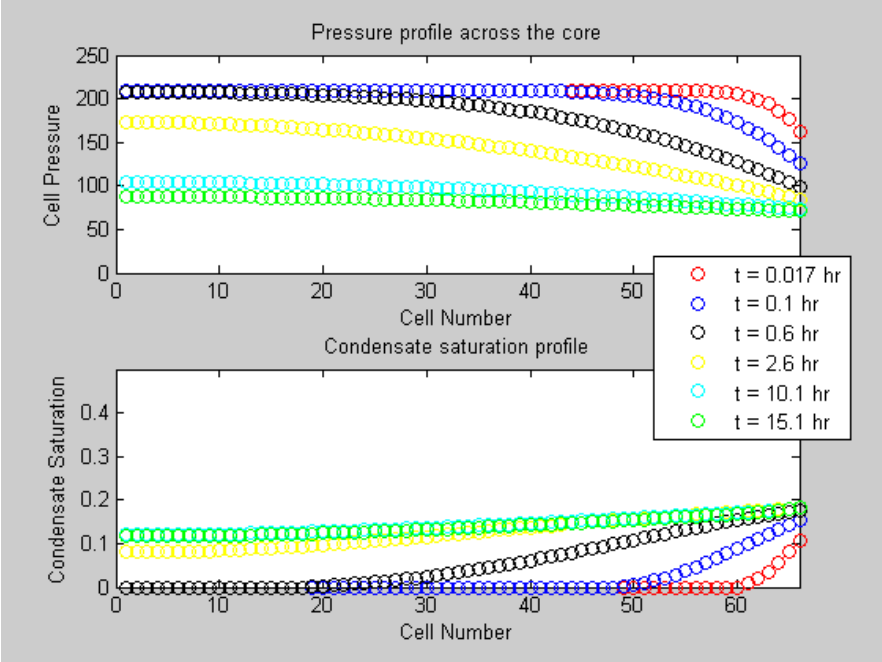

Figure 26: Pressure and condensate saturation profile during the core flowing experiment at 1,000 psi (68 atm) BHP without an injector

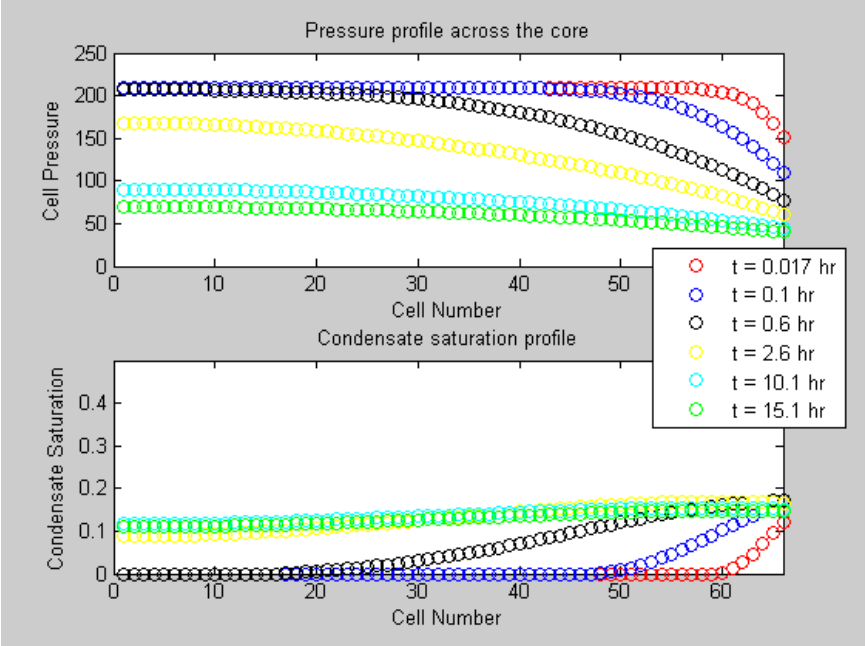

Figure 27: Pressure and condensate saturation profile during the core flowing experiment at 500 psi (34 atm) BHP without an injector

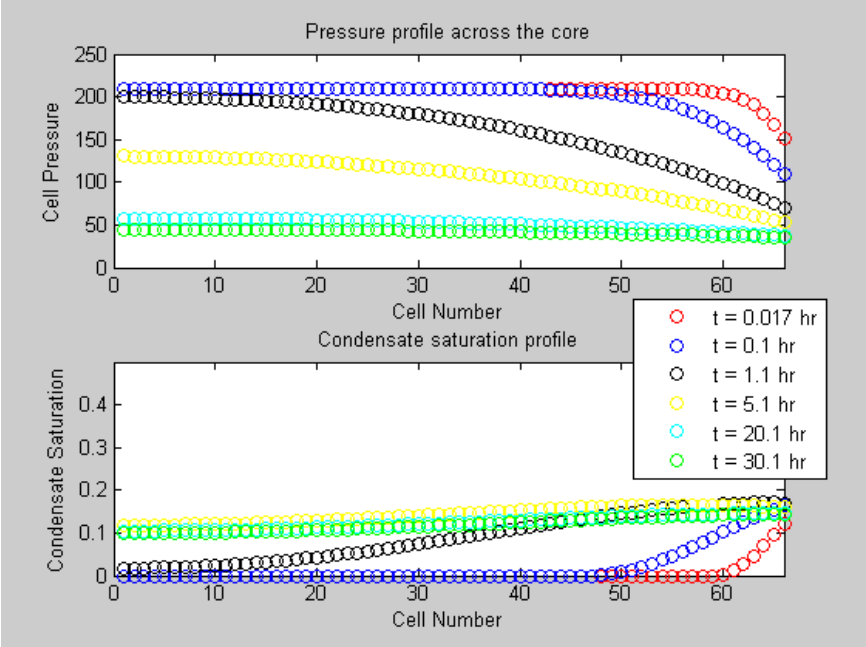

Figure 28: Pressure and condensate saturation profile during the core flowing experiment at 500 psi (34 atm) BHP without an injector

B. Marcellus shale coreflooding experiment

The shale core obtained from the Marcellus (Figure 29) was loaded into the core holder. Prior to conducting the core flooding experiment with the natural gas fluid, Helium gas was injected at 2,500 psi upstream pressure in order to pressure test the system. During the pressure test, a leak between the confining pressure and the pore pressure was observed. After troubleshooting the system, a few O-rings in the core holder were found to be defective because they could not sustain the high temperature of the experiment. After extensive search, proper O-rings were found and installed and the system was pressure-tested successfully.

Figure 29: 2-in diameter Marcellus shale core

The procedures for conducting the coreflooding experiment on the Berea sandstone core was followed for this core. However, due to the tight nature of the Marcellus shale core, the valve downstream of the core was closed while injecting the gas into the core. The injection pressure was 3,000 psi, which is the dew-point pressure of the Marcellus gas mixture as indicated earlier.

Figure 30 shows the upstream and downstream pressures during the experiment. The plot indicates that it took 12 hours for the pressure pulse to reach the downstream side. However, due to limited gas supply, the upstream valve was closed after 48 hours of injection. After that, several gas samples were collected through the sampling ports 1, 2 and 4 across the Marcellus core as shown on Figure 31. Upstream and downstream samples were collected as well.

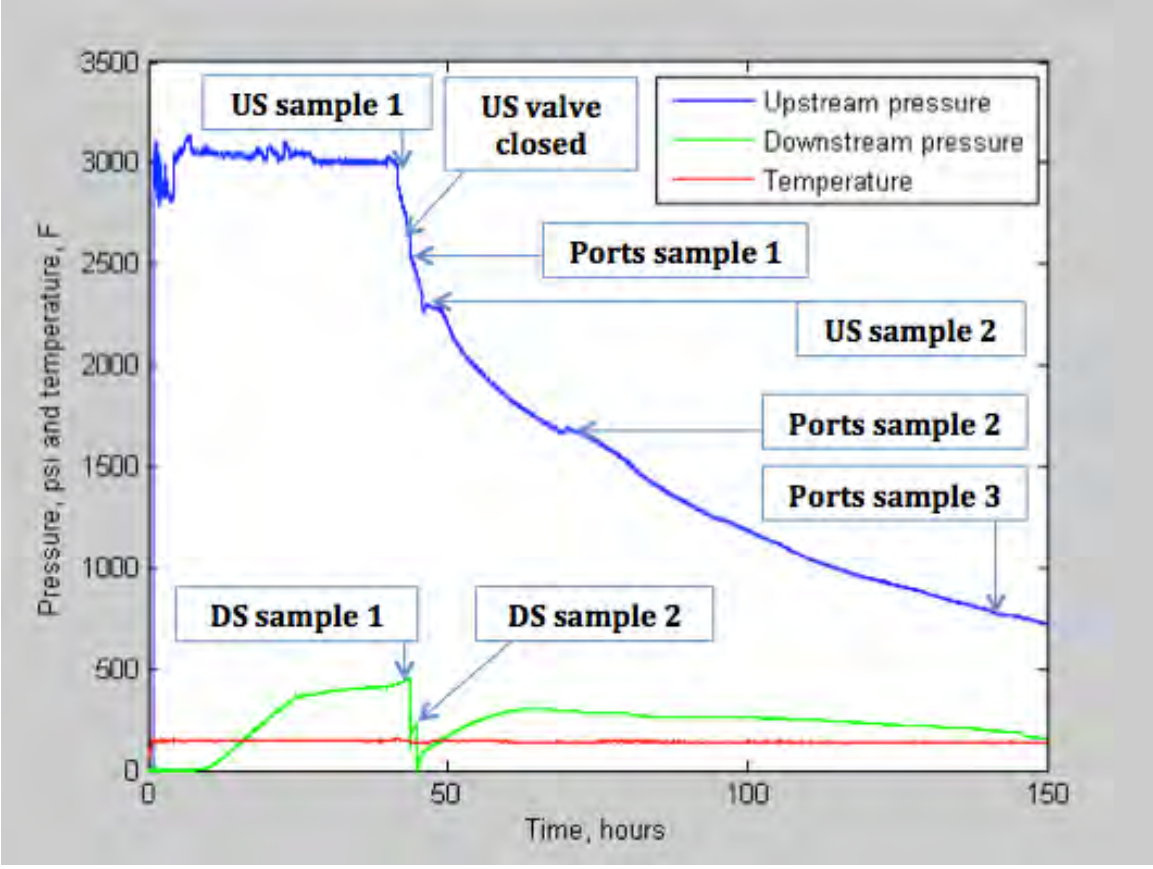

Figure 30: Marcellus gas coreflooding experiment into shale core. US = upstream, DS = downstream.

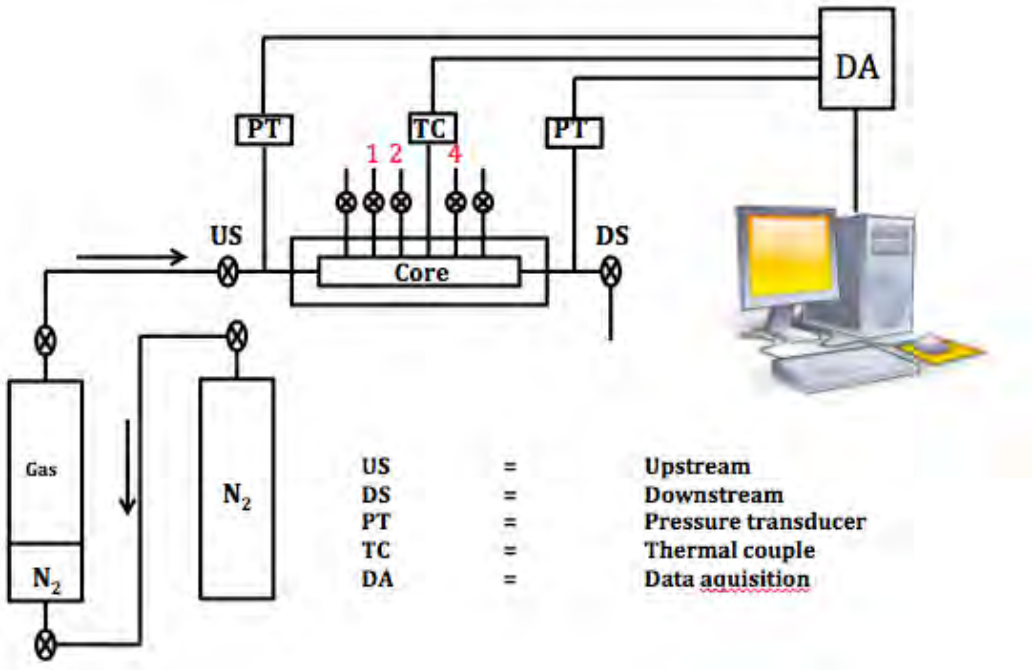

Figure 31: Experimental apparatus showing sampling ports 1, 2 and 4

The collected samples were characterized using the Gas Chromotography (GC) to identify the concentrations of the gas components. Figure 32 shows the propane, i-butane and n-butane concentrations for ports sample # 2. The results indicate that the concentrations of the heavy components are decreasing from the upstream side (port 1) to the downstream side (port 4). The results confirm the findings obtained from the coreflooding experiment on the Berea sandstone presented earlier.

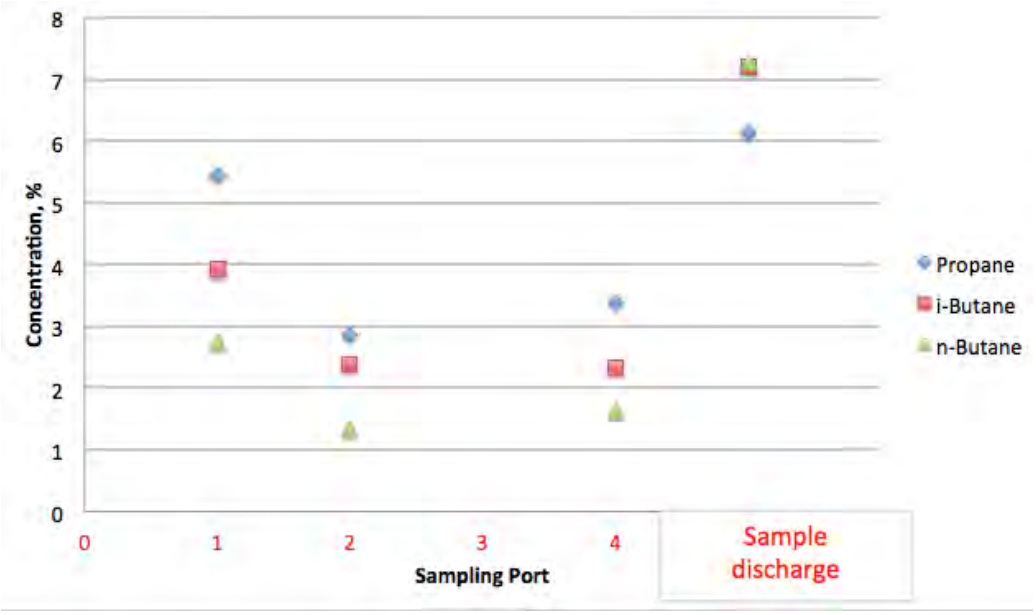

Figure 32: C3, iC4 and nC4 concentrations for ports sample # 2 and discharge sample

The GC characterization results of a discharged sample from the downstream side are also plotted on Figure 32. The concentrations of propane, i-butane and n-butane for the discharged sample are high. This confirms that the liquid condensate dropped out in the core is rich of heavy hydrocarbons. Similar behavior was observed by Vo (2010) when he conducted the experiment on Berea sandstone using binary (methane and n-butane) gas-condensate mixture.

Figure 33 compares the propane, i-butane and n-butane concentrations between ports sample # 2 and ports sample # 3. The plot shows that the component concentrations decreased for ports sample # 3, which were collected when the upstream pressure was 755 psi. Ports sample # 2 were collected at 1,520 psi upstream pressure. This is an indication that the additional pressure drop between the two samples caused additional liquid dropout. As a result, more condensate dropped out which caused the propane, i-butane and n-butane concentrations in the gas phase to go down.

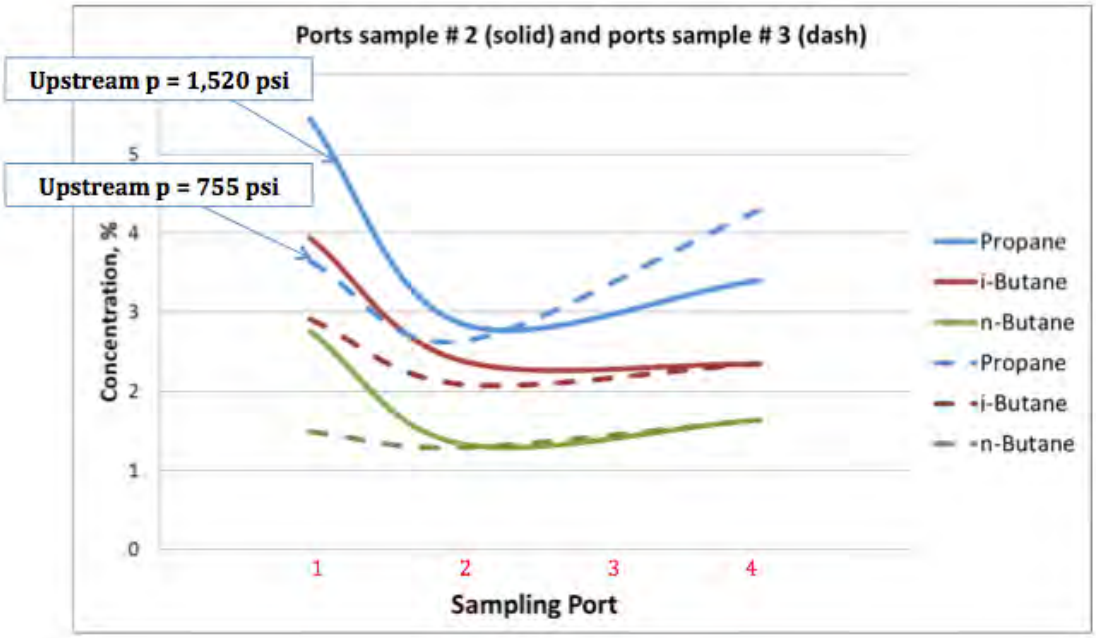

Figure 33: C3, iC4 and nC4 concentrations for ports sample # 2 and ports sample # 3

Conclusion

The coreflooding experiment of the Berea sandstone and the Marcellus shale core using the Marcellus gas-condensate gas mixture confirm the expectation based on earlier experiments (which used synthetic binary gas mixtures) that the composition of Marcellus shale gas mixture would change during production. The change in the gas composition is caused by the dropout of the heavier components into the liquid condensate phase below the dew point pressure.

References

Brace, W.F., Walsh, J.B., and Frangos, W.T., 1968, Permeability of Granite under High Pressure: Journal of Geophysical Research, v. 73, p. 2225-2236.

Coats, K. H. and Smart, G. T.: 1986, Application of a Regression-Based EOS PVT Program to Laboratory Data, *SPE Reservoir Engineering,* May 1986*,* 277-299.

Kwon, O., Kronenberg, A.K., Gangi, A.F., and Johnson, B., 2001, Permeability of Wilcox shale and its effective pressure law: Journal of Geophysical Research, v.106, p. 19339-19353.

Pedersen, K. S., Fredenslund, Aa. and Thomassen, P.: 1989, Properties of Oils and Natural Gases, Gulf Publishing Company, Houston, TX.

Shi, C., 2009, "Flow Behaviors of Gas Condensate Wells", PhD Dissertation, Stanford University, California.

Vo, H., 2010, "Composition Variation During Flow of Gas Condensate Wells", MS Thesis, Stanford University, California.

Appendix H – Fracture Characterization at the Marcellus Level

GTI

RPSEA Project 9122-04

GTI Project 21100

Penn State Subcontract

Task 6.2 Characterization of Hydraulic Fracturing at the Marcellus Level

Final Report

Terry Engelder, Prof Geosciences, Penn State

Yunhui Tan, Ph.D. Candidate, Penn State

Dec 20, 2012

Summary: The principal objective of this study is to understand and characterize the hydraulic fracture process within gas shale through a detailed analysis of microseismic events during stimulation of the Devonian Marcellus shale from four laterals drilled by Range Resources LLC at the Troyer pad in Washington County, PA. The technique for this analysis was the inversion and decomposition of the seismic moment tensor for the largest of the microseismic events caused by the stimulation. 34 out of the 50 largest events identified from a downhole linear array of Schlumberger accelerometers were processed by Microseismic Inc. using data from a surface array with a star pattern. 11 of the 34 events took place on subvertical planes with a downdip slip vector. The average strike of the nodal planes from these subvertical events was N49°E. Some of these 11 subvertical events had a relatively large volumetric component whereas other events were mainly double couple. Dip-slip motion is consistent with the majority of regional stress data from the eastern edge of the North American continental lithosphere where the maximum stress is vertical. The subvertical orientation of these brittle structures is consistent in orientation with the J_1 joint set populating black shale of the Appalachian Basin (Engelder et al., 2009).

Introduction

A commonly held view is that microseismic events induced by hydraulic fracturing during reservoir stimulation are a manifestation of shear failure. This argument is largely based on high S-to P amplitude ratios associated with the microseismic events (Phillips et al., 1998). The shear-slip interpretation was called to question by work on the European Hot Dry Rock Program at Soultz-sous-Forets (Cuenot et al., 2006) and analysis of the Carthage Cotton Valley tight sand gas field experiments (Rutledge and Phillips, 2003). In the latter case the fault planes were so close to the maximum horizontal stress that the fault must have been subject to a very low shear stress while being in an orientation that favored a significant volumetric component (Rutledge et al., 2004).

Gas shale with permeability on the order of 100 nd must be stimulated (i.e. fractured) to allow economic gas flow. Massive slickwater hydraulic fracturing is employed for this purpose. One of the most contentious questions about the stimulation of gas shale concerns the extent to which hydraulic fracturing causes rupturing the intact rock as opposed to opening pre-existing fractures. If intact rock is ruptured by high fluid pressure, then the product is a crack that should exhibit a large component of volumetric strain with no shear slip. If the fracture stimulation is the opening of pre-existing fractures, the seismic slip commonly posited as the cause of failure for microseismic events gives no indication whether the pre-existing fractures are joints or faults?

In the Appalachian Basin, gas shales observed in outcrop contain fractures in the form of both joints and veins (Engelder et al., 2009). The most common orientation for faulting is parallel to bedding in the form of slickenside surfaces (Evans, 1994). Based on their presence in both outcrop and core, it is reasonable to presume that stimulation of gas shale such as the Marcellus opens a network of pre-existing joints. If this is indeed the case, it stands to reason that fluid invading these joints should be reflected by a relatively large volumetric component of seismic radiation, a hypothesis worth testing. This hypothesis may be tested with the calculation of moment tensors for the largest of the events during gas shale stimulation. The principal objective of this study is then to understand and characterize fracture opening and slip during the hydraulic fracturing process within the Marcellus gas shale through a detailed analysis of microseismic events caused by stimulation of the Marcellus.

Background

Microseismic source mechanisms are traditionally assumed to reflect shear strain parallel to the slipping fault. The volume of the fault zone neither increases nor decreases. Fracture stimulation of gas shale by massive slickwater hydraulic fracturing involves a volumetric expansion on the order of 0.4% (i.e., a 50 feet thick section of Marcellus stimulated by 5 million gallons of hydraulic fracture fluid). This should show up as a positive volumetric component of the seismic moment tensor. Thus, the microseismic events associated with stimulation of gas shale can be of two types (Vavryčuk, 2001). The first type of event is much like a laboratory acoustic emission which is a single couple seismic mechanism. A single couple event is the record of the noise associated with walls of the crack moving normal to the plane of the crack. In linear elastic fracture mechanics this is known as Mode I crack propagation (Lawn, 1993).

Here, the motion of the walls of the crack is defined by the angle, α, between motion of the walls of the crack, U_i, and the plane of the crack defined by its normal vector, n_j. A single couple mechanism with α=±90° is a consequence of either pure extension (i.e. seen in nature as a tensile crack) or a pure closure (i.e. seen in nature as disjunctive cleavage which forms with the motion of the walls of an anti-crack in compression). The second type of event is typical of faulting where the slip vector on the crack is parallel to the plane of the crack. In this case, the seismic event is a double couple mechanism where slip is parallel to the fault plane (i.e. α=0°). Seismic acoustic energy from Mode I cracking tends toward the relatively low energy end of the seismic spectrum. During shear slip, a relatively large amount of seismic energy is released compared to the pure opening of a crack. Seismic radiation during fault slip is the signal most easily detected by microseismic techniques associated with stimulation of gas shales (Rutledge et al., 2004).

In addition to the motion of the walls of a crack which can be either a joint or a fault, the radiation pattern can be represented by equivalent body forces in the form of force couples (Stein and Wysession, 2003). Single couples can be offset in the direction the force is acting, thus generating no torque, or offset normal to the direction of the force couple, thus generating a torque. Two offset force couples are combined at right angles to produce a double couple that allows slip on a fault without subjecting the fault to a net torque. Magnitude of the equivalent body forces is the scalar seismic moment of a microseismic event. Body forces of unit magnitude define the fault (or crack) geometry including motion of its wall.

Location of Microseismic Events

One of the primary uses of microseismic data is to map the location where the rock is breaking and estimate the stimulated reservoir volume based on the distribution of such locations (Mayerhofer et al., 2008b). This result is commonly known as “dots in a box” (Eisner et al., 2010).

However, the calculation of the location and estimation of the uncertainty of that location remain the most challenging problems in current microseismic monitoring operations (Eisner et al., 2011). Different service providers often come up with widely varying microseismic locations for the same event (Hayles et al., 2011). This is exactly the case for microseismic data from the Troyer experiment. The locations of events determined by Microseismic Inc. and Schlumberger differ as much as 200 ft. (Figure 1). Microseismic Inc.’s results are consistently above the Schlumberger results. One explanation of this difference is the choice of velocity models used by the two companies. The Troyer experiment does not have a sonic log. Therefore, the two companies used sonic logs from adjacent wells for their location calculation algorithm. Another reason for differences in location is that neither of the two surveys had a vertical component: Microseismic Inc.’s was a 2-D surface array while Schlumberger’s was a one dimensional array in an adjacent wellbore (Figure 2 and Figure 3). Both surveys are biased to some extent because of the lack of control in the vertical direction. The third problem is that neither company used a variable velocity model to account for the change in sonic velocity during fracture stimulation.

Estimates suggest that the change in velocity can be as high as 20% (Eisner et al., 2011). If that is true, data processing requires a recalibration of a velocity model after every stage for.

The specific algorithms used for calculation of locations of events were released by neither companies. Microseismic Inc. used their own patented software called PSET (Passive Seismic Emission Tomography) (Duncan et al., 2010) to process the data. They claimed to use a "beam forming method" to restore the event location. However, we don't really understand the details of their algorithm. Schlumberger has similar patented algorithms to process their data too, which is called CMM (Continuous Microseismic Mapping) (Khadhraoui et al., 2009). An early version of this algorithm uses Geiger's algorithm for calculation of hypocenter and origin time and this algorithm can minimize the residual time of P-wave arrival time with spatial variation (Menke, 2012).

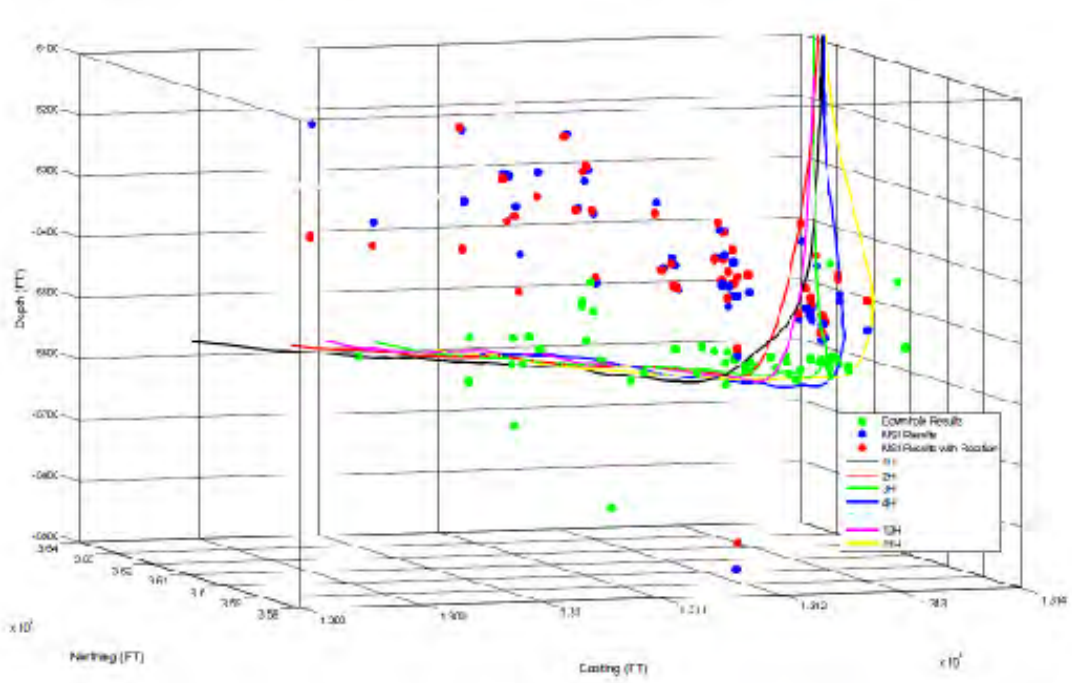

Figure 1, Plot of the locations of events calculated by Schlumberger (green) and Microseismic Inc. (blue and red). The blue dots are the locations calculated without rotation; the red dots are after rotation. Vertical scale is about 100 ft for each grid box.

Moment Tensor Representation of Source Mechanism

The physical meaning of a moment tensor is simply the relative displacement of a crack face during growth (Pollard and Segall, 1987). The moment tensor can also be interpreted as the volume integral of stress released associated with the microseismic event (Snoke, 2009).

Gilbert (Gilbert, 1971) first introduced the moment tensor as a means of characterizing of the point source of the microseismic event. When convoluted with the elastodynamic Green's function, moment tensors are able to stipulate the displacement field associated with an microseismic event.

Seismic events reduce to simple point sources as long as the dimension of the fault is smaller than the wave length of the seismic waves generated by slip on the fault, which is true in our case. Moment tensors are widely used in the seismologist community. For example, the Harvard Global Centroid Moment Tensor Catalog uses a full waveform inversion of moment tensor to characterize the source mechanisms of natural earthquakes.

Moment Tensor Inversion

The forward modeling of a microseismic event involves the generation of a synthetic seismogram. The algorithm for producing this synthetic seismogram, especially to convert the velocity model to a Green's function is quite complex. To make the inversion process simpler and also be more confident about the data source, for now, we used only the first motion of the P-wave of each event. The linear relationship between seismic moment tensor and P wave first motion can be expressed as follows (Julià et al., 2009):

$$\mathbf{u} = c\mathbf{F}\colon \mathbf{M}$$

Due to the symmetry of moment tensor and excitation matrix, the equation above can be written as:

$$u_j = \sum_k c_j^i f_k^i m_k \qquad i = P, SV, SH \qquad j = 1, \dots, n,$$

Where n is the number of data points (number of traces used for P-wave first motion in our case).

Excitation matrix for P wave:

$$\mathbf{F}^p = \begin{bmatrix} sin^2\theta cos^2\varphi & 1/2sin^2\theta sin2\varphi & 1/2sin2\theta cos\varphi \\ 1/2sin^2\theta sin2\varphi & sin^2\theta sin^2\varphi & 1/2sin2\theta sin\varphi \\ 1/2sin2\theta cos\varphi & 1/2sin2\theta sin\varphi & cos^2\theta \end{bmatrix}$$

θ and φ are the takeoff angle and azimuth respectively. The takeoff angle is zero in the downward direction and azimuth is zero in a clockwise direction from the north.

The P-wave first motion can be picked up from the seismograms recorded on each trace in time domain directly if the noise and frequency of the signal is relatively low, which is the case in surface microseismic monitoring. However, when we study the downhole microseismic data, high frequency data becomes another challenge (Eisner et al., 2011). One possible solution to this problem is to use the amplitude in the frequency domain instead of the time domain. A time window needs to be picked on the P-wave first arrival wave train.

Microseismic Inc. performed the moment tensor inversion using their proprietary program PSET. Therefore, we do not know the details of the algorithm. However, for a future study we'd like to perform our own moment tensor inversion to conduct an independent check of their results. In addition, we might use different inversion methods to test the robustness and stability of the inverted results.

Moment Tensor Decomposition

After we calculate the moment tensor from wave-form data, decomposition is usually routinely performed. Through the decomposition of moment tensor of each microseismic event, the double-couple (shearing, mode II or III fracturing) and non-double-couple (explosion or implosion, mode I fracturing) components could be quantitatively assessed.

The procedure decomposition of moment tensors are as follows:

$$\begin{bmatrix}\lambda_1 & 0 & 0\\ 0 & \lambda_2 & 0\\ 0 & 0 & \lambda_3\end{bmatrix} = \begin{bmatrix}E & 0 & 0\\ 0 & E & 0\\ 0 & 0 & E\end{bmatrix} + \begin{bmatrix}\lambda_1' & 0 & 0\\ 0 & \lambda_2' & 0\\ 0 & 0 & \lambda_3'\end{bmatrix}$$

Moment Tensor Isotropic Anisotropic

$$E = \frac{1}{3}(\lambda_1 + \lambda_2 + \lambda_3)$$

Here $\lambda_1, \lambda_2, \lambda_3$ are the three eigenvalues of the moment tensor; E is the average of the eigenvalues. The moment tensor could be first split into two parts: isotropic (explosion or implosion) and anisotropic. This tensor split is unique.

Then the anisotropic part can be further split into two parts: double couple (DC) and compensated linear vector dipole (CLVD). This tensor split is non-unique, which means there are many other ways of splitting the tensor, like two DC, one DC and two CLVD.

$$\begin{bmatrix}\lambda_1' & 0 & 0\\ 0 & \lambda_2' & 0\\ 0 & 0 & \lambda_3'\end{bmatrix} = \begin{bmatrix}\lambda_1' + \lambda_3'/2 & 0 & 0\\ 0 & -\lambda_1' - \lambda_3'/2 & 0\\ 0 & 0 & 0\end{bmatrix} + \begin{bmatrix}-\lambda_3'/2 & 0 & 0\\ 0 & -\lambda_3'/2 & 0\\ 0 & 0 & \lambda_3'\end{bmatrix}$$

Anisotropic Moment Tensor DC CLVD

We use the parameter $\varepsilon = \frac{\lambda_3'}{\lambda_1'}$ to estimate the component of non-double-couple mechanisms. According to the Harvard Global Centroid Moment Tensor Catalog, only 4 percent of all natural earthquakes have$|\varepsilon| > 0.3$ (Stein and Wysession, 2003). Hence, natural earthquakes are considered to be predominantly double-couple.

The moment tensor of Mode I cracking can be decomposed in the following way:

$$M = \begin{bmatrix} \lambda & 0 & 0 \\ 0 & \lambda & 0 \\ 0 & 0 & \lambda + 2\mu \end{bmatrix} = \begin{bmatrix} E & 0 & 0 \\ 0 & E & 0 \\ 0 & 0 & E \end{bmatrix} + \begin{bmatrix} -2/3\mu & 0 & 0 \\ 0 & -2/3\mu & 0 \\ 0 & 0 & 4/3\mu \end{bmatrix}$$

Here, λ is the Lame's first constant; μ is the shear modulus. The Mode I cracking can be decomposed into an isotropic component and a CLVD component, but there is no double couple component for this style of brittle fracture. Double couple components only appear with shearing mechanisms.

The moment tensors inverted for this particular experiment were all decomposed and the percentage of each component are listed in Figure 12 along with the full moment tensor using the method provide by (Vavryčuk, 2001).

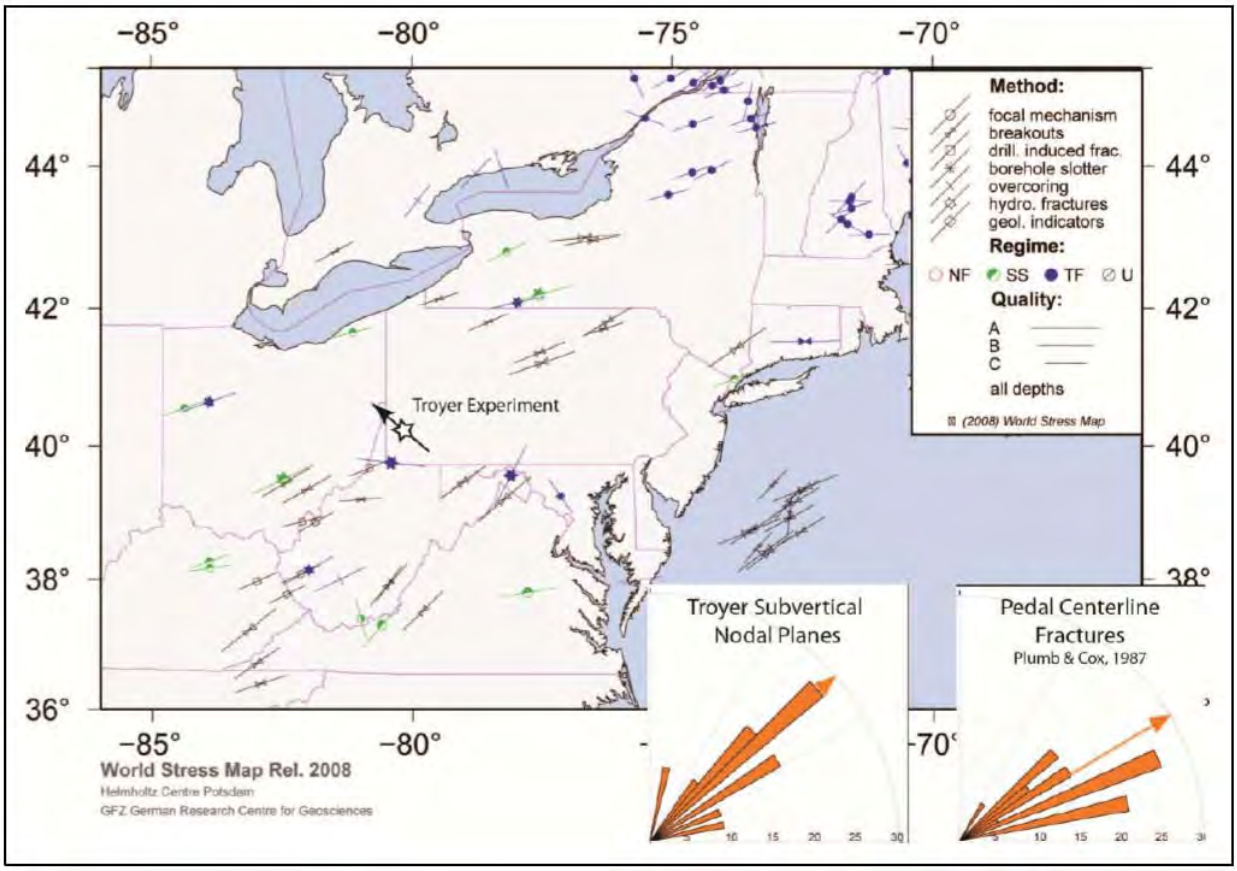

Figure 2, the location of the Troyer experiment (star) located on a map of contemporary tectonic stress in the northeastern USA and southeast Canada (source: World Stress Map project). The direction of the Troyer laterals is shown by a heavy arrow pointing N50W. The orientation of the maximum horizontal stress (S_{Hmax} which is generally ENE) is shown along with rose diagrams of the strike of subvertical nodal planes (source: Microseismic Inc.) and the strike of drilling induced pedal centerline fractures; source: (Plumb and Cox, 1987).

The Troyer Microseismic Experiment Overview

The Troyer microseismic experiment was managed by Range Resources Inc. from a well pad (i.e., the Troyer) in Washington County, PA. The experiment consisted of an array of five laterals known as the Troyer 2H, 3H, 10H, and 11H plus an observation well. Each lateral was drilled N50°W which is at least 20° from the average direction of the least horizontal stress (S_{hmin}) across the Appalachian Basin (Figure 2). The idea is that the growth of a stimulated reservoir volume favors the direction of the maximum contemporary tectonic stress (S_{Hmax}) which is to the ENE in eastern North America.

Microseismic Inc. was engaged to lay out a star surface array of geophones (Figure 3). Schlumberger was engaged to insert an array of accelerometers in the horizontal section of the observation well (Figure 4). Four wells were stimulated in a sequence that alternated between the wells starting in the toe section of each well. Ultimately, more than a dozen stages were stimulated within each well.

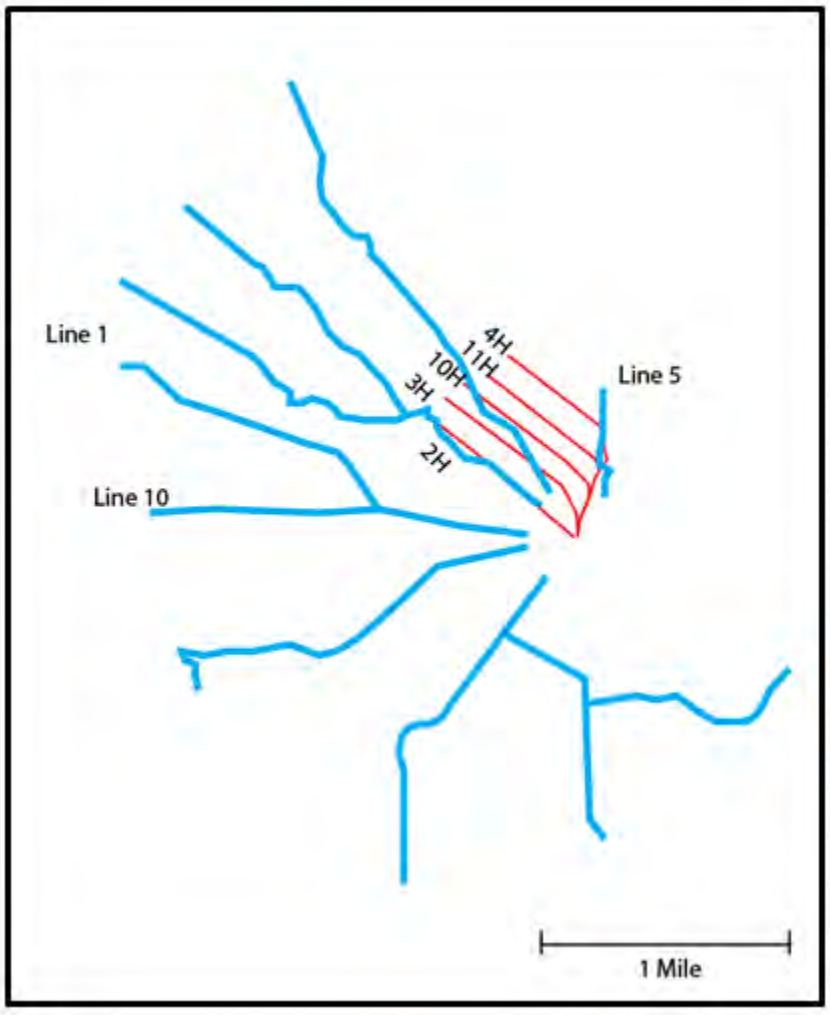

Figure 3, Surface microseismic geophone array and trajectory of stimulated wells, adapted from Microseismic Inc. report presentation.

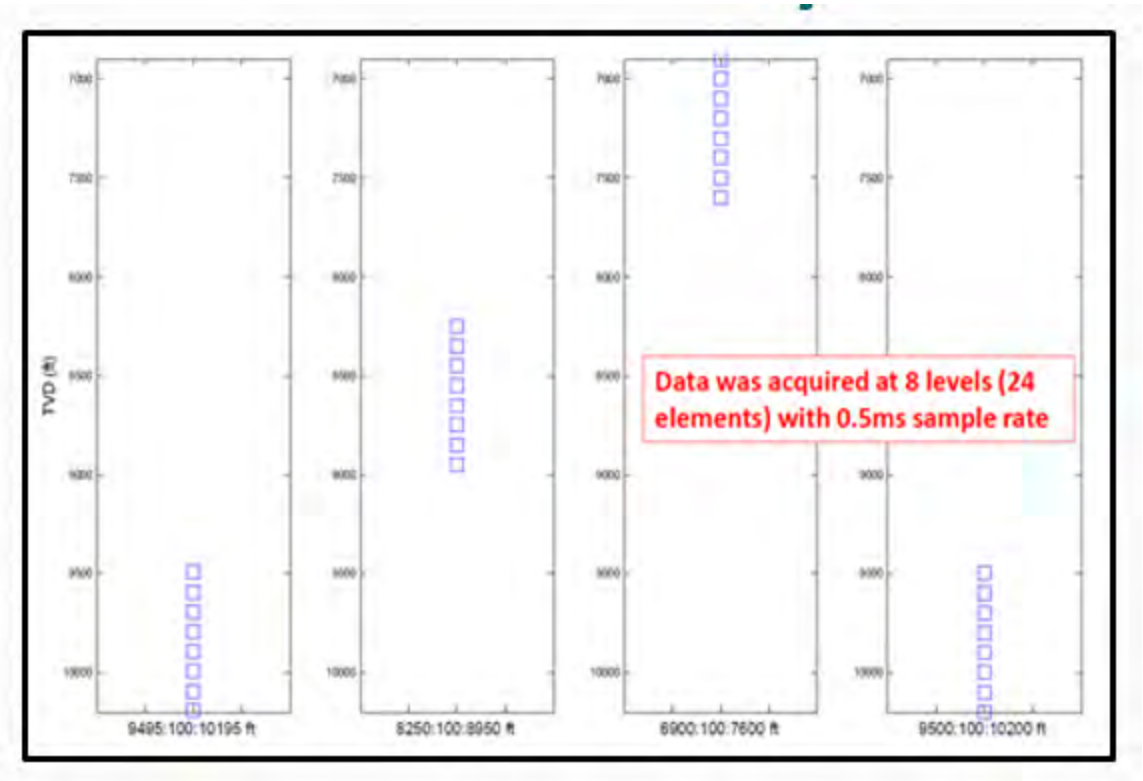

Figure 4, Downhole microseismic geophone array used by Schlumberger. 8 3-component geophones slide back and forth to get closest to the events. Only the direction of one component along the wellbore direction is fixed. The other two components can rotate perpendicular to the wellbore direction.

Analysis of the Microseismic Seismograms

The raw data were recorded in SEGY format, which is the standard recording format used in the exploration geophysics industry. By plotting some of the largest events' seismograms, we have a quick overview of the microseismic events recorded in this experiment.

Since Microseismic Inc. only used 1 component geophones (vertical, orthogonal to the surface), it does not show the SH wave component in the record. However, in Figure 4, we can still pick up the P wave arrival and S wave arrival. Each array leg is laid out from near the wellbore to farther away. Therefore, we expect a hyperbolic travel-time curve, which is exactly what is seen in Figure 5. The S wave closer to the well site is not well shown because the ray paths are mostly straight upward from the source towards the surface. We observe the polarity reversal of P wave first motion on the seismogram directly (Figure 6).

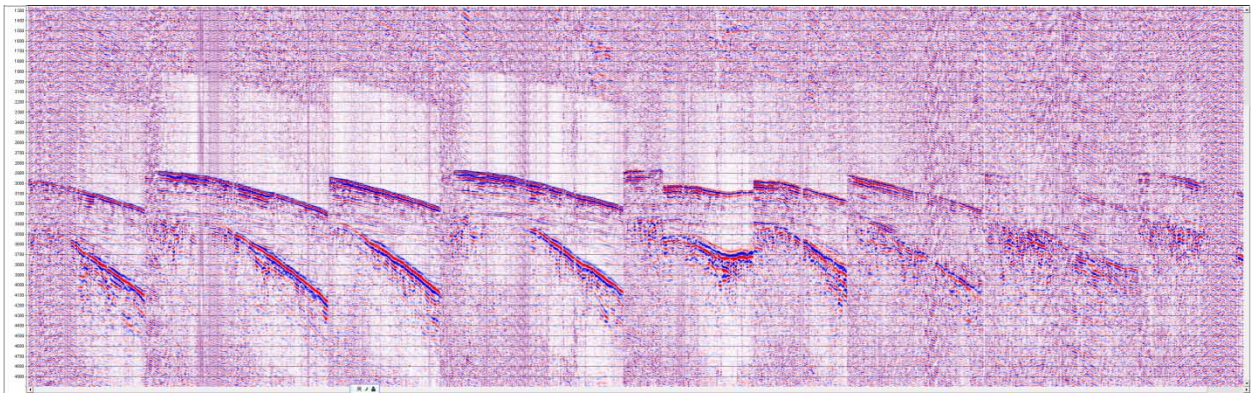

Figure 5, surface microseismic record showing one microseismic event; the first strong reflector is the P wave and the second one is S wave. There are multiple reflections of P wave, which might potentially be used to model the reflection of seismic rays on Onondaga and Tully limestone interfaces.

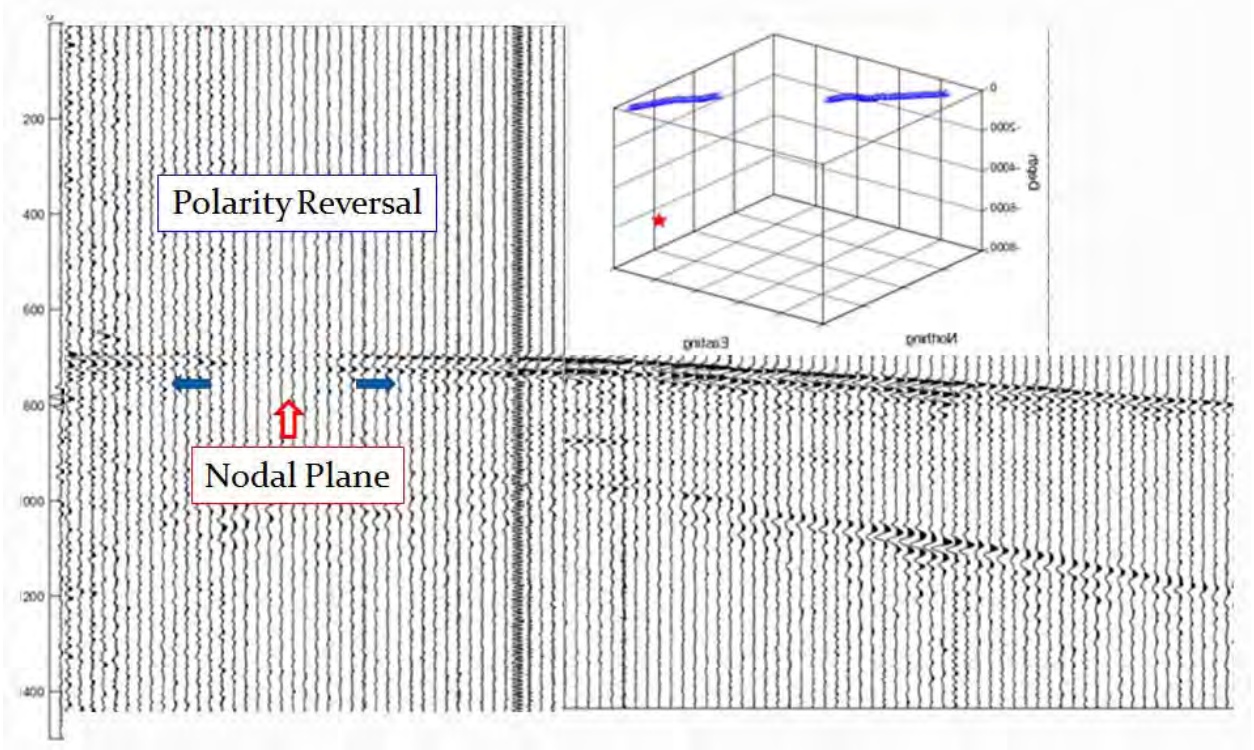

Figure 6, seismogram showing the polarity reversal of P wave of one event. The relative location of geophone traces and event location is shown in the picture on the upper right.

Observation of the wave form is clearer with the downhole array because it uses 3 component geophones. We can identify P wave and S wave arrival confidently (Figure 7). Although the azimuthal coverage is very limited with the downhole array, it is still possible to see the polarity reversal on the seismograms, as for example in Figure 6 where we can see the change of amplitude of P and S waves as we go from the left to the right, which is characteristic of P and S wave radiation patterns from one microseismic event event.

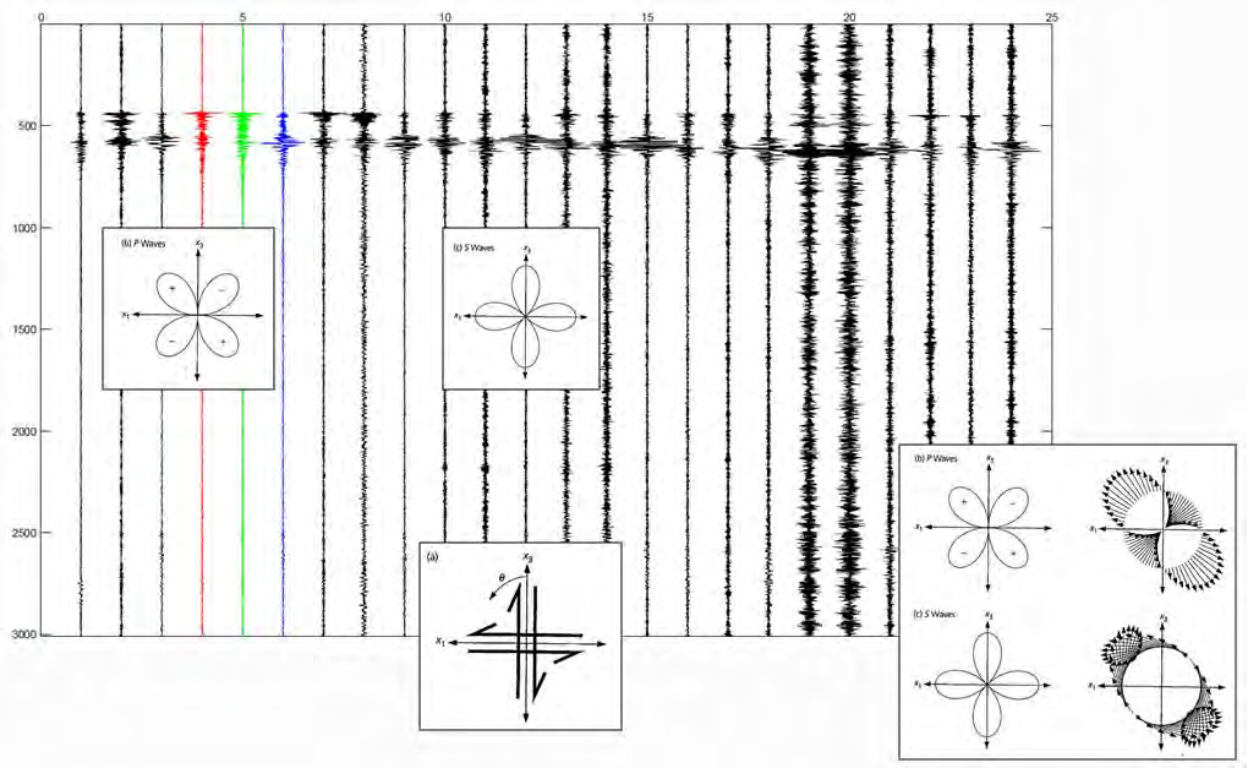

Figure 7, Downhole microseismic seismogram showing the polarity reversal of one event. Each 3 component of one geophone is put together. We did not do the rotation. But the change of amplitude of P and S wave is still apparent.

Aside from the difference in the waveforms, another important difference between the surface and downhole data is the frequency of the seismic data. Due to wave attenuation, the high frequency components are quickly filtered out during seismic wave propagation through several thousand feet of rock in traveling to the surface. On Figure 8, we can see that the highest signal-to-noise ratio for surface microseismic data falls in the 20Hz range while that of the down hole data falls within the 200Hz range. Although the downhole instruments recorded acceleration instead of velocity, which naturally will have more high frequency component, the differences in frequency components are apparent.

High frequency data masks picking P and S wave first motion data for the moment tensor inversion based on (Eisner et al., 2011). The high frequency portion of the wave spectrum is also affected by heterogeneity and anisotropy of the transport medium (i.e., rocks) more so than low frequency signals. However, this also provides a chance of looking into the petrophysical properties of the medium. Since the seismic ray paths are mostly within the gas shale formation for the downhole data (Marcellus in this experiment), this might provide valuable information regarding the anisotropy (fracture distribution) in the gas shale. Shear wave splitting is also a possibility for further study.

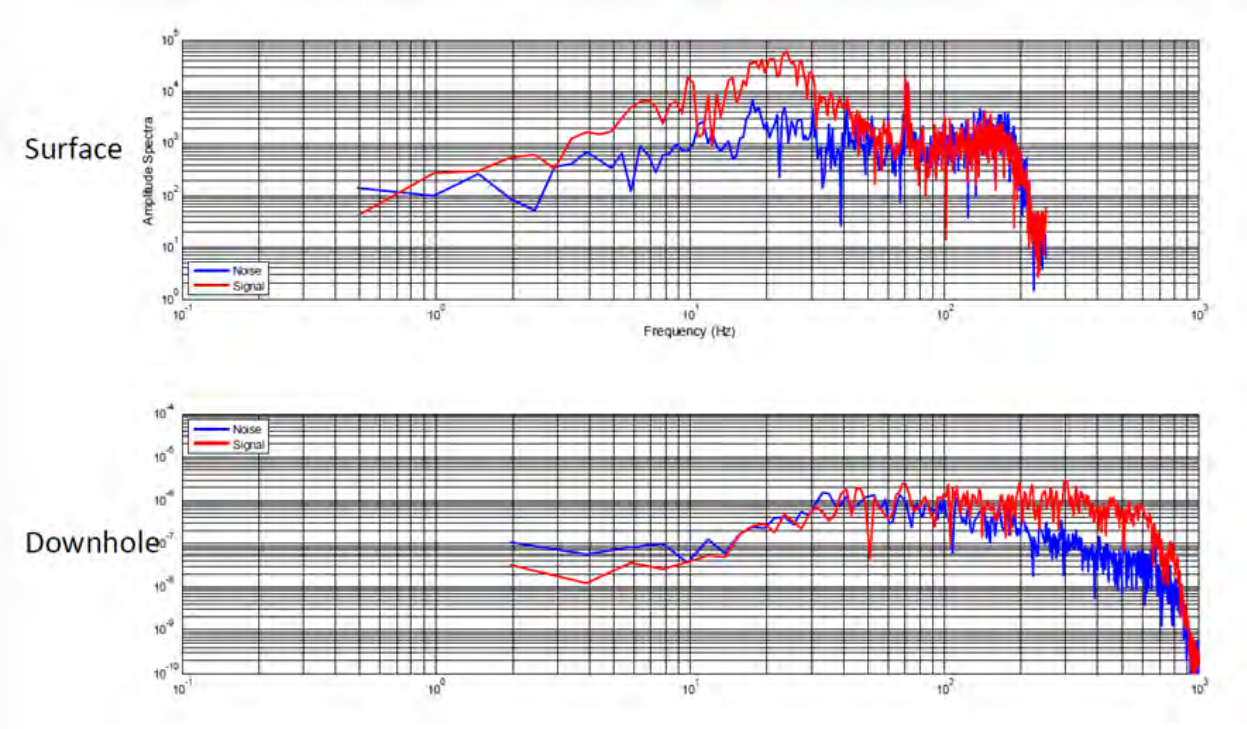

Figure 8, comparison of the spectrum of surface and downhole data; the red curve is the signal and blue is the background noise.

Microseismic Events and the Pumping Record

Schlumberger identified more than 16,000 events using a cutoff signal noise ratio of 3, while Microseismic Inc. identified less than 2,000 events. The difference between the surface star array and the downhole array is largely one of detection limit. Some events take place at less than 600 ft. (i.e. the distance between laterals) from the accelerometers of the Schlumberger subsurface array. The surface geophones on the star array were greater than 6000 ft. away from the microseismic events. Naturally, smaller events could be detected by the subsurface array.

Another important distinction between the two arrays is that the velocity model for the surface array is time-invariant largely because the ray paths immediately travel upward out of the stimulated zone and into undisturbed rock. An array in the horizontal portion of an observation well is sampling events whose ray paths must travel through a rock volume with changing properties because it is being stimulated. One presumes that a velocity model for such a situation is time dependent but more so for the Schlumberger records.

A typical stimulation is illustrated with a pair of curves showing pressure and slurry rate versus time (Figure 9). The surface pressure at breakdown is about 9000 psi. After breakdown the slurry rate is gradually increased to reach 72bbl/min about 45 minutes after breakdown. The evolution of microseismic events more closely follows the slurry rate with microseismic events reaching their maximum lateral spread once the slurry rate has reached a maximum of 72bbl/min (Figure 10).

In a typical frac job, the proppant will be changed in the middle of pumping procedure from a finer 40/70 mix to a 20/40 mix. Higher concentration of proppant will increase the hydrostatic pressure of the mud. Therefore, the decrease of surface pressure shown in Figure 9 doesn't necessarily mean that the downhole pressure has decreased. To get the true downhole pressure, we need to add the weight of the slurry in the wellbore, which generally is not readily available.

Some researchers tried to read the ISIP (Instantaneous Shut In Pressure) to get the minimum principle stress (S_{hmin} in this particular experiment) (Vermylen and Zoback, 2011). There may be concern about the water hammer effect at the end of the pumping. As a result, the breakdown pressure and fracture propagation pressure might be a better indicator of the in-situ stress.

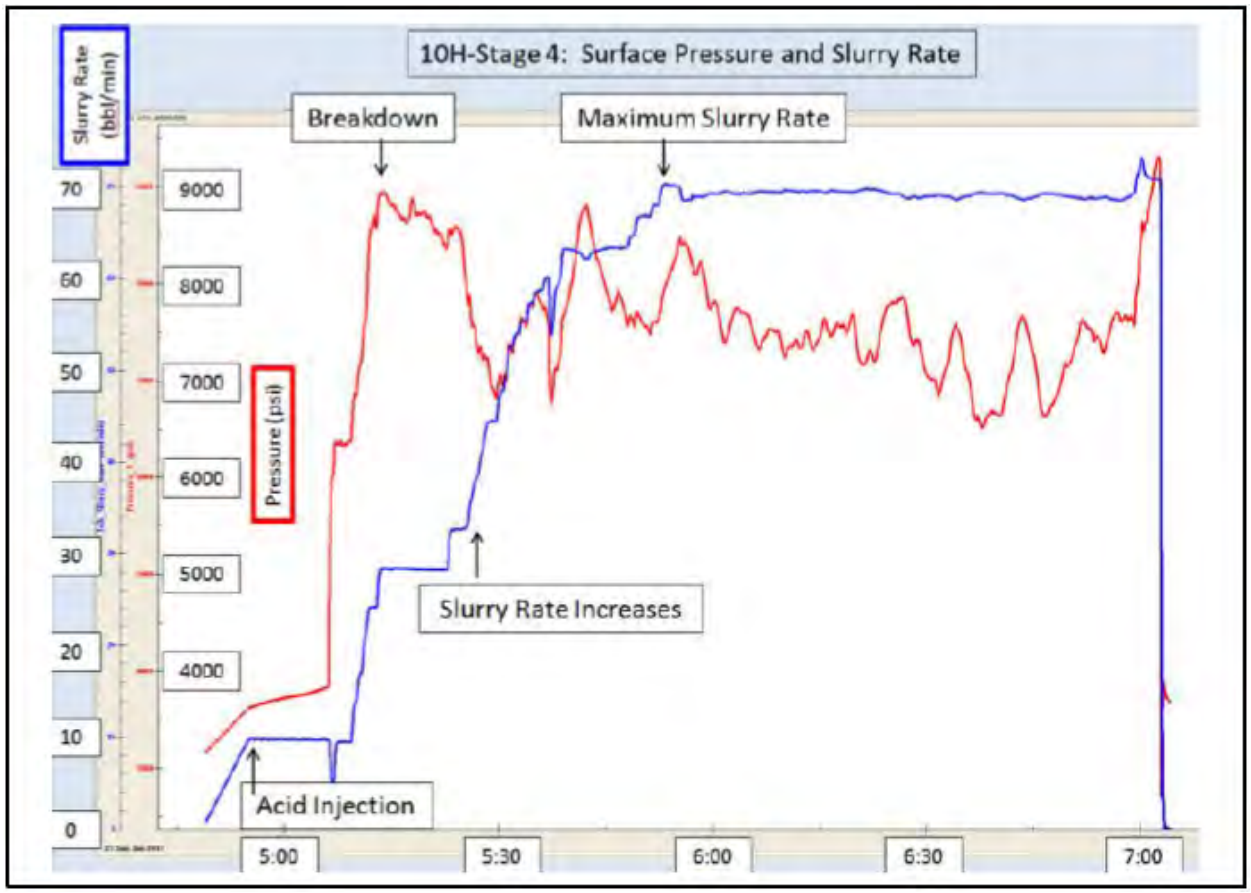

Figure 9, Surface pressure (psi) and slurry rate (bbl/min) versus time (hr) for the Troyer 10- stage 4 stimulation.

Schlumberger sorted their stimulation data by stage and provided a record for 16,721 microseismic events. The distribution of microseismic events shows maximum growth of the stimulated reservoir volume toward the direction of S_{Hmax} in eastern North America (Figure 2). Not all stages were equally well stimulated with three zones separated by stimulated volumes containing very few microseismic events (Figure 11). The location of microseismic events in the Microseismic Inc. presentations of the Troyer experiment show the same development of three zones with the growth of the stimulated reservoir volume pointing about N47°E which is not at right angles to Troyer laterals nor is the direction of growth toward the regional S_{Hmax} of the contemporary tectonic stress field.

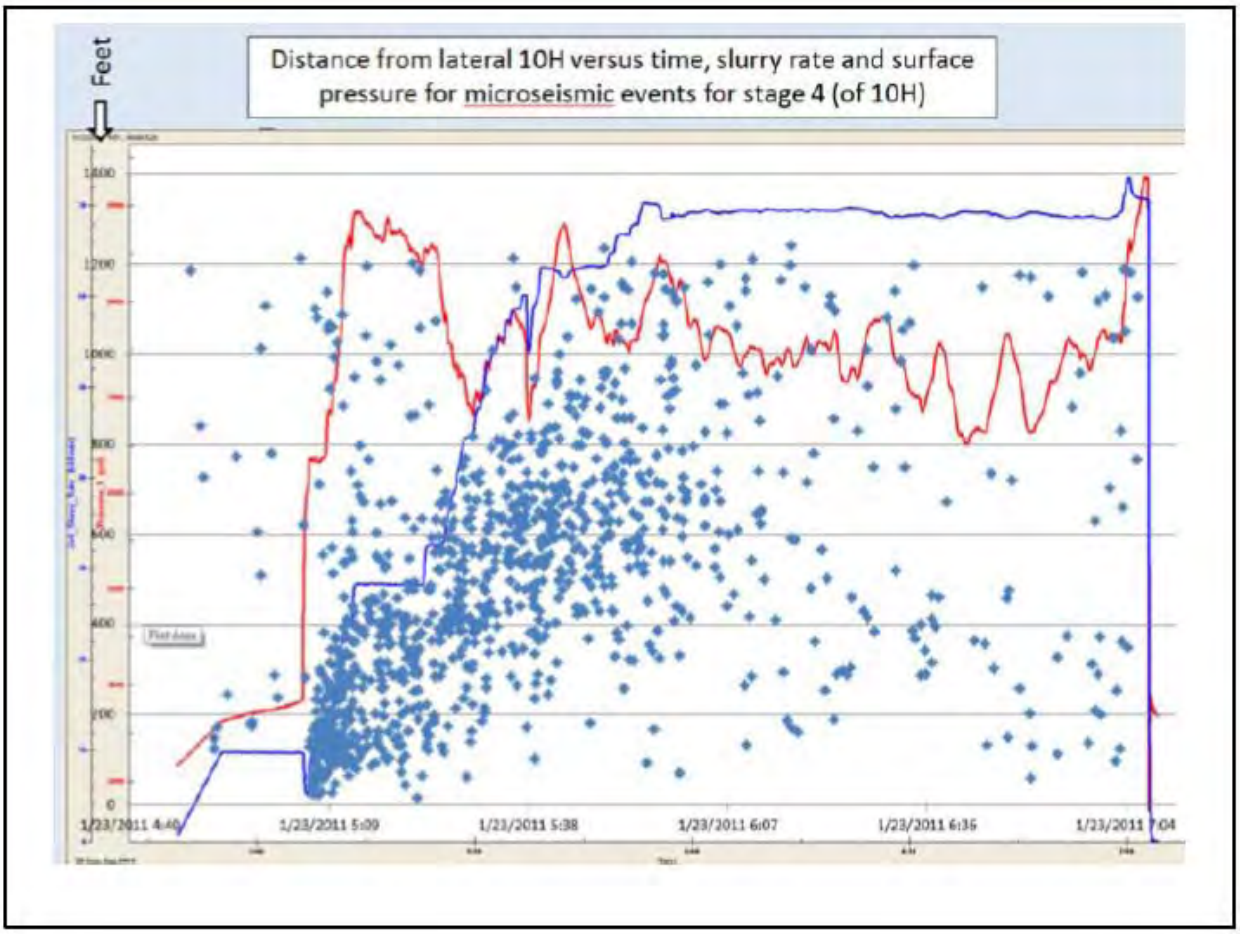

Figure 10, Distance (ft) for microseismic events versus time (hr) for the Troyer 10-stage 4 stimulation.

One interesting phenomenon shown in Figure 10 is that, microseismic events are detected almost instantaneously after pumping. Given the distance of the events from the wellbore, there is no chance that these events are actually opened by the high pressure frac fluid. Intuitively, tensile cracking caused by the injection of fluid shouldn't exceed the speed of fluid migration.

One important feature observed by the microseismic services companies (for example, Microseismic Inc.) is called Stimulated Reservoir Volume (SRV) (Mayerhofer et al., 2008a), which means the volume stimulated by the injected frac fluid. Currently the method of estimating the SRV is only based on the location of the microseismic events (i.e. wherever there is microseismic event, it falls within the SRV).

If some events are not really opened by the frac fluid, there is a chance that they are not directly connected with the gas flow pathways created by the frac fluid and supported by the proppant. Therefore, their contribution to the production must be different from those artificially created hydraulic fractures.

The SRV should be further classified according to the source mechanism to get a better estimate of the completion results.

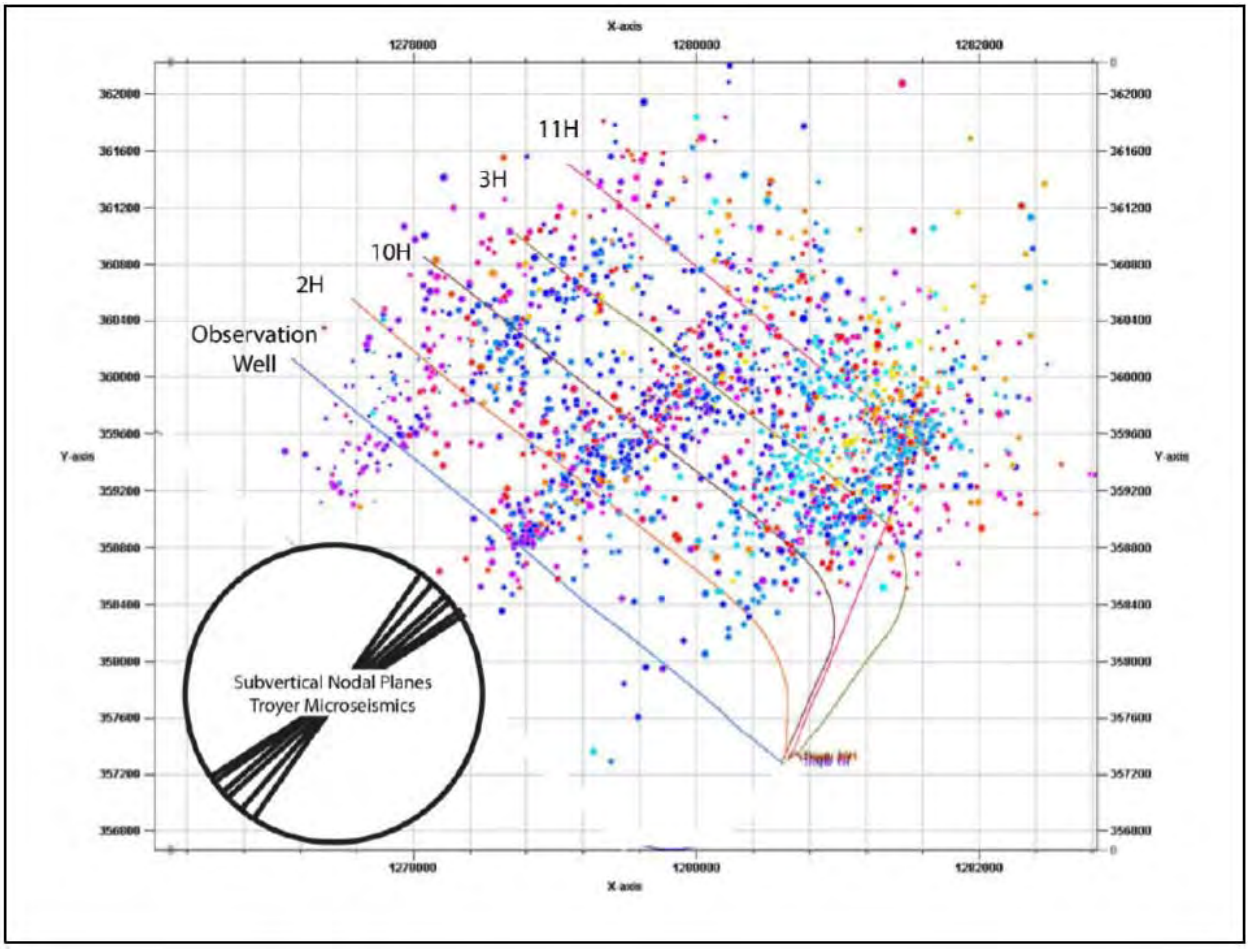

Figure 11, Microseismic events located by the Schlumberger down-hole accelerometers. These data are filtered leaving only those events showing a moment magnitude > -1.224. The orientations of six subvertical nodal planes for microseismic focal mechanisms are shown in the form of a rose diagram. These data were provided by Microseismic Inc.

Analysis of Microseismic Moment Tensor of Troyer Experiment

The moment tensor results inverted by Microseismic Inc. are presented in Figure 12 and 13 on a lower hemisphere stereonet plot (beach ball). While doing the moment tensor inversion, we first run the full moment tensor inversion to get the results in Figure 12. Then an additional constraint of zero volumetric component was put on the inversion procedure to get the results in Figure 13.

Only 34 out of the largest 50 events were clear enough to be seen on the surface microseismic seismogram. There are clear waveforms on the surface seismograms at all without stacking to reduce the noise. This is an indication that the deeper wells drilled in the gas shale plays will be detected using arrays on the surface.

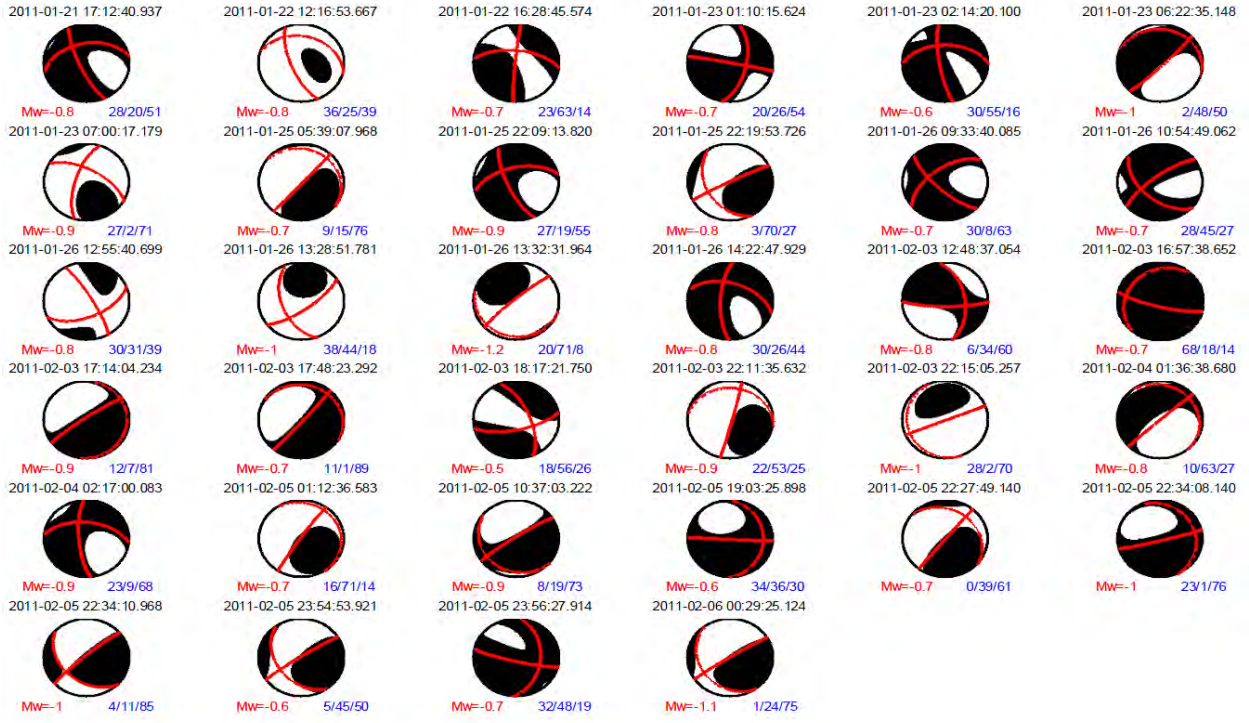

Figure 12, full moment tensor results plotted on a lower hemisphere projection with nodal planes marked in red. The magnitude and three moment tensor components (Volumetric/CLVD/Double Couple) listed below the beach ball.

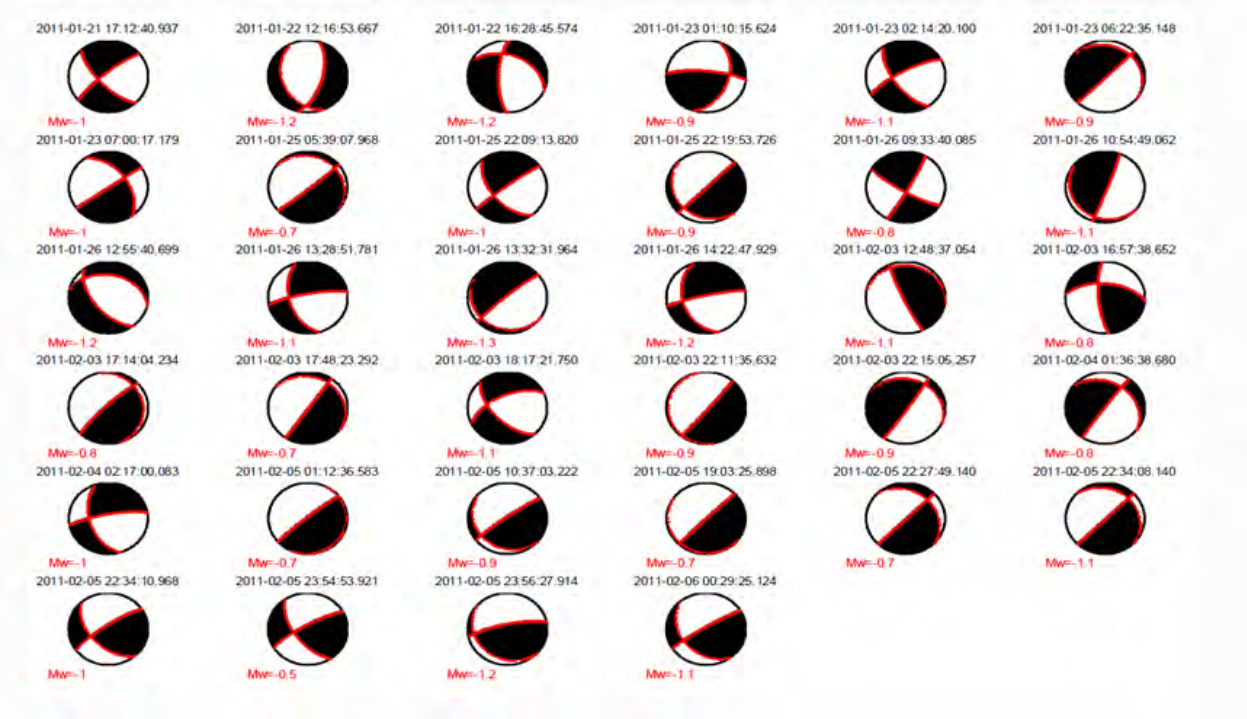

Figure 13, double couple moment tensor plotted on a lower hemisphere projection with nodal planes marked in red. The magnitude and three moment tensor components (Volumetric/CLVD/Double Couple) listed below the beach ball.

One important objective of this project is to the distribution of the events caused by tensile opening relative to shearing of pre-existing natural fractures. To develop a criterion for classifying the event category, we did a theoretical calculation based some measured rock properties (Jaeger et al., 2007).

In Figure 14, we plotted the inverted events on a ternary plot based on the percentage of each component. Most of the events are near that region, which could be interpreted as a combination of shearing and opening mode fracturing. The events with very large CLVD components might be a result of failing to resolve the isotropic component on the moment tensor inversion process. Another possibility is that two nearby double couple events combined might look like a CLVD event.

On the other hand, the events with a large double couple component might actually be pure double couple. Here, the noise in the data was amplified during the inversion process.

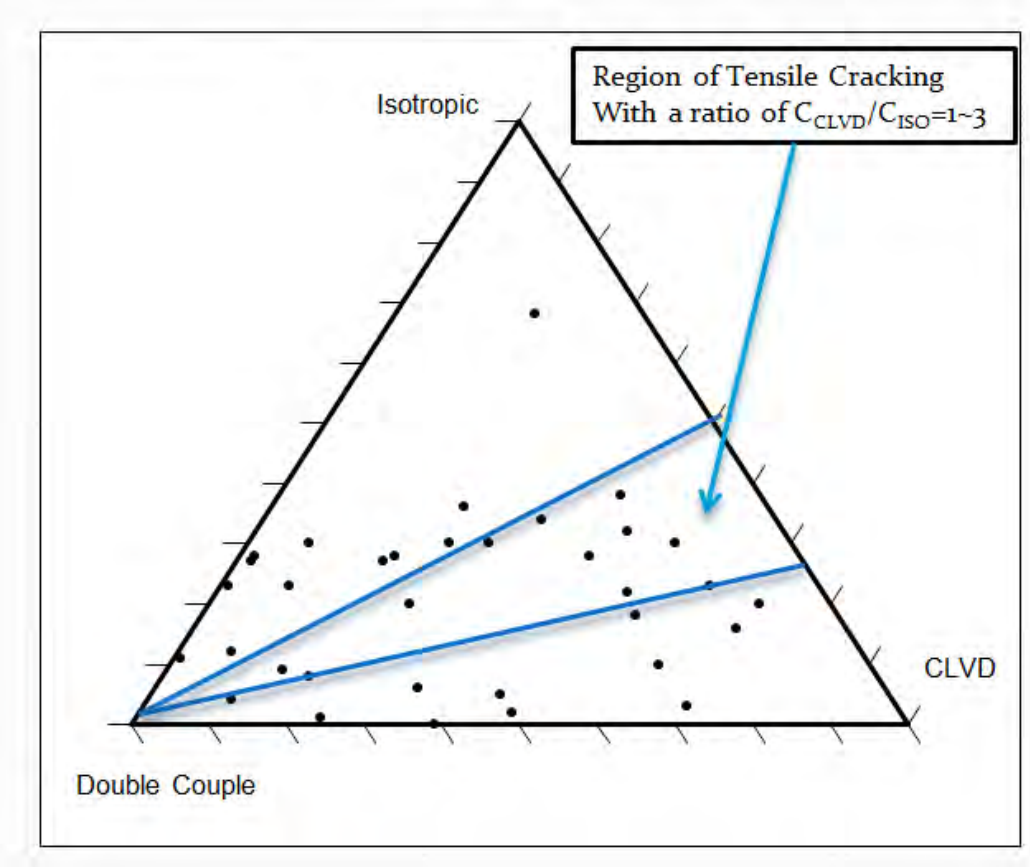

Figure 14, Ternary plot of moment tensor components. The region contained by the two blue lines is the region of tensile cracking, with a ratio of CLVD/ISO component of 1-3 based on the theoretical data calculated above.

Brittle Structures Observed in Adjacent Wells

The vertical sections of a number of wells (i.e., the Hardie, Paxton, and Stewart Nancy) in the vicinity of the Troyer pad were logged with dipole sonic and FMI tools, both of which are capable of detecting a fracture fabric either directly (FMI) or indirectly (dipole sonic). Fractures in these wells included faults and open joints (Figure 15). Subvertical (dip>70°) fractures are classified by Schlumberger as open joints (stars in Figure 15). Brittle fractures interpreted as faults all have a dip less than 60°. Several joint sets appear in the subsurface near the Troyer pad including J_1 joints in the Stewart Nancy well with a strike of ENE (i.e.N52°). Poles to J_2 joints are seen in all three wells with a strike of approximately 310°. The Hardie well also has a joint set striking NNE.

Faults appear in all three wells (squares in Figure 15). Poles to low-angle faults cluster in two groups with faults dipping off to the NW and SE (i.e., average strike about N39°E) with dips of 45° or less. The slip on these faults is unknown although a good number of these faults have a low enough dip so that slip might have been reverse rather than normal.

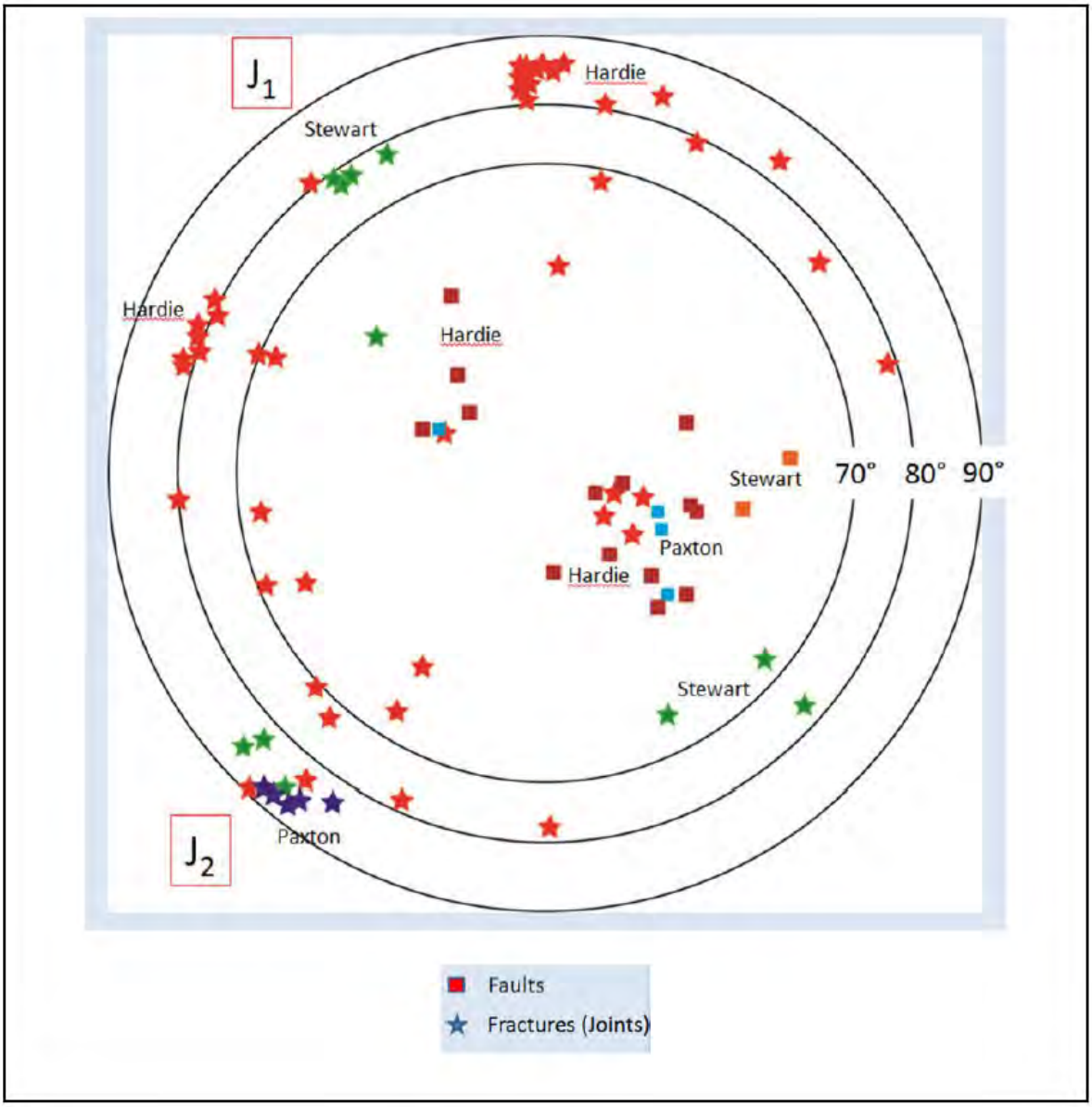

Figure 15. Lower hemisphere projection of the poles to fractures (open joints) and faults as they appear and have been interpreted by Schlumberger FMI logs run in adjacent wells: Hardie Unit #1, Paxton Issac Unit #1, and Stewart Nancy #4.

The dipole sonic log from the Steward Nancy well detected shear wave anisotropy (Figure 16). The fast horizontal velocity was to the NE (i.e. approximately N52°E). While this sonic anisotropy appears not to be subparallel to the strike of the low angle faults, the average fast shear wave is within a degree of the average strike of the J_1 joints seen in the Stewart Nancy well.

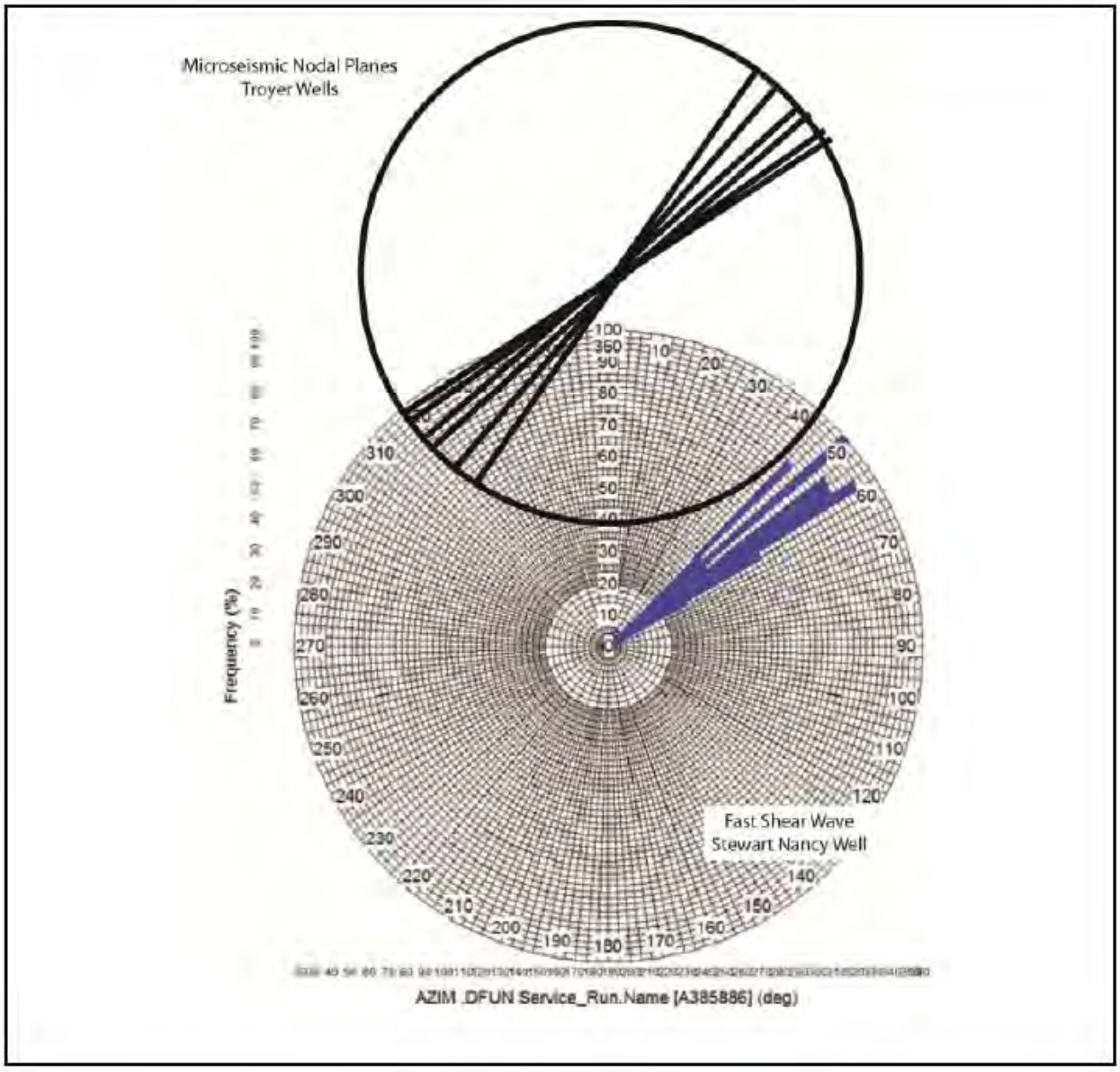

Figure 16. Orientation of the fast shear wave in the Marcellus Shale of the Stewart Nancy #4. The orientations of subvertical nodal planes for microseismic focal mechanisms are shown in the form of a rose diagram (top). These data were provided by Microseismic Inc. and plotted as focal mechanisms in Figure 13.

Interpretation

The distribution of brittle structures in Appalachian Basin gas shales includes subvertical planes which are either joints or strike-slip faults with a subhorizontal slip vector (i.e. slip vector parallel to strike). No vertical faults were observed in EGSP core (Cliffs Minerals, 1982). Fractures with planes dipping between 20° and 70° are commonly faults with a slip vector normal to the strike of the fracture. Slickensided

surfaces in EGSP core from the Marcellus are examples (Evans, 1994). The only subhorizontal fractures known in gas shales of the Appalachian Basin are populations of horizontal microcracks developed during catagenesis (Lash and Engelder, 2005).

Both faults and joints are found in the vicinity of the Troyer pad while subhorizontal fractures were not observed. The question is whether the subvertical nodal planes striking NE (i.e. average strike= N47.5°E) revealed by the moment tensors of the Troyer microseismic events delineate the opening of pre-existing joints, slip on very steep faults or the rupture of intact Marcellus by hydraulic splitting. Regardless, a vertical plane with dip-slip motion would seem to be driven by a gravitational stress nearly parallel to the fracture plane. There are other examples of microseismic activity driven by a regional stress nearly parallel with the rupture plane. In the Carthage Cotton Valley gas field, east Texas, fault planes of composite source mechanisms were close to S_{Hmax} (Rutledge et al., 2004). These Texas data were reinterpreted assuming that the moment tensor was, in part, the consequences of tensile fracturing (Šílený et al., 2009). The reanalysis of the Texas data showed the presence of an additional isotropic component because the moment tensor vector did coincide with the double couple (DC) vector. If the moment tensor has a minor DC component, and the contents of the ISO component are larger than half the percentage of the CLVD, the non-DC portion of the moment tensor describes a process that approaches a tensile crack (Šílený et al., 2009).

The decomposition of the moment tensors from the Troyer experiment shows that some of those fault plane solutions with vertical nodal planes had a relatively low DC component (left column in Figure 12). However, these events have an ISO component that is less than half the percentage of the CLVD which is not necessary consistent with a tensile crack according to Sileny et. al . (2009). Some of the events with subvertical nodal planes have large percentage of the seismic moment in the DC component (Figure 12). In this regard, the behavior of the events in the Troyer experiment are different from those of the Carthage Cotton Valley gas field, east Texas where the maximum principle stress was horizontal and close to the plane of the fault but the ISO component was larger.

With a subvertical slip vector, the Troyer events are consistent with a regional stress field favoring normal faulting. In fact, the majority of stress measurements within several hundred km of the Troyer pad are consistent with normal faulting. Faulting with a subvertical slip vector is, presumably, driven by vertical maximum principle stress which is gravitational. However, the locations of the P and T-axes with plunges of about 45° for the Troyer events are not consistent with a gravitationally induced stress (Figure 13). This makes the events with subvertical nodal planes more difficult to understand although not inconsistent with the microseismic events from the Carthage Cotton Valley gas field, east Texas, where the maximum compressive stress was close to the slip plane. The interpretation of the east Texas events was that they were the result of fluid invading pre-existing fractures (Rutledge et al., 2004).

If the east Texas experience applied to Troyer events, then there should be evidence for pre-existing fractures in the Marcellus of Washington County, PA. Based on brittle structures observed on FMI logs from three nearby wells, the strike of the subvertical nodal planes are within 5° of a J_1 joint set in the Stewart Nancy #4 well (Figure 15). Presumably the fast shear wave direction of the seismic anisotropy field of the Stewart Nancy #4 was a reflection of the presence of this J_1 joint set.

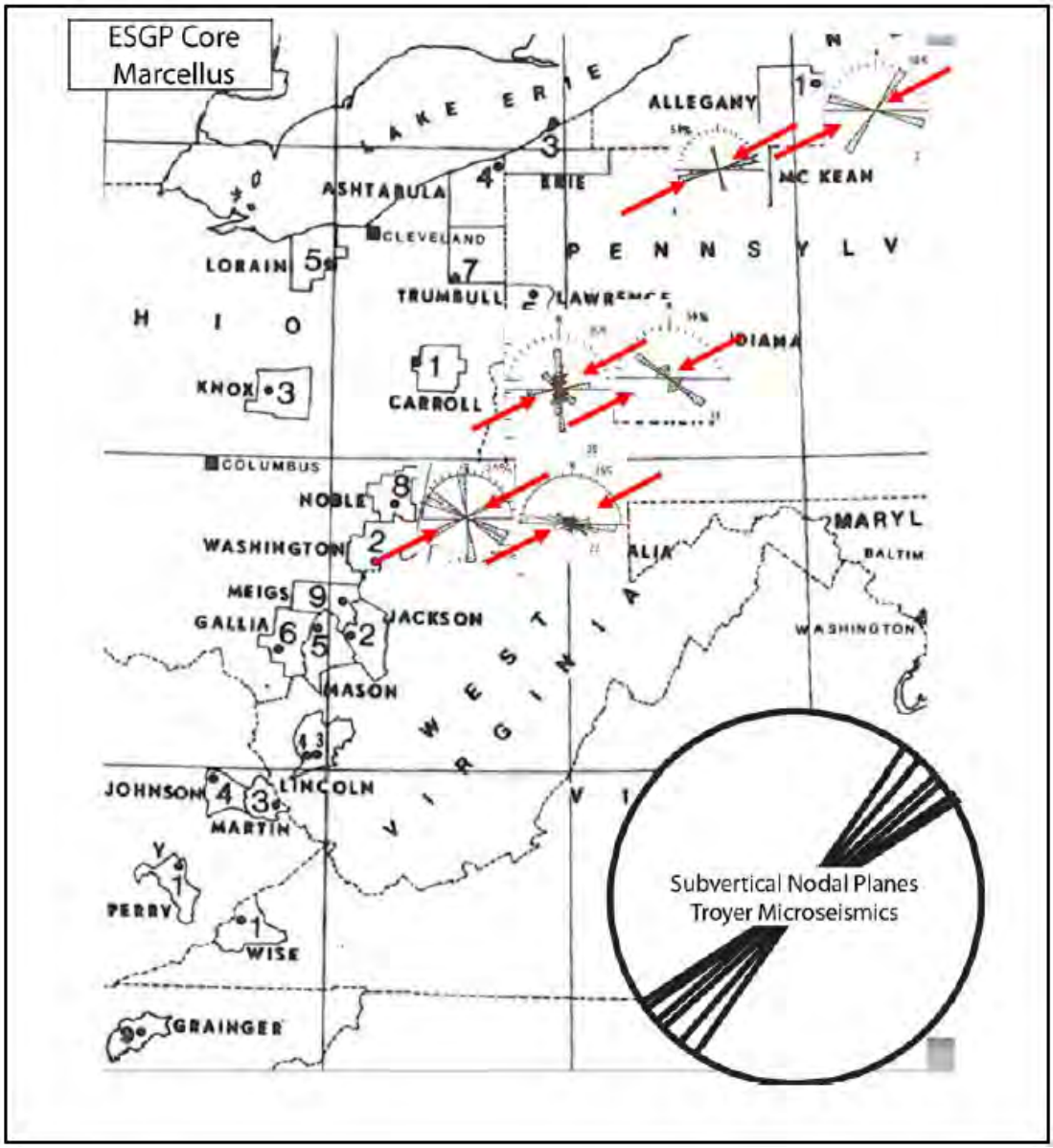

Figure 17. Rose diagram of the orientation of joints in six Marcellus cores collected by the Eastern Gas Shale Project (EGSP). Arrows denote the orientation of a J_1 joint that would have a strike of N70E. The orientations of subvertical nodal planes for microseismic focal mechanism are shown in the form of a rose diagram (lower right). These data were provided by Microseismic Inc. and plotted as focal mechanisms in Figure 13.

The J_1 joint set is a regional set found developed in late Paleozoic rocks along much of the Central and Southern Appalachian Mountains (Engelder, 2004; Engelder and Whitaker, 2006). While this joint set may appear in other rocks of the late Paleozoic, it is best developed in the black shale of the Appalachian Basin (Engelder et al., 2009; Lash and Engelder, 2009). J_1 joints in outcrop exposures of the Marcellus on both the foreland and hinterland side of the gas rich Appalachian Plateau are consistent with the hypothesis that this joint set is also present at depth in the Marcellus reservoir rocks of the Appalachian Plateau. If so, the J_1 joint set should appear in core from the deep Appalachian Plateau. The best set of core samples of the Marcellus comes from Eastern Gas Shale Project (EGSP) (Cliffs Minerals, 1982). J_1 joints are not well developed in these core samples (Figure 15). However, in four of six core samples from EGSP, candidates for J_1 joints in the Marcellus cluster between N70°E and N90°E. In all six ESGP core from the Marcellus, there are no joints within a 10° window of the average strike of the vertical nodal planes (i.e., N49°E) derived from seismic moment analyses of the Troyer wells and seen in Steward Nancy #4.

Are there structures in the vicinity of the Troyer experiment that occur in other core of the Marcellus? The Hardie Unit #1 has a joint set striking EW which correlates with a nearby EGSP well, the WVA-6 (Figure 17&18). While the J_1 joint set has traditionally been restricted to a fairly narrow range of orientations between N60E and N70E (Whitaker and Engelder, 2006), such a joint set may have a larger range of orientations. In the extreme, the J_2 joint set of the Appalachian Basin consists of several subsets and with the change in strike of the oroclinal bend of the Appalachian fold belt, the orientation of the J_2 joint may cover a range of up to 60° (Engelder and Geiser, 1980). If this is true, the orientation of the J_1 set may differ significantly across the basin.

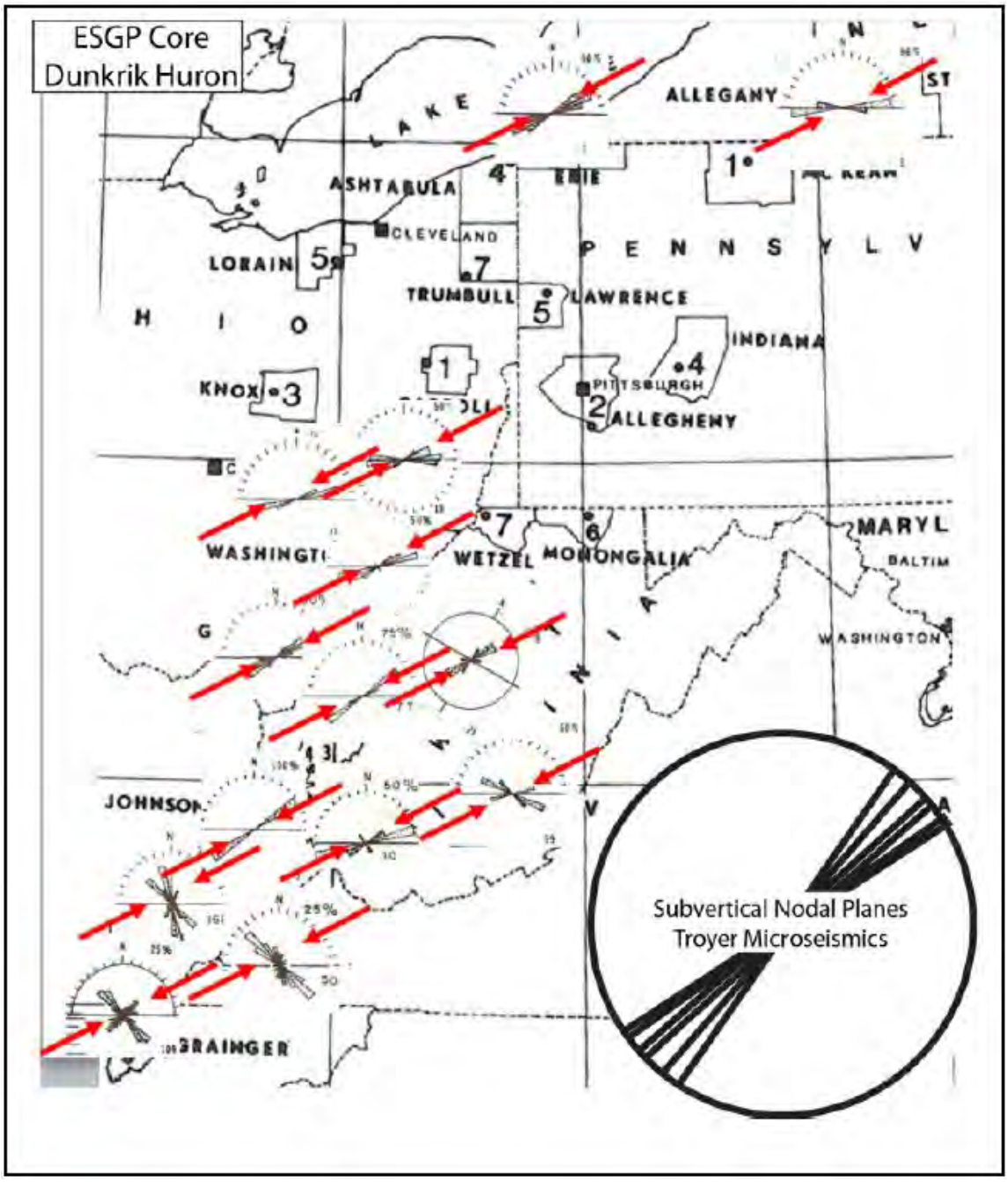

Figure 18, Rose diagrams of the orientation of joints in fourteen Dunkirk Huron cores collected by the Eastern Gas Shale Project (EGSP). Arrows denote the orientation of a J_1 joint that would have a strike of N70°E. The orientations of subvertical nodal planes for microseismic focal mechanisms are shown in the form of a rose diagram (lower right). These data were provided by Microseismic Inc. and plotted as focal mechanisms in Figure 13.

In core, the best developed J_1 joints come from the Dunkirk Huron interval of the EGSP samples (Figure 18).When comparing the orientation of the subvertical nodal planes of Troyer experiment with J_1 joints of the Dunkirk Huron interval, there is a mismatch of 10° or more. All of this is to say that the subvertical nodal planes may represent a Marcellus joint set that is significantly misaligned from the 'classic' J_1 joint set with a strike between N60°E and N70°E.

A second interpretation of subvertical nodal planes is that they are faults related to ongoing slip on Rome Trough structure. One of the earliest maps showing the orientation of the Rome Trough in Washington County PA was based on growth faulting during the rifting of Laurentia during the period spanning the deposition of Cambrian and Ordovician carbonates. The rift basin is bounded by a normal fault striking N33°E (Figure 19).

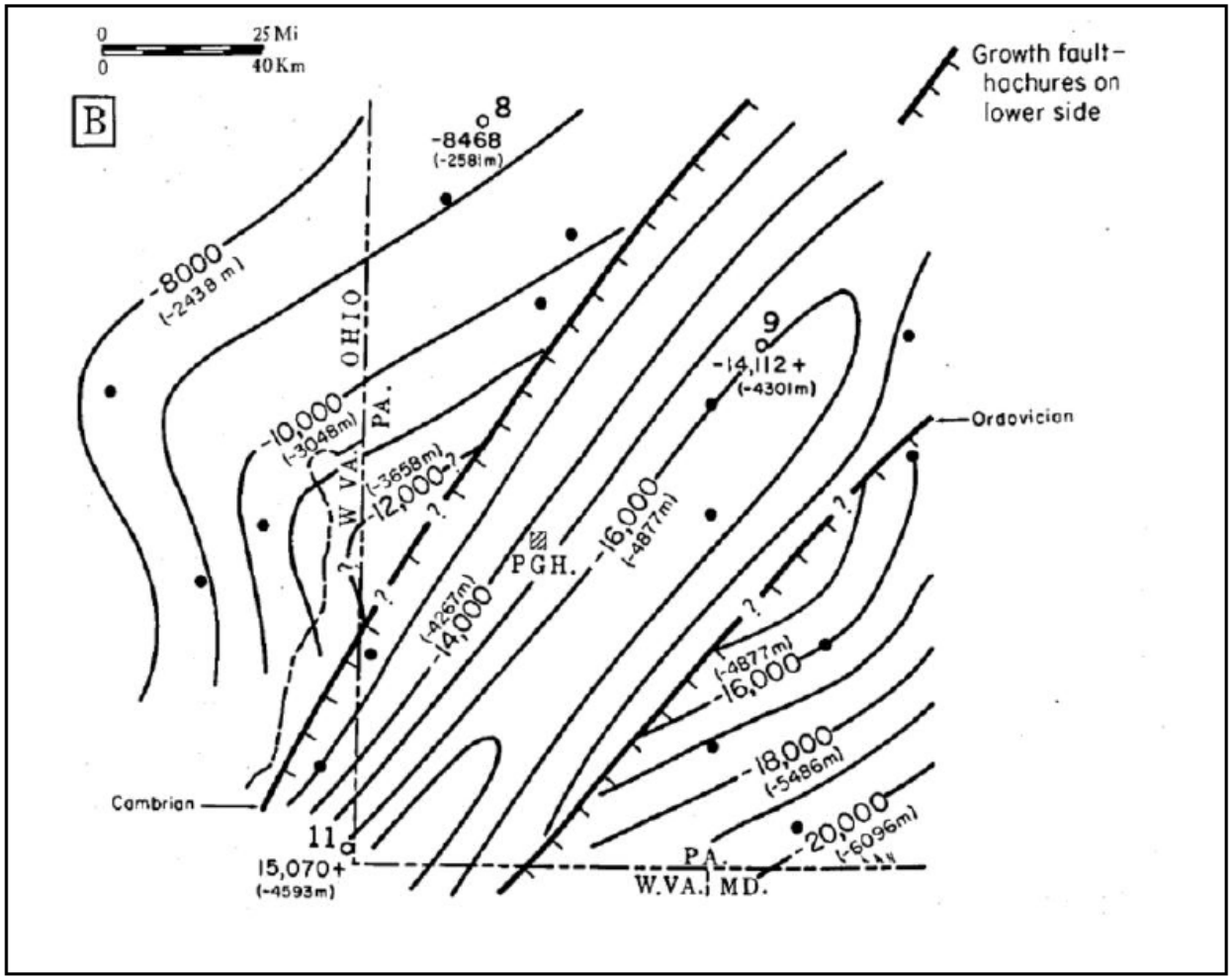

Figure 19, the orientation of the Rome Trough in the vicinity of the Troyer pad based on inferences for growth faulting from stratigraphic thickness of the Cambrian and Ordovician sections of SW PA (Wagner, 1976).

The Alleghanian folds of western PA are also known to occur over the Rome Trough system of normal faults (Figure 20). The orientation of these faults is between N30°E and N35°E. Because of the mismatch in strike between the subvertical nodal planes from the Troyer stimulation and the basement faults, it seems unlikely that the nodal planes in the Marcellus have anything to do with growth faulting which is believed to have continued through the Devonian (McDaniel, 2006). Of interest is the correlation strike between the low angle faults observed in FMI logs for wells in the vicinity of the Troyer pad (i.e. average strike about N39°E) and the general trend of the growth faults of SW PA (Figure 19).

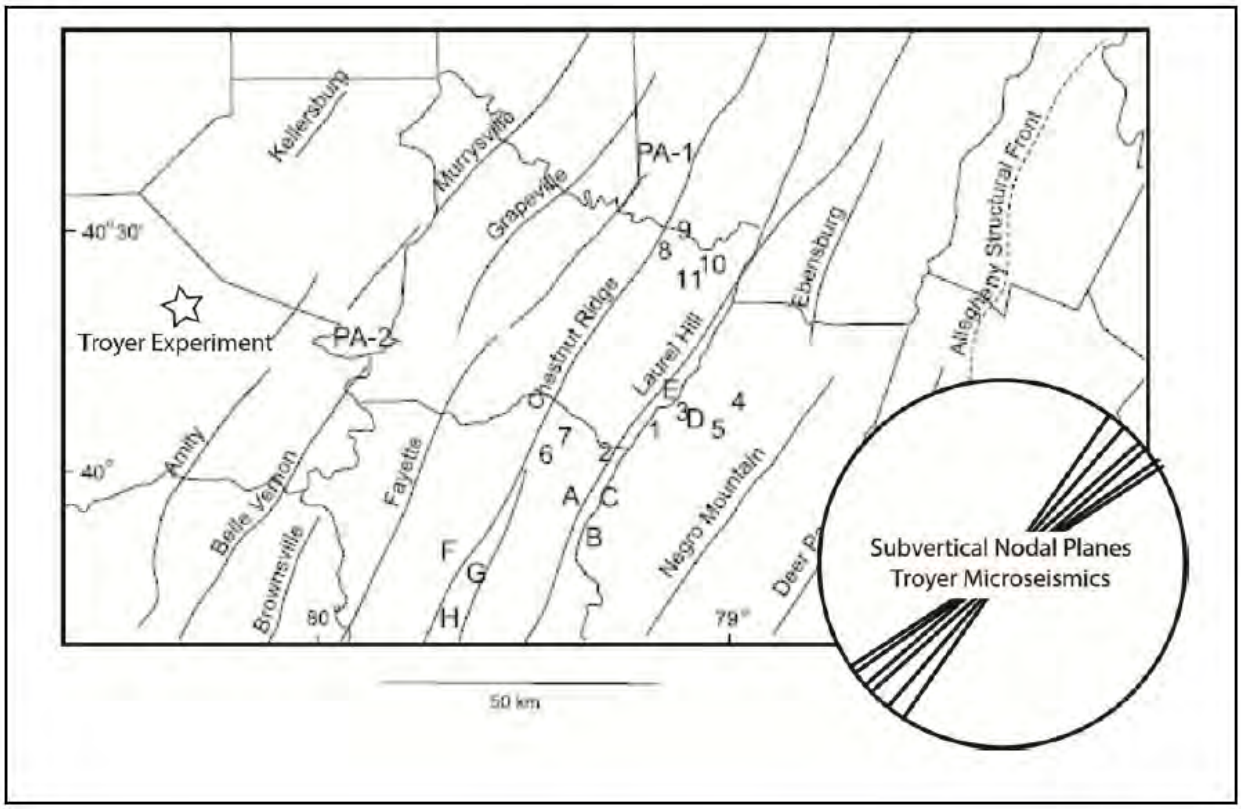

Figure 20, the folds of western PA. At least the Laurell Hill, Chestnut Ridge, and Bell Vernon anticlines are located over basement normal faults of the Rome Trough system (Scanlin and Engelder, 2003)

The mechanism for the correlation between the faults of the observation wells around the Troyer pad may be found in a model from Haper and Laughery (1979) (Figure 21). In this model, faults occur directly above a basement growth fault (Figure 21B). This mechanism is not perfect because Harper and Laughrey (1979) propose fairly steep faults consistent with normal faults in basement. It is, however, noteworthy that the average strike of the low angle faults is parallel to folds of the SW PA Appalachian Plateau. Such faults would be reverse faults of the type imaged in the core of several of the Appalachian Plateau folds (Scanlin and Engelder, 2003).

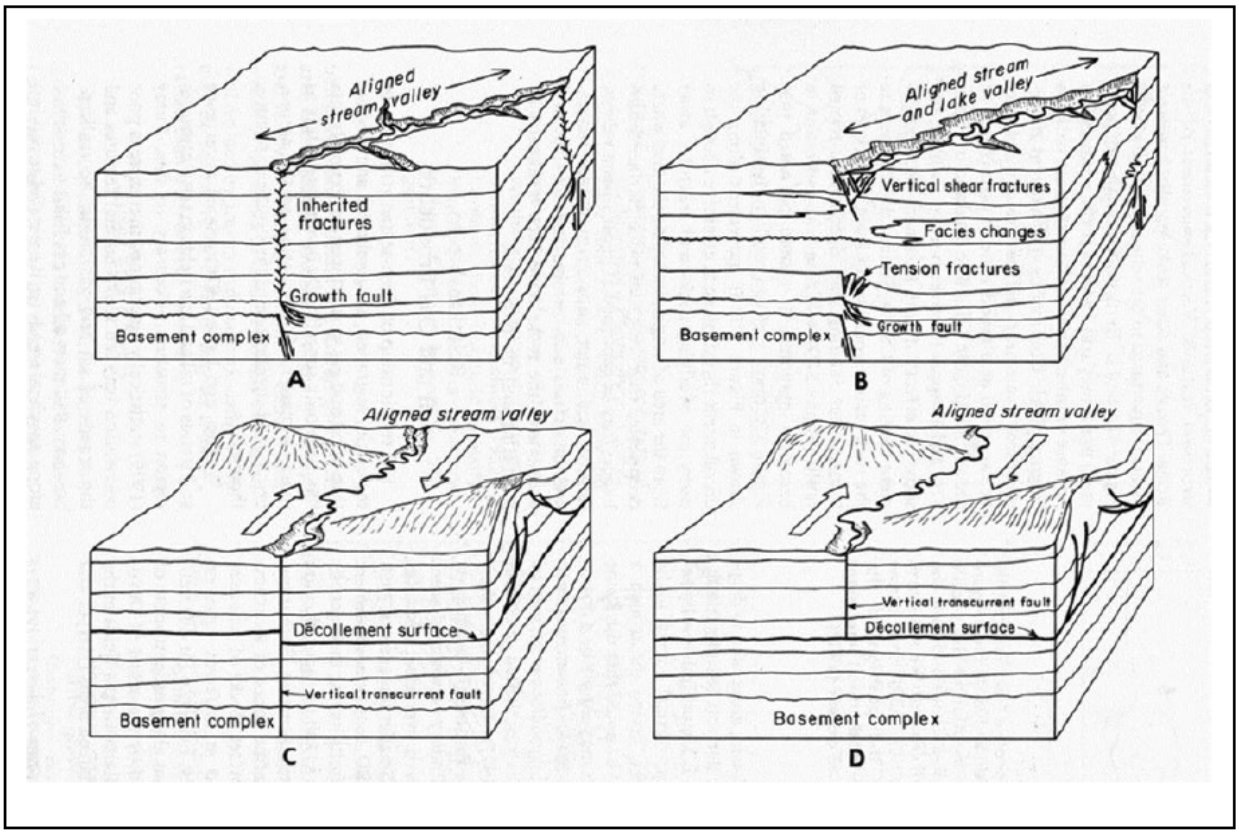

Figure 21, Four models for deep-seated basement movement affecting shallow structures (Harper and Laughrey, 1979).

Remaining Questions:

Conundrum 1: Spatial heterogeneity of microseismic events

Not all frac stages are created equal. It is true in a sense of production as well as producing microseismic events. Engineers think 70% of the production from one well might come from 30% of the perforations (Doug Cook, personal communication). One example of the non-uniform production of different perforations is shown in Figure 22. 70 % of the production comes from three perforations and half of the perforations produced nothing.

This problem may be solved by resolving the volumetric component of microseismic events. However, this requires the production logs, which were not available in this experiment.

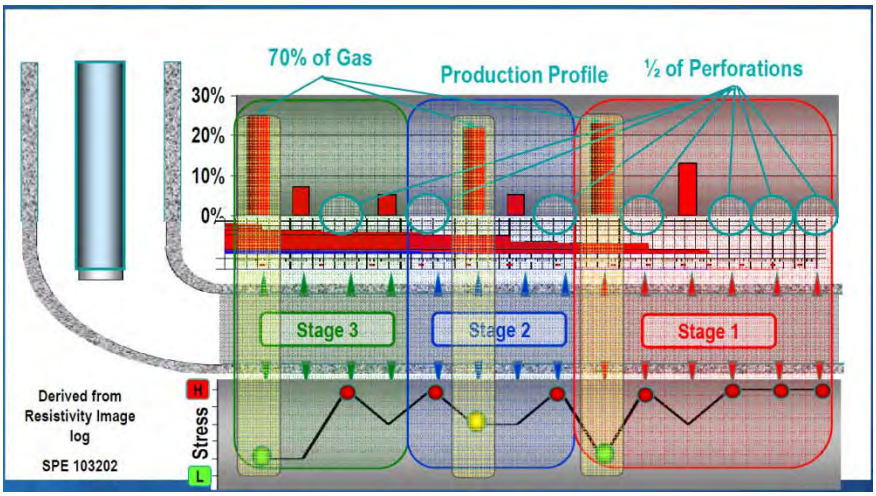

Figure 22. Production log from each perforation of three frac stages from one well (Cipolla, 2011).

Conundrum 2: Uncertainties in the Moment Tensor Inversion

One important quality control step to do is to look into the volumetric component of moment tensors caused by the noise in the data. Fortunately, there has been work on this problem.

The two figures below show the increase of the percentage of volumetric components with noise level (inverse of signal noise ratio). In the dip slip example, if signal/noise is one, moment tensor will have 10% volumetric component caused by noise. In the strike slip example, the percentage increased to 20%.

In our experiment, we have a cutoff value of signal noise ratio of 3 in the downhole record and 2.5 on the surface, which allowed us to constraint the volumetric component uncertainty to only a few percent.

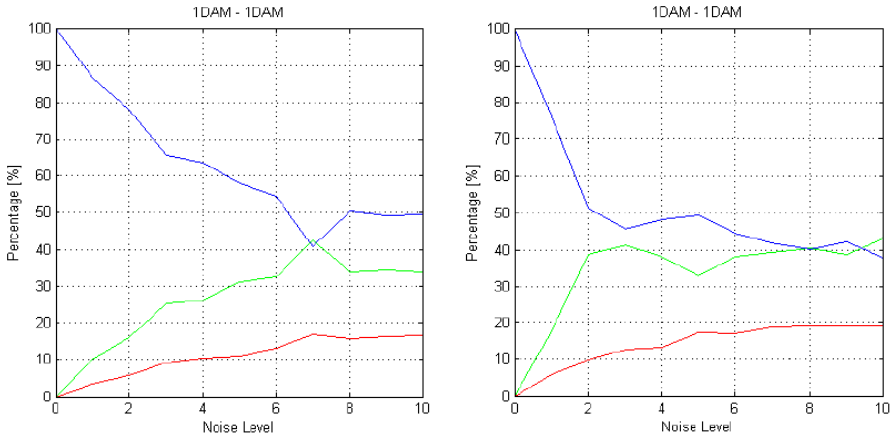

Figure 23, decomposition of moment tensor inverted from amplitude for strike-slip (left) and for di-slip (right) mechanisms for star array. Blue line represents DV, green line CLVD and red line ISO. Noise level is the inverse of signal noise ratio (Staněk et al., 2012).

Conclusions

A subvertical nodal plane characterized a number of focal mechanisms from the largest microseismic events during the stimulation of four horizontal wells drilled by Range Resources at the Troyer pad in Washington County PA. The moment tensors of some of these subvertical-nodal-plane events have a significant volumetric component, consistent with opening mode cracking. The orientation of these nodal planes was in the direction of the maximum contemporary tectonic stress of the Appalachian Basin. This correlation lends some strength to the conclusion that these nodal planes are characteristic of the geological boundary conditions in southwestern portion of PA.

These subvertical nodal planes correlate best with a local joint set seen downhole and a shear-wave velocity anisotropy in the Stewart Nancy #4 well. The most likely brittle structure for microseismic events associated with subvertical nodal planes is the early Alleghanian J_1 set (Engelder et al., 2009). Otherwise, we would interpret the vertical nodal planes as representing the rupture of intact rock by hydraulic fracturing in the contemporary tectonic stress field.

References

Cipolla, C., 2011, Application of Microseismic Hydraulic Fracture Monitoring, 2011 Schlumberger Microseismic Workshop: Pittsburg, PA.

Cliffs Minerals, I., 1982, Analysis of the Devonian Shales in the Appalachian Basin, U.S. Department of Energy contract DE-AS21-80MC14693, Final Report: Washington D.C., Cliffs Minerals Inc., p. 314.

Cuenot, N., Charlety, J., Dorbath, L., and Haessler, H., 2006, Faulting mechanisms and stress regime at the European HDR site of Soultz-sous-Forets, France: Geothermics, v. 35, p. 561-575.

Duncan, P.M., Lakings, J.D., and Flores, R.A., 2010, Method For Passive Seismic Emission Tomography, Microseismic, Inc.

Eisner, L., Thornton, M., and Griffin, J., 2011, Challenges For Microseismic Monitoring, SEG Annual Meeting: San Antonio.

Eisner, L., Williams-Stroud, S., Hill, A., Duncan, P., and Thornton, M., 2010, Beyond the dots in the box: The Leading Edge, v. 29, p. 326-333.

Engelder, T., and Geiser, P., 1980, On the use of regional joint sets as trajectories of paleostress fields during the development of the Appalachian Plateau, New York: Journal of Geophysical Research.

Engelder, T., Lash, G., and Uzcátegui, R.S., 2009, Joint sets that enhance production from Middle and Upper Devonian gas shales of the Appalachian Basin: AAPG Bulletin.

Evans, M.A., 1994, Joints and décollement zones in Middle Devonian shales: Evidence for multiple deformation events in the central Appalachian Plateau: Geological Society of America Bulletin, v. 106, p. 447.

Gilbert, F., 1971, Excitation of the normal modes of the Earth by earthquake sources: Geophysical Journal of the Royal Astronomical Society, v. 22, p. 223-226.

Hayles, K., Horine, R.L., Checkles, S., and Blangy, J.P., 2011, Comparison of Microseismic Results From the Bakken Formation Processed By Three Different Companies: Integration With Surface Seismic And Pumping Data, SEG 2011 Annual Meeting: San Antonio, TX.

Jaeger, J.C., Cook, N.G.W., and Zimmerman, R.W., 2007, Fundamentals of Rock Mechanics (Fourth Edition), Blackwell Publishing.

Julià, J., Nyblade, A.A., Durrheim, R., Linzer, L., Gök, R., Dirks, P., and Walter, W., 2009, Source Mechanisms of Mine-Related Seismicity, Savuka Mine, South Africa: Bulletin of the Seismological Society of America, v. 99, p. 2801-2814.

Khadhraoui, B., Leslie, H.D., Michaud, G., and Leaney, W.S., 2009, Continuous Microseismic Mapping for Real-Time 3D Event Detection and Location, Schlumberger K.K.

Lash, G.G., and Engelder, T., 2005, An analysis of horizontal microcracking during catagenesis: Example from the Catskill delta complex: AAPG Bulletin, v. 89, p. 1433.

Lawn, B., 1993, Fracture of Brittle Solids, Cambridge University Press.

Mayerhofer, M.J., Lolon, E., Warpinski, N.R., Cipolla, C.L., Walser, D.W., and Rightmire, C.M., 2008a, What is Stimulated Reservoir Volume (SRV)?, SPE Shale Gas Production Conference: Fort Worth, Texas, USA, Society of Petroleum Engineers.

Mayerhofer, M.J., Lolon, E.P., Warpinski, N.R., Cipolla, C.L., Walser, D., Rightmire, C.M., and Garb, F.A., 2008b, What is Stimulated Reservoir Volume (SRV)?: SPE.

McDaniel, B.A., 2006, Subsurface stratigraphy and depositional controls on Late Devonian-Early Mississipian sediments in southwestern PA, West Virginia University

Menke, W., 2012, Geophysical Data Analysis: Discrete Inverse Theory, Academic Press.

Phillips, W.S., Fairbanks, T.D., Rutledge, J.T., and Anderson, D.W., 1998, Induced microearthquake patterns and oil-producing fracture systems in the Austin chalk: Tectonophysics, v. 289, p. 153-169.

Plumb, R.A., and Cox, J.W., 1987, Stress directions in eastern North America determined to 4.5 km from borehole elongation measurements: Journal of Geophysical Research, v. 92, p. 4805-4816.

Pollard, D., and Segall, P., 1987, Theoretical displacements and stresses near fractures in rock: with applications to faults, joints, veins, dikes, and solution surfaces, *in* Atkinson, B.K., ed., Fracture mechanics of rock, Academic Press, p. 277-349.

Rutledge, J.T., and Phillips, W.S., 2003, Hydraulic stimulation of natural fractures as revealed by induced microearthquakes, Carthage Cotton Valley gas field, east Texas: Geophysics, v. 68, p. 441-452.

Rutledge, J.T., Phillips, W.S., and Mayerhofer, M.J., 2004, Faulting Induced by Forced Fluid Injection and Fluid Flow Forced by Faulting: An Interpretation of Hydraulic-Fracture Microseismicity, Carthage Cotton Valley Gas Field, Texas: Bulletin of the Seismological Society of America, v. 94, p. 1817-1830.

Scanlin, M., and Engelder, T., 2003, The Plateau Climb-out Zone beneath the Allegheny Front and Deer Park Anticline, Southwest Pennsylvania: Characterization of a Geologic Speed Bump, 68th Annual Field Conference of Pennsylvania Geologists, p. 42-54.

Šílený, J., Hill, D.P., Eisner, L., and Cornet, F.H., 2009, Non–double-couple mechanisms of microearthquakes induced by hydraulic fracturing: Journal of Geophysical Research, v. 114, p. B08307.

Snoke, J.A., 2009, FOCMEC: FOCal MEChanism Determinations Manual.

Staněk, F., Eisner, L., and Moser, T.J., 2012, Stability of source mechanisms inverted from P-wave amplitude microseismic monitoring data acquired at surface, 2012 SEG Annual Meeting: Las Vegas.

Stein, S., and Wysession, M., 2003, An Introduction to Seismology, Earthquakes, and Earth Structure, Blackwell Publishing.

Vavryčuk, V., 2001, Inversion for parameters of tensile earthquakes: J. Geophys. Res., v. 106, p. 16339-16355.

Vermylen, J., and Zoback, M.D., 2011, Hydraulic Fracturing, Microseismic Magnitudes, and Stress Evolution in the Barnett Shale, Texas, USA, SPE Hydraulic Fracturing Technology Conference: The Woodlands, Texas, USA.

Wagner, W.R., 1976, Growth faults in Cambrian and lower Ordovician rocks of western Pennsylvania: AAPG Bulletin, v. 60, p. 414-427.

Whitaker, A., and Engelder, J.T., 2006, Characterizing Stress fields in the upper crust using joint orientation distributions: Journal of Structural Geology, v. 27.

Appendix I – Reservoir Engineering

Top-Down Modeling of Marcellus Shale Gas

Shahab D. Mohaghegh

PEARL - West Virginia University

Marcellus Gas Shale
Final Report

Abstract

This is the final technical report submitted by West Virginia University under award identification number, 2009UN001 for the project entitled “Marcellus Gas Shale”.

This report covers all activities undertaken during the project at PEARL (Petroleum Engineering and Analytics Research Lab - WVU) that include data collection and quality control, data mining of the collected data, preparation of the data for reservoir modeling using Top-Down Modeling technology, training, calibrating and validating a comprehensive Top-Down reservoir simulation model that included history matching all the individual wells in the asset, and finally analysis of the Top-Down Model (TDM) and forecasting asset performance. The details of each task are explained in monthly reports presented throughout the life of the project. This report provides a summary of the main features of methodology, approach, results of history matching and TDM predictions.

The first chapter of the report is devoted to the conventional method in reservoir modeling and simulation versus the Top-Down Modeling (TDM). The outlines of each method in simulation and modeling of Shale gas reservoirs are discussed. In the second chapter, the steps that have been taken in spatio-temporal database compilation are discussed. The third chapter covers the workflow of history matching process, and the fourth chapter is dedicated to the application of TDM in prediction of reservoir performance in the Marcellus Shale Asset.

Table of contents

Abstract 1
Table of contents 2
List of Figures 3
Chapter 1: Introduction 5
1-1 Reservoir Simulation 5
1-2 Shale Gas Reservoir Simulation 6
1-3 Top-Down Modeling 7
Chapter 2: Spatio-Temporal Database Development 10
2-1 Database 10
2-2 Preliminary Statistical Analysis 10
2-3 Decline Curve Analysis 19
2-4 Fuzzy Pattern Recognition 20
2-5 Reservoir Dynamic Behavior 24
Chapter 3: History Matching 26
3-1 Workflow 26
3-2 Base Case 27
3-3 Effect of Offset Wells 28
3-4 Effect of Well Types 29
3-5 Effect of Flow Regimes 30
3-6 Effect of Distances 32
3-7 Best History Matching Model with Least inputs 33
3-8 Error Calculation 35
Chapter 4: Forecast 36
4.1 Scenario 1 36
4.2 Scenario 2 36
4.3 Scenario 3 38
Chapter 5: Conclusion 42
References 43
Appendix A: Best History Matching Results 44
Appendix B: Forecasting Results- Scenario 1 112

List of Figures

Figure 1: Conventional Reservoir Simulation 6
Figure 2: Top-Down Modeling Workflow 8
Figure 3: List of Available Data 11
Figure 4: Key Performance Indicators (KPI) for 30 day cum gas production. 12
Figure 5: Key Performance Indicators (KPI) for 30 day cum condensate production 13
Figure 6: Relative impact of different categories of parameters on 30 days cumulative gas production. 13
Figure 7: Relative impact of different categories of parameters on 30 days cumulative condensate production 14
Figure 8: Relative impact of different categories of parameters on 90 days cumulative gas production. 14
Figure 9: Relative impact of different categories of parameters on 90 days cumulative condensate production 15
Figure 10: Relative impact of different categories of parameters on 120 days cumulative gas production. 15
Figure 11: Relative impact of different categories of parameters on 120 days cumulative condensate production 16
Figure 12: Relative impact of different categories of parameters on 180 days cumulative gas production. 16
Figure 13: Relative impact of different categories of parameters on 180 days cumulative condensate production 17
Figure 14: Relative impact of different categories of parameters on cumulative gas production as a function of time. 18
Figure 15: Relative impact of different categories of parameters on cumulative condensate production as a function of time. 18
Figure 16: Relative impact of all different parameters on Gas & Condensate Production 19
Figure 17: Decline Curve Analysis for Well#10002 20
Figure 18: Fuzzy Pattern Recognition- First 3 Month-Cumulative Gas (MCF) 21
Figure 19: Fuzzy Pattern Recognition- First 6 Month-Cumulative Gas (MCF) 22
Figure 20: Fuzzy Pattern Recognition- First 9 Month-Cumulative Gas (MCF) 22
Figure 21: Fuzzy Pattern Recognition- First Year-Cumulative Gas (MCF) 23
Figure 22: Fuzzy Pattern Recognition- First 3 Years-Cumulative Gas (MCF) 23
Figure 23: Production Logs in Well 10020 24
Figure 24: Production Profile for Well# 10041 25
Figure 25: Marcellus shale AI-Based Full-field history matching process 26
Figure 26: KPI Result for Most Influential Parameters in Base Case 27

Figure 27: Entire Field History Matching Results and two wells as examples- Base Case 28
Figure 28: Entire Field History Matching Results and two wells as examples- Effect of Offset Well 28
Figure 29: Different Well Types 29
Figure 30: Entire Field History Matching Results and two wells as examples- Effect of Well Types 30
Figure 31: Log-log plot of production rate as a function of time for one of 135 wells 31
Figure 32: Entire Field History Matching Results and two wells as examples- Effect of Flow Regimes 31
Figure 33: Inside and closest outside distance 32
Figure 34: Entire Field History Matching Results and two wells as examples- Effect of Distances 33
Figure 35: Cross plots for Training, Calibration and Verification for Best history matching Model 34
Figure 36: Entire Field History Matching Results and two wells as examples- Best History Matching Model 34
Figure 37: List of Parameters in Best History Matching Model 35
Figure 38: History Matching Error in Best History Matching Model 35
Figure 39: Blind History Matching and additional Forecasting for Two Well in Scenario 1 37
Figure 40: Blind history matching of last four months and additional year of forecasting for entire field 37
Figure 41: Location and Pattern of New Wells 38
Figure 42: Forecasting the Production Performance for New Well # 1 39
Figure 43: Forecasting the Production Performance for New Well # 2 39
Figure 44: Forecasting the Production Performance for New Well # 3 40
Figure 45: Forecasting the Production Performance for New Well # 4 40
Figure 46: Forecasting the Production Performance for New Well # 5 41

Chapter 1: Introduction

1-1 Reservoir Simulation

Reservoir simulation is the process of inferring the behavior of a real reservoir from the performance of a model of that reservoir. Reservoir simulation is a primary tool for reservoir managements that has become an integral part of the oil and gas business over the last 50 years.

Over the past decades, the use of numerical reservoir simulation with high-speed electronic computers has gained wide acceptance throughout the petroleum industry for making engineering studies of a wide variety of oil and gas reservoirs and for helping to make large capital decisions, estimating reserves and diagnosing and improving the performance of producing reservoirs throughout the world.

In general, a reservoir simulation study involves four steps:

- Selecting the model and approach: During this critical step decisions are made regarding the physics (flow dynamics) of the fluid flow that is going to be modeled. Making decision about model coordinate's system, compositional versus black oil models, using the specialized models for unconventional reservoirs (dual porosity, dual permeability, etc.) is an important step at the start of a reservoir simulation project.
- Gathering and preparing the input data: One of the most laborious aspects of reservoir simulation study is data gathering and preparation. Oftentimes, this requires collaboration among technical personnel with varying level of expertise and background. Because of the large volume of data being processed at this stage, and the likelihood of internal inconsistencies in the data, the engineers and scientists involved in this process must have strong organizational skills and sound judgment. This step include development of the geo-cellular model as well as up-scaling it to the appropriate dimensions for use in the reservoir simulation model.
- Planning the computer runs in terms of history matching and/or performance prediction: In simulation studies, time (both the engineers' and the computers') is of the essence. A typical simulation study requires a large number of simulation runs which must be carefully orchestrated to yield the desired information.
- Analysis and interpretation of the results: Perhaps the most important step in a simulation study is analysis and interpretation of the results generated from multiple simulation runs.

As schematic diagram that shows thee conventional reservoir simulation workflow is presented in Figure 1.

A reservoir simulation study's ultimate objective is to forecast reservoir performance. If we have selected the correct model, adequately prepared the data, completed the appropriate number of runs and made good, informed analyses, we should be confident of our ability to predict performance. Any mistakes in each of the steps will have a cumulative impact on performance prediction.

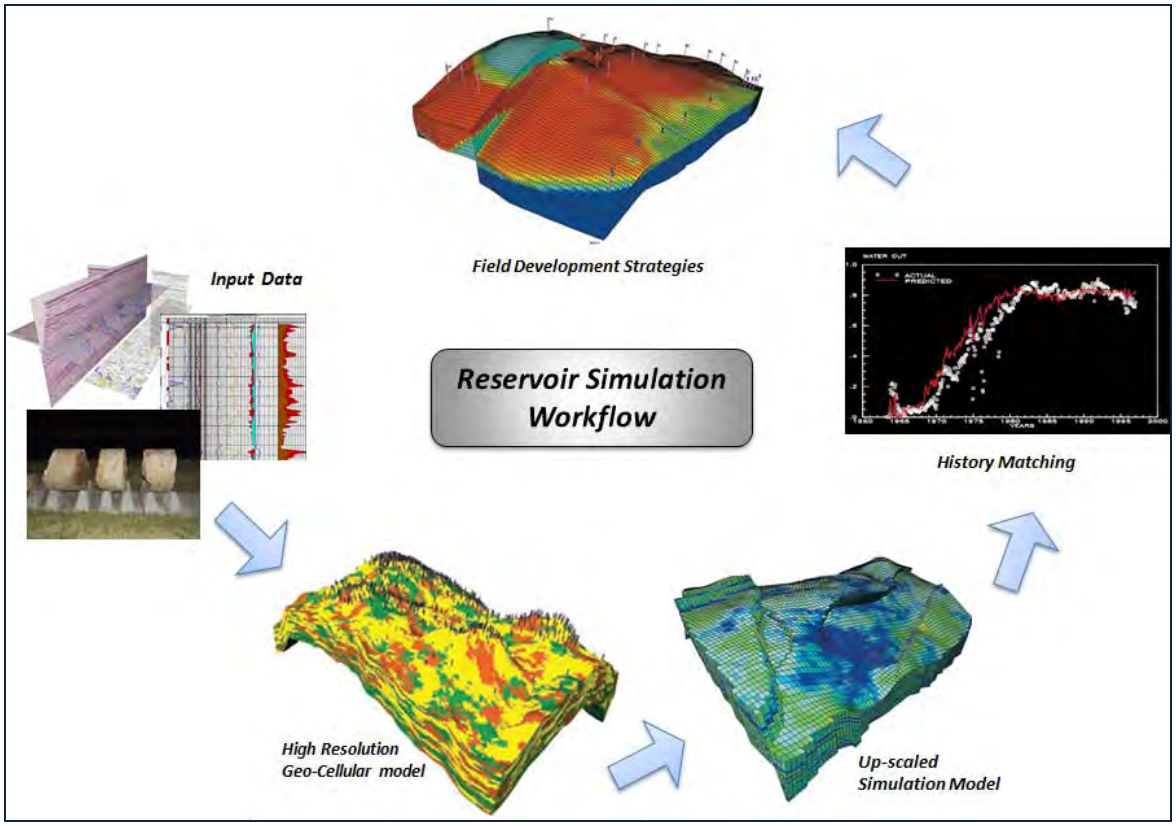

Figure 1: Conventional Reservoir Simulation

1-2 Shale Gas Reservoir Simulation

Shale gas is a tremendous potential resource that has the potential to completely change the energy landscape in the United States and in the world. Efforts to understand the transport mechanism through this unconventional resource and to model its behavior are proceeding rapidly. Shale reservoirs are characterized by extremely low permeability rocks that have a number of unique attributes, including high organic content, high clay content, extremely fine grain size, plate-like micro-porosity, little to no macro-porosity, and coupled Darcy and Fickian flow through the rock matrix.

Understanding reservoir properties like lithology, porosity, organic carbon, water saturation and mechanical properties of the rock, which includes stresses, beforehand and planning completions based on that knowledge is the key to production optimization. Therefore, the final objective is to increase our ability to integrate proprietary laboratory and petrophysical measurements with geochemical, geological, petrologic, and geomechanical knowledge, to develop a more solid understanding of shale plays and to provide better assessments, better predictions, and better models. Reservoir simulation has played an important role in this aspect. However, there are still many challenges to overcome. One is that the physics of fluid flow in shale rocks have not been fully understood, and are undergoing continuous development as the industry learns more (Lee and Sidle, 2010). Another one is that detailed reservoir simulation is resource intensive and time consuming.

1-3 Top-Down Modeling - TDM

Top-Down Modeling (TDM)[1], a new technology that has been recently introduced to the oil and gas industry, is a comprehensive and formalized, full-field empirical reservoir model, which takes into account all aspects of production from a reservoir. TDM incorporates well location and configuration, reservoir characteristic (through well logs and core analysis), details of completion and stimulation practices as well as production history from all the producing and injection wells. In this project TDM is applied to a Marcellus Shale asset in southwestern Pennsylvania.

Unlike the common practice in shale modeling using a conventional approach, which is usually done at the well level (Strickland et al.2011), Top-Down Modeling is capable of performing history matching for all individual wells in addition to the full field by taking into account the effect of offset wells. Top-Down Modeling is classified as an Artificial Intelligent (AI)-based reservoir model.

Following are the major steps in the development of a Top-Down Model for Shale reservoirs:

a. **Spatio-temporal database development**- The first step in developing a data driven shale model is preparing a representative spatio-temporal database (data acquisition and preprocessing). The extent at which this spatio-temporal database actually and accurately represents the fluid flow behavior of the reservoir, determines the potential degree of success in developing a successful Top-Down Model. The nature and class of the AI-based shale reservoir model is determined by the source of this database. The term spatio-temporal defines the essence of this database and is inspired from the physics that controls this phenomenon (Mohaghegh 2011). An extensive data mining and analysis process should be conducted at this step to fully understand the data that is housed in this database. The data compilation, curation, quality control and preprocessing are the most important and time consuming steps in developing an AI-based Reservoir Model.

b. **Simultaneous training and history matching of the reservoir model-** In conventional numerical reservoir simulation the base model will be modified to match production history, while AI-based reservoir modeling starts with the static model and try to honor it and not modify it during the history matching process. We will analyze and quantify the uncertainties associated with this static model at a later stage in the development. The model development and history matching in AI-based shale reservoir model are performed simultaneously during the training process. The main objective is to make sure that the AI-based shale reservoir model learns fluid flow behavior in the shale reservoir being modeled. The spatio-temporal database developed in the previous step is the main source of information for building and history matching the AI-based Reservoir Model.

   In this work, multiple, multilayer neural networks are used as part of the Top-Down Model. The neural networks consist of one hidden layers with different number of

[1] Top-Down, Intelligent Reservoir Modeling (TDM) technology has been introduced to the E&P industry by Intelligent Solutions, Inc.

hidden neurons, which have been optimized based on the number of data records and the number of inputs in training, calibration and verification process.

It is extremely important to have a clear and robust strategy for validating the predictive capability of the AI-based Reservoir Model. The model must be validated using completely blind data that has not been used, in any shape or form, during the development of the TDM. Both training and calibration datasets that are used during the initial training and history matching of the model are not considered to be part of the blind data for validation purposes.

As noted by Mohaghegh (2011), some may argue that the calibration - also known as testing dataset - is also blind. This argument has some merits but if used during the development of the AI-based shale reservoir model can compromise validity and predictability of the model and therefore such practices are not recommended.

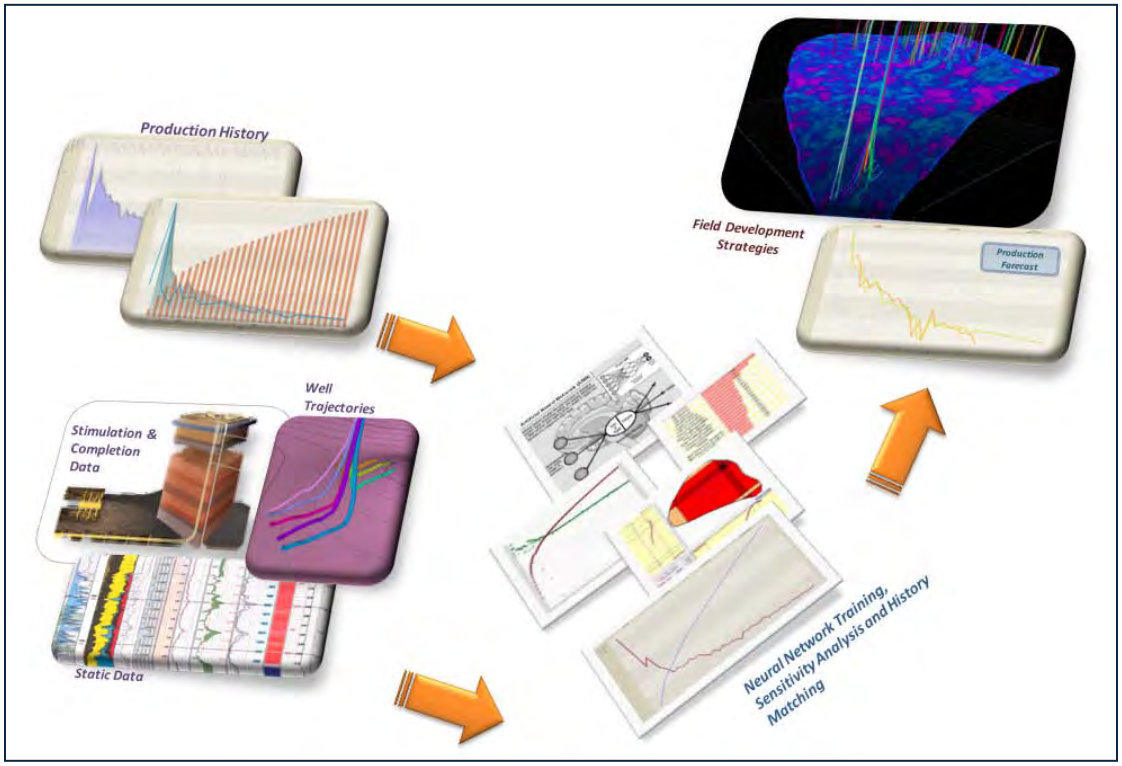

Figure 2: Top-Down Modeling Workflow

c. **Sensitivity analysis and quantification of uncertainties-** During the model development and history matching that was defined in the previous step, the static model is not modified. Lack of such modifications may present a weakness of this technology, given the fact that the static model includes inherent uncertainties. To address this, the AI-based Reservoir Modeling workflow includes a comprehensive set of sensitivity and uncertainty analyses. During this step, the developed and history matched model is thoroughly examined against a wide range of changes in reservoir characteristics and/or

operational constraints. The changes in pressure or production rate at each well are examined against potential modification of any and all the parameters that have been involved in the modeling process. These sensitivity and uncertainty analyses include single- and combinatorial-parameter sensitivity analyses, quantification of uncertainties using Monte Carlo simulation methods and finally development of type curves. All these analyses can be performed on individual wells, groups of wells or for the entire field.

d. **Deployment of the model in predictive mode-** Similar to any other reservoir simulation model, the trained, history matched and validated AI-based shale reservoir model is deployed in predictive mode in order to be used for performing reservoir management and decision making purposes.

Figure 2 show the workflow of Top-Down Modeling approach.

This approach has been applied on 136 horizontal wells in multiple pads, different landing targets, and well lengths and reservoir properties. The full-field history matching process was completed successfully. Artificial Intelligence (AI)-based model proved its capability in capturing the production behavior with acceptable accuracy for individual wells and for the entire field.

Chapter 2: Spatio-Temporal Database Development

This chapter presents the details of data used in this analysis along with the process through which the spatio-temporal database was developed. The data set used in this project includes 135 wells from a total of 43 pads. These wells include different landing targets, and well lengths and reservoir properties. During this step all available data including static, dynamic, completion, hydraulic fracturing, and operational constraints have been analyzed. Also in this chapter, the behavior of the reservoir by using PLT data, production history, Decline Curve analysis and fuzzy pattern recognition will be shown.

2-1 Database

The data set includes more than 1,200 hydraulic fracturing stages. Some wells have up to 17 stages of hydraulic fracturing while others have been fractured with as few as four stages. The perforated lateral length ranges from 1400 to 5600 ft. The total injected proppant in these wells ranges from a minimum of about 97,000 lbs up to a maximum of about 8,500,000 lbs and total slurry volume of about 40,000 to 181,000 bbls. Following table shows the number of pads and the corresponding number of laterals in each of the pads.

Description of pads	Number of each pad
Pads with Single Laterals	12
Pads with 2 Laterals	13
Pads with 3 Laterals	2
Pads with 4 Laterals	5
Pads with 5 Laterals	1
Pads with 6 Laterals	6
Pads with 7 Laterals	1
Pads with 8 Laterals	3

The Porosity of Upper Marcellus varies from 5 to 10 percent while its gross thickness is measured to be between 43 to 114 ft with Total Organic Carbon Content (TOC) between 0.8 to 1.7 percent. The reservoir characteristics of Lower Marcellus include porosity of 8 to 14 percent, gross thickness between 60 to 120 ft and TOC of 2 to 6 percent. A complete list of data that are included in main data set for development of the base model is shown in Figure 3.

2-2 Preliminary Statistical Analysis

Some statistical analyses have been performed for each of production indicators of 30, 90, 120 and 180 days of cumulative gas and condensate production. The analyses have been done separately and compared with one another.

To perform the analyses that are presented in this report two software applications were used, Data-Driven Analytics tool[2] for completion optimization and Top-Down Modeling tool[3].

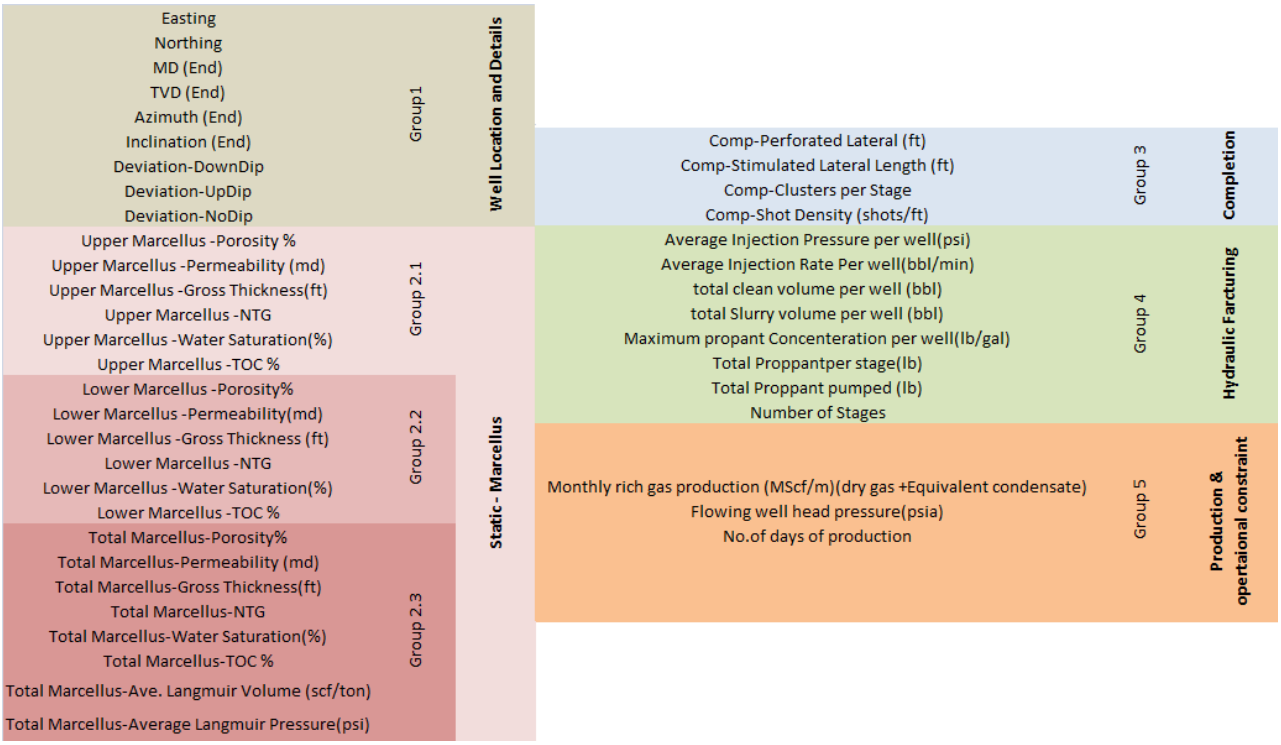

Figure 3: List of Available Data

Using the Data-Driven Analytics software for completion optimization, Fuzzy Pattern Recognition (FPR) was performed in order to identify the most influential parameters (a.k.a. Key Performance Indicators – KPI) for the 30 day cumulative gas production index. Figure 4 shows that Fuzzy Pattern Recognition (FPR) identifies the top 5 influential parameters for the 30 day cumulative gas production in this particular asset of Marcellus shale to be the *Gross Thickness* of the entire Marcellus, the *Net to Gross* ratio of Upper Marcellus, *Gross Thickness* of the Lower Marcellus, the *Easting End point* of the well (location) and finally the *Porosity* of the Upper Marcellus, noting that all these parameters are geology related.

The first design related parameter that is a completion related parameter (*Number of Clusters per Stage*) appears as KPI number 9 followed by *Total Number of Stages, Total Amount of Proppant Injected, Shot Density* and finally the *Average Injection Pressure* as KPIs 10 through 13 all being design related parameters.

Figure 5 shows the KPIs for the 30 days cumulative condensate production and the top 5 ranking parameters are also reservoir characteristics such as, Easting end of the well (location), gross thickness of the Lower Marcellus, Water Saturation of the Lower Marcellus, the Net to

[2] IMprove acquired from Intelligent Solutions, Inc.
[3] IMagine acquired from Intelligent Solutions, Inc.

Gross ratio of lower Marcellus and finally gross thickness of the entire Marcellus. It is interesting to note that three of the five are related to Lower Marcellus while the other two also have implicit indications of lower Marcellus. Completion and Stimulation design parameters such as number of stages, amount of clean fluid volume injected, length of perforated lateral and stimulated lateral length that are all design parameters are ranked 6 to 9.

This leads us to believe the Lower Marcellus plays an important role in condensate production in part of the Marcellus Shale.

In addition, the relative importance of different parameters associated with gas and condensate production in Marcellus Shale is examined. In the next several figures (bar charts) the y axis are FPR scales that only have relative meaning (relative to each other). For example Figure 6 shows the relative impact of different categories of parameters on 30 days cumulative gas production. The scale on the y-axis is a normalized relative impact that is essentially dimensionless and only provides a comparison of impact of different groups of parameters.

Figure 6 and 7 show that the most influential group of parameters for early (30 days Cum.) gas production in Marcellus shale is the static reservoir parameters of the Upper Marcellus while for condensate production is the static reservoir parameters of the Lower Marcellus. Figure 8 through 13 show similar plots for 90, 120 and 180 days cumulative gas and condensate production, respectively.

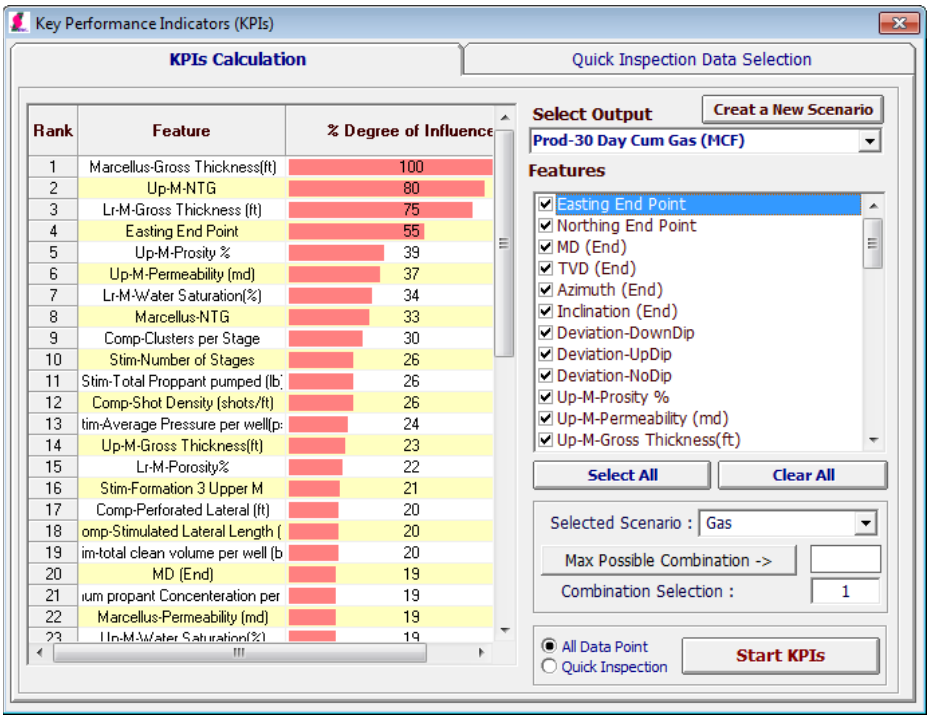

Figure 4: Key Performance Indicators (KPI) for 30 day cum gas production.

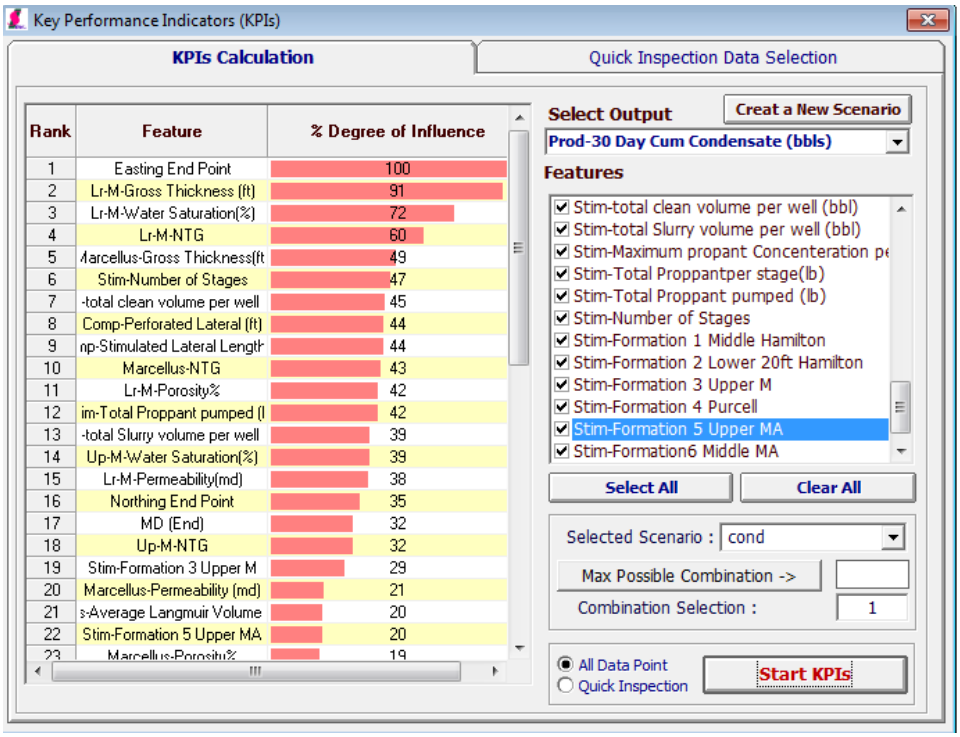

Figure 5: Key Performance Indicators (KPI) for 30 day cum condensate production.

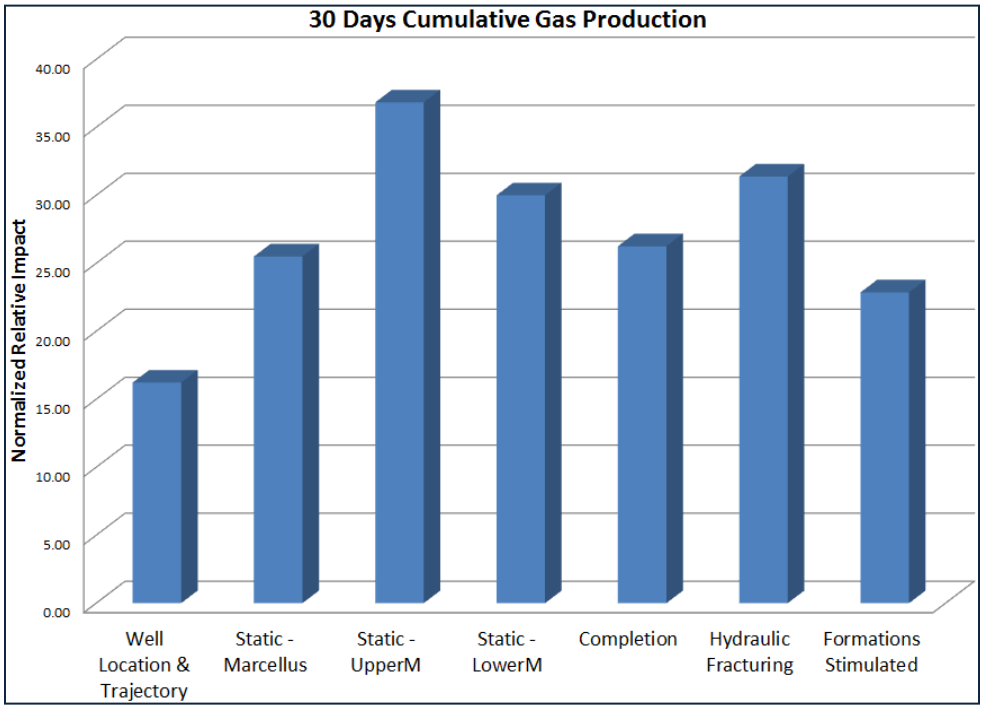

Figure 6: Relative impact of different categories of parameters on 30 days cumulative gas production.

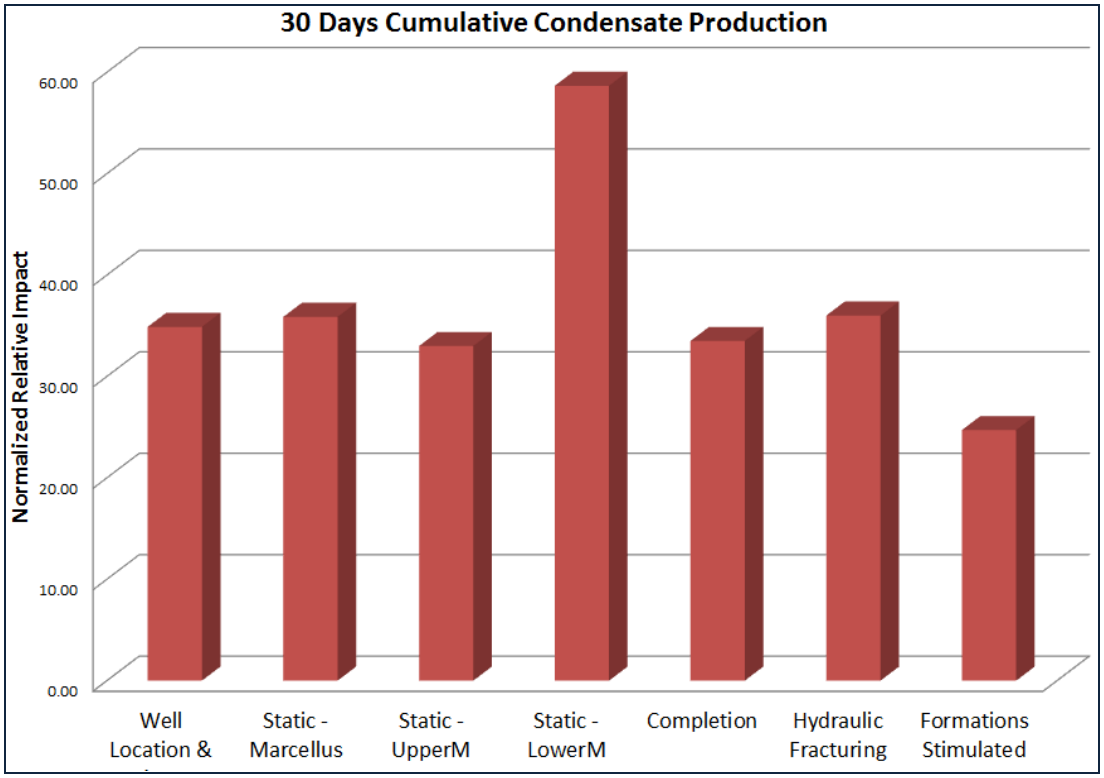

Figure 7: Relative impact of different categories of parameters on 30 days cumulative condensate production.

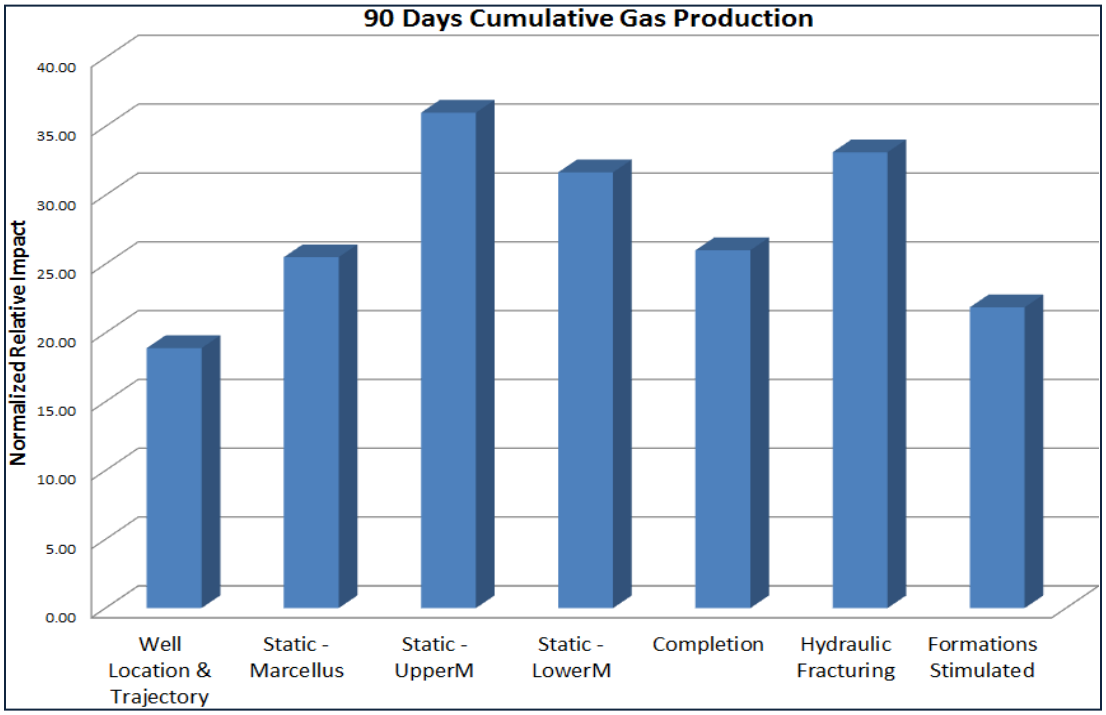

Figure 8: Relative impact of different categories of parameters on 90 days cumulative gas production.

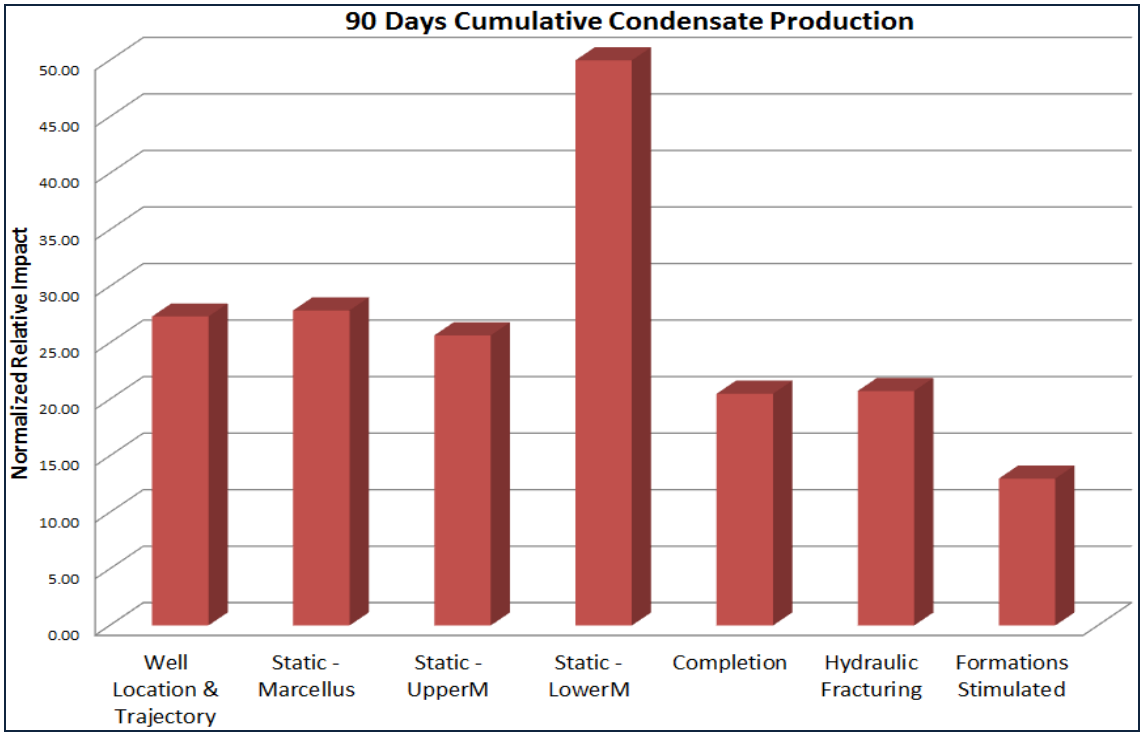

Figure 9: Relative impact of different categories of parameters on 90 days cumulative condensate production.

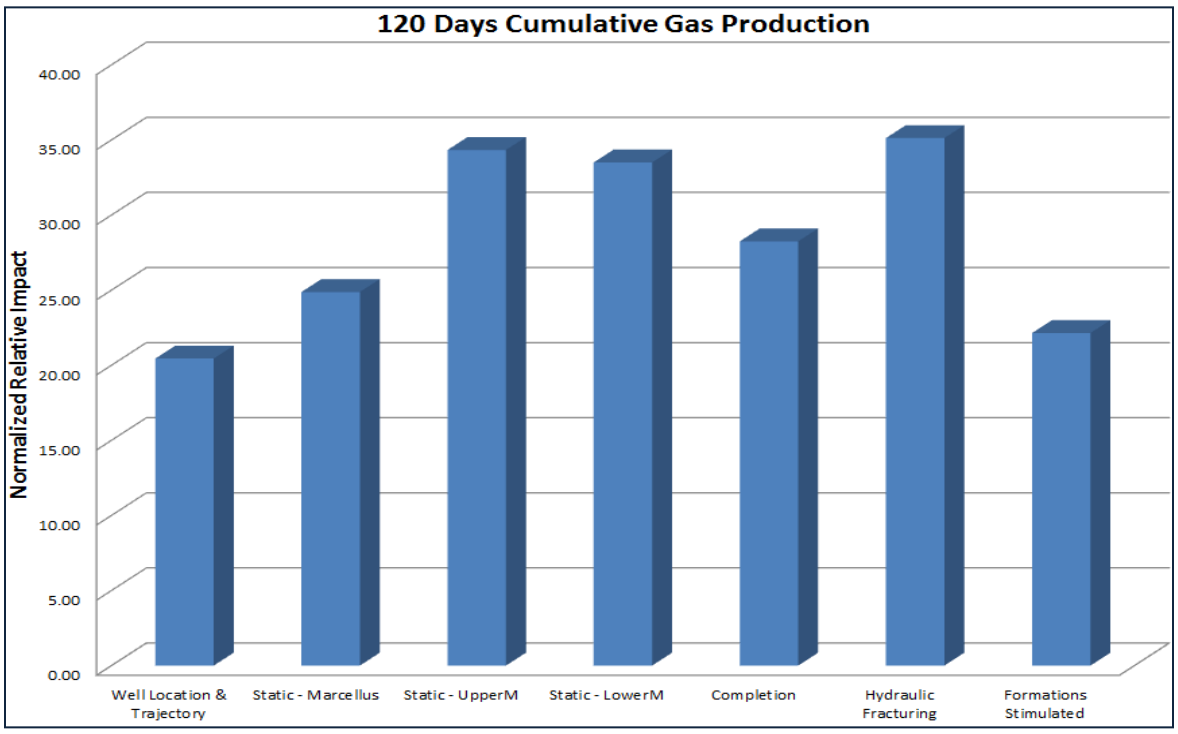

Figure 10: Relative impact of different categories of parameters on 120 days cumulative gas production.

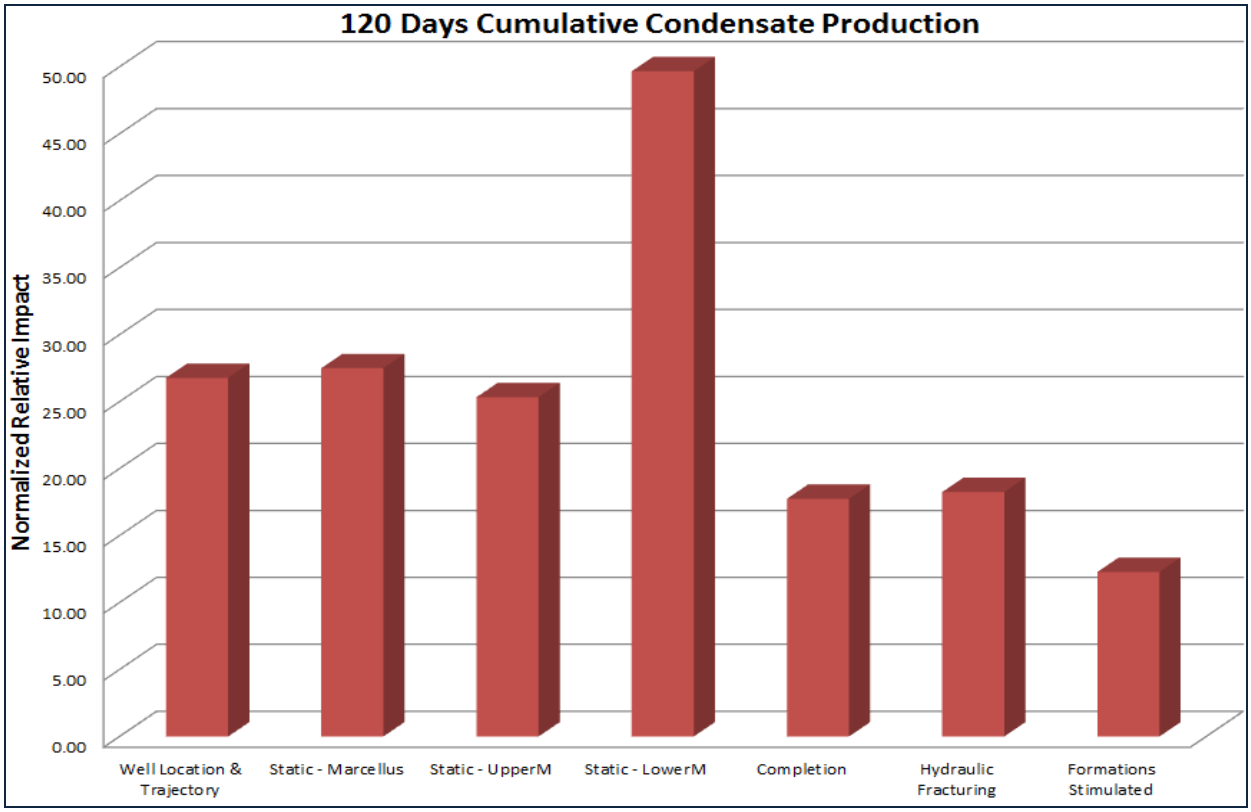

Figure 11: Relative impact of different categories of parameters on 120 days cumulative condensate production.

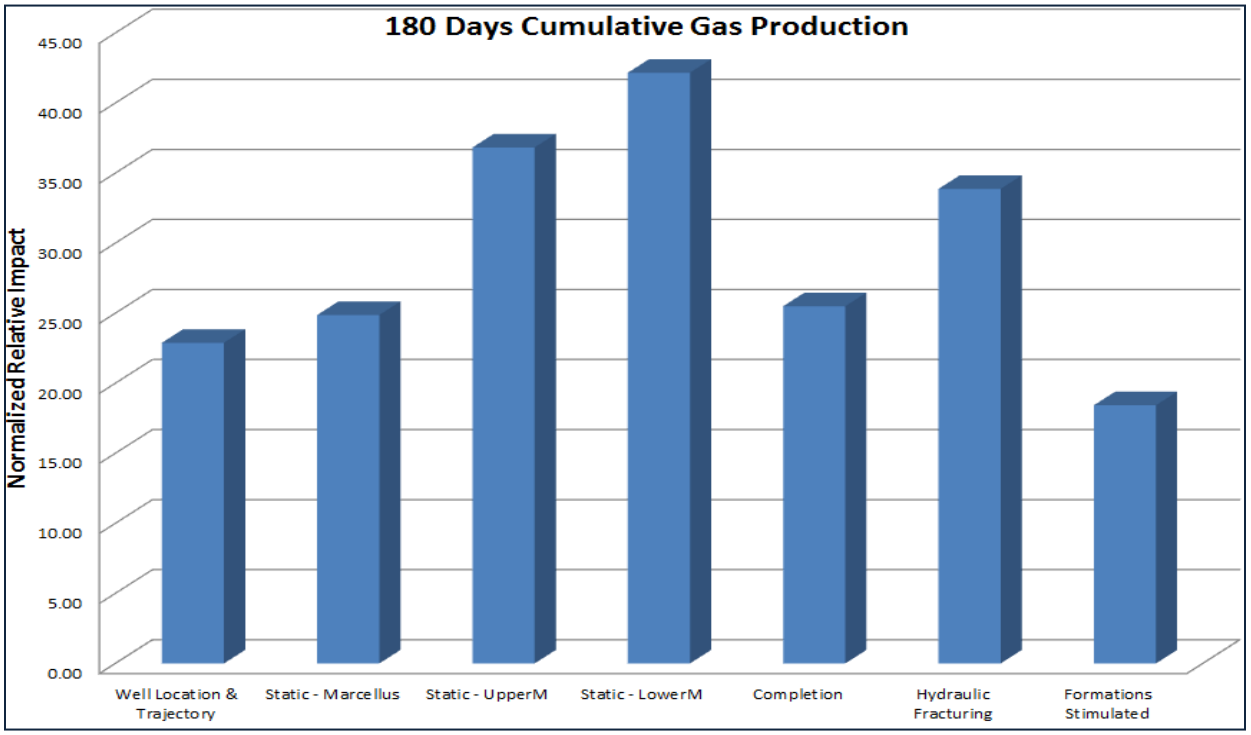

Figure 12: Relative impact of different categories of parameters on 180 days cumulative gas production.

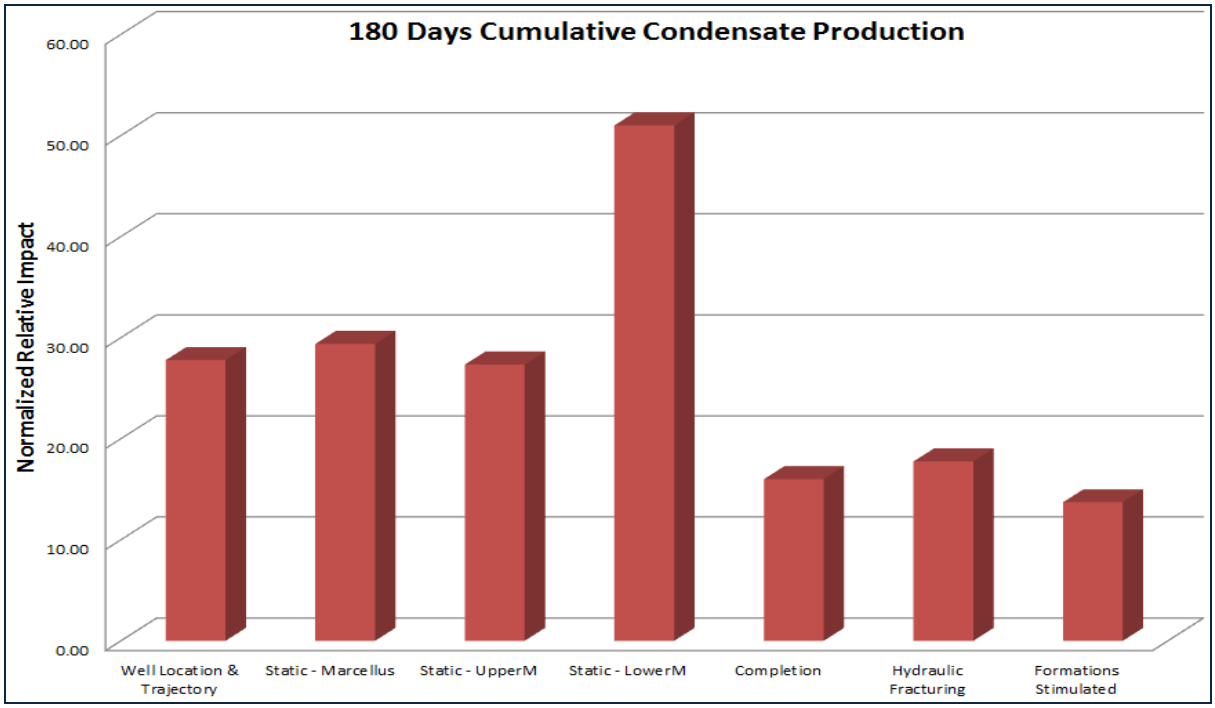

Figure 13: Relative impact of different categories of parameters on 180 days cumulative condensate production.

Figure 14 summarized all the numbers and trends that are shown in Figures 6 through 13 for cumulative gas production while Figure 15 summarized all the numbers and trends that are shown in Figures 6 through 13 for cumulative condensate production. While the major trends of impact of groups of parameters seem to stay reasonably constant from 30 to 180 days of production, certain trends become apparent. For example, Figure 14 shows that impact of well location and trajectory on gas production increases as the duration of the production (age of the well) increases.

On the other hand, figure 14 shows that the impact of static reservoir characteristics of the overall Marcellus Shale remains the same throughout the age of the well (up to 180 days of production). Another group of parameters that show an increase in impact as a function of time of production of gas is the static reservoir characteristics of Lower Marcellus formations. Influence of this group of parameters increases significantly, when 180 days of cumulative gas production is analyzed.

Completion and stimulation parameters do not show any lasting trends as we move from 30 to 180 days of cumulative gas production in Marcellus Shale.

Figure 15 shows that unlike the cumulative gas production, in cumulative condensate production the impact of design parameters such as completion and stimulation are most significant at the start of the production. It also shows that the impact of these parameters diminishes as number of days of production increases.

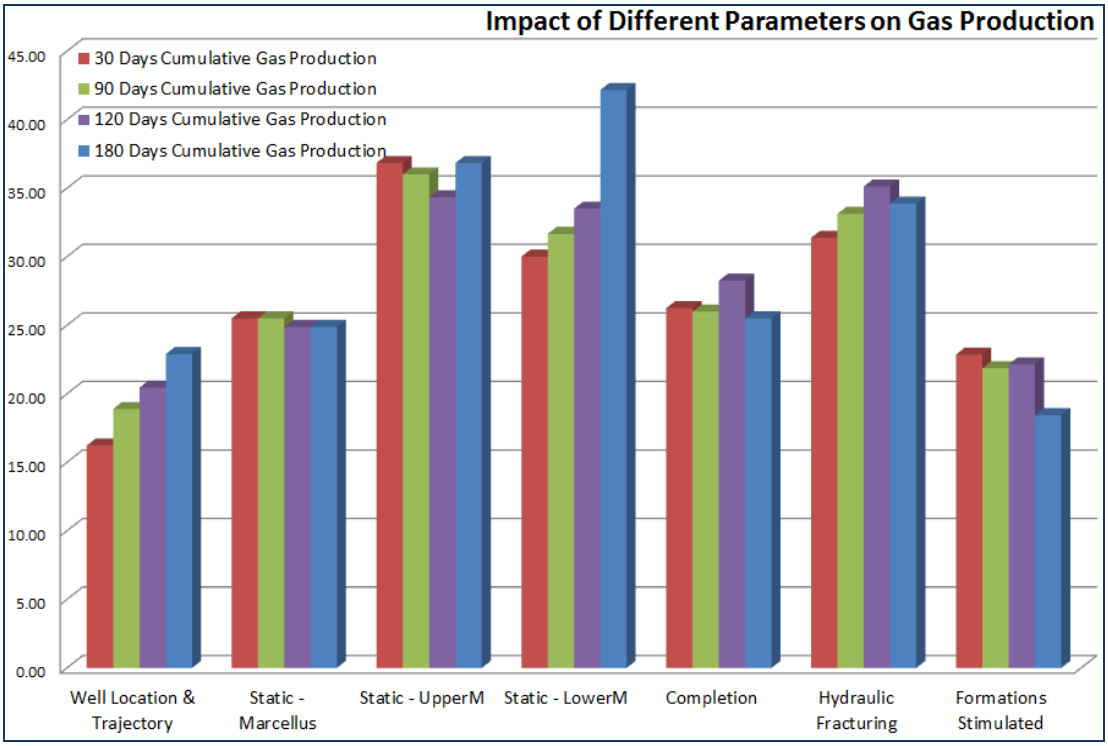

Figure 14: Relative impact of different categories of parameters on cumulative gas production as a function of time.

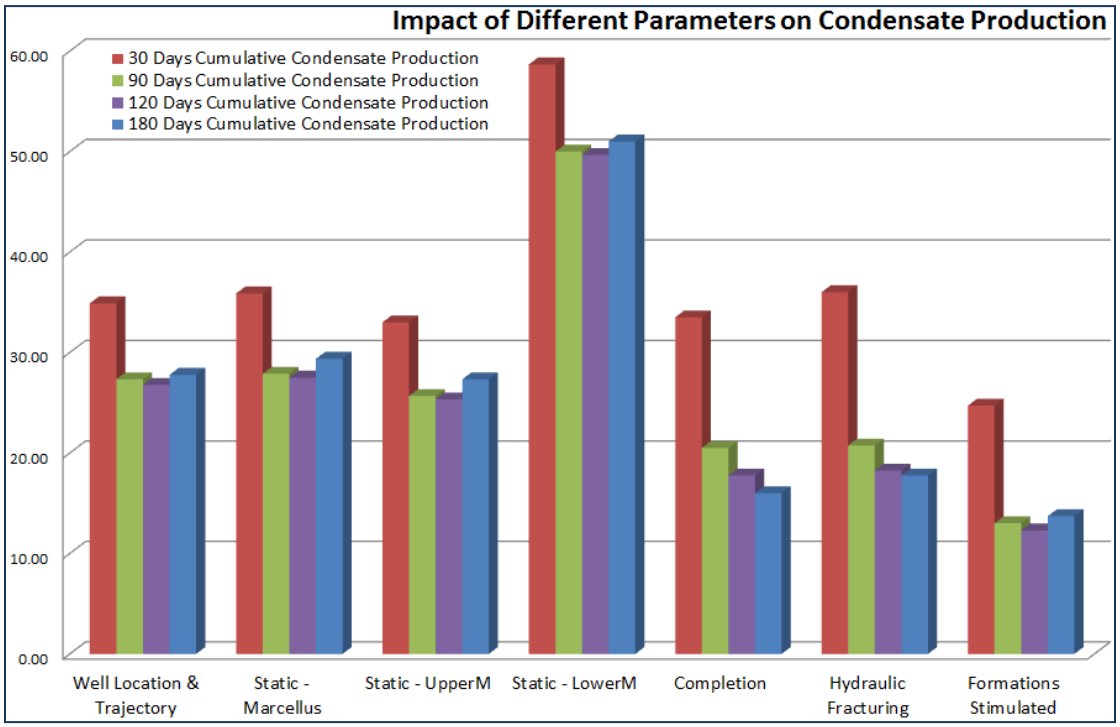

Figure 15: Relative impact of different categories of parameters on cumulative condensate production as a function of time.

Figure 16 compares the overall impact of groups of parameters on both gas and condensate production. In this figure the normalized relative importance scale of gas and condensate have been summed and normalized for 30, 90, 120 and 180 days of cumulative production, respectively. This figure shows that (relatively speaking) completion and stimulation parameters have impact that is more significant on gas production they do on condensate production. For condensate production role of static parameters (reservoir characteristics and well location and trajectory) are more significant than those of hydraulic fracturing.

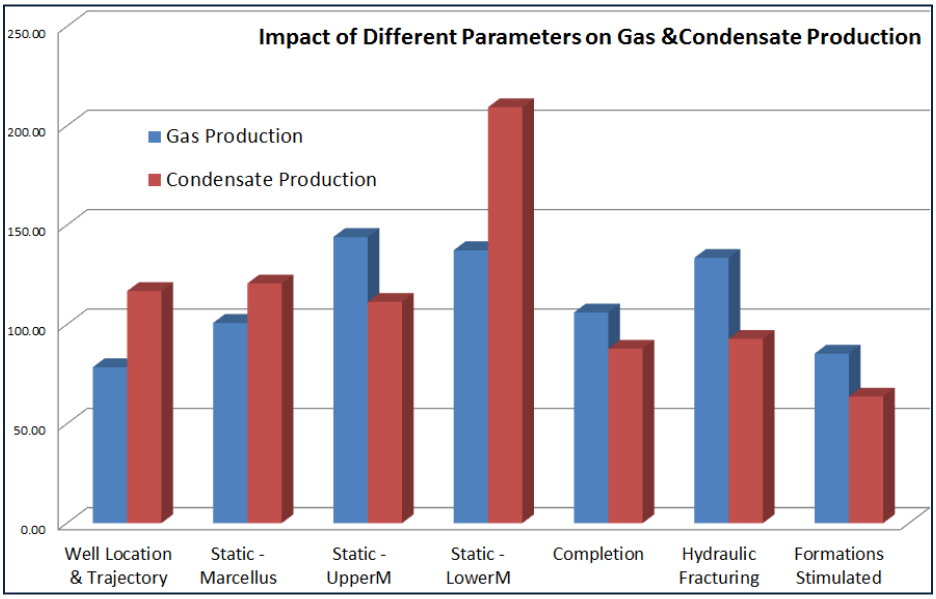

Figure 16: Relative impact of all different parameters on Gas & Condensate Production

2-3 Decline Curve Analysis

After quality control of production data, Conventional hyperbolic decline curve analysis is performed on daily gas production of all the wells. An optimization routine based on genetic algorithms identifies the best decline curve for the given well, as both the rate versus time and the cumulative production versus time are simultaneously matched.

This is illustrated in figure 17 for well 10012. In this figure green dots show the actual gas rate, red dots show the actual cumulative gas and blue and red lines show the estimated decline rate and cumulative respectively.

As it has shown in this figure and it was observed in other wells, the hyperbolic constant for most of the wells in this reservoir is more than 1. It should be noted that since we had concluded that decline curve analysis is an unreliable method for predicting the production behavior in Shale assets, we have not used the results in our analysis. Nevertheless, decline curve analyses were performed to be used as a base line for comparison.

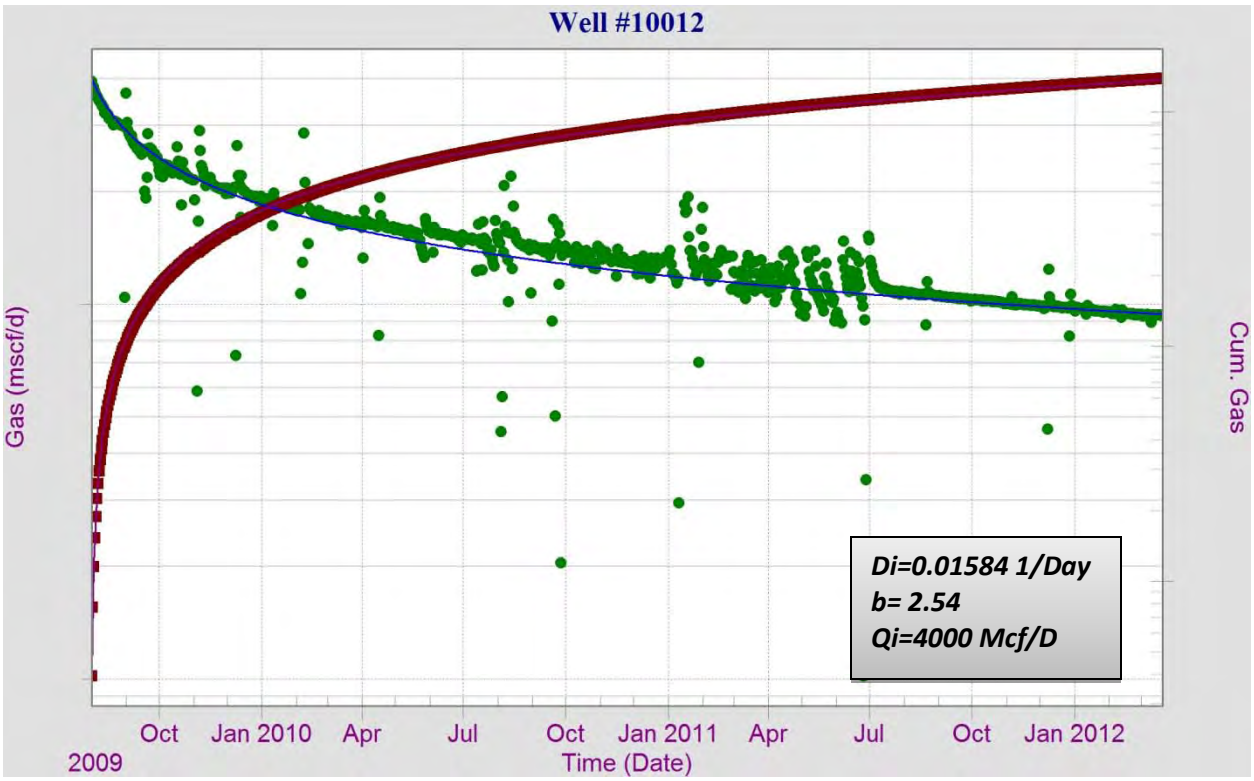

Figure 17: Decline Curve Analysis for Well#10002

2-4 Fuzzy Pattern Recognition

One of the unique features of the Top-Down Modeling workflow is a field development design tool that assists engineers in making reservoir management decisions. This is done by using Fuzzy Pattern Recognition that has the capability of taking large amounts of data with little or no apparent trend and extract patterns that can lead to effective decision making. This design tool can identify the portions of the shale formation that has contributed the most to the production during the first 3, 6, 9 months, and first 1 and 3 years.

As shown in Figure 18 through 22, the reservoir is delineated into several Relative Reservoir Quality Indices (RRQIs) shown in different colors. The portion of the reservoir that is shown with the darkest color represents RRQI of 1. This is the portion of the reservoir that has made the largest contribution to production followed by RRQI 2, 3, and 4. The colors of other RRQIs gradually get lighter until the region for RRQI 5 become light yellow.

The contribution of the delineated RRQIs to production is calculated taking into account the number of wells that are included in each of the RRQI regions. Furthermore, these regions refer to depletion in the Marcellus shale formation since locations that have the highest amount of production are, relatively speaking, the most depleted parts of the reservoir. For example RRQI 1 is shown with dark red (almost black) color in Figure 18.

This region is small in the three months FPR map (top-right) and shifts as a function of time toward the northeastern part of reservoir during the first year of production, but in third year the increase in size of RRQI and its movement toward the west is noticeable.

This change in size of RRQI 1 and location of it can be corresponded to production of free gas from natural fractures, instant desorbed gas or any other available pore spaces.

During the first year of production the sorption is not dominant and does not contribute that much on flow .Therefore noticeable change of pattern in figure 22 which correspond to the first 3 years of Cumulative production may shows the role of sorption of gas from the matrix.

Because sorption is a timely process, therefore having more production history can be helpful to track the contribution of desorbed gas from organic material on production.

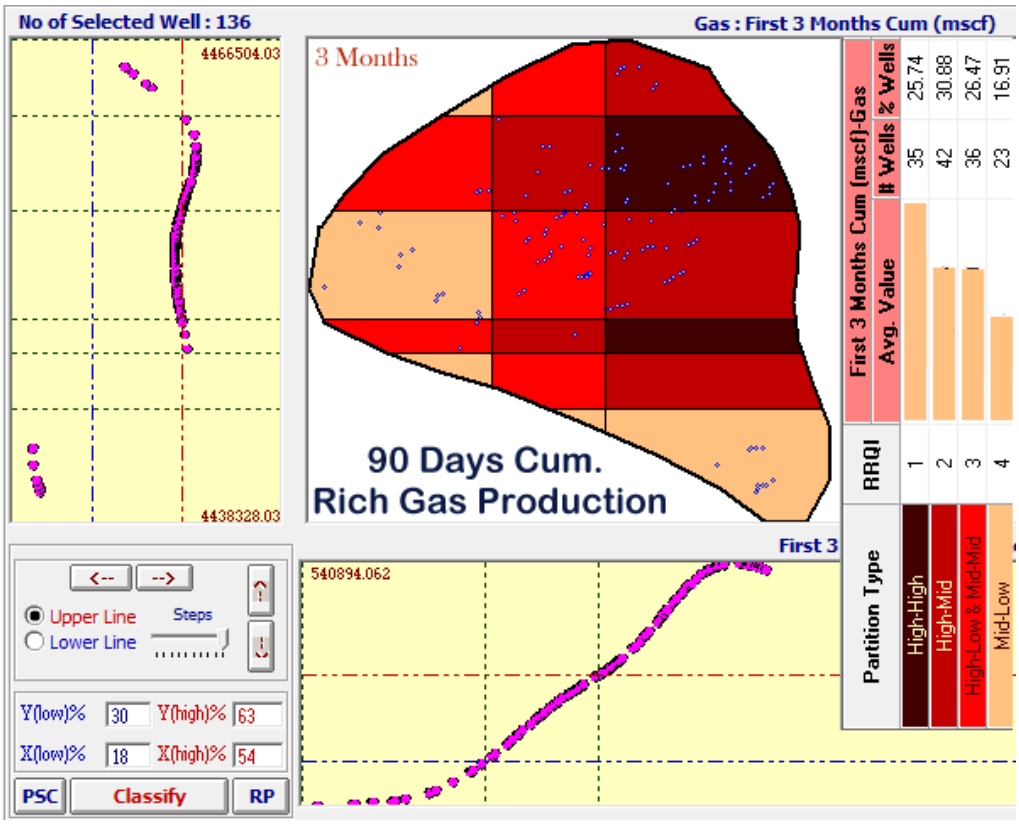

Figure 18: Fuzzy Pattern Recognition- First 3 Month-Cumulative Gas (MCF)

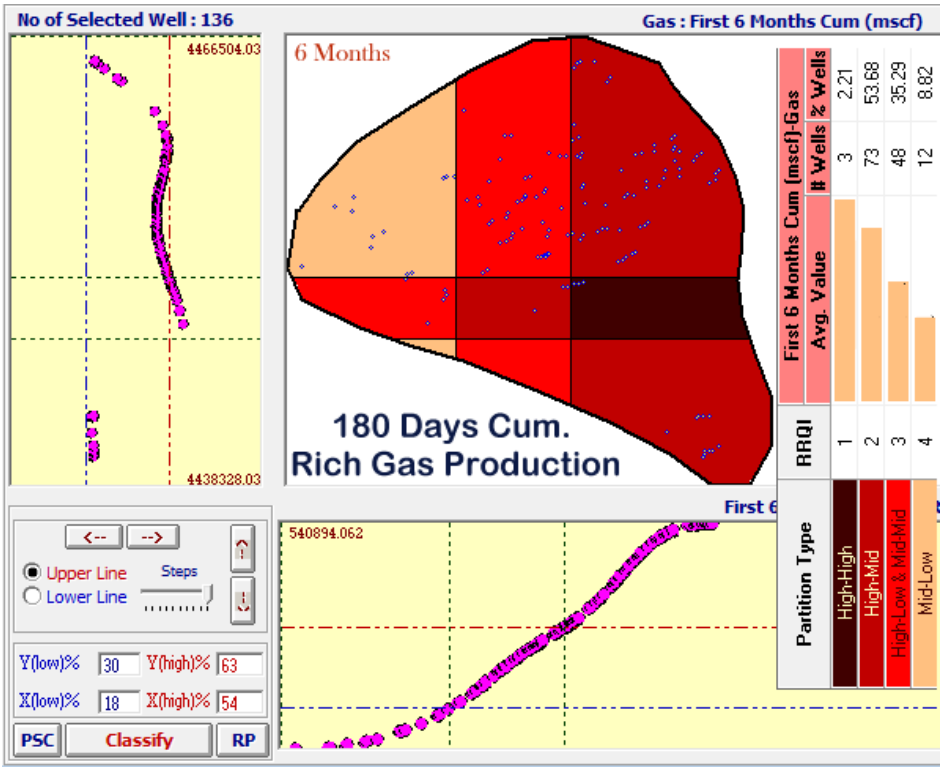

Figure 19: Fuzzy Pattern Recognition- First 6 Month-Cumulative Gas (MCF)

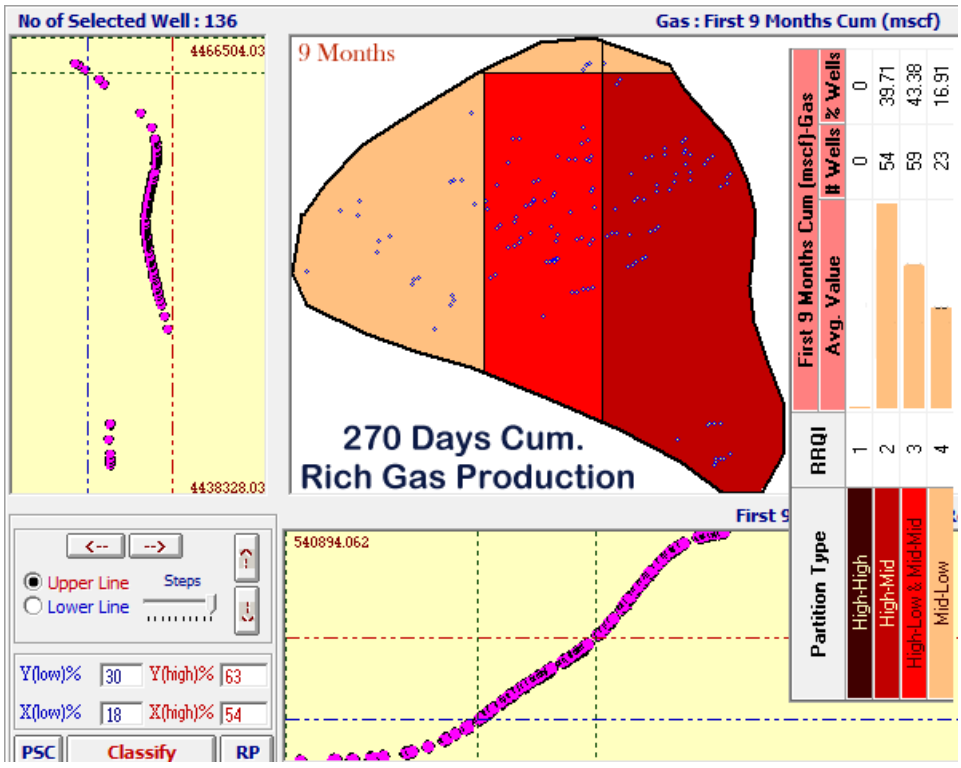

Figure 20: Fuzzy Pattern Recognition- First 9 Month-Cumulative Gas (MCF)

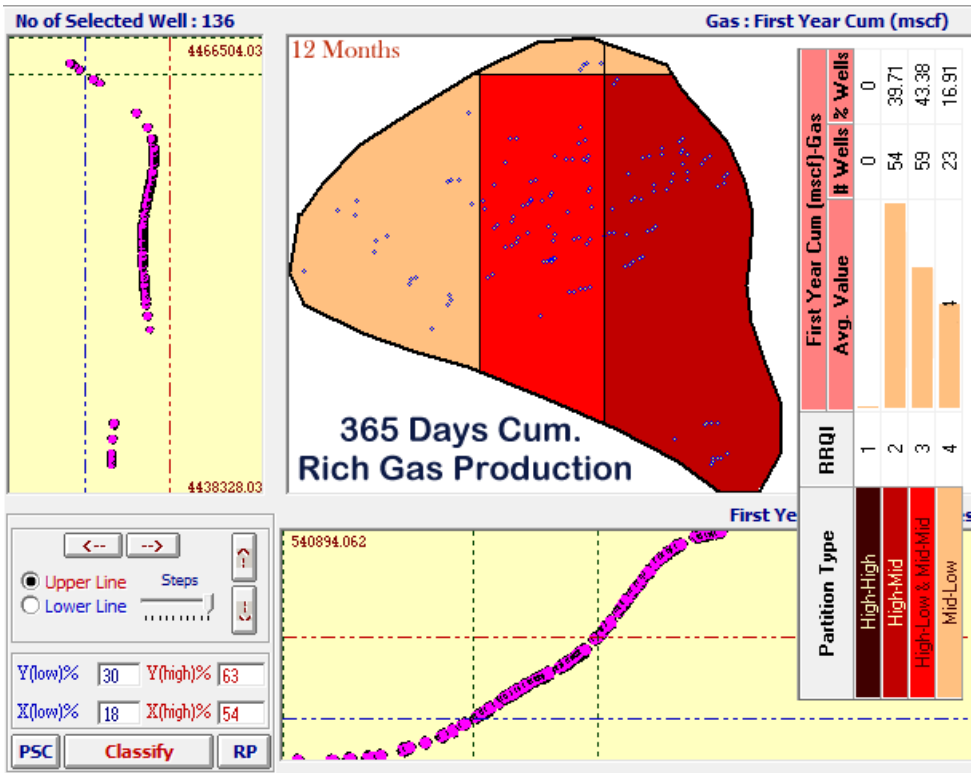

Figure 21: Fuzzy Pattern Recognition- First Year-Cumulative Gas (MCF)

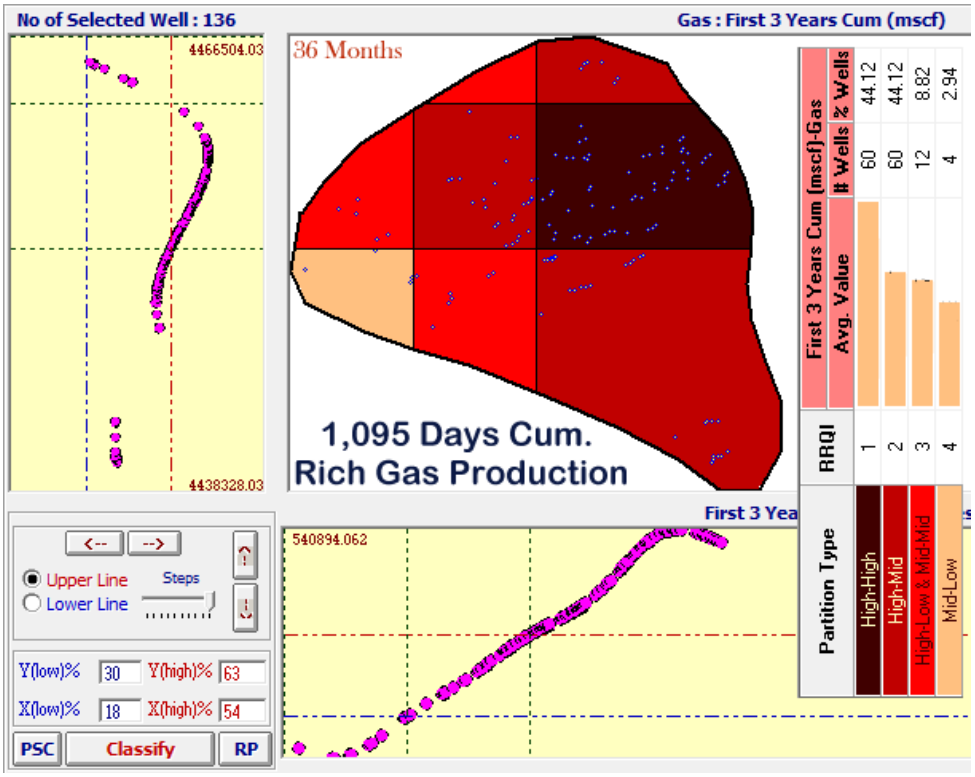

Figure 22: Fuzzy Pattern Recognition- First 3 Years-Cumulative Gas (MCF)

2-5 Reservoir Dynamic Behavior

Production Logs

The production log are carried out to determine the performance of well in different time intervals of well life and it is very crucial for reservoir management in areas such as reservoir simulation, voidage control, pressure maintenance and workover decisions.

PLTs enable the identification of fluid entry, type of fluid and most important, and the proportion of fluid entering each layer or set of perforations.

Two sets of PLT data (performed at different time intervals in the same well) was included in the data set. The first PLT for this well (Well#10020) was run at the start of production and the second PLT was run after 2 years of production. Figure 23 shows the contribution of each stage on production of this well in both PLTs.

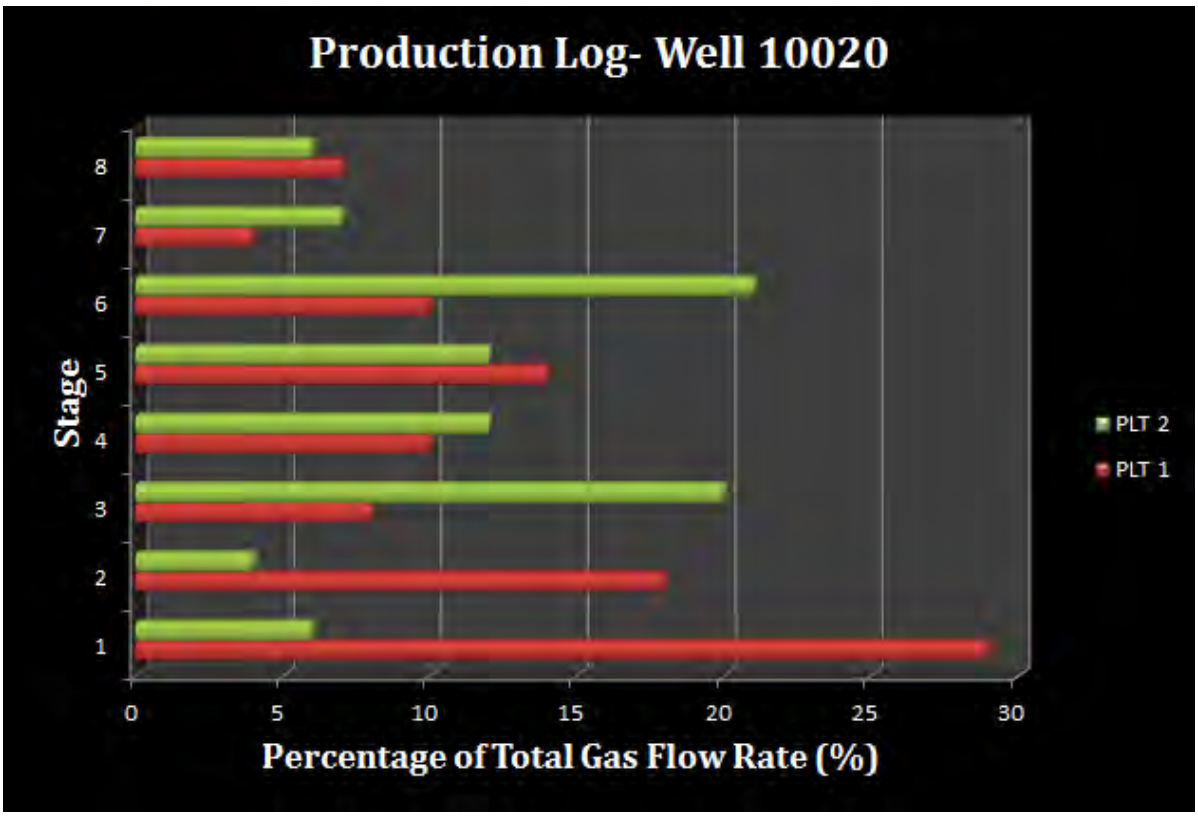

Figure 23: Production Logs in Well 10020

As it has shown in this figure the contribution of each stage on production is changing versus time and it might be because of different dominant flow regimes and/or existing of open natural fractures in different stages at different time of production in well life.

Production History

In order to monitor well behavior and find potential anomalies in production rates, the gas, condensate, and water production rates are plotted for each individual well and carefully studied.

Figure 24 shows the production profile for a well that is located in a pad with total of five laterals.

As it is shown in this figure, the water production is negligible during the production life, although the initial water production is higher, most probably, due to the flow back of injected water. For the short period of time, some anomalies can be observed in production of the wells that are located in the same pad. This probably occurs do to commingling wells during flow-back and estimating individual well rates for a short time period.

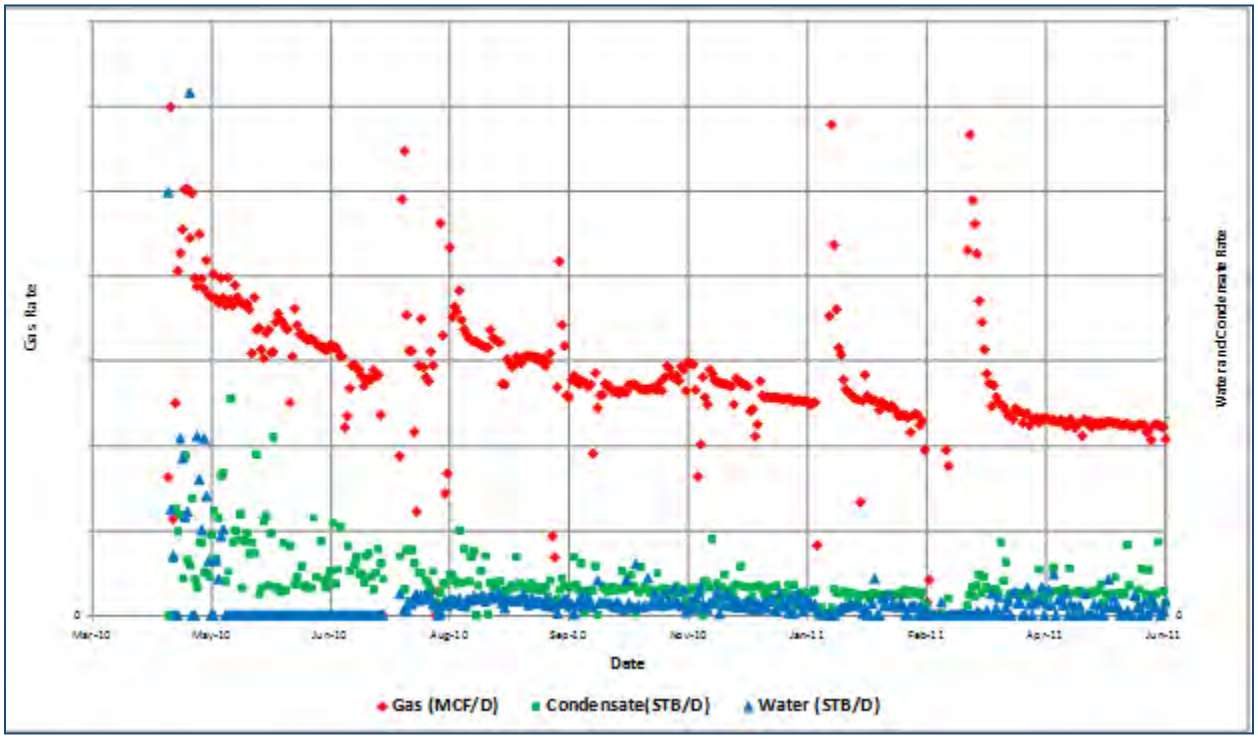

Figure 24: Production Profile for Well# 10041

Chapter 3: History Matching

3-1 Workflow

After performing all analysis, the model is ready to be trained and history matched. A flowchart that show the evolution process of developing the Top-Down model for Marcellus Shale from base model to the best history match model is illustrated in Figure 25.

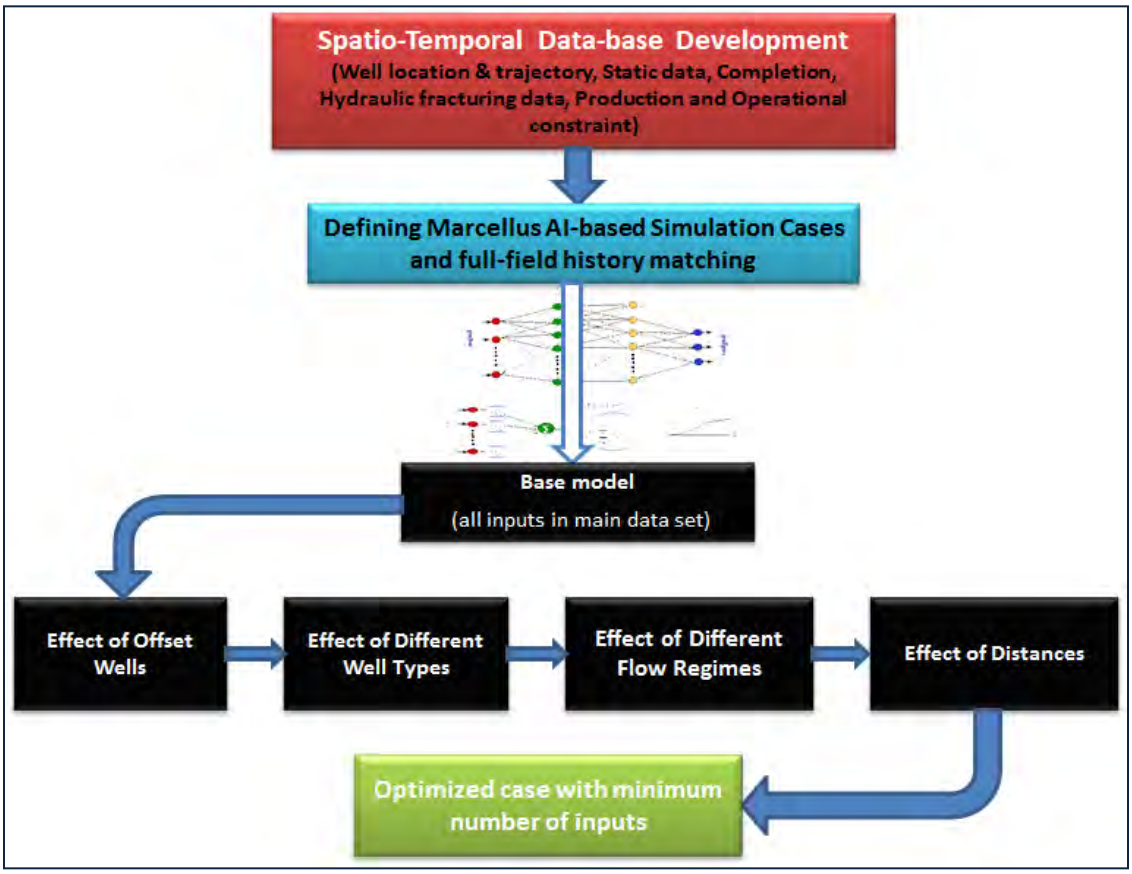

Figure 25: Marcellus shale AI-Based Full-field history matching process

As it has shown in figure 25, different cases were defined in order to incorporate all available data and to improve the result in each step. The details and result of each case will be discussed in following sections. In all defined cases, the equivalent gas from produced condensate at surface was calculated and final product as rich gas was used as production history. Also the cumulative production of rich gas in each month as well as average corresponding wellhead pressure in each month was considered.

Likewise, in all cases, 80 percent of the data was randomly used for neural network training and 20 percent for calibration and verification (10 percent for each).

3-2 Base Case

The base model was built by incorporating all available data which was listed in figure 3. This model has 55 inputs. The Key Performance Indicator of 10 most influential parameters in this model is shown in figure 26. The history matching result for entire field and two samples of those wells with good and bad results are shown in figure 27. In this graph, the orange dots represent the actual monthly rate for the entire field while the green solid line shows the Top-Down model results. The orange shadow represents the actual cumulative production while the green one is corresponding to cumulative production output by AI-based model. The red bar chart at the bottom of the plots shows the number of active Marcellus wells as a function of time. Moreover, in graph of each individual well, the dark red line show the actual gas rate while the light orange represents the Top-Down model results for gas rate. The pink line also shows the actual cumulative gas and the purple line represents the Top-Down model results for cumulative gas.

As illustrated in figure 27, from the beginning of the production to third quarter of 2009, a good match is achieved because of less number of wells in comparison with the period of late 2009 to the end of production. (Most of the wells are completed in this period).

Rank	Feature	% Degree of Influence
1	Mrcls-GThick(ft)	100
2	UpM-TOC(%)	100
3	LrM-GThick(ft)	98
4	Stim-TotPropInj(lb)	87
5	Stim-TotNoStages	79
6	MD(ft)	74
7	Pressure (psi)(t-1)	74
8	Pressure (psi)(t-2)	72
9	Stim-FVol(bbl)	70
10	Comp-LatPerf(ft)	69

Figure 26: KPI Result for Most Influential Parameters in Base Case

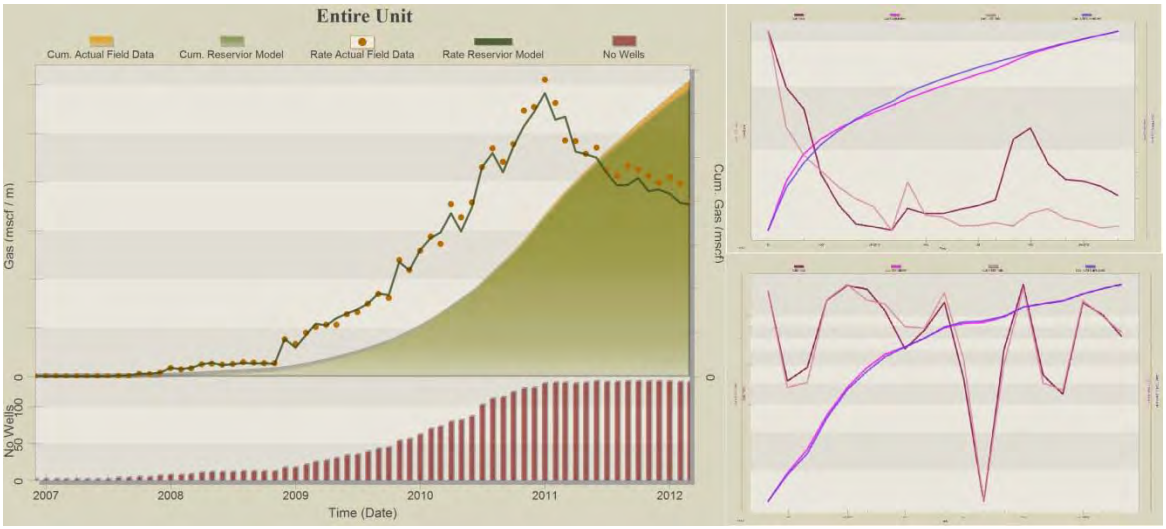

Figure 27: Entire Field History Matching Results and two wells as examples- Base Case

3-3 Effect of Offset Wells

In order to consider the effect of offset wells and taking into account any well interference effects, all aforementioned properties for closest offset well were included in the modeling. The history matching result for entire field and two wells with good and bad result are shown in figure 28. This figure shows some over-estimation of production at the early life of the reservoir. The reasoning for that behavior might be because of no or negligible impact of well interference at the early stage of the development. Since in this case all information for offset well included in the model, therefore it may cause confusion for neural network. Still the end of production was not captured completely by the Top-Down model.

Figure 28: Entire Field History Matching Results and two wells as examples- Effect of Offset Well

3-4 Effect of Well Types

Since drilling multiple wells from a pad is a common practice in the Marcellus shale, three main types of laterals have been defined as follows (Figure 29) and based on that a new parameter was added to the dataset as "Type" of the well by assigning a value of 1 to 3 in order to incorporate such information:

- ***Type one Lateral:*** This type of lateral has no neighboring laterals and does not share drainage area. It does not experience any "Frac Hits"* from wells in the same pad and its reach will be as far as its hydraulic fractures.

- ***Type two Lateral:*** The second type of lateral has only one neighboring lateral and therefore; it shares part of the drainage area and "Frac Hits" are possible from laterals in the same pad.
- ***Type three Lateral:*** The last type, is bounded by two neighboring laterals thus; the drainage area will be shared and "Frac Hits" are possible from both sides in the same pad.

(*"Frac Hit" refers to the process where an offset well is being fractured and it pushes water into existing wells.)

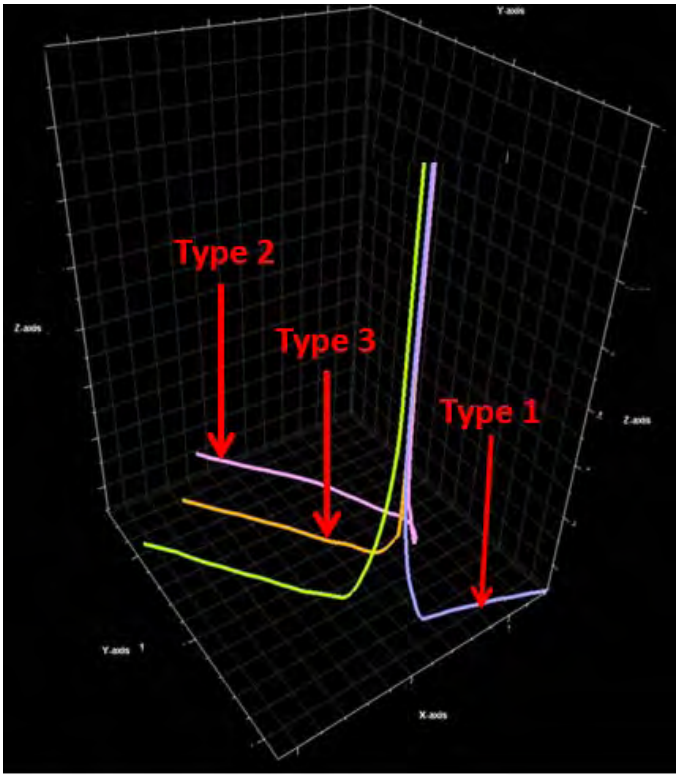

Figure 29: Different Well Types

By adding this parameter for both main and offset well, the model would have 85 inputs. Figure 30 shows the history matching result for the entire field and two wells with good and bad

result. In this case, different well configurations on pad were introduced to the neural network in order to make sure that the neural network does not treat all the wells similarly. As it has shown in figure 30, the initial over-estimation problem was solved by this action but still the history matching result needs further improvement.

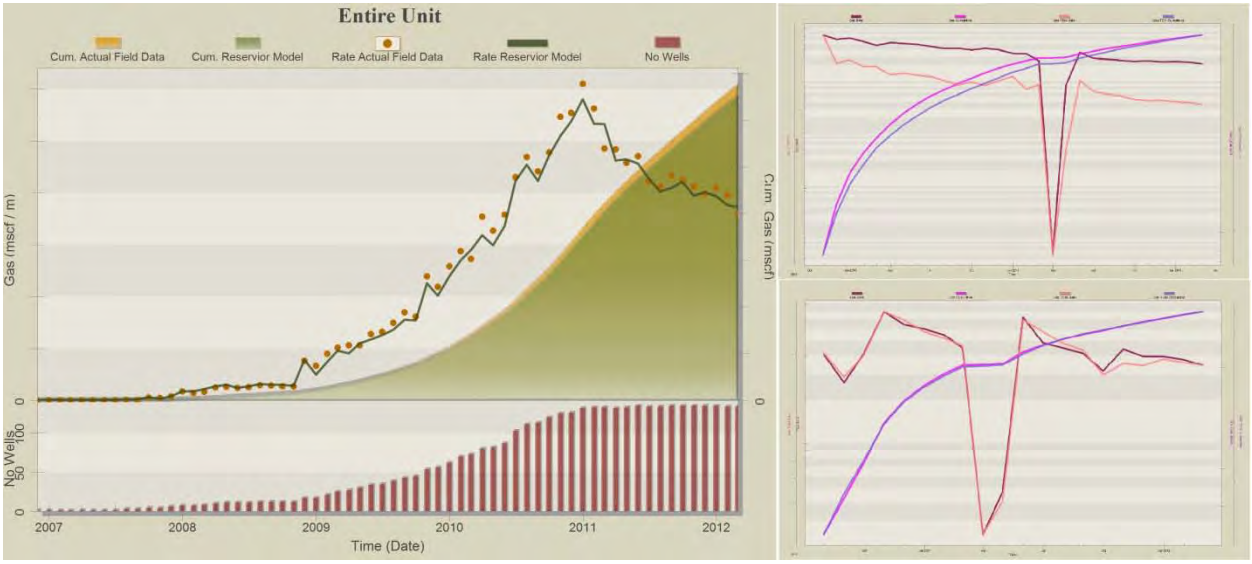

Figure 30: Entire Field History Matching Results and two wells as examples- Effect of Well Types

3-5 Effect of Flow Regimes

Two distinct flow regimes can be observed in all the wells as shown in figure 31. The first flow regime is corresponding to the initial free gas in fracture/pore spaces, which is immediately available for production and it may last a few days to a few months (Flow regime type one). Most of the wells have been observed to exhibit transient linear behavior as the main flow regime (Flow regime type two) .This transient linear behavior is characterized by a one-half slope on a log-log plot of rate against time.

This transient linear flow regime is expected to be caused by transient drainage of low-permeability matrix blocks into adjoining fractures. Many researchers (e.g., Bello et al. (2010)) also investigated this behavior. These two flow regimes where introduced in neural network as dynamic property.

Figure 32, shows the history matching result for the entire field and two wells with good and bad result.

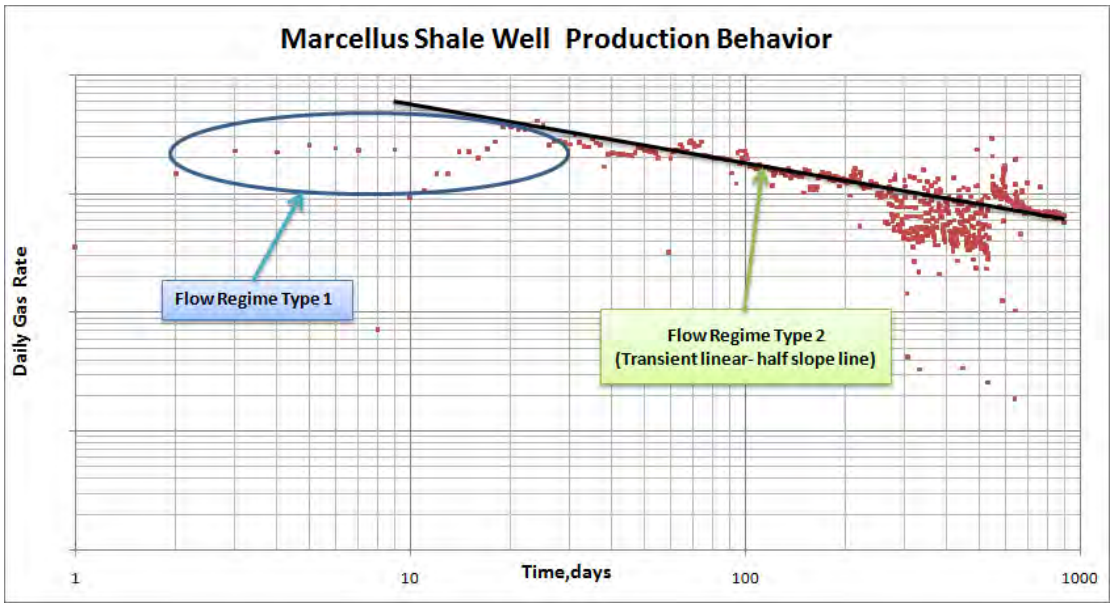

Figure 31: Log-log plot of production rate as a function of time for one of 135 wells

Figure 32: Entire Field History Matching Results and two wells as examples- Effect of Flow Regimes

Different flow regimes were introduced to the model as a dynamic parameter by assigning the value of 1 and 2 to each individual well at each time and the history match result (Figure 32) slightly improved for the whole field but the improvement was tangible for some of the wells especially for the period that flow regime one is governing.

3-6 Effect of Distances

In order to consider the impact of location (distance from other laterals in the same pad and closest lateral from offset pad), two distances were defined and fed to the neural network for training (Figure 33):

- Distance between laterals of the same pad
- Distance to closest lateral of a different pad

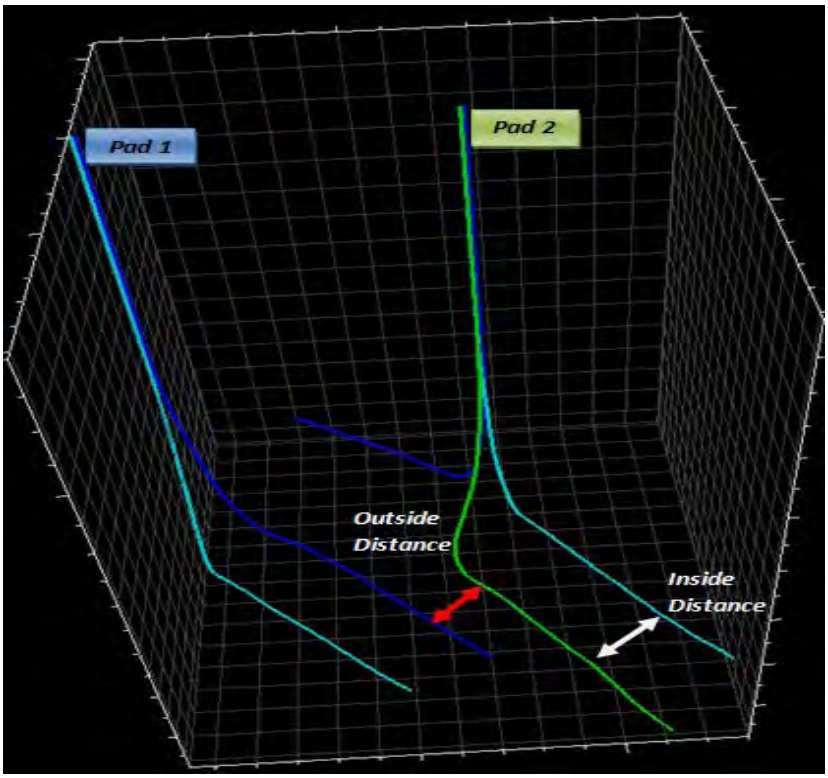

Figure 33: Inside and closest outside distance

By adding these new parameters, the model will have 103 inputs which is the largest case in terms of number of inputs. The history matching result of entire field and two sample wells for this case is shown in figure 34.

The history match result shown in figure 34 still needs some improvements and one may reasonably argue that dealing with large number of inputs is not a correct and effective way for modeling through neural network training, calibration and verification process.

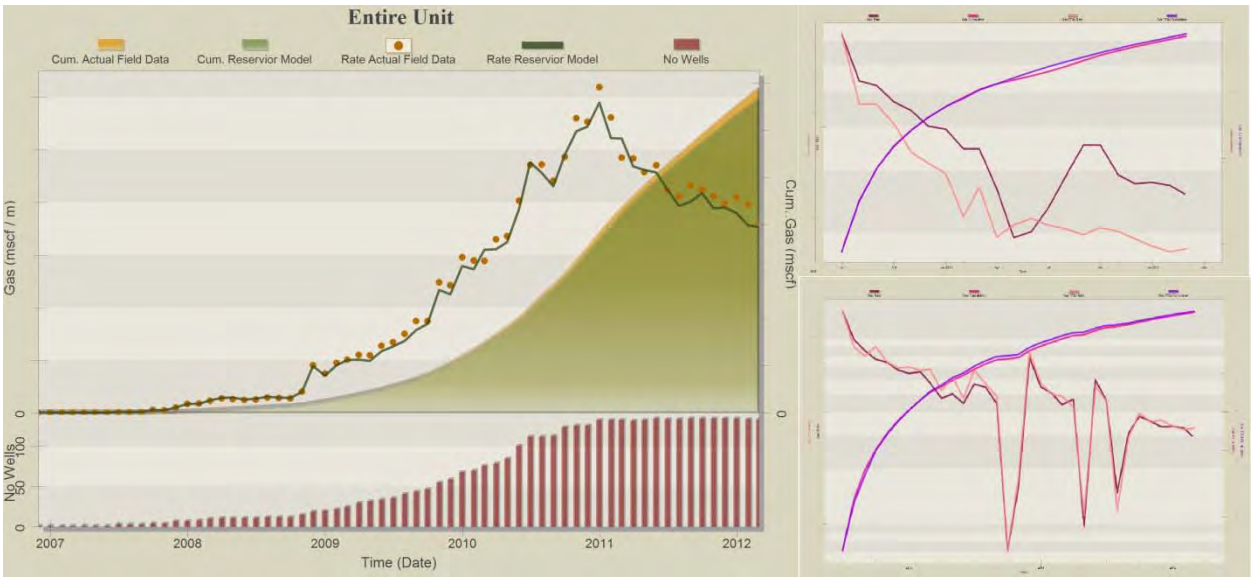

Figure 34: Entire Field History Matching Results and two wells as examples- Effect of Distances

3-7 Best History Matching Model with Least inputs

As it has shown in previous sections, adding several parameters will be concluded to a model with 103 inputs which the result shows still needs to be improved. Therefore, several attempts have been done by defining variety of scenarios which is each of them; some parameters were removed from the list of inputs in order to achieve an acceptable history matching results for each individual well and for the entire field. Finally the best history matching model was achieved by using 38 inputs.

List of the inputs that were removed and reasoning for removing them are briefly explained below:

- Since there was no allocated production from upper and lower Marcellus available, therefore the average static data for the entire Marcellus was used in case six.
- The perforated lateral length and total stimulated length were included in the data set. Since these two values had consistent difference (the length of stimulated lateral is 100 ft. longer than the length of perforated lateral), therefore the total perforated lateral length was removed from the model.
- Instead of including stage based hydraulic fracturing data, the total slurry volume; Proppant amount etc. was used in the optimized case. In addition, the average injection rate and pressure that were not changing considerably were removed instead; the breakdown pressure was included in the model.
- Since the inside and closest outside distance from an offset was included for each individual well in case five, therefore there is no need to include these two distances for offset well.

As it was mentioned before, 80 percent of the data was randomly used for neural network training and 20 percent for calibration and verification (10 percent for each). Figure 35 shows the cross plot of neural network training, calibration, and verification, which shows a good AI-based Marcellus shale model. In this figure, the x-axis is the predicated monthly gas rate by neural network while the y-axis is the actual gas production rate.

The history matching result for this case was also improved and showed an acceptable match of monthly gas rate and also cumulative production for the entire field (Figure 36).

Figure 37 shows the list of inputs that used in best history matching model.

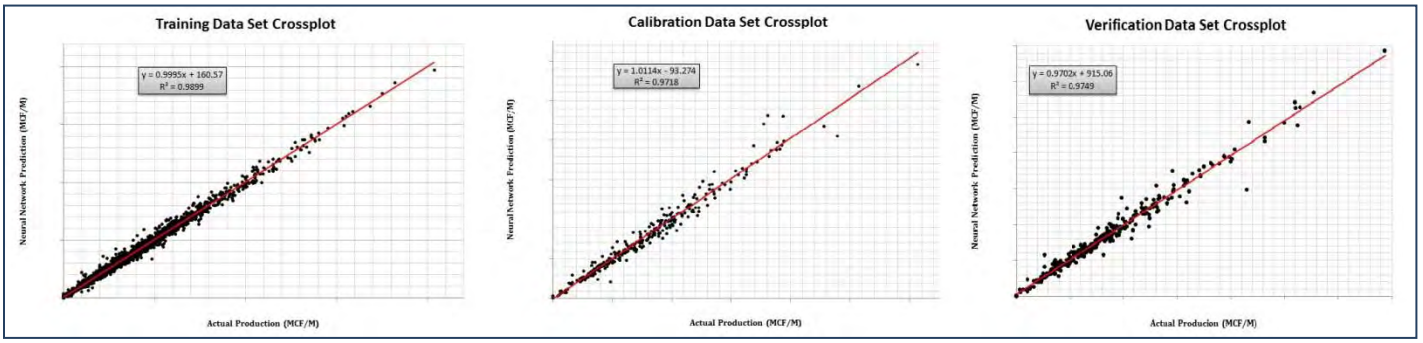

Figure 35: Cross plots for Training, Calibration and Verification for Best history matching Model

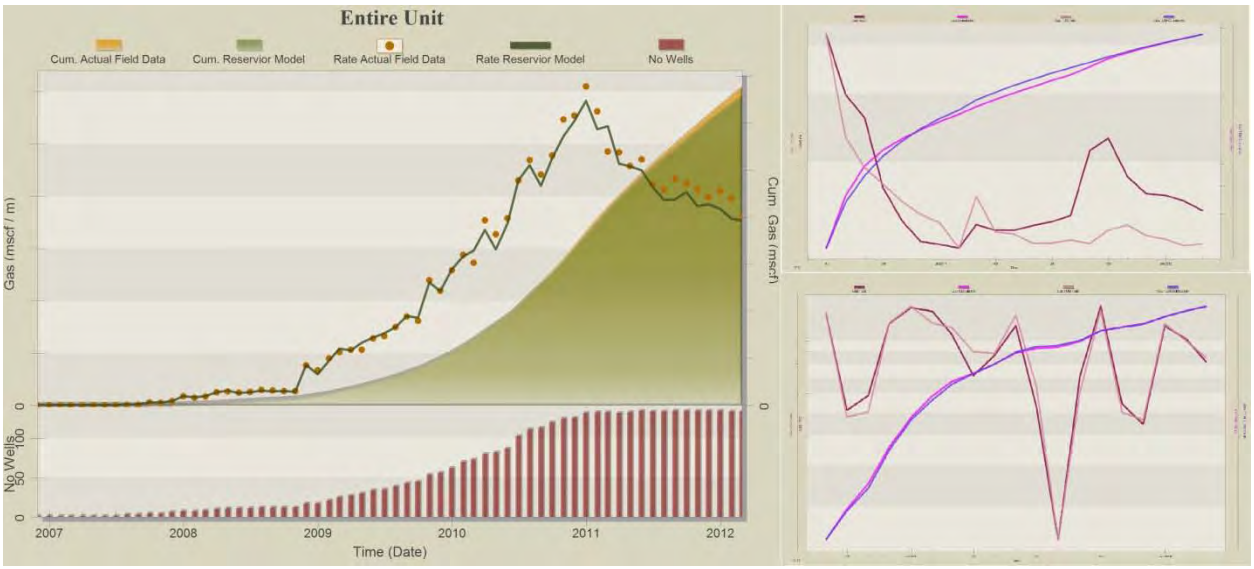

Figure 36: Entire Field History Matching Results and two wells as examples- Best History Matching Model

Easting (Main Well and its Offset) Northing (Main Well and its Offset) MD (Main Well)	Group 1	Well Location	Breakdown Pressure (Main Well and Its Offset) total Slurry volume per well (bbl)(Main Well and Its Offset) Total Proppant pumped (lb) (Main Well) Total Number of Clusters (Main Well)	Group 4	Hydraulic Farcturing
Porosity% (Main Well and its Offset) Net Thickness(ft)(Main Well and its Offset) Water Saturation(%)(Main Well and its Offset) TOC %(Main Well and its Offset)	Group 2,3	Static - Marcellus	Monthly rich gas production (MScf/m)(dry gas +Equivalent condensate) Flowing well head pressure(psia) No.of days of production	Group 5	Production & opertaional constraint
Comp-Stimulated Lateral Length (ft) (Main Well and its Offset)	Group 3	Completion	Flow Regimes (Main Well and its Offset) Inside and Outside Distances (Main Well) Well Type (Main Well and its Offset)	Group 6	Additional Parametres

Figure 37: List of Parameters in Best History Matching Model

3-8 Error Calculation

The error percentage of monthly gas production rate for all 135 wells was calculated using the following equation:

$$MAPE = \frac{\sum_{t=1}^{Nt(i)} \left| Y_{i,t}^{TDM} - Y_{i,t}^{m} \right| / Y_{i,t}^{m}}{Nt(i)} .100\%$$

Where:

$Y_{i,t}^{TDM}$ is the predicted production by TDM (AI-based model)

Yi, is the Actual Field data

ΔY_i^m is the measured maximum change in actual production data

$t(i)$ is the number of month of production

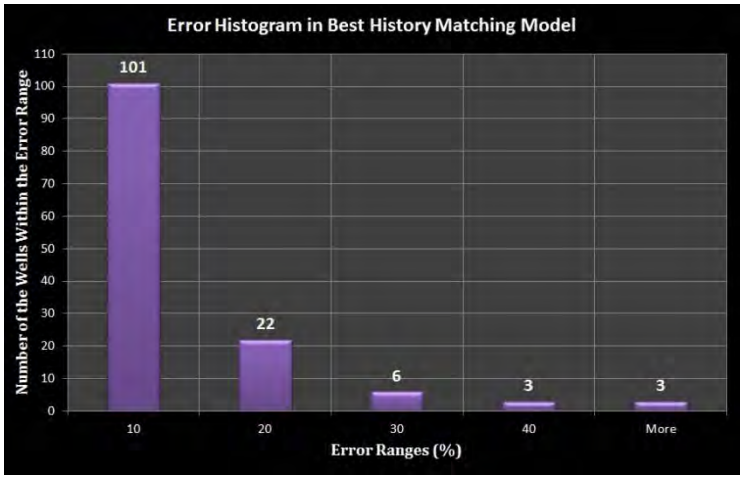

Figure 38: History Matching Error in Best History Matching Model

Chapter 4: Forecast

After completion of history matching process, the best history matching model was used to forecast the well/reservoir performance to assist in planning field development strategies. To examine the model validity in the forecasting mode, the well and field data were partially matched and then attempted forecasting (Scenario 1 and 2). Taking validation one-step further, the production performance of a recently drilled well, which was completely blind to the model (was not involved during training and initial validation), was predicted and compared with actual field measurement (Scenario 3).

4.1 Scenario 1

In the first step, 20% of last production history was removed from the training data set. Since the length of production for 135 wells is varying between 16 and 67 months, therefore last 4 to 14 months of production were removed to examine the forecasting ability of the model (Blind history match). Additionally, the AI-based model was run to forecast additional 12 months. For blind history matching of last 4 to 14 months, the number of days of production for that period was included in the training set. The averaged flowing wellhead pressure for the last three months was used as a constraint for the blind history matching forecasting period (4 to 14 months and an additional year).

Figure 39 shows the blind history matching and additional one year forecasting results for two wells with 16 and 44 months of production history correspondingly as an example. In this graph, the orange dots represent the actual monthly rate while the green solid line shows the Top-Down model results. The black dots show the actual production data that was removed from the training and tried to be predicted by model. The yellow part of graph represents the one year of forecast which there is no production history is available.

In these two wells last four and nine months of production were removed from training (20% of total month of production) and Top-Down model could predict the production behavior of those periods with acceptable accuracy.

4.2 Scenario 2

As a complement to scenario 1, last four months of production were consistently removed for all the wells and tried to predict the production rate for those months. The wellhead pressure for these 4 months is an average of last 3 months and is kept constant for both these 4 months and additional one year of forecast.

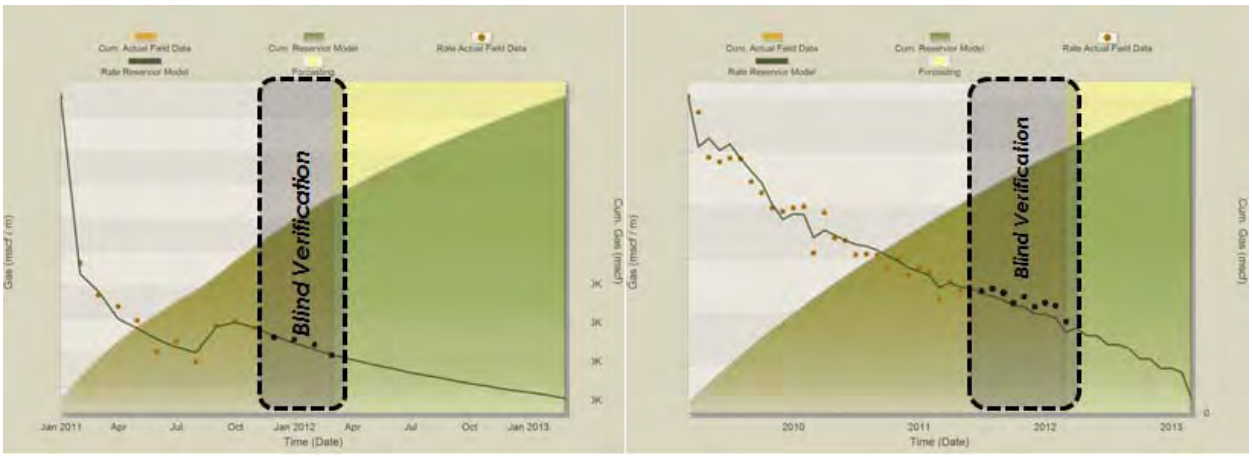

Figure 39: Blind History Matching and additional Forecasting for Two Well in Scenario 1

Figure 40 shows the blind history matching results as well as forecasting for additional year. By looking at actual production for the last four months, a sudden increase in rate at second month can be clearly observed, that might be because of high demand of natural gas over the winter, and then the production followed its natural declining behavior at fourth month. Therefore, the model could predict total production rate for the first and fourth month good enough but it underestimate the total rate for second and third months.

The error for predicting the production rate of those four months is varying from 1.4 to 9.2%, for each individual, which shows the capability of model in prediction mode.

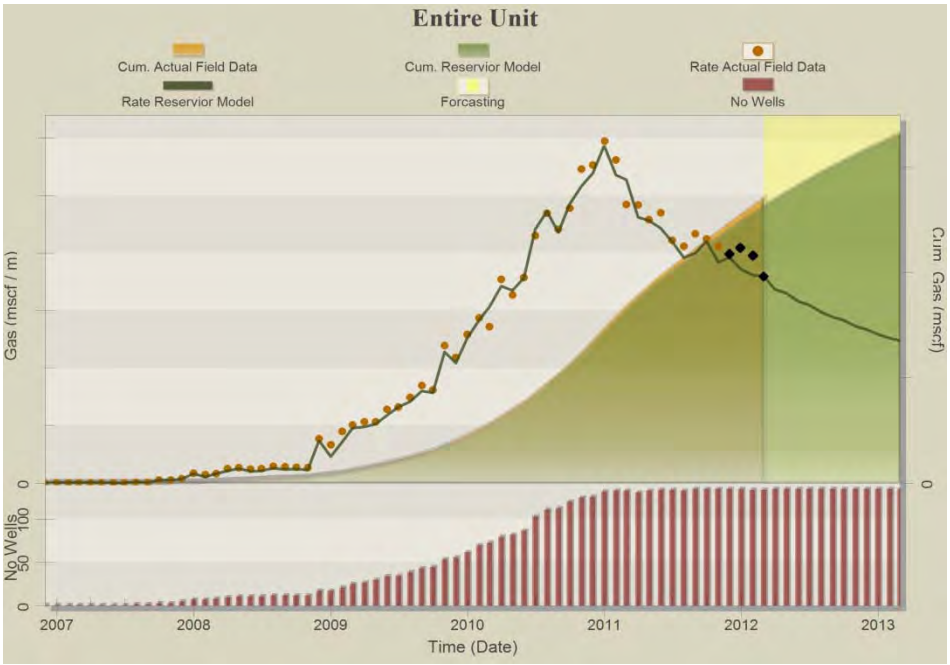

Figure 40: Blind history matching of last four months and additional year of forecasting for entire field

4.3 Scenario 3

In this scenario, the capability of the model for forecasting was tested by prediction of production performance of a newly drilled pad in area.

The operator provided the location of a new pad including five recently drilled wells that are producing for five month in the study area (Figure 41) The wellhead pressure for all the wells was kept at 200 psi (based on the closest offset wells).

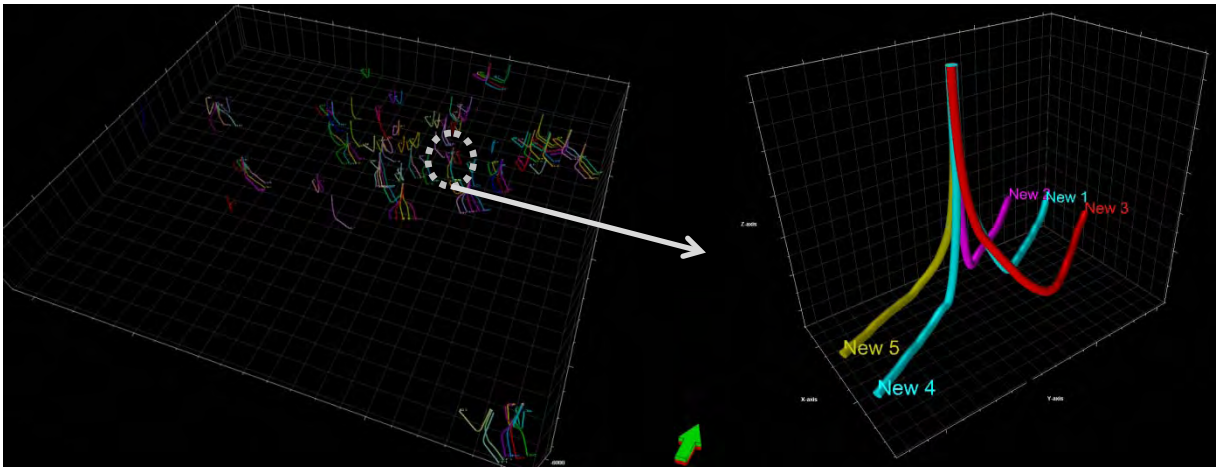

Figure 41: Location and Pattern of New Wells

For the first run, number of days of production was not included in the model and it was assumed that all the wells are producing for whole month. In the second run, the provided number of days of production was included in predictive model. The forecasting results for all five new wells and the location of them in part of area of study are shown in figures 42 to 46.

In these figures, the red line represents the completely blind forecasted cumulative production without including the no. of days of production while the blue dashed line shows forecasted cumulative production by including the no. of days of production. The black dots are actual cumulative production for five months. Additional seven months of forecasting are identified by a grid dashed box.

Figures 42 to 46 show the range of error for forecasted cumulative production, for those new wells with five months of history, between 8.7 to 21.7%. More than 10% error in the forecast might be attributed to very short production history for those new wells. Nevertheless Top-Down Marcellus Shale model shows its capability on predicting and forecasting of new well/s performance. It has to be mentioned that the properties of the new wells were not available and Top-Down Model used the average static parameter, completion and stimulation data from the nearby wells.

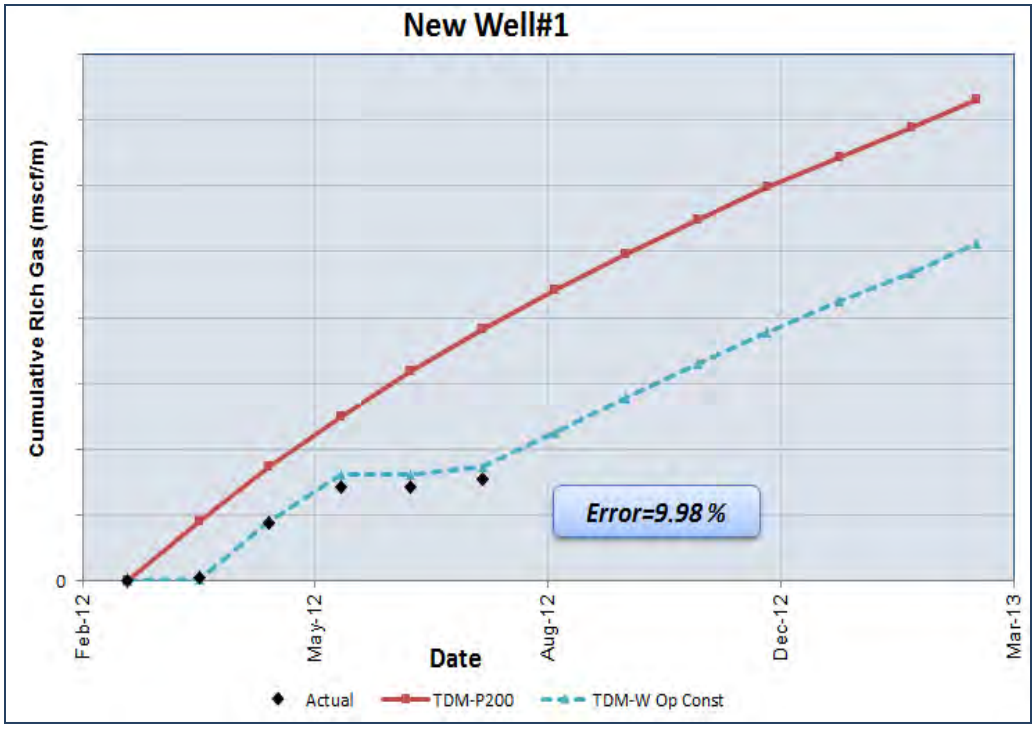

Figure 42: Forecasting the Production Performance for New Well # 1

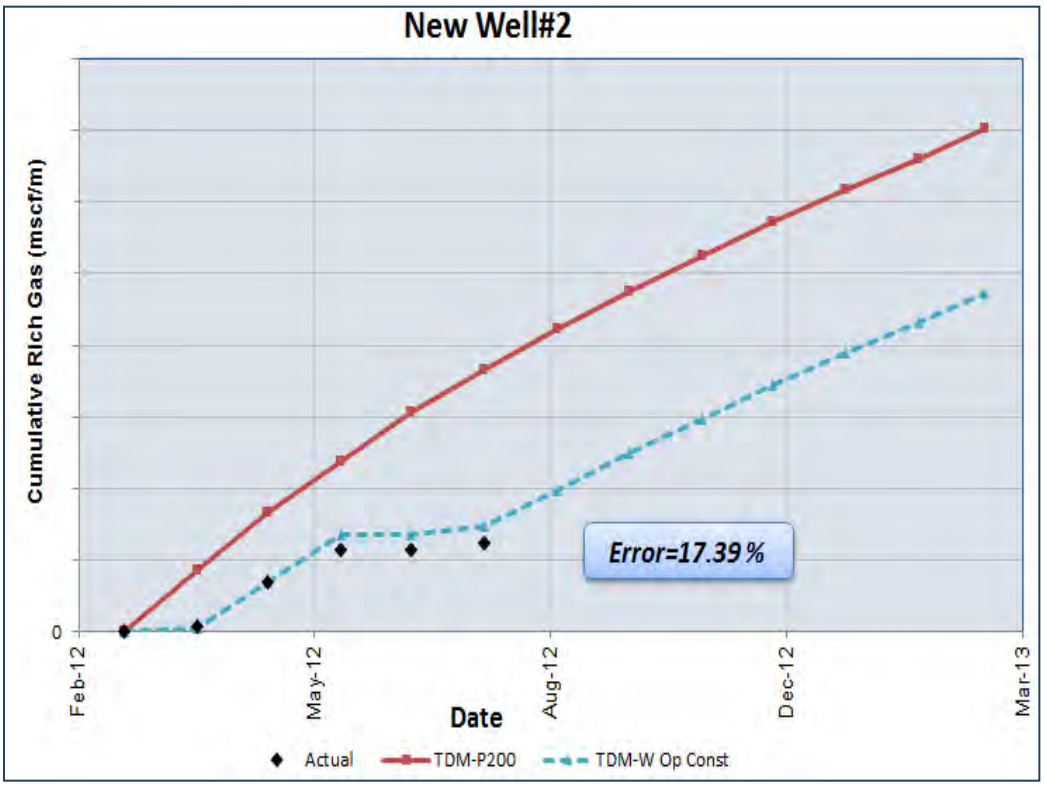

Figure 43: Forecasting the Production Performance for New Well # 2

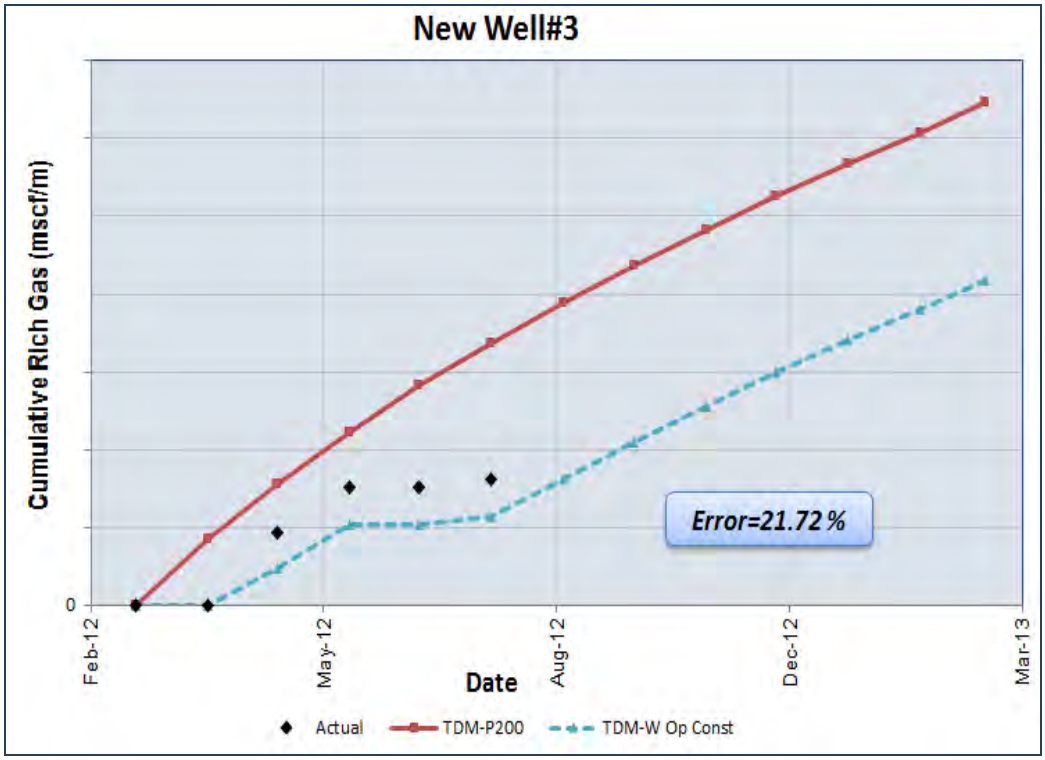

Figure 44: Forecasting the Production Performance for New Well # 3

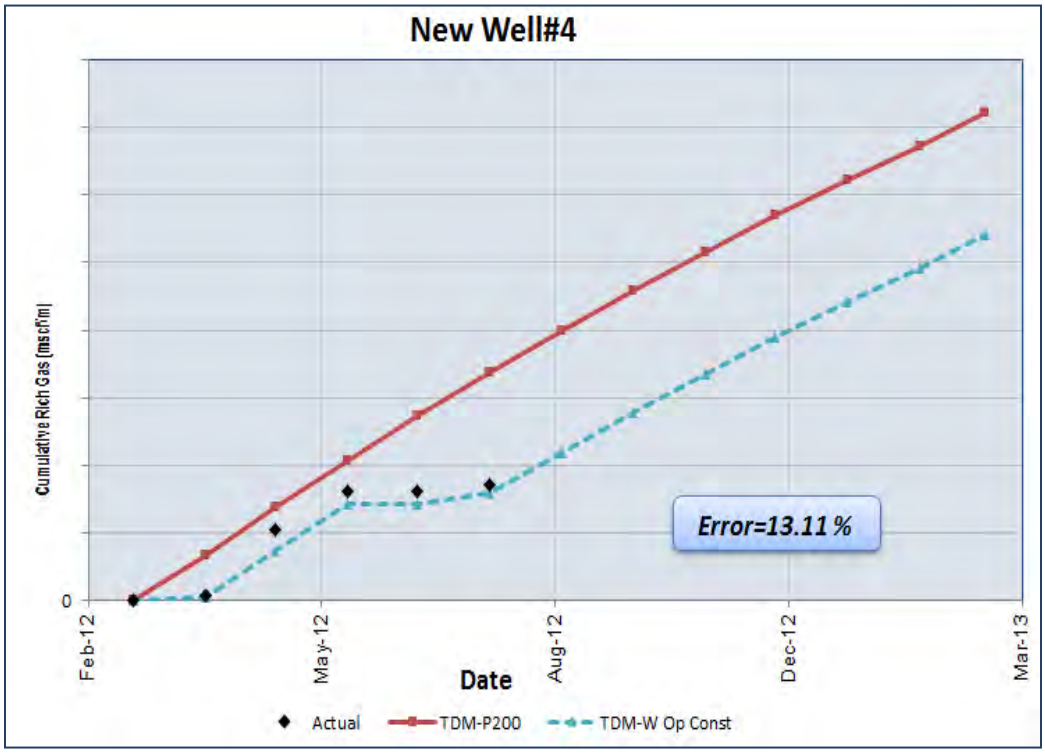

Figure 45: Forecasting the Production Performance for New Well # 4

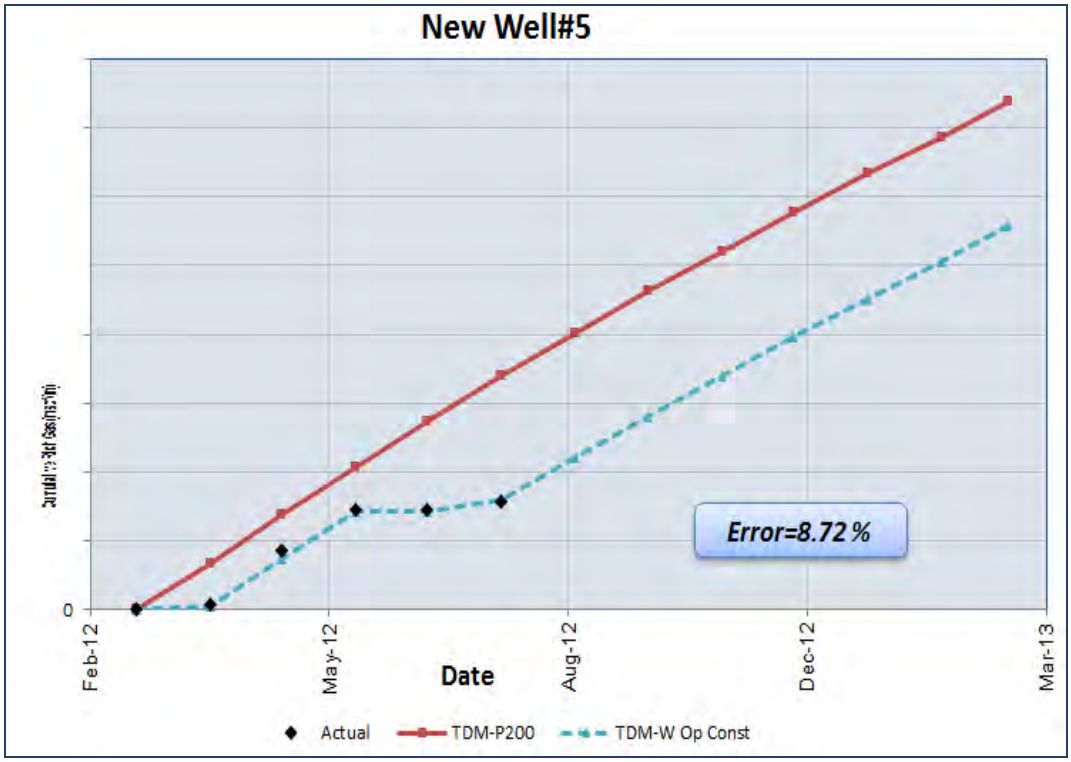

Figure 46: Forecasting the Production Performance for New Well # 5

Chapter 5: Conclusion

In this project, a Top-Down Model for Marcellus Shale Gas Reservoir was developed with the aim of overcoming current issues in numerical modeling and simulation of this kind of reservoirs. The beauty of this technology is its capability to handling and incorporating all the data and instead of imposing our vague knowledge of flow and transport mechanism in shale system, let the data identify its functional relationship using pattern recognition approach in a non-linear and complex system.

The process of full-field history matching has been explained in details and the result were shown very acceptable match between actual data and TDM.

The best history matching model was used for forecasting the well/reservoir performance. Results of different scenarios in chapter 4 showed that the TDM is fully capable of forecasting the well/reservoir performance.

The best history matching results and prediction results of all wells are shown in appendices A and B respectively.

References

1. *Virtual Intelligence Applications in Petroleum Engineering: Part 1; Artificial Neural Networks.* **D.Mohaghegh, Shahab.** s.l. : Journal of Petroleum Technology, 2000.

2. *Virtual Intelligence Applications in Petroleum Engineering: Part 2; Evolutionary Computing.* **D.Mohaghegh, Shahab.** s.l. : Journal of Petroleum Technology, 2000.

3. *Virtual Intelligence Applications in Petroleum Engineering: Part 3; Fuzzy Logic.* **D.Mohaghegh, Shahab.** s.l. : Journal of Petroleum Technology, 2000.

4. *Reservoir Modeling of New Albany Shale.* **Kalantari,Amirmasoud.** Master Thesis, 2010.

5. Esmaili S., Kalantari-Dahaghi A., Mohaghegh S.D." *Modeling and History Matching Hydrocarbon Production from Marcellus Shale using Data Mining and Pattern Recognition Technologies*" SPE161184,Easetrn Regional Meeting, Lexington ,KY, US.

6. Esmaili S., Kalantari-Dahaghi A., Mohaghegh S.D." *Forecasting, Sensitivity and Economic Analysis of Hydrocarbon Production from Shale Plays using Artificial Intelligence and Data Mining*" SPE162700,SPE Canadian unconventional Resources Conference, Calgary, US.

Appendix A: Best History Matching Results

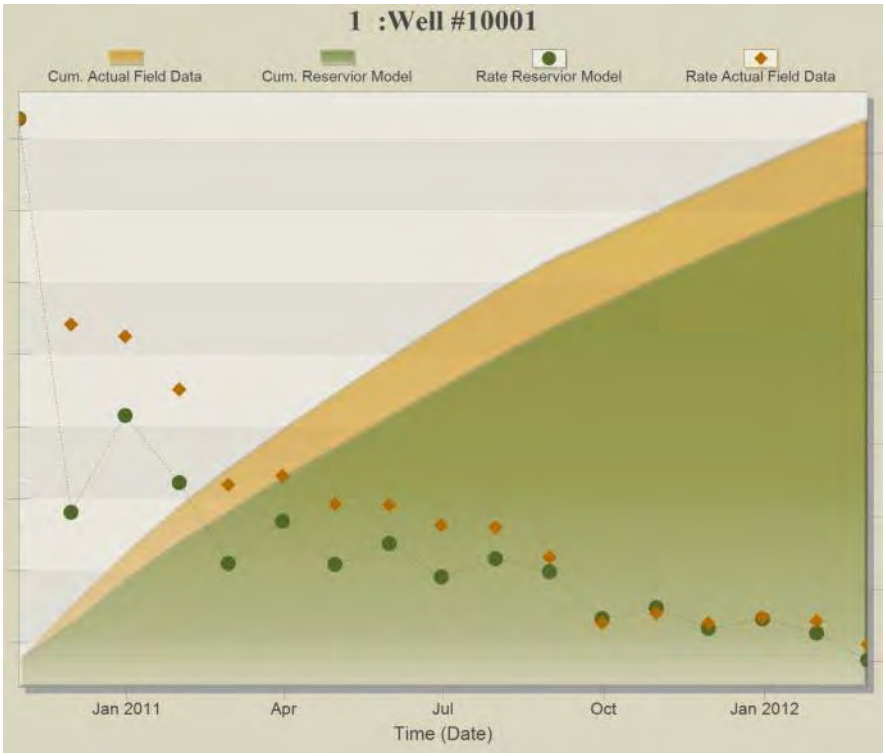

Figure A- 1: History Matching Results of Well#10001

Figure A- 2: History Matching Results of Well#10002

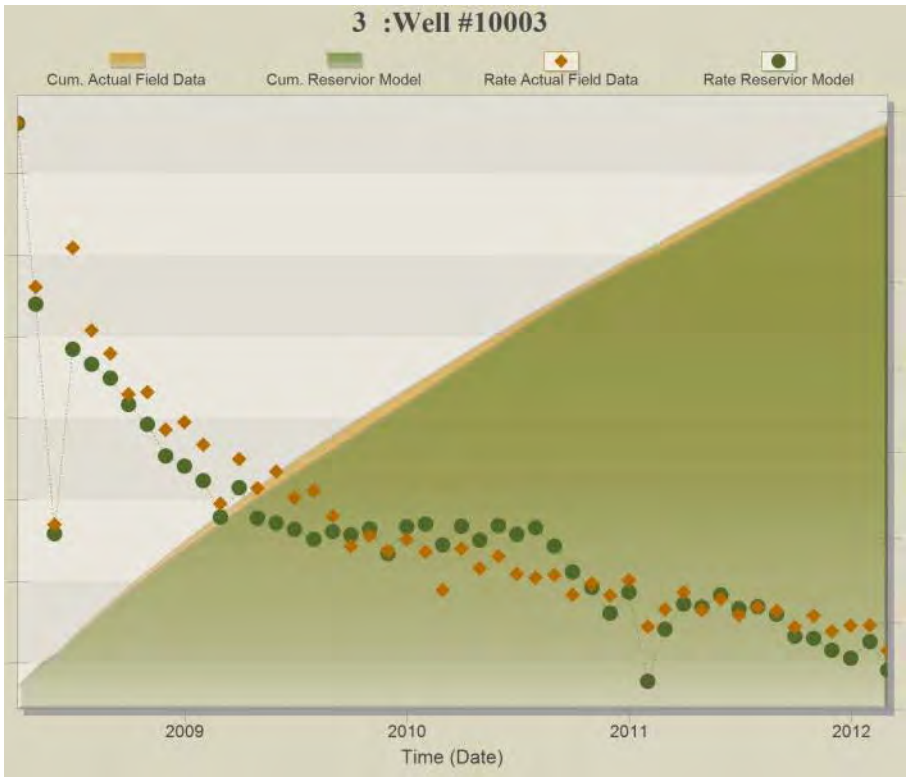

Figure A- 3: History Matching Results of Well#10003

Figure A- 4: History Matching Results of Well#10004

Figure A- 5: History Matching Results of Well#10005

Figure A- 6: History Matching Results of Well#10006

Figure A- 7: History Matching Results of Well#10007

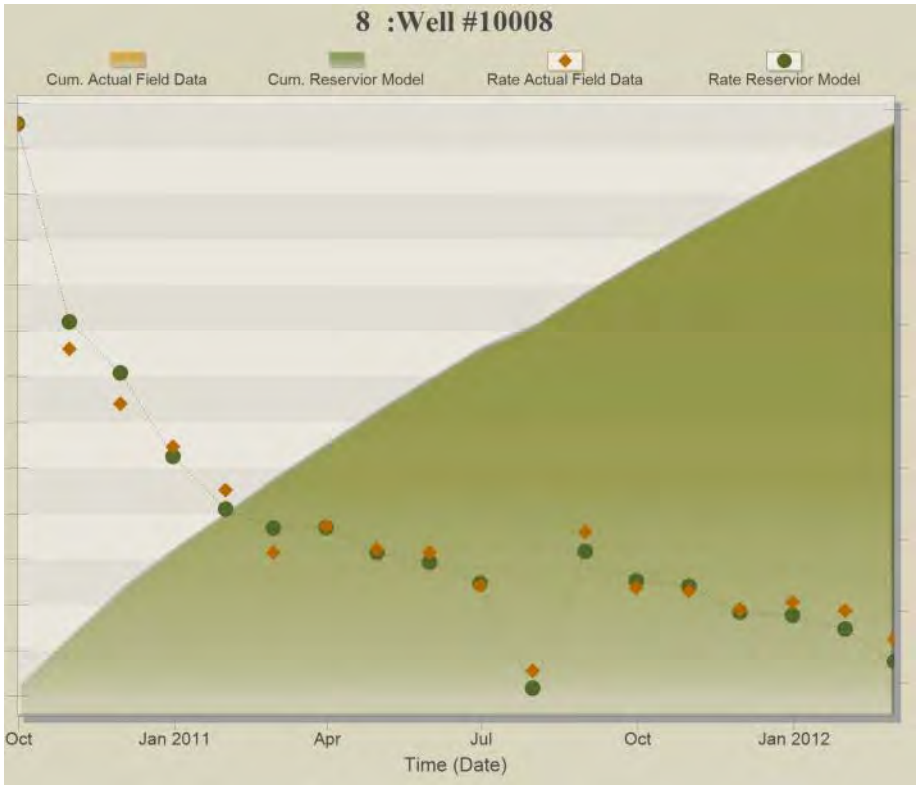

Figure A- 8: History Matching Results of Well#10008

Figure A- 9: History Matching Results of Well#10009

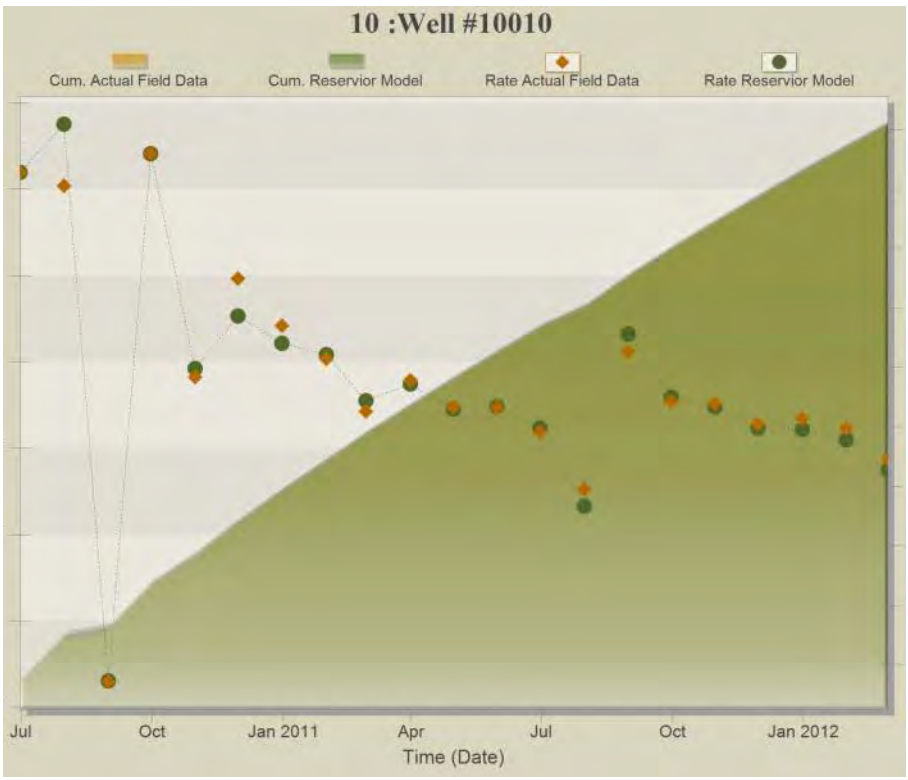

Figure A- 10: History Matching Results of Well#10010

Figure A- 11: History Matching Results of Well#10011

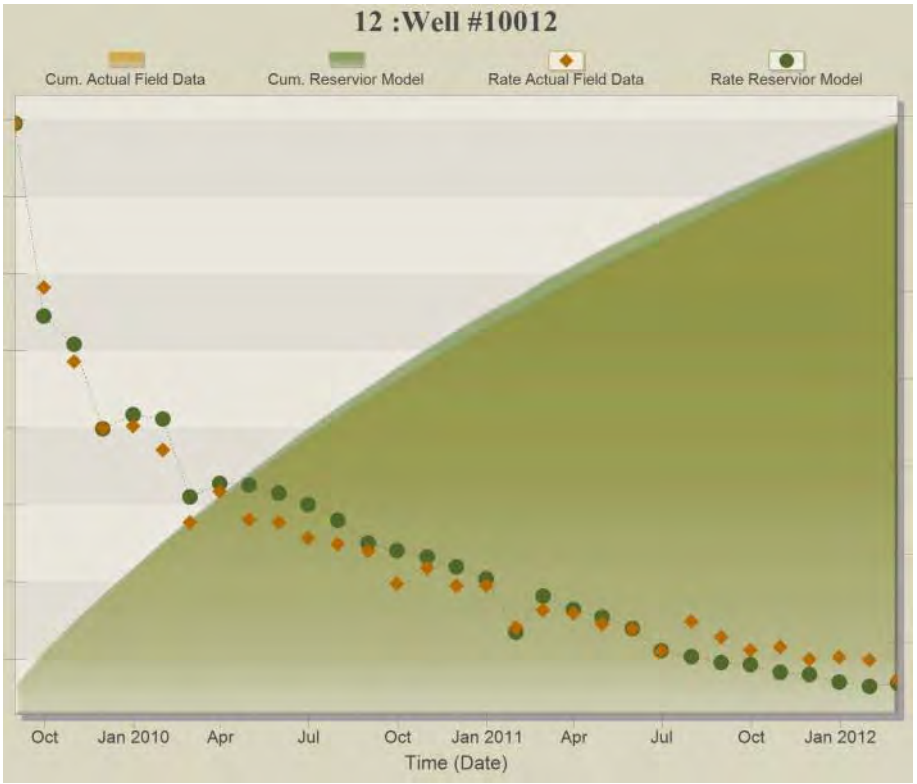

Figure A- 12: History Matching Results of Well#10012

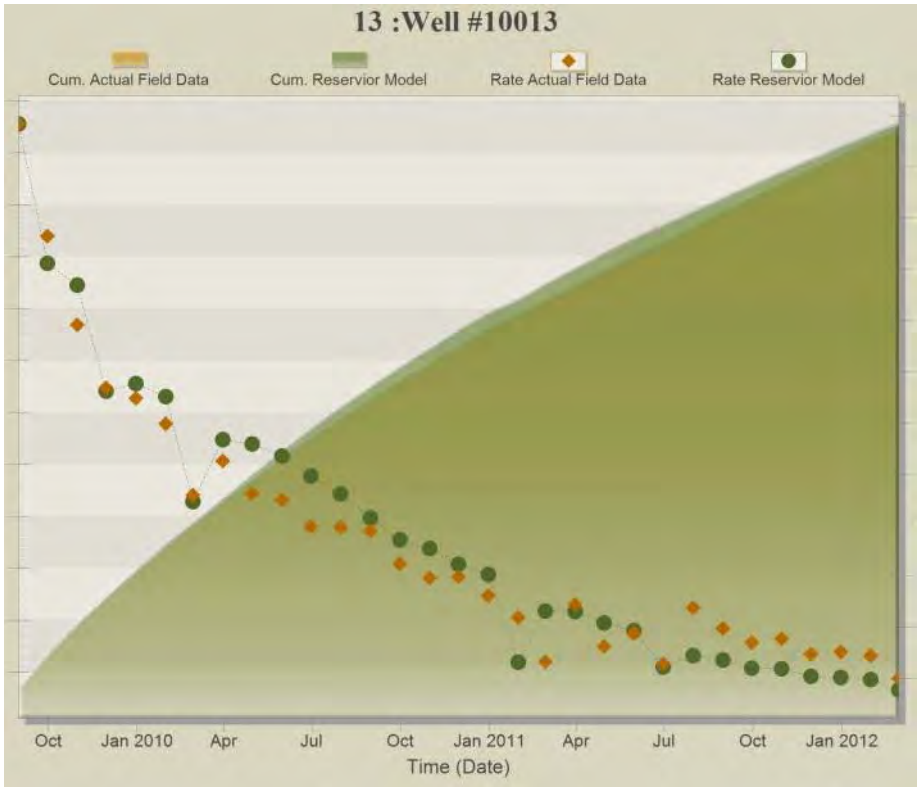

Figure A- 13: History Matching Results of Well#10013

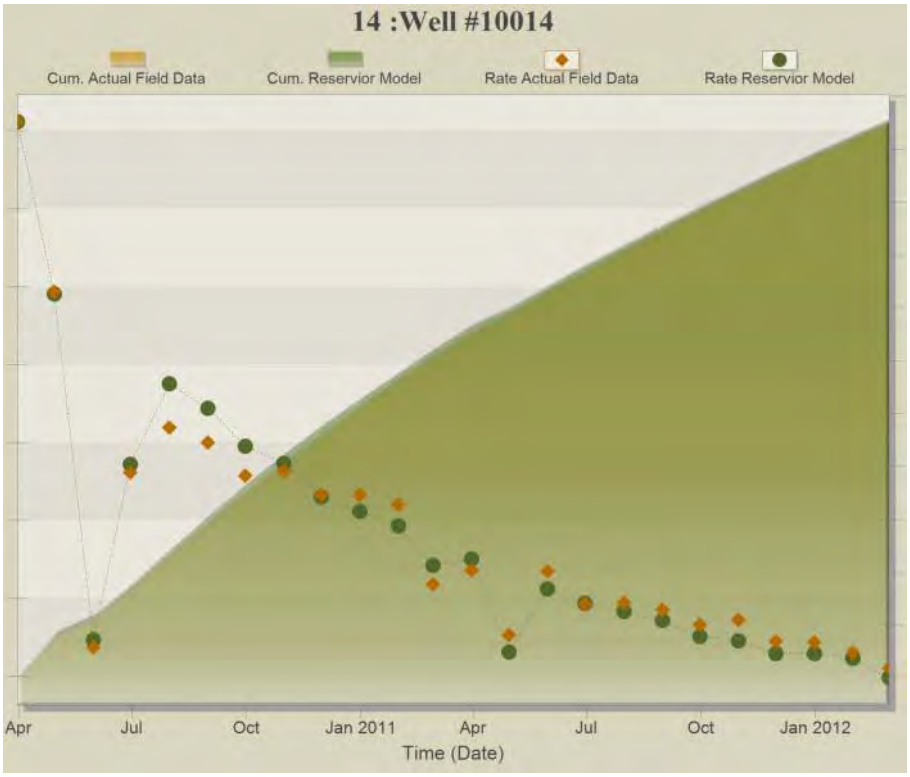

Figure A- 14: History Matching Results of Well#10014

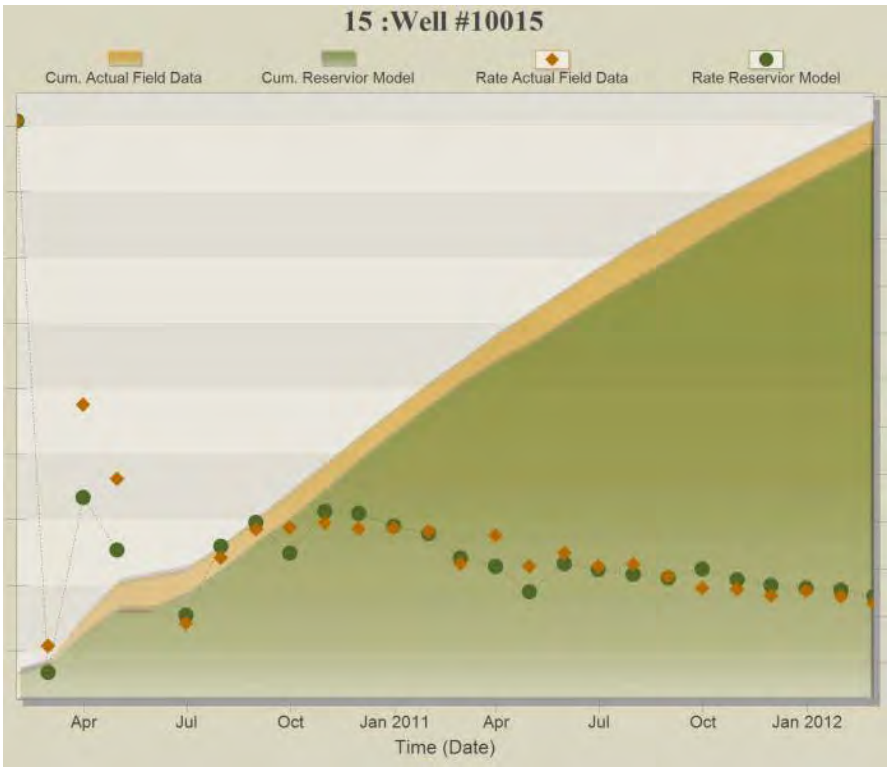

Figure A- 15: History Matching Results of Well#10015

Figure A- 16: History Matching Results of Well#10016

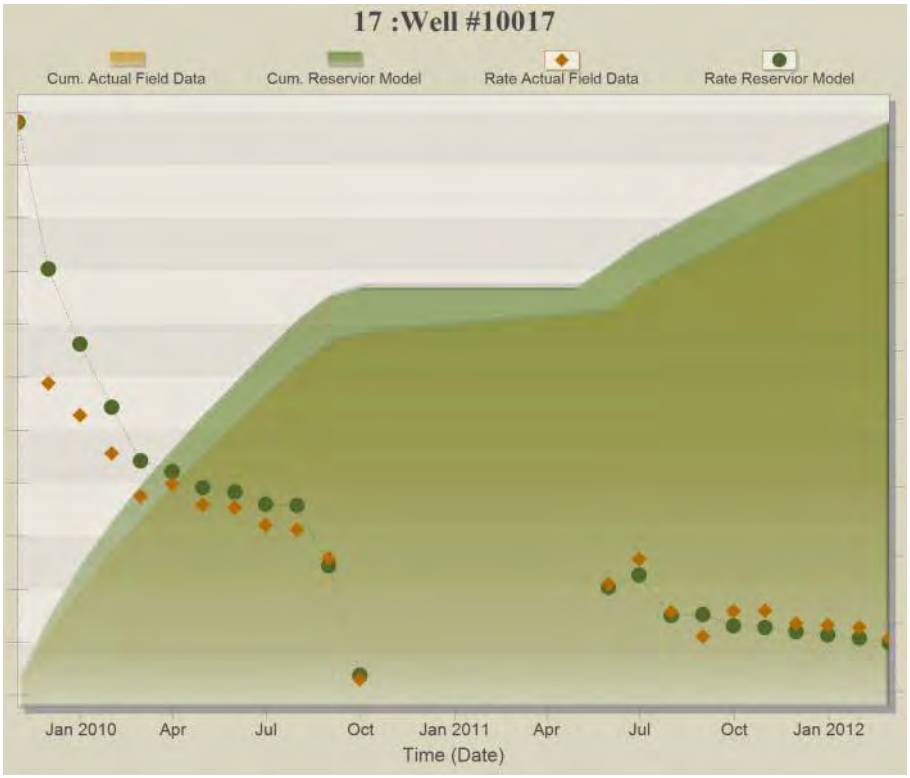

Figure A- 17: History Matching Results of Well#10017

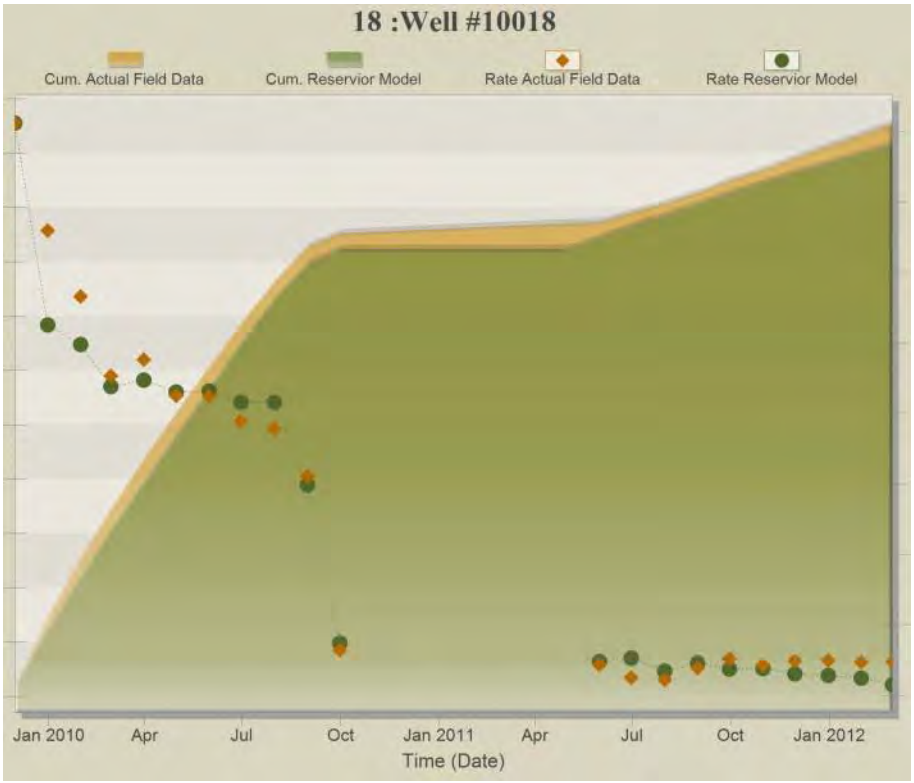

Figure A- 18: History Matching Results of Well#10018

Figure A- 19: History Matching Results of Well#10019

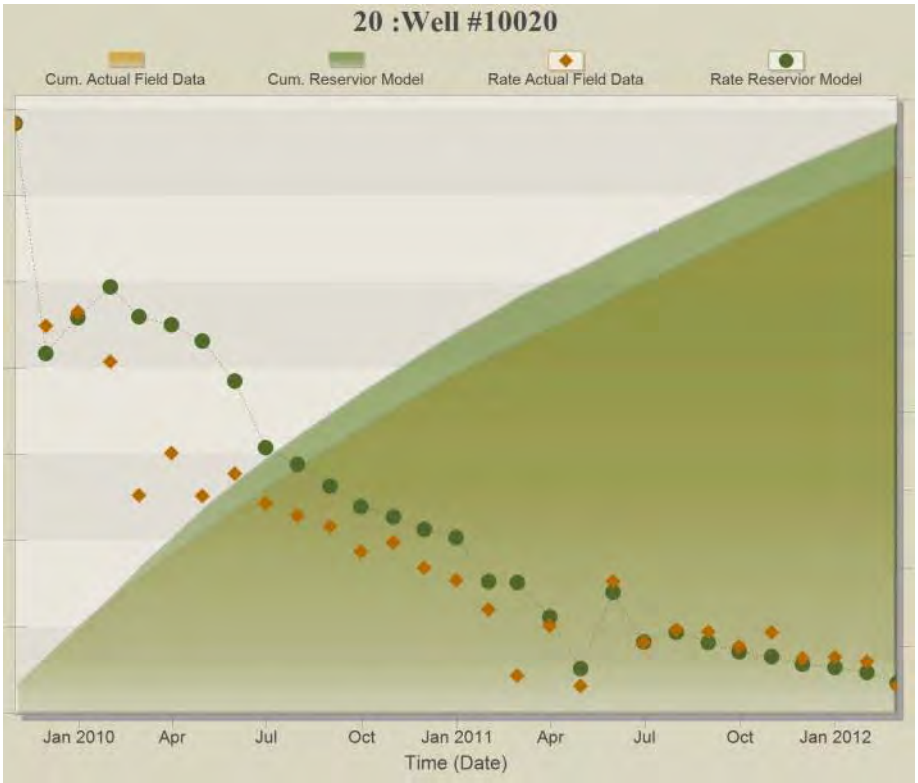

Figure A- 20: History Matching Results of Well#10020

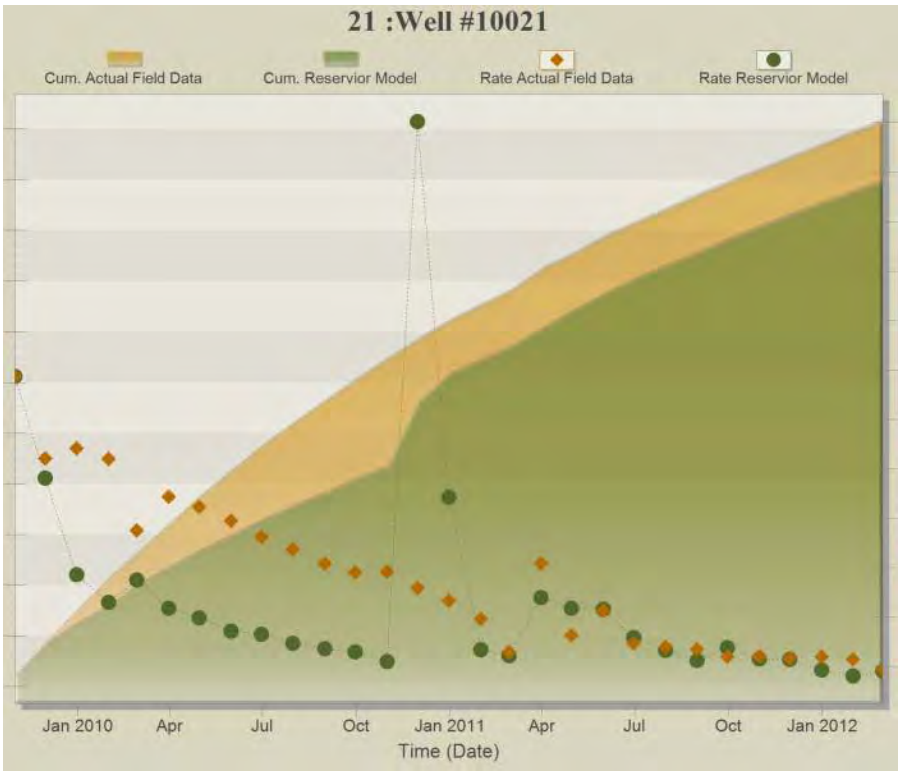

Figure A- 21: History Matching Results of Well#10021

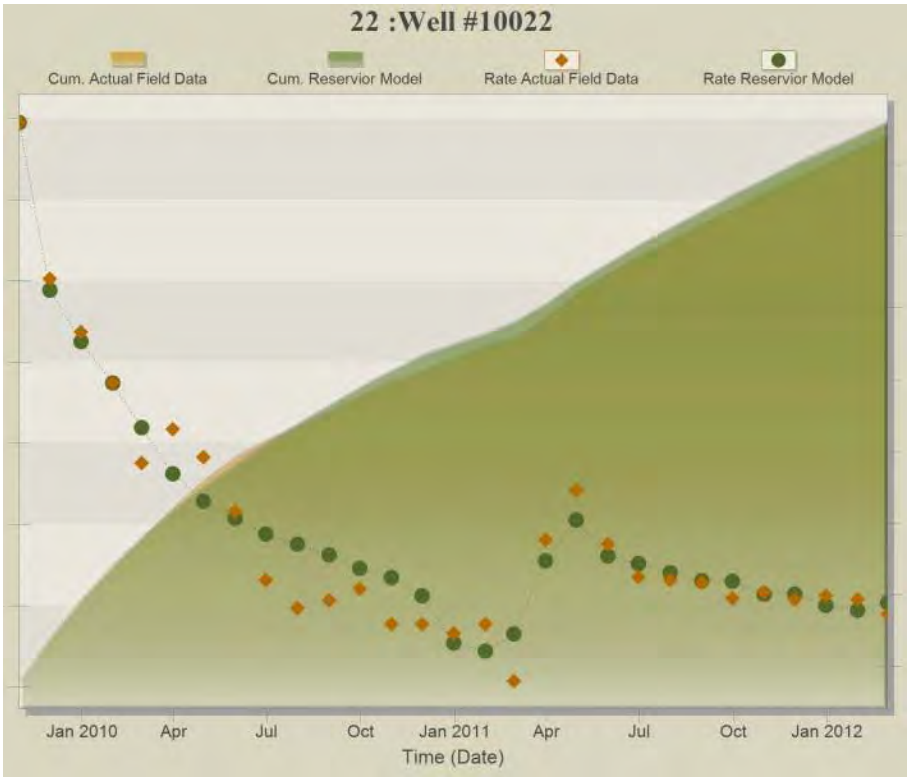

Figure A- 22: History Matching Results of Well#10022

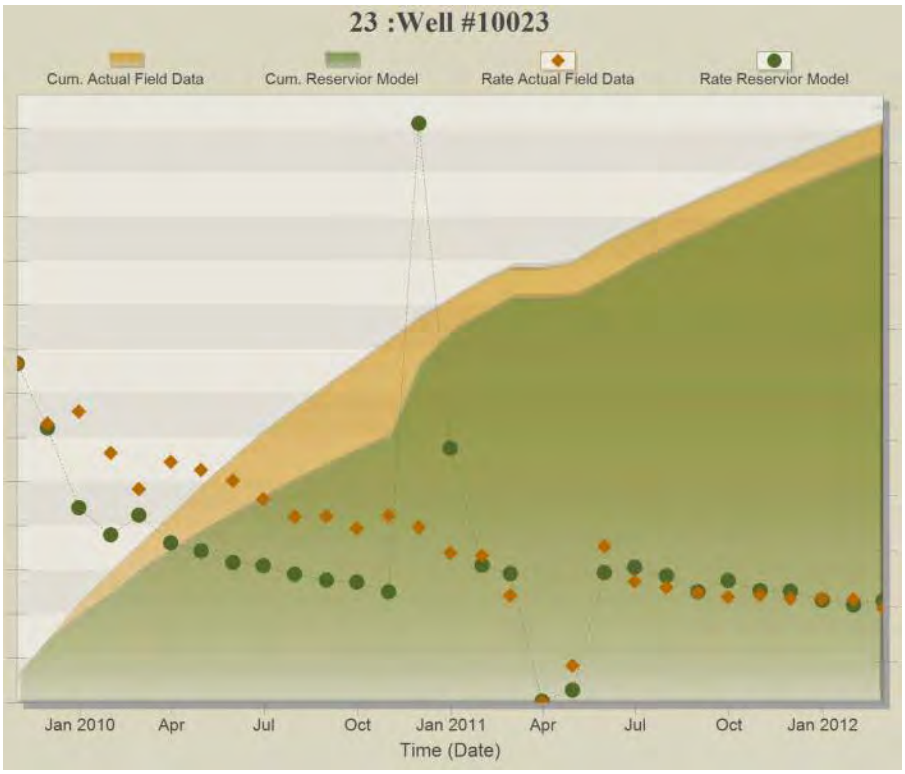

Figure A- 23: History Matching Results of Well#10023

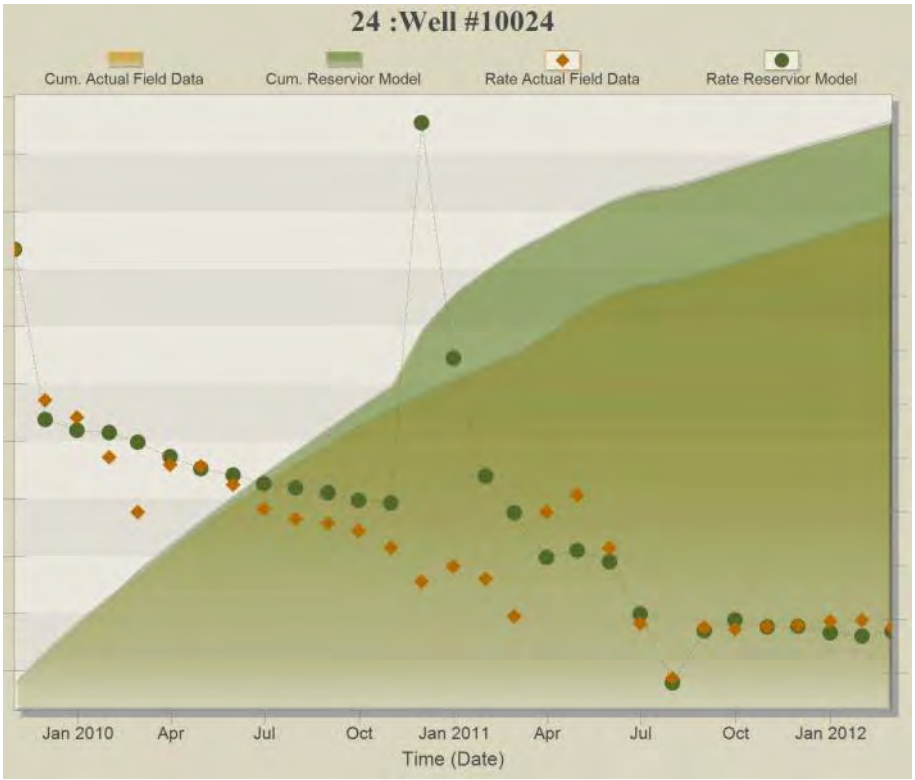

Figure A- 24: History Matching Results of Well#10024

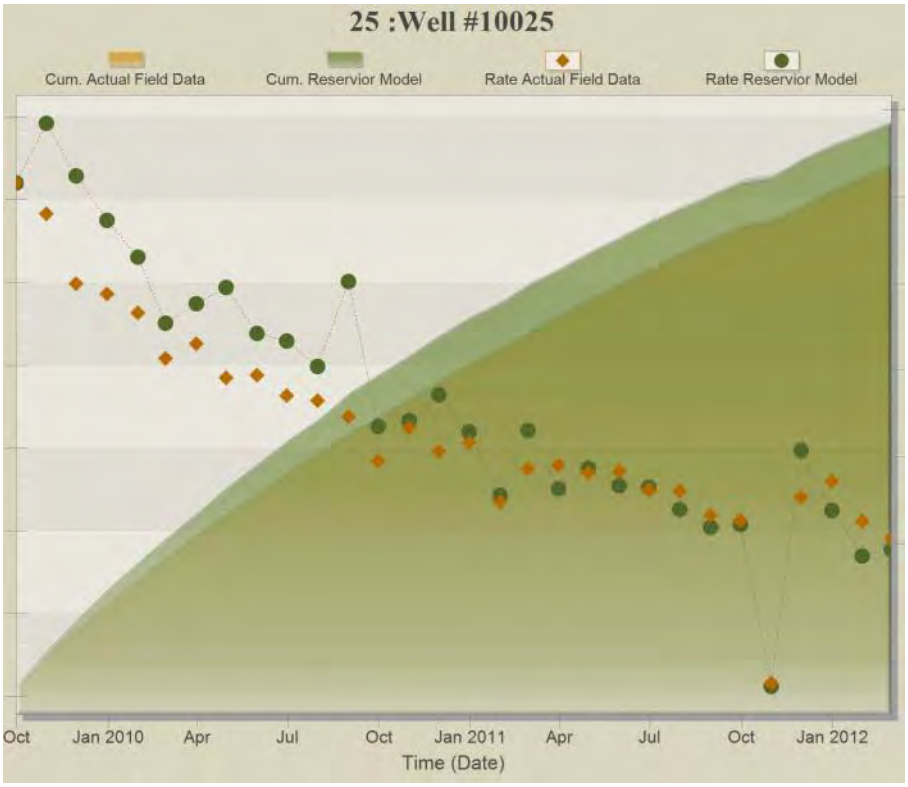

Figure A- 25: History Matching Results of Well#10025

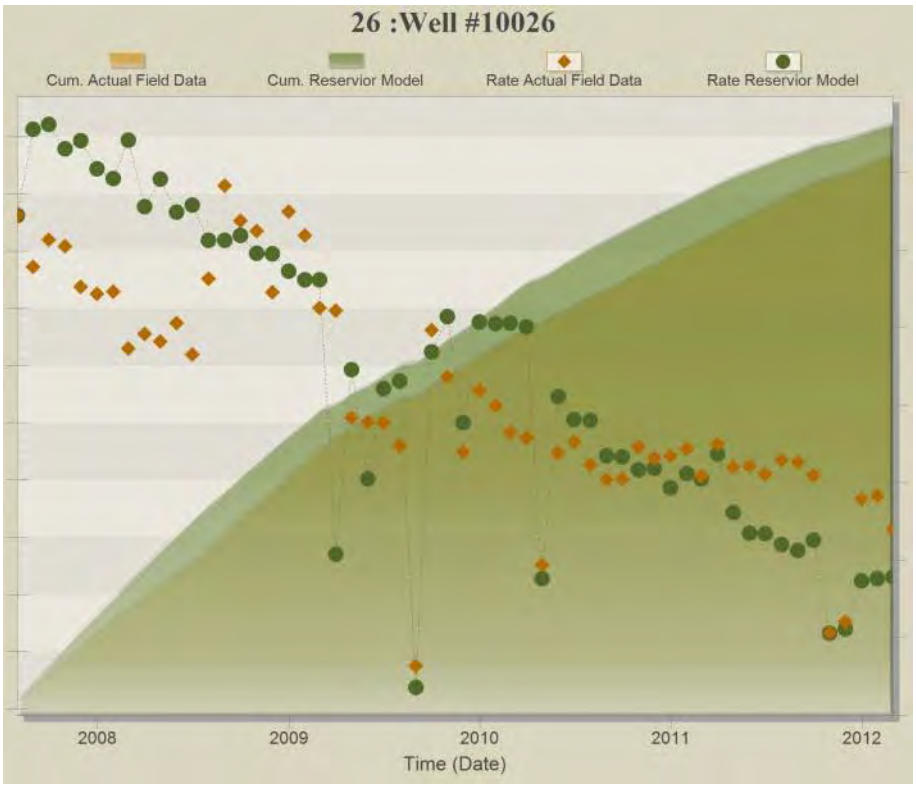

Figure A- 26: History Matching Results of Well#10026

Figure A- 27: History Matching Results of Well#10027

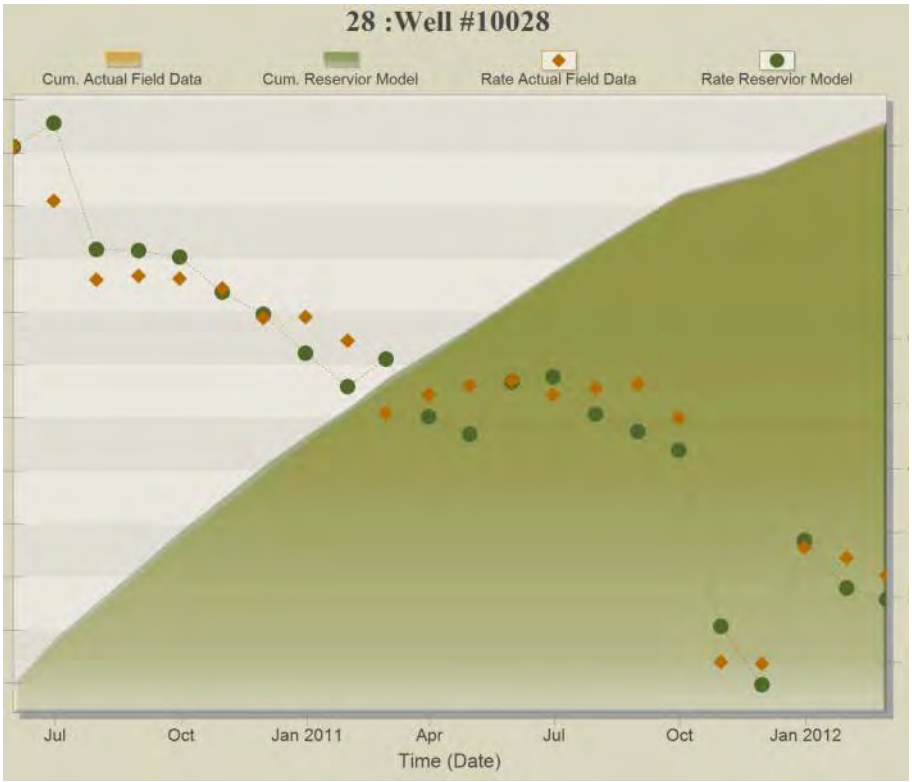

Figure A- 28: History Matching Results of Well#10028

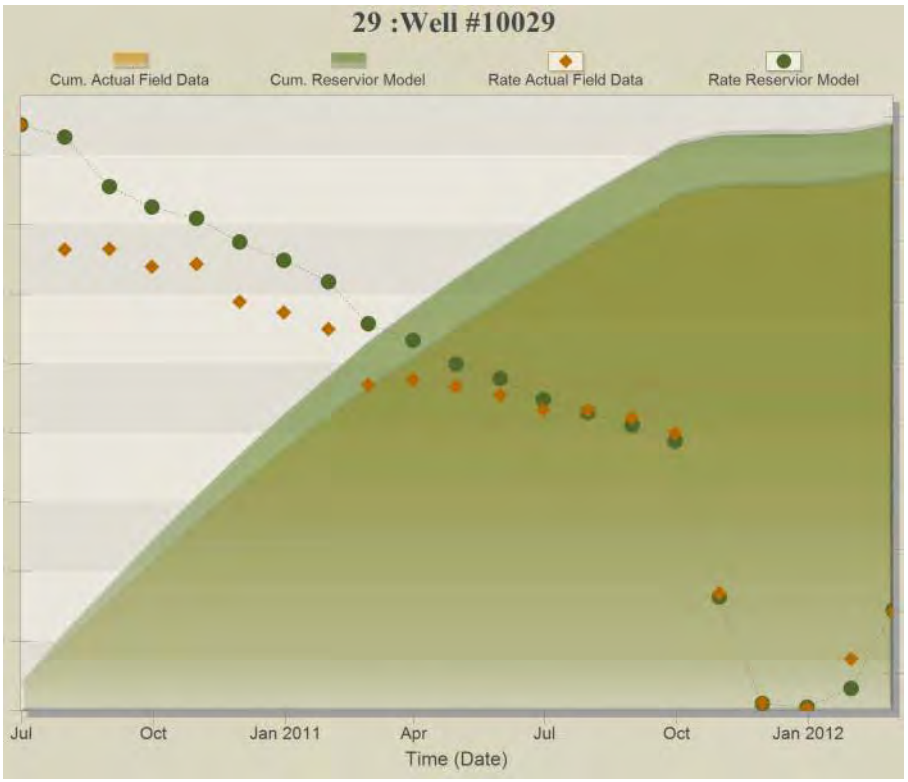

Figure A- 29: History Matching Results of Well#10029

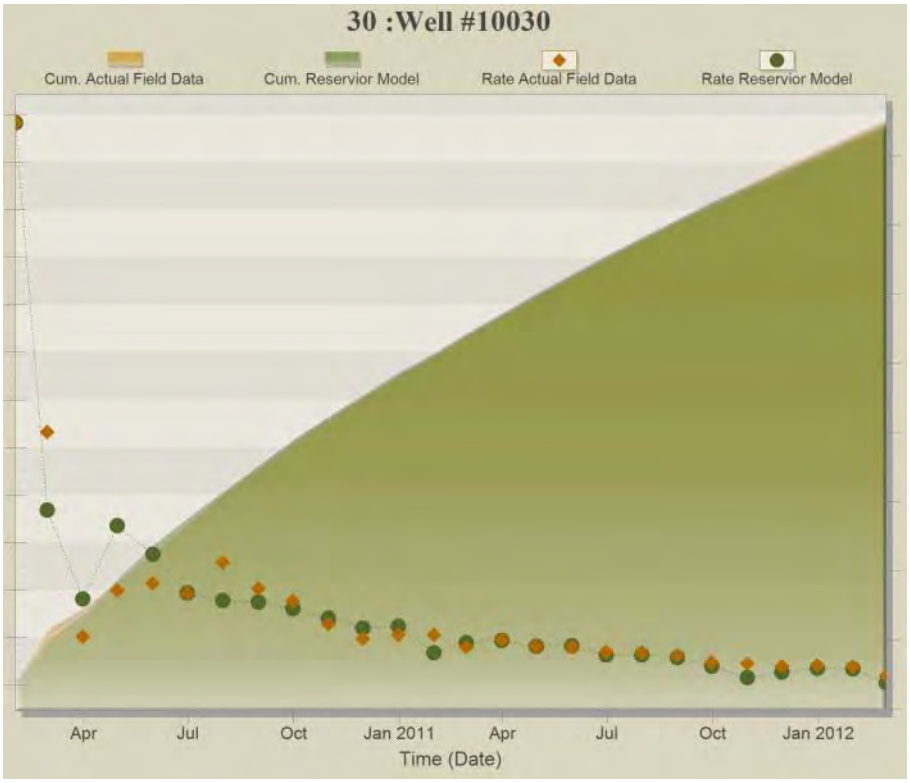

Figure A- 30: History Matching Results of Well#10030

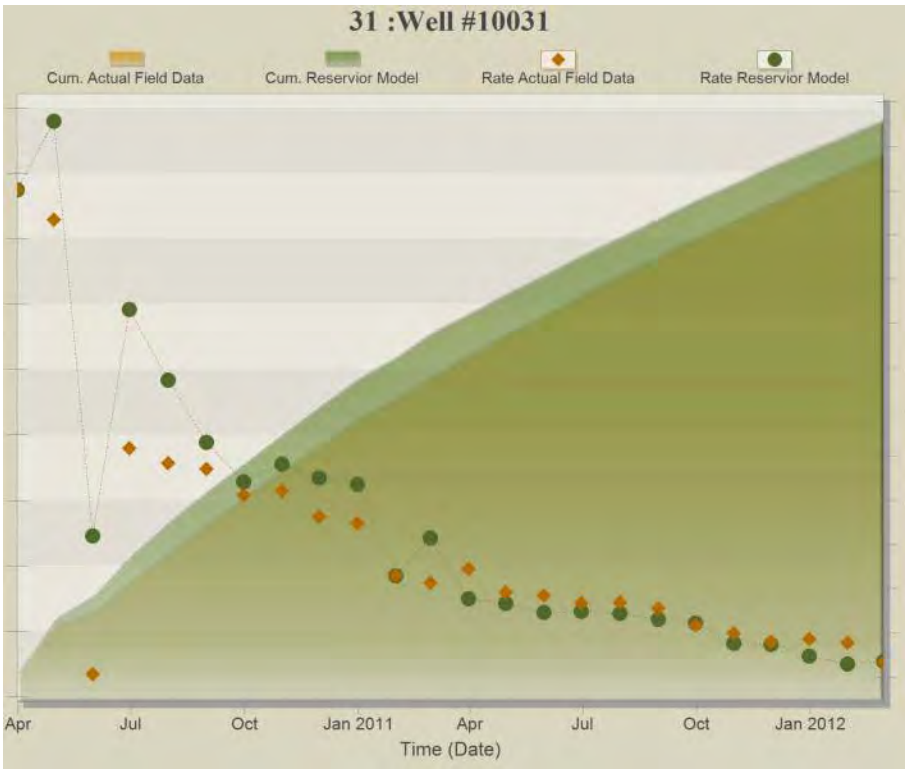

Figure A- 31: History Matching Results of Well#10031

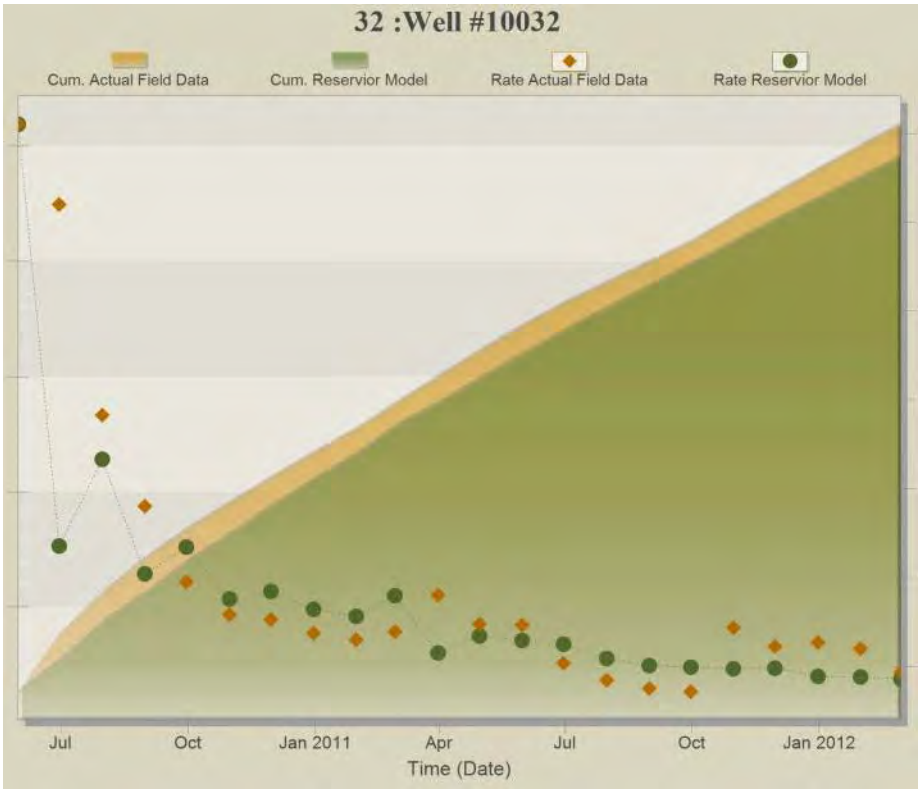

Figure A- 32: History Matching Results of Well#10032

Figure A- 33: History Matching Results of Well#10033

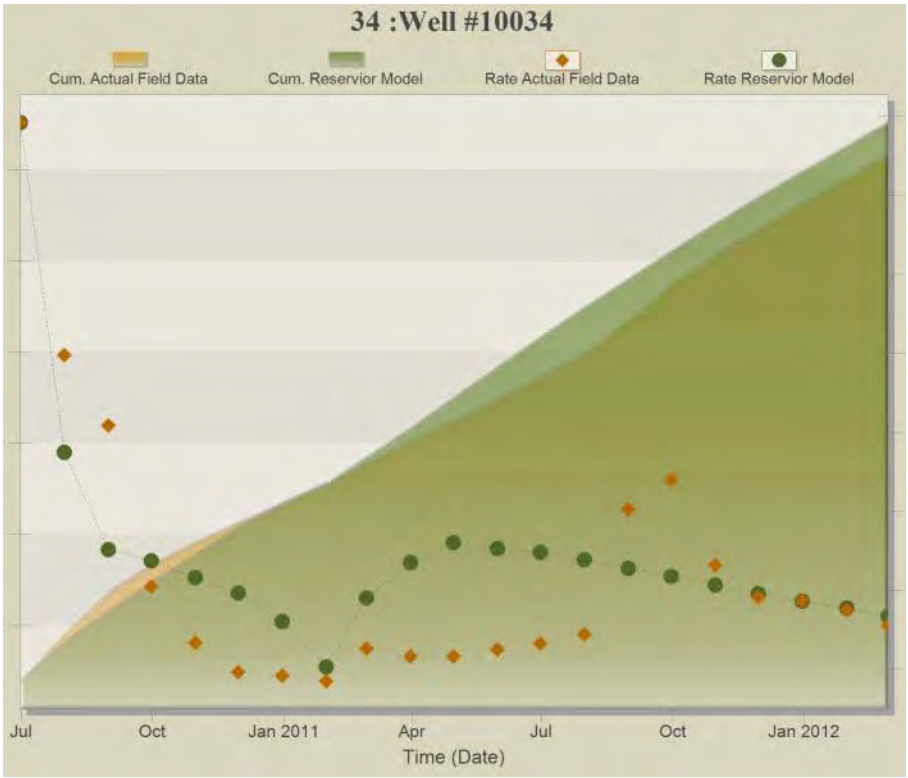

Figure A- 34: History Matching Results of Well#10034

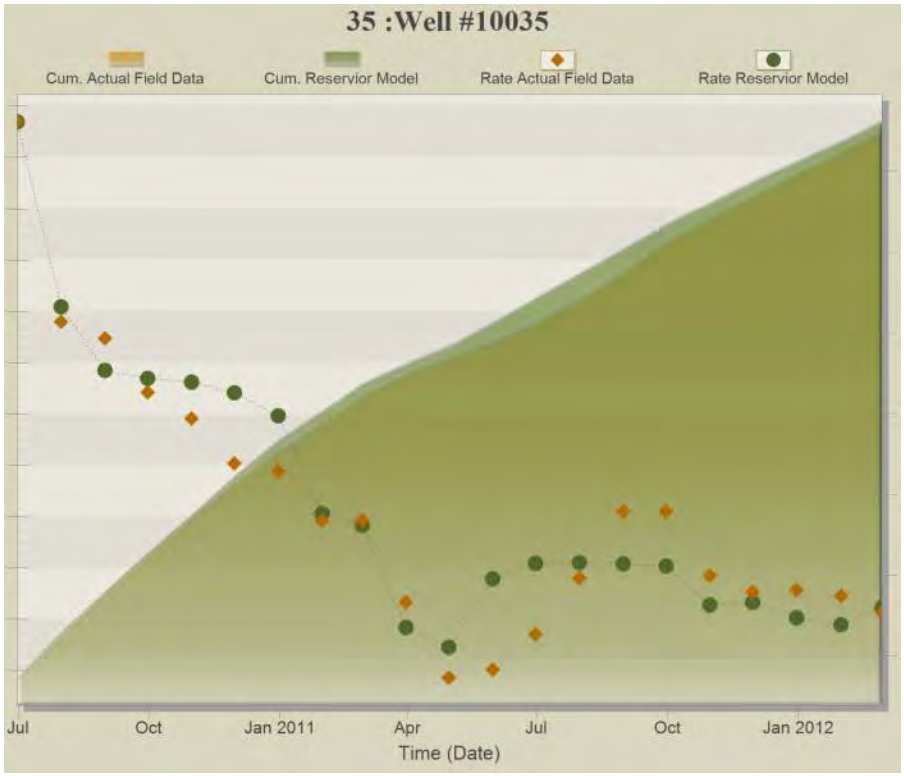

Figure A- 35: History Matching Results of Well#10035

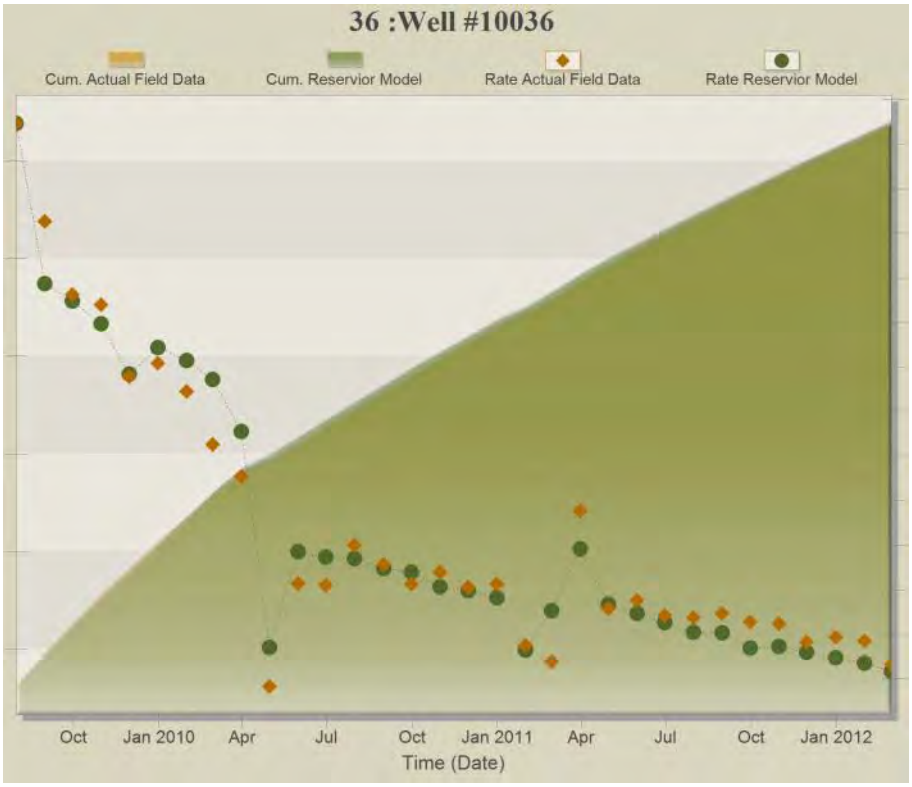

Figure A- 36: History Matching Results of Well#10036

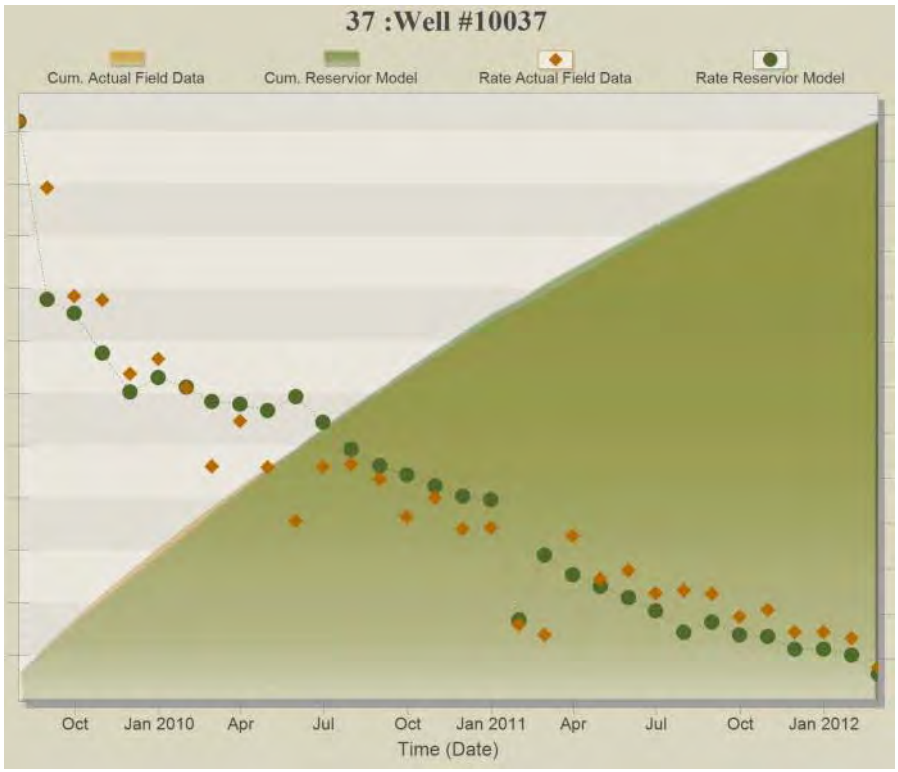

Figure A- 37: History Matching Results of Well#10037

Figure A- 38: History Matching Results of Well#10038

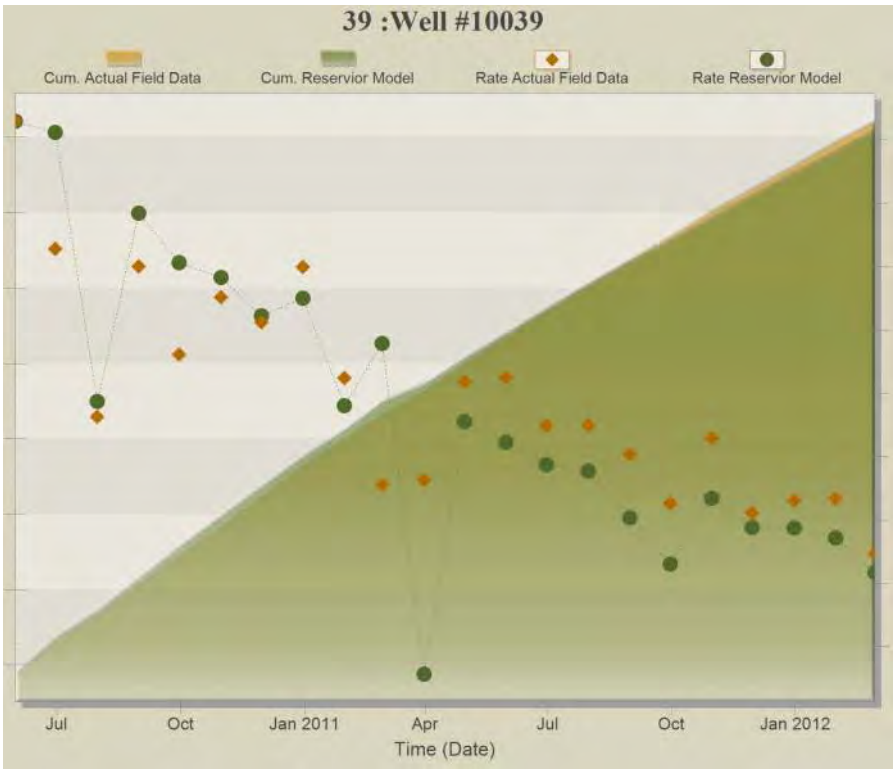

Figure A- 39: History Matching Results of Well#10039

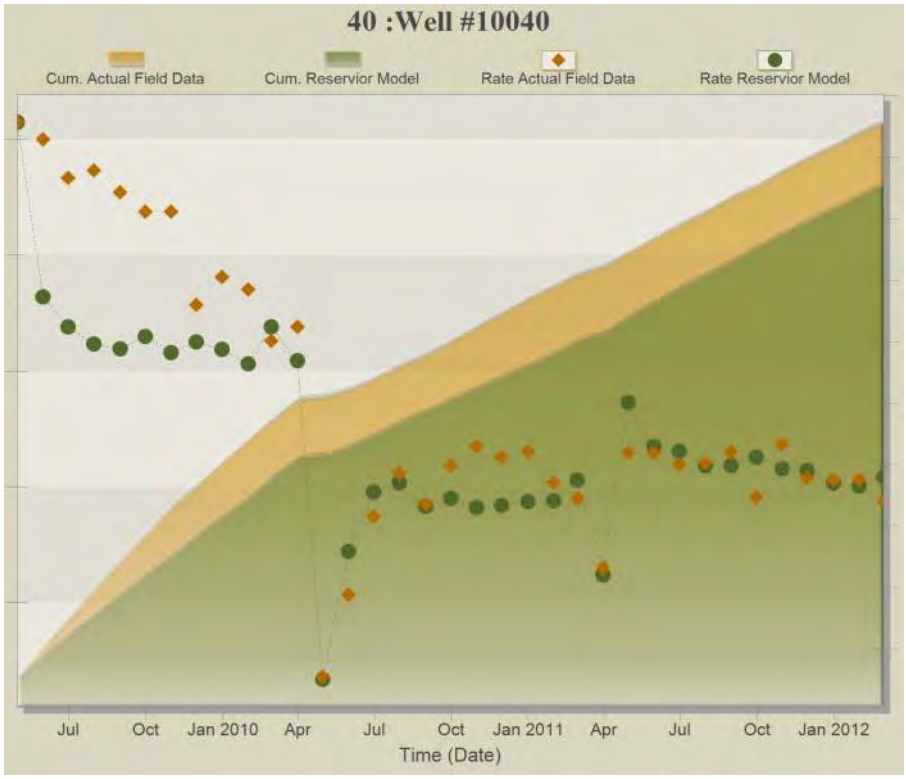

Figure A- 40: History Matching Results of Well#10040

Figure A- 41: History Matching Results of Well#10041

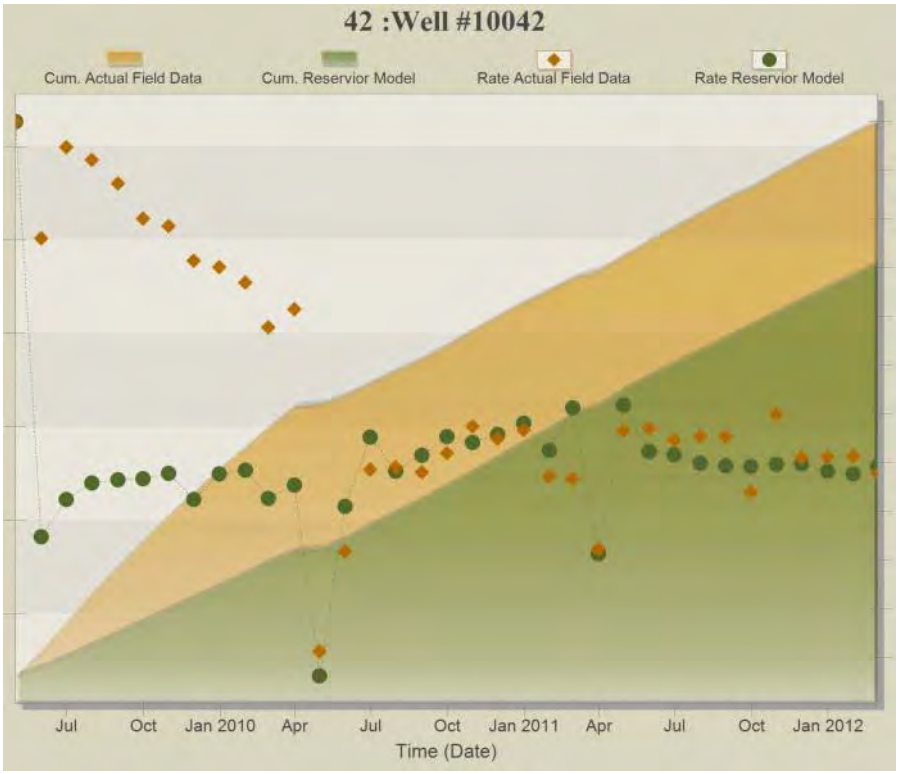

Figure A- 42: History Matching Results of Well#10042

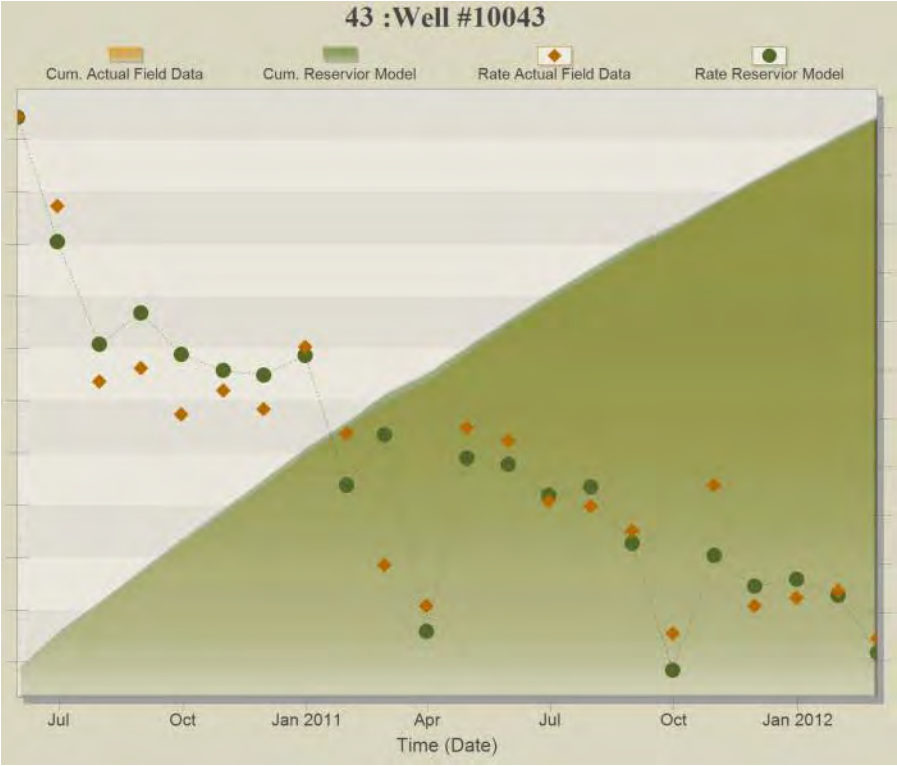

Figure A- 43: History Matching Results of Well#10043

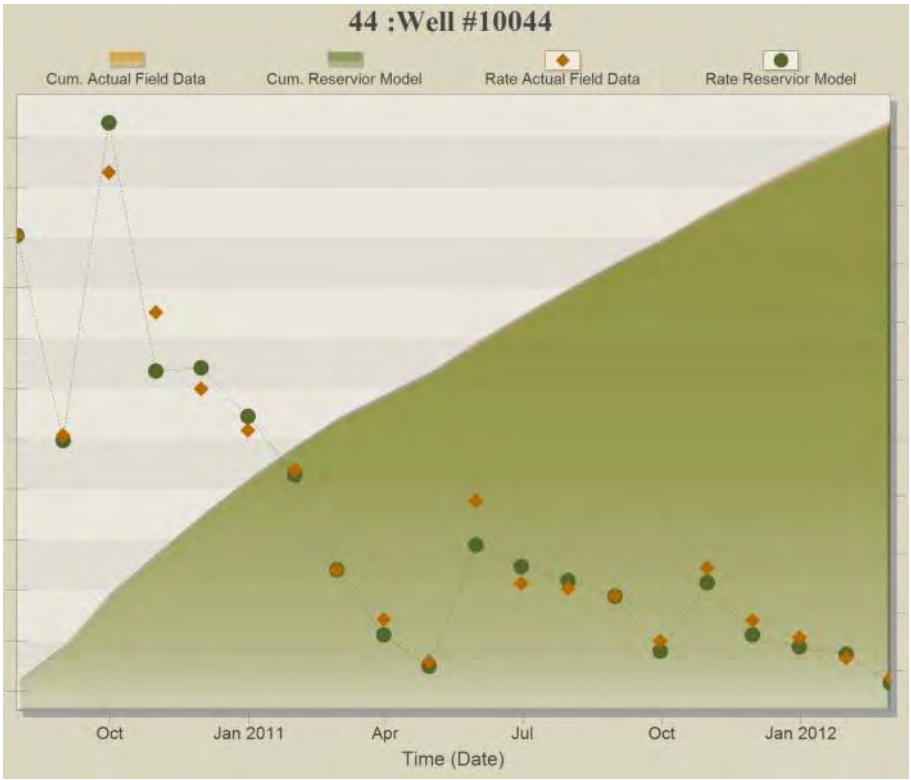

Figure A- 44: History Matching Results of Well#10044

Figure A- 45: History Matching Results of Well#10045

Figure A- 46: History Matching Results of Well#10046

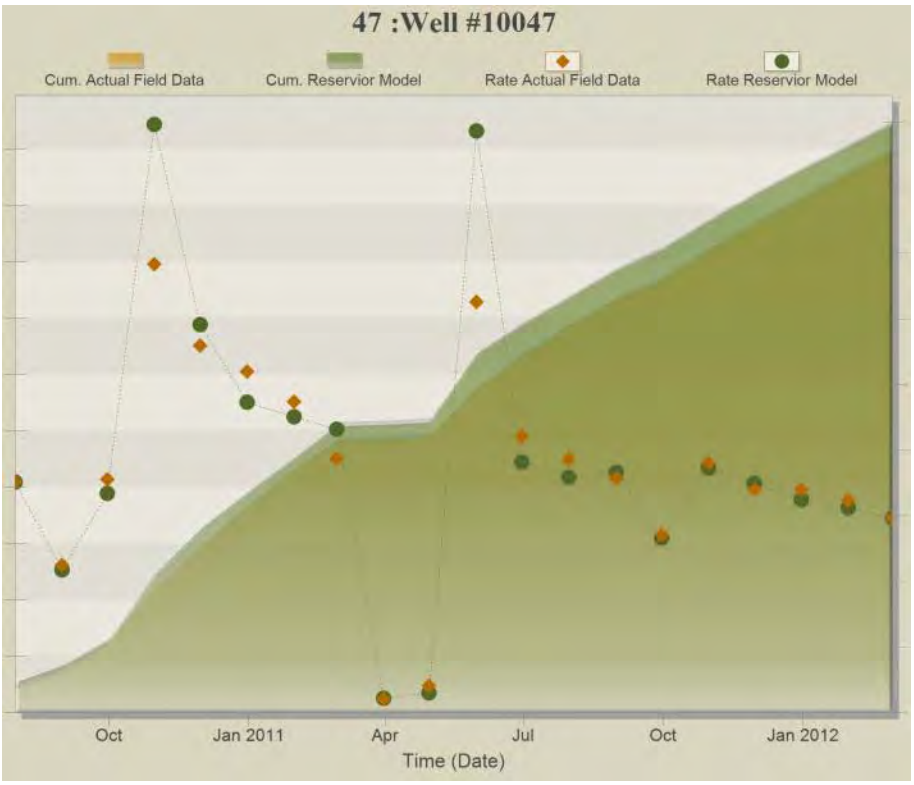

Figure A- 47: History Matching Results of Well#10047

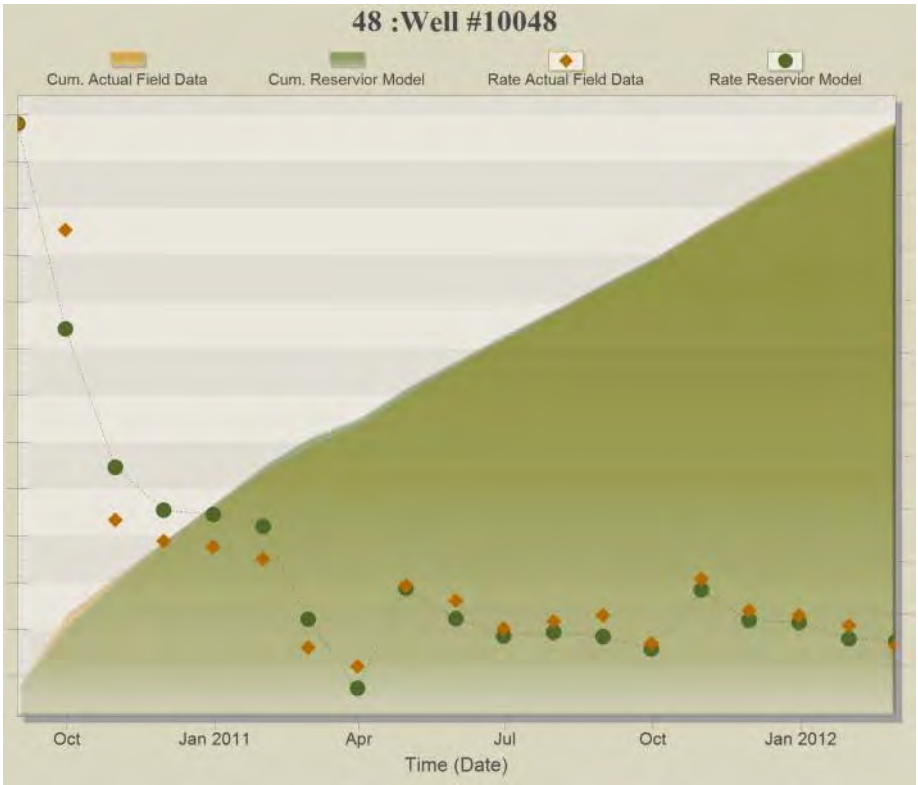

Figure A- 48: History Matching Results of Well#10048

Figure A- 49: History Matching Results of Well#10049

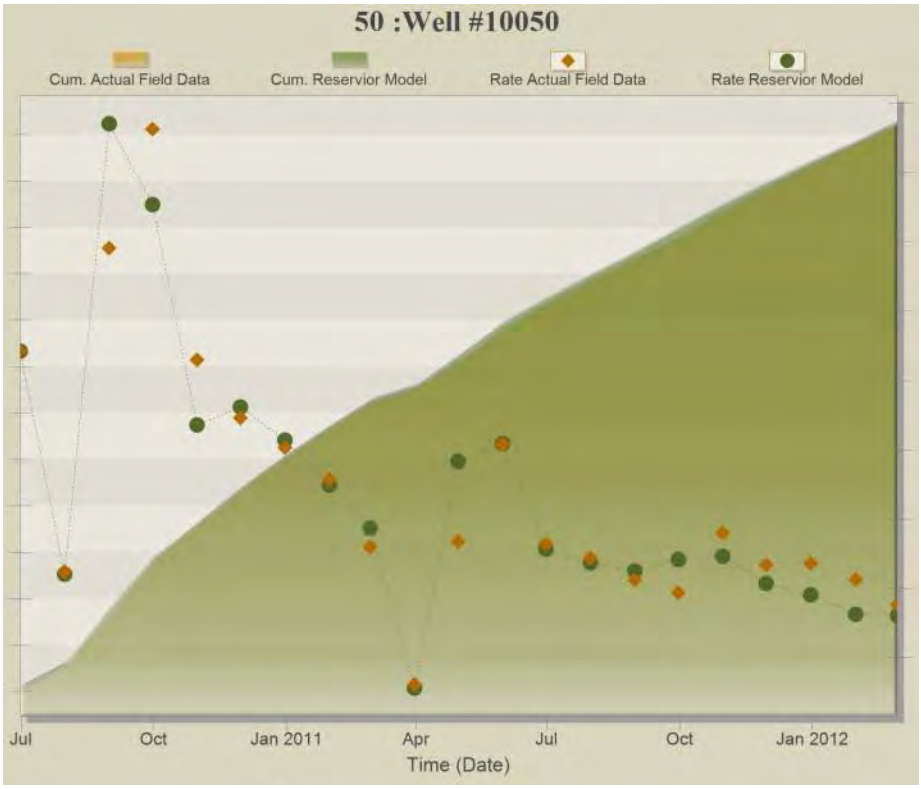

Figure A- 50: History Matching Results of Well#10050

Figure A- 51: History Matching Results of Well#10051

Figure A- 52: History Matching Results of Well#10052

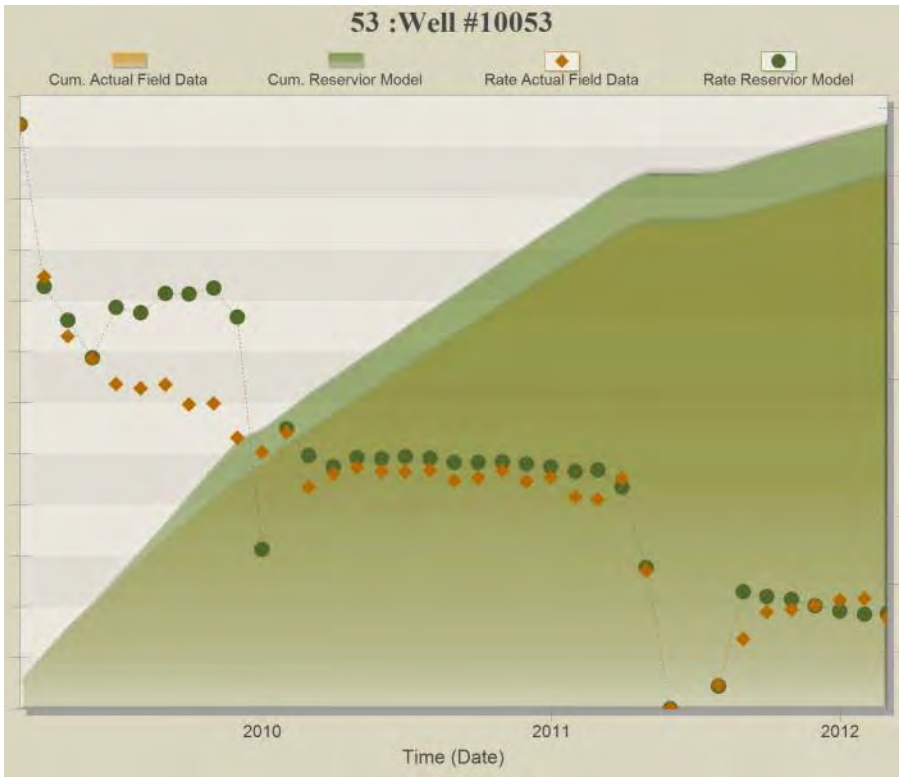

Figure A- 53: History Matching Results of Well#10053

Figure A- 54: History Matching Results of Well#10054

Figure A- 55: History Matching Results of Well#10055

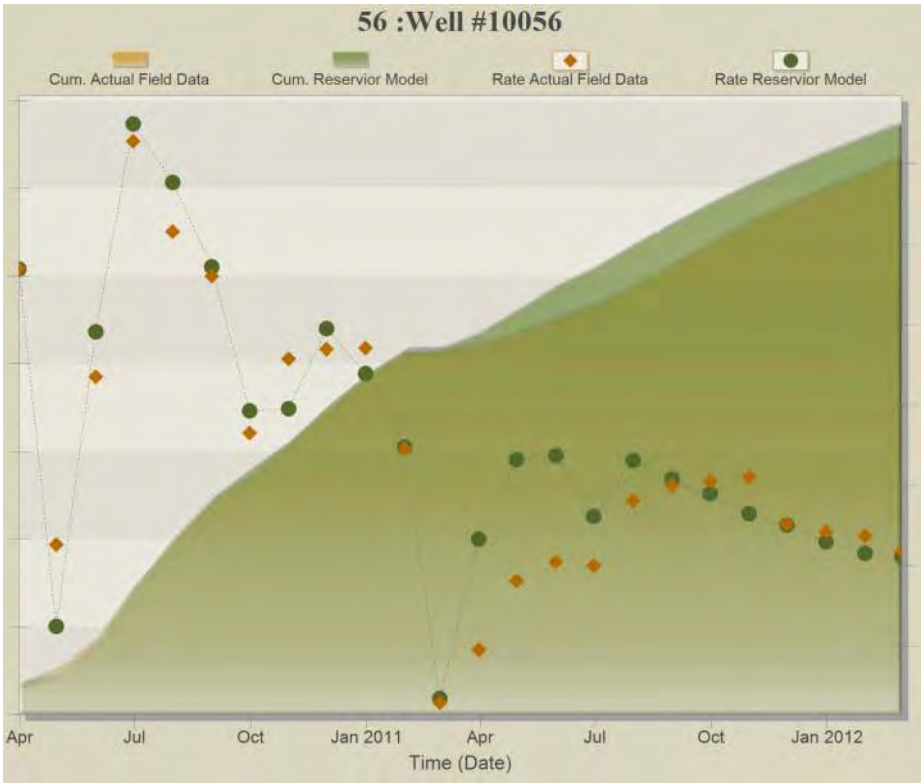

Figure A- 56: History Matching Results of Well#10056

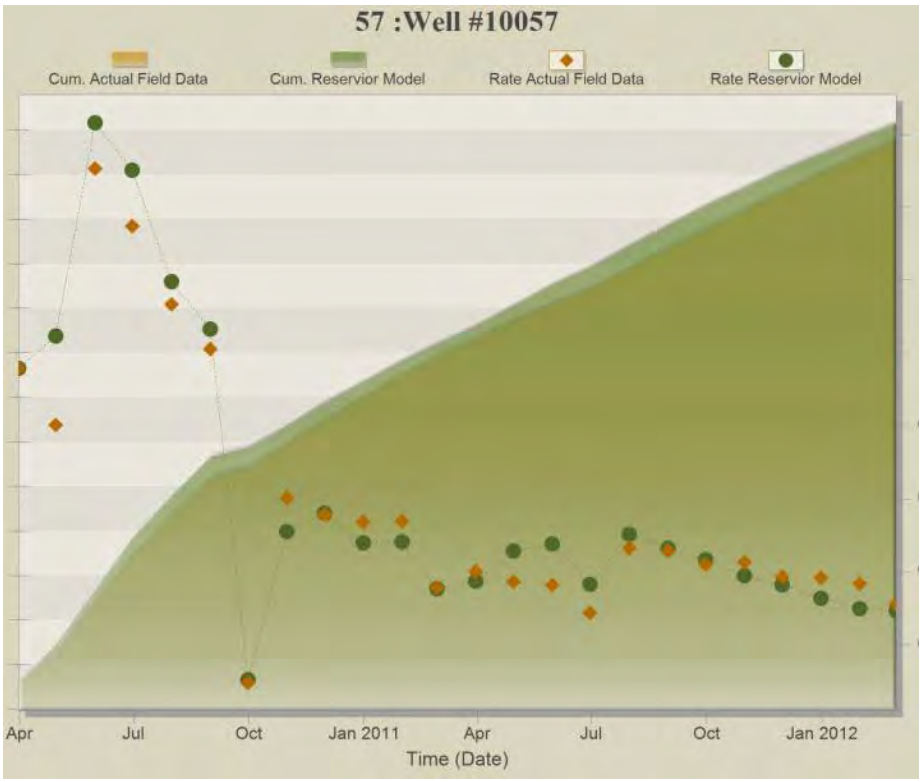

Figure A- 57: History Matching Results of Well#10057

Figure A- 58: History Matching Results of Well#10058

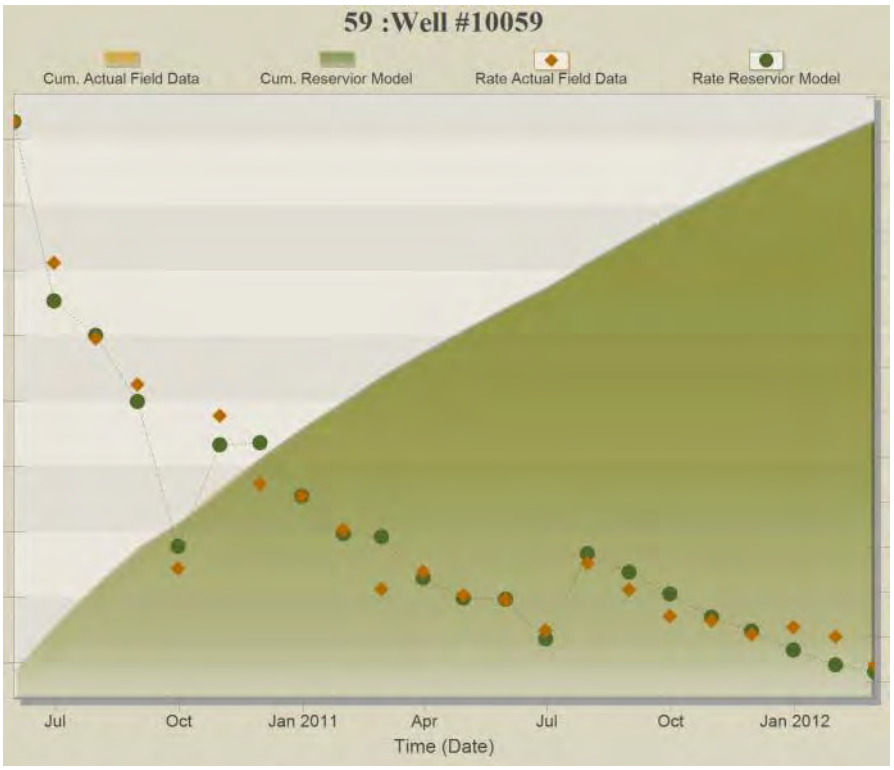

Figure A- 59: History Matching Results of Well#10059

Figure A- 60: History Matching Results of Well#10060

Figure A- 61: History Matching Results of Well#10061

Figure A- 62: History Matching Results of Well#10062

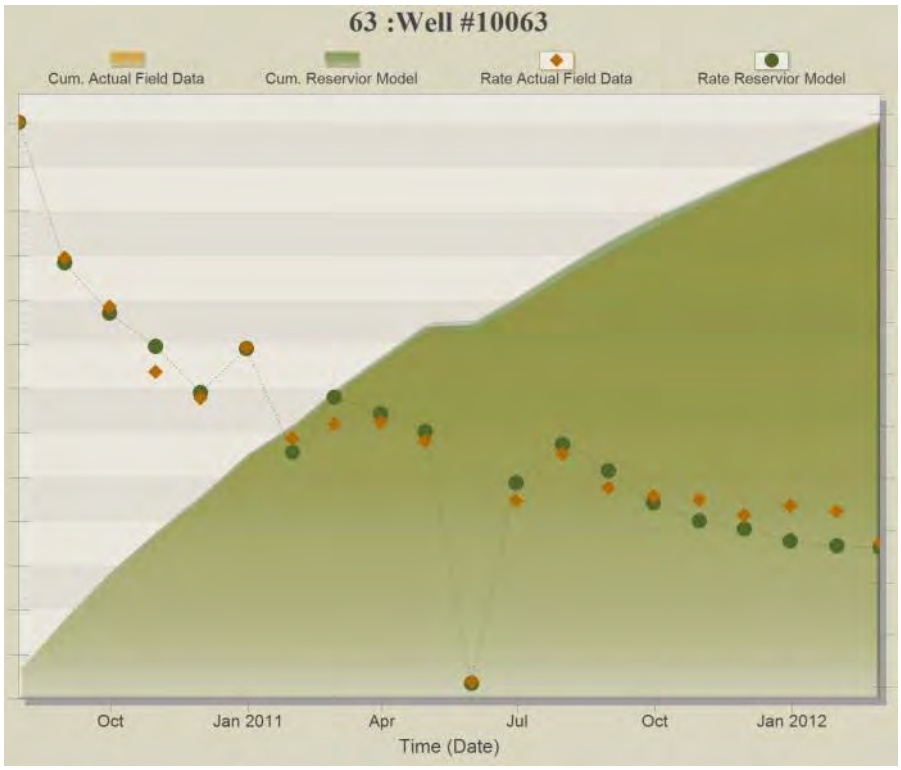

Figure A- 63: History Matching Results of Well#10063

Figure A- 64: History Matching Results of Well#10064

Figure A- 65: History Matching Results of Well#10065

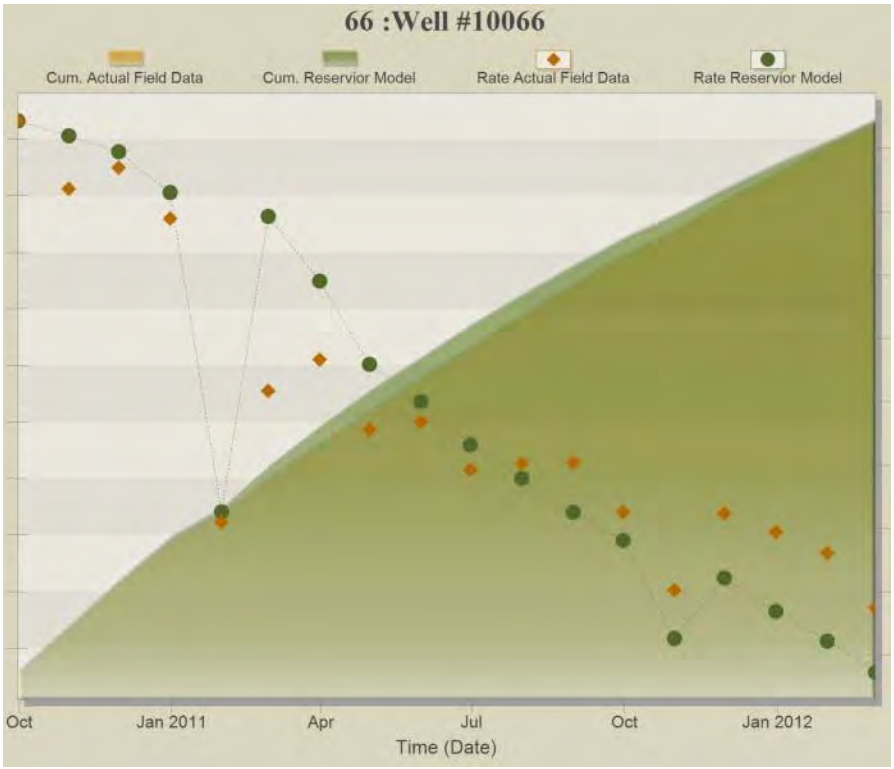

Figure A- 66: History Matching Results of Well#10066

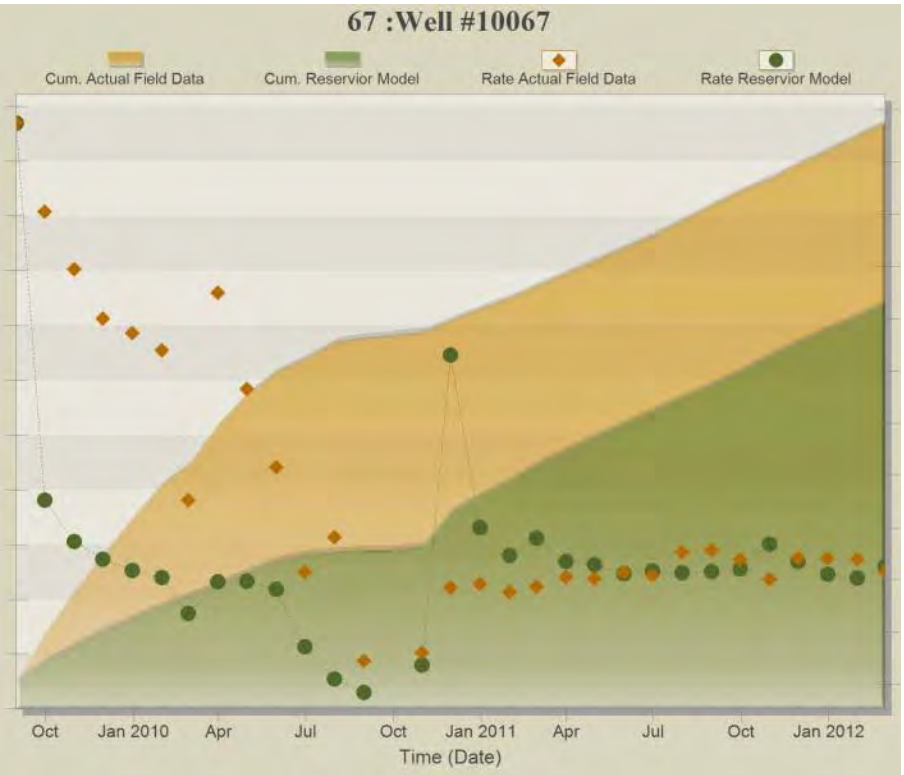

Figure A- 67: History Matching Results of Well#10067

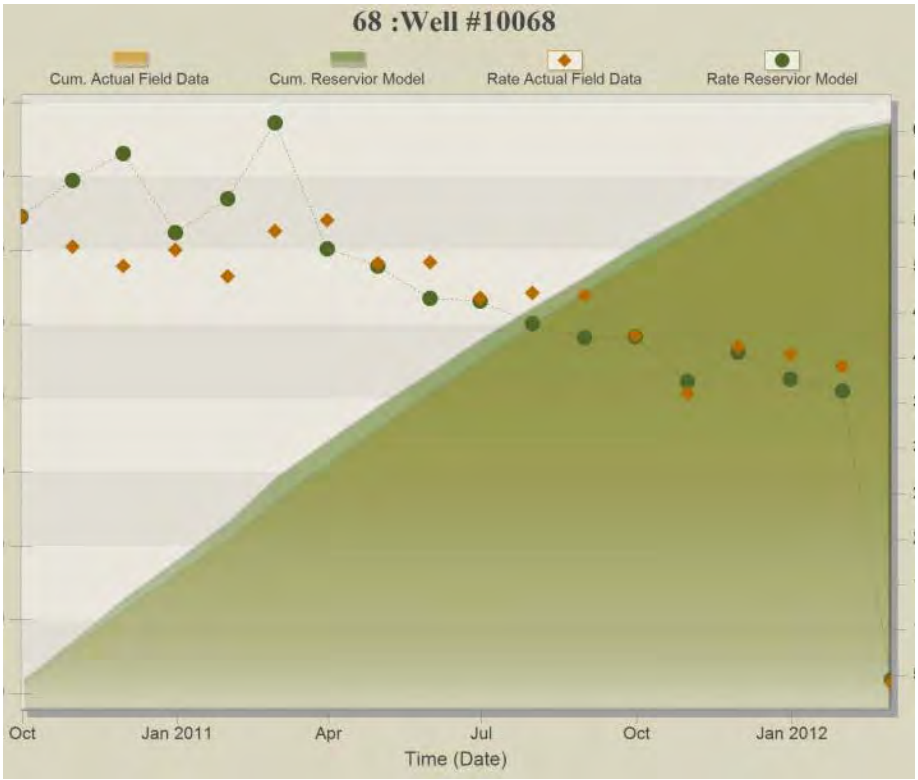

Figure A- 68: History Matching Results of Well#10068

Figure A- 69: History Matching Results of Well#10069

Figure A- 70: History Matching Results of Well#10070

Figure A- 71: History Matching Results of Well#10071

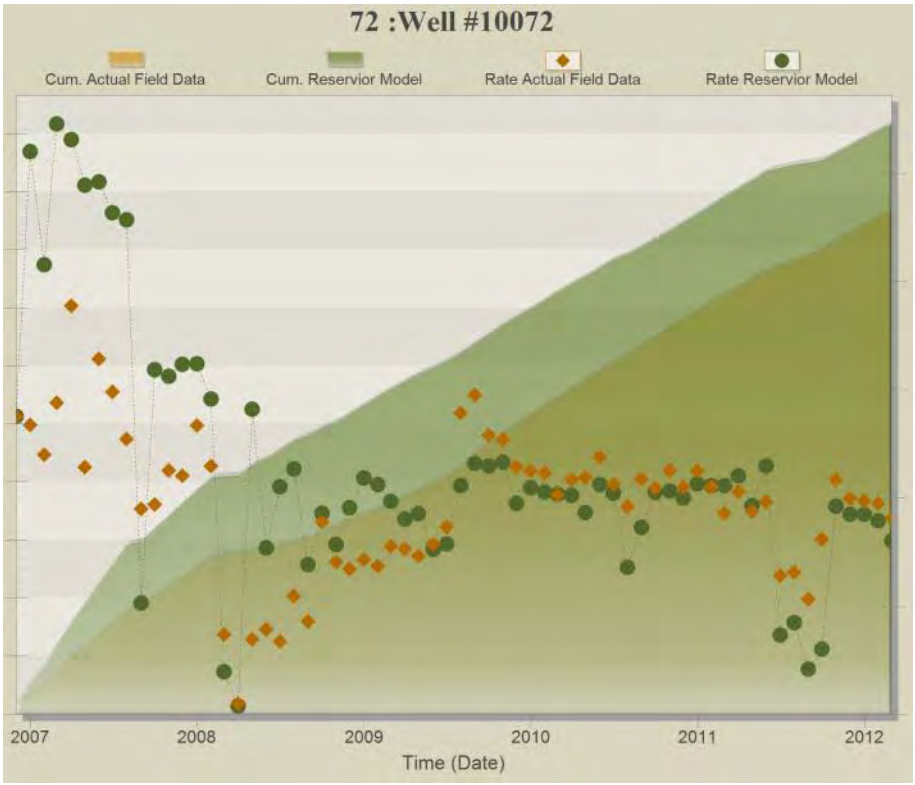

Figure A- 72: History Matching Results of Well#10072

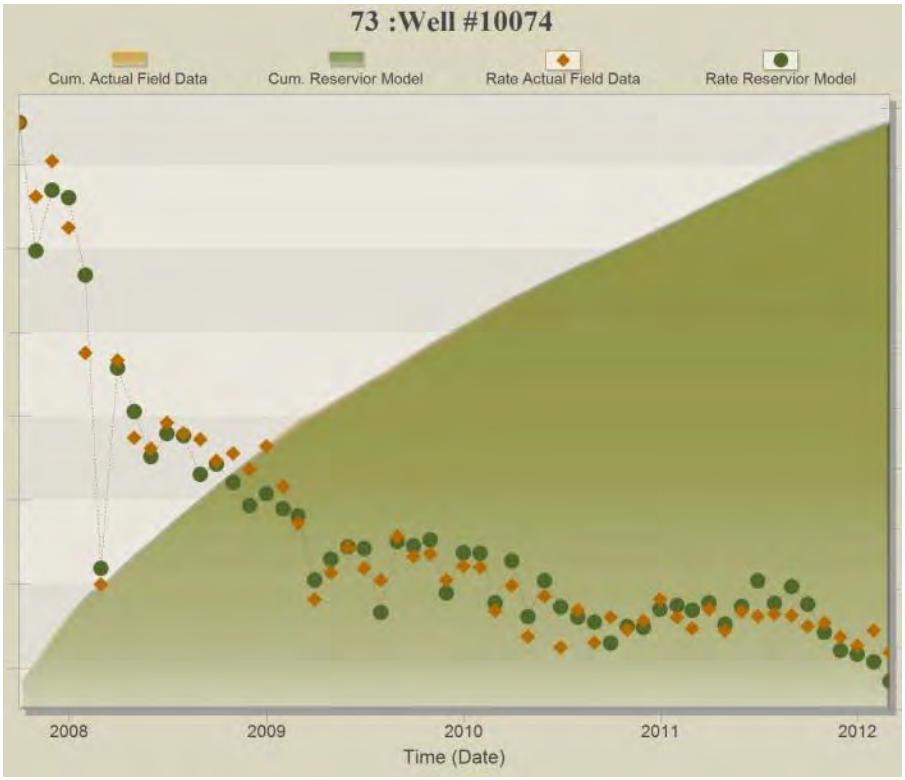

Figure A- 73: History Matching Results of Well#10074

Figure A- 74: History Matching Results of Well#10075

Figure A- 75: History Matching Results of Well#10076

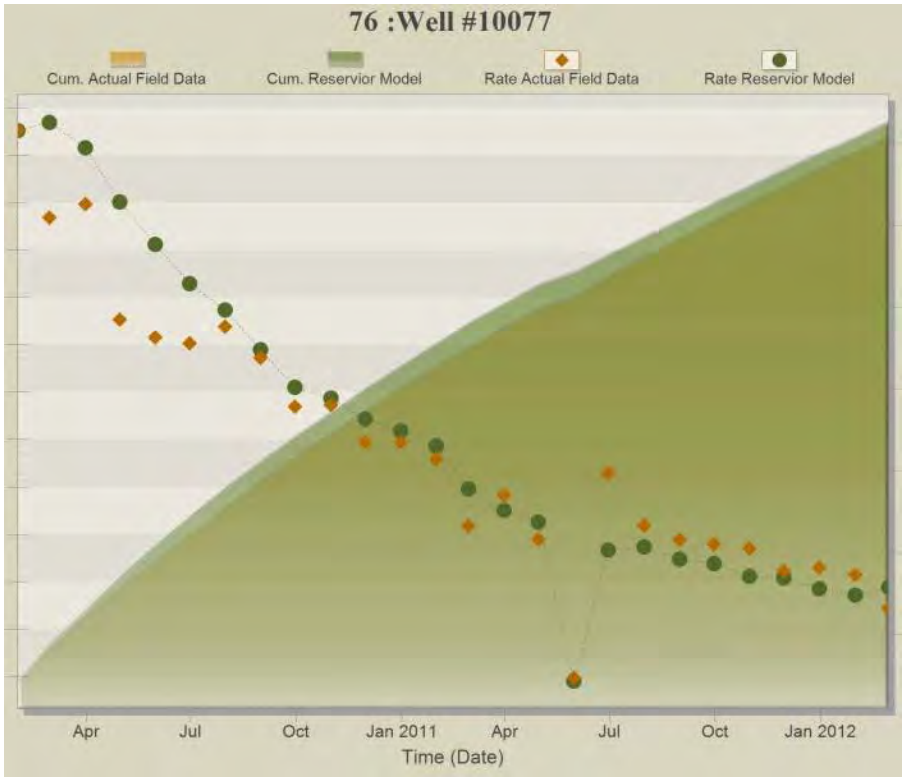

Figure A- 76: History Matching Results of Well#10077

Figure A- 77: History Matching Results of Well#10078

Figure A- 78: History Matching Results of Well#10079

Figure A- 79: History Matching Results of Well#10080

Figure A- 80: History Matching Results of Well#10081

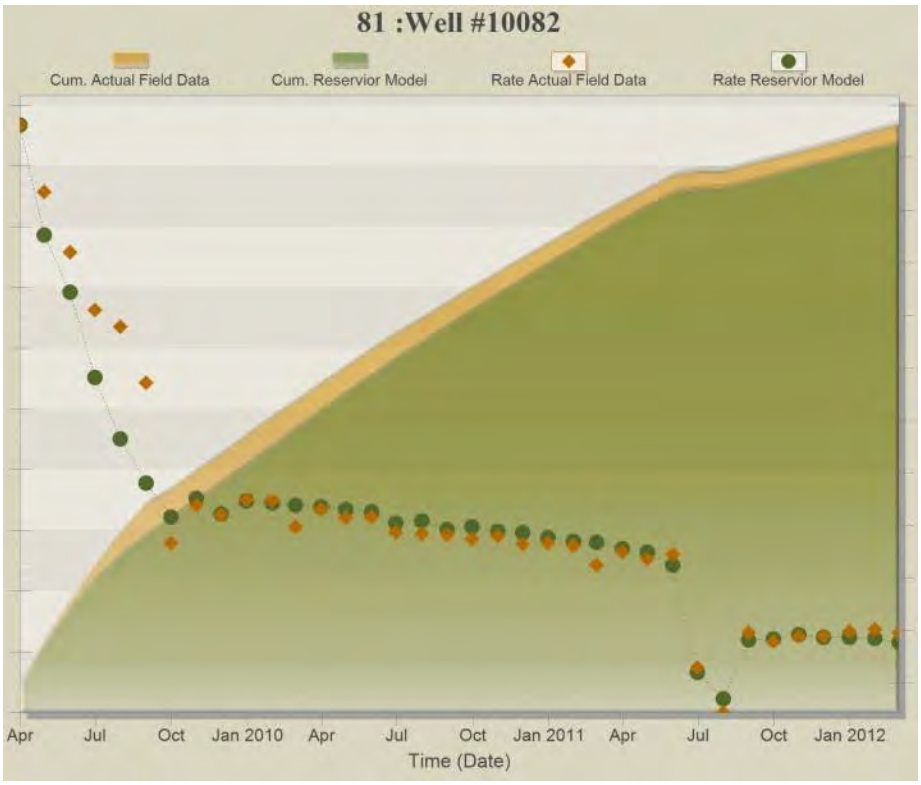

Figure A- 81: History Matching Results of Well#10082

Figure A- 82: History Matching Results of Well#10083

Figure A- 83: History Matching Results of Well#10084

Figure A- 84: History Matching Results of Well#10085

Figure A- 85: History Matching Results of Well#10086

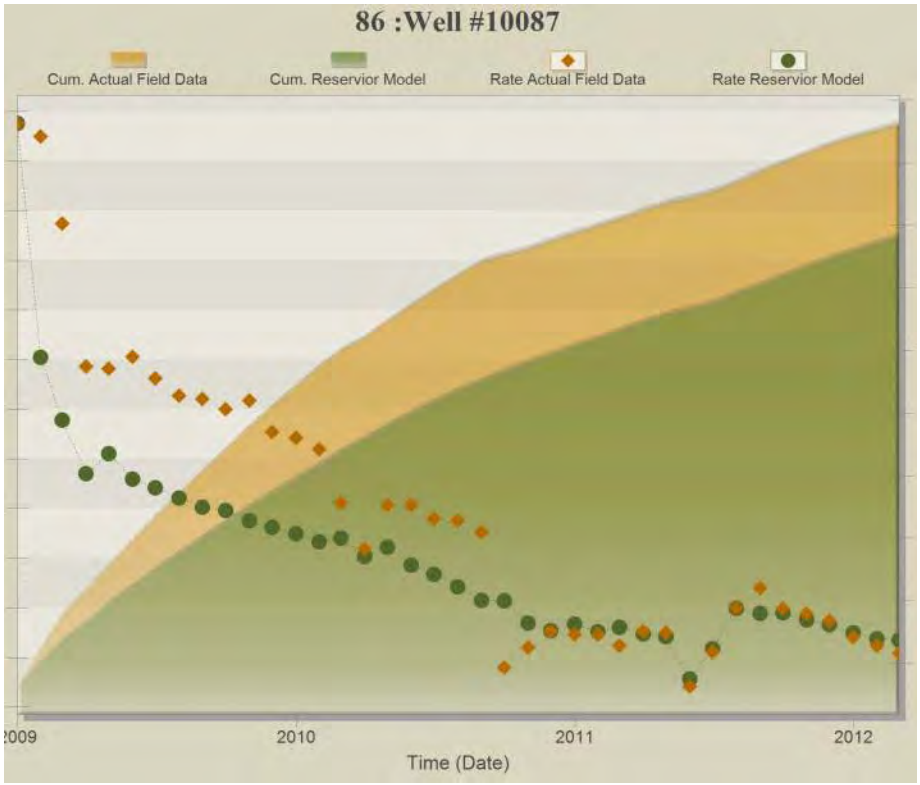

Figure A- 86: History Matching Results of Well#10087

Figure A- 87: History Matching Results of Well#10088

Figure A- 88: History Matching Results of Well#10089

Figure A- 89: History Matching Results of Well#10090

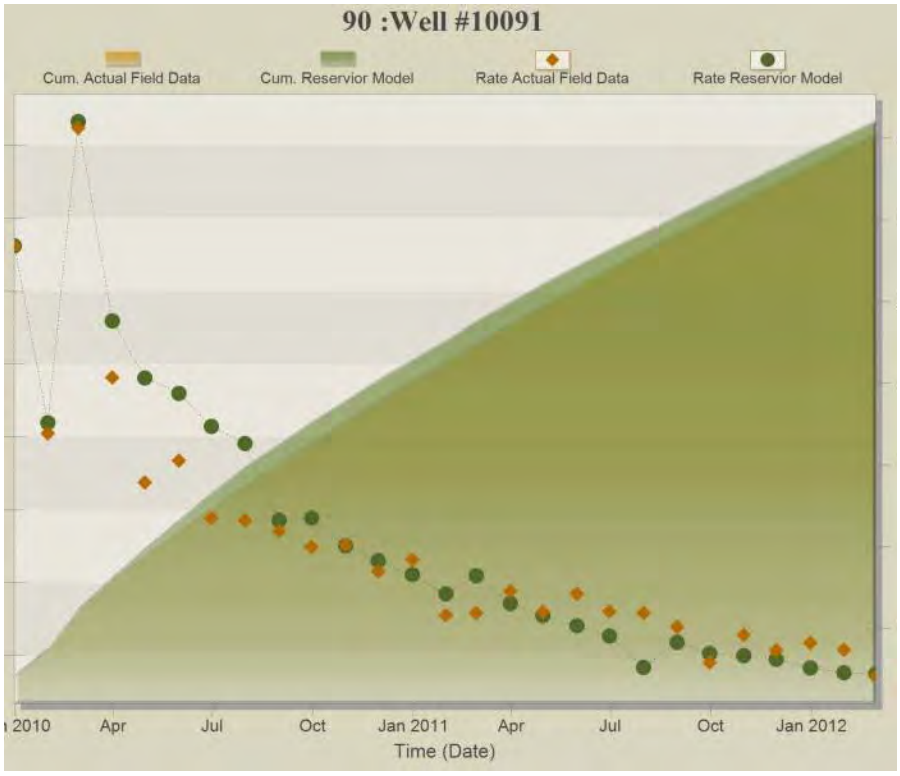

Figure A- 90: History Matching Results of Well#10091

Figure A- 91 : History Matching Results of Well#10092

Figure A- 92: History Matching Results of Well#10093

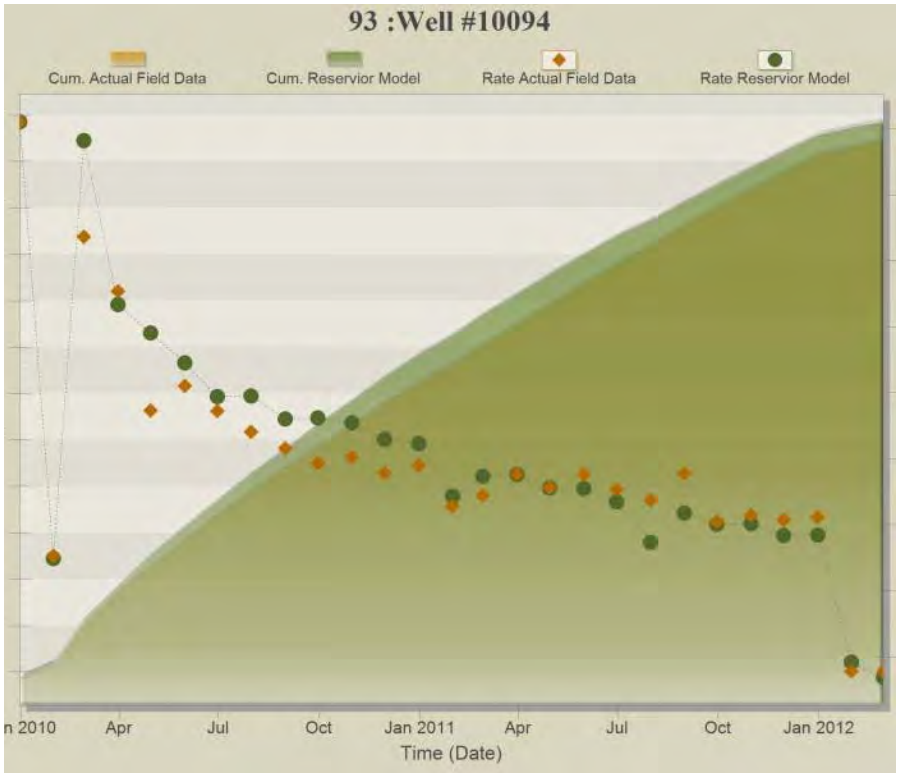

Figure A- 93: History Matching Results of Well#10094

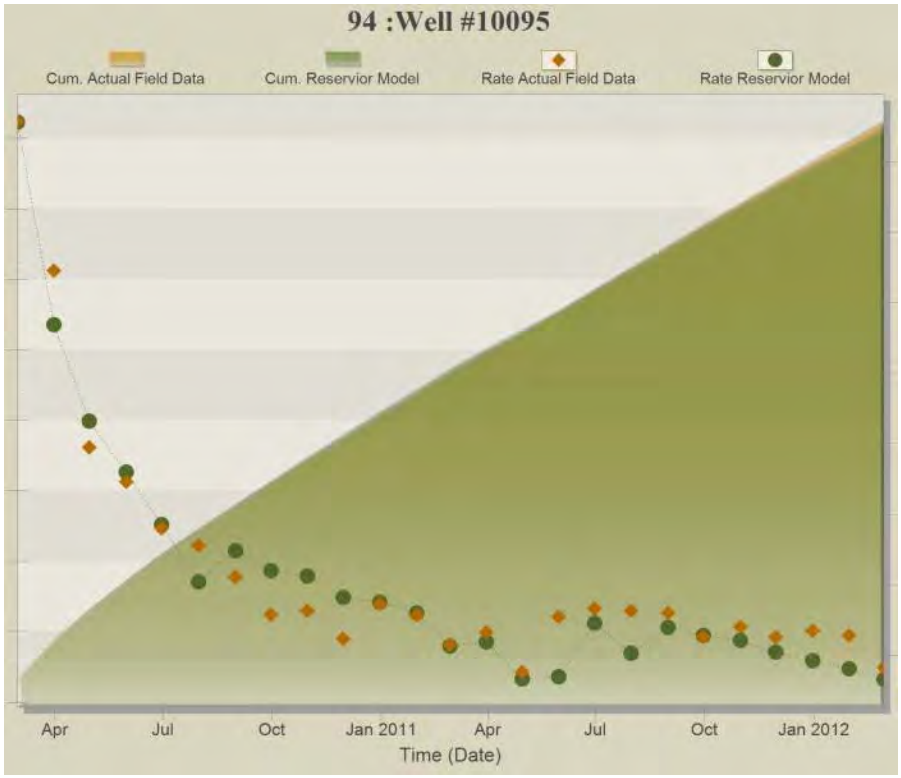

Figure A- 94: History Matching Results of Well#10095

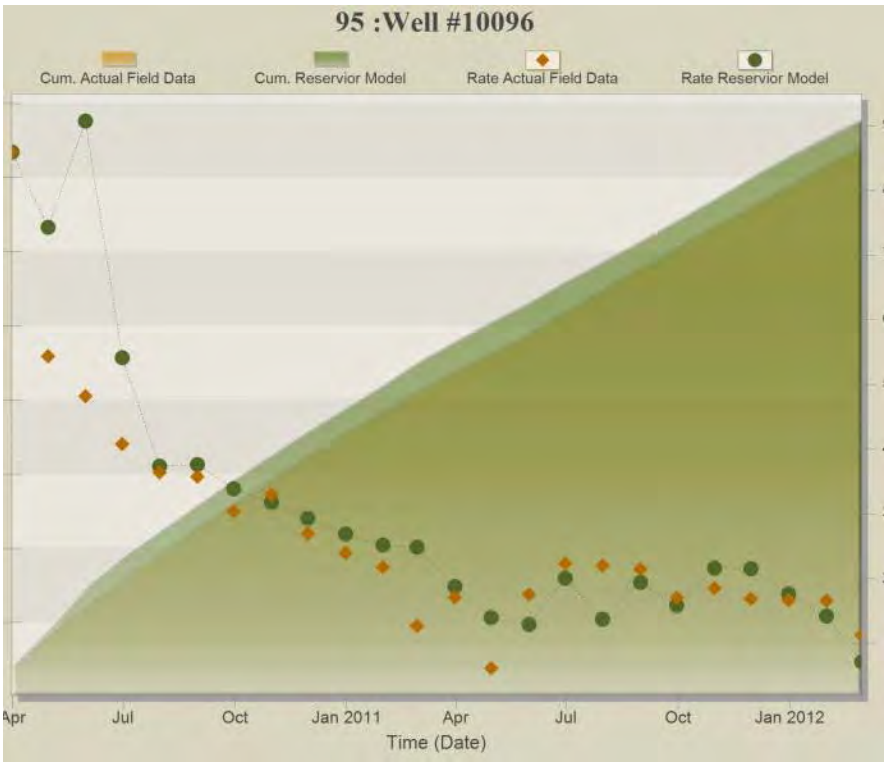

Figure A- 95: History Matching Results of Well#10096

Figure A- 96: History Matching Results of Well#10097

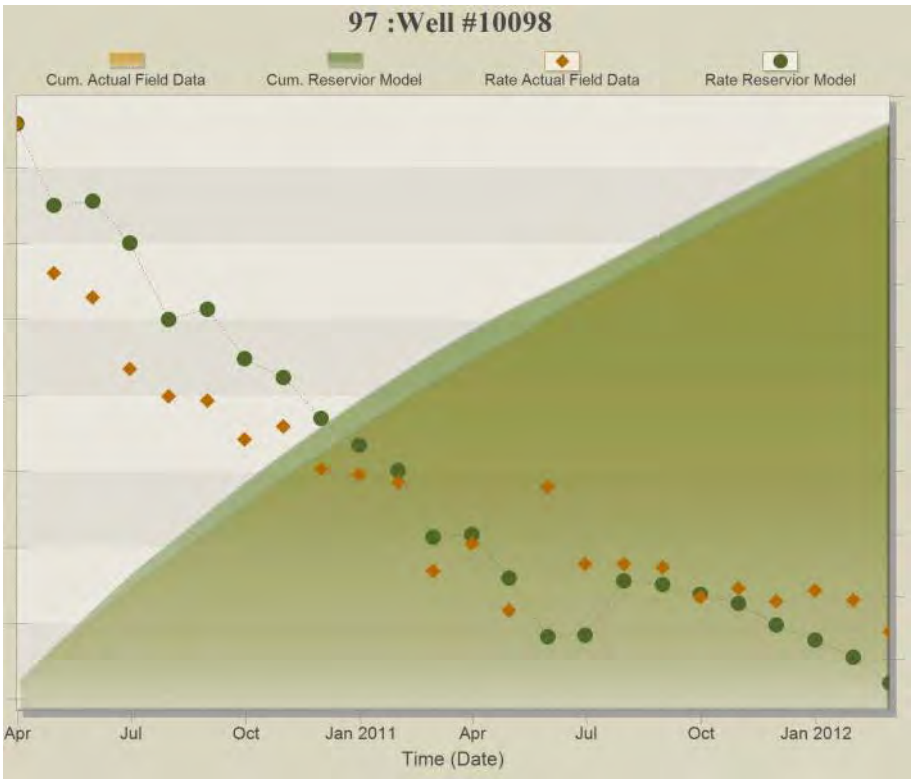

Figure A- 97: History Matching Results of Well#10098

Figure A- 98: History Matching Results of Well#10099

Figure A- 99: History Matching Results of Well#10100

Figure A- 100: History Matching Results of Well#10101

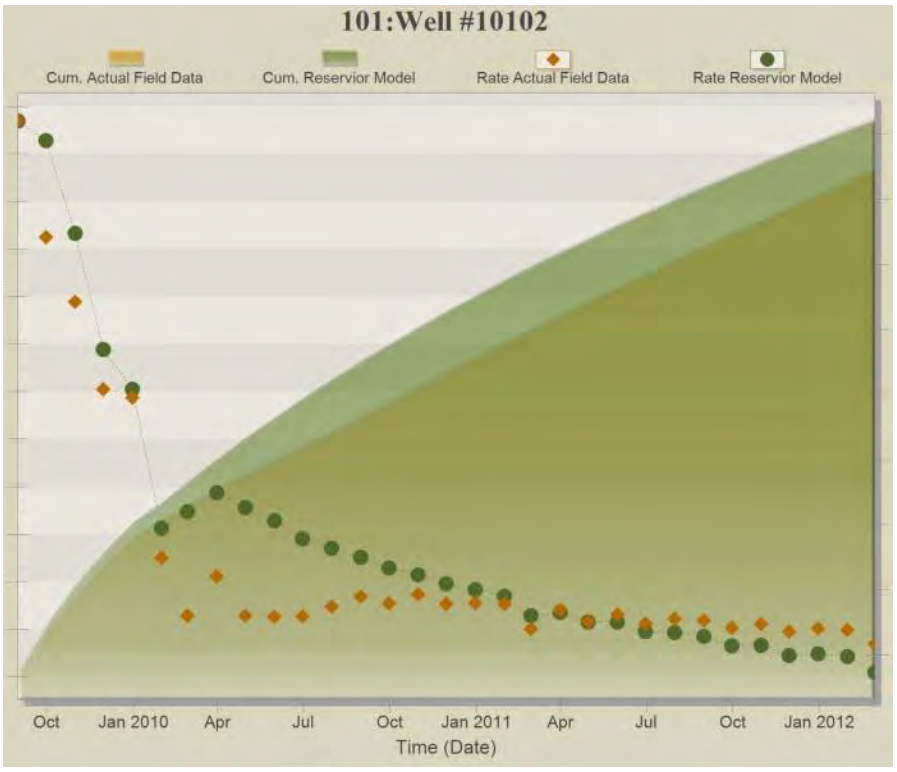

Figure A- 101: History Matching Results of Well#10102

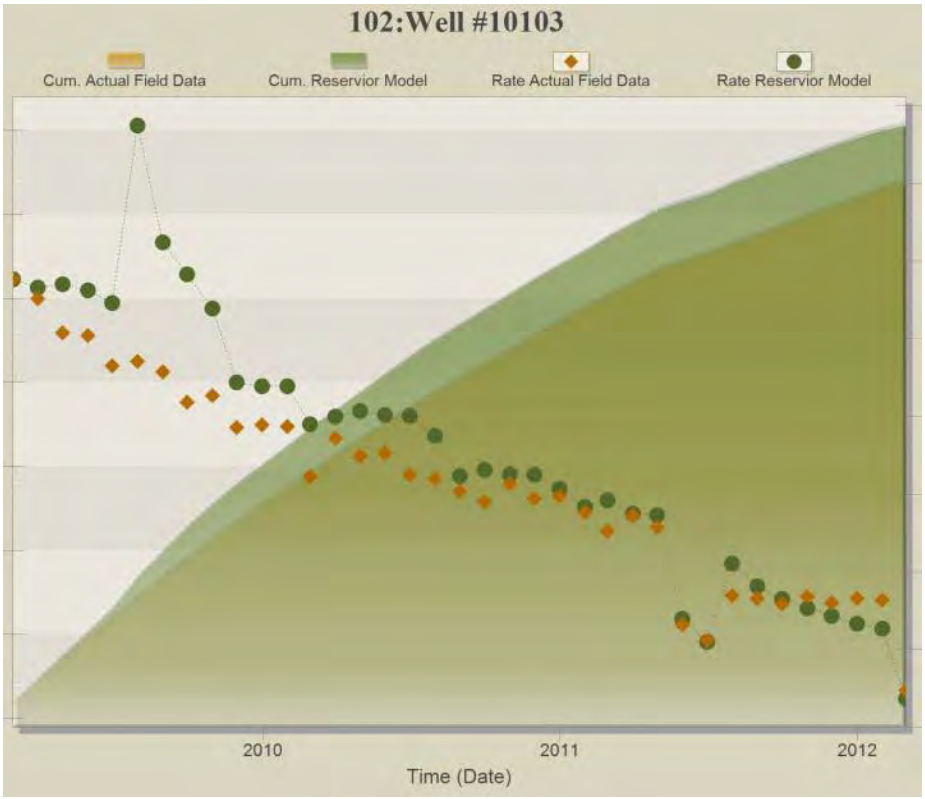

Figure A- 102: History Matching Results of Well#10103

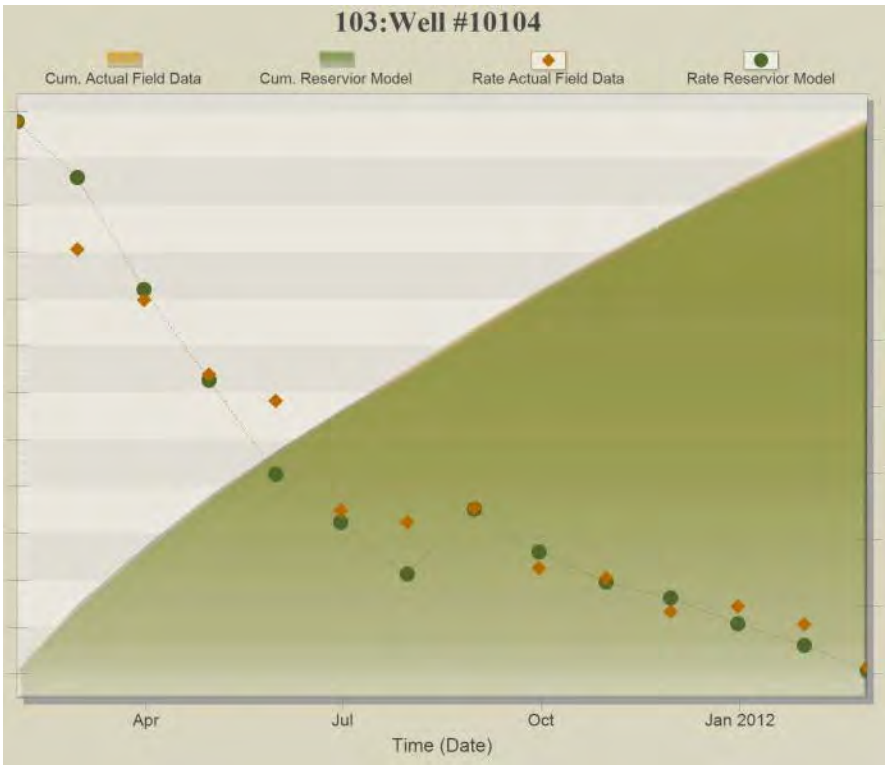

Figure A- 103: History Matching Results of Well#10104

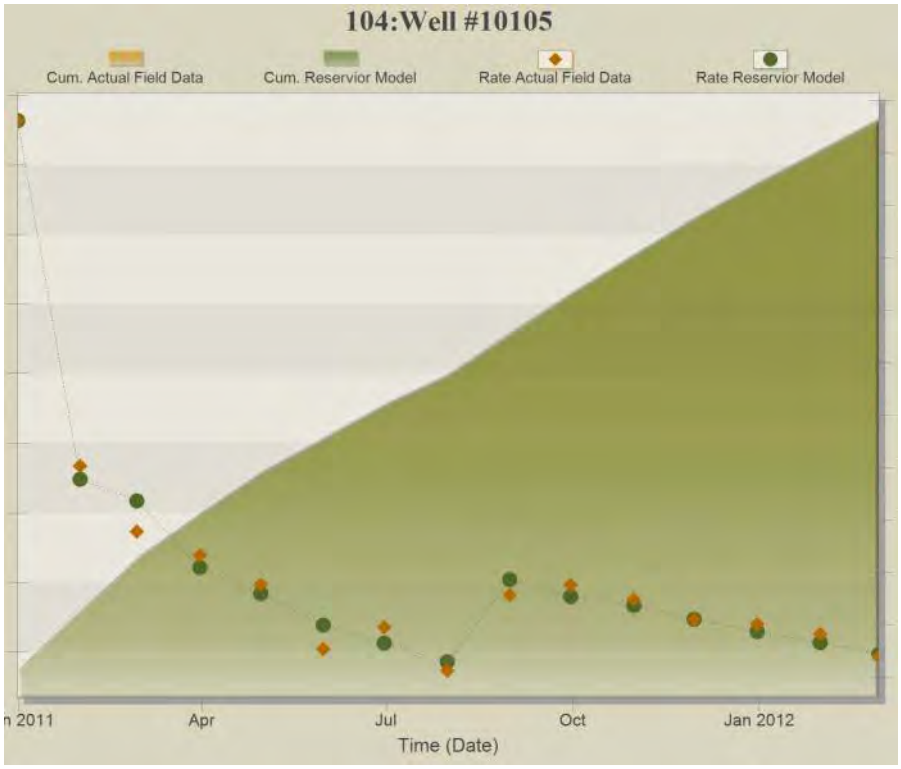

Figure A- 104: History Matching Results of Well#10105

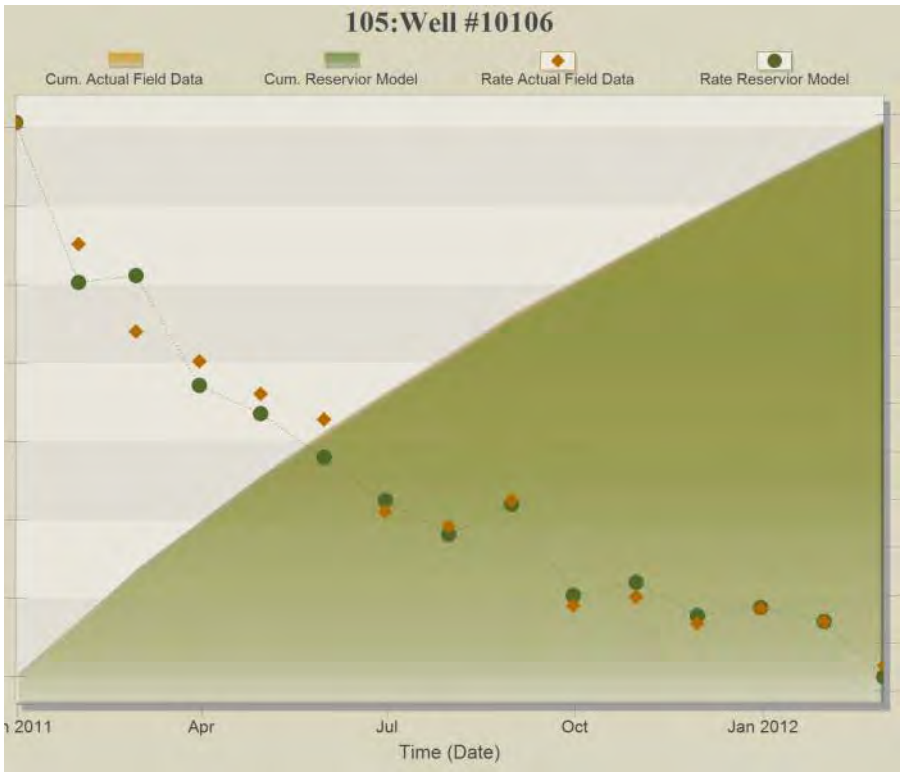

Figure A- 105: History Matching Results of Well#10106

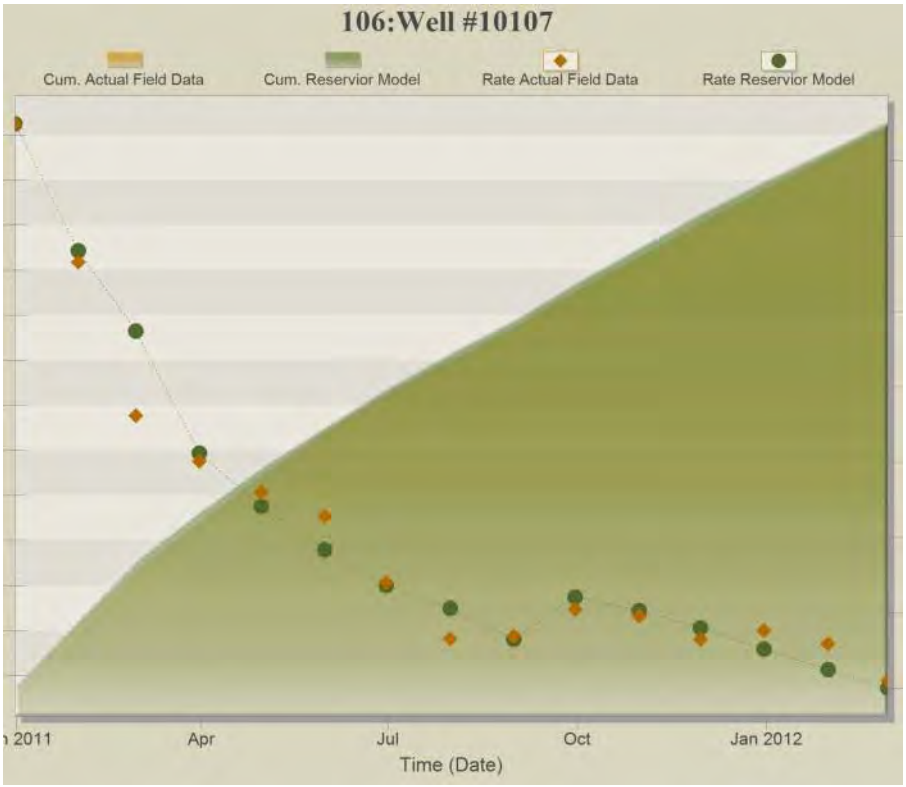

Figure A- 106: History Matching Results of Well#10107

Figure A- 107: History Matching Results of Well#10108

Figure A- 108: History Matching Results of Well#10109

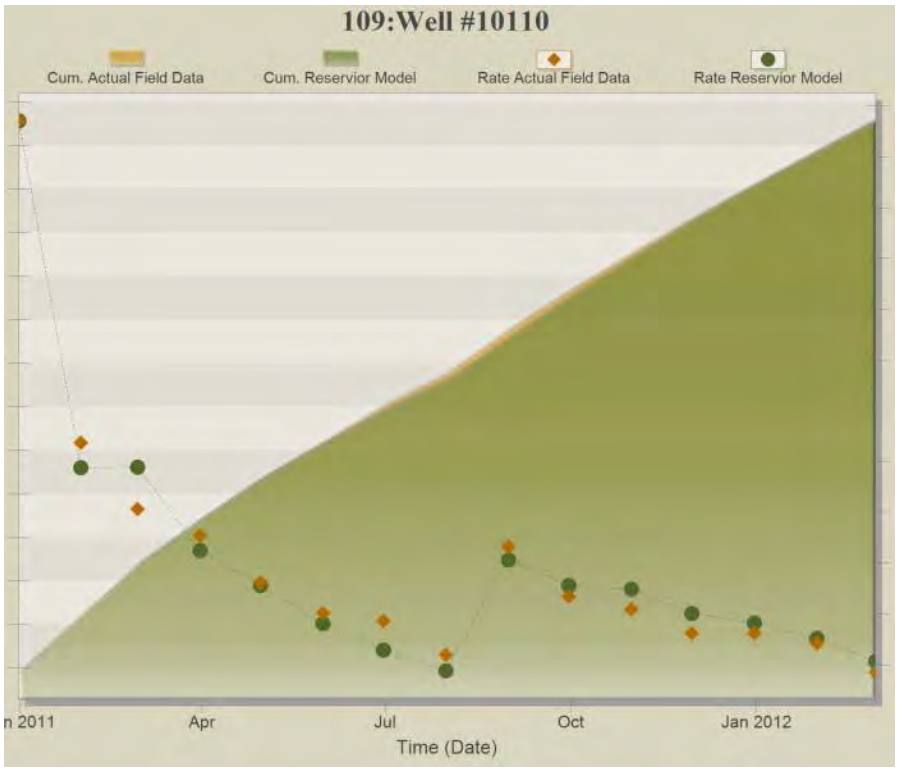

Figure A- 109: History Matching Results of Well#10110

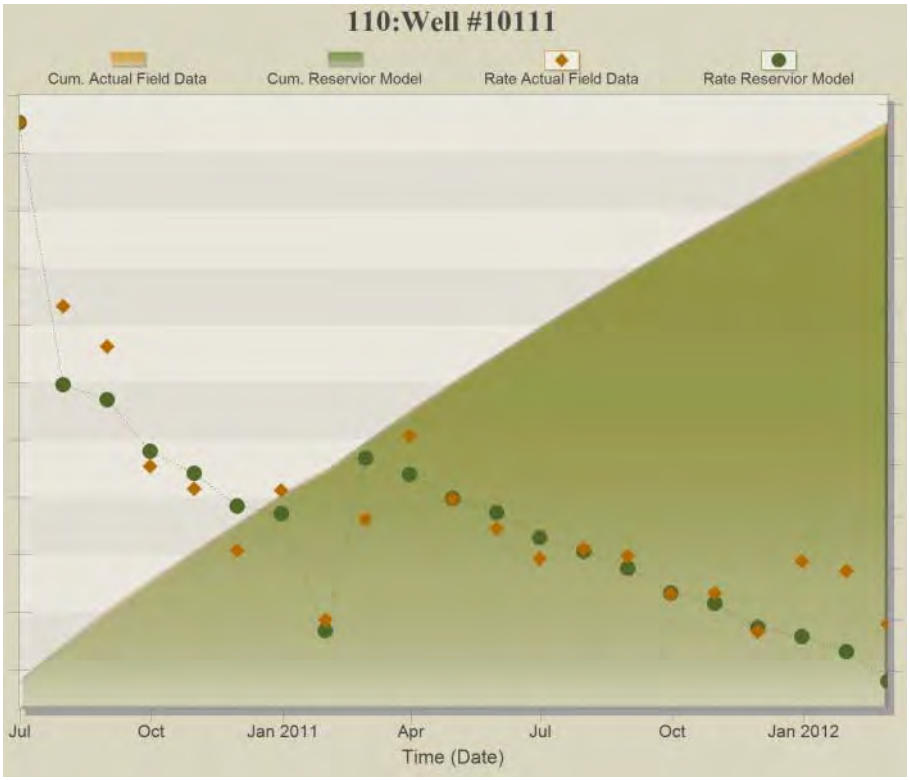

Figure A- 110: History Matching Results of Well#10111

Figure A- 111: History Matching Results of Well#10112

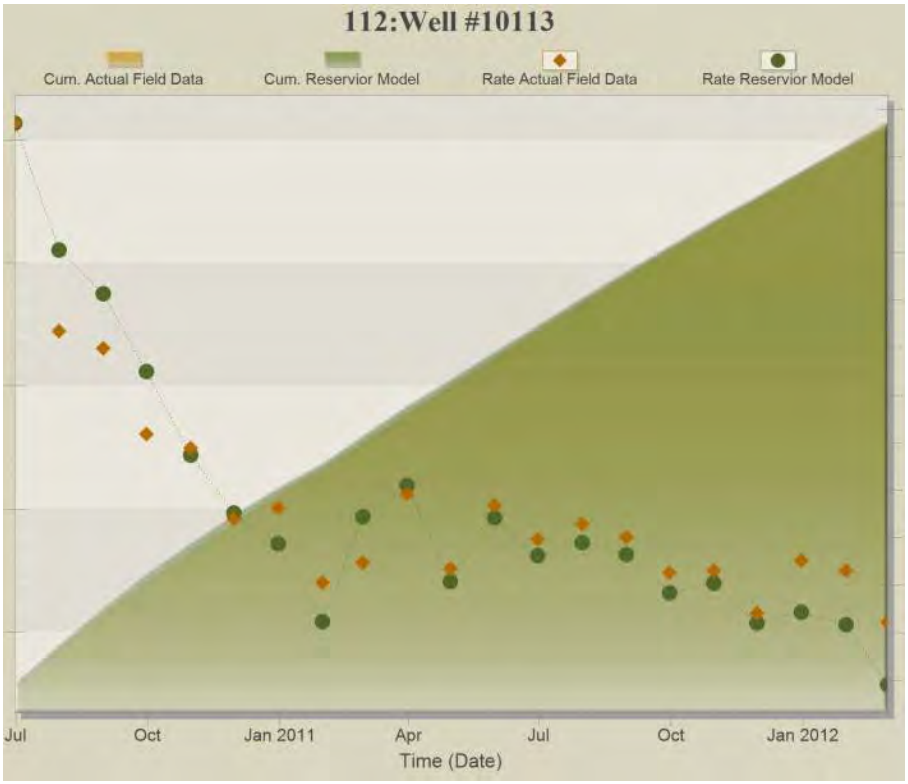

Figure A- 112: History Matching Results of Well#10113

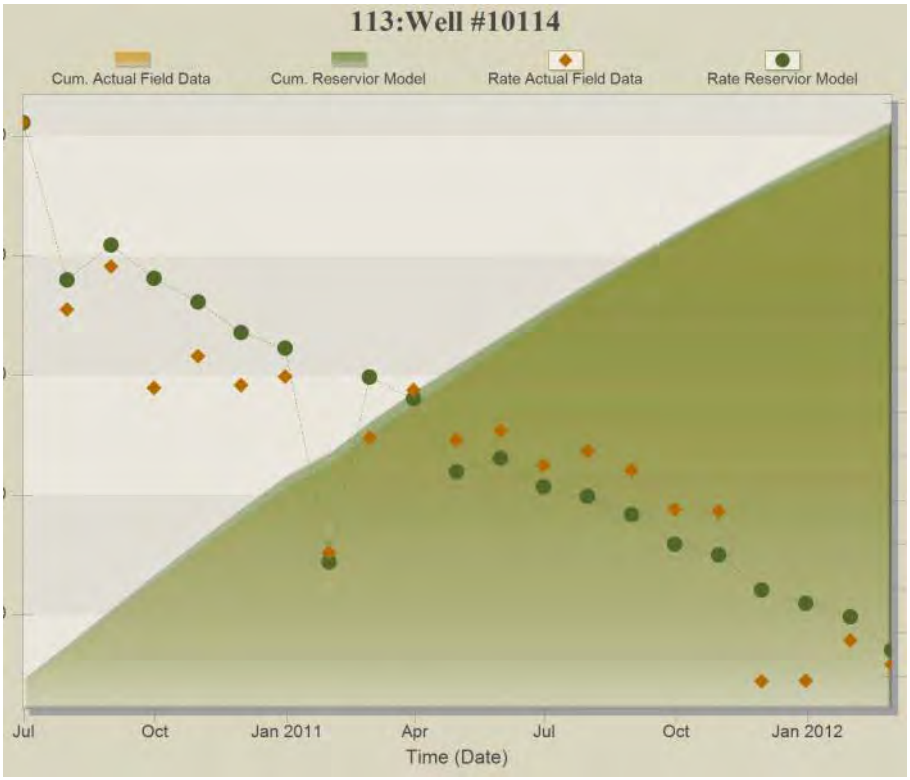

Figure A- 113: History Matching Results of Well#10114

Figure A- 114: History Matching Results of Well#10115

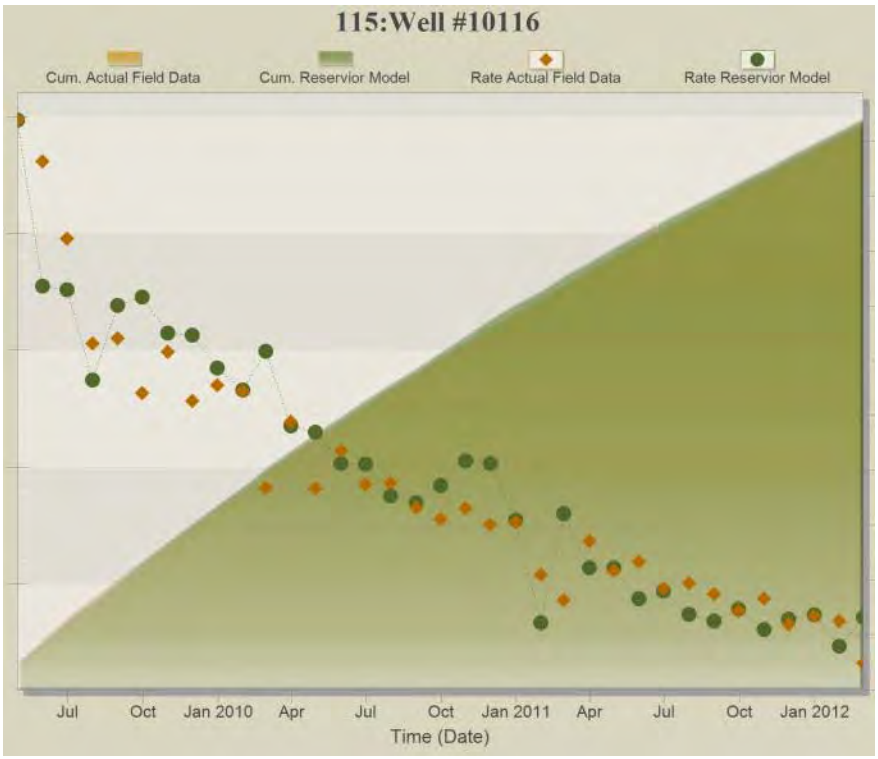

Figure A- 115: History Matching Results of Well#10116

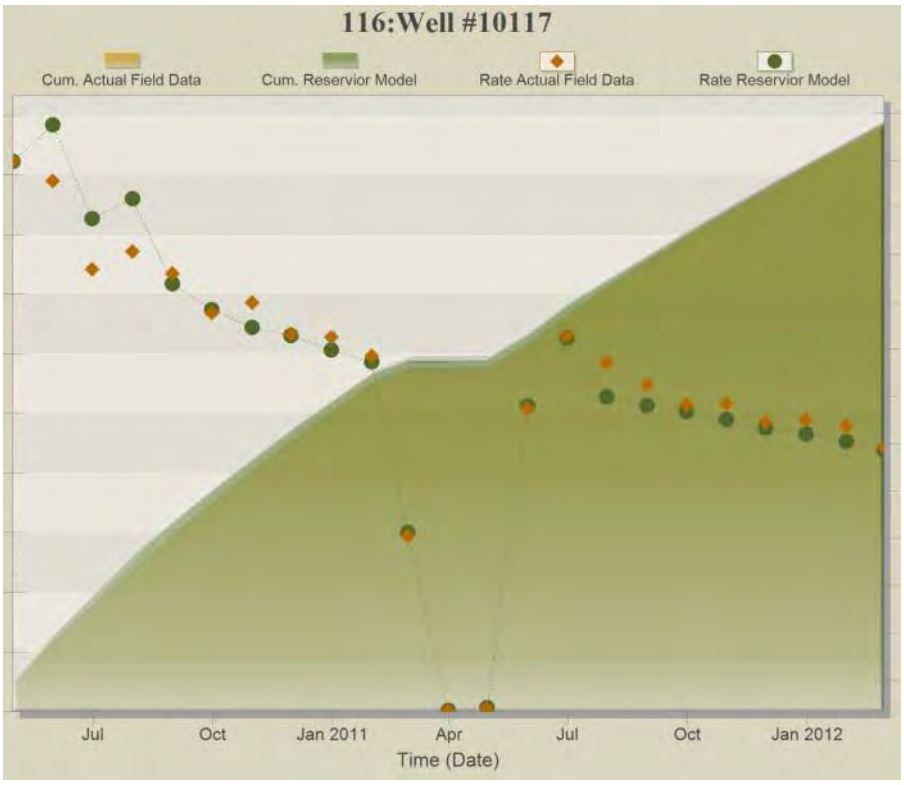

Figure A- 116: History Matching Results of Well#10117

Figure A- 117: History Matching Results of Well#10118

Figure A- 118: History Matching Results of Well#10119

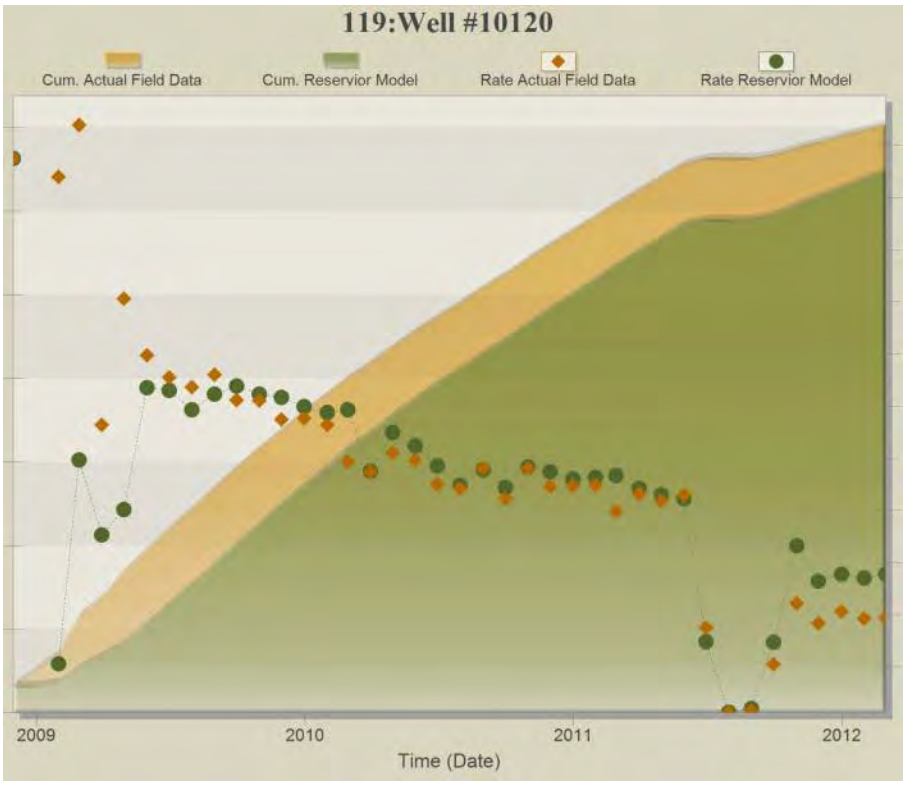

Figure A- 119: History Matching Results of Well#10120

Figure A- 120: History Matching Results of Well#10121

Figure A- 121: History Matching Results of Well#10122

Figure A- 122: History Matching Results of Well#10123

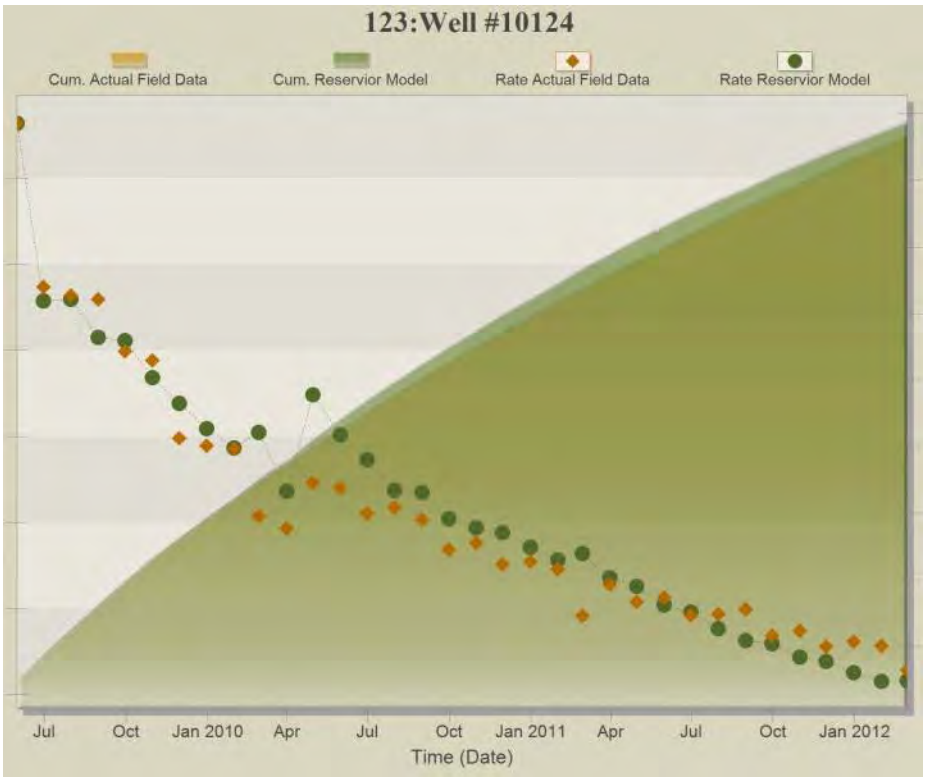

Figure A- 123: History Matching Results of Well#10124

Figure A- 124: History Matching Results of Well#10125

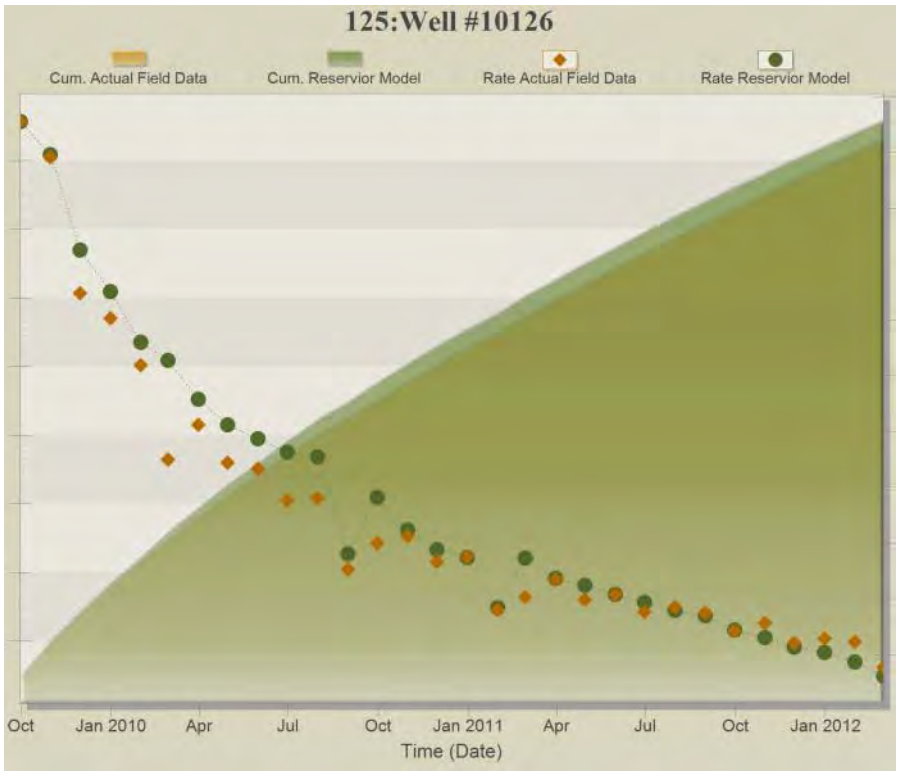

Figure A- 125: History Matching Results of Well#10126

Figure A- 126: History Matching Results of Well#10127

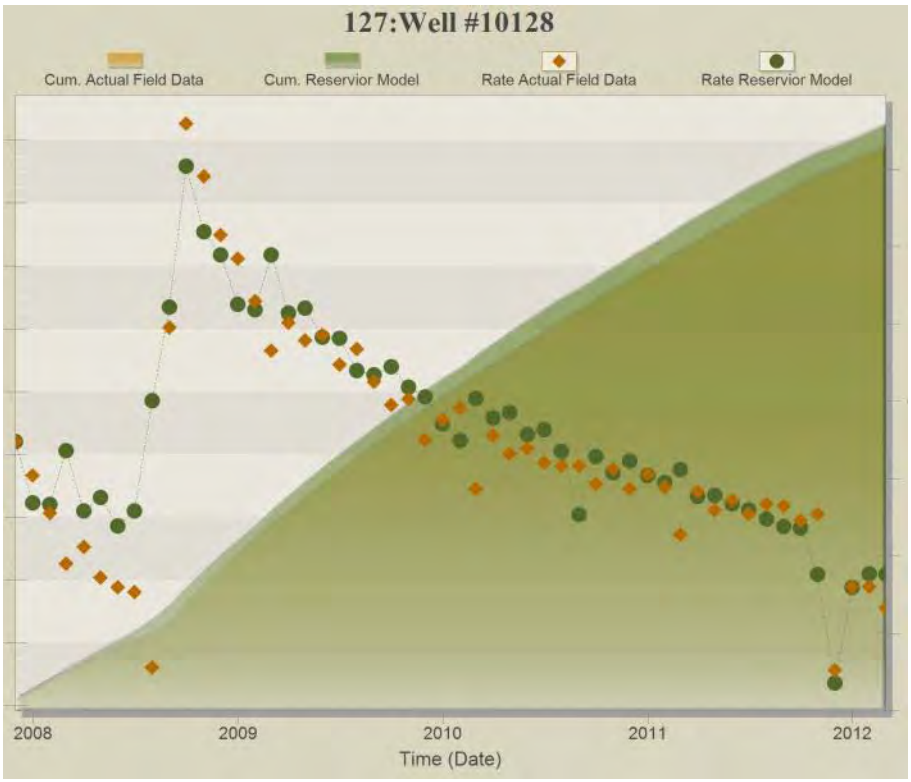

Figure A- 127: History Matching Results of Well#10128

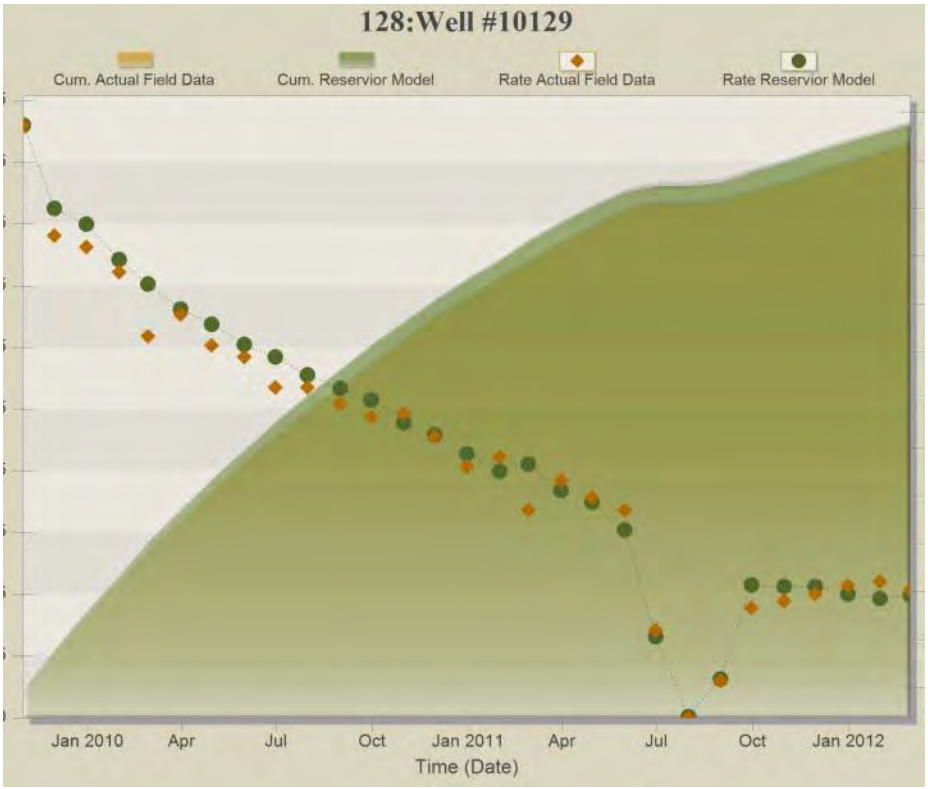

Figure A- 128: History Matching Results of Well#10129

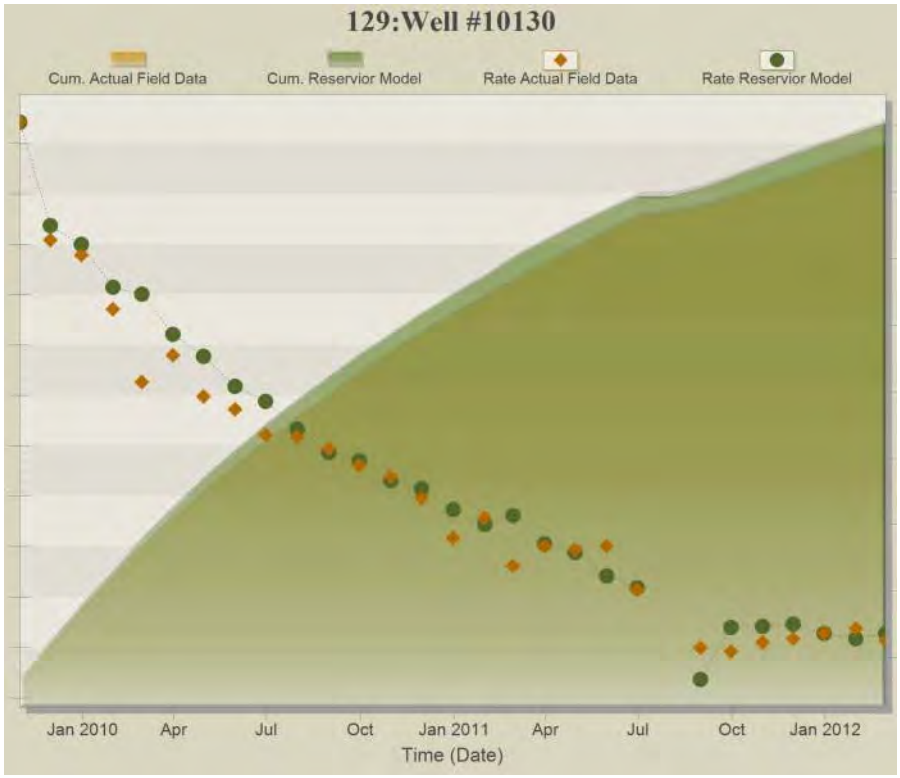

Figure A- 129: History Matching Results of Well#10130

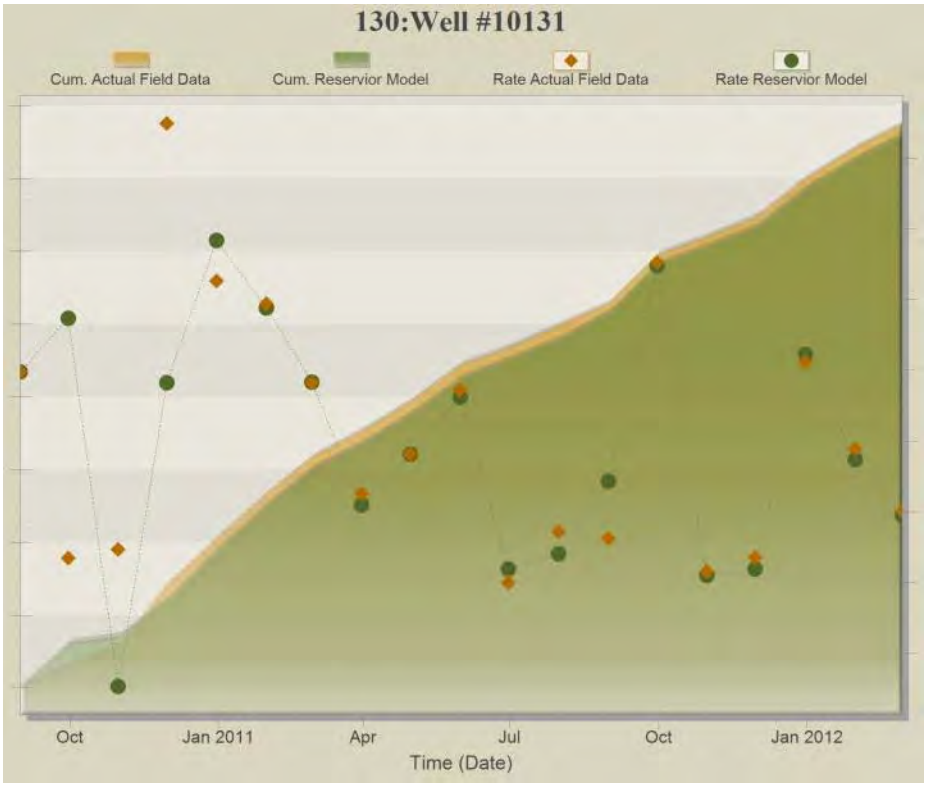

Figure A- 130: History Matching Results of Well#10131

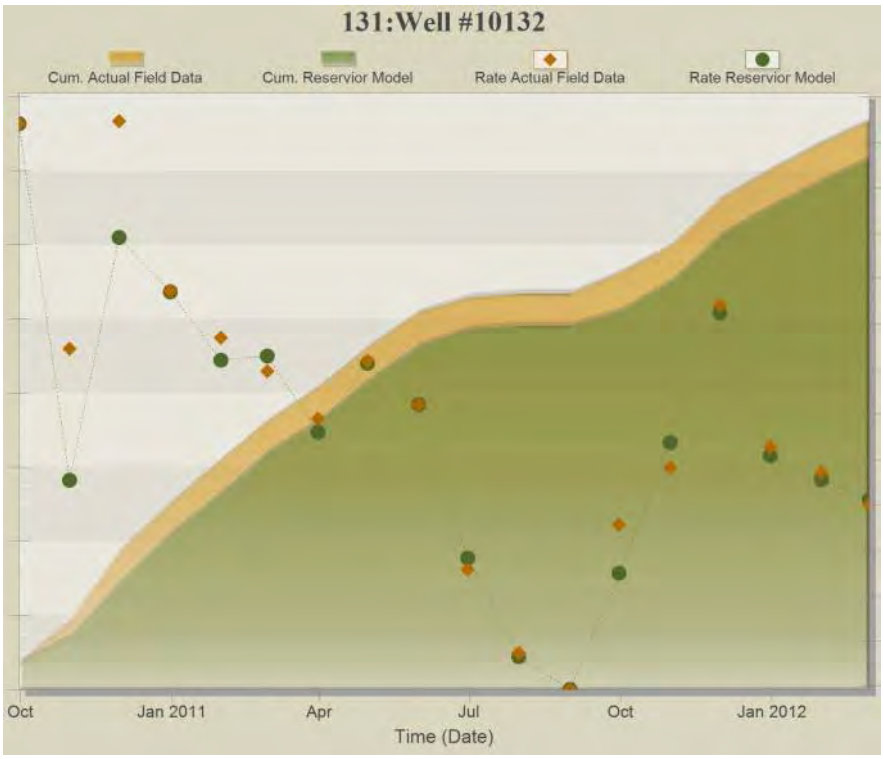

Figure A- 131: History Matching Results of Well#10132

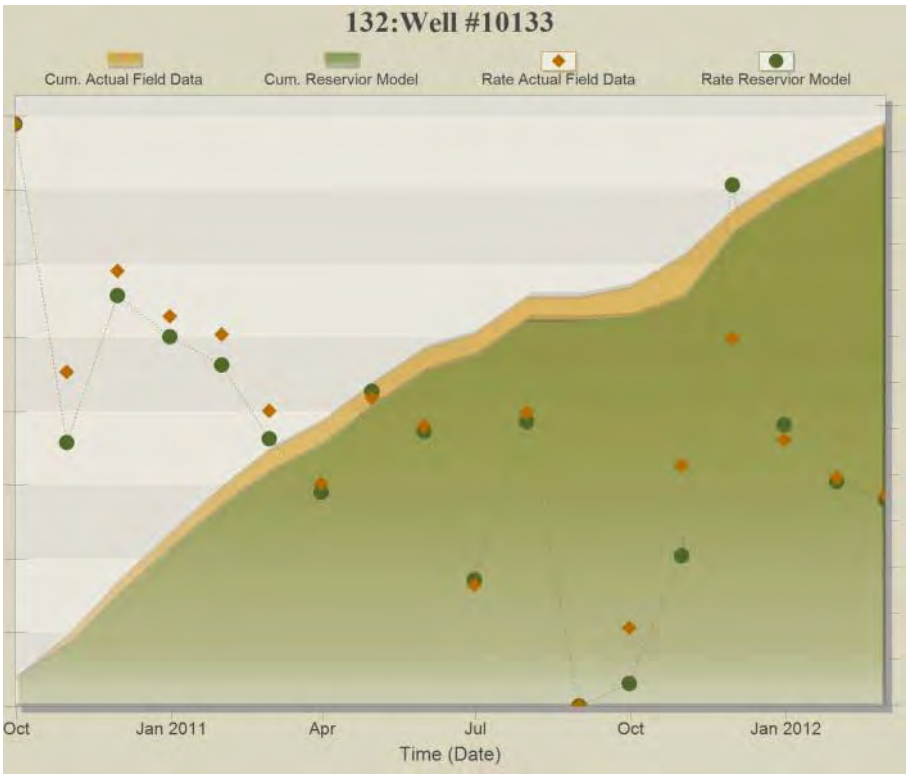

Figure A- 132: History Matching Results of Well#10133

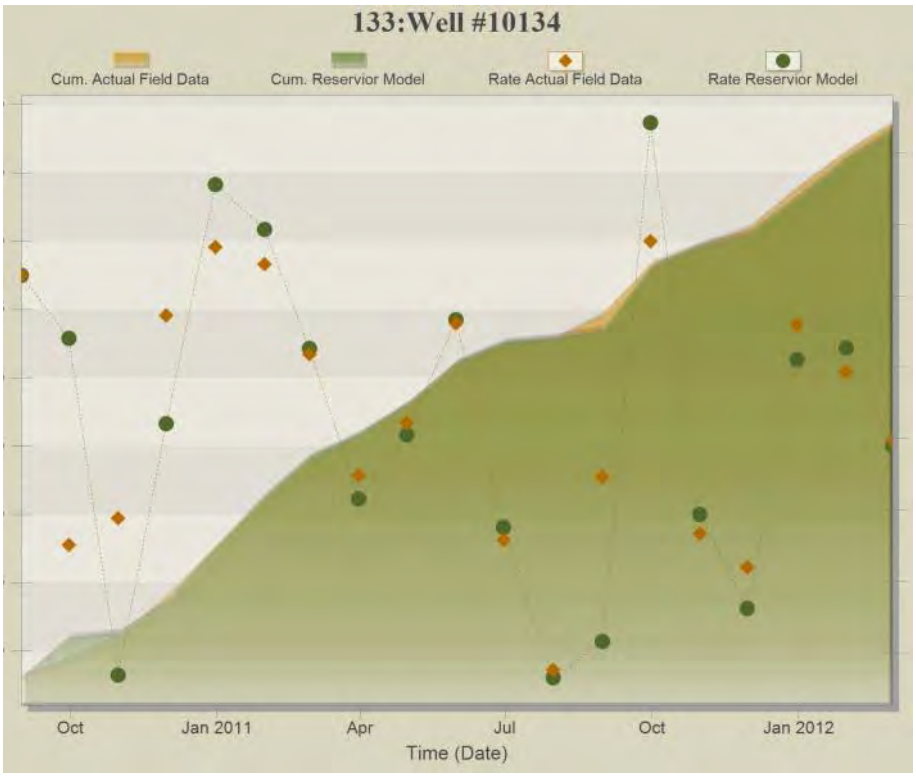

Figure A- 133: History Matching Results of Well#10134

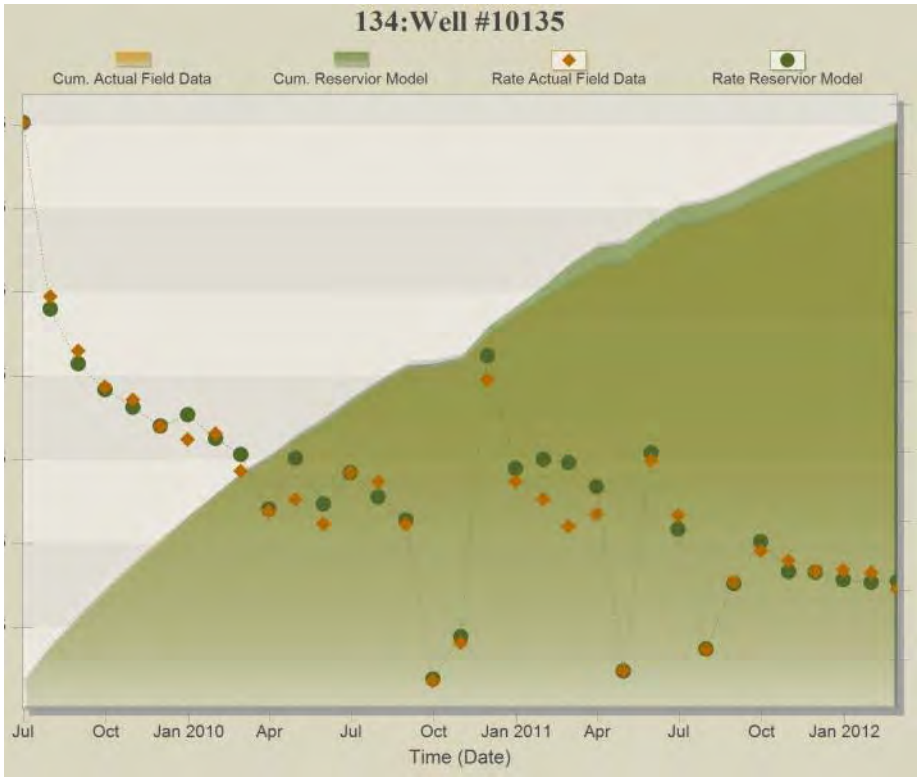

Figure A- 134: History Matching Results of Well#10135

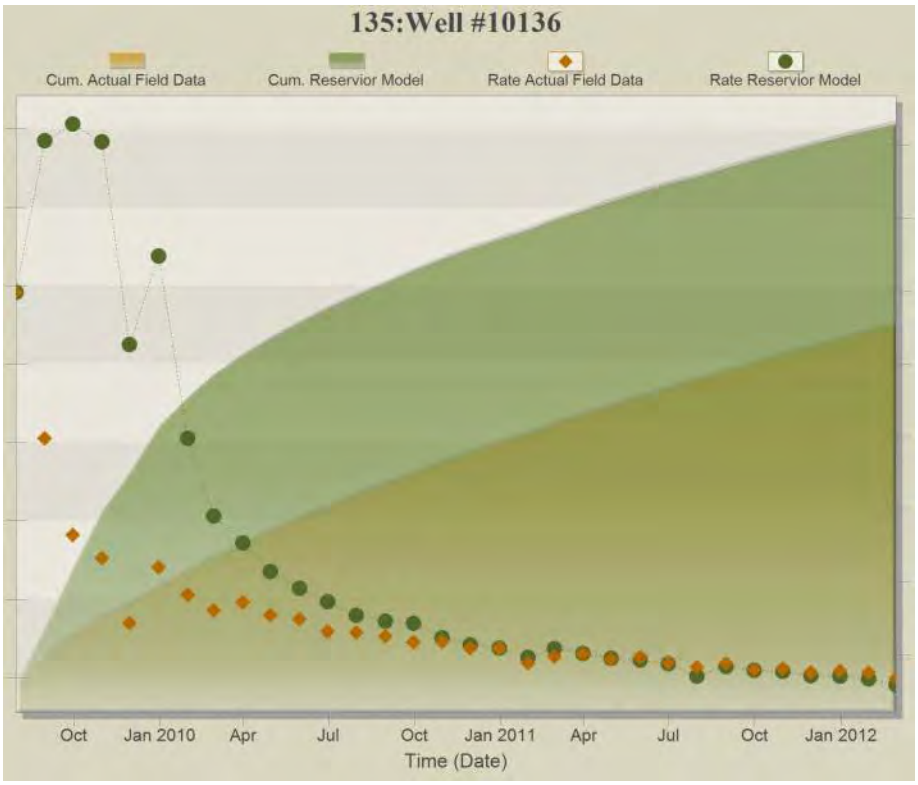

Figure A- 135: History Matching Results of Well#10136

Appendix B: Forecasting Results- Scenario 1

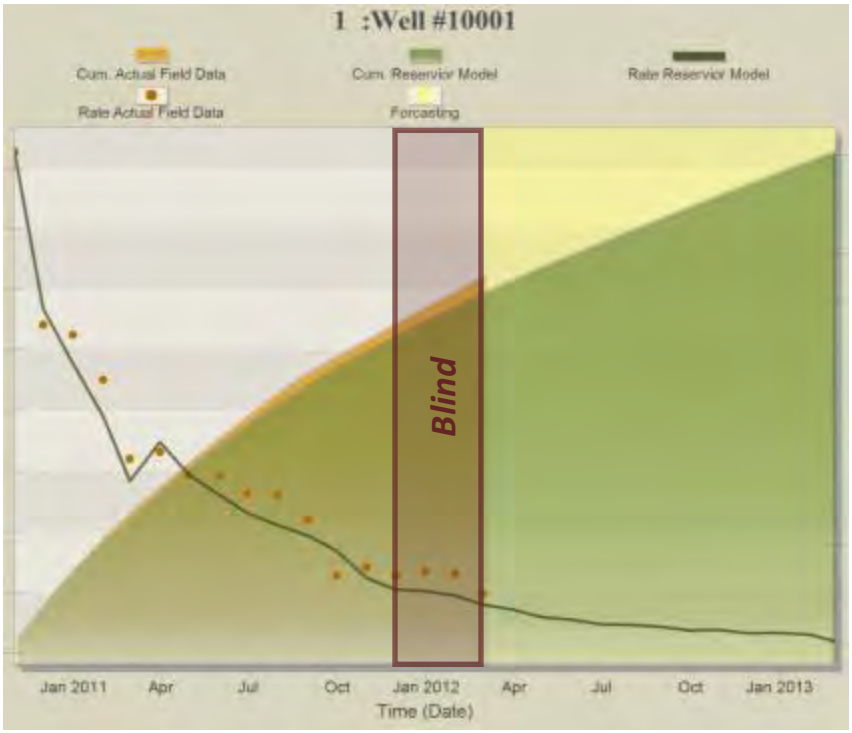

Figure B- 136: Prediction Results for Well#10001

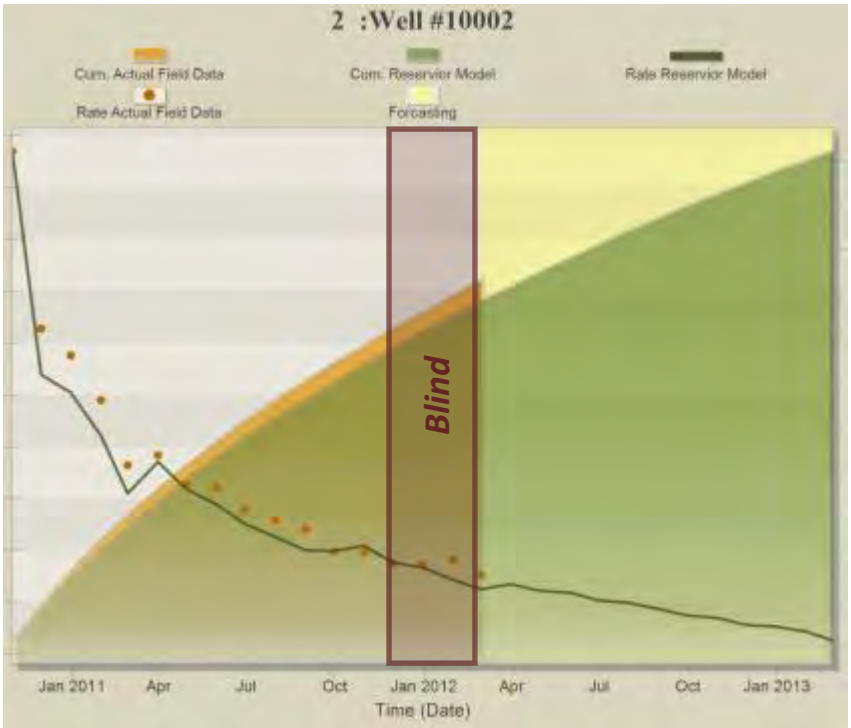

Figure B- 137: Prediction Results for Well#10002

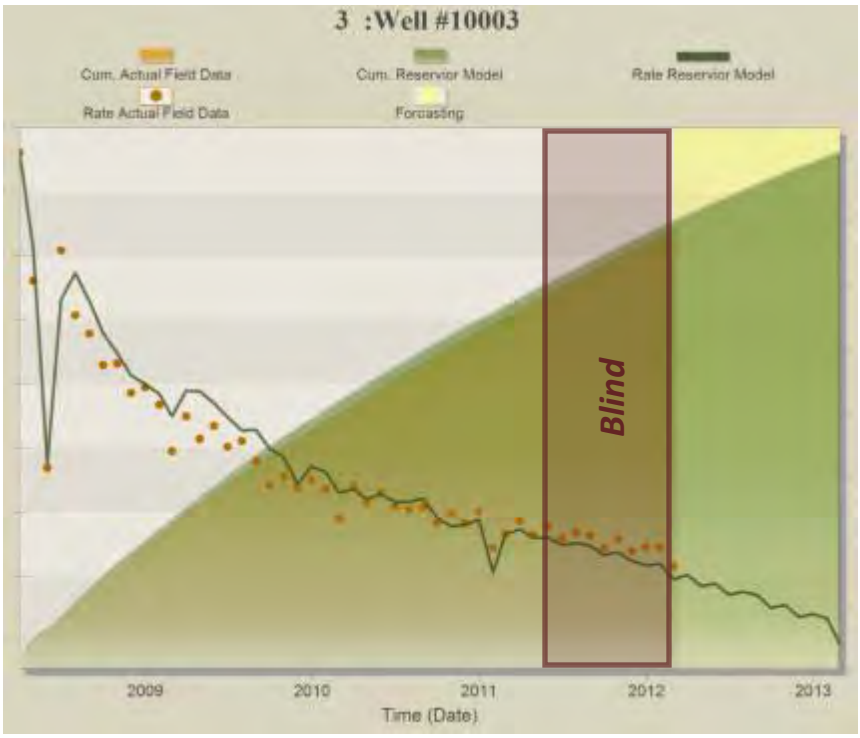

Figure B- 138: Prediction Results for Well#10003

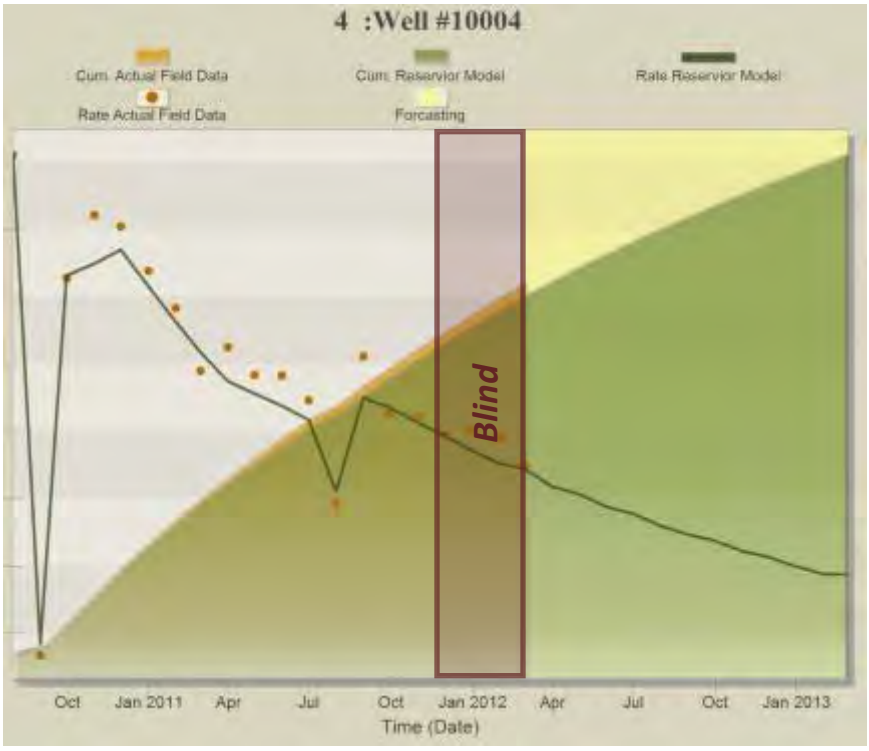

Figure B- 139: Prediction Results for Well#10004

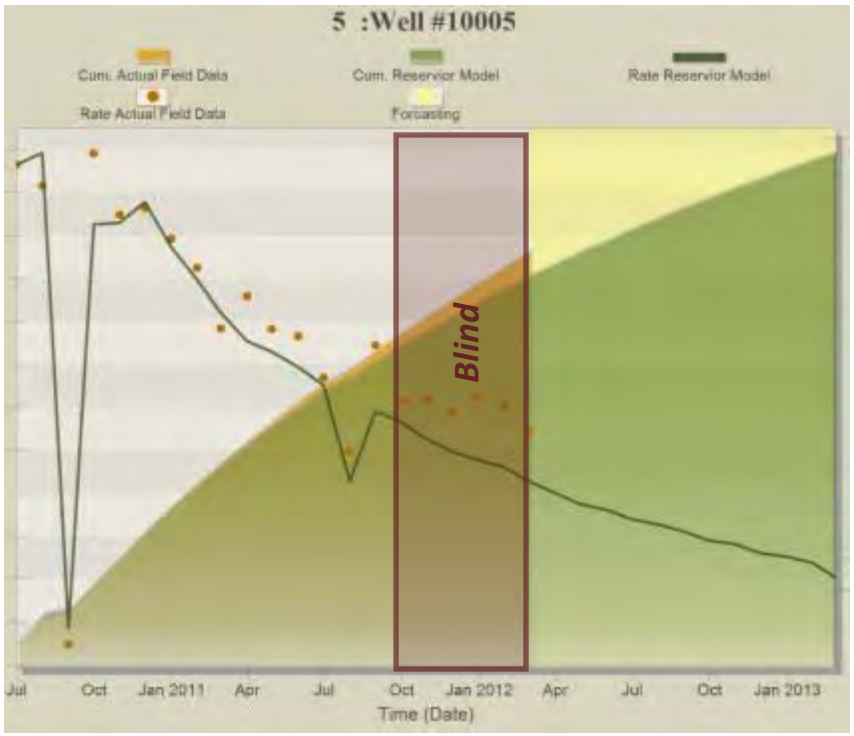

Figure B- 140: Prediction Results for Well#10005

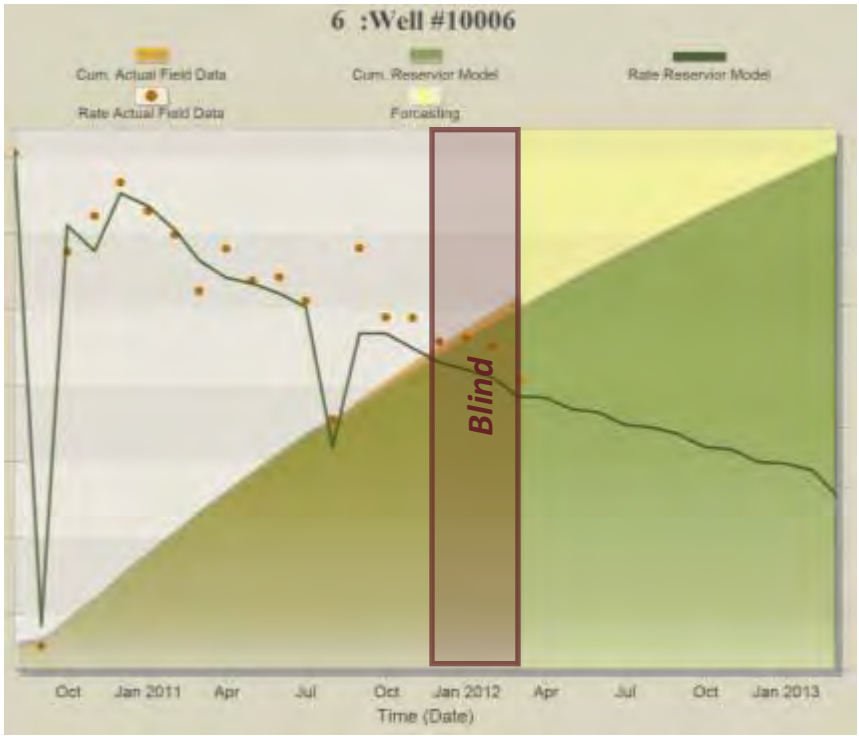

Figure B- 141: Prediction Results for Well#10006

Figure B- 142: Prediction Results for Well#10007

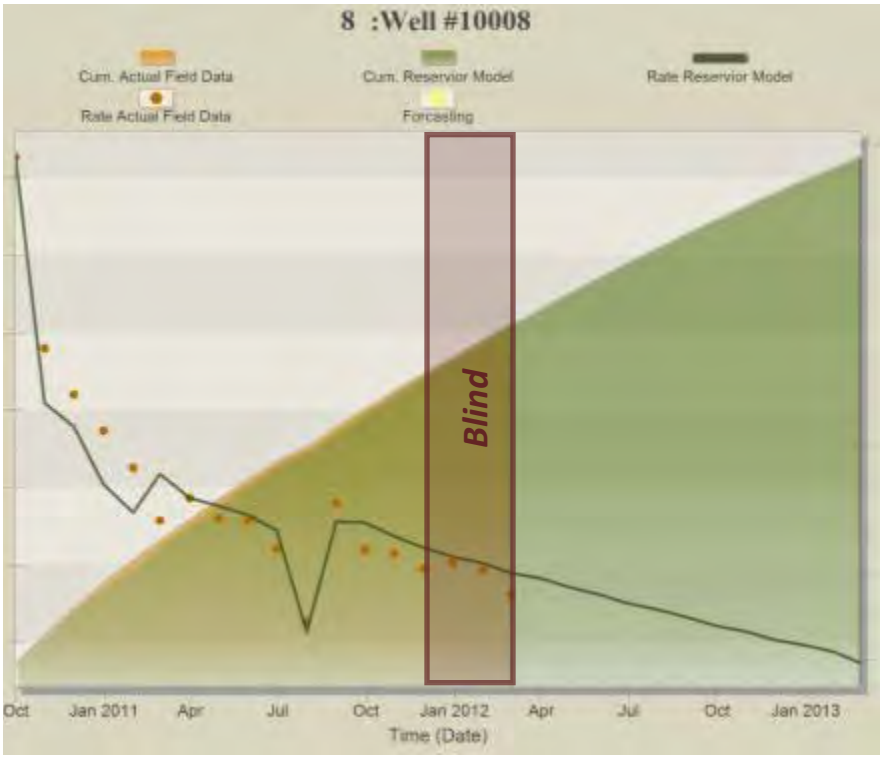

Figure B- 143: Prediction Results for Well#10008

Figure B- 144: Prediction Results for Well#10009

Figure B- 145: Prediction Results for Well#10010

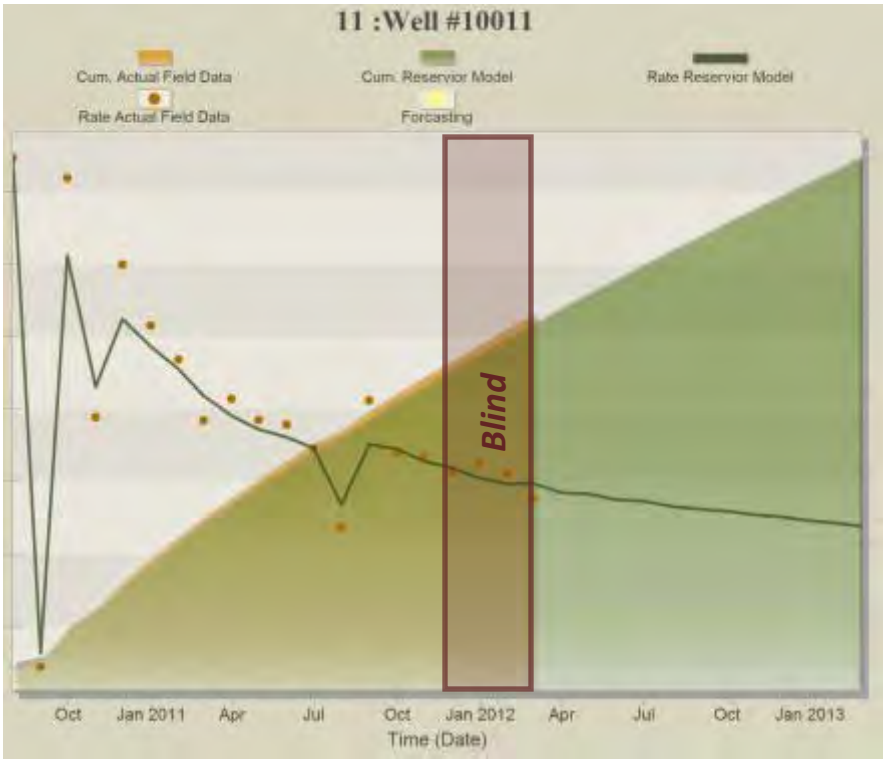

Figure B- 146: Prediction Results for Well#10011

Figure B- 147: Prediction Results for Well#10012

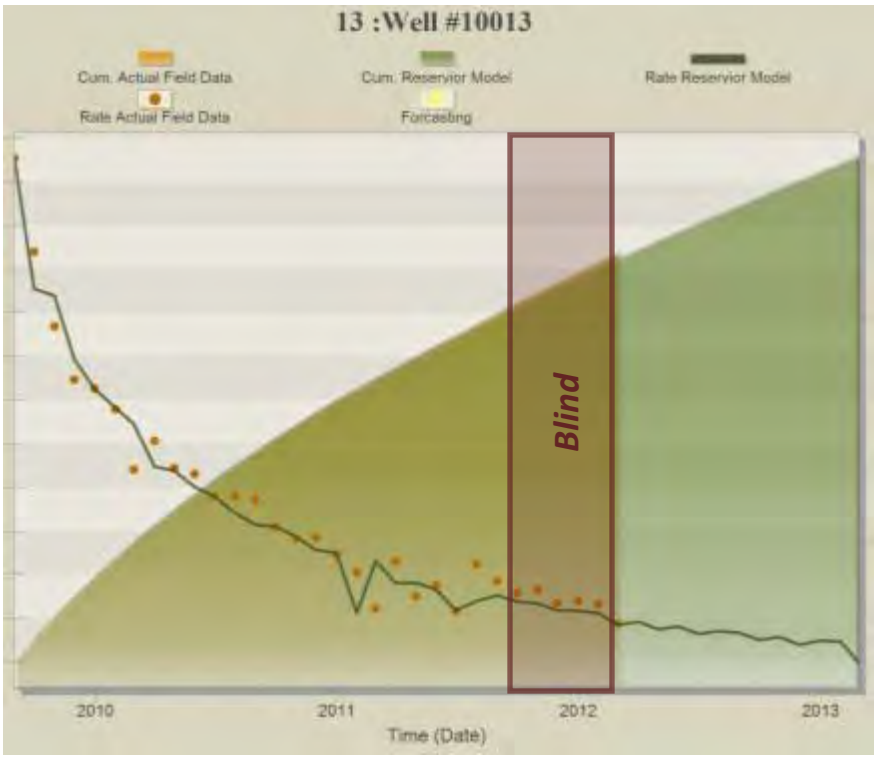

Figure B- 148: Prediction Results for Well#10013

Figure B- 149: Prediction Results for Well#10014

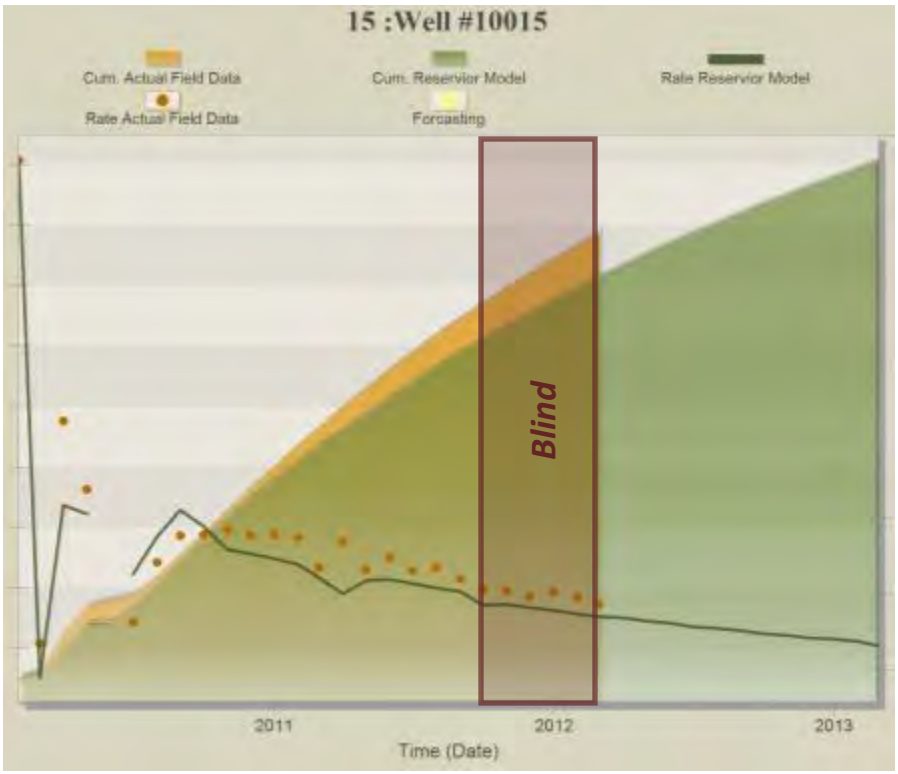

Figure B- 150: Prediction Results for Well#10015

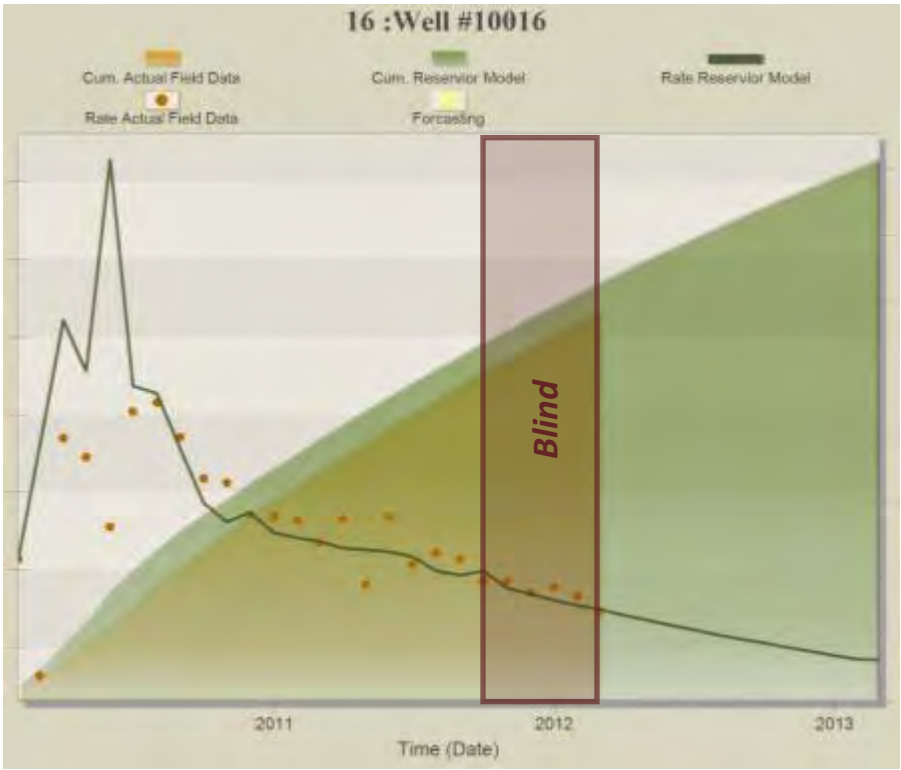

Figure B- 151: Prediction Results for Well#10016

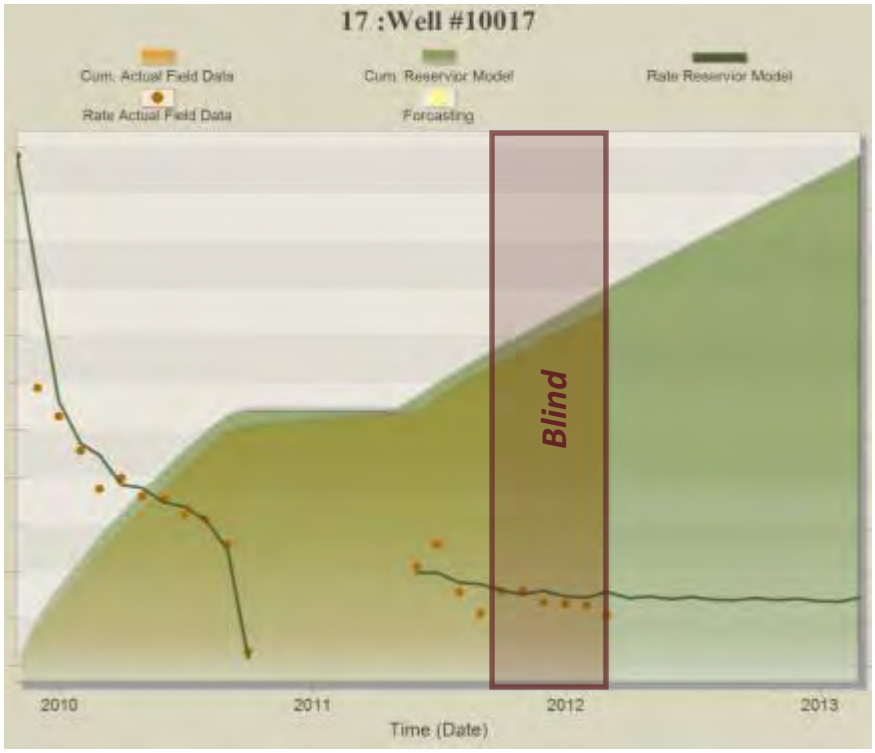

Figure B- 152: Prediction Results for Well#10017

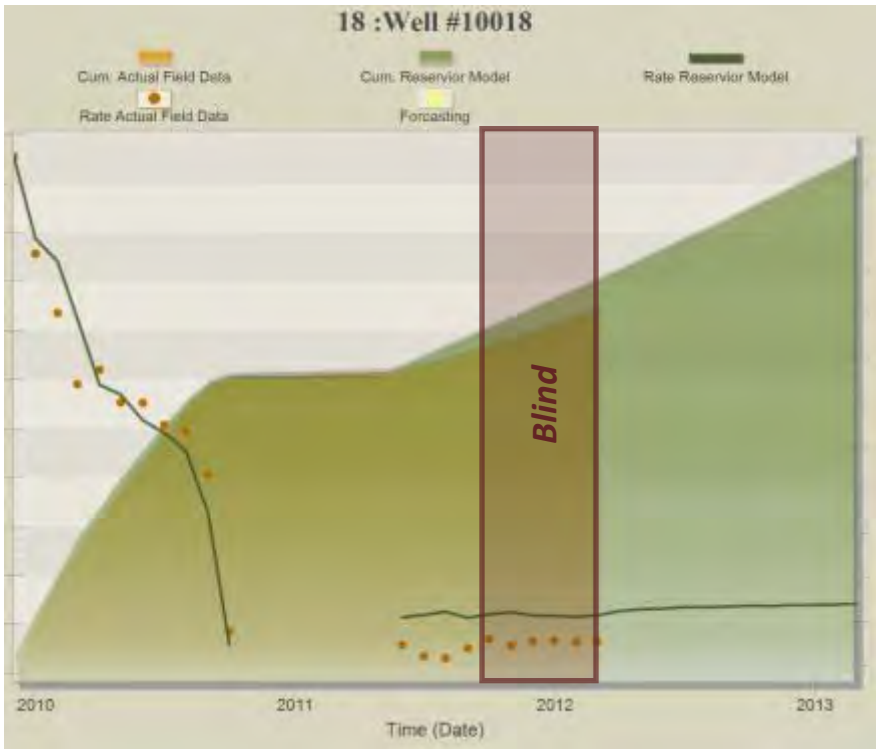

Figure B- 153: Prediction Results for Well#10018

Figure B- 154: Prediction Results for Well#10019

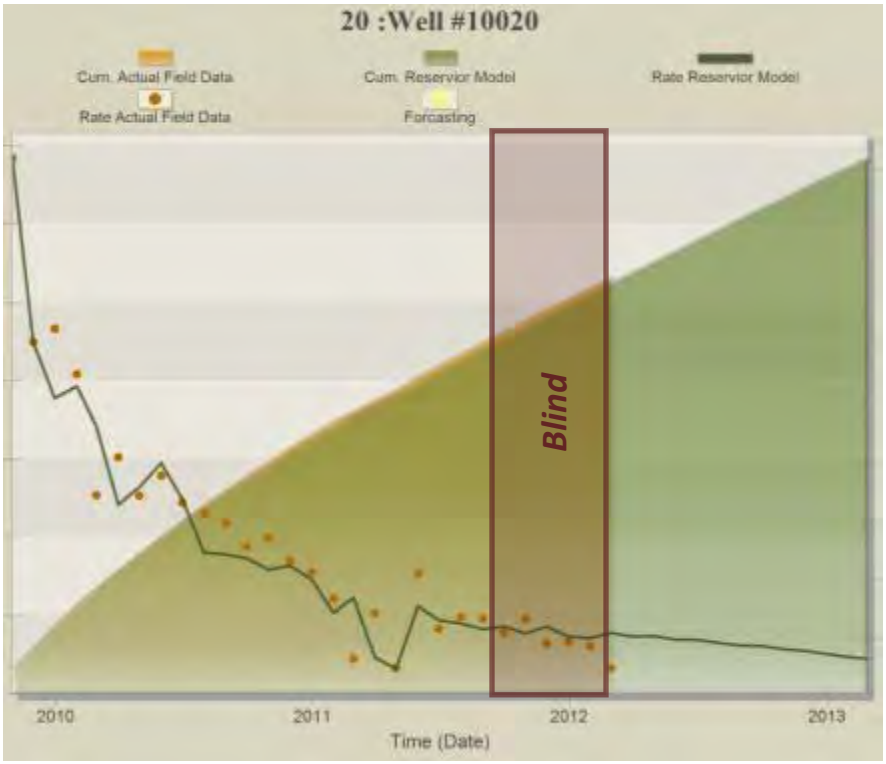

Figure B- 155: Prediction Results for Well#10020

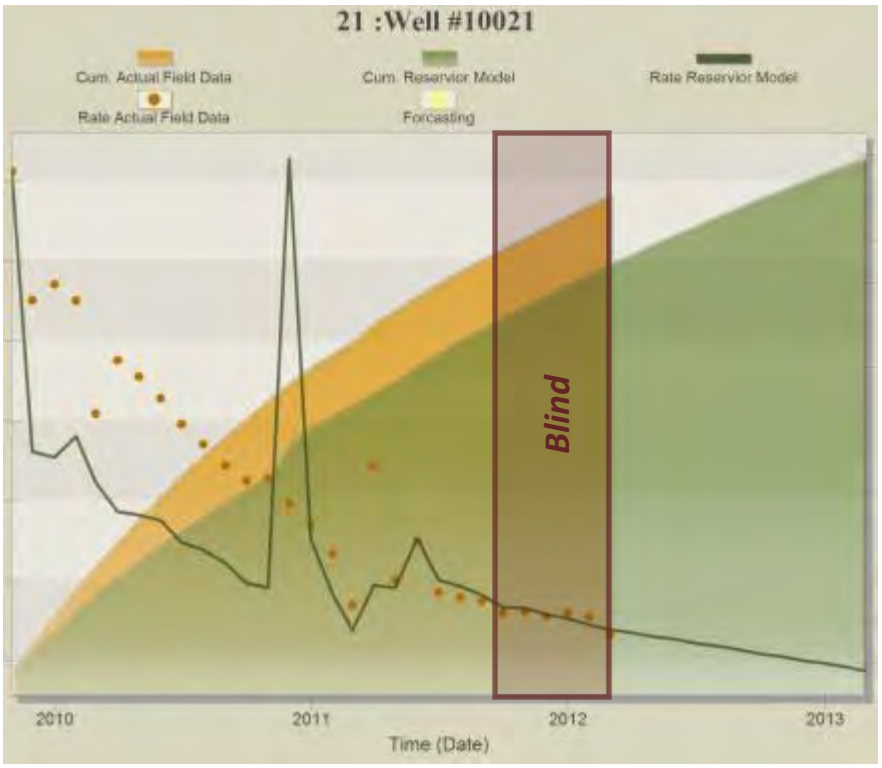

Figure B- 156: Prediction Results for Well#10021

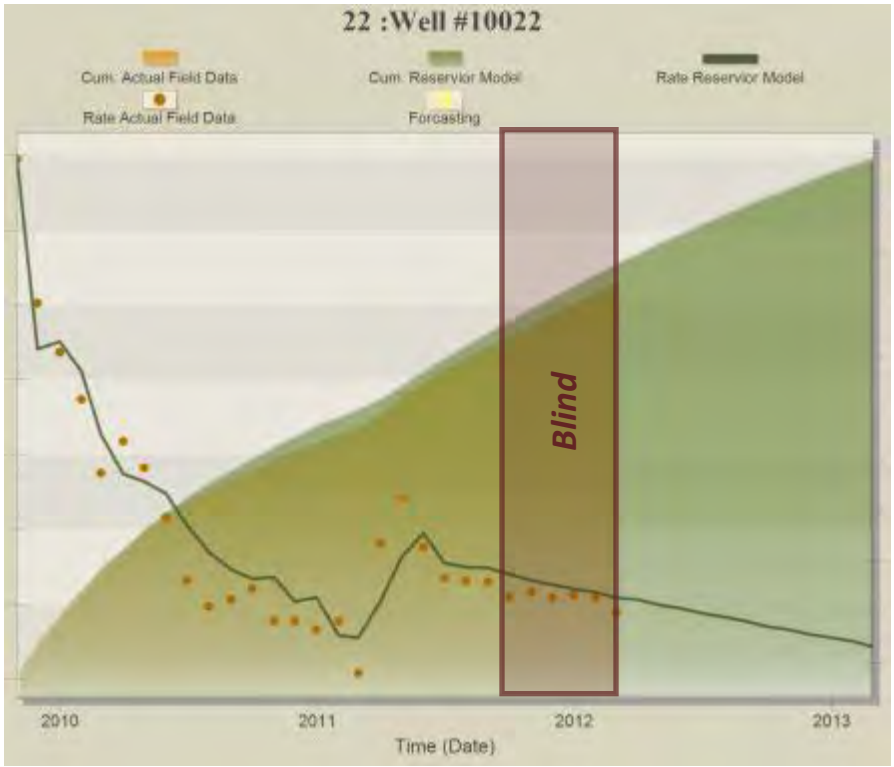

Figure B- 157: Prediction Results for Well#10022

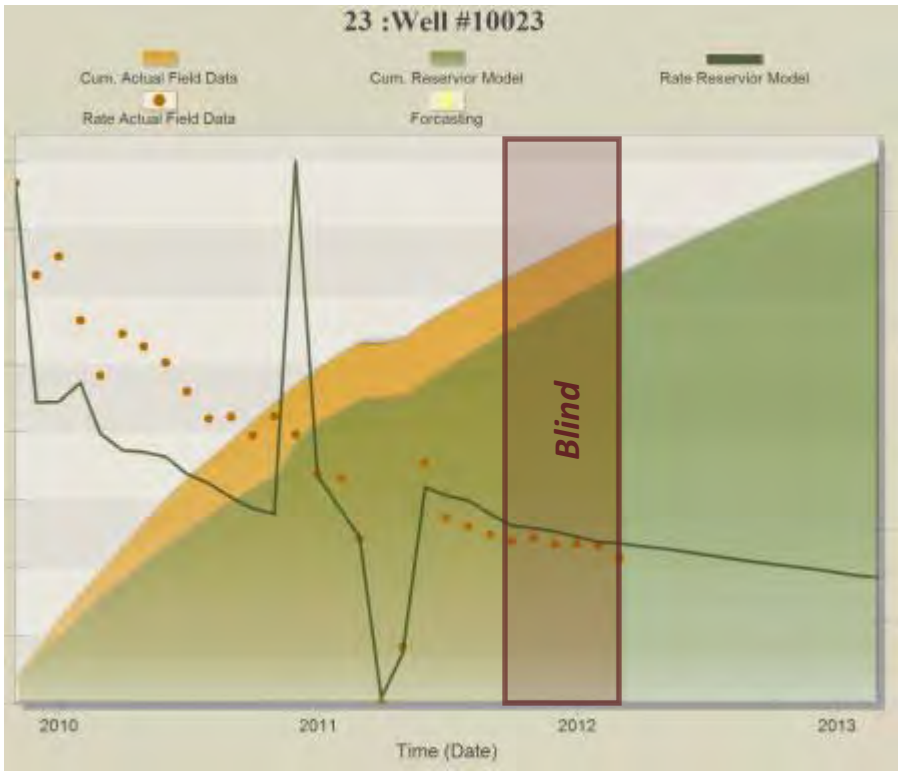

Figure B- 158: Prediction Results for Well#10023

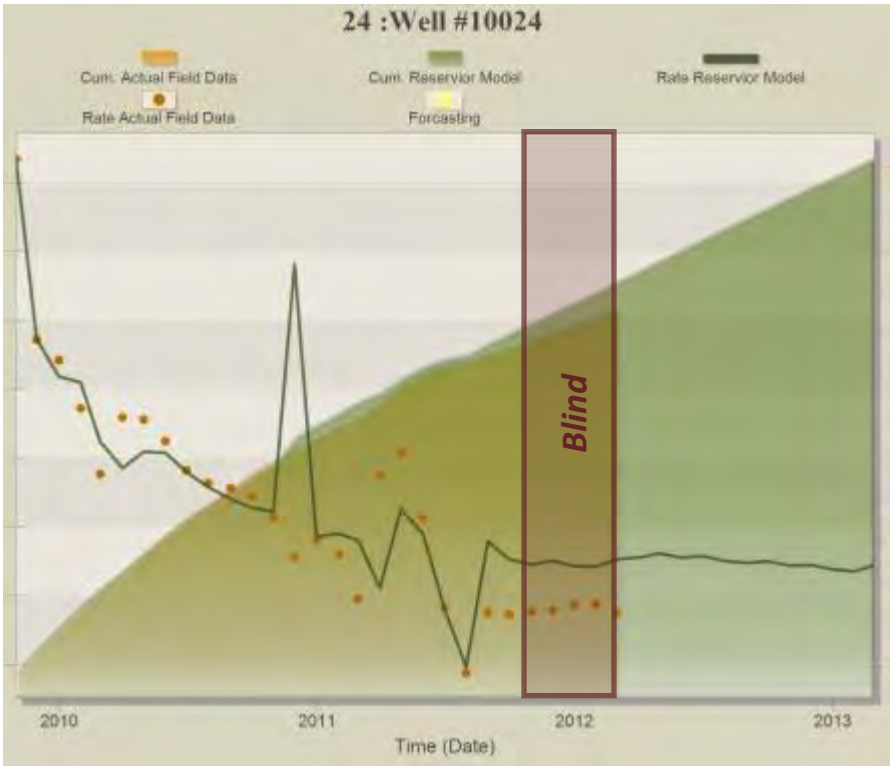

Figure B- 159: Prediction Results for Well#10024

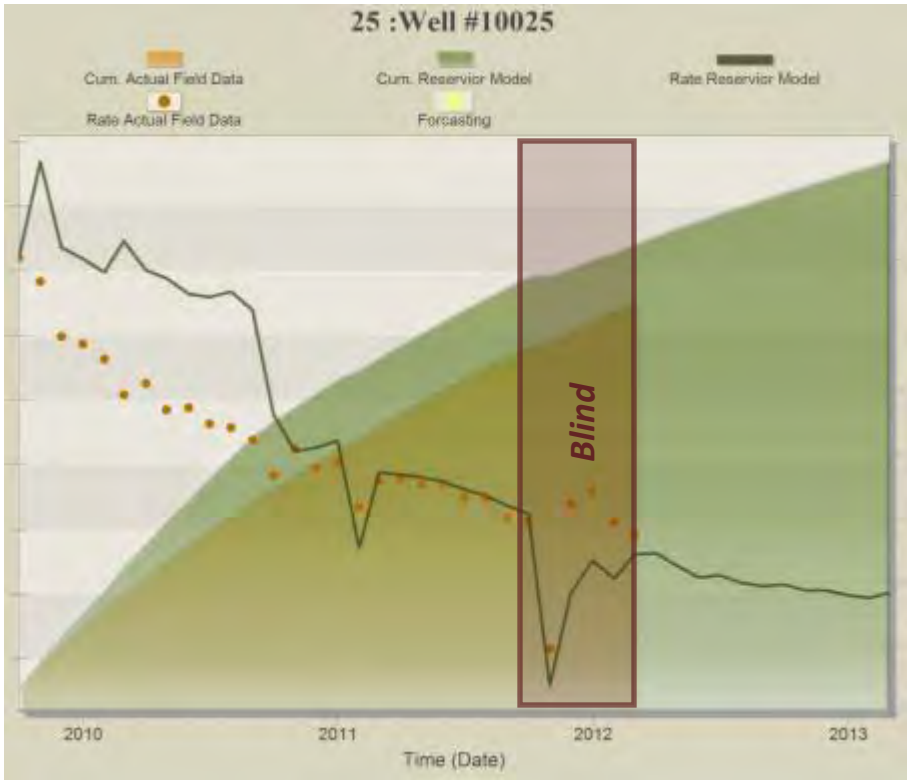

Figure B- 160: Prediction Results for Well#10025

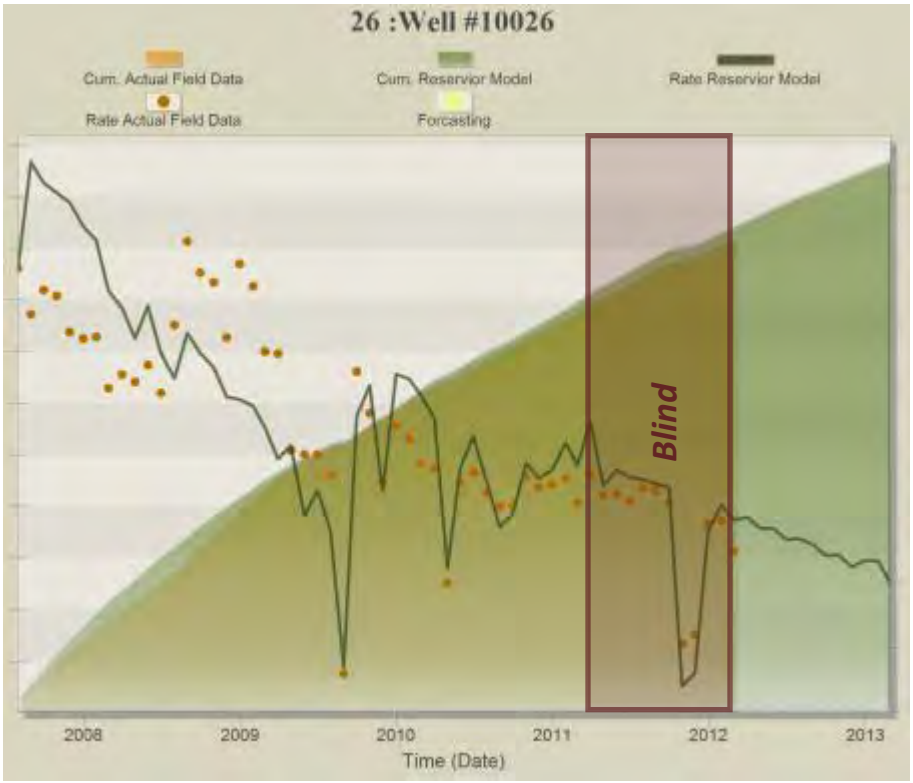

Figure B- 161: Prediction Results for Well#10026

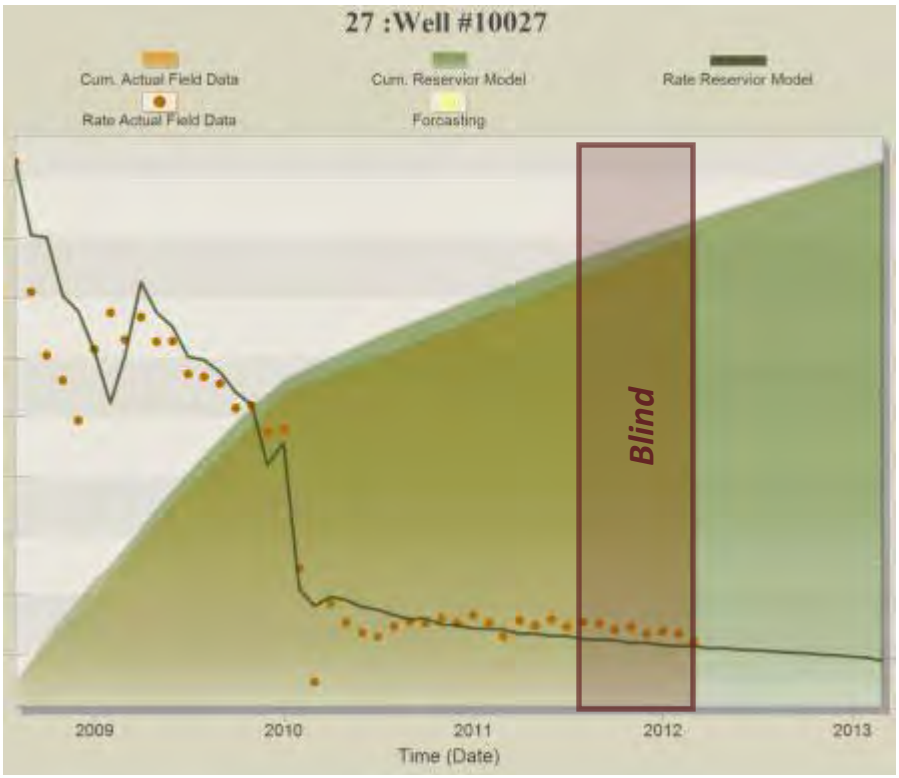

Figure B- 162: Prediction Results for Well#10027

Figure B- 163: Prediction Results for Well#10028

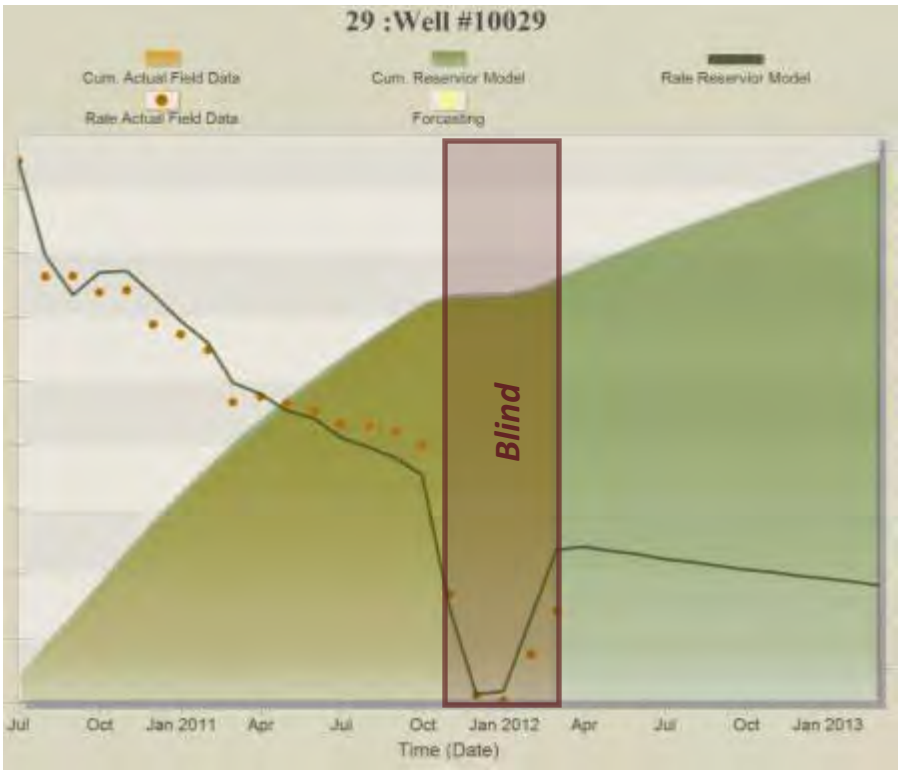

Figure B- 164: Prediction Results for Well#10029

Figure B- 165: Prediction Results for Well#10030

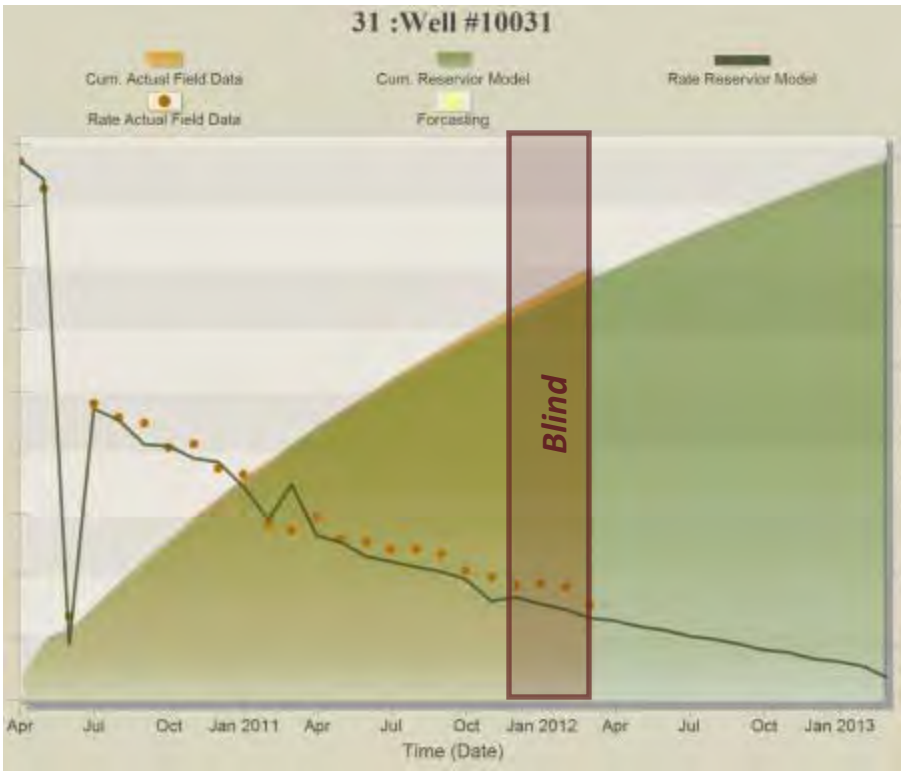

Figure B- 166: Prediction Results for Well#10031

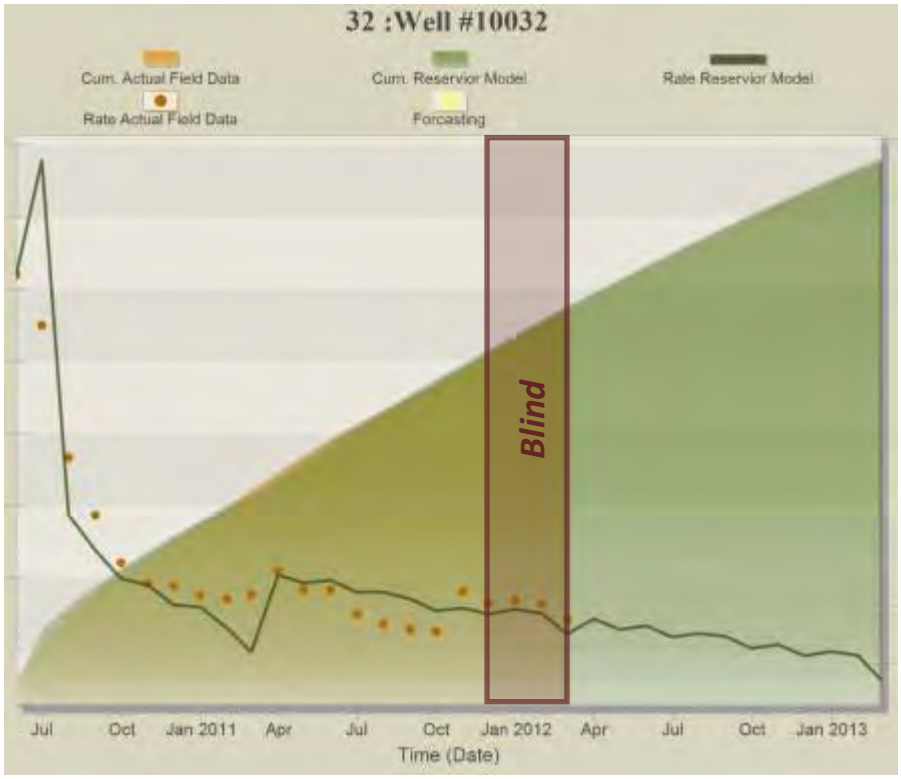

Figure B- 167: Prediction Results for Well#10032

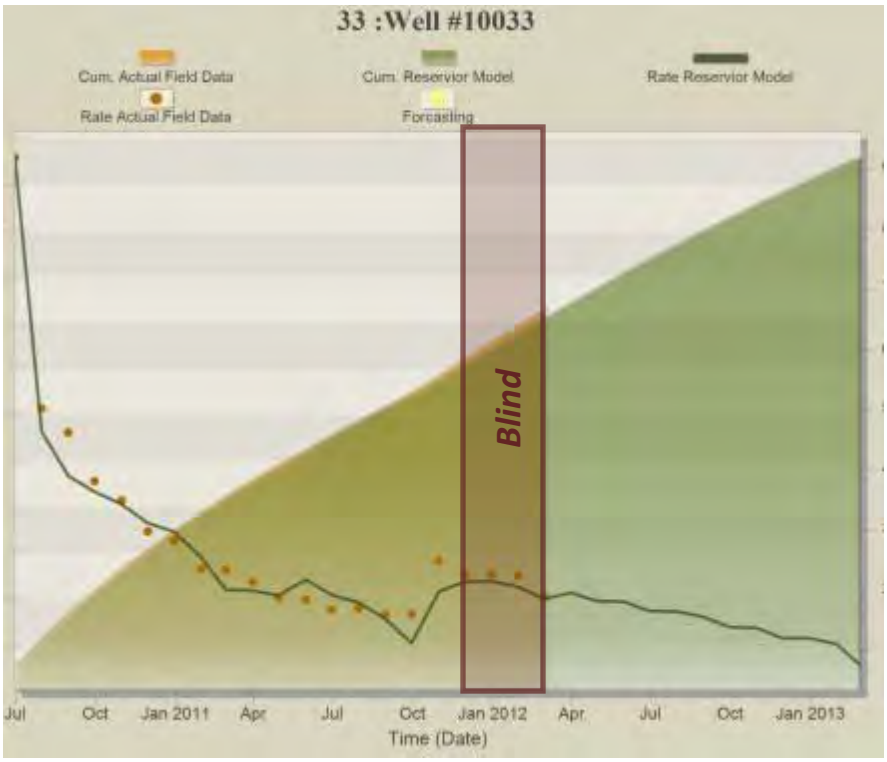

Figure B- 168: Prediction Results for Well#10033

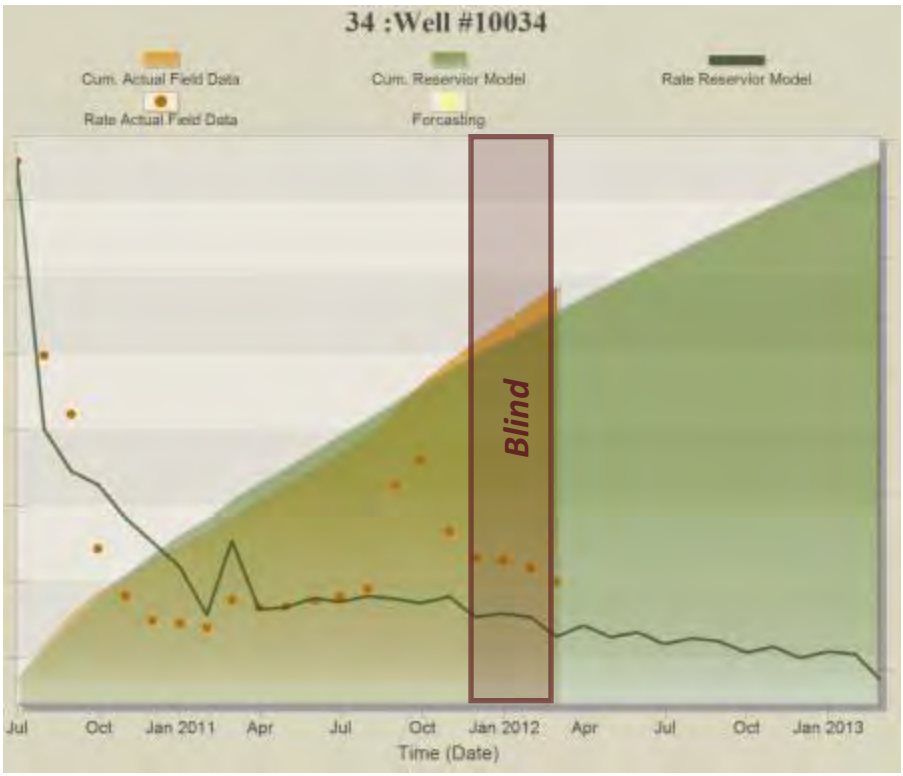

Figure B- 169: Prediction Results for Well#10034

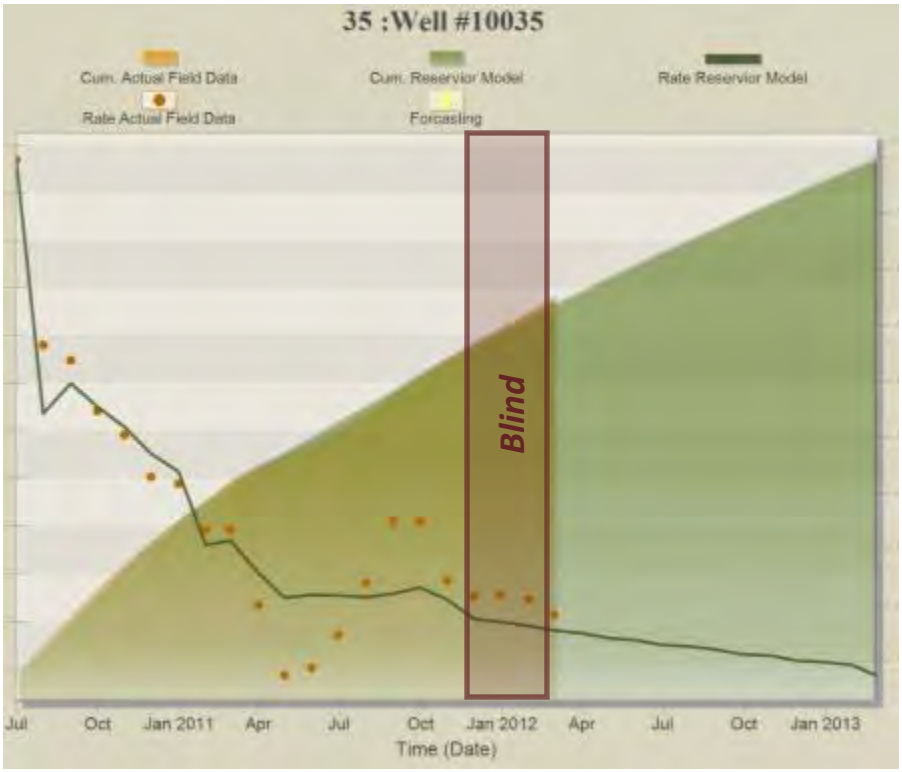

Figure B- 170: Prediction Results for Well#10035

Figure B- 171: Prediction Results for Well#10036

Figure B- 172: Prediction Results for Well#10037

Figure B- 173: Prediction Results for Well#10038

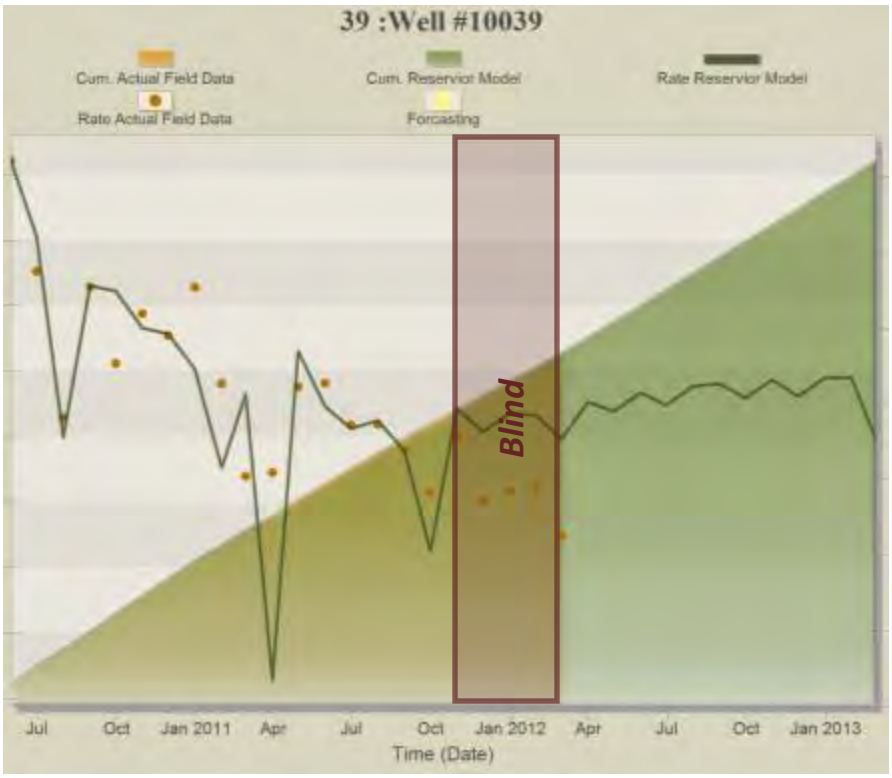

Figure B- 174: Prediction Results for Well#10039

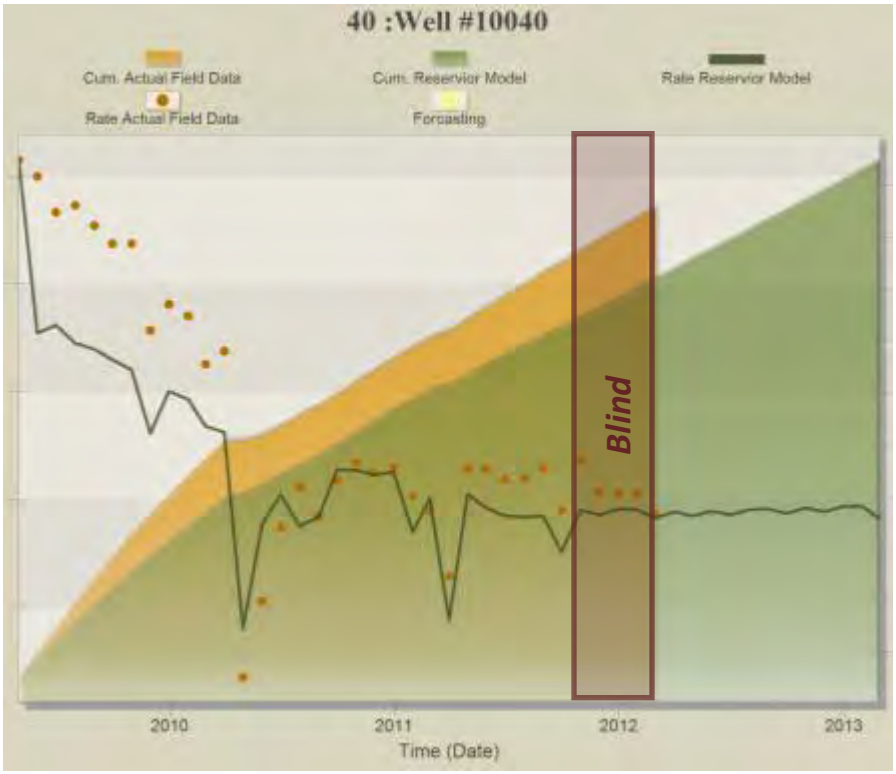

Figure B- 175: Prediction Results for Well#10040

Figure B- 176: Prediction Results for Well#10041

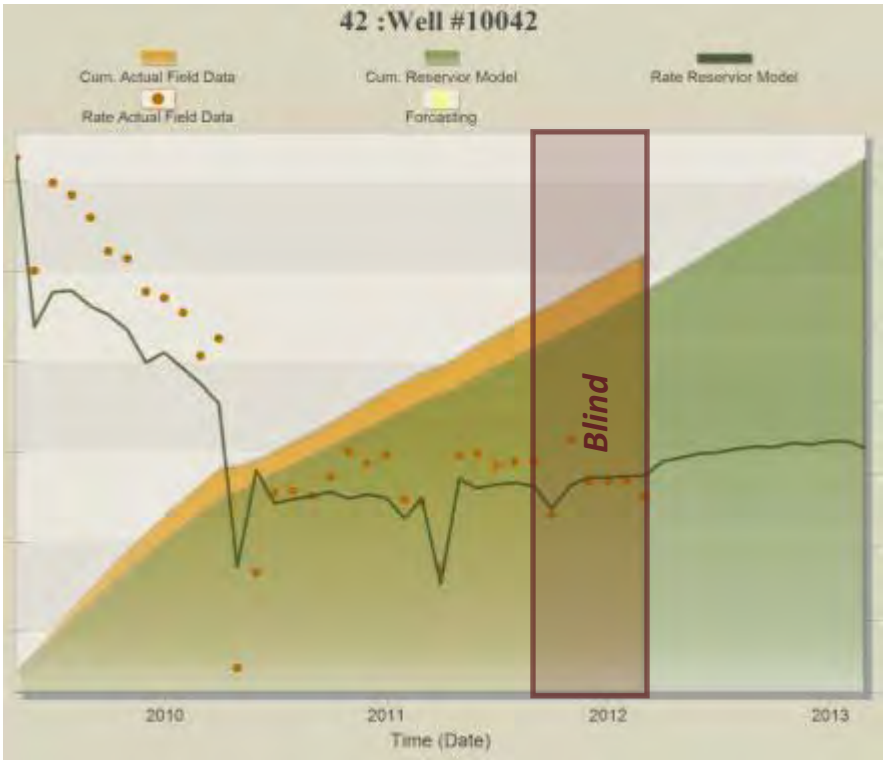

Figure B- 177: Prediction Results for Well#10042

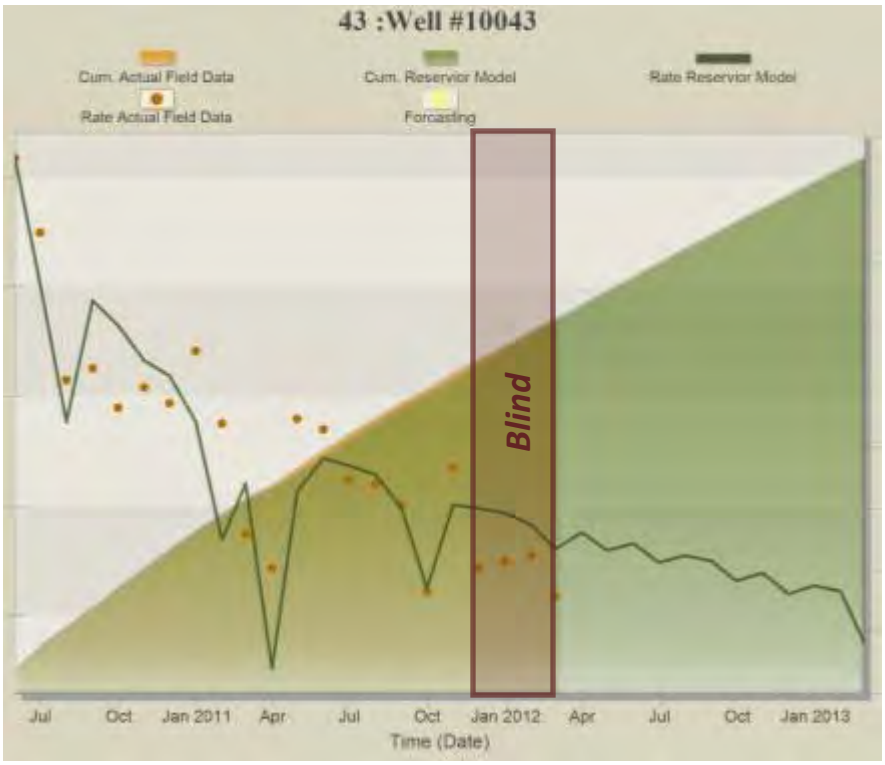

Figure B- 178: Prediction Results for Well#10043

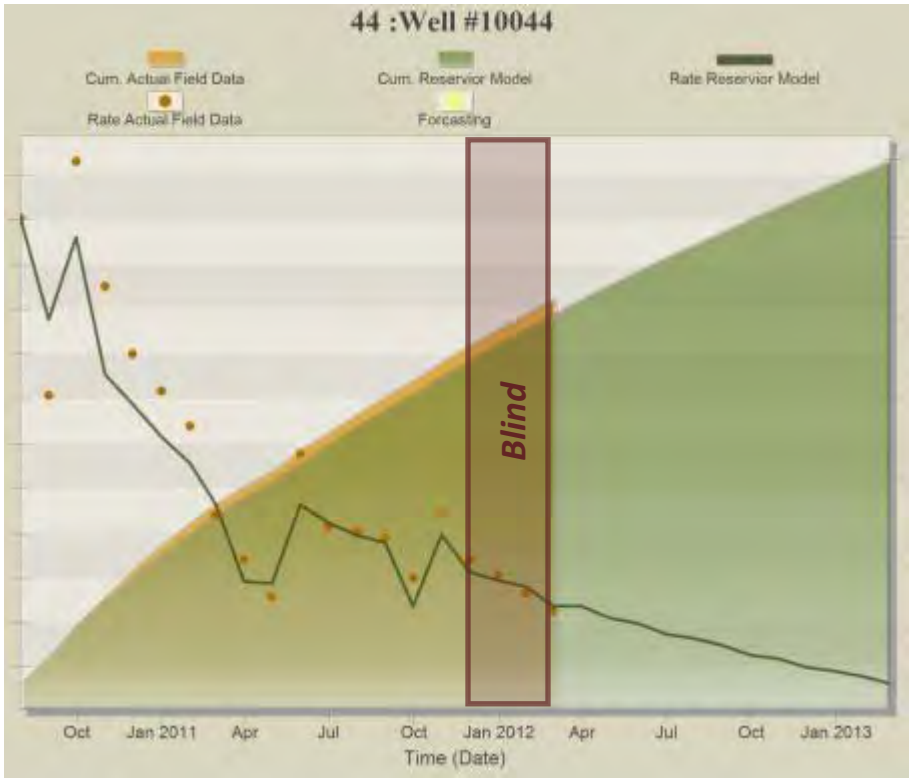

Figure B- 179: Prediction Results for Well#10044

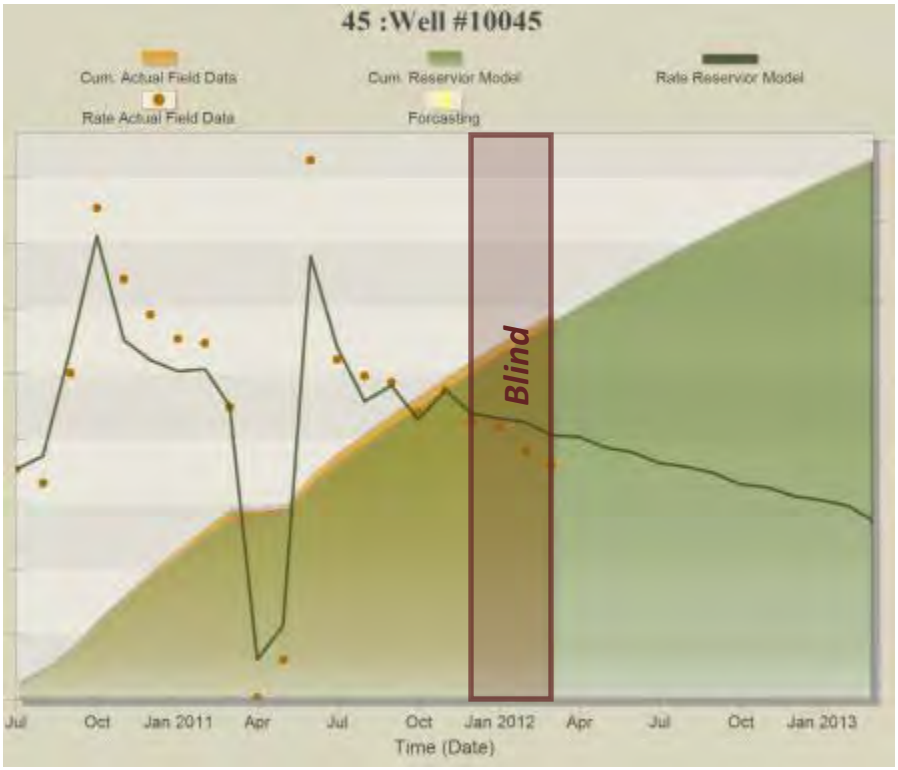

Figure B- 180: Prediction Results for Well#10045

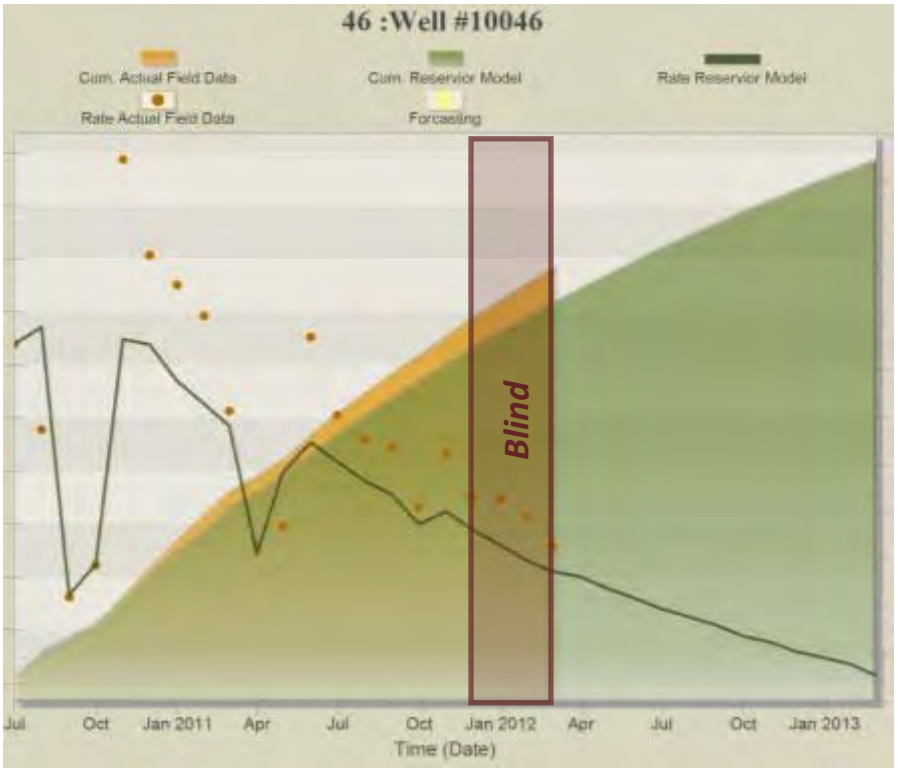

Figure B- 181: Prediction Results for Well#10046

Figure B- 182: Prediction Results for Well#10047

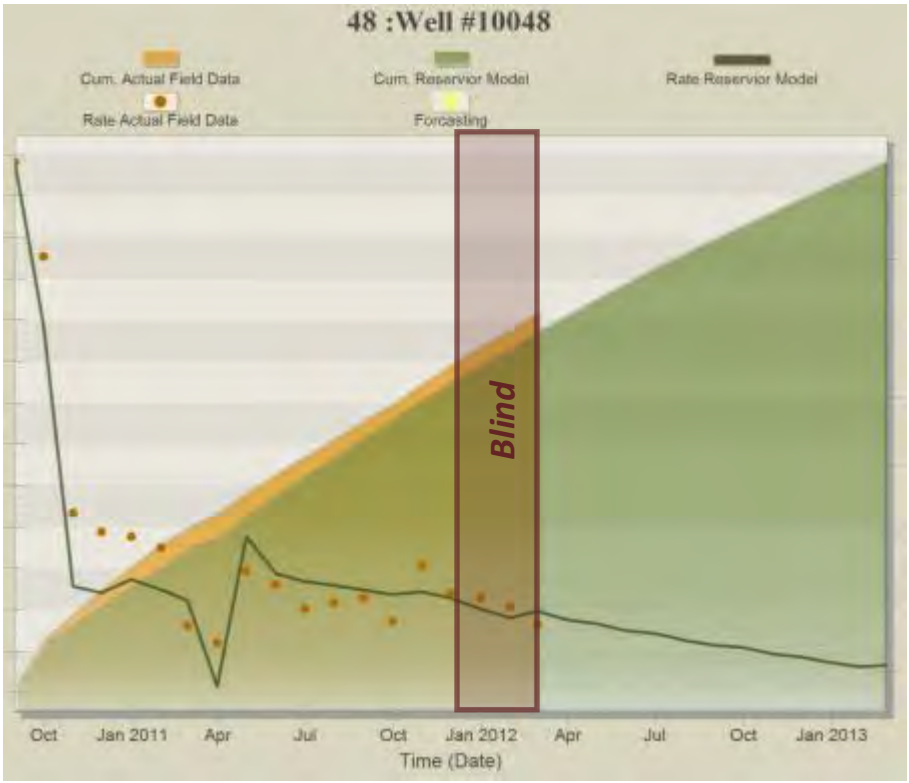

Figure B- 183: Prediction Results for Well#10048

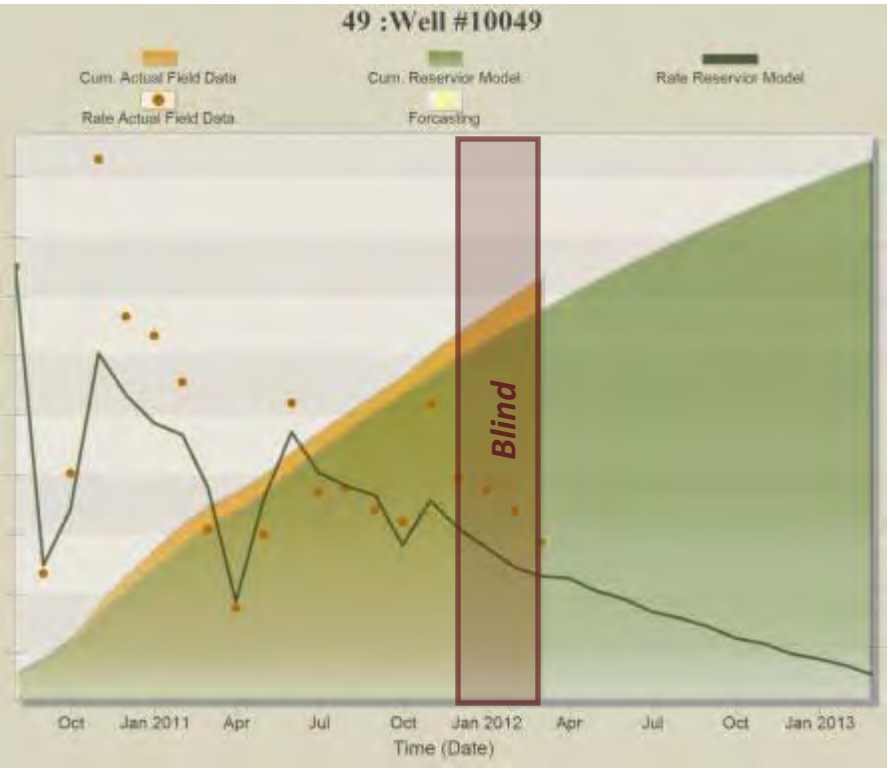

Figure B- 184: Prediction Results for Well#10049

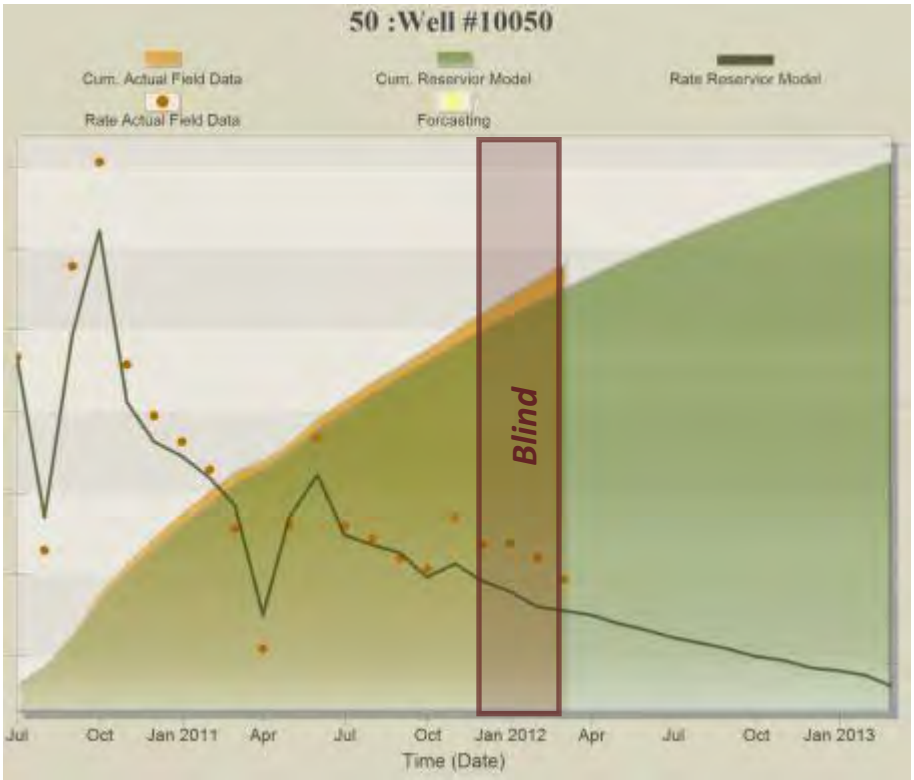

Figure B- 185: Prediction Results for Well#10050

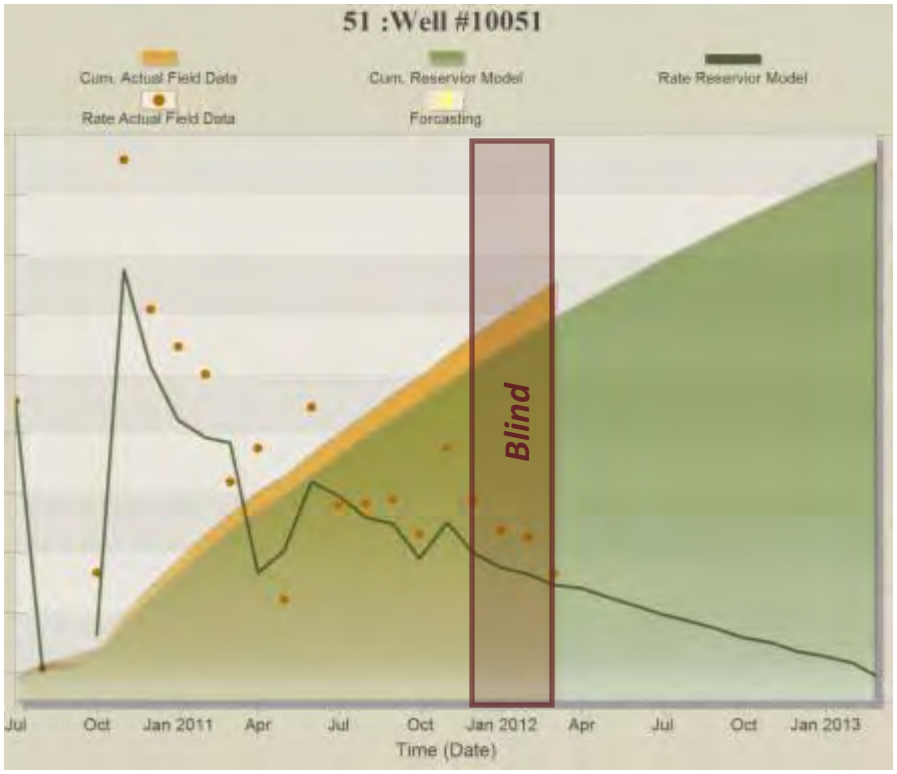

Figure B- 186: Prediction Results for Well#10051

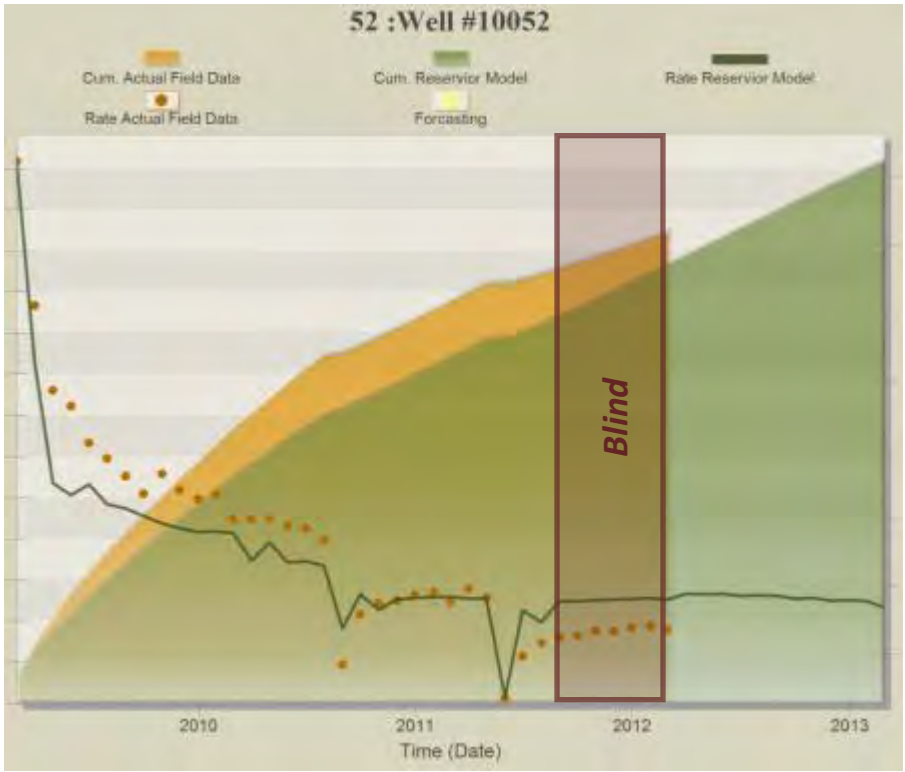

Figure B- 187: Prediction Results for Well#10052

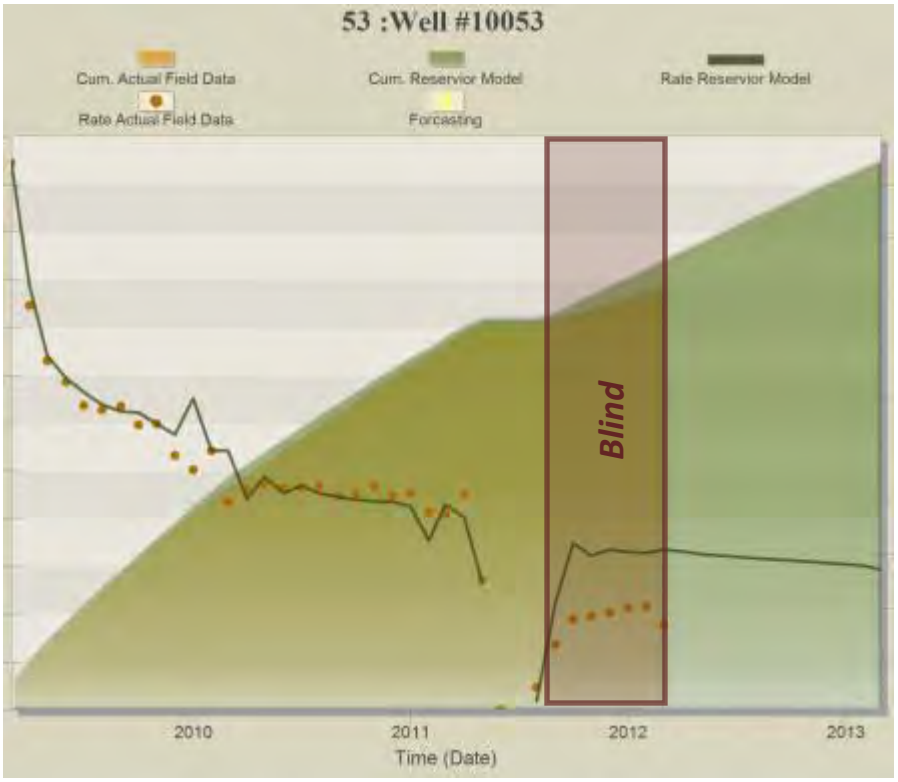

Figure B- 188: Prediction Results for Well#10053

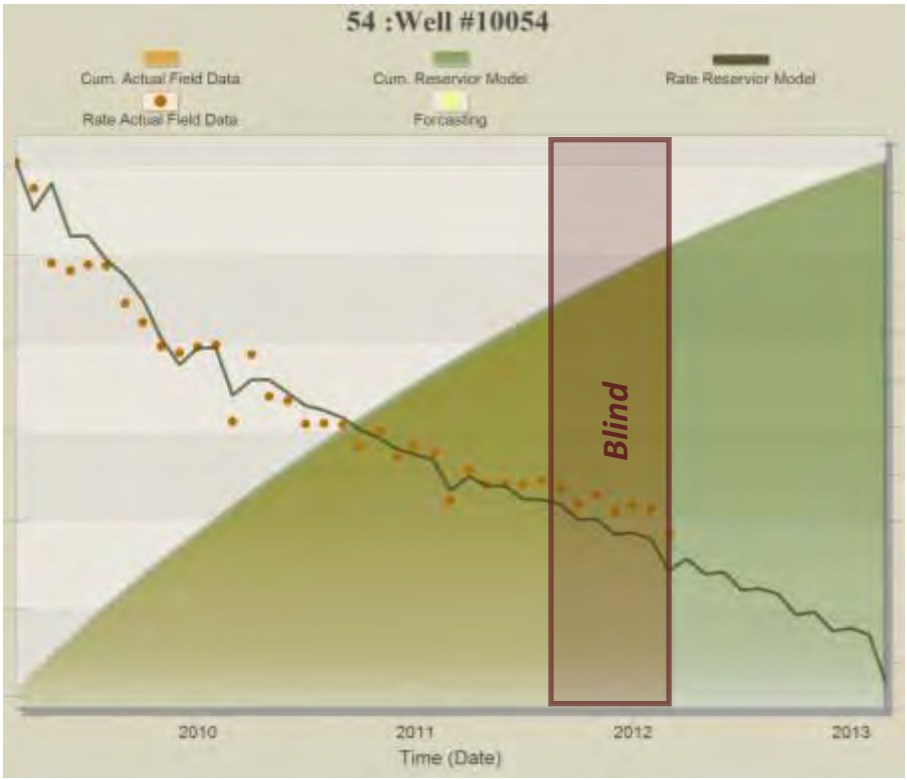

Figure B- 189: Prediction Results for Well#10054

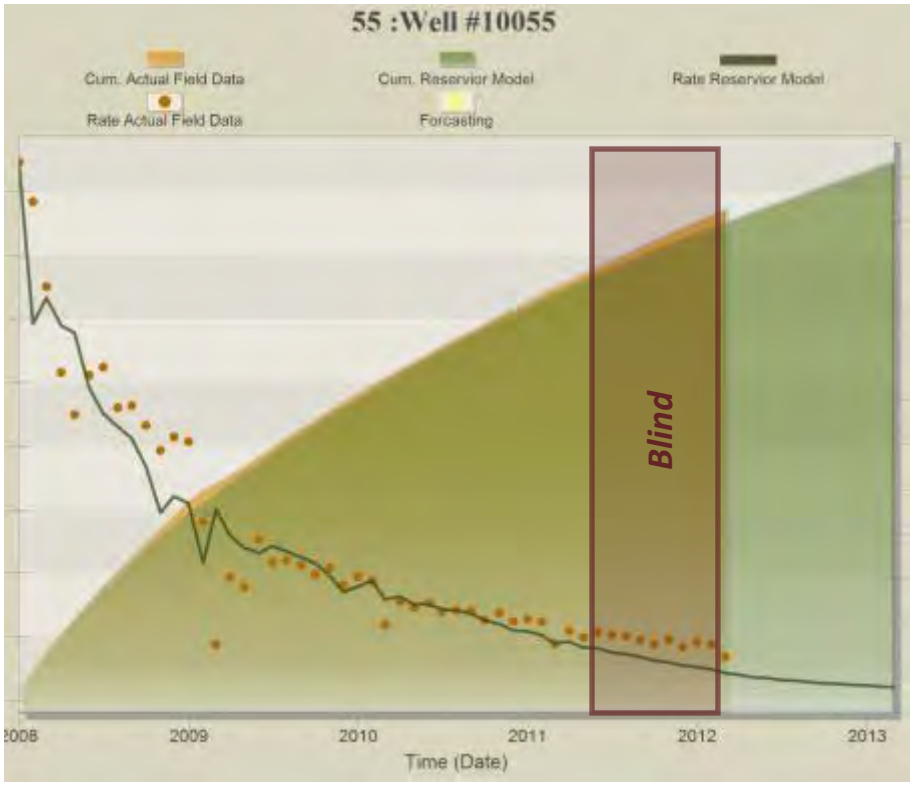

Figure B- 190: Prediction Results for Well#10055

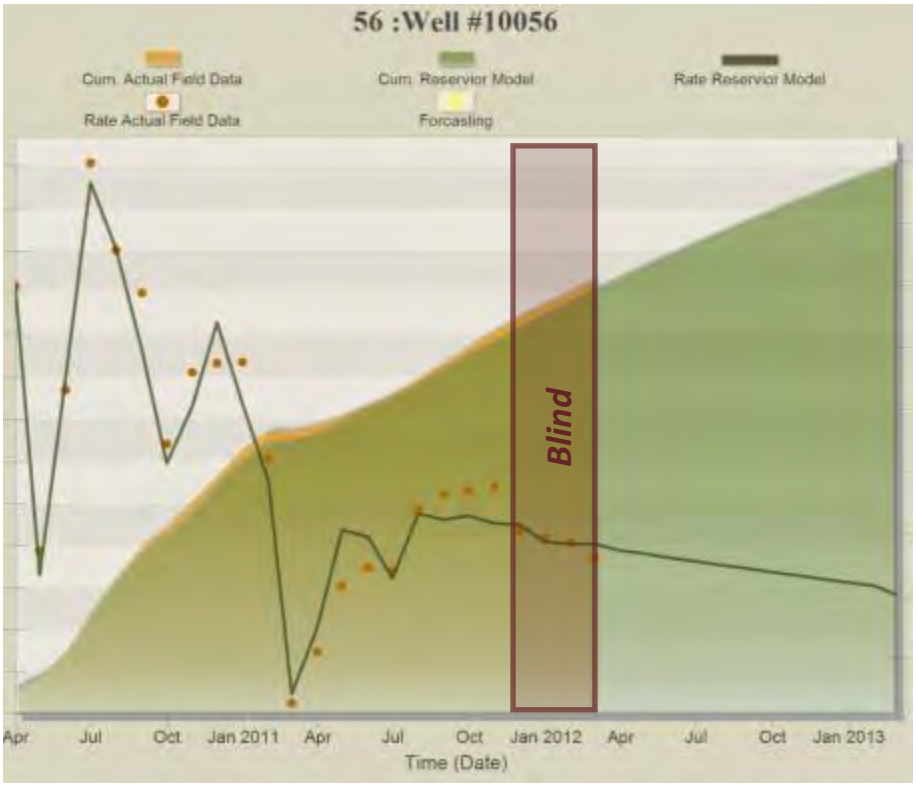

Figure B- 191: Prediction Results for Well#10056

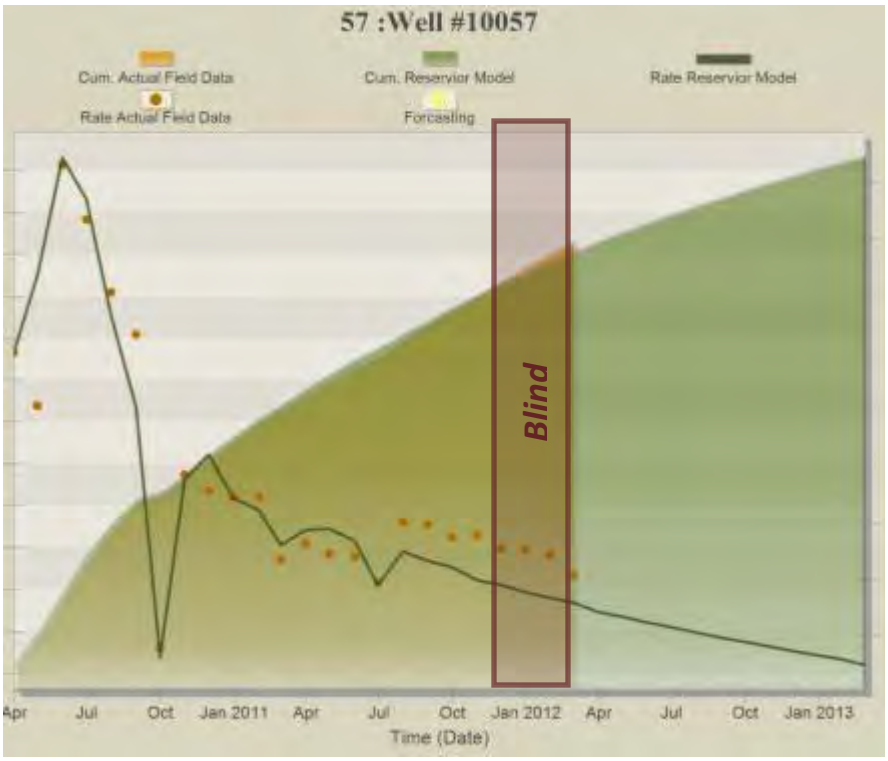

Figure B- 192: Prediction Results for Well#10057

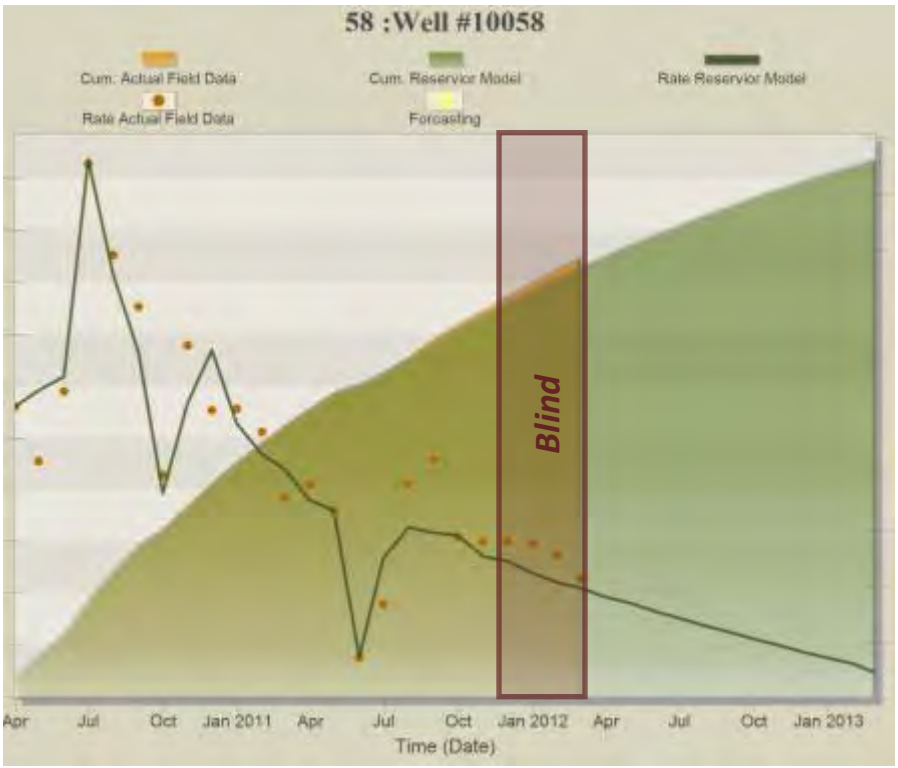

Figure B- 193: Prediction Results for Well#10058

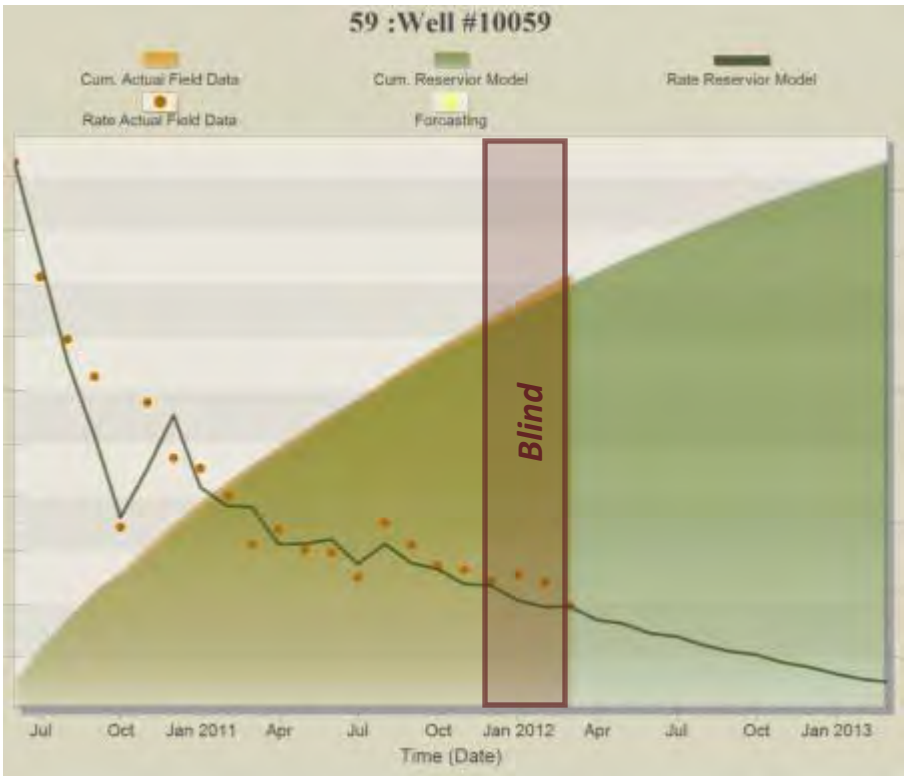

Figure B- 194: Prediction Results for Well#10059

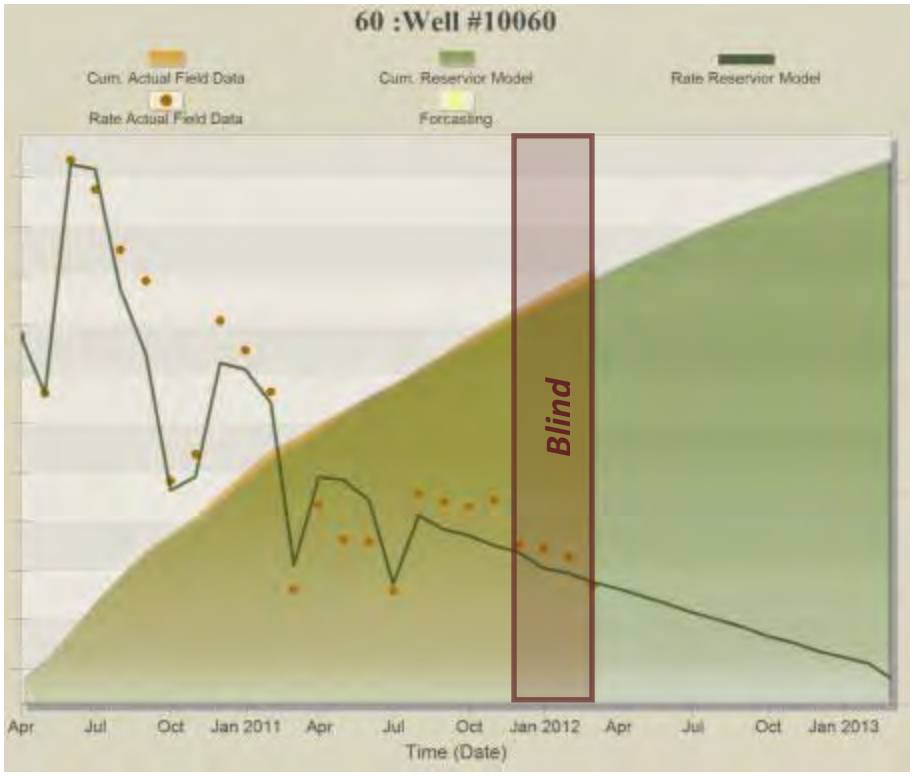

Figure B- 195: Prediction Results for Well#10060

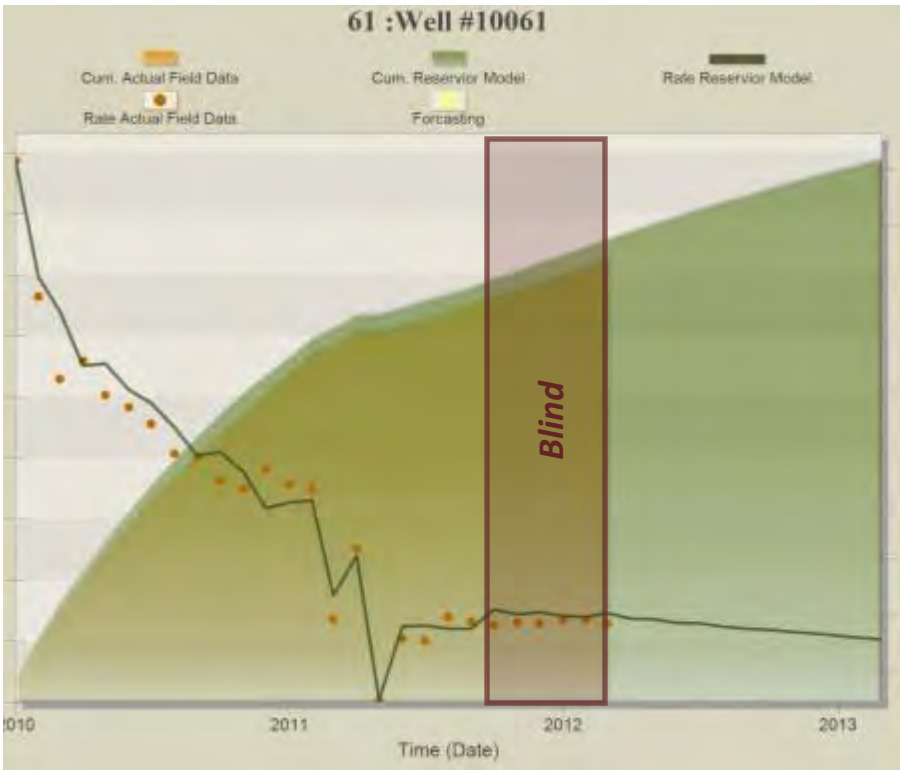

Figure B- 196: Prediction Results for Well#10061

Figure B- 197: Prediction Results for Well#10062

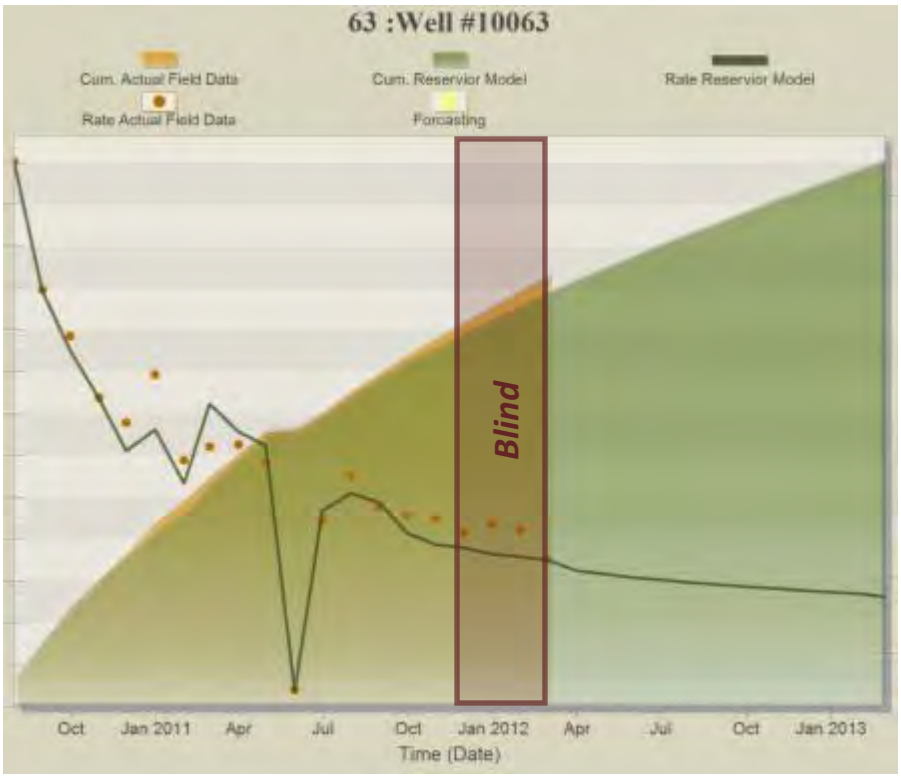

Figure B- 198: Prediction Results for Well#10063

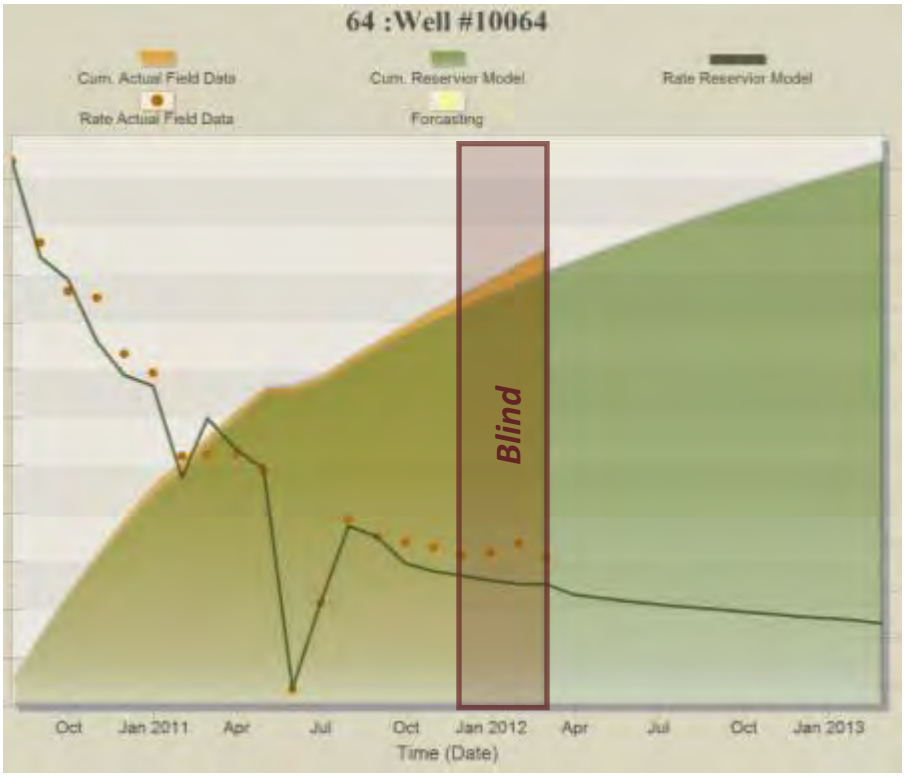

Figure B- 199: Prediction Results for Well#10064

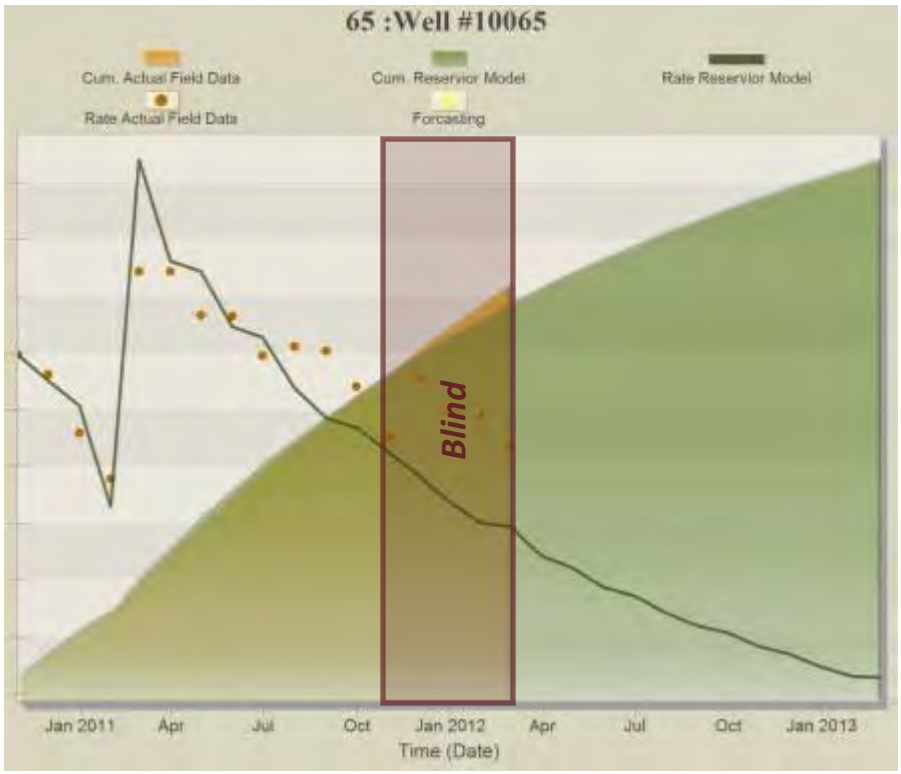

Figure B- 200: Prediction Results for Well#10065

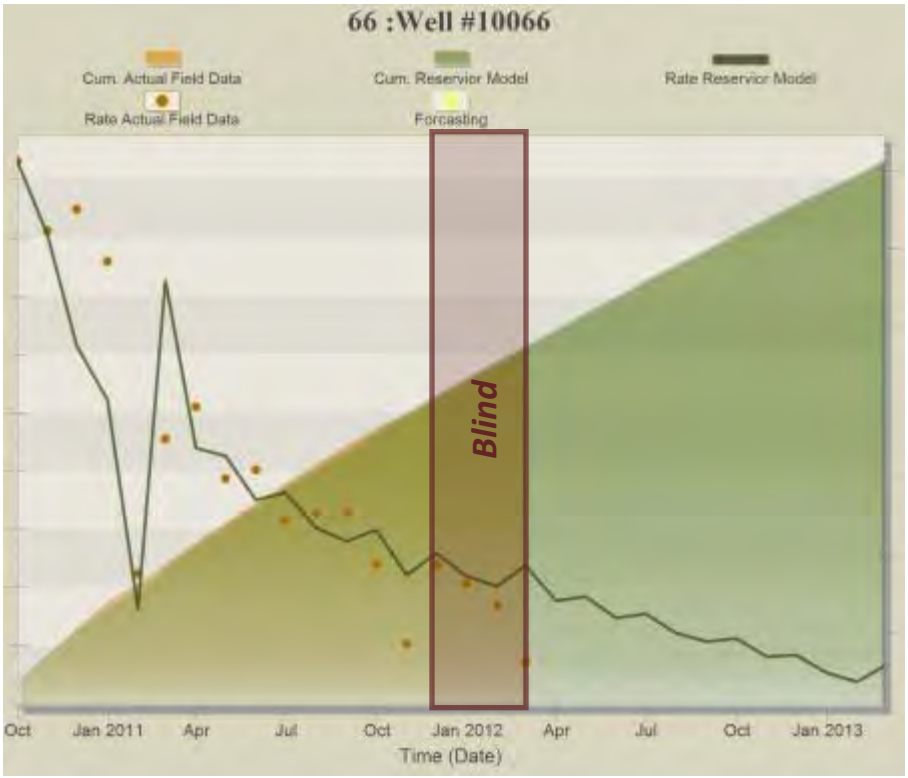

Figure B- 201: Prediction Results for Well#10066

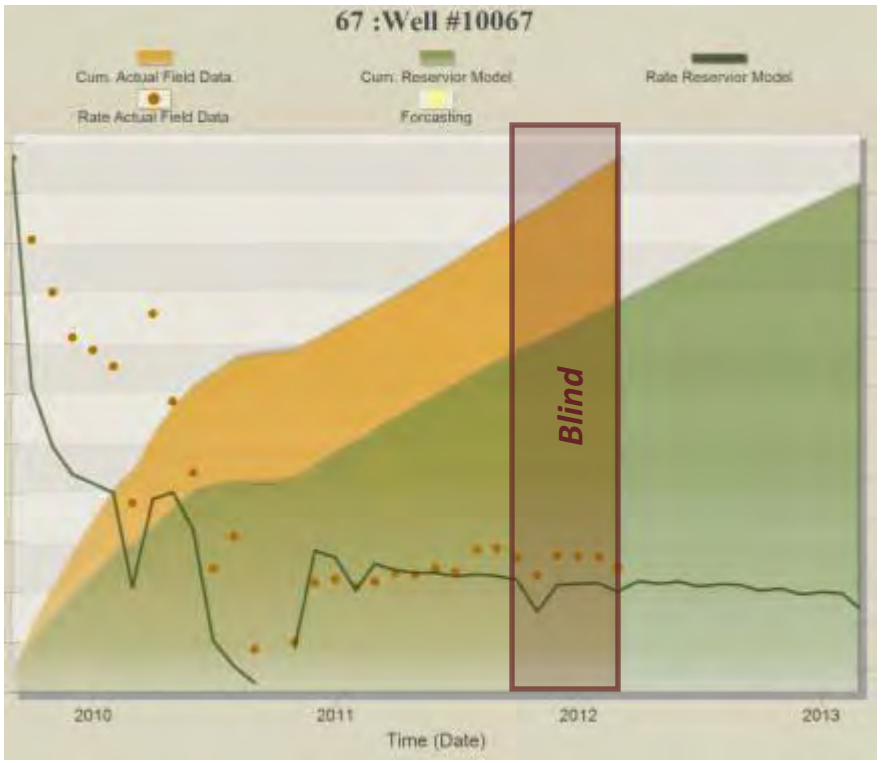

Figure B- 202: Prediction Results for Well#10067

Figure B- 203: Prediction Results for Well#10068

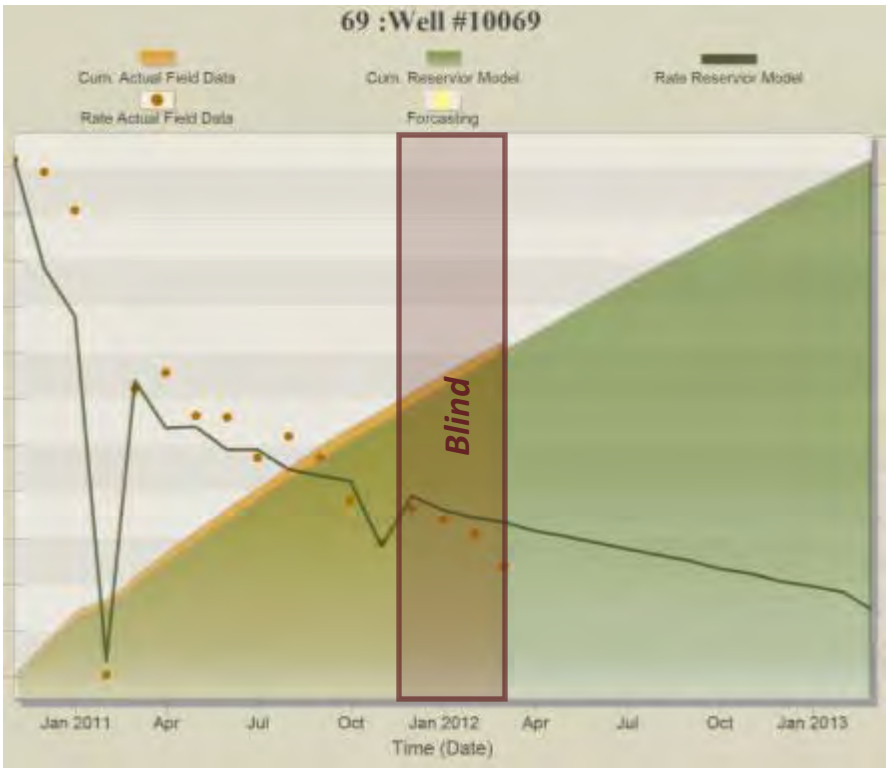

Figure B- 204: Prediction Results for Well#10069

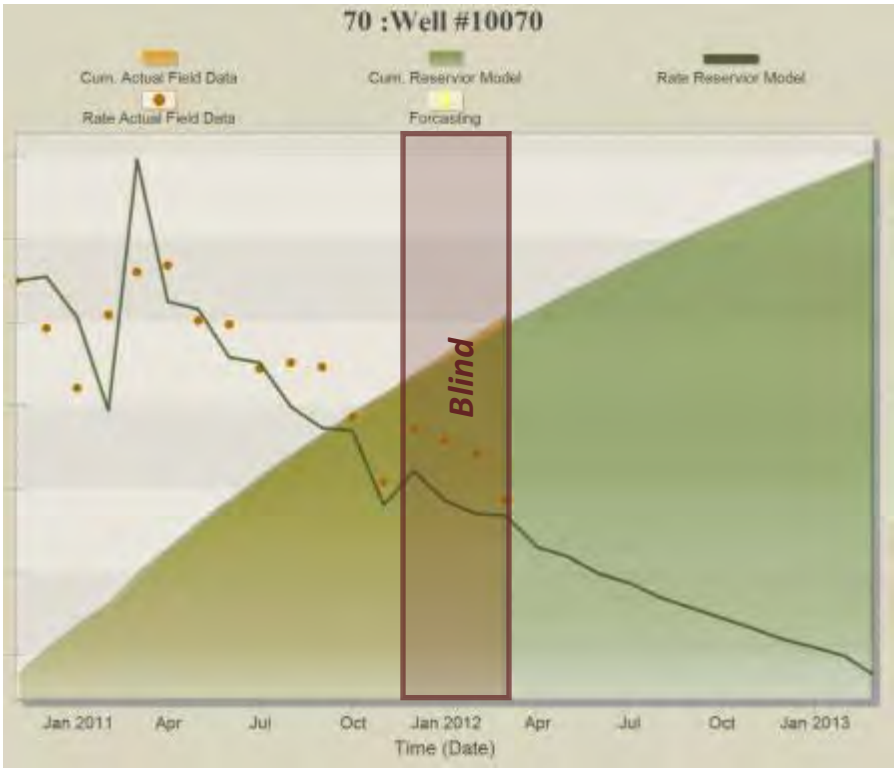

Figure B- 205: Prediction Results for Well#10070

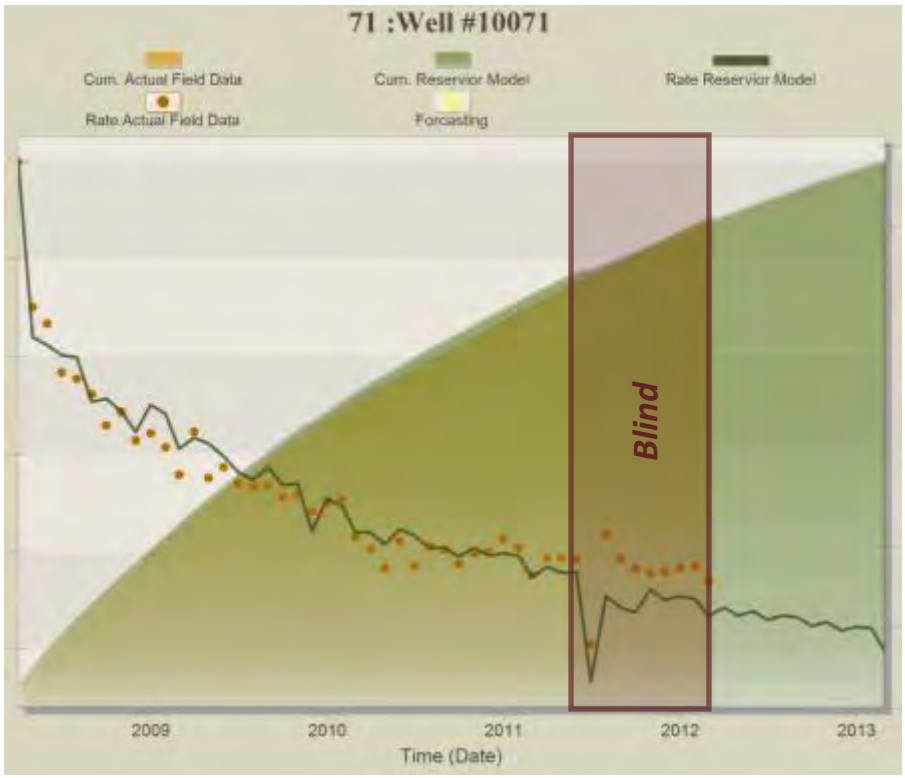

Figure B- 206: Prediction Results for Well#10071

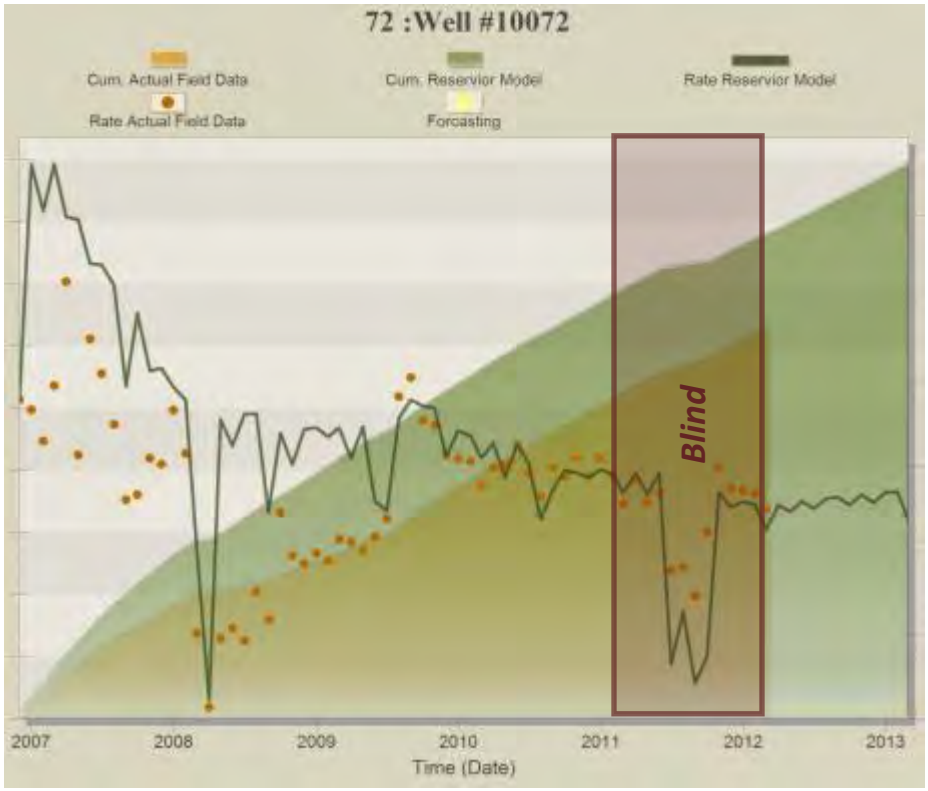

Figure B- 207: Prediction Results for Well#10072

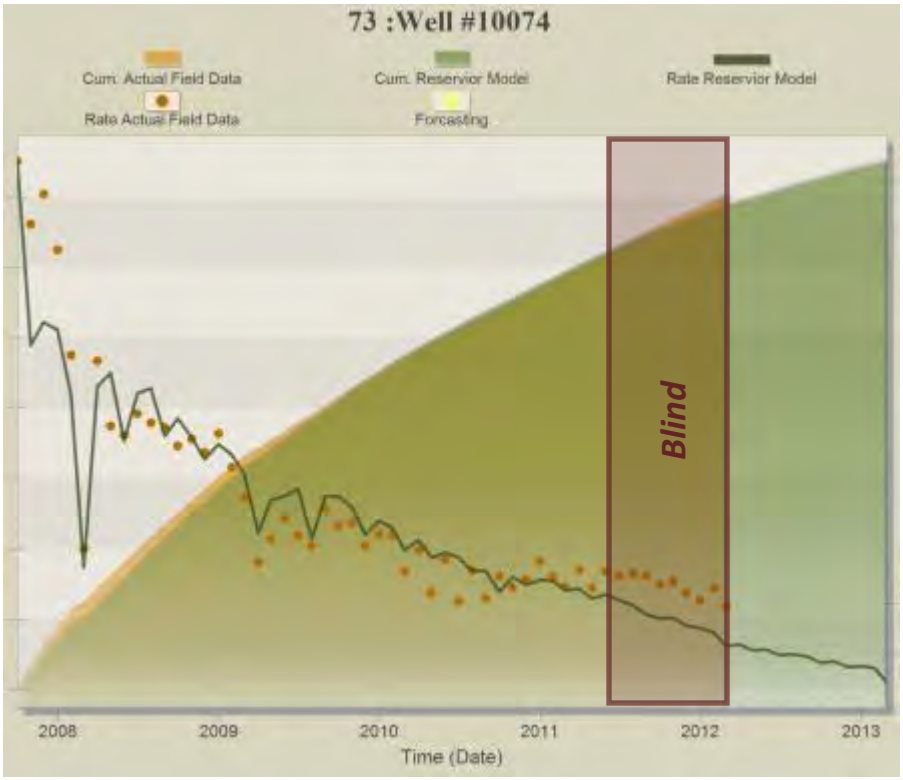

Figure B- 208: Prediction Results for Well#10074

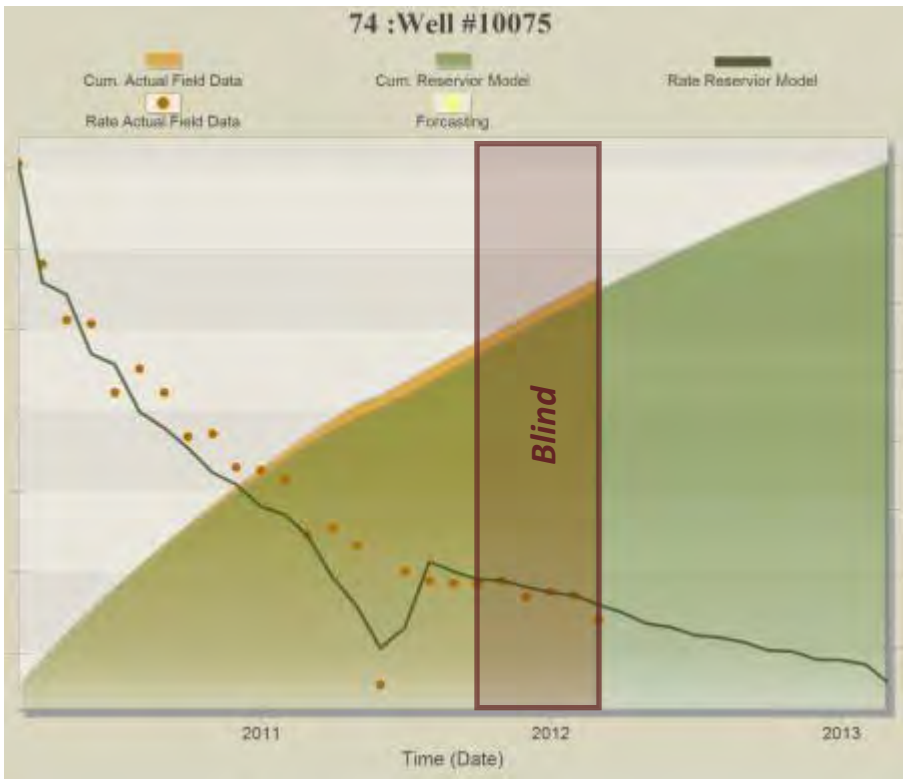

Figure B- 209: Prediction Results for Well#10075

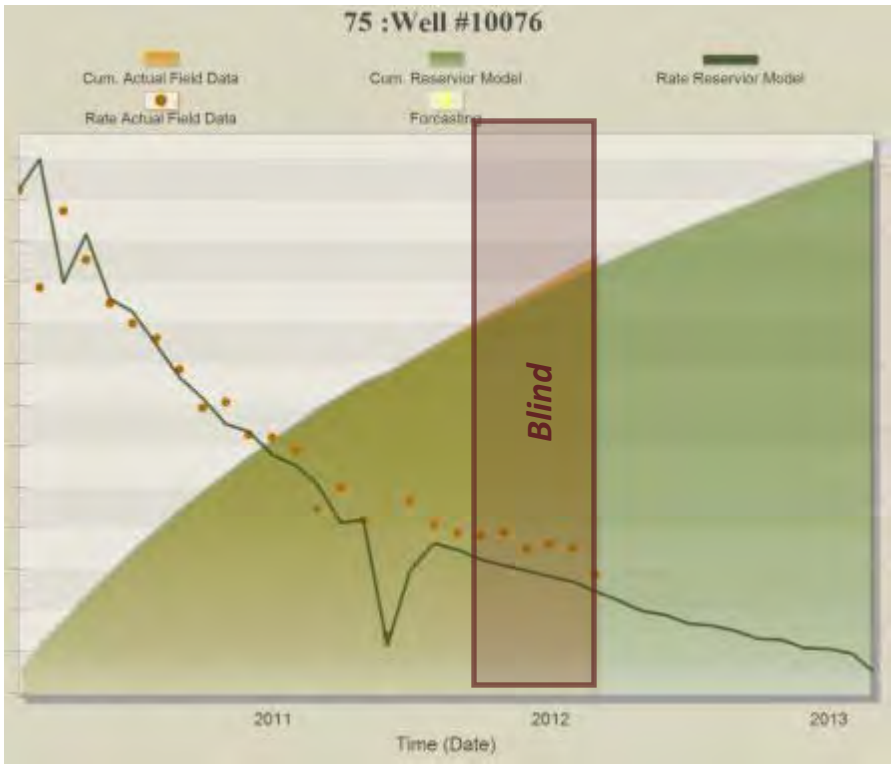

Figure B- 210: Prediction Results for Well#10076

Figure B- 211: Prediction Results for Well#10077

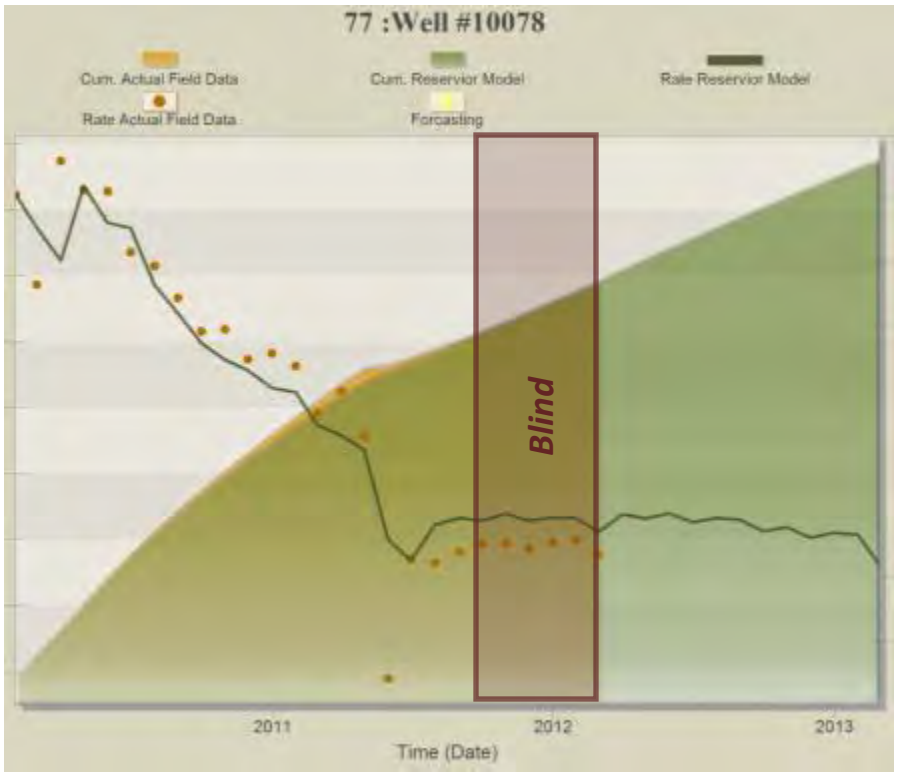

Figure B- 212: Prediction Results for Well#10078

Figure B- 213: Prediction Results for Well#10079

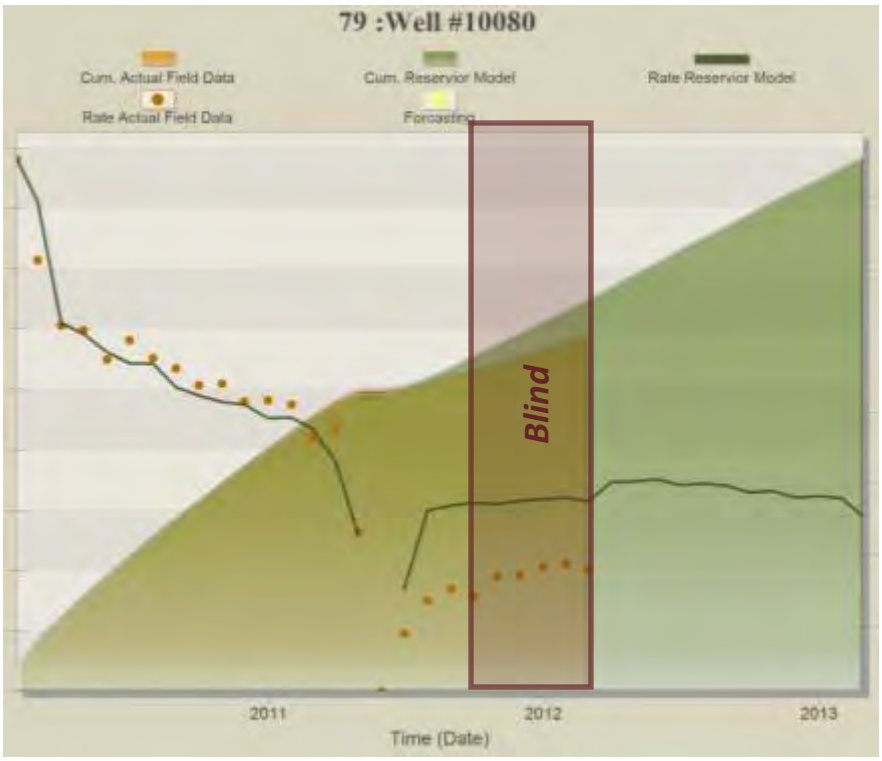

Figure B- 214: Prediction Results for Well#10080

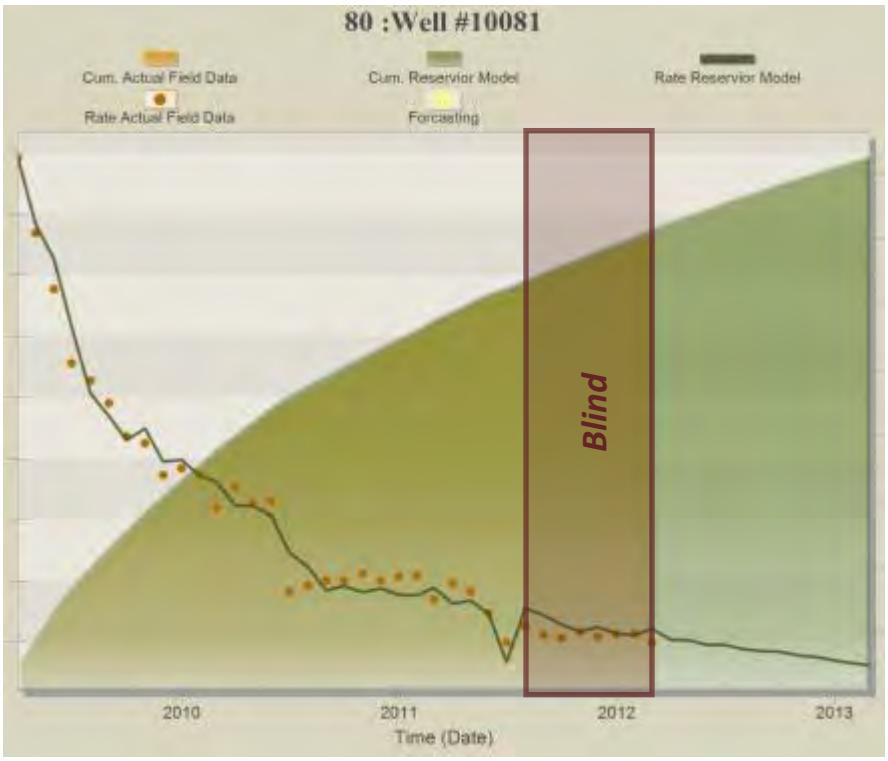

Figure B- 215: Prediction Results for Well#10081

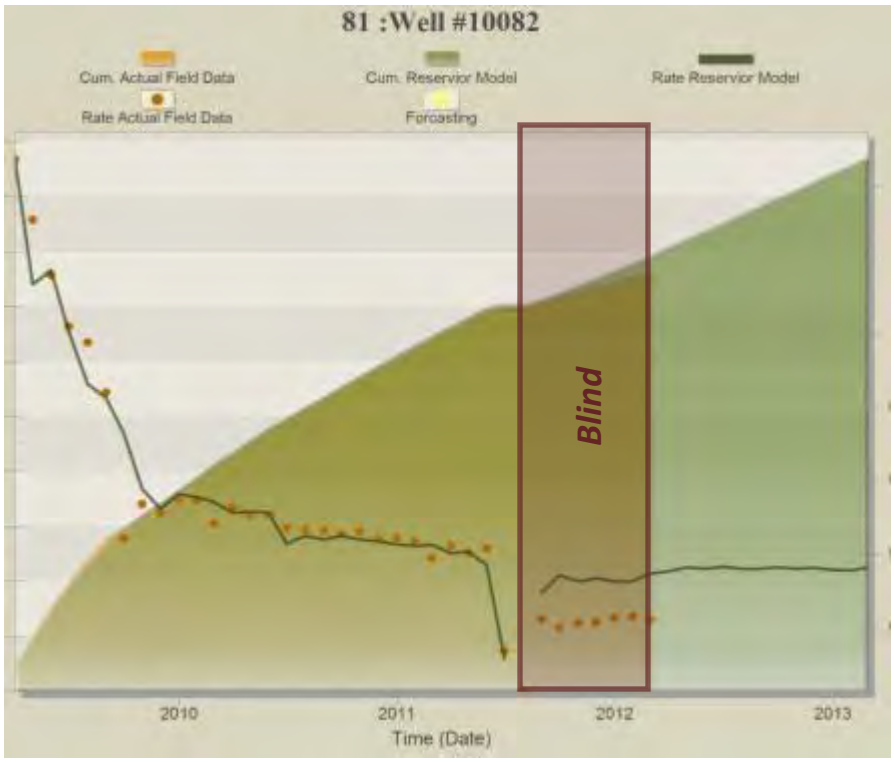

Figure B- 216: Prediction Results for Well#10082

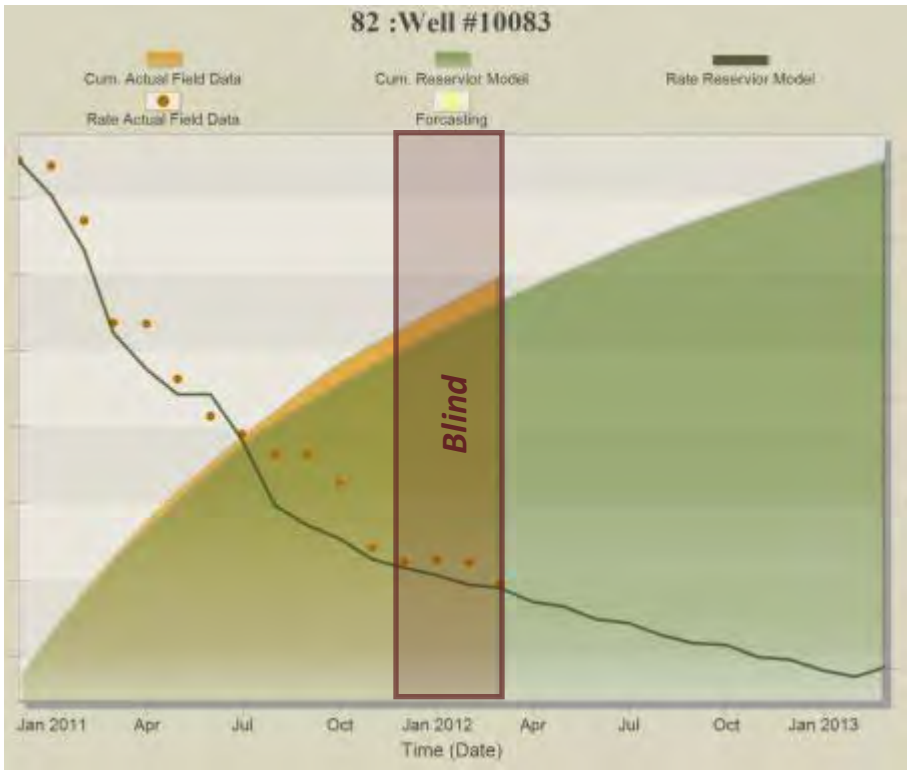

Figure B- 217: Prediction Results for Well#10083

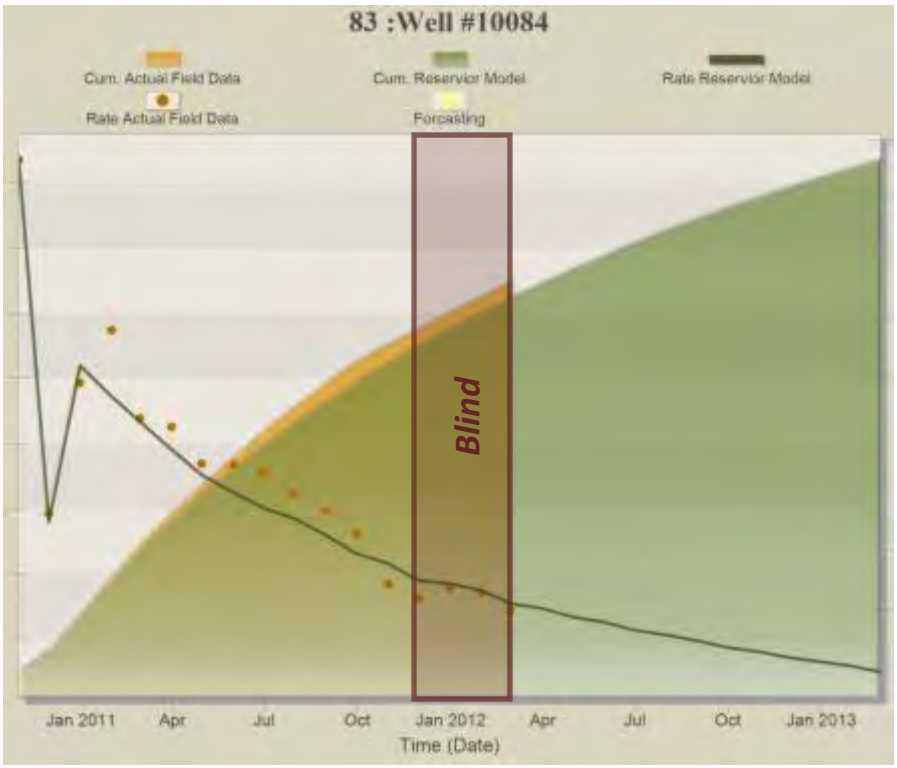

Figure B- 218: Prediction Results for Well#10084

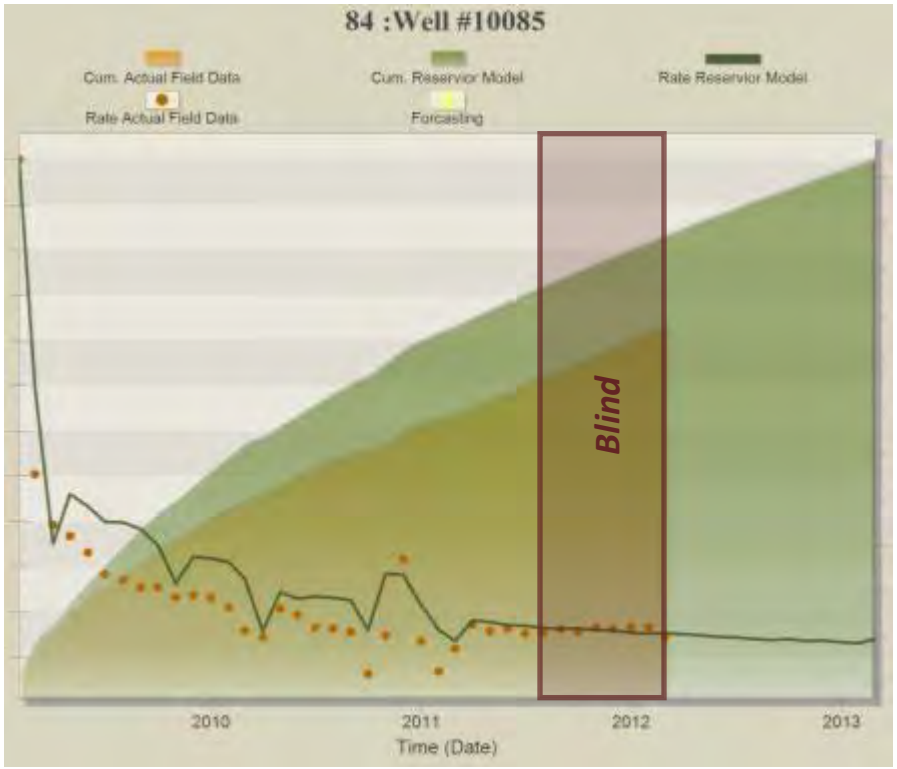

Figure B- 219: Prediction Results for Well#10085

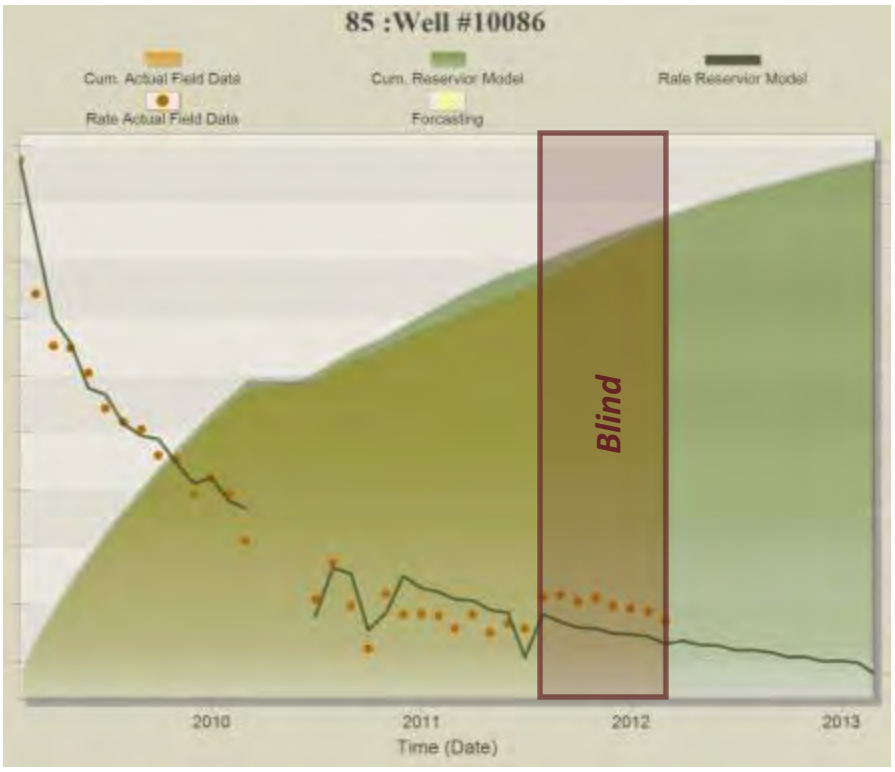

Figure B- 220: Prediction Results for Well#10086

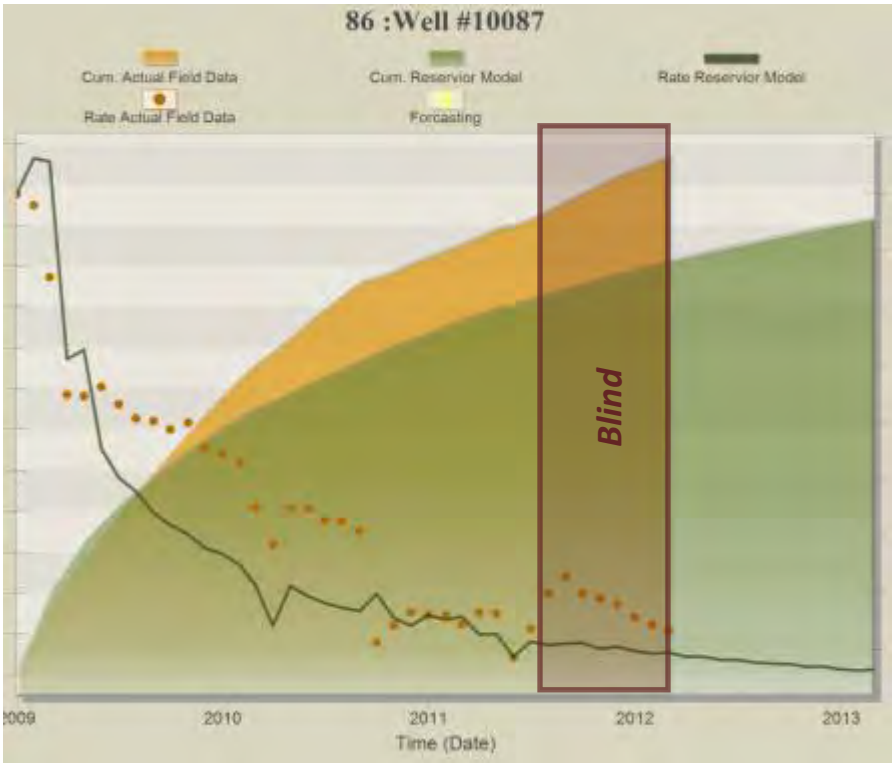

Figure B- 221: Prediction Results for Well#10087

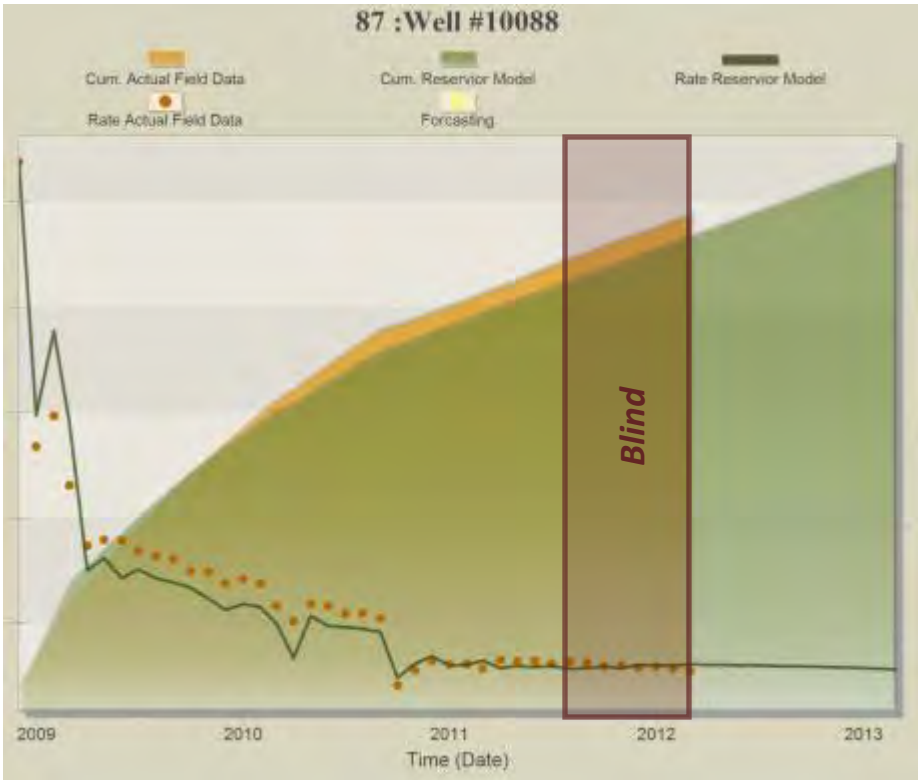

Figure B- 222: Prediction Results for Well#10088

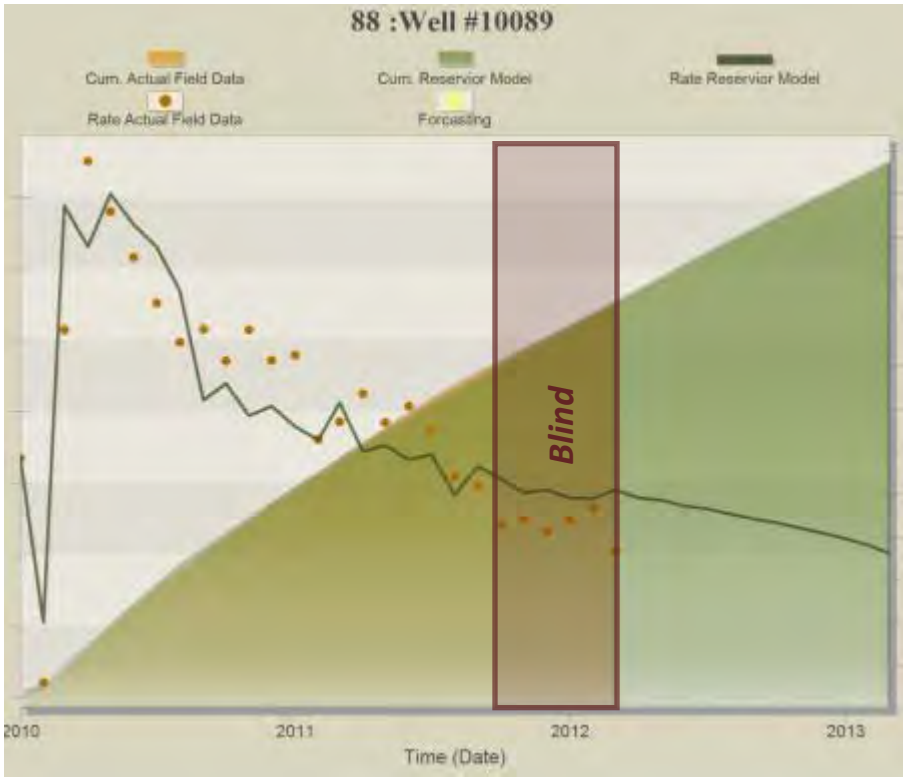

Figure B- 223: Prediction Results for Well#10089

Figure B- 224: Prediction Results for Well#10090

Figure B- 225: Prediction Results for Well#10091

Figure B- 226: Prediction Results for Well#10092

Figure B- 227: Prediction Results for Well#10093

Figure B- 228: Prediction Results for Well#10094

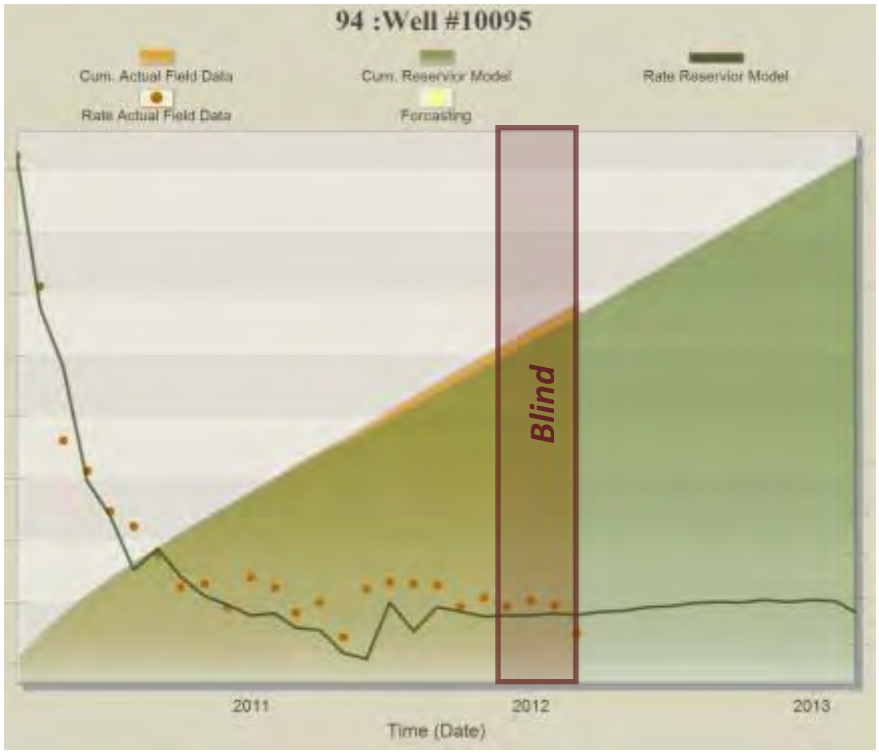

Figure B- 229: Prediction Results for Well#10095

Figure B- 230: Prediction Results for Well#10096

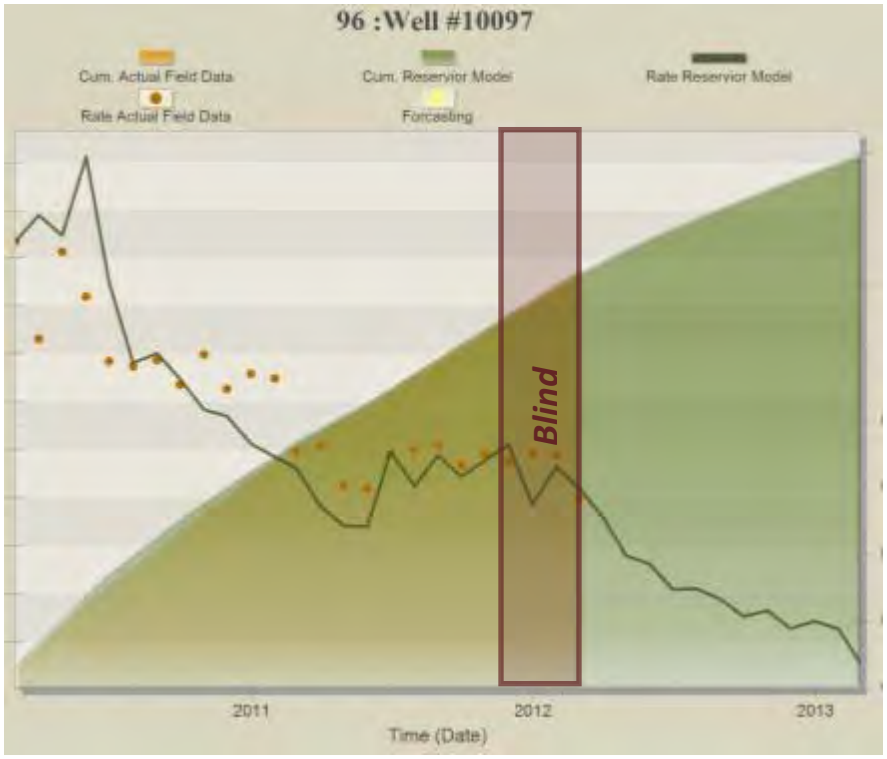

Figure B- 231: Prediction Results for Well#10097

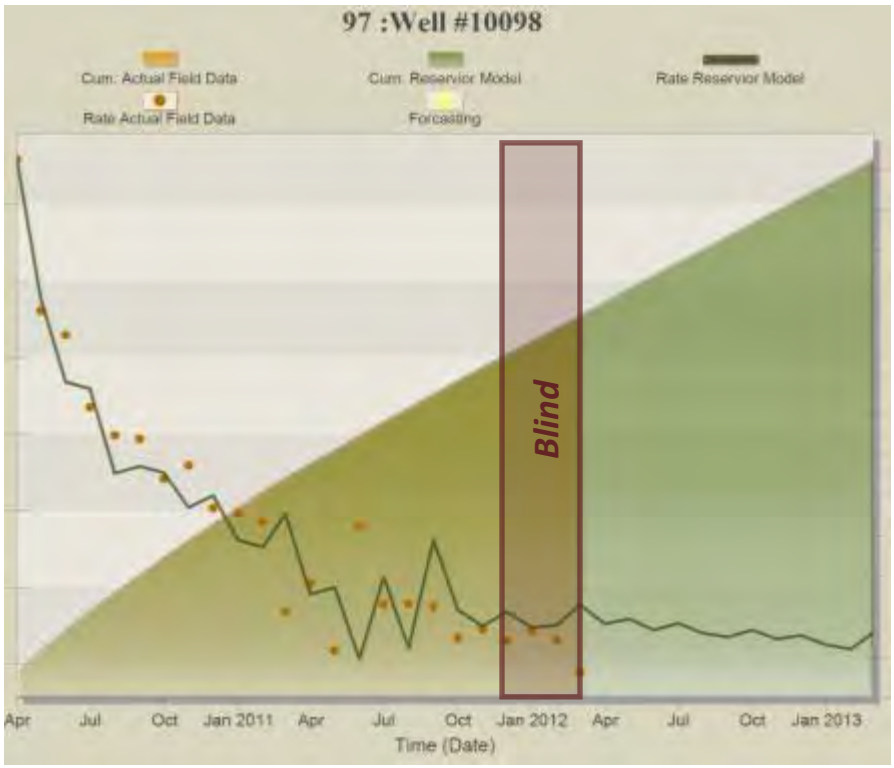

Figure B- 232: Prediction Results for Well#10098

Figure B- 233: Prediction Results for Well#10099

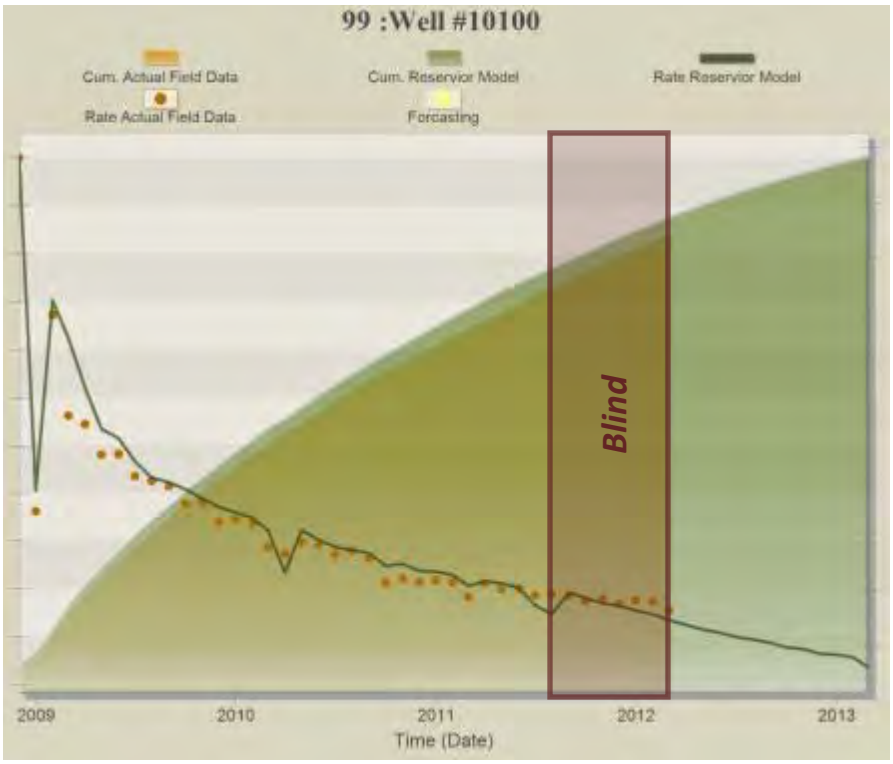

Figure B- 234: Prediction Results for Well#10100

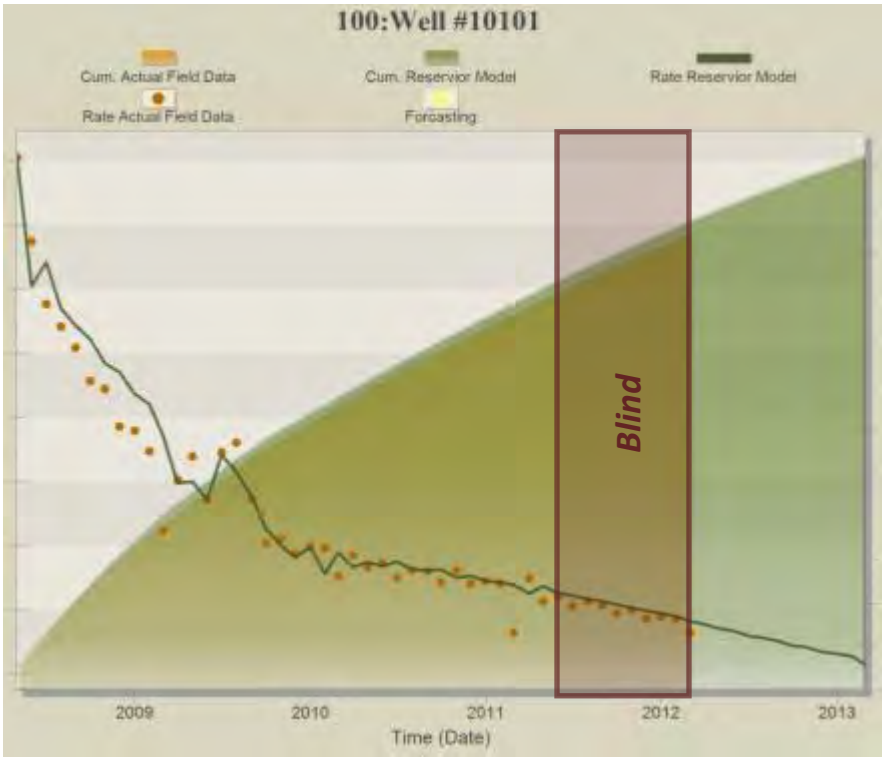

Figure B- 235: Prediction Results for Well#10101

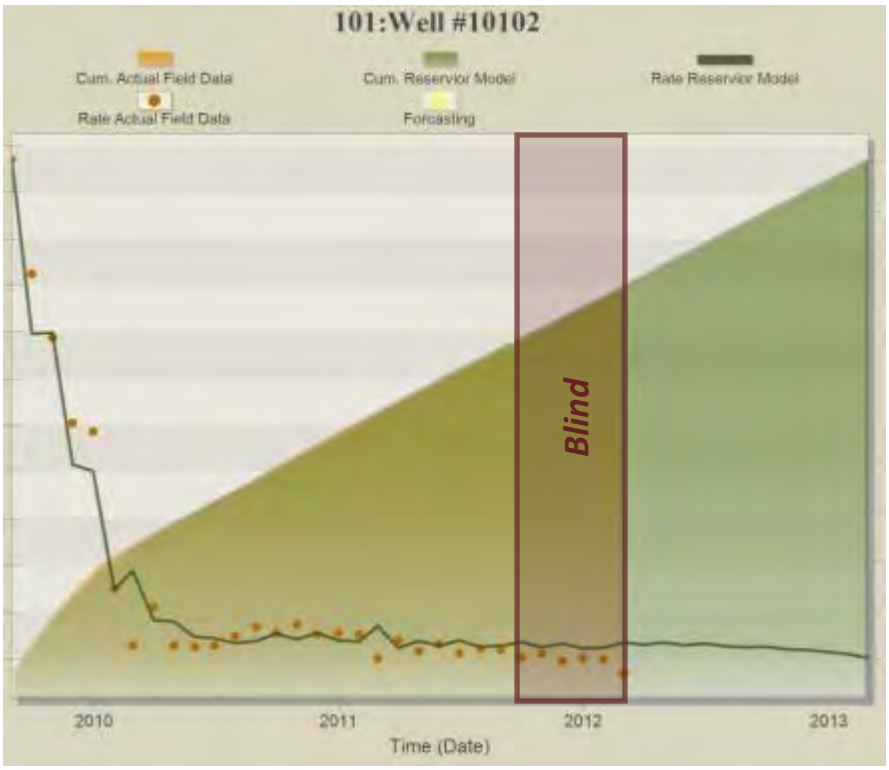

Figure B- 236: Prediction Results for Well#10102

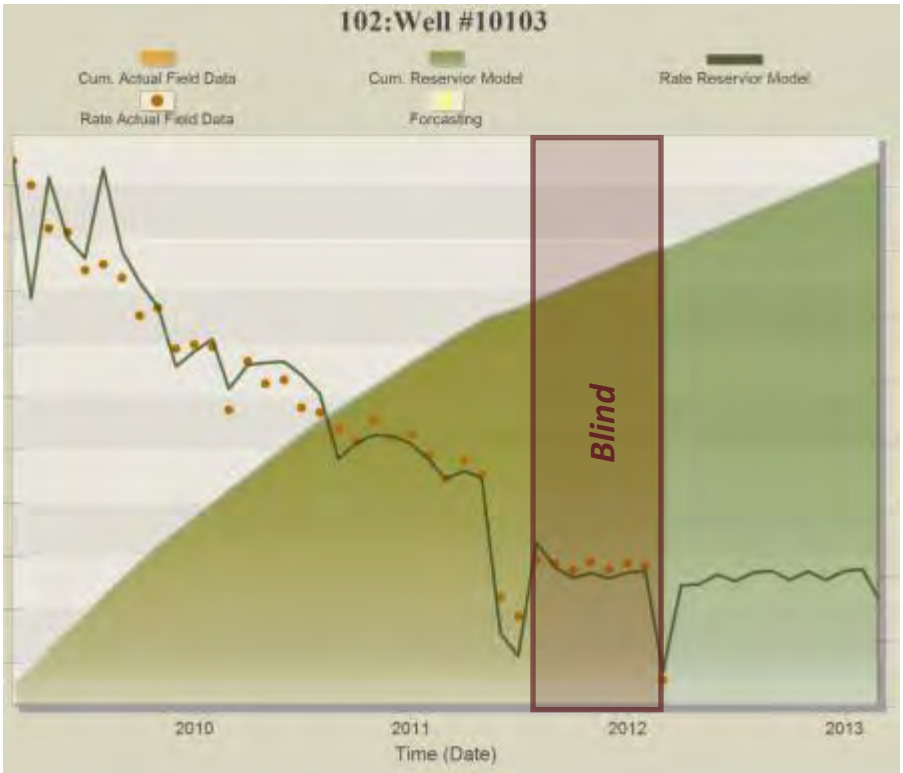

Figure B- 237: Prediction Results for Well#10103

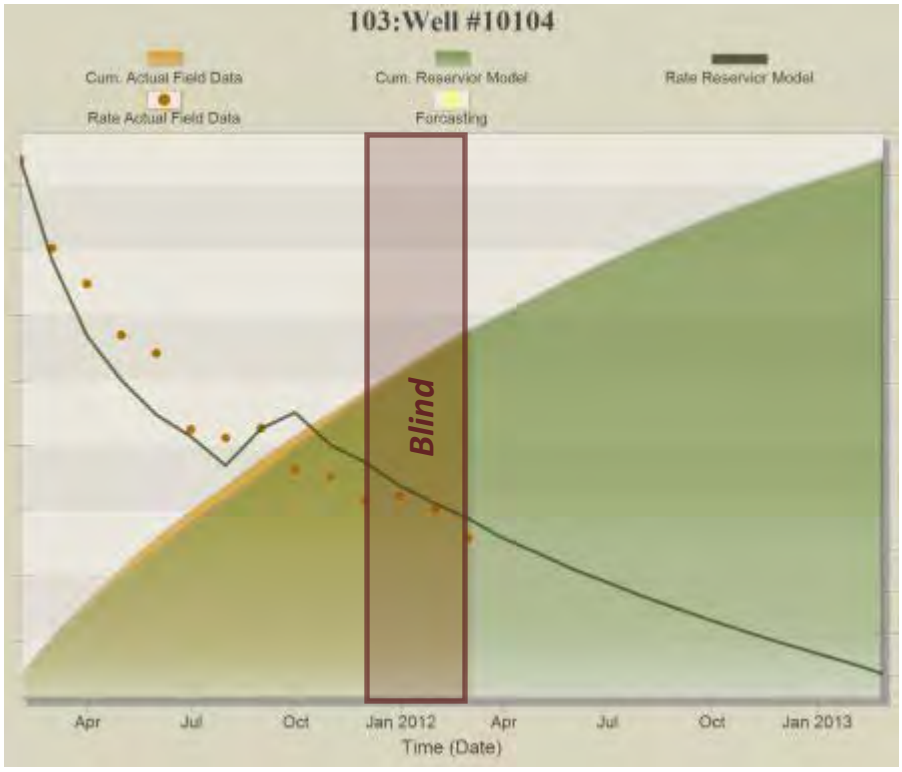

Figure B- 238: Prediction Results for Well#10104

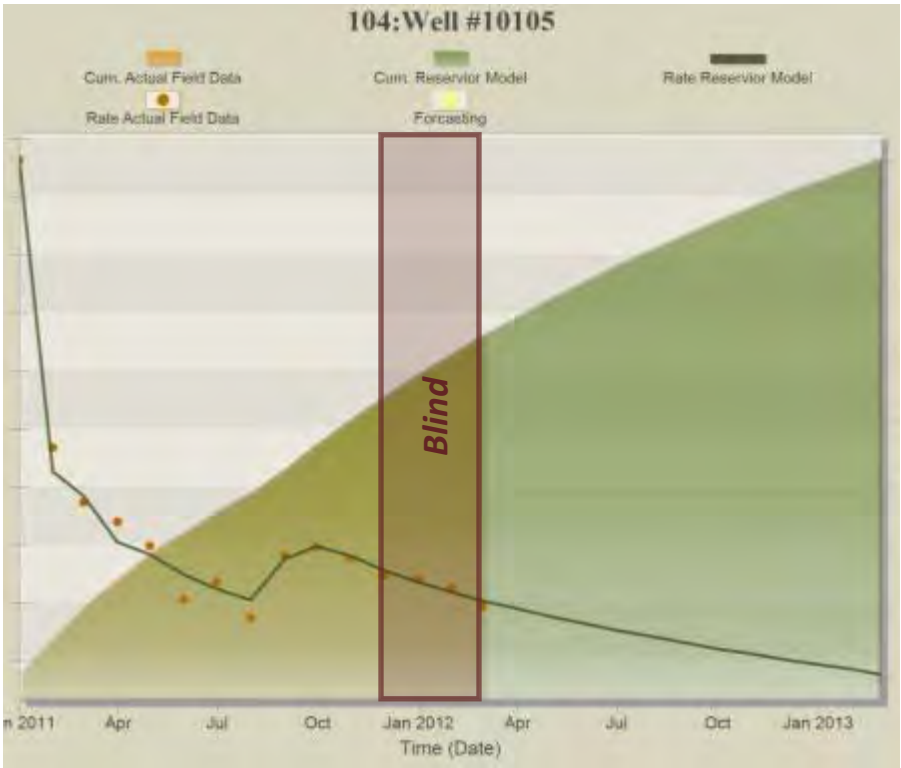

Figure B- 239: Prediction Results for Well#10105

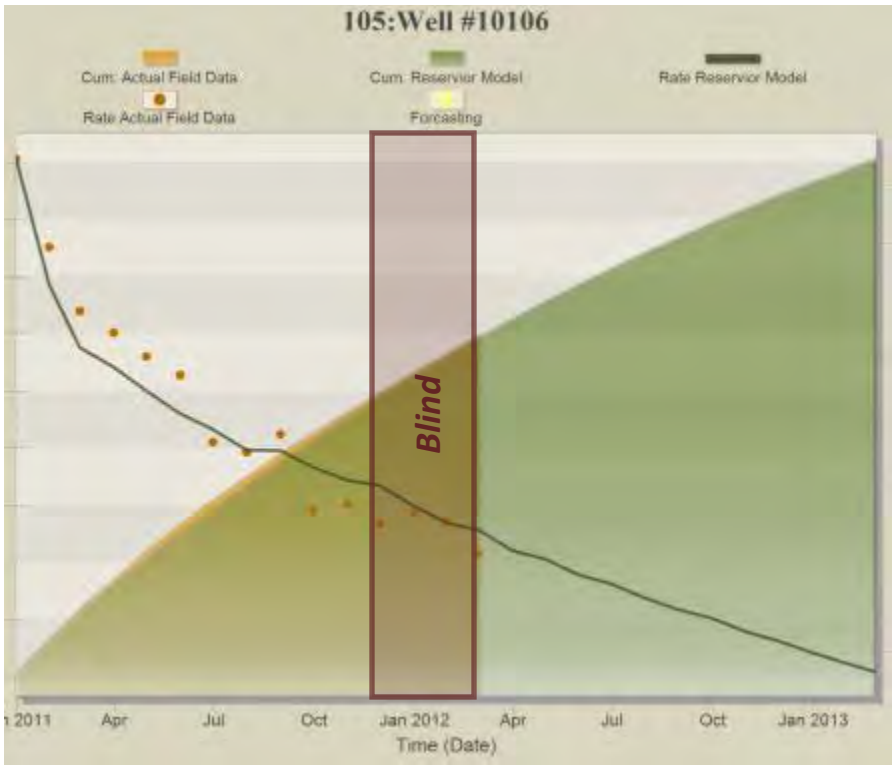

Figure B- 240: Prediction Results for Well#10106

Figure B- 241: Prediction Results for Well#10107

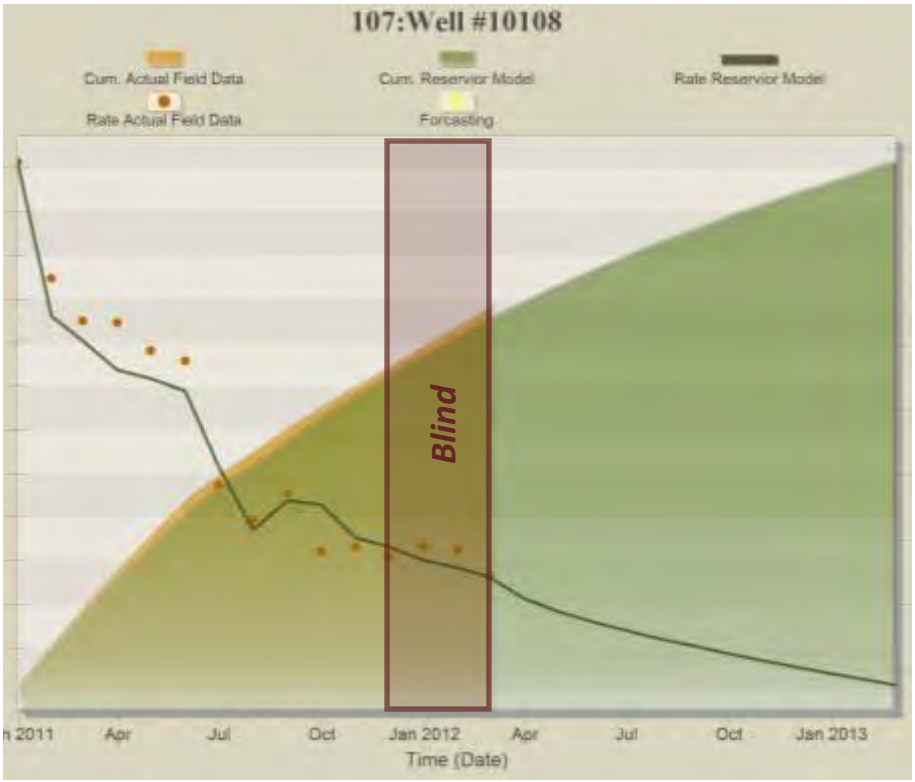

Figure B- 242: Prediction Results for Well#10108

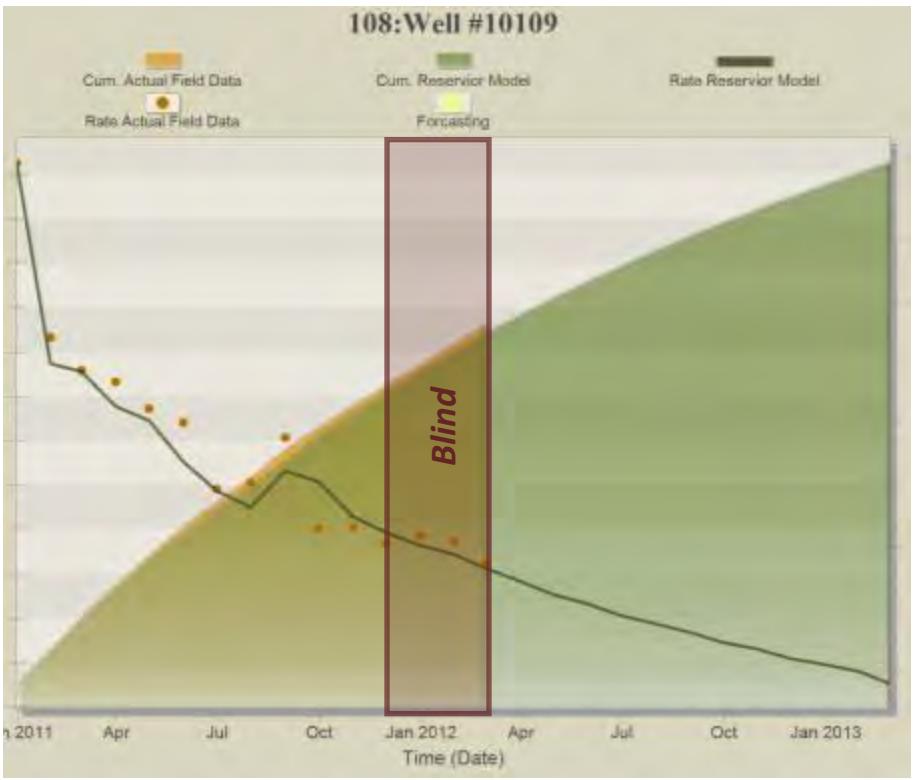

Figure B- 243: Prediction Results for Well#10109

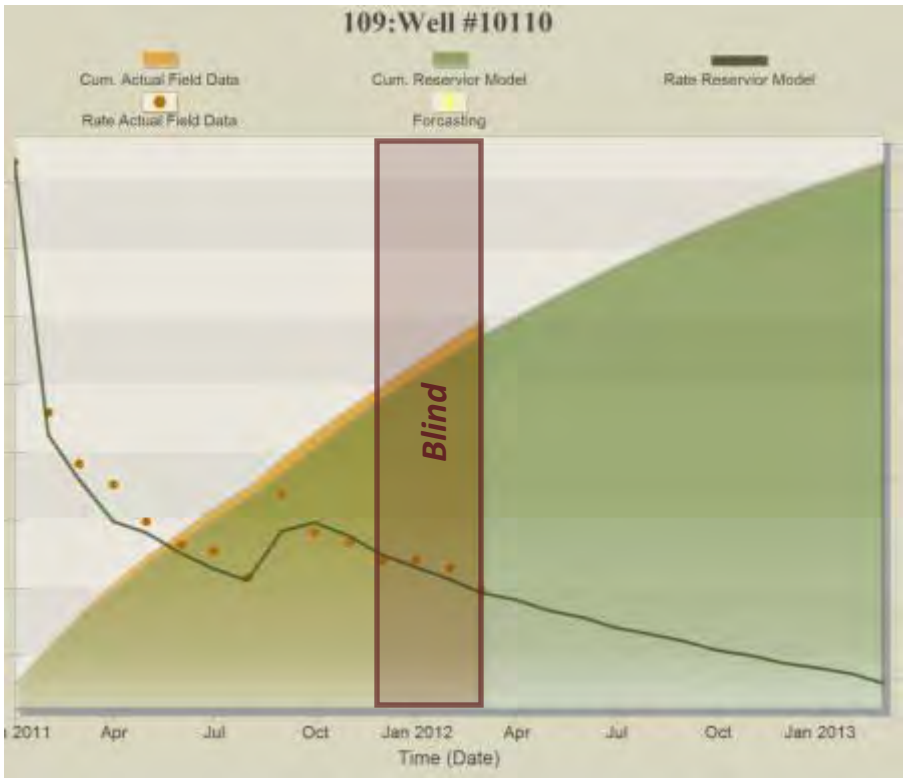

Figure B- 244: Prediction Results for Well#10110

Figure B- 245: Prediction Results for Well#10111

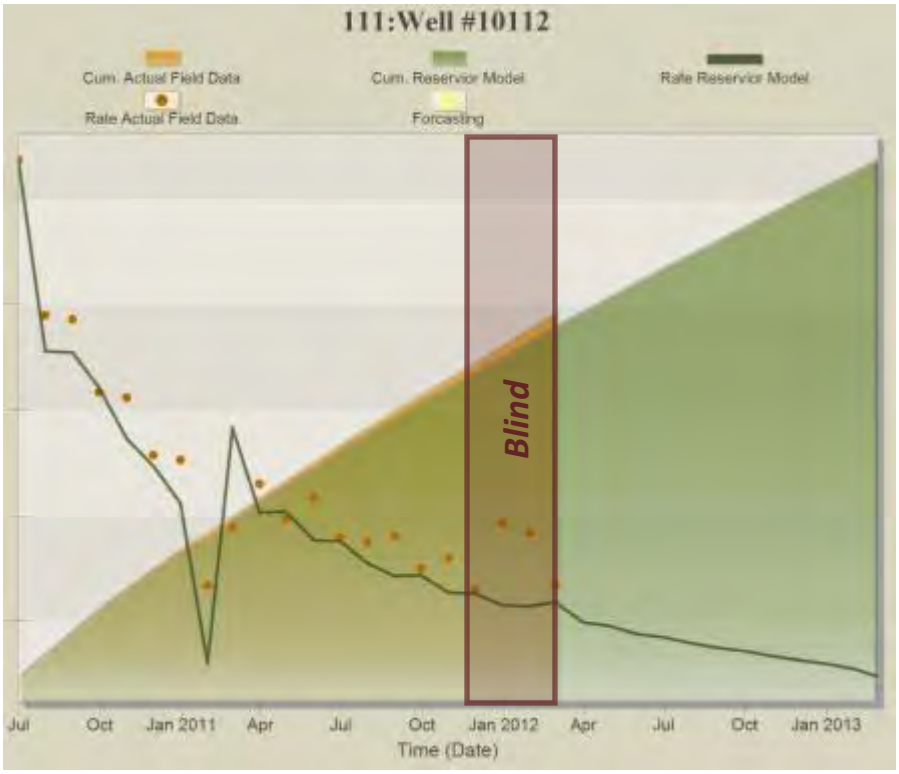

Figure B- 246: Prediction Results for Well#10112

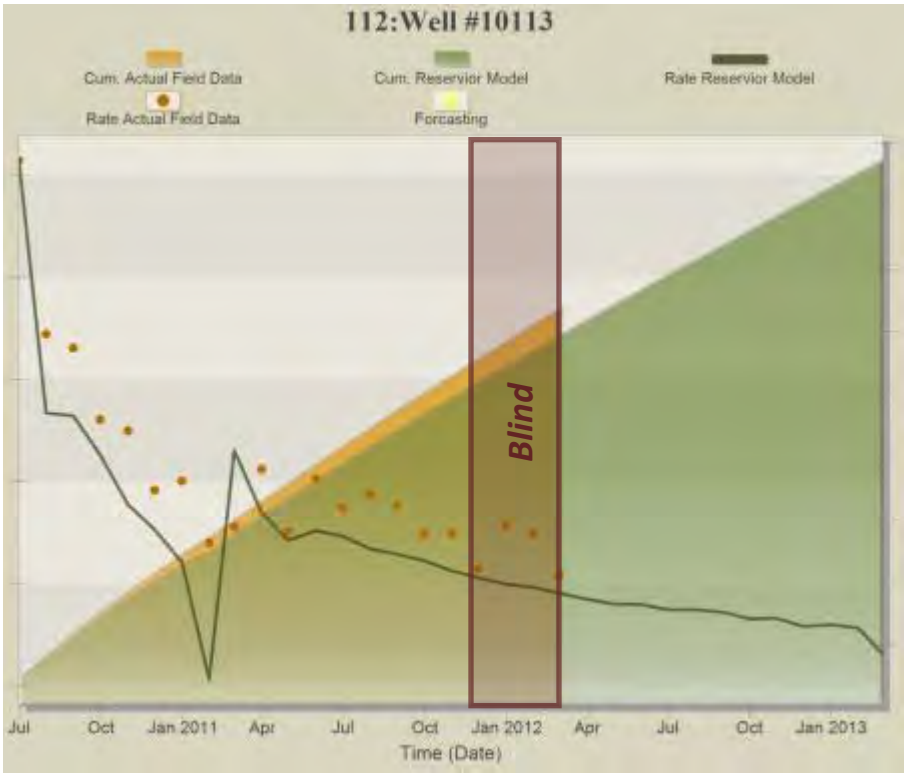

Figure B- 247: Prediction Results for Well#10113

Figure B- 248: Prediction Results for Well#10114

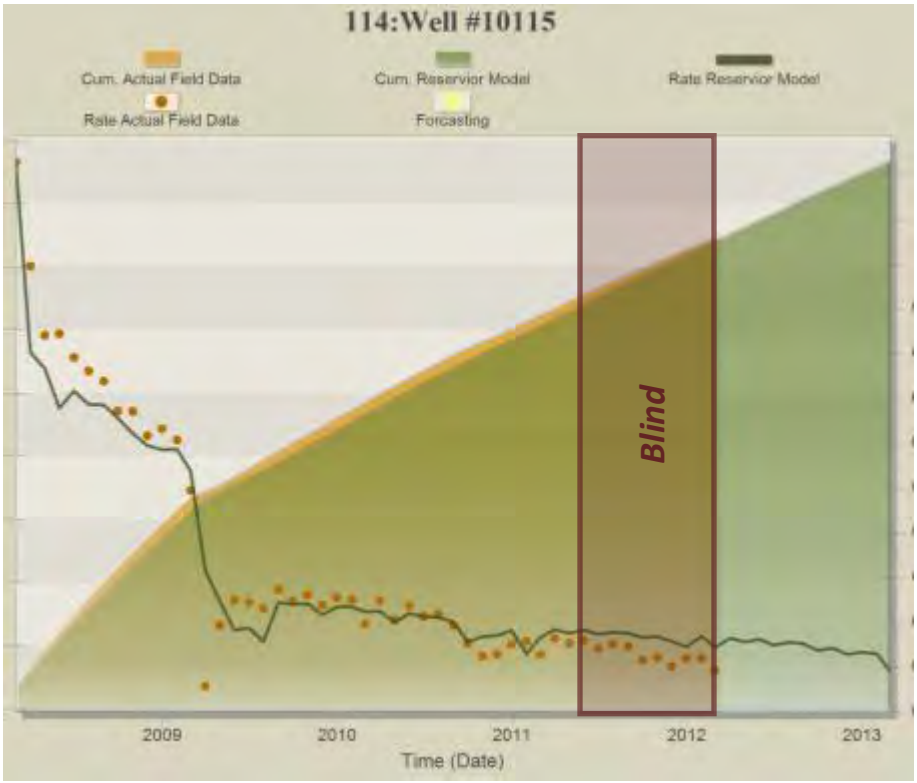

Figure B- 249: Prediction Results for Well#10115

Figure B- 250: Prediction Results for Well#10116

Figure B- 251: Prediction Results for Well#10117

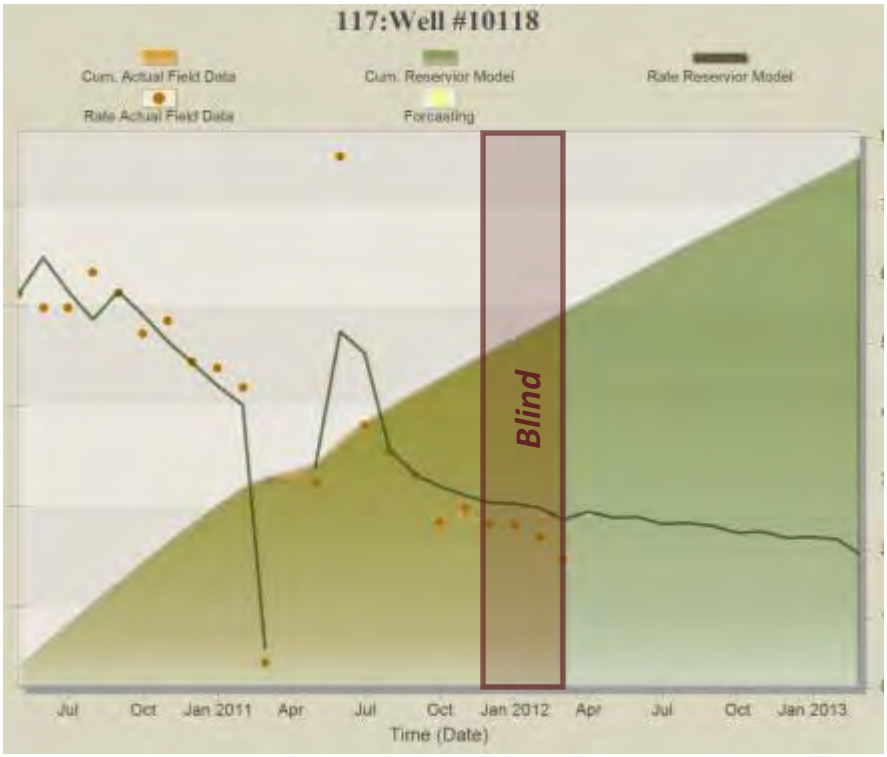

Figure B- 252: Prediction Results for Well#10118

Figure B- 253: Prediction Results for Well#10119

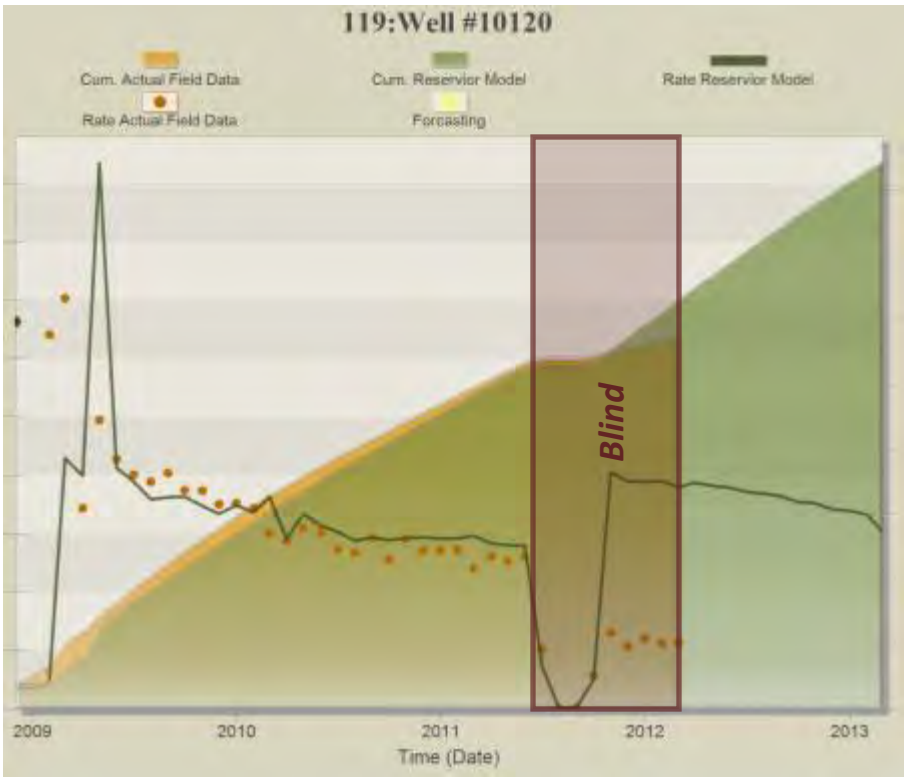

Figure B- 254: Prediction Results for Well#10120

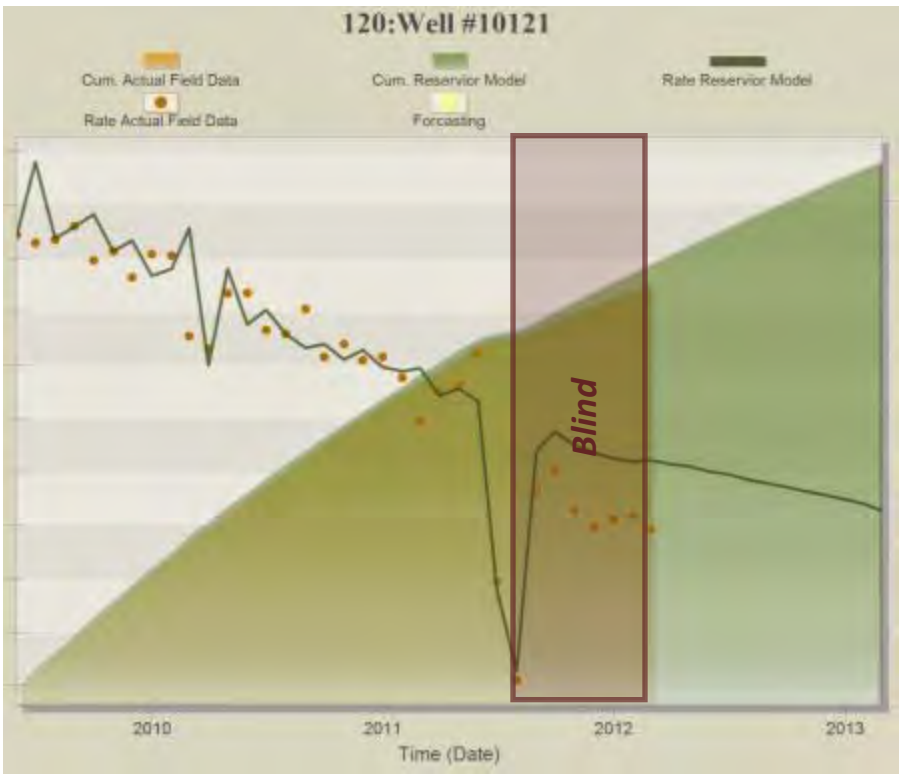

Figure B- 255: Prediction Results for Well#10121

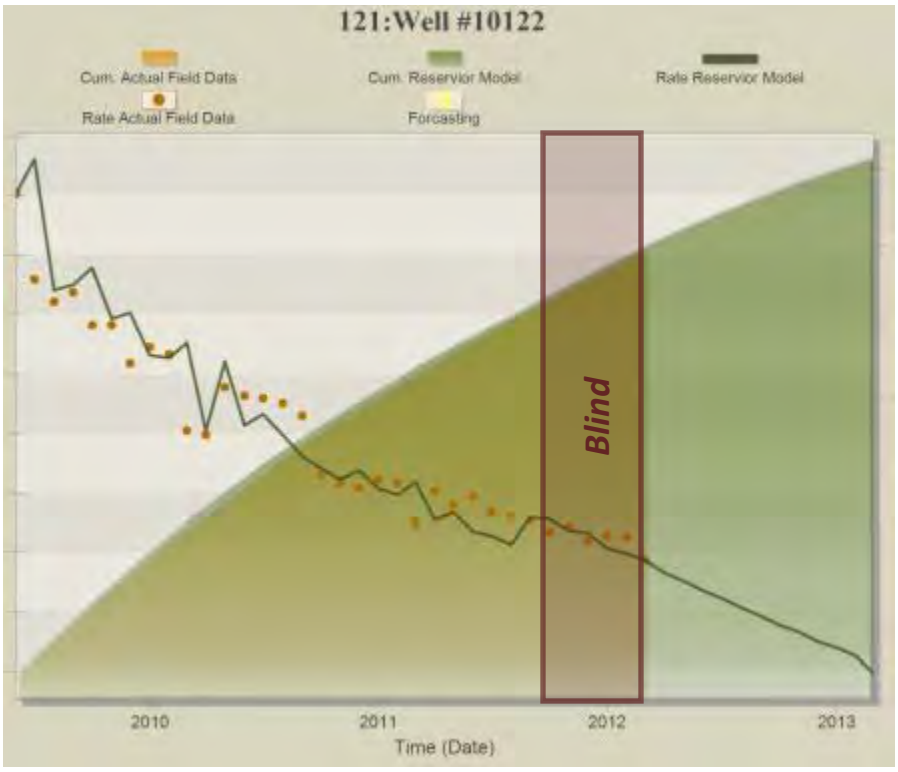

Figure B- 256: Prediction Results for Well#10122

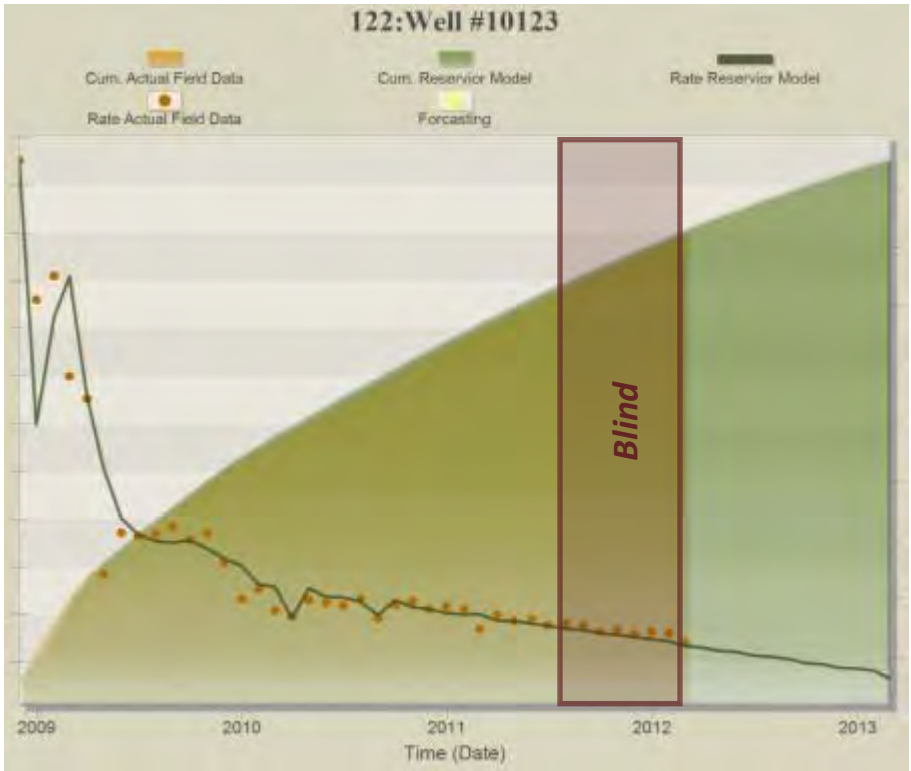

Figure B- 257: Prediction Results for Well#10123

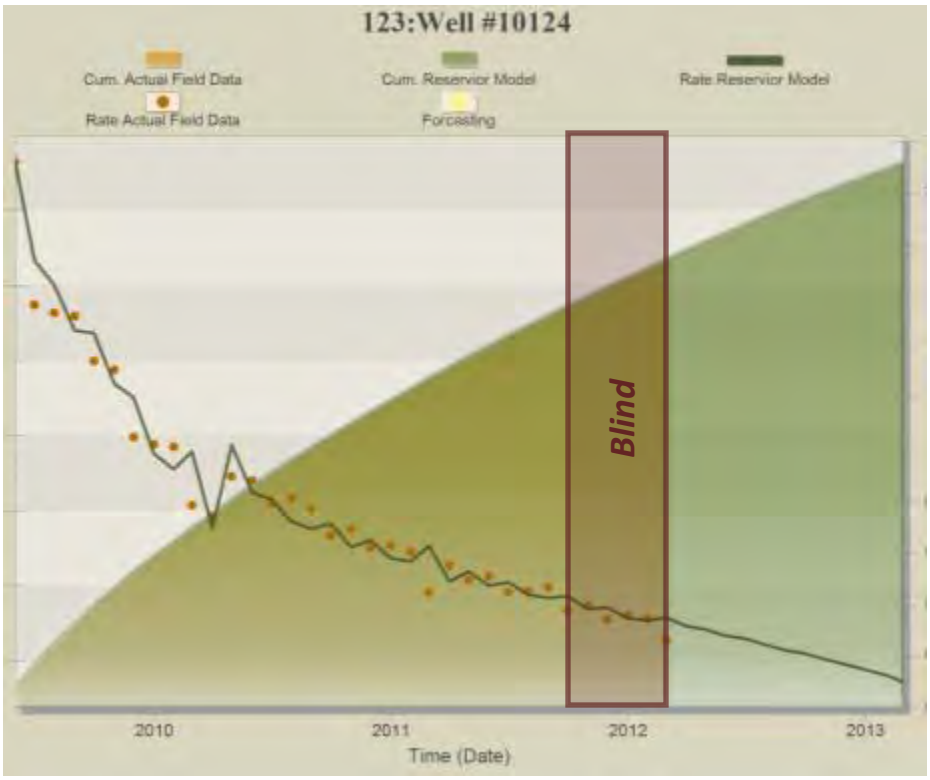

Figure B- 258: Prediction Results for Well#10124

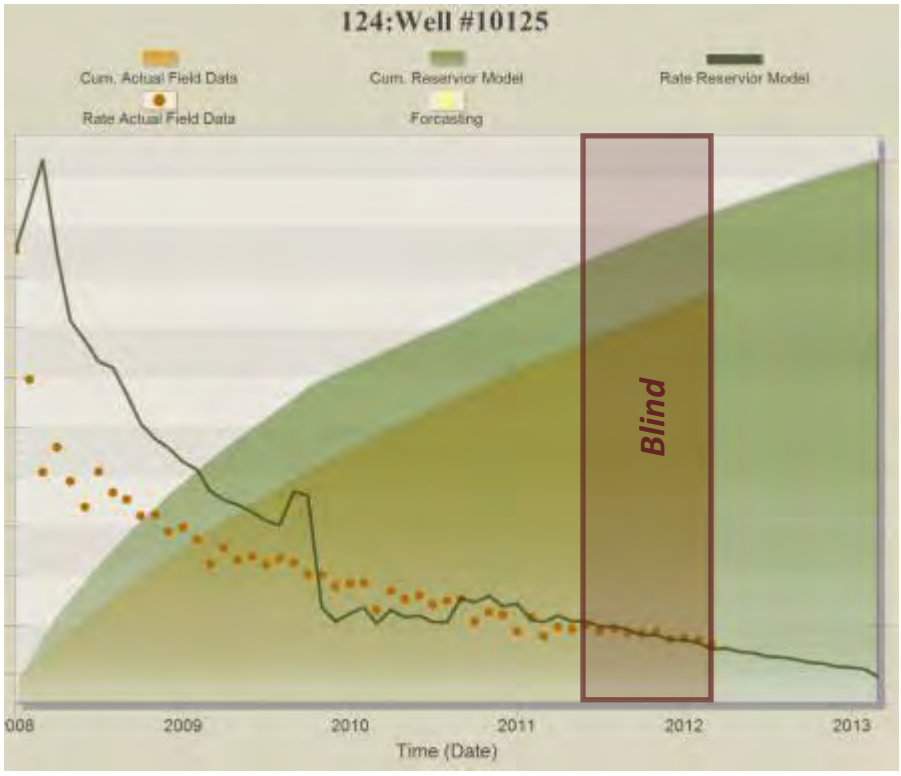

Figure B- 259: Prediction Results for Well#10125

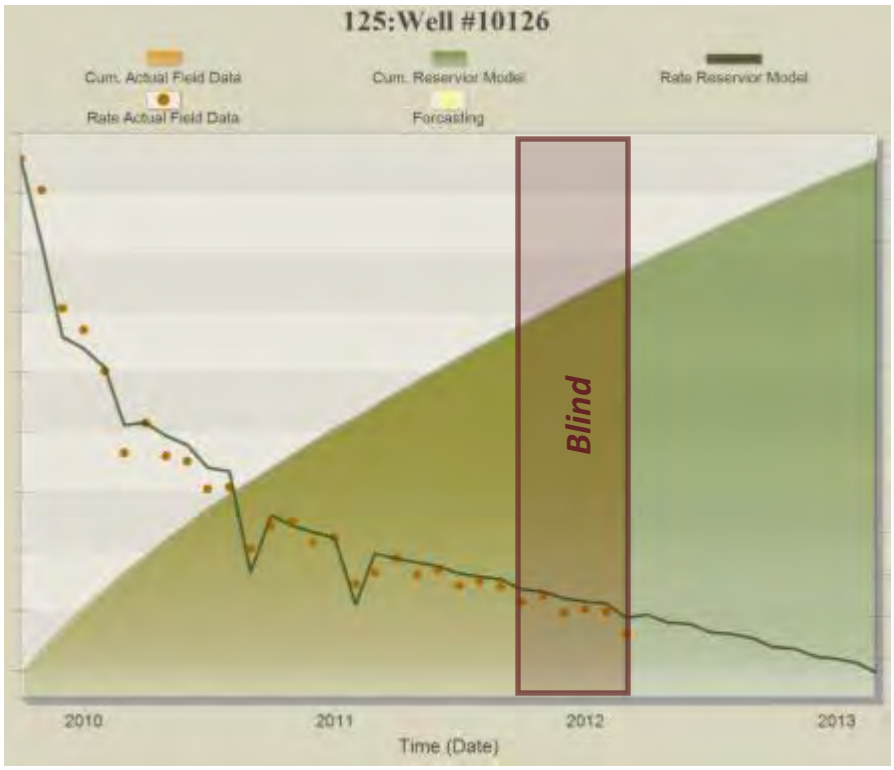

Figure B- 260: Prediction Results for Well#10126

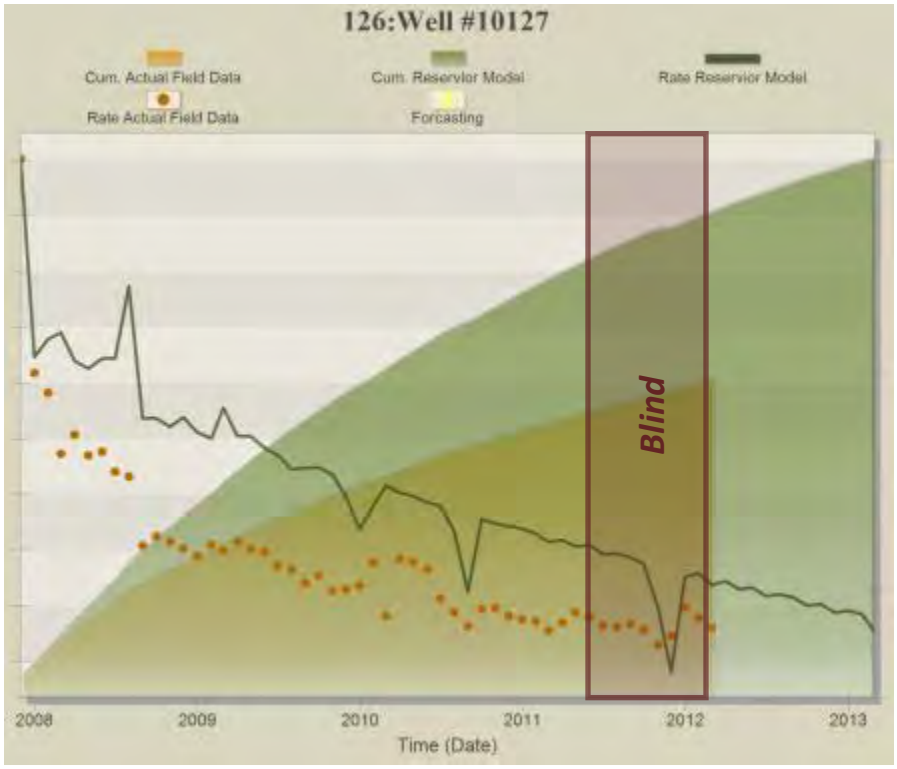

Figure B- 261: Prediction Results for Well#10127

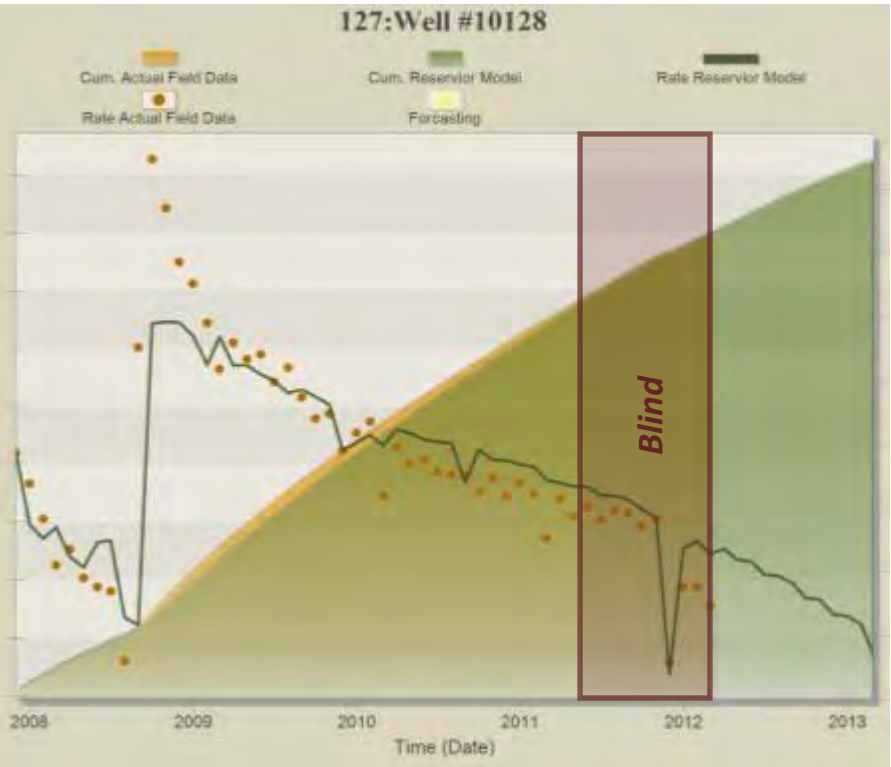

Figure B- 262: Prediction Results for Well#10128

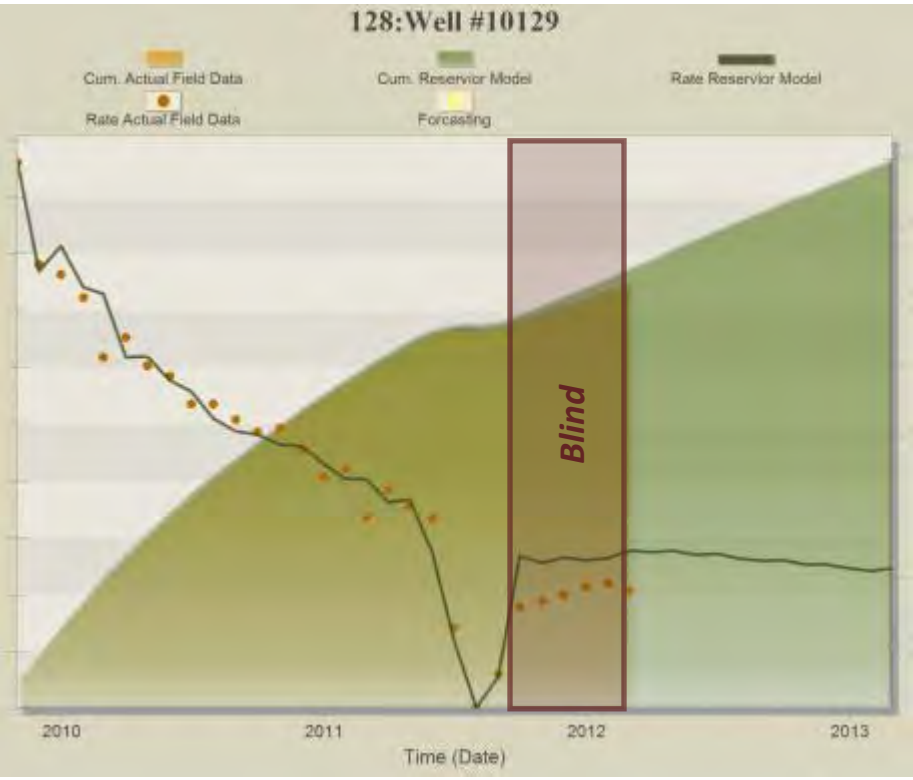

Figure B- 263: Prediction Results for Well#10129

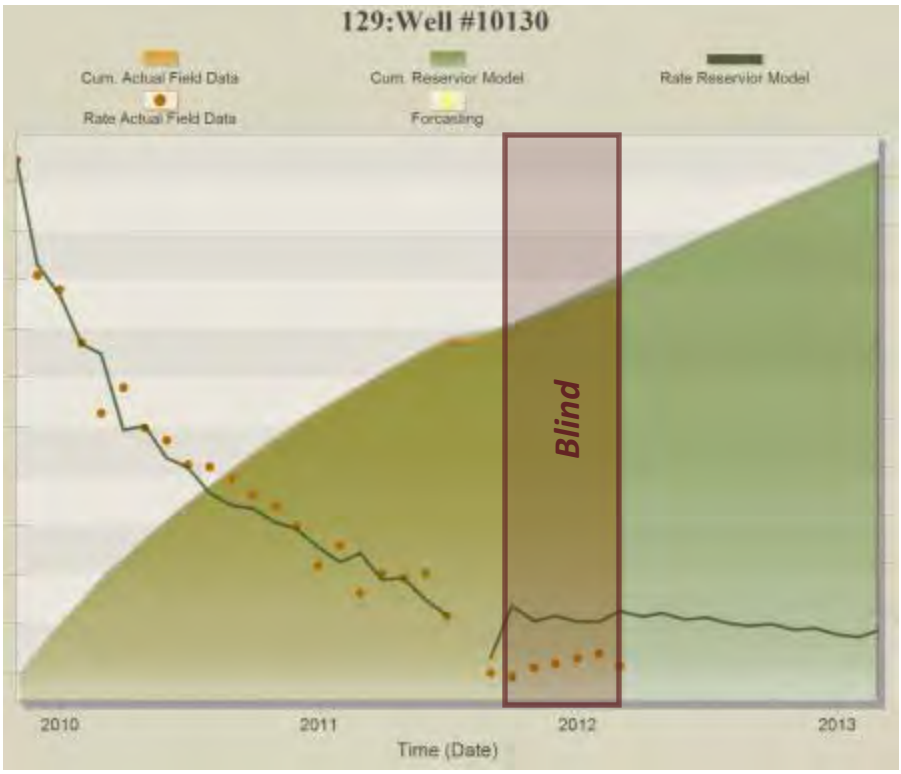

Figure B- 264: Prediction Results for Well#10130

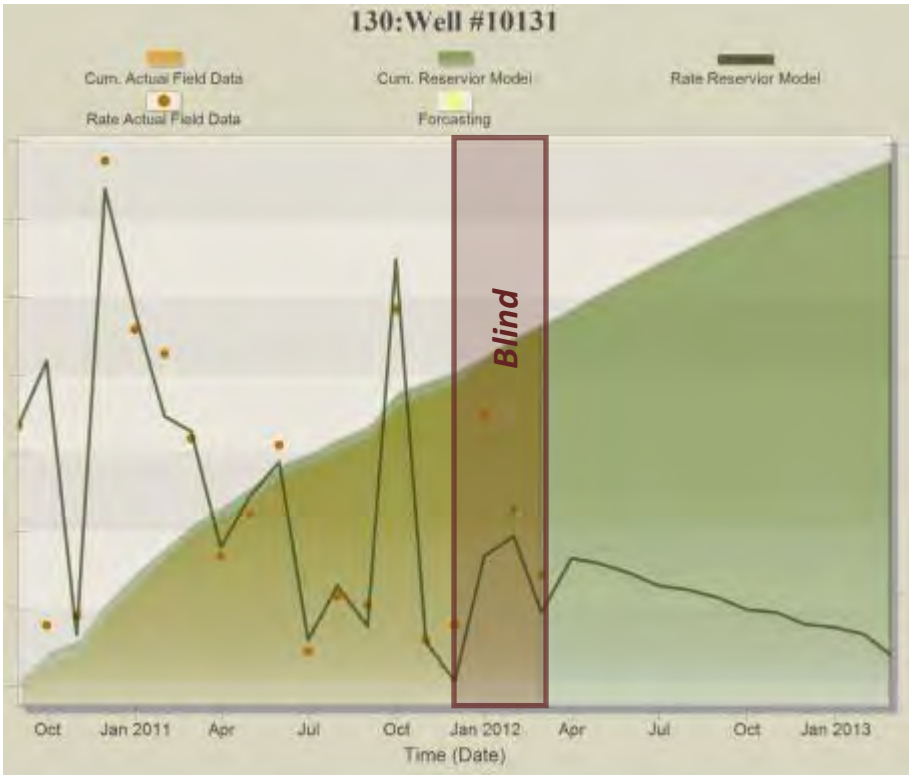

Figure B- 265: Prediction Results for Well#10131

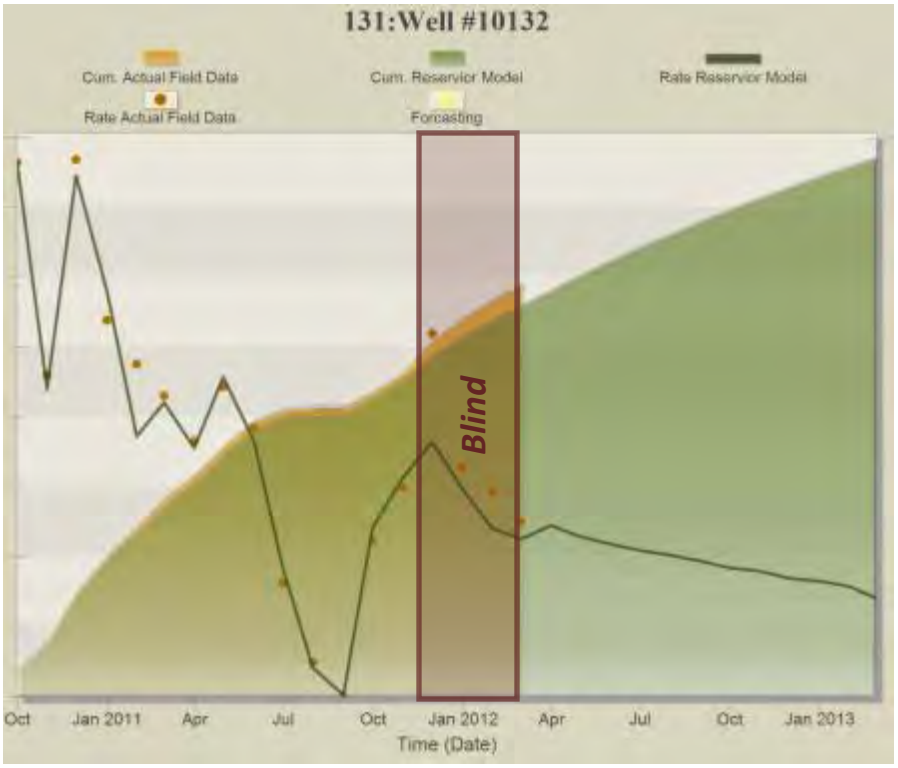

Figure B- 266: Prediction Results for Well#10132

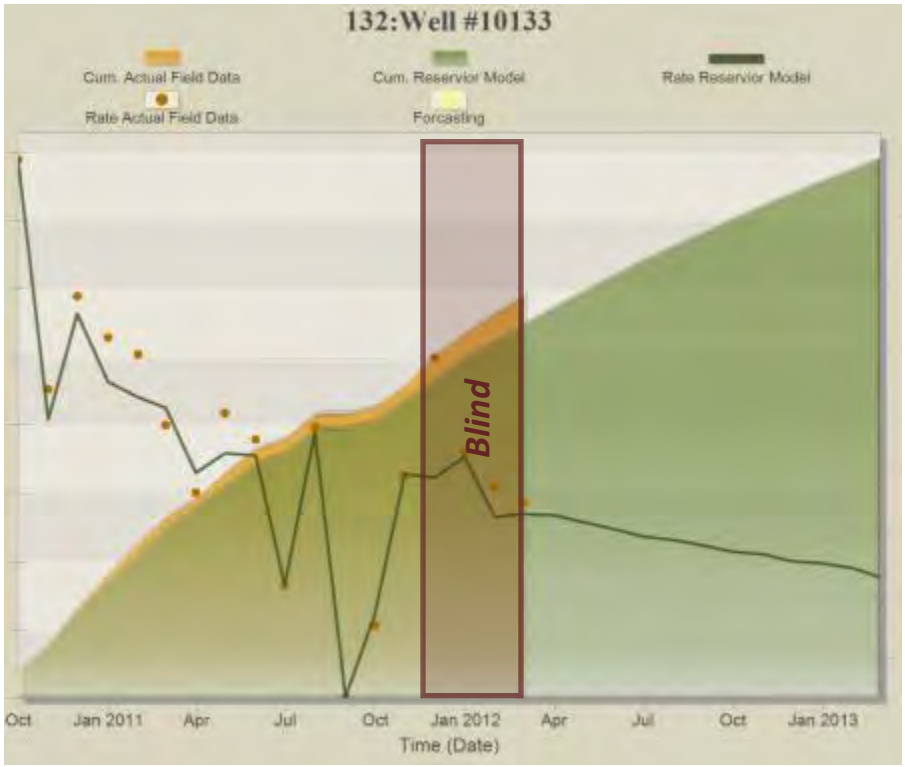

Figure B- 267: Prediction Results for Well#10133

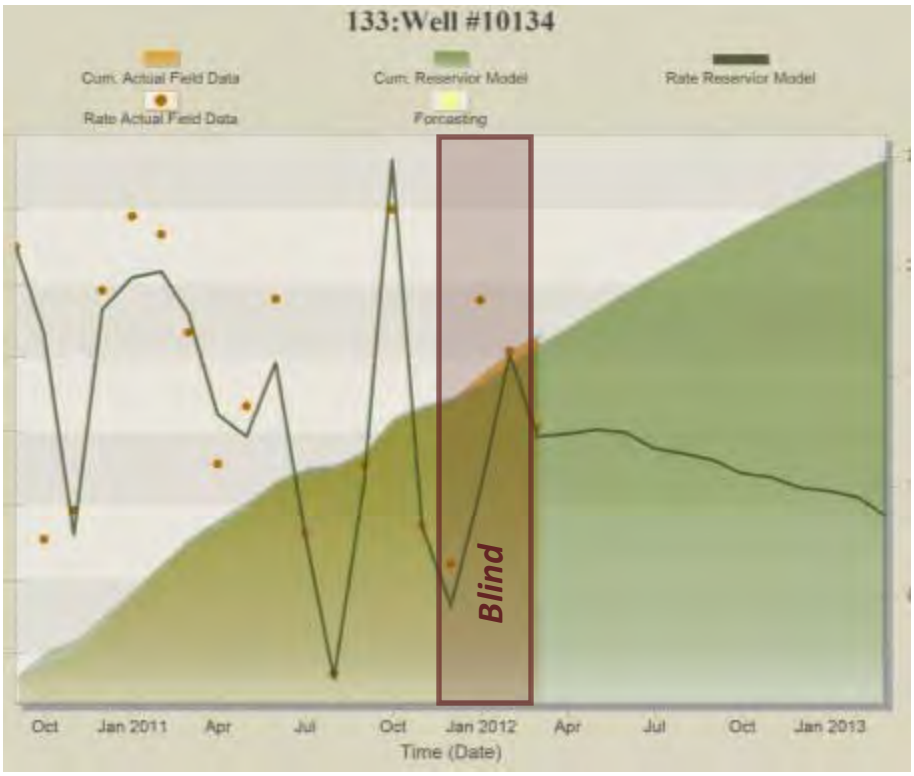

Figure B- 268: Prediction Results for Well#10134

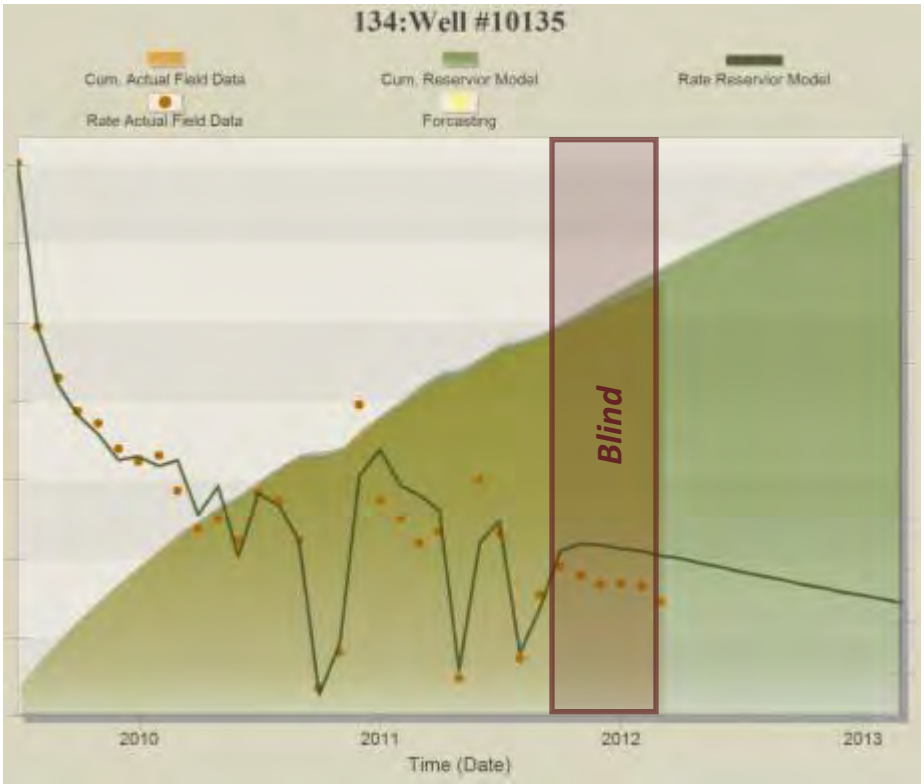

Figure B- 269: Prediction Results for Well#10135

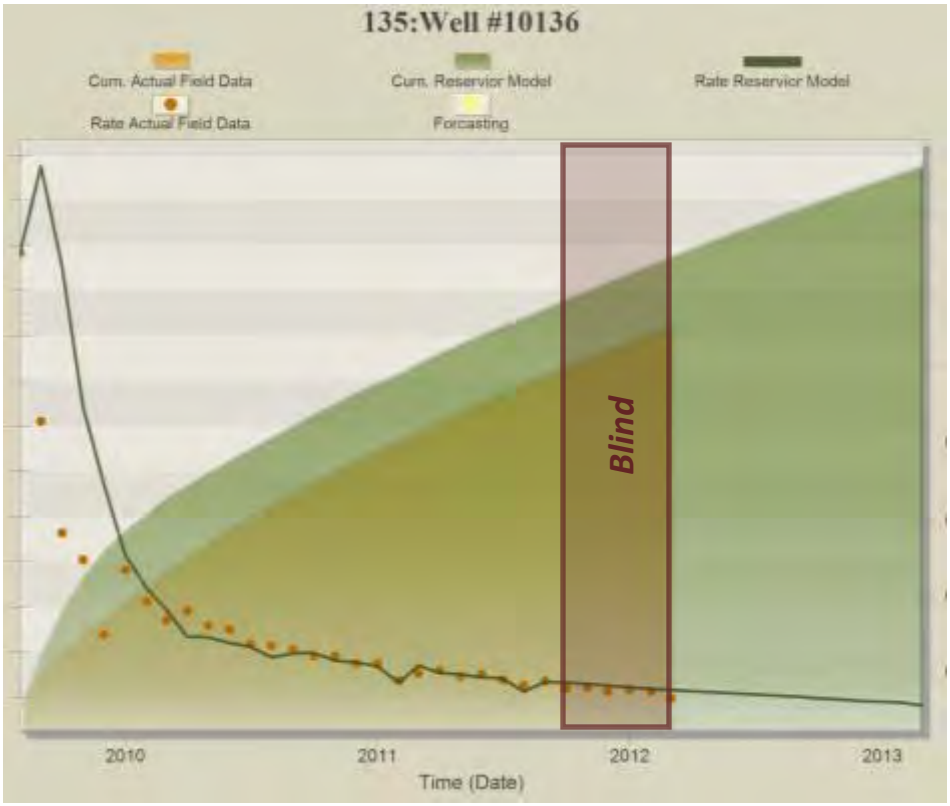

Figure B- 270: Prediction Results for Well#10136